



Dublin City University
Ollscoil Chathair Bhaile Átha Cliath

Electrohydrodynamic Focusing and Light Propagation in 2- Dimensional Microfluidic Devices for Preconcentration of Low Abundance Bioanalytes

by
Tomasz Piasecki, B. Sc.

A thesis submitted for the degree of
Doctor of Philosophy

School of Mechanical and Manufacturing Engineering
Faculty of Engineering and Computing
Dublin City University

Supervisor: Dr Dermot Brabazon (DCU, Dublin, Ireland)
External Supervisors: Prof Mirek Macka (UTAS, Hobart, Australia)
and Prof Brett Paull (UTAS, Hobart, Australia)

September 2011

I hereby certify that this material, which I now submit for assessment on the programme of study leading to the award of Doctor of Philosophy is entirely my own work, that I have exercised reasonable care to ensure that the work is original, and does not to the best of my knowledge breach any law of copyright, and has not been taken from the work of others save and to the extent that such work has been cited and acknowledged within the text of my work.

Signed: Tomasz Piasecki

ID No.: 57127140

Date: September 2011

Dedication

I dedicate this thesis to my wife Jusitne for constant support and help even in the most difficult moments and to my parents for all their efforts and that allowed me for better understanding the world and arriving to this moment.

Acknowledgements

I would like to express my greatest thanks to my supervisor Dr Dermot Brabazon, School of Mechanical Engineering and Manufacturing, Dublin City University, for his guidance, hard work, support and efforts, allowing me to finish this thesis. I would like to thank my co-supervisors Prof Brett Paull and Prof Mirek Macka, School of Chemical Sciences, University of Tasmania, for help encouragement and valuable suggestions during my research.

I would like to thank School of Mechanical Engineering and Manufacturing of Dublin City University, Irish Separation Science Cluster and Science Foundation Ireland for financial support of my research.

I would like to express my heartiest gratitude for Prof Cornelius F. Ivory, Washington State University for his personal help and hospitality provided during my visit in Pullman for learning computer modelling.

I would like to thank Prof Bohuslav Gas and Dr Viliam Kolivoska, department of Physical and Macromolecular Chemistry, Charles University in Prague for their time, help and hospitality during my stay in Prague for learning of the electromigration processes.

I would like to thank Dr Silvja Abele for her help and time, when I was starting my PhD studies at DCU.

I would like to express my thanks to all lecturers, technicians, and other students from School of Chemical Sciences and School of Mechanical Engineering and Manufacturing for their assistance, friendship, support and constant encouragement.

Table of contents

Dedication	III
Acknowledgements.....	IV
Table of contents	V
List of figures.....	XI
List of tables	XXI
Publications from this work	XXIII
Abbreviations.....	XXV
Nomenclature	XXVII
Abstract.....	XXIX
Chapter 1 – Introduction.....	1
1.1. Electrohydrodynamic focusing as an alternative for the sample pre-concentration.....	1
1.2. Research questions and hypotheses	3
1.3. Project aims and adopted methodology	4
1.4. Gap in the literature filled by this work.....	7
1.5. Merits and limitations of the study	9
1.6. Scope of the thesis	9
Chapter 2 – Literature review	11
2.1. MEMS and Microfluidics.....	11
2.1.1. Overview and brief history of microfluidics.....	11
2.1.2. Fabrication methods.....	12
2.1.3. Micro Total Analysis Systems (μ -TAS).....	13
2.1.4. Physics of microfluidics	14
2.1.5. Benefits and limitations of microfluidics	19
2.1.6. Technologies of microfluidic devices	20
2.1.7. Applications of microfluidic devices	21
2.2. Focusing.....	22
2.2.1. Overview of different focusing methods.....	22
2.2.2. Isocratic separations.....	25
2.2.3. Isotachic separations	25
2.2.4. Non-equilibrium gradient methods (NEGM)	26
2.2.5. Equilibrium gradient methods (EGM).....	27
2.3. Modelling.....	29
2.3.1. Modelling of fluid dynamics	29

2.3.2.	Computational Fluid Dynamics (CFD)	30
2.3.3.	Independently developed modelling software.....	32
2.3.4.	COMSOL Multiphysics software	32
2.4.	Illumination for visualisation – choice of Solid State Light (SSL) sources.....	33
2.4.1.	Light sources in chemistry	33
2.4.2.	Advantages and limitations of LEDs.....	34
2.5.	Detection and data acquisition	39
2.5.1.	LEDs in photometric detection	40
2.5.2.	LEDs in fluorometric detection	42
2.6.	Electro-hydrodynamic focusing (EHDF) as a development of EGM methods.....	44
2.7.	Conclusions from the literature review.....	45
Chapter 3 – Materials, methods and procedures.....		47
3.1.	Numerical modelling of microfluidic systems	47
3.1.1.	Computers used.....	47
3.1.2.	Software used and model procedure development.....	48
3.1.2.1.	Model design	48
3.1.2.2.	Subdomain definitions	49
3.1.2.3.	Boundary definitions	51
3.1.2.4.	Meshing	52
3.1.2.5.	Solving	54
3.1.2.6.	Postprocessing and result visualisation	54
3.1.3.	Model setups	54
3.1.3.1.	Analysis of the mesh density impact on a simulation results	55
3.1.3.2.	1 st Navier-Stokes flow with convection and diffusion in a multi-outlet chip	56
3.1.3.3.	2 nd Navier-Stokes flow with convection and diffusion in a multi-outlet chip	57
3.1.3.4.	The mesh type assessment: comparison of triangular and quadrangle meshes	58
3.1.3.5.	Modelling of the Conductivity Gradient Focusing	59
3.1.3.6.	Investigation of the multi-outlet chip properties	60
3.1.3.7.	Development of an optimal chip for the EHDF	62
3.1.3.8.	Models incorporating pressure-drive flow and electromigration with the selected chip layout	65
3.1.3.9.	The first model of EHDF	66
3.1.3.10.	The second model for EHDF	67
3.2.	Experiments with microfluidic systems.....	67
3.2.1.	Instrumentation.....	67

3.2.1.1.	Microfluidic chips	67
3.2.1.2.	Pumps used	69
3.2.1.3.	High voltage source	69
3.2.1.4.	HPLC tubing, fittings and connectors	69
3.2.1.5.	Optical detection equipment	69
3.2.1.6.	Microscopes	69
3.2.1.7.	Camera	70
3.2.1.8.	Power supply unit	70
3.2.1.9.	Computer used in microfluidic experiments	70
3.2.1.10.	Other equipment	70
3.2.2.	Materials (chemicals and consumables).....	71
3.2.3.	Description of the general experimental setup.....	71
3.2.4.	Procedure of the concentration and its error calculation using digital photos...	72
3.2.5.	Absorbance measurements in the chip.....	76
3.2.6.	Individual conditions for experiments on EHD focusing in microfluidic chip.....	78
3.2.6.1.	Problems observed during the initial stage of experiments	79
3.2.6.2.	Experiment 2P-14	81
3.2.6.3.	Experiment 2P-22	81
3.2.6.4.	Experiment 2P-30	82
3.2.6.5.	Experiment 2P-47	82
3.2.6.6.	Experiment 2L-15	82
3.2.6.7.	Experiment 2L-16	83
3.2.6.8.	Experiment 2L-17	83
3.2.6.9.	Experiment 2L-26	84
3.2.6.10.	Experiment 2L-40	84
3.2.6.11.	Experiment 2L-41	85
3.2.6.12.	Experiment 3T-20	85
3.2.6.13.	Experiment 3T-21	86
3.2.6.14.	Experiment 3T-24	86
3.2.6.15.	Experiment 3T-31	87
3.2.6.16.	Experiment 3T-36	87
3.2.6.17.	Experiment 3T-43	88
3.2.6.18.	Experiment 3T-58	88
3.2.6.19.	Reproducibility of the EHDF	89
3.3.	Modelling and experiments of the light propagation in microfluidic systems	89
3.3.1.	Software used	89

3.3.2.	Materials and chemicals used in experiments on light propagation.....	90
3.3.3.	Materials and chemicals used in experiment with photopolymerisation of monoliths in capillaries	90
3.3.4.	Procedure of development of the light propagation model	91
3.3.5.	Light propagation model verification procedure.....	95
3.3.6.	Procedure of obtaining monoliths by photopolymerisation in capillaries for observation of light propagation changes.....	97
3.4.	Summary of experimental approach.....	97
Chapter 4 –	Modelling of microfluidic systems: results and discussion	99
4.1.	Analysis of mesh density impact on simulation results.....	99
4.2.	1 st Navier-Stokes flow with convection and diffusion in multi-outlet chip	105
4.3.	2 nd Navier-Stokes flow with convection and diffusion in a multi-outlet chip	107
4.4.	The mesh type assessment: comparison of triangular and quadrangle meshes	108
4.5.	Modelling of the Conductivity Gradient Focusing.....	112
4.6.	Investigation of the multi-outlet chip properties.....	117
4.7.	The development of an optimal chip for the EHDF.....	125
4.8.	Models incorporating pressure-drive flow and electromigration with the selected chip layout	129
4.9.	The first model of EHDF.....	136
4.10.	The second model for EHDF	138
4.11.	Conclusions and the key modelling results	139
Chapter 5 –	Experiments in microfluidic systems: results and discussions	141
5.1.	Description of experiments	141
5.2.	Results of the experiment 2P-14.....	142
5.3.	Results of the experiment 2P-22.....	144
5.4.	Results of the experiment 2P-30.....	146
5.5.	Results of the experiment 2P-47	149
5.6.	Results of the experiment 2L-15	150
5.7.	Results of the experiment 2L-16	152
5.8.	Results of the experiment 2L-17	153
5.9.	Results of the experiment 2L-26	154
5.10.	Results of the experiment 2L-40	157
5.11.	Results of the experiment 2L-41	158
5.12.	Results of the experiment 3T-20.....	160
5.13.	Results of the experiment 3T-21	162
5.14.	Results of the experiment 3T-24	163

5.15. Results of the experiment 3T-31	164
5.16. Results of the experiment 3T-36	166
5.17. Results of the experiment 3T-43	168
5.18. Results of the experiment 3T-58	169
5.19. Repeatability of the EHDF	171
5.20. Comparison of the modelling and experimental results	174
5.21. Proposed mechanism of microdrople electrohydrodynamic focusing	177
5.22. Conclusions from the conducted experiments	180
Chapter 6 – Modelling and experiments for the light propagation: results and discussion	181
6.1. The experimental verification of the developed light propagation model	181
6.1.1. Experimental and model results for first macro-simulation tests (set A).....	181
6.1.2. Experimental and model results for second macro-simulation tests (set B).....	184
6.1.3. Micro-scale experiments and model results for intensity distribution tests	186
6.1.4. Discussion of the developed light propagation model	188
6.1.5. Conclusions from the model verification.....	189
6.2. Growth of the monolithic polymers in photoinitiated polymerisation in non-illuminated region	190
6.2.1. Results of the monoliths growth	190
6.2.2. Discussion of the results	191
6.2.3. Conclusions from the monolith photopolymerisation	198
Chapter 7 – Conclusions.....	200
7.1. Conclusions form the scientific work	200
7.1.1. Testing of the hypotheses.....	203
7.2. Future work	205
References	207
Appendix A – Brief history of computers.....	i
Appendix B – Description of different methods used in CFD	iv
8.1. Finite Difference Method (FDM)	iv
8.2. The Finite Volume Method (FVM).....	iv
8.3. The Finite Elements Method (FEM).....	iv
8.4. Other methods	v
Appendix C – Brief history of Solid State Lighting.....	vi
Appendix D – Physical principles of LEDs.....	viii
Appendix E – Experiments on real time visualisation of fluorescent dye in a microfluidic chip .	xv
Appendix F – Mesh structures and convergence graphs.....	xx
Appendix G – Technical drawings for the microfluidic chip for EHDF	xxv

Appendix H – Mesh parameters used for comparison of mesh typesxxxiii
Appendix I – Photos of all presented microfluidic experiments.....xxxix

List of figures

FIGURE 1: A SIMPLIFIED DIAGRAM SHOWING THE GENERAL PRINCIPLE OF ELECTRO-HYDRODYNAMIC FOCUSING (EHDF), BLUE ARROWS REPRESENT VECTORS OF HYDRODYNAMIC FORCES F_H (IMPOSED BY PRESSURE-DRIVEN FLOW), RED ARROWS REPRESENT VECTORS OF ELECTROMAGNETIC FORCES F_E (IMPOSED BY APPLIED ELECTIC FIELD) AND GREEN ARROWS REPRESENT THE VECTOR SUMMATION OF BOTH. PURPLE AREA SHOWS WHERE THE EHDF TAKES PLACE.	1
FIGURE 2: SCHEMATIC ILLUSTRATION OF MICROFLUIDIC DEVICE FOR ELECTRO-HYDRODYNAMIC FOCUSING.	4
FIGURE 3: A SCHEMAT OF MICROFLUIDIC CHIP USED FOR GENERATING CONDUCTIVITY GRADIENT FOCUSING, AFTER (8).	7
FIGURE 4: PICTURES OF FLOW PATTERNS ACHIEVED USING PRESSURE-DRIVEN FLOW IN MICROFLUIDIC CHIP (15).	8
FIGURE 5: LAMINAR FLOW BUILD-UP AND SIMPLIFIED TIME EVOLUTION OF VELOCITY DISTRIBUTION AS FUNCTION OF THE DISTANCE FROM THE WALL (AFTER (41)).	15
FIGURE 6: GRAPH OF LENNARD-JONES POTENTIAL $V(E)$ VERSUS DISTANCE $rm = 216\sigma$, WHERE E IS MAXIMAL ATTRACTION ENERGY AND σ IS CHARACTERISTIC MOLECULE DIAMETER (43).	16
FIGURE 7: A SCHEMAT SHOWING THE PRINCIPLE OF MEMBRANELESS H-FILTER. FOR A SPECIFIC LENGTH l , ONLY THE TARGET ANALYTE (BLUE) WITH APPROPRIATE DIFFUSIVITY WILL MERGE INTO THE OTHER STREAM, WHILE IMPURITIES (RED DOTS) WILL BE WASHED AWAY (44).	18
FIGURE 8: MINIATURISATION OF FLUIDIC SYSTEMS ALLOWING FOR MULTIPLE PROCESSES AND SAMPLE DETECTION IN BIOLOGICAL AND CHEMICAL APPLICATIONS (39).	20
FIGURE 9: DIAGRAM OF ISOCRATIC SEPARATION (PEAKS NOT TO SCALE), AFTER (118).	25
FIGURE 10: DIAGRAM SHOWING FORMATION OF SEPARATE ZONES DURING ISOTACHOPHORESIS, AFTER (118).	26
FIGURE 11: SCHEMATIC OF FORMATION OF SEPARATE PEAKS IN NON-EQUILIBRIUM GRADIENT METHOD. AS IT IS SHOWN GRADIENT TRAVELS TOGETHER SAMPLE ALONG SEPARATION CHANNEL, AFTER (118).	27
FIGURE 12: SCHEMATIC OF PEAK FORMATION AROUND FOCAL POINT BY NET FORCE (RED) AS A SUM OF EXTERNAL FORCE GRADIENT (BLUE) AND DIFFUSION FORCE (GREEN). PEAK SHAPE COLOURED WITH GREY, AFTER (123).	28
FIGURE 13: CROSS-SECTION OF EFGF FOCUSING UNIT SHOWING CURRENT LINES (A) AND FLOW LINES (B), (127).	29
FIGURE 14: NUMBER OF PUBLICATIONS AND PATENTS FOR LEDs FROM 1960 TILL 2008. SEARCH CONDITIONS: SCI FINDER SCHOLAR DATABASE (APR 2011), SEARCH TOPIC "LIGHT EMITTING DIODES".	34
FIGURE 15: COMPARISON OF SIGNAL STABILITY FOR DEUTERIUM LAMP (PINK) AND LED (BLUE). SIGNAL COMING FROM TRADITIONAL LIGHT SOURCE (PINK) HAS SIGNIFICANTLY LARGER FLUCTUATIONS OF INTENSITY COMPARED TO SOLID STATE LIGHT SOURCE (184).	37
FIGURE 16: EXAMPLE OF THE MEASURED SPECTRUM OF RGB-TYPE WHITE LED (THREE DIFFERENT DIODE CHIPS RED, GREEN AND BLUE IN ONE CASING.	38
FIGURE 17: EMISSION SPECTRA OF WHITE 'BLUE + PHOSPHORUS' LEDs: 3 DIFFERENT LEDs OF VARYING LIGHT TEMPERATURE: BLUE LINE – COLD WHITE; GREEN – NEUTRAL WHITE; RED – WARM WHITE, CCT – CORRELATED COLOUR TEMPERATURE (195).	39
FIGURE 18: SCHEMATIC OF LIGHT INTENSITY WITH SAMPLE LOCATED FOR PHOTOMETRIC DETECTION (199).	40

FIGURE 19: ILLUSTRATION OF FRANCK-CONDON PRINCIPLE. BLUE ARROWS REPRESENTS LIGHT ABSORPTION, GREEN ARROWS REPRESENTS LIGHT EMISSION PEAK HEIGHT REPRESENTS TRANSITION INTENSITY. TRANSITIONS WITHIN E_1 STATES ARE NOT MARKED (237).	43
FIGURE 20: JABLONSKI DIAGRAM SHOWING THE MOST IMPORTANT TRANSITION TYPES WITHIN ILLUMINATED FLUOROPHORE (238).	43
FIGURE 21: PHOTO OF A MICROFLUIDIC CHIP WITH REGION OF PRECONCENTRATED MALACHITE GREEN USING FIELD GRADIENT FOCUSING (253).	45
FIGURE 22: COMSOL DRAWING INTERFACE WITH TYPICAL DRAWING OF THE EHD FOCUSING CHIP.	48
FIGURE 23: ENGINEERING SCHEMATIC OF THE MODEL USED FOR SIMULATIONS.	50
FIGURE 24: SCHEMATIC OF THE PLAN VIEW OF THE VELOCITY PROFILE INSIDE A MICROFLUIDIC CHAMBER.	51
FIGURE 25: EXAMPLE OF TRIANGULAR MESH STRUCTURE.	53
FIGURE 26: CLOSE-UP OF EMPLOYED MESH STRUCTURE AROUND INLETS.	53
FIGURE 27: CONCENTRATION OSCILLATIONS DUE TO INADEQUATE MESH DENSITY.	53
FIGURE 28: AN EXAMPLE OF POSSIBLE RESULT DISPLAY: COLOR MAP SHOWS CONCENTRATION OF MODEL COMPOUND (BLUE INDICATES LOW CONCENTRATION, RED FOR HIGH); STREAMLINES (RED) – THE VELOCITY; AND ARROWS (YELLOW) – THE TOTAL FLUX OF MODEL COMPOUND.	54
FIGURE 29: CHIP GEOMETRY AND LOCATION OF INLETS AND OUTLETS USED FOR MESH QUALITY EVALUATION.	55
FIGURE 30: SCHEMATIC OF CHIP USED TO MODEL THE EXPERIMENT SHOWN IN FIGURE 4D DRAWN IN COMSOL FOR SIMULATIONS WITH DESCRIPTION OF INLETS (BLUE AND YELLOW ARROWS) AND OUTLETS (RED ARROWS).	57
FIGURE 31: SCHEMATIC OF CHIP USED TO MODEL THE EXPERIMENT SHOWN IN FIGURE 4E DRAWN IN COMSOL FOR SIMULATIONS WITH DESCRIPTION OF INLETS (BLUE AND YELLOW ARROWS) AND OUTLETS (RED CIRCLE).	58
FIGURE 32: CHIP GEOMETRY FOR COMPARISON BETWEEN TRIANGULAR AND QUAD MESH.	59
FIGURE 33: SCHEMATIC OF THE CHIP USED FOR THE MODELLING OF THE CONDUCTIVITY GRADIENT FOCUSING.	60
FIGURE 34: SCHEMATIC ILLUSTRATION OF MICROFLUIDIC DEVICE FOR ELECTRO-HYDRODYNAMIC FOCUSING (253). RED ARROWS INDICATE “BACKFLOW” WHEN THE CENTRAL INLET WAS IN LINE WITH AUXILIARY INLETS.	61
FIGURE 35: LAYOUT OF MICROFLUIDIC CHIP WITH THREE MAIN AND SIX AUXILIARY OUTLETS.	61
FIGURE 36: LAYOUT OF MICROFLUIDIC CHIP WITH THREE MAIN AND EIGHT AUXILIARY OUTLETS.	61
FIGURE 37: LAYOUT OF MICROFLUIDIC CHIP WITH THREE MAIN AND TEN AUXILIARY OUTLETS.	62
FIGURE 38: TEST OF GATE-LIKE INLETS AND OUTLETS.	63
FIGURE 39: TEST OF GATE-LIKE INLETS AND OUTLETS.	63
FIGURE 40: TEST OF GATE-LIKE WITH OUTLETS ROUNDED ENTRANCE WITH AN OPEN-END OUTLET.	64
FIGURE 41: TEST OF GATE-LIKE WITH OUTLETS ROUNDED ENTRANCE WITH TWO MAIN OUTLETS LOCATED ASIDE EACH OTHER.	64
FIGURE 42: TEST OF LONG SEPARATION CHAMBER WITH TWO MAIN OUTLETS LOCATED ASIDE EACH OTHER.	65
FIGURE 43: SCHEMATIC DRAWING OF NEW CHIP FOR TESTING OF SIMULTANEOUS PRESSURE- AND ELECTRO-DRIVEN FLOW.	65
FIGURE 44: BOUNDARIES WITH CHANGED BOUNDARY CONDITION ARE MARKED WITH BLACK LINE. ALL OTHER SETTINGS AS IN FIGURE FIGURE 43.	67
FIGURE 45: (A) 3D SCHEMATIC OF THE ASSEMBLED MICROFLUIDIC CHIP AND (B) PTFE GASKET.	68
FIGURE 46: PHOTO OF THE EXPERIMENTAL SETUP FOR THE EHD FOCUSING.	72

FIGURE 47: CALIBRATION CURVES FOR THE MICROFLUIDIC CHIP WITH A 500MM GASKET FOR IMAGES FROM DIGITAL CAMERA (BLUE AND RED) AND FOR SPECTROPHOTOMETER (GREEN). AU STANDS FOR ARBITRARY UNIT.	73
FIGURE 48: CALIBRATION CURVE FOR 500MM GASKET WITH LIGHT INTENSITY CORRECTION BASED ON LUMINOSITY OF THE REFERENCE WHITE AREA.	75
FIGURE 49: LOCALISATIONS OF THE TEST AREAS FOR LUMINOSITY MEASUREMENTS AND CONCENTRATION CALCULATIONS (A) 20×20MM AERA USED DURING FILLING THE CHIP WITH TRIS-HCL BUFFER, (B) 3×3MM AERA USED DURING FOCUSING.	75
FIGURE 50: COMPARISON OF THE CONCENTRATION CALCULATIONS USING NON-CORRECTED (BLUE POINTS) AND NORMALISED LUMINOSITY (RED POINT). LUMINOSITY OF THE TEST AREA (GREEN POINTS) IS PRESENTED AS A REFERENCE.	76
FIGURE 51: SCHEMATIC OF THE ABSORBANCE MEASUREMENTS SETUP USING LED ILLUMINATION AND FIBRE OPTIC SPECTROPHOTOMETER AS ABSORBANCE DETECTOR (PICTURE IN SCALE).....	77
FIGURE 52: 430NM LED EMISSION SPECTRUM (BLUE LINE) FOR USE AS A LIGHT SOURCE IN ABSORBANCE PHOTOMETRIC DETECTION OF MALACHITE GREEN (RED LINE).	77
FIGURE 53: PLAN SCHEMATIC OF THE MICROFLUIDIC CHIP USED IN FOCUSING EXPERIMENTS.....	78
FIGURE 54: SCHEMATIC OF THE INLETS AND OUTLETS AND OUTLETS USED IN THE 2P-SERIES EXPERIMENTS.....	78
FIGURE 55: SCHEMATIC OF THE INLETS AND OUTLETS AND OUTLETS USED IN THE 2L-SERIES EXPERIMENTS.	79
FIGURE 56: SCHEMATIC OF THE INLETS AND OUTLETS AND OUTLETS USED IN THE 3T-SERIES EXPERIMENTS.....	79
FIGURE 57: SCHEMATIC OF THE EXPECTED PATTERN OF MALACHITE GREEN DURING A FOCUSING EXPERIMENT.	79
FIGURE 58A-F: PHOTOS OF OBSERVED PROBLEMS WITH FLOW STABILITY INSIDE THE CHIP.	80
FIGURE 59: LIGHT INCIDENT ON BOUNDARY OF TWO DIFFERENT DIELECTRICS.	91
FIGURE 60: SCHEMATIC OF LIGHT TRANSMISSION THROUGH, (A) A FLAT TRANSPARENT MATERIAL AND (B) A CYLINDRICAL CAPILLARY, SHOWING CURVATURE AFFECTS ON ANGLE OF INCIDENCE AND TRANSMITTANCE.....	92
FIGURE 61: SCHEMATIC OF REFERENCE LINES AND POINTS, AND LIGHT RAY PATH CALCULATED BY EACH SUB-ROUTINE FOR LIGHT PASSING THROUGH A THREE LAYER SYSTEM IN WHICH THE LIGHT RAY PATH IS PASSING THROUGH A COATED HOLLOW CAPILLARY.....	94
FIGURE 62: SCHEME OF METHOD USED BY ALGORITHM FOR ALLOCATION OF CELL X AND Y REFERENCE VALUES TO A LIGHT RAY FOR CALCULATION OF RELATED LIGHT INTENSITY VALUES AT EACH LOCATION.	95
FIGURE 63: SCHEMATIC PLAN VIEW OF INITIAL POSITIONS OF LASER WITH THE (A) 80x74MM PC AND 70x60MM PMMA CONCENTRIC CYLINDERS (SET A) AND THE AND (B) 80x70MM PMMA AND 70x64MM PC CONCENTRIC CYLINDERS (SET B).....	95
FIGURE 64: (A) ABSORBANCE SPECTRUM OF TARTRAZINE, (B) RELATIVE EMISSION SPECTRUM OF THE 430NM VIOLET LED, AND (C) RELATIVE EMISSION SPECTRUM OF THE WHITE LED.	96
FIGURE 65: SCHEMATIC OF THE EXPERIMENTAL SETUP FOR THE LIGHT INTENSITY DISTRIBUTION MEASUREMENTS INSIDE THE 100MM INNER BORE CAPILLARY.	97
FIGURE 66: MODELLING RESULT FOR EXTREMELY COARSE MESH GRIND. THE COLOUR TO CONCENTRATION ASSIGNMENT IS ON THE LEFT. WHITE AREAS SHOW WHERE CALCULATED CONCENTRATION EXCEEDS GIVEN RANGE FROM 0 TO 0.1M.....	100
FIGURE 67: MODELLING RESULT FOR COARSER MESH GRID. THE COLOUR TO CONCENTRATION ASSIGNMENT IS ON THE LEFT. WHITE AREAS SHOW WHERE CALCULATED CONCENTRATION EXCEEDS GIVEN RANGE FROM 0 TO 0.1M.	100

FIGURE 68: MODELLING RESULT FOR NORMAL MESH GRID. THE COLOUR TO CONCENTRATION ASSIGNMENT IS ON THE LEFT. WHITE AREAS SHOW WHERE CALCULATED CONCENTRATION EXCEEDS GIVEN RANGE FROM 0 TO 0.1M.	101
FIGURE 69: MODELLING RESULT FOR FINER MESH GRID. THE COLOUR TO CONCENTRATION ASSIGNMENT IS ON THE LEFT. WHITE AREAS SHOW WHERE CALCULATED CONCENTRATION EXCEEDS GIVEN RANGE FROM 0 TO 0.1M.	102
FIGURE 70: MODELLING RESULT FOR EXTREMELY FINE MESH GRID. THE COLOUR TO CONCENTRATION ASSIGNMENT IS ON THE LEFT. WHITE AREAS SHOW WHERE CALCULATED CONCENTRATION EXCEEDS GIVEN RANGE FROM 0 TO 0.1MM.....	102
FIGURE 71: GRAPH SHOWING COMPARISON OF NUMBER OF MESH ELEMENTS, DEGREES OF FREEDOM, SOLUTION TIMES AND MEMORY USAGE FOR DIFFERENT MESH DENSITIES.....	103
FIGURE 72: COMPARISON OF THE CONCENTRATION VALUES ALONG A-A (FIGURE 70) FOR DIFFERENT MESH DENSITIES.....	104
FIGURE 73: COMPARISON OF THE CONCENTRATION VALUES ALONG B-B (FIGURE 70) FOR DIFFERENT MESH DENSITIES.	104
FIGURE 74: COMPARISON OF STANDARD DEVIATIONS FOR DIFFERENT MESH DENSITIES.	105
FIGURE 75: COMPARISON OF (A) EXPERIMENTALLY ACHIEVED FLOW PATTERN WITH (B) NUMERICAL SIMULATION. YELLOW ARROW INDICATES INLET OF THE TEST COMPOUND FOR THE MODEL, BLUE ARROWS INLETS OF WATER AND RED ARROWS OUTLETS.	106
FIGURE 76: VELOCITY FIELD MAP ASSOCIATED WITH THE EXPERIMENT SHOWN IN FIGURE 75. BLUE COLOUR REPRESENTS THE MINIMUM, RED THE MAXIMUM.	106
FIGURE 77: COMPARISON OF (A) EXPERIMENTALLY ACHIEVED FLOW PATTERN WITH (B) NUMERICAL SIMULATION. YELLOW ARROW INDICATES INLET OF THE TEST COMPOUND FOR THE MODEL, BLUE ARROWS INLETS OF WATER AND RED CIRCLE LOCALISES USED OUTLET.....	107
FIGURE 78: VELOCITY FIELD MAP ASSOCIATED WITH THE EXPERIMENT SHOWN IN FIGURE 77. BLUE COLOUR REPRESENTS THE MINIMUM, RED THE MAXIMUM.	107
FIGURE 79: MODELLING RESULT FOR NORMAL DENSITY TRIANGULAR MESH.	109
FIGURE 80: MODELLING RESULT FOR NORMAL DENSITY QUAD MESH.	109
FIGURE 81: MODELLING RESULT FOR “10% GROWTH” DENSITY TRIANGULAR MESH.....	110
FIGURE 82: MODELLING RESULT FOR “10% GROWTH” DENSITY QUAD MESH.....	110
FIGURE 83: COMPARISON OF MODEL PROPERTIES FOR FOUR MESH DENSITIES USING TWO DIFFERENT MESHING METHODS.	111
FIGURE 84: COMPARISON OF CALCULATION PERFORMANCES FOR FOUR MESH DENSITIES USING TWO DIFFERENT MESHING METHODS.....	111
FIGURE 85: CONCENTRATION OF MALACHITE GREEN AFTER 930 S FROM BEGINNING OF SIMULATION – MOMENT WHEN THE HIGHEST CONCENTRATION WAS OBSERVED.....	112
FIGURE 86: CONCENTRATION PROFILE ALONG A-A FROM FIGURE 85.	113
FIGURE 87: CONCENTRATION OF MG (A) AFTER 1730S AND (B) AFTER 2000S. CONCENTRATION SCALE AS IN FIGURE 85	113
FIGURE 88: GRAPH OF IONIC CONDUCTIVITY [S/M] AT 600S WITH OVERLAY OF LINES OF ELECTRIC FIELD.....	114
FIGURE 89: SPATIAL DISTRIBUTION OF ELECTRIC FIELD INTENSITY AT 600S.	114
FIGURE 90: FORMATION OF REGION OF INCREASED CONCENTRATION OF ANALYTE. ARROWS SHOW DIRECTION OF ELECTRIC FORCE FOCUSING CATIONIC DYE (MG) IN FRONT OF HIGH CONDUCTIVITY BUFFER (TRIS). BLACK LINES ARE LINES OF ELECTRIC FIELD.	116
FIGURE 91: MODELLED CONCENTRATION DISTRIBUTION AFTER 2000S IN CGF.	117
FIGURE 92: PHOTO OF THE CGF EXPERIMENT AT A TIME OF 1980S.	117

FIGURE 93A: GRAPH OF FLOW PATTERN FOR VELOCITIES RATIO 1:10.	119
FIGURE 94A: GRAPH OF FLOW PATTERN FOR VELOCITIES RATIO 2:10.	120
FIGURE 95A: GRAPH OF FLOW PATTERN FOR VELOCITIES RATIO 4:10.	121
FIGURE 96A: GRAPH OF FLOW PATTERN FOR VELOCITIES RATIO 1:1.	122
FIGURE 97: VELOCITY (A) X-COMPONENT NEAR AUXILIARY OUTLET AND (B) Y-COMPONENT NEAR AUXILIARY OUTLET.	123
FIGURE 98: GRAPH OF FLOW PATTERN FOR VELOCITIES RATIO 2:10 WITH 4 PAIRS OF AUXILIARY OUTLETS.	124
FIGURE 99: GRAPH OF FLOW PATTERN FOR VELOCITIES RATIO 2:10 WITH 5 PAIRS OF AUXILIARY OUTLETS.	124
FIGURE 100: TEST OF CIRCULAR INLETS AND OUTLETS REPLACED BY SIDE CHANNELS WITH SEMI-CIRCLES.....	126
FIGURE 101: TEST OF TRAPEZOIDAL SIDE CHANNELS WITH SEMI-CIRCLES. POSITION OF END OUTLETS (O) WAS SHIFTED COMPARED TO PREVIOUS TEST.....	127
FIGURE 102: TEST OF THE UNRESTRICTED OUTFLOW WITH AUXILIARY OUTLETS. TRAPEZOIDAL SIDE OUTLETS WERE REPLACED WITH RECTANGULAR WITH SMOOTH ARCS CONNECTING CHANNEL WITH MAIN CHAMBER.	127
FIGURE 103: TEST OF THE CHIP WITH TWO MAIN AND FOUR AUXILIARY OUTLETS.	128
FIGURE 104: TEST OF THE CHIP WITH ONLY TWO MAIN OUTLETS LOCATED ASIDE.	129
FIGURE 105: CONCENTRATION DISTRIBUTION OF MG IN NEW CHIP AT 980s.	130
FIGURE 106: CONCENTRATION DISTRIBUTION OF MG IN NEW CHIP AT 1420s OVERLAY OF PRESSURE-DRIVEN FLOW STREAMLINES.....	130
FIGURE 107: CLOSE-UP OF HIGH CONCENTRATION REGION FROM FIGURE 106. ARROWS ARE SHOWING DIRECTION OF TOTAL FLUX FOR MALACHITE GREEN AT 1420s.	131
FIGURE 108: CONCENTRATION PROFILE IN THE CENTRE OF THE CHIP BETWEEN OUTLETS.....	131
FIGURE 109: DISTRIBUTION OF CONCENTRATION OF MG AFTER 960s, FOR 1400V.....	132
FIGURE 110: DISTRIBUTION OF CONCENTRATION OF MG AFTER 3000 s, FOR 1400V.....	133
FIGURE 111: MAP OF THE VELOCITY VALUE WITH STREAMLINES FOR PRESSURE DRIVEN FLOW.	133
FIGURE 112: DISTRIBUTION OF CONCENTRATION OF MG AFTER 3000 s, FOR 2000V APPLIED.	134
FIGURE 113: CONCENTRATION PROFILES FOR POINTS LOCATED 60MM FROM THE LEFT CHIP WALL.	134
FIGURE 114: CONCENTRATION PROFILES FOR POINTS LOCATED 50MM FROM THE LEFT CHIP WALL.	135
FIGURE 115: CONCENTRATION DISTRIBUTION OF MG AT 1220s.	136
FIGURE 116: CONCENTRATION DISTRIBUTION OF MG AT 1390s.....	137
FIGURE 117: CONCENTRATION PROFILES FOR POINTS LOCATED 5MM IN FRONT AND BEHIND OUTLETS LINE.....	137
FIGURE 118: CONCENTRATION DISTRIBUTION OF MG AT 1600s.	138
FIGURE 119: CONCENTRATION DISTRIBUTION OF MG AT 2300s.	138
FIGURE 120: CONCENTRATION PROFILES FOR POINTS LOCATED 2MM IN FRONT AND 3MM BEHIND OUTLETS LINE.....	139
FIGURE 121: FOCUSING IN THE MICROFLUIDIC CHIP, EXPERIMENT 2P-14.....	143
FIGURE 122: GRAPH OF CONCENTRATION VS. TIME OF THE FOCUSED ANALYTE FROM EXPERIMENT 2P-14 SHOWN IN FIGURE 121.....	144
FIGURE 123: FOCUSING IN THE MICROFLUIDIC CHIP, EXPERIMENT 2P-22.....	145
FIGURE 124: CONCENTRATION PROFILE FOR EXPERIMENT 2P-22 SHOWN IN FIGURE 123.	146
FIGURE 125: FOCUSING IN THE MICROFLUIDIC CHIP, EXPERIMENT 2P-30.....	147
FIGURE 126: COMPARISON OF THE CONCENTRATION OF MG IN EXPERIMENT 2P-30.	148

FIGURE 127: FOCUSING IN THE MICROFLUIDIC CHIP, EXPERIMENT 2P-47.....	149
FIGURE 128: CONCENTRATION PROFILE FOR EXPERIMENT 2P-47.	150
FIGURE 129: EXPERIMENT 2L-15 - FOCUSING IN THE CENTRAL FLOWSTREAM.	151
FIGURE 130: EXPERIMENT 2L-16 - FOCUSING IN THE CENTRAL FLOWSTREAM.	152
FIGURE 131: EXPERIMENT 2L-17 - FOCUSING IN THE CENTRAL FLOWSTREAM.	153
FIGURE 132: COMPARISON OF CONCENTRATION CHANGES IN THREE EXPERIMENTS (2L-15, 2L-16 AND 2L-17) INVOLVING FOCUSING OF THE MG IN THE CENTRAL FLOWSTREAM.	154
FIGURE 133: EXPERIMENT 2L-26 - FOCUSING IN THE CENTRAL FLOWSTREAM.	155
FIGURE 134: COMPARISON OF CONCENTRATION VALUES CALCULATED FROM PHOTOS (BLUE POINTS) WITH READ FROM SPECTROPHOTOMETER (RED POINTS).	156
FIGURE 135: EXPERIMENT 2L-40 – FOCUSING IN THE CENTRAL FLOWSTREAM WITH 200MM GASKET USED.....	157
FIGURE 136: COMPARISON OF CONCENTRATION VALUES CALCULATED FROM PHOTOS WITH VALUES ACQUIRED USING A SPECTROPHOTOMETER IN EXPERIMENT 2L-40.	158
FIGURE 137: EXPERIMENT 2L-41 – FOCUSING IN THE CENTRAL FLOWSTREAM WITH 200MM GASKET USED.....	159
FIGURE 138: COMPARISON OF CONCENTRATION VALUES CALCULATED FROM PHOTOS WITH VALUES ACQUIRED USING A SPECTROPHOTOMETER IN EXPERIMENT 2L-41.	159
FIGURE 139: EXPECTED FLOW PATTERN FOR SUCCESSFUL LATERAL ELECTROHYDRODYNAMIC FOCUSING.	160
FIGURE 140: EXPERIMENT 3T-20 – LATERAL FOCUSING IN THE MICROFLUIDIC CHIP.	161
FIGURE 141: CONCENTRATION PROFILE FOR THE EXPERIMENT 3T-20.	161
FIGURE 142: EXPERIMENT 3T-21 – LATERAL FOCUSING IN THE MICROFLUIDIC CHIP.	162
FIGURE 143: EXPERIMENT 3L-24 – LATERAL FOCUSING IN THE MICROFLUIDIC CHIP.	163
FIGURE 144: COMPARISON OF ACHIEVED FOCUSING IN EXPERIMENT 3L-21 (FIGURE 142) AND 3L-24 (FIGURE 143).	164
FIGURE 145: EXPERIMENT 3T-31 – LATERAL FOCUSING IN THE MICROFLUIDIC CHIP.	165
FIGURE 146: COMPARISON OF CONCENTRATION VALUES CALCULATED FROM PHOTOS (BLUE POINTS) WITH VALUES MEASURED USING SPECTROPHOTOMETER (RED POINTS) IN THE EXPERIMENT 3L-31.	166
FIGURE 147: EXPERIMENT 3L-36 – LATERAL FOCUSING IN THE MICROFLUIDIC CHIP.	167
FIGURE 148: COMPARISON OF CONCENTRATION VALUES CALCULATED FROM PHOTOS (BLUE POINTS) WITH VALUES MEASURED USING SPECTROPHOTOMETER (RED POINTS) IN THE EXPERIMENT 3L-36.	167
FIGURE 149: EXPERIMENT 3L-43 – LATERAL FOCUSING IN THE MICROFLUIDIC CHIP.	168
FIGURE 150: COMPARISON OF CONCENTRATION VALUES CALCULATED FROM PHOTOS (BLUE POINTS) WITH VALUES MEASURED USING SPECTROPHOTOMETER (RED POINTS) IN THE EXPERIMENT 3L-43.	169
FIGURE 151: EXPERIMENT 3L-58 – LATERAL FOCUSING IN THE MICROFLUIDIC CHIP.	170
FIGURE 152: EXPERIMENT 3L-58 – CONCENTRATION VALUES CALCULATED FROM PHOTOS.....	170
FIGURE 153: PICTURE OF THE MICROFLUIDIC CHIP AT 2040S IN EACH EXPERIMENT UNDER SAME CONDITIONS TO OBSERVE REPEATEABILITY OF THE EHDF.	171
FIGURE 154: PICTURE OF THE MICROFLUIDIC CHIP AT 3120S IN EACH EXPERIMENT UNDER SAME CONDITIONS TO OBSERVE REPEATEABILITY OF THE EHDF.	172
FIGURE 155: CONCENTRATION PROFILES FOR ALL SIX EXPERIMENTS (LABELED 1R, 2R, ETC.) ON REPEATABILITY OF THE FOCUSING.	173

FIGURE 156: AVERAGE CONCENTRATION (WITH EXCLUSION OF THE EXPERIMENT 5R). ERROR BARS REPRESENTS THE STANDARD DEVIATION OF CONCENTRATION VALUES.	173
FIGURE 157: COMPARISON OF THE MALACHITE GREEN CONCENTRATION (A) OBTAINED BY SIMULATION AND (B) EXPERIMENTALLY.	175
FIGURE 158: COMPARISON OF THE PERFORMANCE OF MODELLED EHDF (RED LINE) AND EXPERIMENTAL VALUES (BLUE POINTS).....	176
FIGURE 159: THE COMPARISON OF SCHEMATICS OF (A) A MODELLED FLOW PATTERN AND (B) OBTAINED EXPERIMENTALLY.	177
FIGURE 160: SCHEMATIC OF THE MECHANISM LEADING TO LATERAL ELECTROHYDRODYNAMIC FOCUSING: (A) INITIAL STATE WITH MG PRESENT IN THE CHIP AND TRIS-HCL FILLING THE CENTRAL FLOWSTREAM, (B) SITUATION SHORTLY AFTER APPLYING POSITIVE VOLTAGE, (C) STABILISED LATERAL FOCUSING. DEEP BLUE ARROWS MARK FORCE IMPOSED BY PRESSURE DRIVEN FLOW, LIGHT BLUE ARROWS MARK NET FORCE ACTING ON MG, RED ARROWS MARK NET FORCE ACTING ON CHLORINE, AND YELLOW ARROWS MARK NET FORCE ACTING ON TRIS.....	178
FIGURE 161: PICTURE SHOWING PLAN VIEW OF LASER LIGHT PASSING THROUGH THE OUTER CYLINDER MADE PC, THEN AIR AND THEN THE INNER CYLINDER MADE OF PMMA. THE DRAWN SOLID ARROW LINES (YELLOW) SHOW THE LASER PATH AND CONSTRUCTION LINES (RED) SHOW THE LOCATION OF REFLECTION AND TRANSMISSION ANGLES (θ_{R1} , θ_{T1} AND θ_{T2}).	182
FIGURE 162: COMPARISON OF THEORETICAL CALCULATIONS FROM THE DEVELOPED SOFTWARE (SOLID BLUE LINE) WITH EXPERIMENTALLY MEASURED VALUES FOR THE REFLECTION ANGLES INSIDE THE OUTER CYLINDER (ANGLE θ_{R1} IN FIGURE 161).....	182
FIGURE 163: COMPARISON OF THEORETICAL CALCULATIONS FROM DEVELOPED SOFTWARE (SOLID BLUE LINE) WITH EXPERIMENTALLY MEASURED VALUES FOR THE TRANSMISSION ANGLES BETWEEN THE FIRST CYLINDER AND AIR (ANGLE θ_{T1} IN FIGURE 161).	183
FIGURE 164: COMPARISON OF THEORETICAL CALCULATIONS FROM DEVELOPED SOFTWARE (SOLID BLUE LINE) WITH EXPERIMENTALLY MEASURED VALUES FOR THE TRANSMISSION ANGLES FROM AIR TO THE INNER CYLINDER (ANGLE θ_{T2} IN FIGURE 161).	183
FIGURE 165: PICTURE SHOWING PLAN VIEW OF LASER LIGHT PASSING THROUGH THE OUTER CYLINDER MADE PMMA AND THEN THE INNER CYLINDER MADE OF PC. THE DRAWN SOLID ARROW LINES (YELLOW) SHOW THE LASER PATH AND CONSTRUCTION LINES (RED) SHOW THE LOCATION OF REFLECTION AND TRANSMISSION ANGLES (θ_{R1} , θ_{T1} AND θ_{T2}).	184
FIGURE 166: COMPARISON OF THEORETICAL CALCULATIONS FROM THE DEVELOPED SOFTWARE (SOLID BLUE LINE) WITH THE EXPERIMENTALLY MEASURED VALUES FOR THE REFLECTION ANGLES INSIDE OUTER CYLINDER (θ_{R1} ANGLE IN FIGURE 165).....	185
FIGURE 167: COMPARISON OF THEORETICAL CALCULATIONS FROM THE DEVELOPED SOFTWARE (SOLID BLUE LINE) WITH EXPERIMENTALLY MEASURED VALUES FOR THE TRANSMISSION ANGLES THROUGH AIR (θ_{T2} ANGLE IN FIGURE 165)...	185
FIGURE 168: COMPARISON OF THEORETICAL CALCULATIONS FROM THE DEVELOPED SOFTWARE (SOLID BLUE LINE) WITH EXPERIMENTALLY MEASURED VALUES FOR THE TRANSMISSION ANGLES THROUGH AIR (θ_{T2} ANGLE IN FIGURE 165)...	185
FIGURE 169: (A) 3D THEORETICALLY CALCULATED LIGHT INTENSITY DISTRIBUTION INSIDE THE 100 μ M INNER DIAMETER CAPILLARY FILLED WITH LIGHT ABSORBING SOLUTION (B) AND ITS 2D TOP VIEW PROJECTION. LIGHT WAS INCIDENT ALONG THE Y- AXIS (FROM THE LEFT SIDE IN (B)).	187

FIGURE 170: (A) CAPILLARY FILLED WITH 0.01M TARTRAZINE SOLUTION ILLUMINATED WITH WHITE LED AND (B) A COLOUR MAP REPRESENTING LIGHT INTENSITY DISTRIBUTION INSIDE THE CAPILLARY. ARROWS REPRESENT DIRECTION OF ILLUMINATION.	187
FIGURE 171: (A) CAPILLARY FILLED WITH 0.01M TARTRAZINE SOLUTION ILLUMINATED WITH 430NM VIOLET LED AND (B) A NORMALISED COLOUR MAP REPRESENTING LIGHT INTENSITY DISTRIBUTION INSIDE THE CAPILLARY. ARROWS REPRESENT DIRECTION OF ILLUMINATION.	187
FIGURE 172: (A) SCHEMATIC OF THE LED PLACEMENT VERSUS THE CAPILLARY FOR PERPENDICULAR ILLUMINATION AND (B) FOR ILLUMINATION UNDER 45° ANGLE. RED ARROW MARKS DISTANCE FROM CAPILLARY TO THE LED, BLUE ARROWS MARKS DISTANCE OF THE MONOLITH GROWTH.	190
FIGURE 173: GRAPH SHOWING RELATION BETWEEN DISTANCE FROM THE LIGHT SOURCE AND MONOLITH GROWTH IN NON-ILLUMINATED REGION FOR LED SHINING PERPENDICULARLY TO THE CAPILLARY AND UNDER ANGLE 45°.	191
FIGURE 174: GRAPH OF THEORETICAL REFLECTANCE OF S AND P POLARISED LIGHT INCIDENT ON BOUNDARY PTFE/FUSED SILICA VS. ANGLE OF INCIDENCE CALCULATED FROM EQ. 22.....	192
FIGURE 175: SCHEMATIC OF THE LIGHT PROPAGATION BY MULTIPLE REFLECTIONS INSIDE PTFE-COATED FUSED SILICA CAPILLARY WITH UPPER LIMIT OF THE INITIAL INTENSITY I_0 (NO MORE THAN). DARK BLUE – PTFE, LIGHT BLUE – FUSED SILICA, WHITE – POLYMERISATION MIXTURE, RED – LIGHT PATH	193
FIGURE 176: GRAPH SHOWING THE THEORETICAL REFLECTANCE ON BOUNDARY FUSED SILICA/PTFE VS. ANGLE OF INCIDENCE. REFLECTANCE OF 1 (STARTING AT 64.8°) SHOWS WHERE TOTAL INTERNAL REFLECTION OCCURS AND NO LIGHT IS TRANSMITTED THROUGH THE BOUNDARY (FROM EQ. 22).	194
FIGURE 177: SCHEMATIC OF EXPERIMENTAL SETUP FOR OBSERVING LIGHT WAVEGUIDING INSIDE THE CAPILLARY WITH MONOLITH.	195
FIGURE 178: (A) CAPILLARY WITH MONOLITH AND (B) EMPTY CAPILLARY. IMAGE COLLECTED BY DIGITAL MICROSCOPE USING SETUP FROM FIGURE 177.	196
FIGURE 179: IMAGE OBSERVED WHEN 532 NM GREEN LASER IS USED AS LIGHT SOURCE (SETUP SAME AS ON FIGURE 177).	196
FIGURE 180: SCHEMATIC OF THE DIFFUSE SCATTERING OF INCIDENT LIGHT ON THE POROUS SURFACE OF THE MONOLITH THAT HAS FORMED INSIDE THE CAPILLARY.	197
FIGURE 181: SCHEMATIC SHOWING FORMATION OF THE EVANESCENT FIELD (YELLOW ARROW) OUTSIDE DIELECTRIC INSIDE WHICH LIGHT UNDERGOES TOTAL INTERNAL REFLECTION. DARK BLUE – PTFE, LIGHT BLUE – FUSED SILICA, TRANSPARENT – POLYMERISATION MIXTURE.	197
FIGURE 182: MEMBERS OF THE ENIAC TEAM AT WORK IN THE 1940s (265).	II
FIGURE 183: GRAPH SHOWING EVOLUTION OF MOORE’S LAW FROM 1972 TO 2003 ON SEMICONDUCTORS AND DATA STORAGE DENSITY (270).	III
FIGURE 184: SCHEMATIC COMPARISON OF THE POPULATION OF CHARGE CARRIERS AT 0K IN SEMICONDUCTOR WITH INDIRECT BANDGAP (Si) AND WITH DIRECT BANDGAP (GAAs).	VIII
FIGURE 185: GRAPHICAL REPRESENTATION OF A CARRIER DENSITY DISTRIBUTION AT $T > 0K$; $n(E)$ AND $p(E)$ ARE DENSITY FUNCTIONS FOR NEGATIVE AND POSITIVE CARRIERS.	IX
FIGURE 186: SCHEME OF THE CRYSTAL LATTICE IN DOPED SEMICONDUCTOR: TYPE N ON THE LEFT, TYPE P ON THE RIGHT.	X
FIGURE 187: CARRIER DENSITY DISTRIBUTION FOR N-TYPE DOPED SEMICONDUCTOR.	X

FIGURE 188: CARRIER DENSITY DISTRIBUTION FOR P-TYPE DOPED SEMICONDUCTOR.....	XI
FIGURE 189: ENERGIES OF POSSIBLE TRANSITIONS BETWEEN CONDUCTIVITY BAND AND VALENCE BAND IN A SEMICONDUCTOR AND RESULTING SPECTRUM.....	XI
FIGURE 190: SPECTRUM SHAPE OF THE EMITTED LIGHT FROM LED CHIP, DUE TO CARRIER DISTRIBUTION.	XII
FIGURE 191: DIFFERENT APPROACHES TO MAXIMISE LIGHT EXTRACTION FROM LED CHIP: AS – ABSORBING SUBSTRATE, TS – TRANSPARENT SUBSTRATE, DBR – DISTRIBUTED BRAGG REFLECTOR, RS – REFLECTIVE SUBSTRATE. BLACK CONES REPRESENT ANGLE VALUES FOR WHICH PHOTON CAN MAY ESCAPE THE CHIP AND WILL NOT BE LOST DUE TO TOTAL INTERNAL REFLECTION (294).	XIII
FIGURE 192: MORE MODERN APPROACHES TO MANUFACTURE LED CHIPS: (A) APPLICATION OF SEMI-TRANSPARENT CONTACTS, (B) REFLECTIVE P-CONTACT, (C) APPLICATION OF REFLECTIVE LAYER BETWEEN HOST SUBSTRATE AND SEMICONDUCTOR, (D) COMBINATION OF TECHNIQUES USED IN (B) AND (C).....	XIII
FIGURE 193: GRAPH ILLUSTRATING LOSSES IN LED CHIP, AFTER (294).	XIV
FIGURE 194: PHOTO OF THINKXXS SNAKE MIXER SLIDE SMS 0104 MICROFLUIDIC CHIP.	XV
FIGURE 195: SCHEMATIC OF THE EXPERIMENTAL SETUP FOR REAL-TIME VISUALISATION OF A FLUORESCENT DYE IN THE SMS0104 MICROFLUIDIC CHIP.	XVI
FIGURE 196: PHOTOGRAPHY OF THE EXPERIMENTAL SETUP FOR VISUALISATION OF A FLUORESCENT DYE IN THE SMS0104 MICROFLUIDIC CHIP.	XVII
FIGURE 197: ABSORPTION (A) AND EMISSION (B) SPECTRA OF FLUORESCHEIN WITH OVERLAYING TRANSMISSION SPECTRA FOR TWO EXCITATION FILTERS: RED LINE – BANDPASS FILTER, GREEN LINE – INTERFERENCE FILTER AND BLUE LINE – EMISSION FILTER	XVII
FIGURE 198: IMAGES OF THE FLUORESCHEIN AT (A) 10^{-5} M AND (B) 10^{-6} M RECORDED WITH USED BANDPASS FILTER. WHITE ARROW INDICATED DIRECTION OF THE ILLUMINATION IN THE PICTURE PLANE.	XVIII
FIGURE 199: IMAGES OF THE FLUORESCHEIN AT (A) 10^{-6} M AND (B) 10^{-7} M RECORDED WITH USED INTERFERENCE FILTER. WHITE ARROW INDICATED DIRECTION OF THE ILLUMINATION IN THE PICTURE PLANE.	XVIII
FIGURE 200: EXTREMELY COARSE MESH GRID.....	XX
FIGURE 201: CONVERGENCE GRAPH FOR EXTREMELY COARSE MESH.....	XX
FIGURE 202: COARSER MESH GRID.	XXI
FIGURE 203: CONVERGENCE GRAPH FOR COARSER MESH.....	XXI
FIGURE 204: NORMAL MESH GRID.	XXII
FIGURE 205: CONVERGENCE GRAPH FOR NORMAL MESH.	XXII
FIGURE 206: FINER MESH GRID.	XXIII
FIGURE 207: CONVERGENCE GRAPH FOR FINER MESH.	XXIII
FIGURE 208: EXTREMELY FINE MESH GRID.	XXIV
FIGURE 209: CONVERGENCE GRAPH FOR EXTREMELY FINE MESH.	XXIV
FIGURE 210: LOWER LAYER OF PMMA CHIP FOR EHDF.	XXV
FIGURE 211: THE PTFE GASKET (THICKNESS VARIES) USED IN THE PMMA CHIP FOR EHDF.	XXVI
FIGURE 212: UPPER LAYER OF THE PMMA CHIP USED FOR EHDF.	XXVII
FIGURE 213: DETAILS OF STANDARD 10-32 MICROFLUIDIC PORT (NINE INSTALLED IN THE UPPER LAYER).....	XXVIII
FIGURE 214: SIDE PORTS ORIENTATION.	XXIX

FIGURE 215: DETAILS OF TECHNOLOGICAL PROCESS OF THE MICROFLUIDIC PORT FABRICATION (STEPS ONE AND TWO).....	XXX
FIGURE 216: DETAILS OF TECHNOLOGICAL PROCESS OF THE MICROFLUIDIC PORT FABRICATION (STEPS THREE AND FOUR). .	XXXI
FIGURE 217: DETAILS OF TECHNOLOGICAL PROCESS OF THE MICROFLUIDIC PORT FABRICATION (STEP FIVE).	XXXII
FIGURE 218: EXTREMELY COARSE TRIANGULAR MESH.	XXXIII
FIGURE 219: EXTREMELY COARSE QUAD MESH.	XXXIII
FIGURE 220: NORMAL TRIANGULAR MESH.....	XXXIII
FIGURE 221: (A) RECIPROCAL OF TIME STEP AND (B) ERROR IN EACH ITERATION FOR NORMAL TRIANGULAR MESH.....	XXXIII
FIGURE 222: NORMAL QUAD MESH.....	XXXIV
FIGURE 223: (A) RECIPROCAL OF TIME STEP AND (B) ERROR IN EACH ITERATION FOR NORMAL QUAD MESH.	XXXIV
FIGURE 224: EXTREMELY FINE TRIANGULAR MESH.	XXXIV
FIGURE 225: (A) RECIPROCAL OF TIME STEP AND (B) ERROR IN EACH ITERATION FOR THE EXTREMELY FINE TRIANGULAR MESH.	XXXV
FIGURE 226: EXTREMELY FINE QUAD MESH.....	XXXV
FIGURE 227: (A) RECIPROCAL OF TIME STEP AND (B) ERROR IN EACH ITERATION FOR EXTREMELY FINE QUAD MESH.....	XXXV
FIGURE 228: 10% GROWTH TRIANGULAR MESH.	XXXV
FIGURE 229: (A) RECIPROCAL OF TIME STEP AND (B) ERROR IN EACH ITERATION FOR THE “10% GROWTH” TRIANGULAR MESH.	XXXVI
FIGURE 230: 10% GROWTH QUAD MESH.	XXXVI
FIGURE 231: (A) RECIPROCAL OF TIME STEP AND (B) ERROR IN EACH ITERATION FOR THE “10% GROWTH” QUAD MESH. .	XXXVI
FIGURE 232: 2% GROWTH TRIANGULAR MESH.	XXXVII
FIGURE 233: (A) RECIPROCAL OF TIME STEP AND (B) ERROR IN EACH ITERATION FOR THE “2% GROWTH” TRIANGULAR MESH.	XXXVII
FIGURE 234: “2% GROWTH” QUAD MESH.....	XXXVII
FIGURE 235: (A) RECIPROCAL OF TIME STEP AND (B) ERROR IN EACH ITERATION FOR THE 2% GROWTH” QUAD MESH.	XXXVIII

List of tables

TABLE 1: SCALING LAWS FOR DIFFERENT PHYSICAL QUANTITIES, AFTER (1) AND (45).	17
TABLE 2: NINE BASIC CATEGORIES OF SEPARATIONS (112).	23
TABLE 3: PHYSICAL PARAMETERS OF SUBSTANCES USED IN MODELS WITH NERNST-PLANCK MODE.	49
TABLE 4: MODELLING BOUNDARY CONDITIONS FOR EXPERIMENTAL SETUP SHOWN IN FIGURE 29.	56
TABLE 5: BOUNDARY CONDITIONS FOR EXPERIMENTAL SETUP SHOWN IN FIGURE 30.	57
TABLE 6: BOUNDARY CONDITIONS FOR EXPERIMENTAL SETUP SHOWN IN FIGURE 31.	58
TABLE 7: BOUNDARY CONDITIONS FOR THE EXPERIMENT SHOWN IN FIGURE 32.....	59
TABLE 8: BOUNDARY CONDITIONS FOR EXPERIMENTAL SETUP SHOWN IN FIGURE 33.	60
TABLE 9: BOUNDARY CONDITIONS FOR EXPERIMENTAL SETUP SHOWN IN FIGURE 35.	61
TABLE 10: BOUNDARY CONDITIONS FOR EXPERIMENTAL SETUP SHOWN IN FIGURE 36.	62
TABLE 11: BOUNDARY CONDITIONS FOR EXPERIMENTAL SETUP SHOWN IN FIGURE 37.	62
TABLE 12: BOUNDARY CONDITIONS FOR EXPERIMENTAL SETUP SHOWN IN FIGURE 38.	63
TABLE 13: BOUNDARY CONDITIONS FOR EXPERIMENTAL SETUP SHOWN IN FIGURE 39.	63
TABLE 14: BOUNDARY CONDITIONS FOR EXPERIMENTAL SETUP SHOWN IN FIGURE 40.	64
TABLE 15: BOUNDARY CONDITIONS FOR EXPERIMENTAL SETUP SHOWN IN FIGURE 41.	65
TABLE 16: BOUNDARY CONDITIONS FOR EXPERIMENTAL SETUP SHOWN IN FIGURE 42.	65
TABLE 17: BOUNDARY CONDITIONS FOR EXPERIMENTAL SETUP SHOWN IN FIGURE 43.	66
TABLE 18: BOUNDARY CONDITIONS FOR EXPERIMENTAL SETUP SHOWN IN FIGURE 43.	66
TABLE 19: BOUNDARY CONDITIONS FOR EXPERIMENTAL SETUP SHOWN IN FIGURE 44.	67
TABLE 20: TABLE OF CHEMICALS USED DURING EXPERIMENTS ON EHD FOCUSING.	71
TABLE 21: CONDITIONS FOR THE EXPERIMENT 2P-14.	81
TABLE 22: CONDITIONS FOR THE EXPERIMENT 2P-22.	81
TABLE 23: CONDITIONS FOR THE EXPERIMENT 2P-30.	82
TABLE 24: CONDITIONS FOR THE EXPERIMENT 2P-47.	82
TABLE 25: CONDITIONS FOR THE EXPERIMENT 2L-15.....	83
TABLE 26: CONDITIONS FOR THE EXPERIMENT 2L-16.....	83
TABLE 27: CONDITIONS FOR THE EXPERIMENT 2L-17.....	84
TABLE 28: CONDITIONS FOR THE EXPERIMENT 2L-26.....	84
TABLE 29: CONDITIONS FOR THE EXPERIMENT 2L-40.....	85
TABLE 30: CONDITIONS FOR THE EXPERIMENT 2L-41.....	85
TABLE 31: CONDITIONS FOR THE EXPERIMENT 3T-20.	86
TABLE 32: CONDITIONS FOR THE EXPERIMENT 3T-21.	86
TABLE 33: CONDITIONS FOR THE EXPERIMENT 3T-24.	87
TABLE 34: CONDITIONS FOR THE EXPERIMENT 3T-24.	87
TABLE 35: CONDITIONS FOR THE EXPERIMENT 3T-36.	88
TABLE 36: CONDITIONS FOR THE EXPERIMENT 3T-43.	88

TABLE 37: CONDITIONS FOR THE EXPERIMENT 3T-58.	89
TABLE 38: CONDITIONS FOR THE EXPERIMENT ON REPEATABILITY.	89
TABLE 39: LIST OF CHEMICALS USED IN EXPERIMENTS ON LIGHT PROPAGATION.....	90
TABLE 40: LIST OF CHEMICALS USED FOR PHOTOPOLYMERISATION OF MONOLITHS IN CAPILLARIES FOR VERIFICATION OF THE LIGHT PROPAGATION MODEL.....	91
TABLE 41: SUMMARY OF THE EXPERIMENT SERIES, EXPERIMENT NUMBERS AND RELEVANT CHIP LAYOUT.	142
TABLE 42: MONOLITH GROWTH DEPENDING ON LIGHT SOURCE POSITION.....	191
TABLE 43: TABLE OF CHEMICALS USED DURING EXPERIMENTS ON REAL-TIME VISUALISATION OF THE FLUORESCENT DYES IN MICROFLUIDIC CHIP.....	XV
TABLE 44: SUMMARY OF THE EXTREMELY COARSE MESH.....	XX
TABLE 45: SUMMARY OF THE COARSER MESH.....	XXI
TABLE 46: SUMMARY OF THE NORMAL MESH.....	XXII
TABLE 47: SUMMARY OF THE FINER MESH.....	XXIII
TABLE 48: SUMMARY OF THE EXTREMELY FINE MESH.....	XXIV
TABLE 49: SUMMARY OF THE NORMAL TRIANGULAR MESH.....	XXXIII
TABLE 50: SUMMARY OF THE NORMAL QUAD MESH.....	XXXIV
TABLE 51: SUMMARY OF THE EXTREMELY FINE TRIANGULAR MESH.....	XXXIV
TABLE 52: SUMMARY OF THE EXTREMELY FINE QUAD MESH.....	XXXV
TABLE 53: SUMMARY OF THE “10% GROWTH” TRIANGULAR MESH.....	XXXVI
TABLE 54: SUMMARY OF THE “10% GROWTH” QUAD MESH.....	XXXVI
TABLE 55: SUMMARY OF THE “2% GROWTH” TRIANGULAR MESH.....	XXXVII
TABLE 56: SUMMARY OF THE “2% GROWTH” QUAD MESH.....	XXXVII

Publications from this work

Scientific publications: journal papers:

1. **Tomasz Piasecki**, Michael Breadmore, Mirek Macka, *White LEDs as broad spectrum light sources for spectrophotometry: Demonstration in the visible spectrum range in a diode array spectrophotometric detector*, *Electrophoresis*, 31, 3737-3744, **2010**
2. **Tomasz Piasecki**, Mirek Macka, Brett Paull, Dermot Brabazon, *Numerical model for light propagation and light intensity distribution inside coated fused silica capillaries*, *Optics and Lasers in Engineering*, 49, 924-931, **2011**

Scientific publications: conference papers:

1. **A. Ben Azouz**, **T. Piasecki**, D. Brabazon, M. Vázquez, M. Macka and B. Paull, *Laser-induced plasma and glass type effects on the process of micro-channel fabrication using CO₂ Laser*, European Physics Society 37th Conference on Plasma Physics, 21st – 25th June **2010**, Dublin, Ireland

Scientific publications: posters

1. **Tomasz Piasecki**, Silvija Abele, Michael Oelgemoeller, Mirek Macka, *Light propagation in capillaries filled with polymerisation mixture to form monoliths: Theoretical models based on optics and photochemistry*, 32th International Symposium on Capillary Electrophoresis, Riva del Garda, Italy, 27 May- 2 June **2008**
2. Amy Smith, **Marketa Ryvolova**, **Tomasz Piasecki**, Eva Mendel, Silvija Abele, Brett Paull, Mirek Macka, *Capillary electrophoresis with in-line derivatisation of amino acids and peptides for the analysis of yeastolaets*, 32th International Symposium on Capillary Electrophoresis, Riva del Garda, Italy, 27 May- 2 June **2008**
3. **Tomasz Piasecki**, Silvija Abele, Michael Oelgemoeller, Mirek Macka, *Studies for photoinitiated polymerisation of monolithic stationary phases: modelling of light propagation in capillaries and light attenuation inside photopolymerisation mixture filling the capillary bore*, ITCBSB, International Conference on Trends in Bioanalytical Sciences and Biosensors, Dublin, Ireland, 26-28 January **2009**
4. **Tomasz Piasecki**, Silvija Abele, Michael Oelgemoeller, Mirek Macka, *Photoinitiated polymerisation of monoliths: How far does the light penetrate into the polymerisation mixture?*, Pittcon 2009, Chicago, IL, USA, 8-13 March **2009**
5. **Tomasz Piasecki**, Cornelius F. Ivory, Mirek Macka, *Computer Modelling of Electrohydrodynamic Focusing in 2-D Planar Microfluidic Devices for Preconcentration of Low-Abundance Analytes*, 21st IISC International Ion Chromatography Symposium, Dublin, Ireland, 20-23 September **2009** – awarded 2nd prize
6. **Tomasz Piasecki**, Dermot Brabazon, Mirek Macka, *Light propagation in coated fused silica capillaries in photo-initiated polymerization of monolithic stationary phases: a three-dimensional model and light intensity distribution*, MicroBiological Separations MSB 2010, 21-25 March **2010**
7. **Tomasz Piasecki**, Dermot Brabazon, Mirek Macka, *What are the invisible differences between PTFE and Polyimide coated fused silica capillaries? Three-dimensional model of optical properties, light propagation and intensity distribution*, 34th International Symposium on Capillary Electrophoresis, Riva del Garda, 30 May – 4 June **2010**

8. **Tomasz Piasecki**, Mirek Macka, Brett Paull, Dermot Brabazon, *Light propagation in capillaries: modelling and experiments of ray-tracing and intensity distribution*, 6th Conference on Analytical Sciences Ireland 2011, Dublin, 21-22 February **2011**

Scientific presentations:

1. Markéta Rývolová, **Tomasz Piasecki**, Jan Preisler, Pavel Krásenský, František Foret, Peter C. Hauser, Dermot Brabazon, Brett Paull, Silvija Abele, Mirek Macka, *New Approaches in Detection for Capillary Separation Techniques using LEDs*, Proc. International Ion Chromatography Conference IICS 2008, Portland, OR, USA, 21-24 September **2008**, invited oral presentation
2. Markéta Rývolová, **Tomasz Piasecki**, Jan Preisler, Pavel Krásenský, František Foret, Peter C. Hauser, Dermot Brabazon, Brett Paull, Silvija Abele, Mirek Macka, *New Options in Light Emitting Diode-Based Photometric and Fluorimetric Detection Systems for Capillary Electrophoresis and Microfluidic Chips*, Proc. Vitamins **2008**, Zlín, 9-11 September 2008, invited oral presentation
3. Walsh Z., Abele S., Rývolová M., **Piasecki T.**, Preisler J., Krásenský P., Foret F., Hauser P. C., Paull B., Lawless B., Brabazon D., Oelgemoeller M., Macka M., *Shedding LED light on synergies between analytical science, miniaturisation, photochemistry, and photonics*, Proc. CECE 2008, Brno, Czech Republic, 24-25 November **2008**, invited oral presentation
4. Walsh Z., Abele S., Rývolová M., **Piasecki T.**, Preisler J., Krásenský P., Foret F., Hauser P. C., Paull B., Lawless B., Brabazon D., Oelgemoeller M., Macka M., *Shedding LED light on the synergies between separation science, miniaturisation, photochemistry and photonics*, Proc. ASASS 2008, Hobart, 8-10 December **2008**, invited oral presentation
5. Zarah Walsh, Ugis Danilevics, **Tomasz Piasecki**, Silvija Abele, Brett Paull, Mirek Macka, *Monoliths in Capillary and Microfluidic Chip Formats for Bioseparations: Examples of Fabrication and Modifications*, ICTBSB-2009 - International Conference on Trends in Bioanalytical Sciences and Biosensors, Dublin, Ireland, 26-27th January **2009**, invited oral presentation
6. M. Rývolová, L. Krčmova, **T. Piasecki**, M. Akhter, J. Preisler, F. Foret, P. C. Hauser, P. Maaskant, M. Macka *LEDs as ideal light sources for capillary-based analytical instrumentation?*, 34th International Symposium on Capillary Chromatography, Riva del Garda, Italy, 30 May-4 June **2010**, , invited oral presentation

Other:

7. Instructor on 1.5 day course "Light Emitting Diodes in Chemical Analysis and Chemistry" as Pittcon 2009, Chicago, IL, USA, 8-13 March **2009**

Abbreviations

- BEM – Boundary Element Method
- CACE – Counteracting Chromatographic Electrophoresis
- CE – Capillary Electrophoresis
- Cl – Chlorine, Cl⁻
- CFD – Computational Fluid Dynamics
- CGF – Conductivity Gradient Focusing
- CIE – Commission Internationale d’Eclairage
- CZE – Capillary Zone Electrophoresis
- EDMA – Ethylene Dimethacrylate
- EGM – Equilibrium Gradient Method
- EHD – electrohydrodynamic
- EOF – Electro-Osmotic Flow
- EFGF – Electric Field Gradient Focusing
- EHDF – Electrohydrodynamic Focusing
- FDM – Finite Difference Method
- FEM – Finite Element Method
- FFE – Free Flow Electrophoresis
- FIA – Flow Injection Analysis
- FVM – Finite Volume Method
- FWHM – Full Width at Half Maximum
- GC – Gas Chromatography
- GMA – Glycidyl Methacrylate
- HCl – Hydrochloric Acid
- HPLC – High Performance Liquid Chromatography
- IEF – Isoelectric Focusing
- IeP – Isoelectric Point
- IR – Infra Red
- ITP – Isotachophoresis
- LBM – Lattice Boltzmann Method
- LC – Liquid Chromatography
- LD – laser diode
- LED – Light Emitting Diode

- LOC – Laboratory- or lab-on-a-chip
- MEKC – Micellar Electrokinetic Chromatography
- MEMS – Micro-Electro-Mechanical Systems
- MG – malachite green, $[\text{C}_6\text{H}_5\text{C}(\text{C}_6\text{H}_4\text{N}(\text{CH}_3)_2)_2]^+$
- μ -TAS – Micro Total Analysis System(s)
- NEGM – Non-Equilibrium Gradient Method
- OECE – Overall Energy Conversion Efficiency
- PC – Polycarbonate
- PCR – Polymerase Chain Reaction
- PDE – Partial Differential Equation
- PDMS – Poly Dimethylsiloxane
- PEEK – Polyether Ether Ketone
- PMMA – Poly Methyl Methacrylate
- PTFE – Poly Tetrafluoroethylene
- rt-PCR – Reverse Transcription PCR
- SPE – Solid Phase Extraction
- SSL – Solid State Light
- Tris – tris(hydroxymethyl)aminomethane, $(\text{HOCH}_2)_3\text{CNH}^+$
- UV – Ultra Violet
- WPE – Wall-Plug Efficiency

Nomenclature

- η – viscosity
- τ_{xy} – shear stress, the force in x -direction on a unit area perpendicular to y
- $\frac{d}{dx}$ – derivative with respect to x
- v_x – velocity x -component
- ρ – density
- $\frac{\partial}{\partial t}$ – time derivative
- \mathbf{v}, \mathbf{u} – velocity vectors
- p – pressure
- ∇ – nabla operator (del operator)
- $V(r)$ – a potential as a function of distance r
- ε – potential depth
- σ – distance at which potential is equal zero
- Re – Reynolds number
- v_0 – tangent linear velocity
- l_0 – characteristic linear dimension
- D – the diffusion coefficient
- Pe – Peclet number
- τ – Fourier number, average number of times that a molecule contacts the capillary wall
- Π – backmixing (or axial mixing) within the system (or pressure drop), Bodenstein number
- J – flux density
- $\frac{dc}{dx}$ – concentration gradient along x -dimension
- R – gas constant
- T – temperature
- f – friction coefficient
- c – concentration
- t – time
- n – number of moles (or molecules)
- $F(t), g(t)$ – unspecified functions time dependent only
- W – overall component velocity (sum of drift velocity due to external fields and flow velocity)

- w – effective zone width w
- σ^2 – sample peak variance for Gaussian profiles
- v – velocity value
- μ – effective mobilities
- T – transmittance
- I_0 – initial light intensity
- I – recorded light intensity
- l – length
- α – molar absorptivity coefficient
- f – permeability
- D_p – average gel spherical “particle” diameter
- ξ – volume of empty space (occupied by the pores)

Abstract

This thesis presents work on electrohydrodynamic focusing (EHDF) and photon transmission to aid the development of species preconcentration and identification. EHDF is an equilibrium focusing method, where a target ion becomes stationary under the influence of a hydrodynamic force opposed by an electromigration force. To achieve this one force must have a non-zero gradient. In this research a novel approach of using a 2-dimensional planar microfluidic device is presented with an open 2D-plane space instead of conventional microchannel system. Such devices can allow pre-concentration of large volume of species and are relatively simple to fabricate.

Fluid flow in these systems is often very complex making computer modelling a very useful tool. In this research, results of newly developed simulations using COMSOL Multiphysics® 3.5a are presented. Results from these models were compared to experimental results to validate the determined flow geometries and regions of increased concentration. The developed numerical microfluidic models were compared with previously published experiments and presented high correspondence of the results. Based on these simulations a novel chip shapes were investigated to provide optimal conditions for EHDF. The experimental results using fabricated chip exceeded performance of the model. A novel mode, named lateral EHDF, when test substance was focused perpendicularly to the applied voltage was observed in the fabricated microfluidic chip.

As detection and visualisation is a critical aspect of such species preconcentration and identification systems. Numerical models and experimental validation of light propagation and light intensity distribution in 2D microfluidic systems was examined.

The developed numerical mode of light propagation was used to calculate the actual light path through the system and the light intensity distribution. The model was successfully verified experimentally in both aspects, giving results that are interesting for the optimisation of photopolymerisation as well as for the optical detection systems employing capillaries.

Chapter 1 – Introduction

1.1. Electrohydrodynamic focusing as an alternative for the sample preconcentration

Microfluidics is a major branch of the broader multidisciplinary field known as Micro-Electro-Mechanical Systems (MEMS), which is a relatively new field of study that combines physics, chemistry and engineering. Microfluidics has been defined as the “study of flows that are simple or complex, mono or multi-phasic, which are circulating in artificial microsystems” (1). The term microfluidics is used to refer to objects with geometrical dimension scale ranging typically between 100nm and 300µm (2; 3). In the 1980’s major breakthroughs in miniaturisation allowed the development of systems down to sub-micrometric scales introducing MEMS. Later on, in the 1990’s this spread to a multitude of chemical, biological, biomedical, and analytical applications (1). Microfluidics is regarded as a new application of the old discipline of hydrodynamics to the novel area of lab-on-a-chip type applications, driven by the idea of combining entire laboratories in a small compact form (4).

Electro-hydrodynamic focusing (EHDF) is a novel microfluidic chip-based equilibrium method of preconcentration of an analyte using a combination of electromigration and pressure-driven flow (5). The main principle of EHDF within microfluidic chips is the formation of a region of stable equilibrium between the forces imposed by the pressure-driven fluid flow and by electrophoretic migration driven fluid flow (see Figure 1).

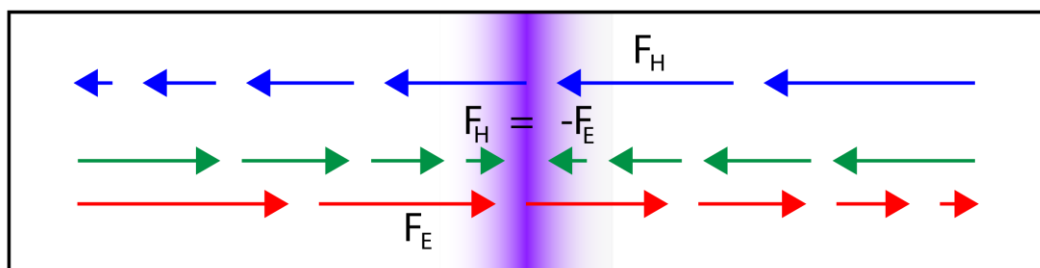


Figure 1: A simplified diagram showing the general principle of electro-hydrodynamic focusing (EHDF), blue arrows represent vectors of hydrodynamic forces F_H (imposed by pressure-driven flow), red arrows represent vectors of electromagnetic forces F_E (imposed by applied electric field) and green arrows represent the vector summation of both. Purple area shows where the EHDF takes place.

In order to create an analyte-specific focusing zone, that will separate the target analyte of known electrophoretic mobility from the matrix that contains it a net motive force must drive it toward the focusing point, ideally regardless of the analytes initial location. EHDF can be achieved by modifying flow pressure and applied potential difference in a specially designed microfluidic device. When all parameters are adjusted suitably a constant increment of concentration of the analyte should be observed within the designated stationary zone when the analyte is introduced into the system.

Currently the most common methods for detection of low-abundance, non-volatile analytes (such as drugs or proteins) in complex matrices (e.g. biological, forensic or environmental samples) are based on adsorption of a target analyte on specially prepared chromatographic columns. Appropriate stationary phases are immobilised on the columns and are subsequently washed by the sample. Elution can then allow for extraction of pre-concentrated and purified analyte. This process is known as Solid Phase Extraction (SPE) (6). Other methods used for preconcentration of low-abundance analytes are based on liquid-liquid extraction, precipitation and crystallisation (7). SPE is a very well established analytical method, but has a few restrictions:

- The possibility of interactions between the adsorbent and the sample content (such as precipitation of proteins)
- The need of specialised, selective materials that are not easily available
- Optimisation of SPE methods is limited to empirical approaches as the modelling of chromatographic materials selectivity is too complex to employ in practice

EHDF is a process with the potential for being a rapid and automated preconcentration method. The design and manufacture of a new device overcoming the limitations of conventional SPE would allow fast and effective pre-treatment of challenging samples. EHDF is a versatile technique that could be adapted to virtually any ionic sample making it simple and cost-effective alternative to SPE.

The concept for EHDF design and development of controlled flow is that the net force imposed by hydrodynamic pressure-driven flow is balanced within a specific chip region by application of the electromagnetic force. A necessary condition is that there is a varying value of at least one force along the selected the dimension (separation dimension). In other words, the gradient of at least one force must be non-zero. To improve the performance and the control within the device for EHDF, it would be better

that both forces could have a non-zero gradient. This is schematically presented in Figure 1.

To achieve the required conditions, both experiments and modelling were performed in a microfluidic chip, inspired by (8), with rectangular chamber, of dimensions 100mm × 20mm, with different thicknesses varying from 50µm to 500µm fitted with multiple openings acting as inlets and outlets. Both ends of the chamber were connected to tanks containing conducting agarose gel, which housed the electrodes. The electrodes were immersed in the conducting agarose gel to prevent undesired electrochemical effects, such as electrolysis and bubble formation on the electrodes. The results from this modelling were used to change the design of chips presented previously in (8).

A non-zero gradient of the electric field was achieved by using solutions with different conductivities that were introduced into the microfluidic chip through separate inlets. During the modelling phase, the installation of multiple outlets was tested to achieve a non-zero gradient of hydrodynamic force. In the experiments a non-zero gradient of hydrodynamic force along the separation dimension was achieved by installation of outlets in such a way that a flowstream was turned from the separation dimension.

1.2. Research questions and hypotheses

In this project the control of multiple fluid flows in microfluidic devices and the detection of said flow patterns was investigated. Presently all practical methods of focusing in microfluidic devices have been based on physical boundaries restricting flow patterns. In this project the implementation of dynamically shaped regions of high and low conductivity giving ability to alter not only intensity but also the shape of the electric field was investigated. Successful identification of the significance of parameters for EHDF in “open space” designed microfluidic chips gives the potential for development of a new generation of chip-based microfluidic devices which could be used for preconcentration and separations. Determination of low-abundance components in complex matrices is a difficult and important problem for science and industry. Development of a method with the potential for full automation could provide a replacement for expensive and time-consuming methods of sample preparation.

Investigation of modern optical detection techniques using cutting-edge light sources is important for developing effective sensor and detectors. The main aim of the visualisation part of this project was to gain knowledge for designing novel optical detection systems such as required for imaging on the microfluidic chip used in the experiments.

The model of device for EHDF was designed based on following hypotheses:

- It is possible to attain a stable high conductivity stream of varying cross-section using multiple inlets and outlets (referred further in this thesis as the flow pattern) in a planar two-dimensional microfluidic chip (see Figure 2)
- The presence of such a flow pattern will allow for the formation of an electric field gradient and velocity gradient along the separation dimension
- A stable trapezoidal flow pattern based on this generated flow pattern will allow for focusing of at least one compound
- Simultaneous concentration measurements can be made across the whole chip with a developed photometric detection system, based and optimised on the investigation of simpler capillary-based microfluidic photometric detection systems

The main difference between the EHDF and other focusing techniques is the replacement of a fixed geometry with an adjustable one in EHDF. Instead of employing channels with predefined geometry with varying cross-sectional area, a rectangular microfluidic chamber can be used with two liquids of different conductivity to create a varying cross-section of high-conductivity (see Figure 2).

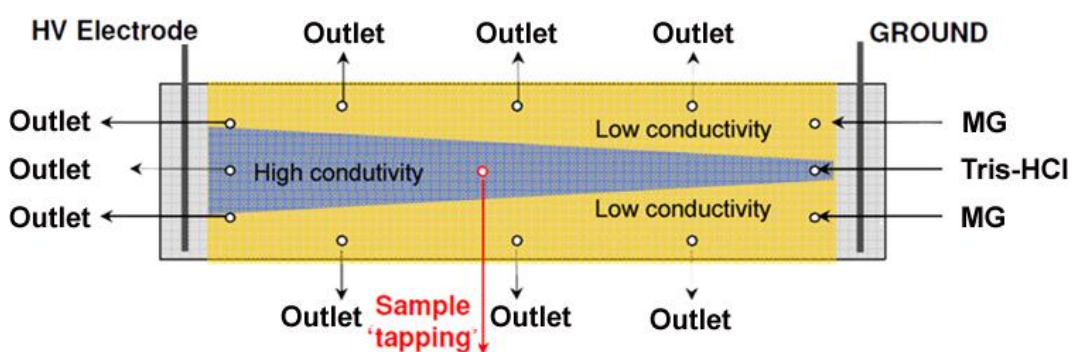


Figure 2: Schematic illustration of microfluidic device for electro-hydrodynamic focusing.

1.3. Project aims and adopted methodology

The development of a two-dimensional model of electrophoresis was regarded as a key element required to understand and develop the EHDF system. Currently there is no commercially available software that allows full modelling of electrophoresis in all

aspects, but there are packages (such as COMSOL) that allow implementing defined equations. Verification of the model with appropriate experiments was a necessary step for validation of developed simulations. This would allow for confirmation or exclusion of the first three research hypotheses.

The experiments in the fabricated microfluidic chip required development of an optical detection method. Light Emitting Diodes (LEDs) were used as light source for numerous reasons, mostly due to their adequate spectral properties in conjunction with the ability to correlate these with the absorbance spectrum of dyes. Investigation of the LED properties as well as their novel application was orientated toward the design of a better optical detection system, with increased performance for miniaturized devices. Modern science generally relies on teamwork where different approaches from different specializations are used to solve existing problems. Identification of the problems and solving them, using synergies of different backgrounds. The study of light propagation in capillaries and microfluidic chips as well as the modelling of EHDF presents an example of the application of multidisciplinary approach for developing the EHDF platform for analyte detection. This addresses the fourth research hypothesis.

Advances in Micro Total Analysis Systems (μ -TAS) are regarded as important for the future development of analytical sciences. Microfluidic chips for electrohydrodynamic focusing will require suitable light sources for optical detection systems. Due to the goals of this project (i.e.: simultaneous visualisation of an entire two-dimensional planar chip) there was no previously implemented cheap and popular method to be employed. A one point of detection can be very precise in that point but does not inform about processes in the other part of the chip. The relatively high thickness (10mm) of PMMA layers inhibited easy direct application of conductivity detection. The necessity of whole chip visualisation led to the choice of a digital camera for detection and data acquisition.

The advantages of LEDs over traditional light sources include that they are small in size compliant with miniaturisation and can be powered with batteries. This can allow to integrated EHDF devices to be developed as a new μ -TAS detection platform. A microfluidic chip with a light source integrated in one chip layer and a CCD or CMOS matrix in the opposite is easy to imagine as a possible sensing system. Within this project a novel μ -TAS device based on such a system layout was developed.

The work presented in this thesis has three main research areas:

1. Numerical modelling of processes in COMSOL Multiphysics®
2. Experimental verification of developed microfluidic models
3. Investigation of the light propagation in microfluidic systems

There is no commercially available software that can directly conduct two or three-dimensional simulations of electrophoresis with existing commercial software being limited to one dimension (9; 10). The two-dimensional model was developed from first principles as a simplified portrayal of the general three-dimensional problem. COMSOL is regarded as a user-friendly commercial package for scientific simulations. It has the capability of handling a multitude of physical simulations ranging from acoustics and electromagnetism, through heat transfer, fluid flow, convection and diffusion.

Initially, a numerical recreation of already conducted experiments was performed with COMSOL. This allowed familiarisation with the modelling environment and demonstrated the suitability of the chosen software options for subsequent work. The next part of the project was devoted toward developing a complete model of EHDF for the designed microfluidic chips, with inclusion of the principal theoretical mechanisms that were driving it. Following this the experimental verification of the constructed models was performed. A new microfluidic chip was fabricated and used to validate the modelling. Finally data acquisition from the two-dimensional microfluidic device, and modelling of the light propagation through the microfluidic devices (capillaries and microfluidic chips) was conducted. Results of this modelling were also verified experimentally.

Microfluidics is a relatively new but already well-established branch. Novel methods of illumination using light emitting diodes (LEDs) and laser diodes (LDs) are discussed extensively (11; 12; 13; 14). LEDs have numerous advantages over traditional light sources, namely high robustness, quasi-monochromaticity, low heat emission, low energy consumption and high compliance with miniaturisation making them a “light-source-of-choice” for microfluidic applications (13).

An important aspect of this project was the implementation of data acquisition in used microfluidic chips and visualisation of flow patterns. Optical properties of the microfluidic chips, light sources and image capturing devices needed to be considered in order to design an appropriate optical detection system. Working with aqueous

solutions and with dyes, in a two-dimensional planar microfluidic chip suggested the application of appropriate photographic equipment.

1.4. Gap in the literature filled by this work

This project was inspired by a combination of previously conducted experiments, which indicated the possibility of coexistence of multiple flowstreams in same microfluidic chamber (15). This combined with successful reported experiments employing conductivity gradient focusing (CGF), using a relatively simple device (see Figure 3) (8), led to the supposition of more general category of focusing techniques and to the development of EHDF. EHDF can be regarded as a general technique, whereas CGF is its particular form. In EHDF there is a velocity gradient present inside the microfluidic chamber, while in CGF fluid velocity was constant. Also a different approach for formation of electric field gradient is used in EHDF: not only flowstreams have different conductivity but also different distribution along the chip cross-section.

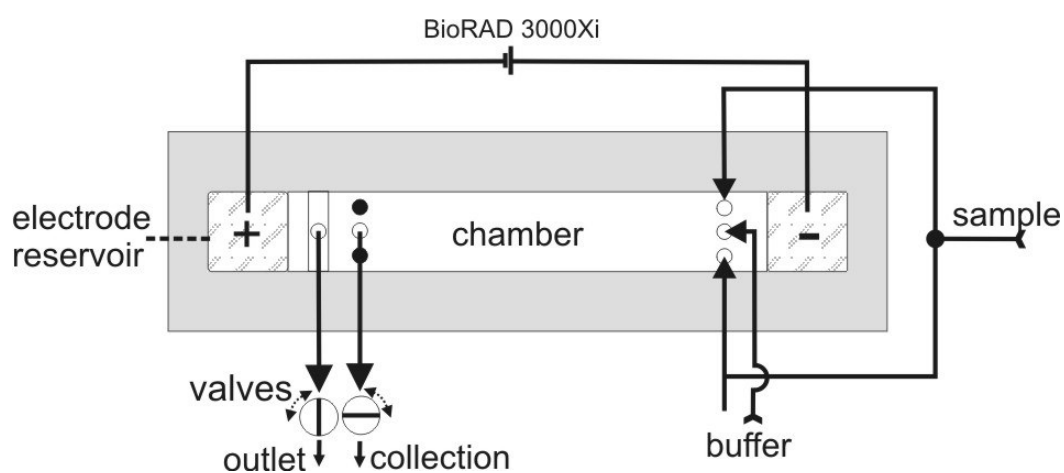


Figure 3: A schemat of microfluidic chip used for generating conductivity gradient focusing, after (8).

This microfluidic device had the form of a rectangular chamber (14cm x 2cm) with a thickness of 200 μ m. This was achieved by placing a micro-scale gasket (spacer) between two sheets of transparent plastic polymethyl methacrylate (PMMA). On the two ends two chambers were drilled and filled with agarose gel that held electrodes immersed in the gel. Difficulties with explanations of two-dimensional electrophoresis observed during experiments with CGF formed the basis in this thesis for development of a theoretical model explaining all properties of the used system. This was addressed in the chapter 4, in section concerning modelling of microfluidic systems.

One of key aspects of work presented in this thesis was the employment of microfluidics. It not only allowed a significant reduction in the amount of used solvents and analytes, but requires consideration of the fundamental changes in the importance of physical properties. Tabeling and others (2; 3) uses the term “microfluidic” to refer to research with at least one linear system dimension being in the order of between 300 to 1 μm (1; 4). Wilkes and others set the lower dimension limit even at 100nm. The change of the scale down to micrometre-size results in a change of the importance of physical properties. For this project the most important aspect is that generally flow in microfluidic systems is laminar. As a consequence, the flow is smooth and gives the possibility of the simultaneous appearance of unmixed fluids in one channel or chamber. The idea of multiple fluids flowing through a microfluidic chip was explored by Dasgupta et al. resulting in series of interesting pictures which are presented in Figure 4 (15).

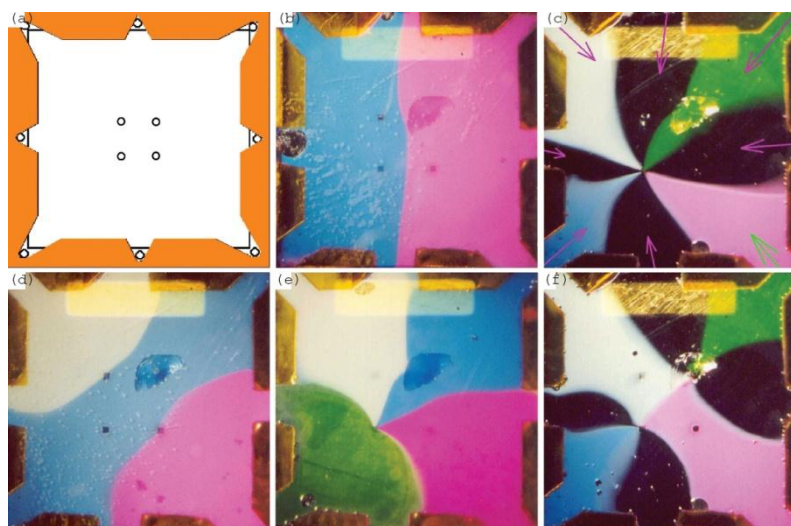


Figure 4: Pictures of flow patterns achieved using pressure-driven flow in microfluidic chip (15).

This experiment was an excellent illustration of the possible co-existence of different flowstreams in the same microfluidic chamber for a relatively large volume (10mm x 10mm, cell volume of 9 μl) as long as a laminar regime was maintained. Also it can be seen in Figure 4 that the formation of even very complicated flow patterns is possible provided appropriate geometry and experimental conditions are employed. Presented results of multiple flowstreams coexisting in one chip were not previously applied for sample separation (15). Application of two flowstreams with different electrical properties combined with shaping of the flow pattern was a key element to achieve successful focusing. The results of microfluidic experiments based on these principles are presented in chapter 5 of this thesis.

1.5. Merits and limitations of the study

- Application of the computer modelling software allows studying of the microfluidic systems in different aspects and gives flexibility not available to traditional experimental systems
- COMSOL Multiphysics software package is a user-friendly environment with numerous adjustable parameters helps identifying potential experimental problems and allows to optimise and the developed system
- Developed numerical model of the EHDF allowed for the prediction of the results
- The developed light propagation model visualised interesting light distribution pattern that can be useful for design and optimisation of capillary-based photodetection and photochemical system
- Numerical models are only an approximation of the real systems and if inadequately defined might produce misleading or physically incorrect results
- Microfluidic devices due to their small dimensions require a high manufacturing precision, which if not maintained may eventually affect the obtained results
- On this step of research the focusing of the only one compound was tested to confirm the research hypotheses and the mechanism of the EHDF

1.6. Scope of the thesis

Chapter 1 is a general introduction to the field of microfluidics applied for sample separation and preconcentration, provides the theme and concepts relevant to the field of study and the thesis, outlines research questions and hypotheses, explains used methodology, unexplored scientific areas and presents strengths and weaknesses of the investigation. In conclusion of the Chapter 1 outlines the scope of the particular chapters in the thesis.

Chapter 2 provides information about current state of knowledge in the areas that are relevant to the thesis: microfluidics, encompassing its brief history, fabrication methods, physical aspects and its applications; different focusing methods, with particular consideration of electrofocusing techniques; numerical modelling including computational fluid dynamics; study of optical detection techniques with application of solid state lighting, especially laser diodes and light emitting diodes. Chapter 2 is concluded by providing information how EHDF is related to the previously published research.

Chapter 3 gives information about used equipment and materials with description of all applied research procedures. The first part of this chapter relates to conducted simulations, with description of used hardware and software and specifies simulation parameters in all presented models. The second part of this chapter provides informations of the developed microfluidic chip, used detection system and individual experimental conditions relevant to all presented microfluidic experiments. The third part relates to modelling and experiments on light propagation and light intensity distribution in microfluidic devices and photopolymerisation of monoliths inside capillaries.

Chapter 4 presents the results of conducted modelling of microfluidic systems. Stating with general assessment of the chosen software and simulation quality, numerical reproduction of previously published experiments and study of the multi-outlet chip properties and development of the optimal chip design for EHDF. This chapter is concluded by presenting the results achieved with the working model of EHDF that was subsequently tested experimentally.

Chapter 5 presents the experimental results obtained with developed microfluidic chip. In the first part of this chapter are presented experiments with chip layout used in numerical simulations and observation of an unexpected phenomenon named “lateral EHDF”. In the second part there are results of studies of formation and equilibration of the lateral EHDF. In the third part are presented results of experiments on lateral EHDF with multiple parallel flowstreams. This chapter is concluded by the comparison of conducted modelling with experimental results.

Chapter 6 presents result of the experimental verification of developed model of the light propagation and light intensity distribution for capillaries. In the first part are presented results of the macro- and micro-scale experiments. In the second part of this chapter an application of the developed model to explanation of the polymerisation within the capillary system is presented.

Chapter 7 presents conclusions for the whole thesis.

Chapter 2 – Literature review

In this chapter, a topical review of microelectromechanics (MEMS) and microfluidics, separations with specific attention on focusing techniques of analytes, different methods of focusing, numerical modelling used in computational fluid dynamics (CFD), illumination and visualisation of the species and application of light emitting diodes (LEDs) for optical detection in microfluidics is provided.

2.1. MEMS and Microfluidics

The first miniaturised chip device was constructed around 1975 and presented in 1979 (16). It was a miniature gas analysis system based on the principles of gas chromatography (GC). The novelty of this device was mostly related to the application of photolithography and chemical etching as micromachining techniques that allowed an unprecedented miniaturisation of the large laboratory device – a gas chromatograph in this case. Achieved results were satisfactory and there was the possibility of performance improvement even within the technology at the time. Despite its small size and rapid separations capability it took almost 25 years to develop the first portable GC system (17), and almost 30 years to couple it with a mass-spectrometer for detection (18). This was due to a lack of deeper interest of separation sciences in applying MEMS and can be attributed to a lack of technological advancement in small device fabrication technology (19). MEMS and microfluidic devices technologies were used extensively in this project and therefore this chapter presents the background of these technologies.

2.1.1. Overview and brief history of microfluidics

In general, the term “microfluidics” is used to refer to all devices that have geometrical dimension typically in order of tens or hundreds micrometres, and which employ fluid flow for its main application (20). Notably, the size definition has also been presented with a lower limit set above 1 micron in 1999 (21), to above 100 nanometres in 2008 (2; 3). This illustrates how rapidly the area of microfluidics is developing. Before the 1990s fluid flow through sub-millimetre channels was discussed in other subject areas such as for fluid transfer in plants (22). In 1990 the novel idea of combining sample handling, analysis and detection in one device was introduced by Manz (23). This is regarded as a major breakthrough and acknowledgement of microfluidic technology as an important quasi-independent interdisciplinary science (19; 24). Initially major

problems were centred on the lack of availability of high pressure pumps compliant with miniaturisation which were needed for efficient transport in microchannels (19). As an alternative electroosmotic pumps were presented, discussed and implemented successfully (25; 26). In 1992 for the first time electrophoresis on a silicon and glass substrate chip were demonstrated (27; 28). After 1994, numerous applications of microfluidics led to the development of range of commercial products from many companies (19). In the mid-90s microfabrication technologies were based on those used in the microelectronic industry (19). Whitesides presented four major pillars that formed a basis for microfluidics development as a quasi-independent science, but definitely, a new technology area (29):

- Microanalytical methods – gas chromatography (GC), high-performance liquid chromatography (HPLC) and capillary electrophoresis (CE) combined with laser-based optical detection
- Need for inexpensive, portable, field-deployable systems to deal with chemical and biological weapons threats
- Need for high throughput methods of microanalysis in molecular biology
- Microelectronics and related technologies for use in microfluidics.

2.1.2. Fabrication methods

New prototyping and manufacturing techniques or their method of application, such as micro-contact printing (30), micro-transfer moulding (31), low temperature bonding (32), and development and application of SU-8 negative photoresist (33; 34), helped engineering microfluidics to cover a broader area of demand especially in chemistry. At the end of 1990's the application of organic polymers begun to revolutionised again the area of microfluidics. Cheap, disposable, easy to produce plastic chips became broadly used and commercialised.

Polydimethylsiloxane (PDMS) chips were introduced in 1993 by Kumar and Whitesides (35). Quick, cheap prototyping method of photolithography with PDMS was presented in 2000 which allowed rapid development and deployment chips for various microfluidic experiments (36). A typically problem associated with PDMS is its porosity and significant gas permeability, allowing vapours created by Joule heating during electrophoresis to penetrate into the bulk material, changing buffer concentration, and rate of electro-osmotic flow (EOF) (3). Typical PMDS chips are made from two pieces of polymer that are bonded together either in a reversible or irreversible manner (36).

Reversible bonding is performed by Van Der Waals contact, which can sustain up to 35kPa. Irreversibly exposing both surfaces to be bonded together by air plasma, and allowing formation of Si-O-Si bonds between the PDMS layers and can sustain typically between 205 to 345kPa (36). Such pressure limits are rather low when compared to modern leading high-end commercial HPLC systems with pressures exceeding 60MPa. Gas permeability and low pressure resilience make PDMS rather unsuited for pressure-driven flows, but electrokinetic driven flow can work very well. The high interest and popularity of PDMS for microfluidic applications can be observed by the number of citations of the pioneering articles. The article with the highest number of citation is “Rapid prototyping of microfluidic systems in polydimethylsiloxane” (37) with 1,793 citations¹, followed by “Fabrication of microfluidic systems in polydimethylsiloxane” (36) with 1,023 citations².

2.1.3. Micro Total Analysis Systems (μ -TAS)

In 1990 Manz *et al.* presented a novel approach to chemical analysis based on microfluidics – miniaturised or micro total analysis system (μ -TAS) (23). The concept of μ -TAS was based on the combination of sampling, sample pretreatment, calibration and detection with a built-in transportation system that would be carrying analyte from the injection point to the waste collection. Initially the idea was not to decrease the size of the sensing system but to increase its separations performance (19; 23). At micrometre dimensions, physical behaviour of the fluid flow changes resulting that a better performance could be achieved with μ -TAS, when compared to more traditional macro-scale laboratory systems. To exploit the full potential of polymer chips, a technology to manufacture vital parts of microfluidic systems such as pumps, valves and mixers was needed. This issue was addressed successfully by Thorsen *et al.* presenting an array of thousands valves and hundreds of individually addressable chambers in a single microfluidic chip (38).

The possibility of better separations efficiency, faster separations and shorter transport time based on miniaturisation and integration with a micro-analytical assembly has been previously presented (23). Later on, the term μ -TAS coming from chemistry origins was broadened to a more general category of laboratory-on-a-chip (or lab-on-chip, LOC). This terminology could be regarded to encompass miniaturised

¹ Retrieved March 7, 2011, by ISI Web of Knowledge

² Retrieved March 7, 2011, by ISI Web of Knowledge

devices that are able to perform various mechanical, chemical and biological tasks, such as synthesis, analysis or treatment of a sample (39).

The μ -TAS as a very rapidly developing field, which requires constant experience exchange and thus in 1994 regular research meetings were started, named “ μ -TAS – the International Conference on Miniaturized Systems for Chemistry and Life Sciences”. Since 2001, RSC Publishing founded new journal entitled “Lab on a Chip” dedicated toward “...significant and original work related to miniaturisation (*on-* or *off-chips*) at the micro- and nano-scale across a variety of disciplines including: chemistry, biology, bioengineering, physics, electronics, clinical/medical science, chemical engineering and materials science, which is likely to be of interest to the multidisciplinary community...” (40)³.

2.1.4. Physics of microfluidics

Sir Isaac Newton’s law of viscosity is presented in Eq. 1, where η is viscosity; τ_{xy} is the force in x -direction on a unit area perpendicular to y ; $\frac{d}{dy}v_x$ is the change of x -component of the velocity along y . Gases and liquids, which follow this law are called Newtonian fluids (41). Newton’s law of viscosity states that shearing force per unit area is proportional to the negative velocity gradient. Microfluidics operates in dimension ranges where a continuity approach is fully valid, and contrary to nanofluidics, no molecular effect has to be discussed (4; 42). Fluids are assumed to be continuous materials incompressible materials, with constant density and viscosity, for which their flow can be described by Navier-Stokes equation (Eq. 2), where ρ is the density, $\frac{\partial}{\partial t}$ is the time derivative; \mathbf{u} the velocity vector; p the pressure; and ∇ is the nabla operator (del operator)⁴.

$$\tau_{xy} = -\eta \frac{dv_x}{dy} \quad \text{Eq. 1}$$

$$\rho \left(\frac{\partial}{\partial t} \mathbf{u} + (\mathbf{u} \cdot \nabla) \mathbf{u} \right) = -\nabla p + \eta \nabla^2 \mathbf{u} \quad \text{Eq. 2}$$

³ Retrieved 9 Mar 2011 from <http://www.rsc.org/Publishing/Journals/LC/about.asp>

⁴ Defined as $\sum_i \delta_i \frac{\partial}{\partial x_i}$

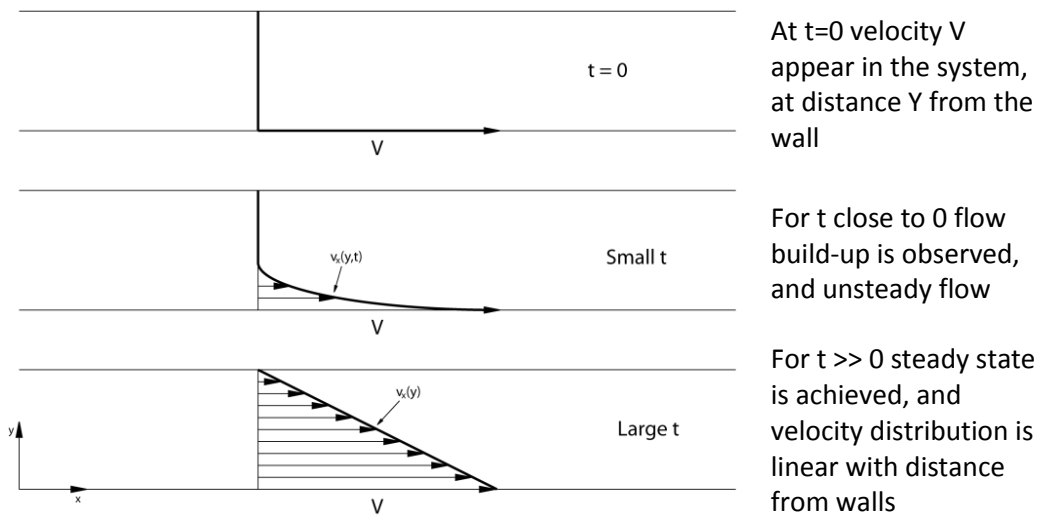


Figure 5: Laminar flow build-up and simplified time evolution of velocity distribution as function of the distance from the wall (after (41)).

Intermolecular forces are the summation of quantum and electromagnetic interactions that in many cases can be expressed in the simplified form of Lennar-Jones potential, see Eq. 3 and Figure 6 (1; 4; 41). At close distances interactions are strongly repulsive but with an increase of the distance become weakly attractive. Typical intermolecular dimensions for liquids are at order of 0.3nm and for gases around 3nm. When compared to typical dimensions of microfluidic devices (order of 10-100 μ m), these can be completely neglected thus allowing the approach of continuous solution fields (1; 4). In microfluidics analytes are carried by a solvent and, although intermolecular interactions are neglected, their effects are not, for example, upon the formation of ions. Ions have a non-zero net charge which is used as a principle element of electromigration.

$$V(r) = 4\varepsilon \left(\left(\frac{\sigma}{r} \right)^{12} - \left(\frac{\sigma}{r} \right)^6 \right) \quad \text{Eq. 3}$$

where $V(r)$ is a potential as a function of distance r , ε is potential depth, and σ is a distance at which potential is equal zero.

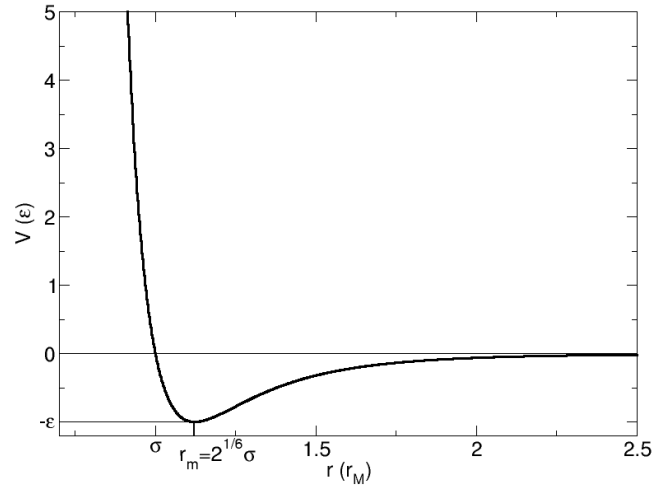


Figure 6: Graph of Lennard-Jones potential $V(\epsilon)$ versus distance $r_m = 2^{(1/6\sigma)}$, where ϵ is maximal attraction energy and σ is characteristic molecule diameter (43).

The scaling of the process is an important subject for chemical engineering. Research conducted in laboratories (analytical scale) typically operates with 10^{-3} litres sized samples, while industrial plants typically use 10^3 litres sized batches. The most relevant up-scaling problems are typically related to heat and mass transfer that can significantly affect overall efficiency of the process (42).

Microfluidic devices are relatively small from our daily point of view. Although the same physical laws regulate the behaviour of the fluids inside microfluidic chip some of them have a much greater importance in micro-scale systems when compared to macro-scale system. The consequence of size scaling on an example of surface forces is considered following paragraph.

As a consequence, volume forces, such as gravity, that are dominant in our daily life become generally negligible on the microscale. Eq. 4 shows that as the linear dimension l goes to the zero ratio between surface forces and volumetric forces goes to positive infinity showing the predominance of surface forces at the micrometre scale (4).

$$\frac{\text{surface forces}}{\text{volume forces}} \propto \frac{l^2}{l^3} = l^{-1} \xrightarrow{l \rightarrow 0} \infty \quad \text{Eq. 4}$$

Janasek *et al.* presents a very detailed method to understanding effects of scaling using dimensionless numbers (42). The most meaningful numbers are:

- Reynolds number, $Re = \frac{v_0 l_0 \rho}{\eta}$ (Eq. 5), where v_0 is tangent linear velocity; l_0 is characteristic linear dimension; ρ is density; η is dynamic viscosity. Re is a ratio

of inertial forces to viscous forces and informs about flow type tendency – laminar or turbulent (41);

- Peclet number, $Pe = \frac{v_0 l_0}{D}$ (Eq. 6), where v_0 is tangent linear velocity; l_0 is characteristic linear dimension; D is the diffusion coefficient. Pe is the number defining ratio of convective to diffusive flux, informs about importance of advection with respect to diffusion (1);
- Fourier number, τ – average number of times molecule contacts the capillary wall (42);
- Bodenstein number Π – backmixing (or axial mixing) within the system (or pressure drop) (42);

Other useful and important dimensionless numbers, provided in excellent review by Squires and Quake (44), are:

- Capillary number as ratio of viscous to interfacial forces;
- Weissenberg number as the ratio of polymer relaxation time to shear rate time;
- Deborah number as the ratio of polymer relaxation time to flow time;
- Elasticity number as the ratio of elastic effects to inertial effects;
- Grayhoff number as the Reynolds number for buoyant flow;
- Rayleigh number as the Peclet number for buoyant flow;
- Knudsen number as the ratio of slip length to macroscopic length;

Using these numbers one can compare an existing or known system of given dimensions to a scaled device and conclude in what way the miniaturised system should work at all. System forces with higher exponents are the first to become less relevant during the system analysis or optimisation.

Quantity	Scaling law
Intermolecular Van der Waals force	l^{-7}
Density of Van der Waals force between interfaces	l^{-3}
Diffusion time	l^{-2}
Fluid velocity, pressure due to surface tension, evaporation rate	l^{-1}
Time, applied pressure	l^0
Capillary force, distance, flow velocity, thermal power transferred by conduction, length	l^1
Electrostatic force, diffusion time, Reynolds number	l^2
Volume, mass, force of gravity, magnetic force with exterior field, electrical motive power	l^3
Magnetic force without an exterior field, centrifugal force	l^4

Table 1: Scaling laws for different physical quantities, after (1) and (45).

The most characteristic feature of flow inside microfluidic devices is its very strong tendency for a laminar flow due to low Reynolds number (Re), typically $Re < 1$ (1; 41; 4; 42; 44; 45). With decreasing Re inertial forces are dominated by viscous forces which results in a steady, non-perturbed flow. For $Re > 1$ the left hand side of Eq. 2 can be disregarded as it is not contributing significantly, leaving a linear Stokes equation (Eq. 7) (46):

$$\eta \nabla^2 \mathbf{u} = \nabla p \quad \text{Eq. 7}$$

As a low Reynolds number results in no time derivative, all motion is directly controlled by the driving force and is symmetric in time, i.e. if any force exerted on the fluid is reversed fluid motion is reversed as well (45). Typically microfluidic devices are characterised by a very low Reynolds number implicating linear and laminar flow within channels and chambers. As miniaturisation increases, inertia plays an even less significant role, and without the nonlinearity provided by the inertial term of Eq. 2, microfluidic flow devices are characterised by predictable and deterministic flow patterns (44).

The ability to contain two unmixed flowstreams in one microfluidic device can be either a helpful or an undesired feature depending on the application. In general mixing occurs due to convection and diffusion. In every day large scale applications convective mixing is predominant. With system dimensions downscaling, convective mixing becomes less relevant compared to the diffusive mixing. The Peclet number (Pe) defines the ratio of these types of mixing. A practical application of low Re and Pe numbers can be, for example, a membraneless H-filter (see Figure 7). In a H-filter, two streams are brought together in one microfluidic channel, and for the chosen channel length, only one species of interest will diffuse across the channel (44; 45).

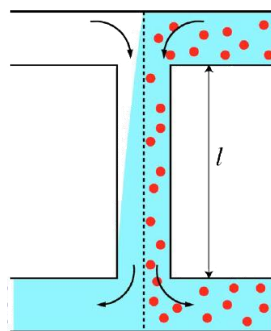


Figure 7: A schemat showing the principle of membraneless H-filter. For a specific length l , only the target analyte (blue) with appropriate diffusivity will merge into the other stream, while impurities (red dots) will be washed away (44).

Many situations require rapid methods of mixing of non-homogenous solutions. This issue has been addressed by many scientists in numerous publications and can be generally grouped in two categories (after (44)):

- Passive mixing, where mixing occurs due to the interaction between the flow and the channel geometry (e.g. staggered herringbone mixer presented by Stroock *et al.* (47))
- Active mixing, where mixing occurs due to the presence of external oscillatory forces (mechanical or electrical) within the channel (e.g. microfabricated rotary mixer presented by Chou *et al.* (48))

2.1.5. Benefits and limitations of microfluidics

Lab-on-a-chip systems were initially developed as an attempt to improve the performance of analytical devices. The first and most obvious advantage of using miniaturised systems is the ability to handle minimum amounts of sample, solvents and reagents thus reducing the amount of waste (29; 39). The ability to work with volumes on the scale of microliters (or less) brings a number of advantages on its own (49; 50):

- Enhanced environmental protection – small waste quantities are easier to handle and will result in less pollution
- Improved economic aspects – solvents and reagents are not cheap, with the reduction of waste comes also reduction of fluid costs and waste disposal costs
- Increased safety – chemicals compounds used in chemical synthesis and analysis are often volatile, harmful or toxic, while smaller volumes are less likely to be dangerous in the case of an accident
- More convenience – miniaturised hand-held devices facilitate operations and allow conducting in-field analysis or diagnose
- Decreasing sample volume size resulted in speeding up analysis, for example for DNA or protein electrophoresis, by an order of magnitude
- Increased detection sensitivity – possibility of detecting single molecule by reducing background signal

Miniature systems allow the integration of multiple units with different functions for reactions, including propelling, mixing, heating, separating and detecting, permitting simplified serial sample processing and the possibility of parallelization for almost no additional cost (see Figure 8) (39). Microfluidic have some limitations, which are related to the generation and control of small feature size, but are not impossible to

overcome. As noted by Whitesides, clinical samples have complex matrices (such as blood) which are typically problematic for analysis (29). Currently there are problems in the analysis of biological species, mostly due to sample preparation and detection. The detection is typically conducted outside of the microfluidic chip typically under a microscope combined with laser-induced fluorescence (LIF). A dominating problem here is the lack of widely available and appropriate miniaturised components and the application of traditional style pumping, valves and power supplies, bottles for solvent and reagent storage, turning small microfluidic lab-on-a-chip devices into heavy, bulky, cumbersome and expensive chip-in-the-lab devices (51).

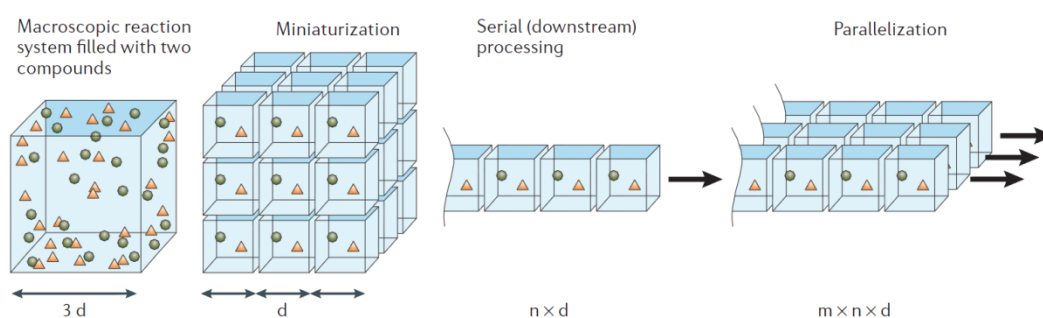


Figure 8: Miniaturisation of fluidic systems allowing for multiple processes and sample detection in biological and chemical applications (39).

2.1.6. Technologies of microfluidic devices

The performance and capabilities of microfluidic devices is dependent on the available technology that is used for fabrication, surface modification and detection (19). Initially micro devices were micro-fabricated in glass and silicon. As time passed and more interest was attracted to the microfluidic field, a wide variety of approaches in manufacturing in different materials were reported. Over 20 years of research developments were covered in a series of review articles (19; 24; 39; 52). These reviews cover almost 2000 journal papers, books, book chapters and conference proceedings, which brought novelty and developed the area of microfluidics. This included descriptions of major advancements in different technologies including micro-contact printing, injection moulding, applications of laser ablation, photopolymerisation, the wide range of photolithographic techniques, different etching methods (electrochemical and plasma), micro-machining, numerous bonding techniques and surface modifications.

2.1.7. Applications of microfluidic devices

Microfluidic devices are most extensively used in chemical and biological engineering. Typical applications revolve around various tasks required for a chemical analysis, synthesis, bioassays, mostly μ TAS-type systems. Typical analytical operations involve sample preparation, injection, fluid and particle handling, separation and detection (53).

Examples of Polymerase Chain Reaction (PCR), measurements of cellular metabolism and flow cytometry using microfluidic chips were presented before the year 1993 (54; 55; 56). Subsequently several electrophoretic separation modes such as Micellar Electrokinetic Chromatography (MEKC) (57; 58), Free Flow Electrophoresis (FFE) (59; 60) and capillary gel electrophoresis (61; 62) were successfully tested in microchips. During this period microfluidics was also applied to biological testing such as high-speed DNA sequencing and separation (63), novel PCR systems (64; 65) and blood serum analysis (66). Detection techniques were focused on absorbance, fluorescence (67), electrochemoluminescence (68; 69) and particle counting (70).

After the year 2000, a multitude of new methods and applications employing microfluidics were presented. Numerous methods of sample preparation have been reported, including: sonication and mechanical cell lysis (71; 72), degassing (73; 74), free flow isoelectric focusing (75; 76), DNA purification from blood (77; 78), microdialysis (79; 80) and liquid-liquid phase extraction (81; 82). Recently more complex systems such as high throughput microfluidic processing (83), coupling of SPE with various techniques such as MEKC or PCR on chip (84; 85; 86), or completely integrated analysis systems entitled "sample-in answer-out" (87) were presented. Typical recent biological applications of microfluidics include DNA purification (88; 89), single molecule isolation (90; 91), sequencing (92; 93), separation (94; 95) and analysis (96; 97), protein preparation (98; 99), cell selection (100; 101), cell lysis (102; 103), cell cytometry (104; 105) and cell separation (106; 107). Microfluidics is gaining popularity in clinical diagnostics, in applications for simultaneous measurements of several biomarkers (108), biomarker detection straight from blood using disposable chips (109), detection of pathogens, reverse transcription PCR (rt-PCR) and toxin detection in whole blood (110). One of the novel and potentially revolutionising microfluidic development is the technology of microdroplets extensively discussed elsewhere (111).

2.2. Focusing

Giddings argued, that separation is as old as the earth, probably as old as the universe itself (112). Separation processes are responsible for formation of celestial phenomena from stars and planets to galaxies and superclusters. Different separation methods accompanied development of human civilisation throughout the ages. From food processing, through plant extract acquisition, dyes, flavours, medicine extraction to metallurgical processes, some kind of separation was required. Separation for analytical purposes dates back to the invention of the chromatography by Tsvet in 1903 (113). Within 100 years, separations became complex, important and an informative branch of science. Today separation sciences are successful in attempting to answer the most basic questions about our life, its origins and history as well as being routinely used in forensics, hospitals and pharmaceutical industry for diagnostic, quality control and product development applications.

Microfluidic separations present new possibilities for separation sciences but are typically currently limited to electro-driven flow and thus are typically compared with capillary electrophoresis (CE) separations. CE is a well-respected separation technique and has numerous advantages such as high efficiency of sample separation, small size that enforces reduction of chemical reagents and solvents and small requirements for sample size. Despite these advantages CE had not been widely introduced for industrial uses except for highly specialised applications such as DNA and protein separations (114). A typical disadvantage associated with the application of CE is the loss of sensitivity when using the most popular photometric detectors. Path length for optical detection is of comparable size with the capillaries used and is in range of tens of micrometres. With the tendency to use of smaller diameter capillaries, which is beneficial for separation efficiency, optical detection becomes more problematic. As the capillary internal diameter decreases, the length for absorption decreases as well making absorbance-based techniques less accurate. Developments in the field of pre-concentration have led to 100 to 1000 fold improvement of detection sensitivity (115).

2.2.1. Overview of different focusing methods

Giddings categorised separation techniques into nine basic categories (112). He introduced chemical potential profile μ^* as the sum of external field effects and intermolecular reactions which he divided into three subcategories of potential profile: continuous (*c*), discontinuous (*d*), and combined (*cd*). As an independent variable he

took flow field and divided it into three categories: static/non-flow (S), flow perpendicular to μ^* gradient (F_{\perp}), and flow parallel to μ^* gradient (F_{\parallel}). The nine separation technique categories based on these defined parameters are presented in Table 2 .

		Chemical potential profile μ^*		
		Continuous (c)	Discontinuous (d)	Combined (cd)
Flow profile	Static/ non-flow	Electrophoresis Isoelectric focusing Isotachopheresis Rate-zonal sedimentation Isopycnic sedimentation	Extraction Adsorption Crystallisation Distillation Evaporation Sublimation Ion exchange Dialysis	Electrodeposition Electrostatic precipitation Electrolytic refining Electrodialysis Equilibrium sedimentation
	$(F_{\perp} \mu^*)$ gradient	Elutriation Countercurrent electro-phoresis	Filtration Ultrafiltration Reverse osmosis Pressure dialysis Zone melting	Electrofiltration
	$(F_{\parallel} \mu^*)$ gradient	Hyperlayer field-flow fractionation	Chromatography Countercurrent distribution Fractional distribution Foam fractionation Multistage two-phase processes	Field-flow fractionation Thermogravitational separation Electrodecantation

Table 2: Nine basic categories of separations (112).

It is a well-known phenomenon that a fluid tends to fill available space. It is particularly valid for gases. One can observe this process in liquids as the colour changes after adding a small sample of colour dye until whole volume reaches the same colour. With removal of all such convective effects, observation of this phenomenon led to the discovery of Fick's first law (Eq. 8), formulated in 1855 (116). Giddings presents the full derivation of Fick's first law from first principles reaching to its well known form (112):

$$J = -D \frac{dc}{dx} \quad \text{Eq. 8}$$

$$\text{where } D = \frac{RT}{f} \quad \text{Eq. 9}$$

where J is flux density; D is diffusion coefficient; $\frac{dc}{dx}$ is concentration gradient. The diffusion coefficient D is related with more fundamental properties in Nernst-Einstein relationship (Eq. 9), where R is gas constant, T is the temperature and f is the friction

coefficient. Studies of transport within a concentration profile led to Fick's second law (Eq. 10):

$$\frac{\partial c}{\partial t} = D \frac{\partial^2 c}{\partial x^2} \quad \text{Eq. 10}$$

Afterwards he considered a 1-dimensional space with a sample of concentration c located at x_0 at time $t=0$, where the concentration profile can then be represented by the following function (Eq. 11):

$$c(x, t) = F(t)e^{-g(t)(x-Wt)^2} \quad \text{Eq. 11}$$

where $c(x, t)$ is concentration dependent on time and space; $F(t)$ and $g(t)$ are unspecified functions time dependent only; W is overall component velocity (sum of drift velocity due to external fields and flow velocity); t is time. This form of the concentration profile allows reduction of the concentration function to a δ -function⁵ as $t \rightarrow 0$ (117). The full analytical solution gives a Gaussian concentration profile (Eq. 12) as a valid solution for the basic diffusion model:

$$c = \frac{n}{\sqrt{4\pi Dt}} e^{\left[\frac{-(x-Wt)^2}{4Dt}\right]} \quad \text{Eq. 12}$$

where n is the number of moles (or molecules) and other symbols as noted previously. The most important conclusion from Eq. 12 is that a Gaussian concentration profile (peak) in the absence of external forces will broaden in time and decrease in its height (112). Focusing in general is an attempt to prevent or minimise this effect.

In this work the emphasis was on electro-focusing methods. Ivory grouped separation techniques into four major categories: isocratic, isotachic, non-equilibrium gradient (NEGM) and equilibrium gradient methods (EGM) (118). He pointed out that EGM methods are unique due to their ability to simultaneously separate and concentrate the target analyte. Moreover EGM are characterised by the existence of a self-correcting stationary state independent of the initial conditions.

⁵ $\delta(x) = \begin{cases} +\infty, & x = 0 \\ 0, & x \neq 0 \end{cases}; \int_{-\infty}^{+\infty} \delta(x) dx = 1$

2.2.2. Isocratic separations

The typical isocratic (equal strength) separation technique is known as High-Performance Liquid Chromatography (HPLC). The sample is injected as a short pulse into a separation channel and driven through by hydrodynamic force (pressure). Constituents separate by either differential migration or by partitioning into a second (stationary) phase. Isocratic separations are characterised by a steady increase of a sample peak variance (σ^2 for Gaussian profiles), while effective zone width w ($w=4\sigma$) is proportionate to square root of variance. As a result the displacement between peak maxima increases more quickly than the peak width itself and separation can occur (112; 118). An inconvenience associated with isocratic separation is that there is no mechanism that could prevent or diminish diffusion. Peak broadening is irreversible in purely isocratic methods, see Figure 9.

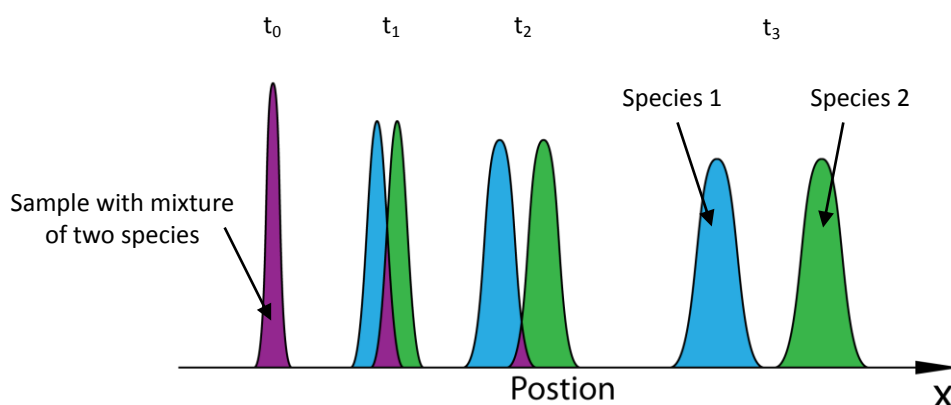


Figure 9: Diagram of isocratic separation (peaks not to scale), after (118).

2.2.3. Isotachic separations

Isotachic (with same speed) separations can be electro-driven – known as isotachopheresis (ITP) or pressure driven – known as displacement chromatography (118; 119). A general principle of isotachic separations is that the species are separated according to their velocities, which is a function of mobility in the mobile phase, from the fastest to the slowest one. As separation occur the first analyte to leave the system is the one with the highest velocity, which was attained due to the highest mobility of the species. In isotachopheresis it is effective ion mobility, which depends on other variables, such as pH, temperature or viscosity (120).

In ITP, initially the separation channel is filled with the leading electrolyte which is composed of the highest mobility ion mixed with a counter-ion⁶ characterised by a good buffering capacity. The sample is introduced between the leading and a terminating buffer which has the lowest mobility of all ions in the system. Afterwards voltage is applied to both ends of the separation channel during which continuous supply of the terminating buffer is provided. Ions are separated according to their velocities v (effective mobilities μ); the fastest ion of the leading electrolyte comes out first (μ_{max}), followed by the slower ones of the sample, until only the ion of the terminating buffer is present (μ_{min}). Forward and rear edges of zones are constantly refocused by the presence of the electric field gradient on the border between electrolytes (120; 121). Figure 10 shows schematically zone formation during ITP. Due to the self-sharpening of zones, isotachic separations are an excellent choice as a first step in multidimensional separations. Moreover, ITP is the only known isotachic separation that has a stationary state when used in conjunction with pressure-driven flow. Applying a counter-flow velocity between the leading and terminating buffer operator can stop outflow at any desired point (118).

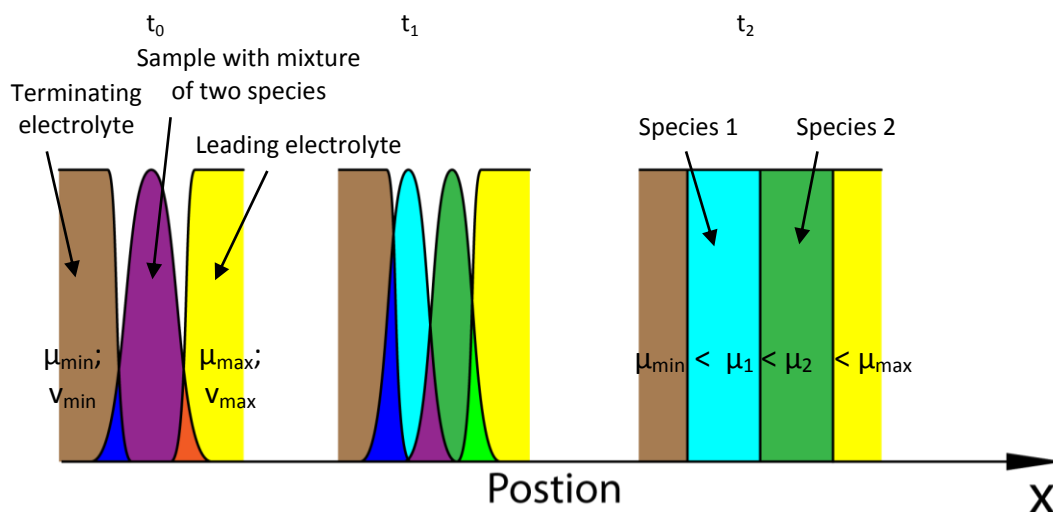


Figure 10: Diagram showing formation of separate zones during isotachopheresis, after (118).

2.2.4. Non-equilibrium gradient methods (NEGM)

Non-equilibrium gradient methods are generally gradient-elution adsorptive chromatographies (122). The NEGMs ability to focus components to high concentration and separate peak at very high resolution is due to the presence of a non-stationary gradient that travels along the separation channel (chromatographic column). The

⁶ Counter-ion is an ion of the opposite sign provided in the leading electrolyte

presence of this gradient is sufficient to prevent zone dispersion and form sharp peaks. A benefit of NEGM is its ability of peak's self-sharpening which allows correction after temporary increment of dispersion (see Figure 11). NEGM does not have stationary state formation and typically requires some additional length of column to allow formation of a slowly changing quasi-steady state (118).

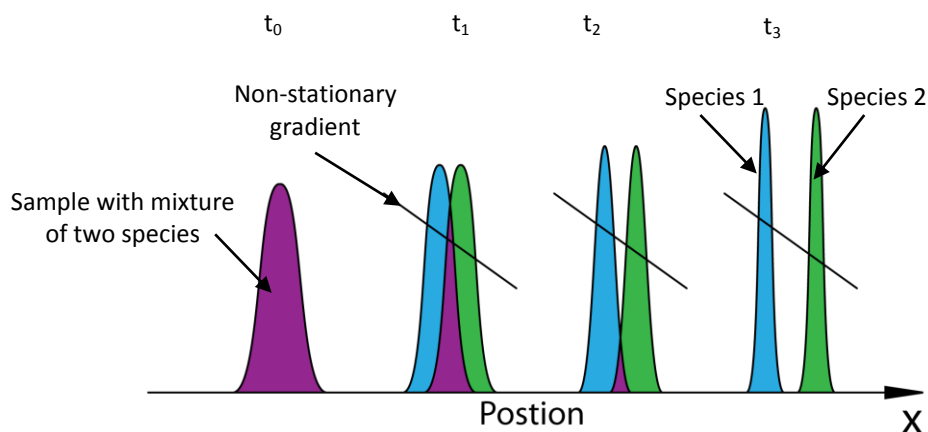


Figure 11: Schematic of formation of separate peaks in non-equilibrium gradient method. As it is shown gradient travels together sample along separation channel, after (118).

2.2.5. Equilibrium gradient methods (EGM)

Equilibrium gradient methods employ the fact that in the presence of an external linear gradient of “restoring force” for every compound in the solution, the flux equation predicts the existence of Gaussian peaks centred on a unique focal point. A typical “restoring force” is an electric field, schematically shown in 1D in Figure 12. The focal point for the analyte is where the restoring force is zero. Outside the focal point the restoring force is non-zero and increases in value with distance, always pointing toward focal point. Without diffusion, the stationary state of the peak shape would attain a δ -function as $t \rightarrow \infty$. Including diffusion peak assumes a Gaussian shape, as diffusion is overcome and any molecule moving outside the equilibrium zone is moved back by the restoring force prevailing over diffusion. This gives one of the fundamental advantages of EGMs – an existing stationary state independent of the initial sample conditions. In other words, peak position and shape is not a function of time, while in other chromatographic methods they are (118).

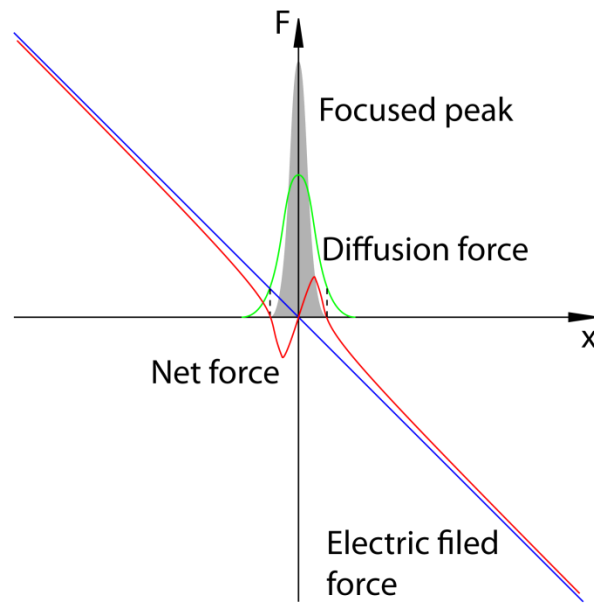


Figure 12: Schematic of peak formation around focal point by net force (red) as a sum of external force gradient (blue) and diffusion force (green). Peak shape coloured with grey, after (123).

Typical well-established EGMs are Isoelectric Focusing (IEF) and Counteracting Chromatographic Electrophoresis (CACE). Isoelectric focusing is a separation technique for zwitterionic analytes or ampholytes – ionic species with ability to become cation or anion depending on pH of the environment. To achieve IEF separation a separation channel is filled with a pH gradient in which the sample is placed. After applying an external electric field the particular species migrate toward their respective isoelectric points (IeP) – the only place where they attain electric neutrality being no longer susceptible to a force imposed by electric field. When a molecule departs from its IeP, it immediately attains a charge due to the different pH and is pushed back toward its IeP (120; 121).

Another EGM technique is known as Electric Field Gradient Focusing (EFGF). The general idea behind EFGF is the application of the electric field gradient by specific device geometry, being balanced by constant convective force. The idea of using a non-uniform electric field to improve the performance of electro-separations has been previously reported. Different approaches were tested, such as area-shaping (124; 125), electrode shaping (126) (127), and the use of multiple electrodes (128). In previously reported EFGF work a Plexiglas cylinder with funnel-like cavity was used with an internal dialysis tube placed at the system symmetry axis (123; 127). The area between the Plexiglas funnel and the dialysis tube was filled with electrolyte to permit current flow. The dialysis tube was used to allow interaction with the electric field but to prevent

contact between the sample and buffer. On the top and bottom surfaces, electrodes were attached. Cross-sections of the channel with smaller area have a higher current density and thus electric field density. The shape was adjusted to achieve a linear electric field gradient (see Figure 13) (123; 127) .

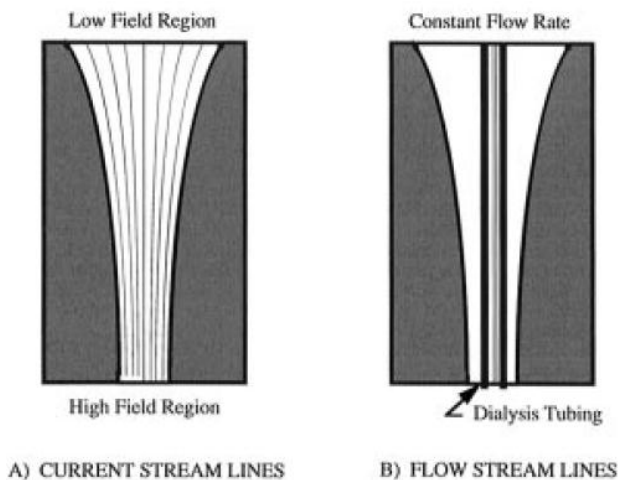


Figure 13: Cross-section of EFGF focusing unit showing current lines (A) and flow lines (B), (127).

2.3. Modelling

2.3.1. Modelling of fluid dynamics

Fluid dynamics is one of the areas where computer simulations can help very significantly. There are two general approaches in fluidic simulations. The first one is based on the infinite possibility of divisions and does not take into account the molecular shape of matter. These types of models are called continuum models. Good accuracy is maintained as long as the properties can be defined as averages over large elements and compared to the size of the molecules therefore making them appropriate when working in macro- and mesoscale (characteristic dimension is above 50 nm) (4). Continuum models are regarded as easier to implement, as they are based on traditional mathematical equations describing material properties, such as heat transfer, fluid motion etc. For a brief history of computers see Appendix A.

The second approach is established on the molecular structure of the matter. This type of simulations uses either deterministic or statistical approaches to describe molecular movement. Such models could be regarded as superior, due to calculating properties such as position, momentum and velocity of all particles at the same time, giving more realistic results, but are not practical in many applications due to limitation of computational power (21; 129).

2.3.2. Computational Fluid Dynamics (CFD)

Some experiments with fluid flows require difficult conditions to implement, while some are close to impossible to conduct. Lack of accessibility to the measurement point or alterations of the experiment itself due to the presence of measuring equipment are typical experimental difficulties. In such cases instead of problematic experiments, a simulation method can be employed (130).

Mathematical modelling is an attempt to describe properties of a system using the language of mathematical formulas (131). Computer modelling is a branch of mathematical modelling where either analytical solutions would take very long to calculate or are not possible to obtain such that some approximations are needed. Initially mathematical modelling was limited to continuum models, somehow per definition, as solving differential equations was one of the first tasks for computers. Early molecular models were developed already in the 1960s (132). Solving problems with continuum model approach in fluid dynamics requires solving of nonlinear partial differential equations (PDE) (such as Navier-Stokes equations) or integro-differential equations, which are still not possible to solve analytically in general form. Although known for over a century, they are still analytically solvable for a narrow quantity of cases.

Employing the computational power of modern machines allows solving many problems not analytically, but rather approximately using numerical methods. The general interest in numerical methods gave birth to the Computational Fluid Dynamics (CFD) as a field of fluid dynamics that relies on numerical simulation using either custom derived programs or commercially available packages. Modern computers deliver high computational power which can be easily employed to solve approximately a set of PDEs using numerical methods (133). Currently there are several commercial packages available for microfluidic simulations such as: CFD ACE+, ANSYS CFX, ANSYS FLUENT, FLOW 3D and COMSOL (134; 135; 136; 137).

CFD has several different methods of solving PDEs that rely on a certain number of similar or even identical techniques. The commencing element of any numerical simulation is a mathematical model that describes the problem as well as possible with available knowledge. Some simplifications are already included in this step, such as limiting the number of dimensions.

The first key element to solve numerically any equation is the discretisation of the solution space where a given macro-field equation is approximated by set of algebraic equations. This gives a limited number of discrete locations in space and time where numerical results are calculated. The quality of discretisation highly influences the final quality of the simulation. The most significant methods are Finite Difference Method (FDM), Finite Volume Method (FVM) and Finite Elements Method (FEM) which are described in Appendix B. Other noteworthy methods are Boundary Elements Method (BEM) and Lattice Boltzmann Method (LBM). After selecting discretization type, a coordinate system (Cartesian, cylindrical, spherical or other) is chosen and numerical grid (also called mesh) based on the discretisation method is composed. There are several types of mesh that can be employed:

- Regular or structured mesh, the simplest mesh structure, where each grid line crosses any other only once. In such grid each grid point (vertex) is uniquely assigned with the number of indices equal to the number of dimensions.
- Block-structured mesh is a grid type with at least two different grids combined together. This type of meshing can be used for precise divisions around points of interest and a coarser grid where high gradient changes are not expected.
- Composite mesh is a sub-type of block structured mesh where two (or more) grids are overlapping.
- Unstructured mesh is generally any that does not fall into any of previous categories. There are no strict rules about the number of lines and crossings, and a single mesh cell can have a different shape along the entire solution domain. The most typically encountered shapes are triangular and tetragonal for 2D geometries and tetrahedral and hexahedral for 3D geometries.

After generation of the geometry an approximation method, solver and convergence criteria are chosen. In the case of commercial packages, these features are typically limited to a certain number as provided by the software developers (130).

There are several properties of a simulation that have to be achieved in order to recognise the numerical approximate solution as the correct one. The error introduced by approximation at a point, called the truncation error, tends toward 0 as the distance between vertices goes to 0. A method with such solution is called consistent. A next

criterion for correct simulation is numerical stability, defined as the lack of magnification of errors that appear during the process of numerically solving the problem. Numerical methods have potential loss of precision at every step. A method is considered stable when all accumulated errors do not influence the overall result. The numerical method must display convergence of the solution. The appearance of artificial sources and drains that are affecting overall simulation must be avoided. The next important quality is boundedness understood as displaying only physically reasonable values, avoiding for example negative mass or concentration. Numerical methods should display realistic solutions as they are not exact experiments and giving extreme conditions may result in meaningless or non-physical solutions (130; 138).

2.3.3. Independently developed modelling software

Computers gave the opportunity to simulate processes that are very difficult and modelling of electro-migration is a good example. The most commonly used theory of electrophoresis was developed by Smoluchowski in 1903 (139). First attempts to simulate electro-migration problems date back to the mid-1970's, after (140). Following the popularisation of personal computers in 1980s, several researchers started intensive work in this field. Works of Thormann, Mosher, Palusinski and others paved way for modern simulations of electromigration (141; 142; 143; 144; 145). Numerical simulation studies led to the development of software used for the investigation of ITP, adsorption effects, thermal effects and migration in microchannels (146; 147; 148; 149; 150; 151). Non-commercial freeware programs for Capillary Zone Electrophoresis (CZE) "Peakmaster" and for more general one dimensional electrophoresis "SIMUL" were developed by Gas *et al.* (9; 10). Works of Ivory *et al.* on a modelling of the focusing shows a practical approach in the application of commercially available packages as well as good agreement of developed simulations with experimental results (118; 152; 153; 154; 155).

2.3.4. COMSOL Multiphysics software

COMSOL Multiphysics® is a commercial software environment based on the Finite Element Method, designed for simulation problems up to three dimensions defined in partial differential equations. First version of COMSOL appeared on the market at end of 90's. Currently it is well established brand in scientific software especially for engineering applications (137). One of the most important features of COMSOL is its ability to handle different problems simultaneously, such as flow and heat

transfer, in the form of the interface called multiphysics. COMSOL has a set of predefined computational modes (like Incompressible Navier-Stokes mode, Brinkman Flow mode, or Nernst-Planck mode) which are particular forms of generic PDE's. COMSOL also allows using the general forms of PDEs with full liberty of defining all terms in the equation. PDEs can be defined in general, coefficient or weak form depending on needs.

COMSOL is well-recognised software in the market of simulation packages. There are hundreds of scientific papers from various disciplines where COMSOL was successfully used: from purely numerical simulations of MEMS, through studies of biological to physics and chemistry applications. (156; 157; 158; 159). There are reported applications of COMSOL for simulating electrokinetic flow in two-dimensional planar microfluidic devices, focusing with ITP or simulations of hydrodynamics in microfluidic systems and others proving reliability and effectiveness of that software in chosen field (160; 161; 162).

At the start of the project, COMSOL presented a unique feature of modelling fluidic subjects with the possibility of implementing any user-defined PDEs combined with significant database of examples from the field of microfluidics. Later on with version 3.5a, a Nernst-Planck mode for electromigration modelling was implemented, which was not available in other leading commercial packages.

2.4. Illumination for visualisation – choice of Solid State Light (SSL) sources

2.4.1. Light sources in chemistry

The potential of LEDs as light sources has been gradually recognised in research including chemical sciences. LEDs have become competitive light sources in optical analytical techniques such as photometry and fluorometry as well as in photochemistry and other areas. As the technical parameters of LEDs continuously improve, a growing number of applications of LEDs in chemistry can be anticipated. With increasing radiative power and life expectancy and decreasing wavelength and cost, LEDs are getting increasingly attractive as alternative light sources to the classical deuterium xenon and other lamps, both in chemistry research and in the industry (163; 164). The number of scientific papers on LEDs published per year has been growing on an exponential scale as shown in Figure 14. The number of publications on LEDs was below

500 publications per year in 1970s and 1980s, even with a declining trend. Then in 1991, the introduction of the blue LED presented a breakthrough in the LED technology and is clearly represented by the growth seen in Figure 14. The last bar represents only a 27 months period already exceeding output of the 1999-2003, 60-months period. For a brief history of Solid State Lighting see Appendix C. For physical principle of LEDs see Appendix D.

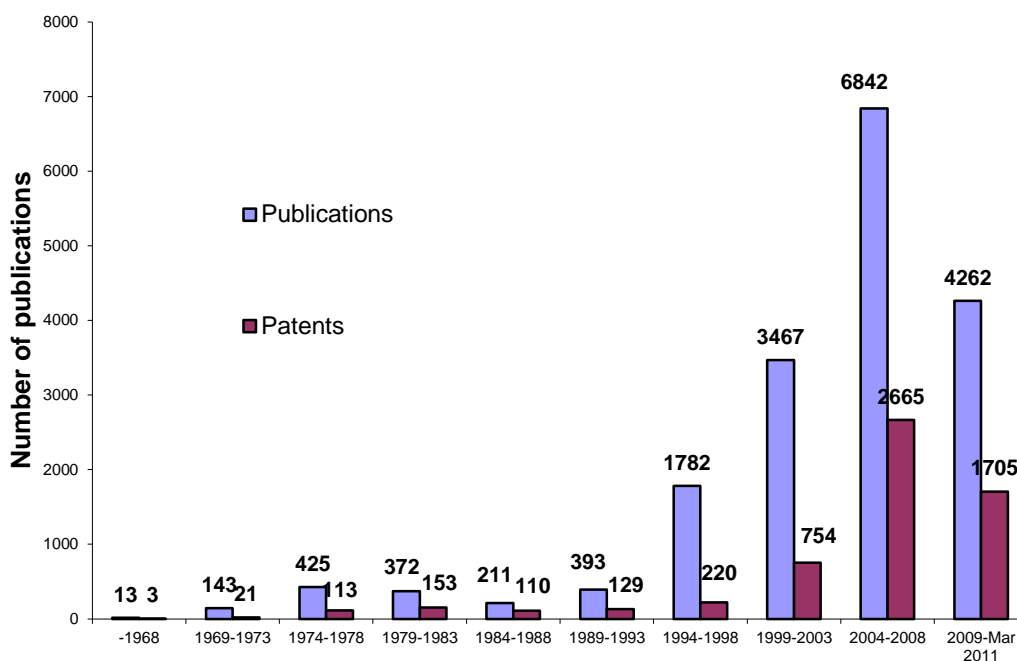


Figure 14: Number of publications and patents for LEDs from 1960 till 2008. Search conditions: Sci Finder Scholar database (Apr 2011), search topic "Light emitting diodes".

2.4.2. Advantages and limitations of LEDs

Justifiably, solid-state (semiconductor) light sources are the light sources of tomorrow. LEDs possess numerous merits that make them increasingly popular in science in general and in chemistry specifically, including: very low prices for well-established LEDs, robustness of solid state technology including long life expectancy, small size compatible with miniaturisation, relatively low power consumption and heat production, cold light sources exhibiting low radiative heating, very low optical noise etc. In the following sections the technical parameters of LEDs in respect to their use are discussed. Some features of light emitting diodes can be either beneficial or undesirable depending on the specific application. Especially deep-UV-LEDs are still at a stage of development and therefore some shortcomings must be mentioned.

The low cost, around or even below \$1 for visible spectral range of emission is a very important advantage of LEDs. Evolution of the prices for LEDs during the last years clearly indicates the trend of decreasing prices for LEDs in the visible emission spectrum range down into UV spectral range. Another benefit is virtually no maintenance is needed for solid state light sources. Only UV-LEDs are still considered expensive with 2011 prices of up to several hundred of \$ per unit (165).

Typical a commercially available light emitting diode has the form of a plastic (the most commonly used is epoxy resin) cylinder with diameter ranging from 3 to 10 millimetres with an integral hemispherical lens at the end (166). They are waterproof and compared to classical light sources such as glass bulbs extremely shock resistant. Some still suffer minor problems such as delamination of epoxy from the chip through temperature cycling which has been suggested is induced by the process of mounting of LEDs (167; 168; 169). One of the future directions of research is the application of ceramic materials with special attention to the mounting process to improve thermo-mechanical properties of LEDs (170).

Light emitting diodes are now providing to the longest working life light sources available. The average life expectancy of LEDs exceeds 10^5 working hours however this life time is achieved when the LED is operated under optimal thermal conditions. With increased ambient temperature LEDs present shorter life expectancy, therefore accelerated tests of lifetime of LEDs are conducted at increased temperature (171; 172).

LEDs have far better scaling properties than incandescent, fluorescent or arc light sources. LEDs are the only light sources considered for any highly miniaturised devices requiring illumination. Consequently on-chip microfabricated LEDs have found utilisation in optical detection in lab-on-chip microfluidic chips (120; 173; 174). A demand for even smaller light sources led to the development of micro-LEDs with a diameter in the order of $10\ \mu\text{m}$ (175). The possibility of using such small light sources opens a new chapter for portable detection devices.

Incandescent and fluorescent light sources have low energy conversion efficiencies resulting in the remainder of the supplied electrical energy being converted to very significant amounts of undesired heat, both radiatively emitted and convectively dissipated. The higher Overall Energy Conversion Efficiency (OECE) of LEDs quasi-monochromatic nature of light is free of undesired infrared radiation. LEDs are heated by the electrical current and convective heat can be observed. LEDs operating in the

ultra violet range are still burdened with several technological problems that result in a high degree of heating of the diode. For instance the external quantum efficiency is lower by two orders of magnitude when compared to blue LEDs. Further due to requirement of wide bandgap carriers can easily undergo non-radiative transition (176). AlGaInN is expected to provide better efficiency for UV emission, but the quality of crystal structure is generally insufficient, resulting in an inferior performance of AlGaInN LEDs over AlGaN (177).

Today SSL sources offer higher luminous efficacy than incandescent light sources in 1999. Currently the most luminous LEDs have reached luminous efficacy of 169 lm/W (178). A typical white 5 mm LED as one of the most common of all LEDs, consumes 80 mW while having a luminosity of 18-20 candelas (165) while the newest super-bright LED consumes 100 mW, giving 25-30 candelas. The OECE reaching 50.8 % for some white LEDs makes SSL the most energy efficient light sources ever manufactured.

Possibly the largest benefit of using LEDs in mass scale is very significant reduction of electricity consumption (179). Ireland was the first European country to ban traditional incandescent light bulbs and it was estimated that it will reduce electricity costs by €185 million and emission of carbon dioxide by 700,000 tons per year (180). By definition LEDs require a direct current power supply but responding to market needs there are currently efforts undertaken to construct LEDs capable to be driven by alternating current. Although mostly at a stage of laboratory research, there have been already reported successful constructions (181).

The optical noise is a combination of several factors: spatial stability, intensity stability, output at a specified wavelength, electronic power source noise, temperature fluctuations, mechanical stability of optics etc. Generally LEDs provide a far more stable signal than traditional light sources (182). Considerably lower overall fluctuations of the emitted light intensity result in lower signal noise thus lowering the limits of optical detection as illustrated in Figure 15 (183). Therefore the usage of LED based optical detectors showed an advantage of using solid state light sources over classical light sources such as deuterium, mercury and tungsten lamps (184; 185; 186).

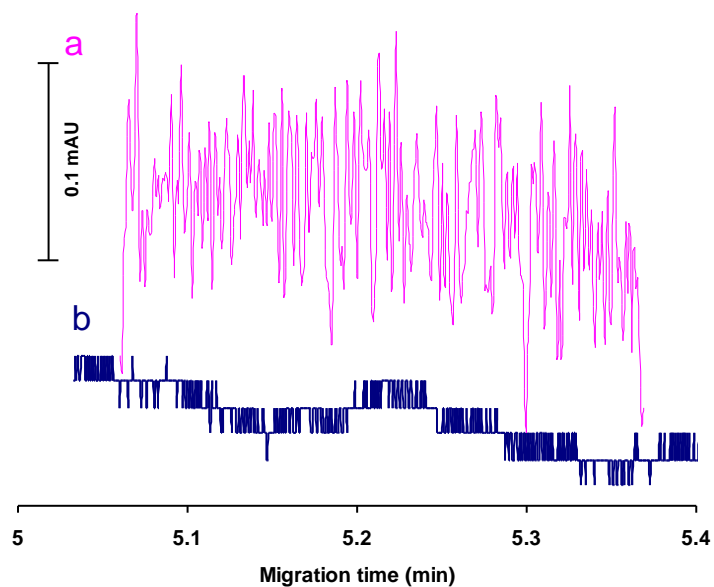


Figure 15: Comparison of signal stability for deuterium lamp (pink) and LED (blue). Signal coming from traditional light source (pink) has significantly larger fluctuations of intensity compared to solid state light source (184).

Well defined narrow band emission spectra of LEDs exhibit typically full width at half intensity maximum (FWHM) bandwidth of around 20-25 nm. It has been shown that this degree of polychromacity of the emitted is applicable for analytical applications such as absorption photometric detection in capillary electrophoresis (186; 187). For most chemistry applications this size of LED emission bandwidth is narrower than the absorption bands of most compounds in solutions and therefore LEDs can be fully acceptable as quasi-monochromatic light sources. They include photochemistry applications (again the typical absorption bandwidth of a compound in solution will be broader) and photometry and photometric detection in flow-through detectors in analytical methods including FIA, CE and LC (174; 188; 189; 190; 191). For other applications, such as fluorometry, where the longer-wavelength portion of the emission spectrum would be interfering with a sensitive detection of the red-shifted emitted light, high quality cut-off or band-width filters have to be additionally applied (192). By the end of 2010 the lowest commercially available wavelength was 245 nm thus defining the limits of the chemistry applications (166), and 210nm is still being developed (193).

Whenever a broad spectrum light source is needed, such as for illumination with white light, visualisation and spectrophotometry, so called white LEDs may be employed. White LEDs are realised in two ways, both of which are commercially available: (i) “RGB LEDs” - combined LEDs containing multiple LEDs with different wavelengths of peak emission within one bulb – a blue, a green and a red emitting chip,

as illustrated in the emission spectra for a 'RGB LED' in Figure 16; (ii) Phosphorus-based white LEDs, based on a blue or UV LED and a broad-spectrum phosphorescence compound admixed to the LED bulb that creates a combined emission spectrum with a peak in the blue region of the visible spectrum and a wide band with a maximum in the green region but reaching well into the red region, thus giving a white light appearance. Depending on the application, either RGB or phosphorus-based white LEDs can be used, but it is important to realise that solid state light sources are not yet true wide-bandwidth emitters.

To make a comparison of different white light sources possible, the Commission Internationale d'Eclairage (CIE) introduced temperature definitions of four standard sources of the white light: A - tungsten at 2856 K, B - direct sunlight of approximately 4870 K, C - overcast sunlight at 6770 K and D65 - daylight at 6504 K (194). In phosphorus-based white LEDs the ratio between the heights of the first maximum in the blue and the second maximum in the green region is described by the temperature of the emitted light. LEDs with a white light temperature of 9000K (cold white) will have an intensity of the blue emission peak significantly higher than the green one, while an LED with a light temperature of 3000 K (warm white) (Figure 17) will have a more intense green peak than blue (195). A different approach is based on additive colour synthesis - white light is obtained by combining three diodes (red, green and blue) in one case ()). The advantage of the RGB white LED is a possibility to mix different relative intensities of the blue, green and red light components. The three emitters can be operated separately (there is 1 common electrode, and an opposite polarity electrode is provided independently for each chip (165) giving more flexibility over light temperature than in phosphorus-based LEDs.

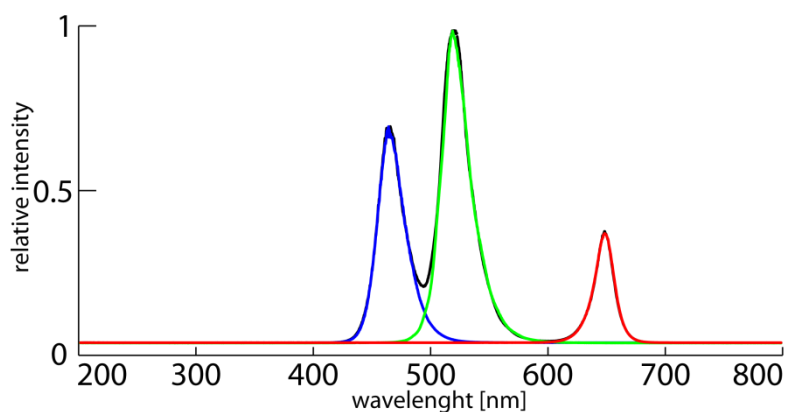


Figure 16: Example of the measured spectrum of RGB-type white LED (three different diode chips red, green and blue in one casing.

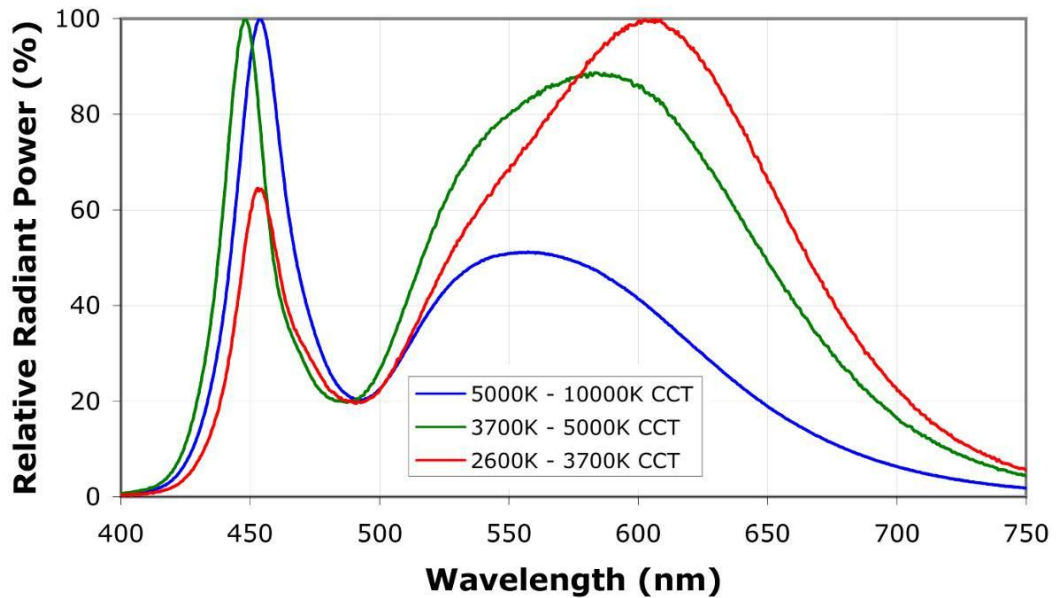


Figure 17: Emission spectra of white 'blue + phosphorus' LEDs: 3 different LEDs of varying light temperature: blue line – cold white; green – neutral white; red – warm white, CCT – Correlated Colour Temperature (195).

LEDs (unlike lasers) do not emit coherent light and in principle are not directional light sources. Currently used photon extraction techniques, especially the application of a reflector on one side of the semiconductor chip, results in these LEDs are pseudo-directional light sources. The high refractive index of used semiconductors (even up to 3.5 in InGaP) also contributes to much higher directionality of emission (196; 197). Also optical elements affixed in front of the emitter or in the form of a hemispherical lens integrated with the polymer body of the LED provides some degree of collimation, and is one of the most vulnerable parts to damage and loss of transparency.

2.5. Detection and data acquisition

An important aspect of the work presented in this thesis is data acquisition from the developed microfluidic chips and visualisation of flow patterns. Microfluidic chips require novel design to provide appropriate or enhanced optical detection systems. Working with aqueous solutions, often dyes, suggests the application of optical detection systems.

Imaging of large two dimensional microfluidic structures can be easily performed using appropriate photographic equipment. In order to design a properly working detection and imaging system for whole-chip visualisation a good

understanding of optical detection techniques, light properties, available light sources and photodetectors is needed.

2.5.1. LEDs in photometric detection

Photometry is a detection technique used to determine concentration of target species in a liquid sample based on interaction between the probe light and species. Typically it is a measurement of the light intensity before and behind the sample or more commonly with and without a sample placed in the light path. A scheme of the light intensity measurement with the sample located for detection is presented on Figure 18. The sample transmittance T is defined as a ratio of the initial light intensity I_0 to the recorded light intensity I (Eq. 13). The I_0 should be measured with the sample holding cuvette empty to correct its value for reflections and potential absorption by the cuvette material. The cuvette length l is known, as well as species molar absorptivity coefficient α , which is an individual characteristic of every species. Light attenuation along the light path is governed by Beer-Lambert's law (Eq. 15) (198):

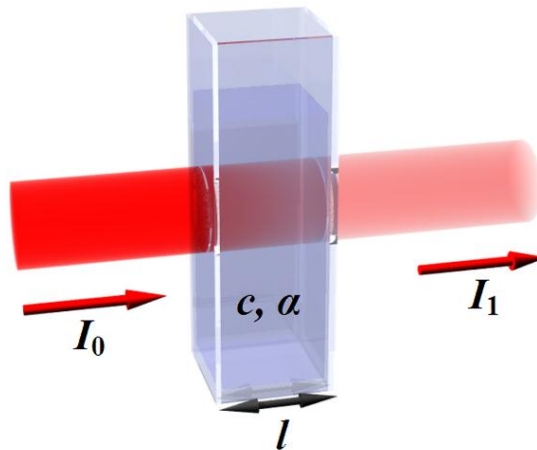


Figure 18: Schematic of light intensity with sample located for photometric detection (199).

$$T = \frac{I_0}{I_1} \quad \text{Eq. 13}$$

$$A = -\log T = \log \frac{I_0}{I_1} \quad \text{Eq. 14}$$

$$I(l) = I_0 \cdot e^{-\alpha c l} = I_0 \cdot e^{-A} \quad \text{Eq. 15}$$

where T is transmission through the sample, I_0 is initial light intensity, I is light intensity behind the sample, A is sample absorbance, α is the species molar absorptivity coefficient, l is length and c is molar concentration.

For optical detection (absorbance measurements) in photometry LEDs can be used as light sources and as LED-based optical detectors. A narrow peak emission wavelength is the key in a photometric detection system, which relies on a matching of the emission intensity maximum with an absorbance maximum of the analyte. Matching spectra lowers the limits of detection and in consequence improves the performance of the detector. As LEDs provide almost monochromatic light they are very appropriate for photometric detections. The small size of these light sources makes them attractive for miniature analytical devices.

The first application of LED for photometric detection was presented by Flashka *et al.* in 1973, but according to authors the first experiments were proposed by Barnes in 1970 (191; 13). The first flow through LED detector was presented by Betteridge *et al.* (200). While the first successful attempt to use light emitting diode coupled with photodiode detector was presented by Anfalt *et al.* (201), this setup was developed and significantly upgraded by Dasgupta and co-workers making photodiodes the most common detectors for LED based photometry (202; 203; 204; 205; 206; 207; 208; 209; 210). The first use of blue LED as a spectroscopic source was presented by Hauser and co-workers (211; 212; 213; 214). A simple reflectometer for colorimetric diffuse reflectance measurements based on green LED was presented by Matias *et al.* (215). LEDs as an almost heatless light source was use for first time in absorption and detection system in capillary electrophoresis by Tong and Yeung in 1995 (216). Subsequent works by Macka *et al.* had shown that light emitting diodes present better stability than tungsten, mercury or deuterium lamps (187). Over the last decade LEDs were used in miniaturised photometric detectors for capillary electrophoresis resulting in lower base line noise and improved detection limits (164; 181; 217). A very simple and effective way of detecting the effective pathlength and stray light has been suggested by Macka values for which would be used to evaluate detector's performance (218).

Several experiments conducted with LED-based detectors showed the broad application of such constructions (185; 219; 220; 221; 222). The use of LEDs in photometric detection is growing as LEDs are becoming better and more widely available. Light emitting diodes were also tested in paired setups with one LED used as the light source and the second acting as the photodetector. The first attempts were

based on the measurement of LED photocurrent which was acting as the photodetector (223; 224; 225). Lau *et al.* presented a novel approach where instead of measuring photocurrent a timer circuit was implemented and discharge time of the photodetector LED was measured. The benefits of such an approach included removing the necessity of using an analogue-digital converter and operation amplifier (226; 227; 228; 229; 230).

Fabrication of a simple flow-through multi-wavelength absorbance/fluorescence detector with additional spectroelectrochemical detection has been suggested by Dasgupta *et al.* (164). LED based broadband photometers have been tested for several years but they have still not been widely accepted commercially and are still a small margin of commercial products (231; 232; 233).

2.5.2. LEDs in fluorometric detection

Fluorescence is defined as a luminescence of the medium that immediately after an excitation is extinguished, typically $\approx 10^{-8}$ s (234). This categorisation comes from times when it was not possible to observe such short events. Currently there is entire branch of fluorometric techniques relying on measurements of the emission spectra decay times (163).

The phenomenon of fluorescence is associated with changes of the electronic states under the influence of an external light. Electrons in the compound molecule move from ground state to excited state upon absorbing light. After reaching the excited state they can return to ground (or less excited) state producing light emission. The difference in energy of initial and final state determines the wavelength of the absorbed/emitted light (Eq. 24). The probability of transition between two states was first explained by the Franck-Condon principle, stating that probability of the electronic transition is proportional to the overlap of the wave functions of both states (235; 236)(Figure 19). Later on it was significantly developed by Jablonski, who is regarded as the father of fluorescence spectroscopy. He presented a theory why absorption and emission spectra are often not symmetrical. Diagrams named after him Jablonski diagrams, are often the starting point for discussion about light absorption and emission and are excellent to show processes occurring in excited molecules (234), see Figure 20.

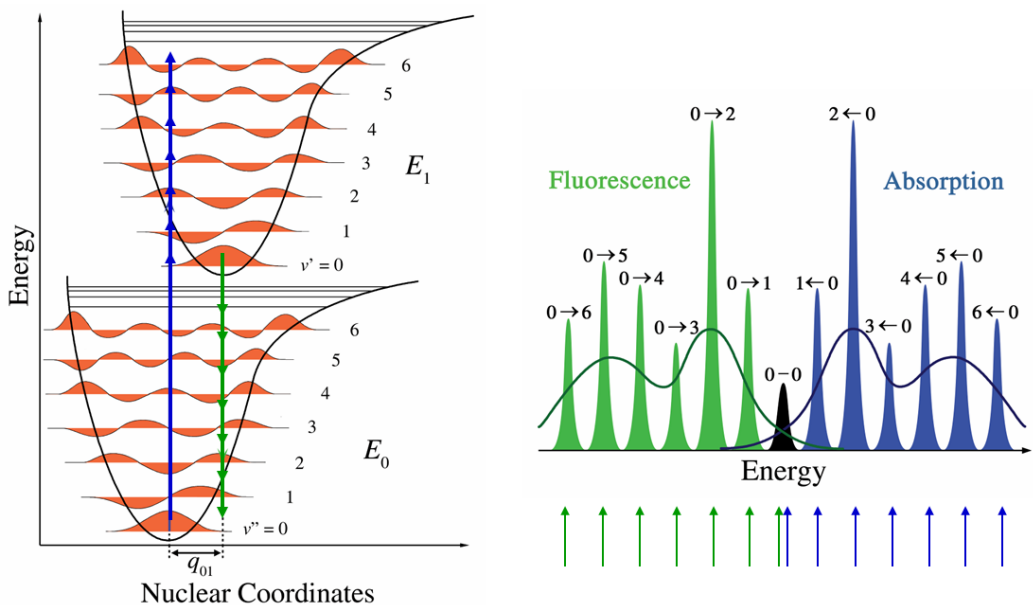


Figure 19: Illustration of Franck-Condon principle. Blue arrows represents light absorption, green arrows represents light emission. Peak height represents transition intensity. Transitions within E_1 states are not marked (237).

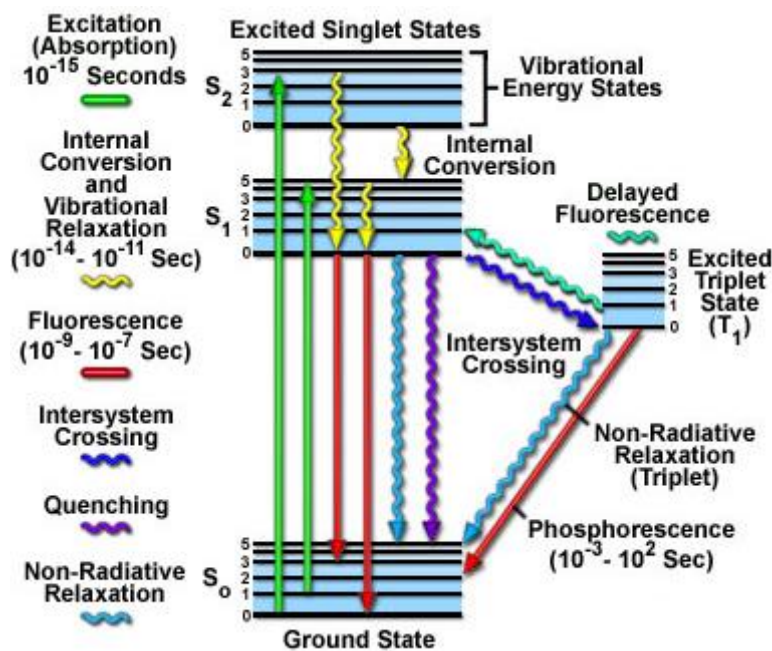


Figure 20: Jablonski diagram showing the most important transition types within illuminated fluorophore (238).

The most important light source for fluorometry is the laser, although with recent breakthroughs in LED construction and materials sciences, resulting in lower emission wavelengths and increased power, light emitting diodes are gaining significant popularity in this field. LEDs are currently used as powerful alternatives to lasers for both time and frequency domain fluorometry. The possibility of direct modulation, their stability resulting in low optical noise, and robustness are principal factors for using LEDs

in fluorometry. First attempts of application of the fast pulsed (300 MHz) LEDs in frequency-domain fluorometry dates back to the year 2000 (239) and 2001 in frequency-domain fluorescence microscopy based on LED illumination (240). Experiments with fast pulsed LEDs conducted by Herman and Vecer show that light emitting diodes can be used in frequency domain fluorometry (241).

LEDs suitable for time-resolved fluorometry have been available for a significantly longer period of time. There are several time-resolved techniques which are explained in detail elsewhere (163). UV-LEDs present an alternative for xenon flash lamps or nitrogen lasers. The most important features giving LEDs the edge over previously mentioned light sources are the reduction of delay time for time-resolved techniques from 60 μ s to 1 μ s and much faster repetition rate (242).

The hindering factor for the application of LEDs in fluorometry is the bandwidth of emitted light (excitation) that can overlap with the emission spectrum (243; 234). In this case the use of commercially available LEDs with built-in filters is needed. Such experiments were conducted by Dang *et al.* (244; 245; 246) and Lucy (247). Another approach was presented by Uchiyama and co-workers. Instead of using sophisticated focusing optics integration of LEDs in chips was presented with only spectral filters used to narrow down emission spectrum (248). The combination of multiple LEDs with different peak emission wavelengths was tested in the field of Excitation Emission Matrix Spectroscopy (EEMS) by Hart and JiJi (249).

A novel approach by using combination of three detection modes was presented by Ryvolova *et al* with a detector measuring simultaneously absorbance, fluorescence and contactless conductivity (250). In presented design the same LED was used as the light source for absorbance photometric detection and as the excitation source for fluorometry.

2.6. Electro-hydrodynamic focusing (EHDF) as a development of EGM methods

Electrohydrodynamic focusing is an equilibrium gradient method of focusing and can be regarded as a development of electric field gradient focusing (EFGF) (127). EHDF has been used for the generation of liquid droplets, by application of large electrical potential difference (251), and has been considered for application in the semiconductor industry (252).

The idea of EHDF is based on the further development of successful experiments with conductivity gradient focusing (8). For CGF, the microfluidic device used in (8) had the form of a rectangular chamber (14cm by 2cm) with a height of 200 μm , made by placing a microscale gasket (spacer) between two sheets of transparent plastic polymethyl methacrylate (PMMA). On both ends two chambers were drilled to be filled with agarose gel and to hold the electrodes. Three inlets and two outlets were placed in the chip. The device was initially filled with 0.2mM malachite green solution (MG) with a conductivity of 71 $\mu\text{S}\cdot\text{cm}^{-1}$. The same concentration of malachite green was introduced through auxiliary inlets (labelled “sample” in Figure 2) with a flowrate of 15 $\mu\text{l}\cdot\text{min}^{-1}$. The central inlet was used to introduce 20 mM citrate buffer (pH 4.9, 403 $\mu\text{S}\cdot\text{cm}^{-1}$) with a flowrate of 2 $\mu\text{l}\cdot\text{min}^{-1}$. A schematic of the used apparatus is presented in Figure 3 (8).

Initially the collection valve was closed and the outlet valve was open. Three separate parallel flowstreams formed inside chamber, as shown in Figure 21, in proximity to the inlets. After 300 seconds a potential difference of 280V was applied. After 1980 seconds, the voltage was turned off, and the sample was collected through the collection valve. The concentration of the sample was determined using absorbance photometric detection. The authors pointed to the fact that the presence of regions of different conductivity affects the electrical field which is deflected toward the central region of higher conductivity. As a result, migration of MG toward the central flowstream was observed to the point where electromigration was equilibrated by pressure driven flow and a region of increased concentration of MG was formed. The development of a numeric model to visualise the electric field distribution of that experiment was mentioned as the direction required for future research.

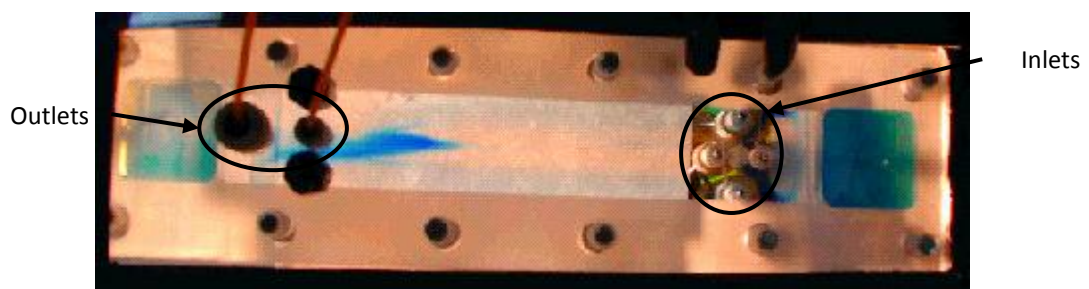


Figure 21: Photo of a microfluidic chip with region of preconcentrated malachite green using field gradient focusing (253)

2.7. Conclusions from the literature review

In this project the control of multiple fluid flows in microfluidic devices and the detection of said flow patterns were investigated. Presently all practical methods of

focusing in microfluidic devices have been based on physical boundaries restricting flow patterns. In this project the implementation of dynamically shaped regions of high and low conductivity giving ability to alter not only intensity but also the shape of the electric field was investigated. The application of unrestricted fluid flow with the simultaneous presence of multiple flows in one microfluidic chamber was not previously explored thoroughly and presents a novel area of research. Due to this fact the computer modelling of processes was selected as the first step of the research to provide constrains for engineering of the microfluidic chip. In the next step fabricated chip was cross-referenced with the developed model to check the model validity and observe actual performance of EHDF.

Successful identification of the significance of parameters for EHDF in “open space” designed microfluidic chips gives the potential for development of a new generation of chip-based microfluidic devices which could be used for preconcentration and separations. Determination of low-abundance components in complex matrices is a difficult and important problem for science and industry. Development of a method with the potential for full automation could provide a replacement for expensive and time-consuming methods of sample preparation.

Investigation of modern optical detection techniques using cutting-edge light sources is important for developing effective sensor and detectors. The main aim of the visualisation part of this project was to gain knowledge for designing novel optical detection systems such as required for imaging on the microfluidic chip used in the experiments.

Chapter 3 – Materials, methods and procedures

This chapter presents the general materials, consumables, chemicals, instruments and procedures used during the research. Results and discussion are presented in the subsequent chapters.

Section 3.1. provides details on the hardware and the software used for numerical modelling, outlines model development procedure, justifies values of used physical parameters and gives all the individual parameters and conditions for all models presented and discussed in this thesis. Results of these simulations are presented in the Chapter 4.

Section 3.2. gives information about the microfluidic chip used for EHDF experiments; all instrumentation and chemicals used with these experiments; outlines the method of concentration calculation using digital camera and the spectrophotometer; provides details on used different sets of outlets; and gives individual parameters for all presented experiments. Results of these experiments are presented and discussed in the Chapter 5. Full photographic documentation of all conducted experiments is given in Appendix I.

Section 3.3. details the methods of calculation the light path and the light intensity distribution in the developed numerical model for the light propagation, outlines experimental procedure with which this model was verified and provides information on photopolymerisation of organic monoliths inside the capillaries. Results of this modelling and experimental work are presented in the Chapter 6.

3.1. Numerical modelling of microfluidic systems

3.1.1. Computers used

A custom-built computer PC-class was assembled to gain a maximum performance for modelling. This consisted of a motherboard Asus® P5E64 WorkStation Evolution, processor Intel® Core™2 Quad Q9450, cooler Zalman CNPS9500A-LED Aero Flow, RAM memory 4GB DDR 3 OCZ PC3-10666 Special Ops Edition, graphic card Asus® GeForce ENGTX 280/HTDP/1Gb DDR3 PCI-E, hard disk drive 2x Seagate Barracuda 7200.11 ST31000340AS 1TB 7200 RPM 32 Mb Cache SATA 3.0Gb/s 3.5" working in Raid

0 mode, optical drive LG 20x DVDRW +/- SATA, power supply unit Antec TruePower Quattro 850W 80PLUS, case Antec Nine Hundred. The operating system used was Microsoft® Windows XP™ 64-bit version 2003, Service Pack 2.

3.1.2. Software used and model procedure development

All fluidic simulations were conducted using COMSOL Multiphysics® 3.5a standard commercial package modelling software with Chemical Engineering Module and MEMS Module (for microelectromechanics and microfluidics) developed by COMSOL AB, Stockholm, Sweden.

3.1.2.1. Model design

COMSOL has a simplified CAD design interface for model drawing. There are no precision drawing tools in COMSOL, but it is possible to implement user defined grid with Snap-On function. This allows drawing simple shapes, but becomes awkward or impractical with more complicated shapes. Some geometries are too complicated to be replicated precisely with this interface. In such a situation it is possible to import a designed geometry from any CAD software with standard *.DWG or *.DXF format. A typical schematic drawing in COMSOL is presented in Figure 22. Once the designed geometry is ready it is possible to add or remove simulation modes.

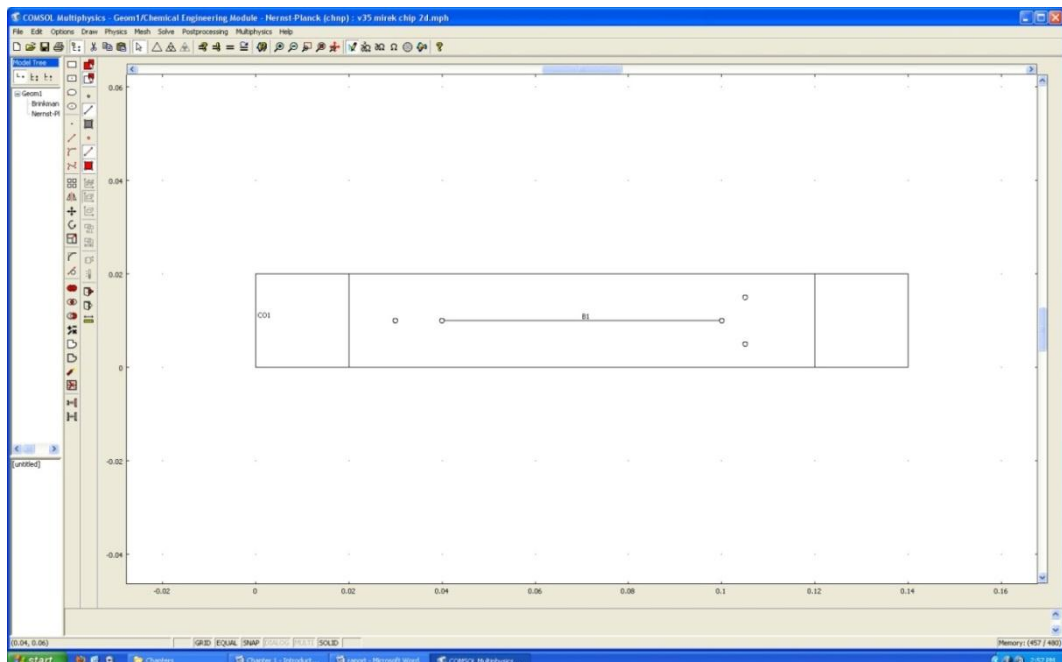


Figure 22: COMSOL drawing interface with typical drawing of the EHD focusing chip.

3.1.2.2. Subdomain definitions

The finished drawing contains a set of regions separated by lines. In COMSOL these regions are called subdomains and relevant equations specified in each region are solved inside thereof. Boundary conditions are defined on these lines. Subdomain settings describe appropriate physics for the associated part of the model and can have the form of constants or space and/or time-dependant functions.

Momentum transport modelling was performed with application of “Incompressible Navier-Stokes” mode or “Brinkman Equations” mode (for simulations involving flow through porous media). Mass transport was modelled with “Nernst-Planck with the electroneutrality condition” mode. For Navier-Stokes and Brinkman flow modes, water with density, $\rho = 1000 \text{ [kg}\cdot\text{m}^{-3}]$ and dynamic viscosity, $\eta=0.001 \text{ [Pa}\cdot\text{s]}$ was used. Diffusion coefficients, electrophoretic mobilities and charge used in Nernst-Planck mode are presented in Table 3:

Name	Diffusion coefficient (isotropic) d	Electrophoretic mobility μ	Charge z
Malachite green	$3\text{e-}10 \text{ [m}^2\cdot\text{s}^{-1}]$	$1.12\text{e-}13 \text{ [mol}\cdot\text{s}\cdot\text{kg}^{-1}]$	+1
Tris(hydroxymethyl)amino-methane	$6.667\text{e-}10 \text{ [m}^2\cdot\text{s}^{-1}]$	$2.69\text{e-}13 \text{ [mol}\cdot\text{s}\cdot\text{kg}^{-1}]$	+1
Chloride	$2.032\text{e-}9 \text{ [m}^2\cdot\text{s}^{-1}]$	$8.02\text{e-}13 \text{ [mol}\cdot\text{s}\cdot\text{kg}^{-1}]$	-1

Table 3: Physical parameters of substances used in models with Nernst-Planck mode.

The entire model domains were drawn on a 1:1 scale, see Figure 23. Three subdomains were defined: one and three as the agarose gel tanks and subdomain two was microfluidic chamber. In subdomain three inlets and two outlets were placed. The entire model consist two layers: the momentum transport was solved with a Brinkman equation for flow through porous media and mass transport solving Nernst-Planck equation. The line between central inlet and outlet 2 (called a “virtual object”) had no physical property and was used to increase mesh density locally.

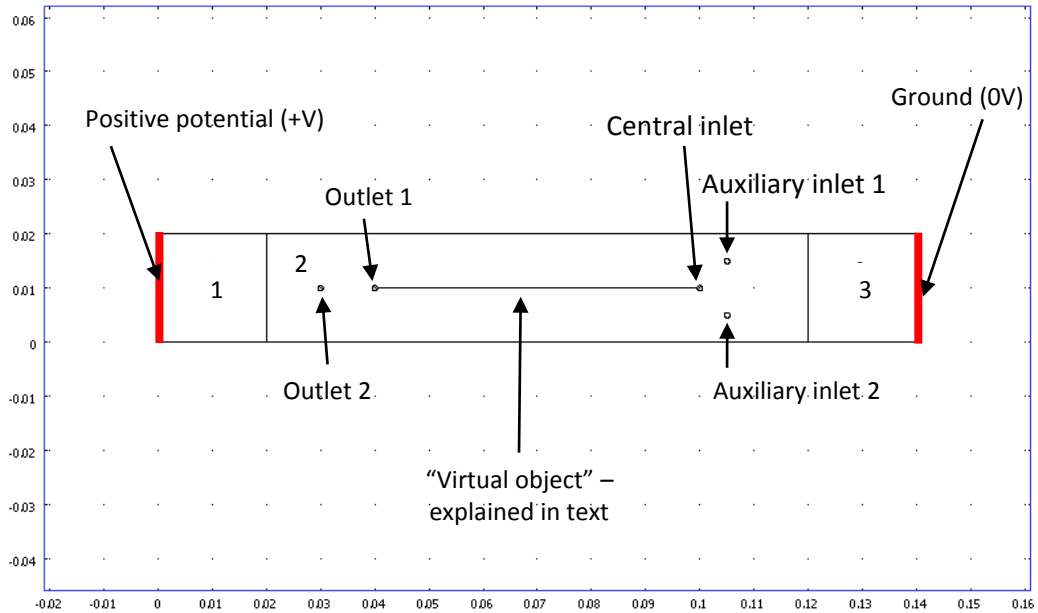


Figure 23: Engineering schematic of the model used for simulations.

The presented model is a two-dimensional approximation of the three-dimensional problem. It assumes that along Z-axis (perpendicular to the model plane) the boundaries extend to the infinity. As in fluid dynamics dimensions that are in order of magnitude of microns can play a significant role, to model fluid flow properly in a thin channel an approximation was needed. To address this problem Brinkman flow mode was used instead of Incompressible Navier-Stokes flow mode. A defined parameter of channel permeability was set to simulate the influence of channel thickness on the fluid flow.

Subdomains one and three were filled with porous media (agarose gel) for which permeability was approximated using the Blake-Kozeny equation (Eq. 16):

$$f = 150 \cdot \frac{\eta(1 - \xi)}{\rho v D_p} \quad \text{Eq. 16}$$

where f is permeability, η is dynamic viscosity, ρ is fluid density, v is fluid velocity, D_p is average gel spherical “particle” diameter, and ξ is volume of empty space (occupied by the pores) per medium unit volume (gel porosity). This equation reproduces experimental data for flow through porous media of identical spheres of given diameter for laminar flow. Sometimes a value of 180 determined from experiments is recommended instead of 150, and then this equation is called Carman-Kozeny (254). For modelling it was assumed that agarose gel was composed of 100 nm spheres and had

90% porosity (void space). Modelled solutions were highly diluted (up to 20 mM/l) and did not contribute significantly to different density and viscosity values.

Subdomain two (main chamber) had three inlets: two auxiliary through which model dye (cationic) and a central inlet through which a buffer was introduced. Only initial concentrations of the dye and the cation in buffer were set in the model. COMSOL automatically adjusts concentration of anion to satisfy electroneutrality.

All models were developed to account for the physics of the electromigration process and no buffering or pH changes were implemented.

3.1.2.3. Boundary definitions

Boundaries for the designed model were of two types: outer boundaries which impose limits and were set according to desired properties (i.e.: walls, inlets, outlets and electrodes) and internal boundaries (between subdomains) on which the continuity requirements were set. COMSOL enforces continuity condition on an internal boundary if a constitutive equation is to be solved in adjacent subdomains.

Boundary conditions, similarly to the subdomain settings, can have the form of a constant value or space and/or time-dependant functions. Features such as inlets and outlets are defined through appropriate boundary conditions.

The velocity for auxiliary inlets was set to $2^{-4} \text{ m}\cdot\text{s}^{-1}$ (malachite green) and the central inlet velocity was set to $2^{-5} \text{ m}\cdot\text{s}^{-1}$ for (buffer). Corresponding experimental values were $15 \mu\text{l}\cdot\text{min}^{-1}$ and $2 \mu\text{l}\cdot\text{min}^{-1}$ respectively. The thickness of the gasket used to produce the chip thickness was $200\mu\text{m}$ and the chamber width was 20mm , which gave a cross-section of 4mm^2 . For a flowrate of $15 \mu\text{l}\cdot\text{min}^{-1}$ with flat profile, a velocity of $3.75 \text{ mm}\cdot\text{min}^{-1}$ is required to satisfy the mass conservation in a time unit. When the flow is pressure driven, then flow profile is parabolic rather than flat, which leads to a situation as shown in Figure 24. This data leads to the integral equation shown in Eq. 17.

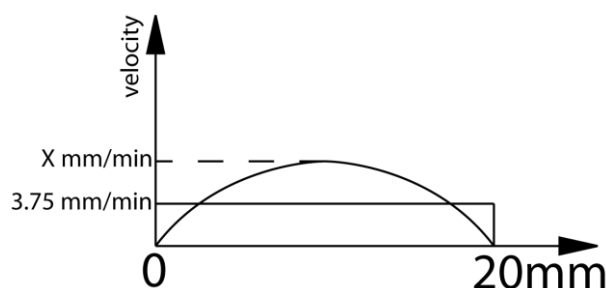


Figure 24: Schematic of the plan view of the velocity profile inside a microfluidic chamber.

$$\int_0^{20} ax(x-20) dx = 75 \quad \text{Eq. 17}$$

Where a is unknown parameter defining the parabolic flow, integration interval is defined by chip width (20mm) and 75 is the surface area given by the chip width and velocity of flat profile ($3.75\text{mm}\cdot\text{min}^{-1} \times 20\text{mm}$).

Solving this equation give $a = -\frac{9}{160}$ and maximum velocity $v = 0.09375 \left[\frac{\text{mm}}{\text{s}} \right]_{x=10}$ which is $5.625\text{mm}\cdot\text{min}^{-1}$. This approximation (correction of the velocity due to parabolic flow profile along only two dimensions) showed that the assumed values were of the correct order of magnitude (i.e. between $2^{-4}\text{mm}\cdot\text{s}^{-1}$ or $12\text{mm}\cdot\text{min}^{-1}$ for the auxiliary inlet and $2^{-5}\text{mm}\cdot\text{s}^{-1}$ or $1.2\text{mm}\cdot\text{min}^{-1}$ for the central inlet).

The applied voltage was defined as a time dependant boundary conditions using either an error function (erf) (Eq. 18) or a smoothed Heaviside step function (flc1hs) with continuous first derivative (Eq. 19).

$$V(t) = V_0 \cdot \frac{1 + \text{erf}[0.1 \cdot (t - 600)]}{2} \quad \text{Eq. 18}$$

$$V(t) = V_0 \cdot \text{flc1hs}(t - 600, 10) \quad \text{Eq. 19}$$

where $V(t)$ = time dependent value of voltage, V_0 = given voltage value, t = time, erf = error function, flc1hs = Heaviside step function with continuous first derivative; the first parameter ($t-600\text{s}$) defined the position of $0.5V_0$ value, (for $t=600\text{s}$, $V=0.5V_0$); the second parameter (10s) was the time during which voltage increase from 0 to V_0 . With this definition $V=0$ for $t=0$ to $t=600-5$ (time taken from the first parameter minus half of the second parameter value) and $V=V_0$ for $t>600+5$ (time taken from the first parameter plus half of the second parameter value). For specific model boundary conditions refer to section “3.1.3 Model setups”.

3.1.2.4. Meshing

The prepared geometric model was partitioned into simple small geometrical figures (triangles or tetragons for 2D models, see Figure 25 and Figure 26). When simulating the migration of species in an aqueous solution sometimes concentration oscillations occur, significantly slowing solving procedure and in some cases leading to incorrect results. These oscillations occur as a result of the numerical solving of partial

differential equations. Increasing mesh density in regions where oscillations were appearing is generally the best method of removing this problem. Example of concentration oscillations appearing in the system is shown in Figure 27. Computational hardware employed for modelling sets a practical limit on the mesh density. In practice models with this system could be solved with a maximum of 40,000 elements (polygons). Denser meshes would result in a very long simulation time and often in memory overload error.

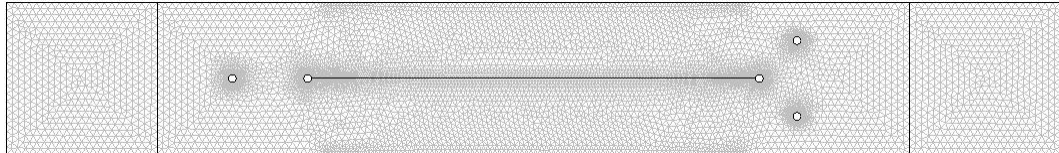


Figure 25: Example of triangular mesh structure.

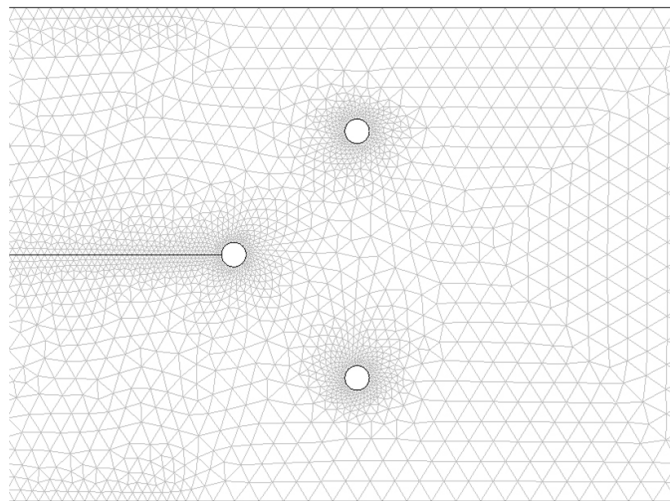


Figure 26: Close-up of employed mesh structure around inlets

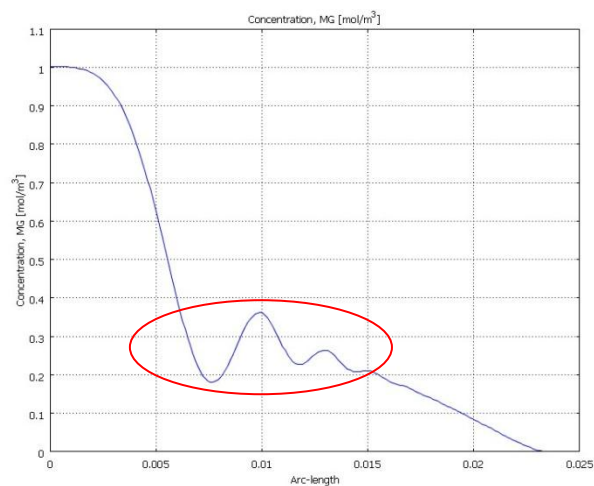


Figure 27: Concentration oscillations due to inadequate mesh density.

3.1.2.5. Solving

There are several different numerical solving methods (solver types) implemented in COMSOL that differ in utilisation of memory, CPU (or multiple cores in CPU), have different methods of linearization and so on. For the PC in this work the most effective solver was the Pardiso solver which employed multi-core support as well as loading the entire model to the computer memory. In case of insufficient memory, GMRES (Generalised Minimum Residual Solver) was used, but this was significantly slower.

Separately there are two types of available solver modes: the stationary solver that calculated only the stationary state for a given set of conditions and time-dependent solver, which conducts the time evolution of the system giving results in predefined intervals for a specified period of time. Typically momentum transport equations (Navier-Stokes or Brinkman mode) were solved using the stationary solver as no changes in the flow field were made and mass transport equations were solved using the time-dependent solver. This coupling allowed the evolution of the species distribution to be determined.

3.1.2.6. Postprocessing and result visualisation

The calculated simulation result could be displayed in many forms. Scalar quantities are typically presented as multi-colour gradient maps with blue representing minimum and red maximum. Vector quantities (like velocity or electric field) are typically displayed as arrows or streamlines (traces left by test particle). A typical example of simulation output is presented in Figure 28.

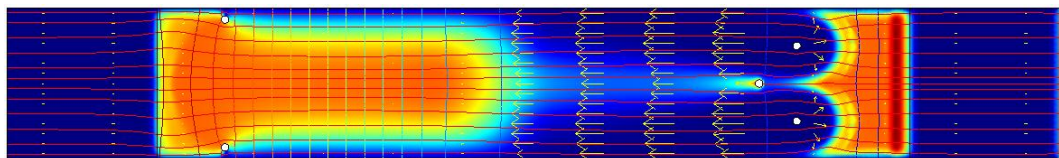


Figure 28: An example of possible result display: color map shows concentration of model compound (blue indicates low concentration, red for high); streamlines (red) – the velocity; and arrows (yellow) – the total flux of model compound

3.1.3. Model setups

This section provides details on the conditions of individual models. Please refer to appropriate section for the results (e.g. results for model setup described in the section 3.1.3.1, are presented in the next chapter in Section 4.1.).

3.1.3.1. Analysis of the mesh density impact on a simulation results

The analysis of the mesh density and mesh quality and how it affects the produced results was conducted early using a relatively simple model with a pressure driven flow and no electromigration implemented.

The chip had a form of a square 20mm by 20mm with eight trapezoidal via ended with semi-circular connector. Six of these were modelled as inlets and two as outlets in the system shown in Figure 29 in order to compare with previous work. The test compound (malachite green) at a concentration of 0.1mM was introduced through three inlets located on the left side of the chip (marked with yellow arrows), and pure solvent (water) was introduced through the inlets located on the right side (marked with blue arrows). Two outlets were installed on top and bottom edge of the chip (marked with red arrows), see Figure 29 for details. The circles located in the central part of the chip had no use in this evaluation.

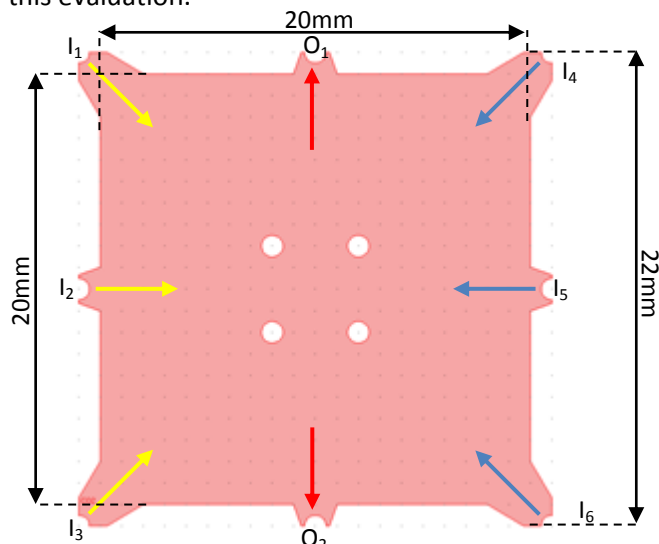


Figure 29: Chip geometry and location of inlets and outlets used for mesh quality evaluation.

COMSOL has pre-defined mesh density types labelled as: extremely coarse, extra coarse, coarser, coarse, normal, fine, finer, extra fine and extremely fine. Five pre-set mesh density types were tested – extremely coarse, coarser, normal, finer and extremely fine. It is possible to define meshing parameters manually for local increase of density or to increase overall density higher than that given by using the “extremely fine” pre-set. This model was developed using “Incompressible Navier-Stokes” flow and “Convection and Diffusion” modes. For exact mesh geometry and mesh parameters see Appendix C. Settings for the boundary conditions are presented in Table 4.

Inlets	I ₁	I ₂	I ₃
Velocity	5·10 ⁻³ m·s ⁻¹	5·10 ⁻³ m·s ⁻¹	5·10 ⁻³ m·s ⁻¹
MG Concentration	0.1M	0.1M	0.1M
Inlets	I ₄	I ₄	I ₆
Velocity	5·10 ⁻³ m·s ⁻¹	5·10 ⁻³ m·s ⁻¹	5·10 ⁻³ m·s ⁻¹
MG Concentration	0	0	0
Outlets	O ₁	O ₂	
Velocity	Pressure = 0, no viscous stress		Pressure = 0, no viscous stress
Concentration	Convective flux option selected		Convective flux option selected
Applied modes	Incompressible Navier-Stokes Convection and diffusion		

Table 4: Modelling boundary conditions for experimental setup shown in Figure 29.

3.1.3.2. 1st Navier-Stokes flow with convection and diffusion in a multi-outlet chip

As a starting example a set of pictures from (15)(see Figure 4), portraying flow of coloured solutions in microfluidic chip with numerous inlets and outlets was chosen. The model was recreated using reasonable parameters (line inflow velocity in order of mm per second) that are typical in other microfluidic systems. This model was developed using “Incompressible Navier–Stokes” flow and “Convection and Diffusion” modes.

The chip schematic was drawn in COMSOL on a 1:1 scale (Figure 30). Semicircles in the corners and in the middle of each side represent the inlets or outlets depending on the boundary settings of particular model variant. Circles in the centre of the chip represent outlets installed in the bottom of the device. The model was developed using the “Navier-Stokes” mode for momentum transport and “Convection and Diffusion” mode for the mass transport. Although the “Navier-Stokes” mode assumes infinite distance along z-axis (perpendicular to the plane of picture), the result of stationary state is the same as when using the Brinkman mode for simulating thin channel flow. To provide a clear description of the model parameters, inlets around the chip are labelled using geographical directions (N, NE, E, and so on) and central outlets were numbered (O₁, O₂, O₃ and O₄) – see Figure 30. Figure 30 represents the experimental setup recorded in Figure 4d which represents the experimental setup presented in Figure 4d. Settings for the boundary conditions are given in Table 5.

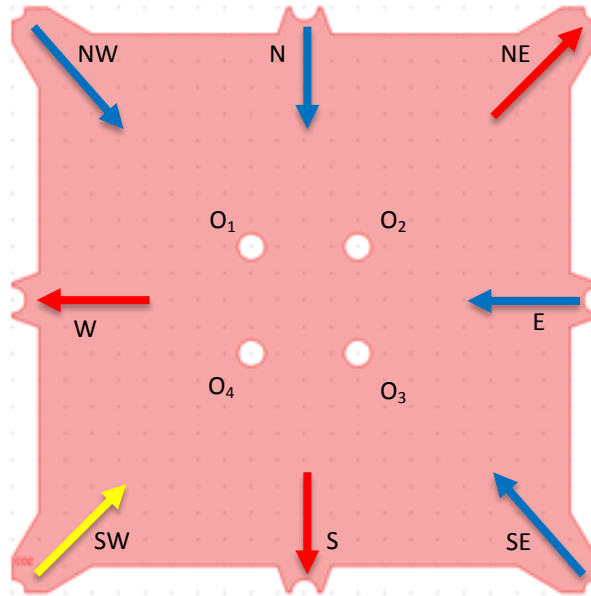


Figure 30: Schematic of chip used to model the experiment shown in Figure 4d drawn in COMSOL for simulations with description of inlets (blue and yellow arrows) and outlets (red arrows).

Inlets	NW	N	E
Velocity	$5 \cdot 10^{-3} \text{ m} \cdot \text{s}^{-1}$	$5 \cdot 10^{-3} \text{ m} \cdot \text{s}^{-1}$	$5 \cdot 10^{-3} \text{ m} \cdot \text{s}^{-1}$
Concentration	0	0	0
Inlets	SE	SW	
Velocity	$5 \cdot 10^{-3} \text{ m} \cdot \text{s}^{-1}$	$5 \cdot 10^{-3} \text{ m} \cdot \text{s}^{-1}$	
Concentration	0	0.1M	
Outlets	NE	W	S
Velocity	Pressure = 0, no viscous stress	Pressure = 0, no viscous stress	Pressure = 0, no viscous stress
Concentration	Convective flux option	Convective flux option	Convective flux option
Outlets	O ₁		O ₂
Velocity	Wall/no slip option		Wall/no slip option
Concentration	Insulation/symmetry option		Insulation/symmetry option
Outlets	O ₃		O ₄
Velocity	Wall/no slip option		Wall/no slip option
Concentration	Insulation/symmetry option		Insulation/symmetry option
Applied modes	Incompressible Navier-Stokes Convection and diffusion		

Table 5: Boundary conditions for experimental setup shown in Figure 30.

3.1.3.3. 2nd Navier-Stokes flow with convection and diffusion in a multi-outlet chip

The flow pattern shown in Figure 4e was selected for comparison of the experimental results with the modelled results. As in the previous setup, this model was developed using “Incompressible Navier-Stokes” and the “Convection and Diffusion”

modes. Figure 31 shows the location of inlets and outlets. Settings for boundary conditions are given in Table 6.

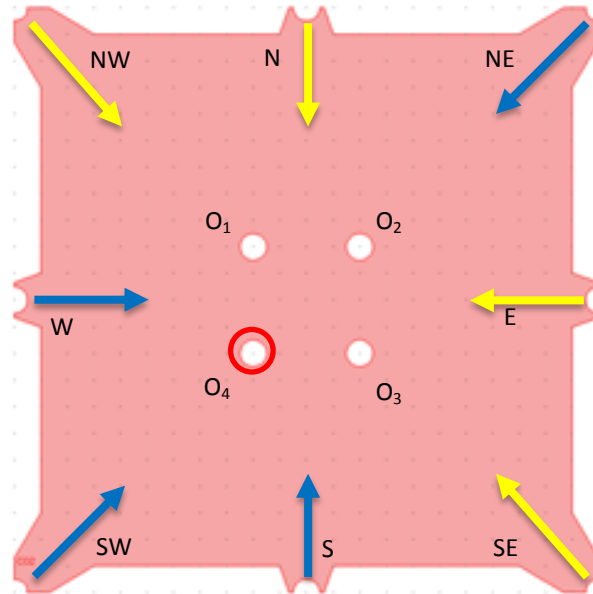


Figure 31: Schematic of chip used to model the experiment shown in Figure 4e drawn in COMSOL for simulations with description of inlets (blue and yellow arrows) and outlets (red circle).

Inlets	NW	N	NE	E
Velocity	$5 \cdot 10^{-3} \text{ m} \cdot \text{s}^{-1}$	$5 \cdot 10^{-3} \text{ m} \cdot \text{s}^{-1}$	$5 \cdot 10^{-3} \text{ m} \cdot \text{s}^{-1}$	$5 \cdot 10^{-3} \text{ m} \cdot \text{s}^{-1}$
Concentration	0.1M	0.1M	0	0.1M
Inlets	SE	S	SW	W
Velocity	$5 \cdot 10^{-3} \text{ m} \cdot \text{s}^{-1}$	$5 \cdot 10^{-3} \text{ m} \cdot \text{s}^{-1}$	$5 \cdot 10^{-3} \text{ m} \cdot \text{s}^{-1}$	$5 \cdot 10^{-3} \text{ m} \cdot \text{s}^{-1}$
Concentration	0.1M	0	0	0
Outlets	O ₁	O ₂	O ₃	O ₄
Velocity	Pressure = 0, no viscous stress	Wall/no slip	Wall/no slip	Wall/no slip
Concentration	Convective flux option	Insulation/symmetry	Insulation/symmetry	Insulation/symmetry
Applied modes	Incompressible Navier-Stokes Convection and diffusion			

Table 6: Boundary conditions for experimental setup shown in Figure 31.

3.1.3.4. The mesh type assessment: comparison of triangular and quadrangle meshes

COMSOL provides two types of meshing: triangular and quadrangular. Triangular meshing, the default method of mesh creation, was used in most cases. Sometimes the solver could not find a solution to a problem even for the most dense mesh grid. In some cases changing the meshing method allowed for solving of the problem. Solving the problems over quadrangular mesh (also called quad mesh) typically takes longer

than with the application of the triangular mesh. Also quad mesh implies more degrees of freedom per mesh element and thus a higher memory usage limiting overall number of mesh elements that can be used effectively. This model was developed using “Incompressible Navier–Stokes” flow and “Convection and Diffusion” modes. Schematic of the used chip layout is shown in Figure 32. Table 7 shows the boundary condition set for this model.

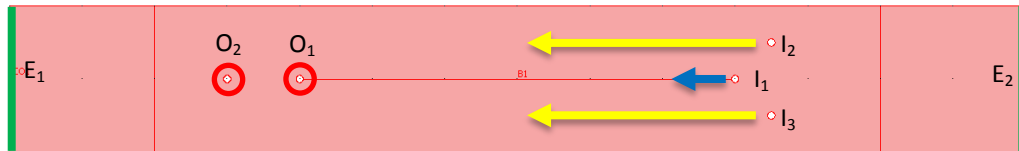


Figure 32: Chip geometry for comparison between triangular and quad mesh.

Inlets	I ₁	I ₂	I ₃
Velocity	$2 \cdot 10^{-5} \text{ m} \cdot \text{s}^{-1}$	$2 \cdot 10^{-4} \text{ m} \cdot \text{s}^{-1}$	$2 \cdot 10^{-4} \text{ m} \cdot \text{s}^{-1}$
MG Concentration	0	0.1mM	0.1mM
Tris-HCl Concentration	20mM	0	0
Outlets	O ₁	O ₂	
Velocity	Pressure = 0, no viscous stress	Pressure = 0, no viscous stress	
Concentration	Convective flux	Convective flux	
Electrodes	E ₁	E ₂	
Potential	0V to 600s, 280V from 600s	0V	
Applied modes	Incompressible Navier-Stokes Convection and diffusion		

Table 7: Boundary conditions for the experiment shown in Figure 32.

3.1.3.5. Modelling of the Conductivity Gradient Focusing

A numerical recreation of the previously conducted and published experiment was recognised as an important step toward successful development of the EHD simulation. Information about the original microfluidic device used for conductivity gradient experiment and its schematics (see Section 1.4 and Figure 3) were taken from (8). The microfluidic models were developed to incorporate electrophoretic and hydrodynamic equilibrium. The recreation of the conducted experiments with the numerical simulation was used to prove the reliability of the COMSOL software as scientific tool and its utility in the field of electrophoresis and microfluidics. A two-dimensional model of was designed to compare the numerical simulation with experimental results (see Figure 33). Settings for boundary conditions are given in Table 8. This model was developed using “Brinkman Equations” and “Nernst-Planck” modes.

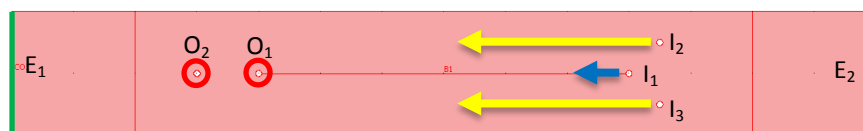


Figure 33: Schematic of the chip used for the modelling of the conductivity gradient focusing.

Inlets	I_1	I_2	I_3
Velocity	$2 \cdot 10^{-5} \text{ m} \cdot \text{s}^{-1}$	$2 \cdot 10^{-4} \text{ m} \cdot \text{s}^{-1}$	$2 \cdot 10^{-4} \text{ m} \cdot \text{s}^{-1}$
MG Concentration	0	0.1mM	0.1mM
Tris-HCl Concentration	20mM	0	0
Outlets	O_1		O_2
Velocity	Pressure = 0, no viscous stress		Pressure = 0, no viscous stress
Concentration	Convective flux		Convective flux
Electrodes	E_1		E_2
Potential	0V to 600s, 280V from 600s		0V
Applied modes	Brinkman Equations Nernst-Planck (with electroneutrality)		

Table 8: Boundary conditions for experimental setup shown in Figure 33.

3.1.3.6. Investigation of the multi-outlet chip properties

The initial layout tested had three inlets (see Figure 35: central inlet I_1 and auxiliary inlets I_2 and I_3), three outlets located on the opposite side to the inlets (later called main outlets O_{1-3}), and six outlets located along walls (later called auxiliary outlets, AO_{1-6}). Settings for boundary conditions are provided in Table 9. Later on layouts with eight and ten auxiliary outlets were tested (see Figure 36 with Table 10 and Figure 37 with Table 11 for details and settings for boundary conditions). Agarose gel tanks were not implemented in this model, as the interest was in the flow pattern inside the microfluidic chamber. The main chamber dimensions were 10cm by 2cm. When all inlets were aligned in a straight line transversal to the chip length (see Figure 34) a stream moving toward the back wall and along side walls (marked with red arrows in) appeared. Presence of such “back-flow” dramatically increased calculation time. Although not critical in this step, it could significantly complicate the model with the introduction of the different conductivity fluids. The central inlet was therefore shifted slightly toward the outlets to avoid this problem (see Figure 35). A second reason for the central inlet shift came from dimensions of the HPLC fittings that are commonly used in the microfluidics. The outer diameter of a typical fingertight connector is 9.2mm and such two connectors’ would not fit together if distance between ports I_1 and I_2 or I_3 was less than about 5mm.

In this model different concentration distributions were tested depending on the velocity ratio between the central and the auxiliary inlets. These models were developed using “Incompressible Navier–Stokes” flow and “Convection and Diffusion” modes.

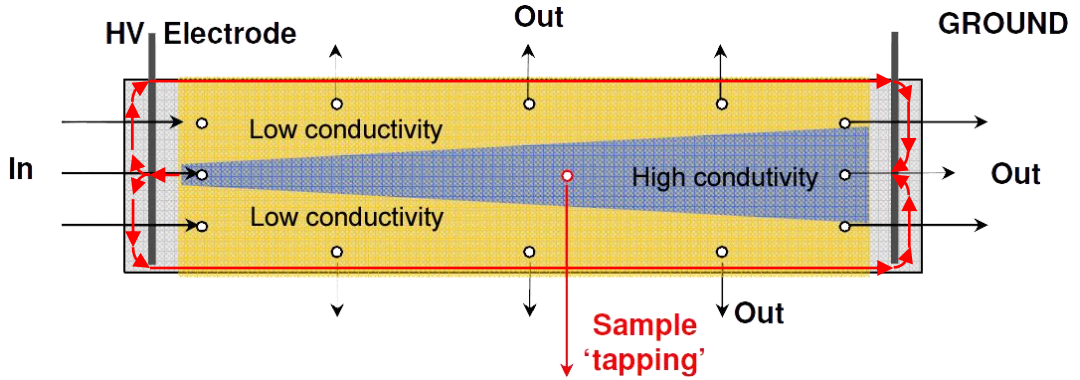


Figure 34: Schematic illustration of microfluidic device for electro-hydrodynamic focusing (253). Red arrows indicate “backflow” when the central inlet was in line with auxiliary inlets.



Figure 35: Layout of microfluidic chip with three main and six auxiliary outlets.

Inlets	I_1	I_2	I_3
Velocity	From $2 \cdot 10^{-5} \text{ m} \cdot \text{s}^{-1}$ to $2 \cdot 10^{-4} \text{ m} \cdot \text{s}^{-1}$	$2 \cdot 10^{-4} \text{ m} \cdot \text{s}^{-1}$	$2 \cdot 10^{-4} \text{ m} \cdot \text{s}^{-1}$
HCl Concentration	1M	0	0
Outlets	O_{1-3}		AO_{1-6}
Velocity	Pressure = 0, no viscous stress		Pressure = 0, no viscous stress
Concentration	Convective flux		Convective flux
Applied modes	Incompressible Navier-Stokes Convection and diffusion		

Table 9: Boundary conditions for experimental setup shown in Figure 35.

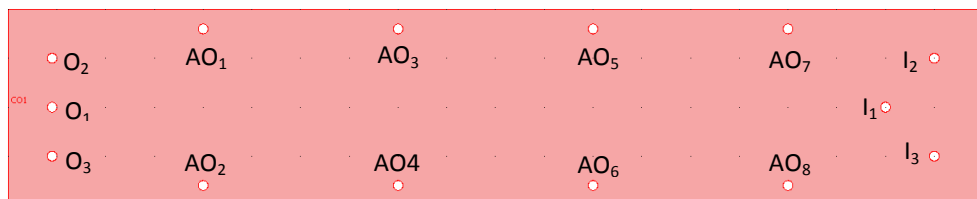


Figure 36: Layout of microfluidic chip with three main and eight auxiliary outlets.

Inlets	I_1	I_2	I_3
Velocity	$4 \cdot 10^{-5} \text{ m} \cdot \text{s}^{-1}$	$2 \cdot 10^{-4} \text{ m} \cdot \text{s}^{-1}$	$2 \cdot 10^{-4} \text{ m} \cdot \text{s}^{-1}$
HCl Concentration	1M	0	0
Outlets	O_{1-3}		AO_{1-8}
Velocity	Pressure = 0, no viscous stress		Pressure = 0, no viscous stress
Concentration	Convective flux		Convective flux
Applied modes	Incompressible Navier-Stokes Convection and diffusion		

Table 10: Boundary conditions for experimental setup shown in Figure 36.

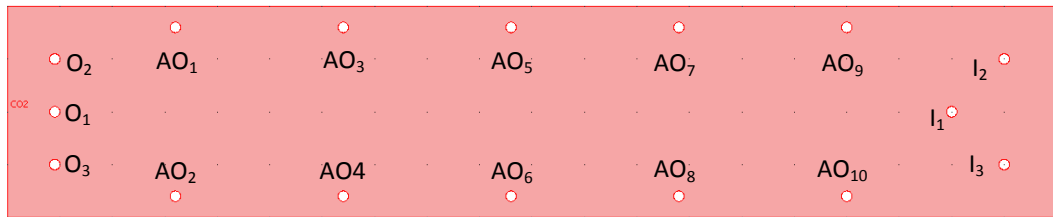


Figure 37: Layout of microfluidic chip with three main and ten auxiliary outlets.

Inlets	I_1	I_2	I_3
Velocity	$4 \cdot 10^{-5} \text{ m} \cdot \text{s}^{-1}$	$2 \cdot 10^{-4} \text{ m} \cdot \text{s}^{-1}$	$2 \cdot 10^{-4} \text{ m} \cdot \text{s}^{-1}$
HCl Concentration	1M	0	0
Outlets	O_{1-3}		AO_{1-10}
Velocity	Pressure = 0, no viscous stress		Pressure = 0, no viscous stress
Concentration	Convective flux		Convective flux
Applied modes	Incompressible Navier-Stokes Convection and diffusion		

Table 11: Boundary conditions for experimental setup shown in Figure 37.

3.1.3.7. Development of an optimal chip for the EHDF

The initial idea for the chip for EHDF is presented in Figure 2. To achieve the trapezoidal flow pattern of the central flowstream the application of additional multiple outlets was proposed. This series of experiments was conducted to determine the optimal shape and location as well as the overall influence of such outlets located along the side walls of the chip.

Basing on the previous simulations and observations of prof. Dasgupta's results a different approach to inlets and outlets was tested. Instead modelling circles, representing tubing collecting fluid, gate-like structures with short collection channels along the walls were implemented. Different shapes and positions were tested until the optimal design was chosen. Schematics are shown in Figure 38-43 with settings for the

boundary conditions provided in the tables below each figure. These models were developed with “Incompressible Navier–Stokes” and “Convection and Diffusion” modes.

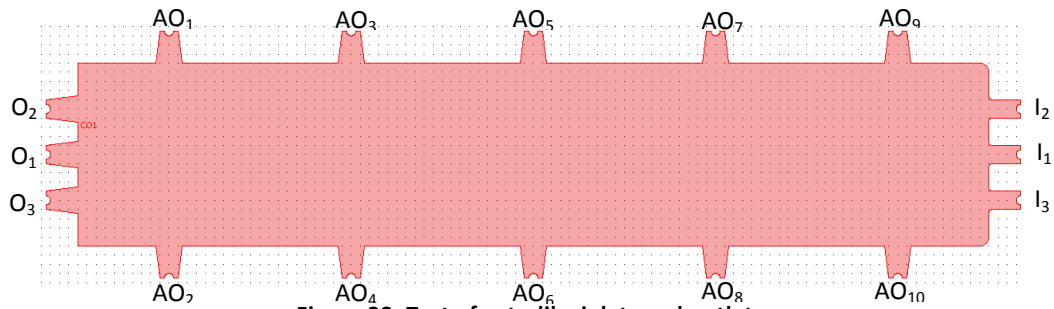


Figure 38: Test of gate-like inlets and outlets.

Inlets	I ₁	I ₂	I ₃
Velocity	$5 \cdot 10^{-5} \text{ m} \cdot \text{s}^{-1}$	$5 \cdot 10^{-5} \text{ m} \cdot \text{s}^{-1}$	$5 \cdot 10^{-5} \text{ m} \cdot \text{s}^{-1}$
HCl Concentration	0.1M	0	0
Outlets	O ₁₋₃		AO ₁₋₁₀
Velocity	Pressure = 0, no viscous stress		Pressure = 0, no viscous stress
Concentration	Convective flux		Convective flux
Applied modes	Incompressible Navier-Stokes Convection and diffusion		

Table 12: Boundary conditions for experimental setup shown in Figure 38.

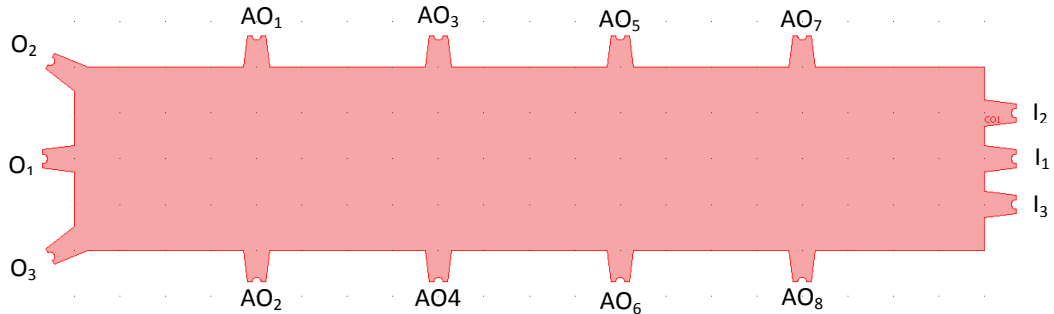


Figure 39: Test of gate-like inlets and outlets.

Inlets	I ₁	I ₂	I ₃
Velocity	$5 \cdot 10^{-5} \text{ m} \cdot \text{s}^{-1}$	$5 \cdot 10^{-5} \text{ m} \cdot \text{s}^{-1}$	$5 \cdot 10^{-5} \text{ m} \cdot \text{s}^{-1}$
HCl Concentration	0.1M	0	0
Outlets	O ₁₋₃		AO ₁₋₈
Velocity	Pressure = 0, no viscous stress		Pressure = 0, no viscous stress
Concentration	Convective flux		Convective flux
Applied modes	Incompressible Navier-Stokes Convection and diffusion		

Table 13: Boundary conditions for experimental setup shown in Figure 39.

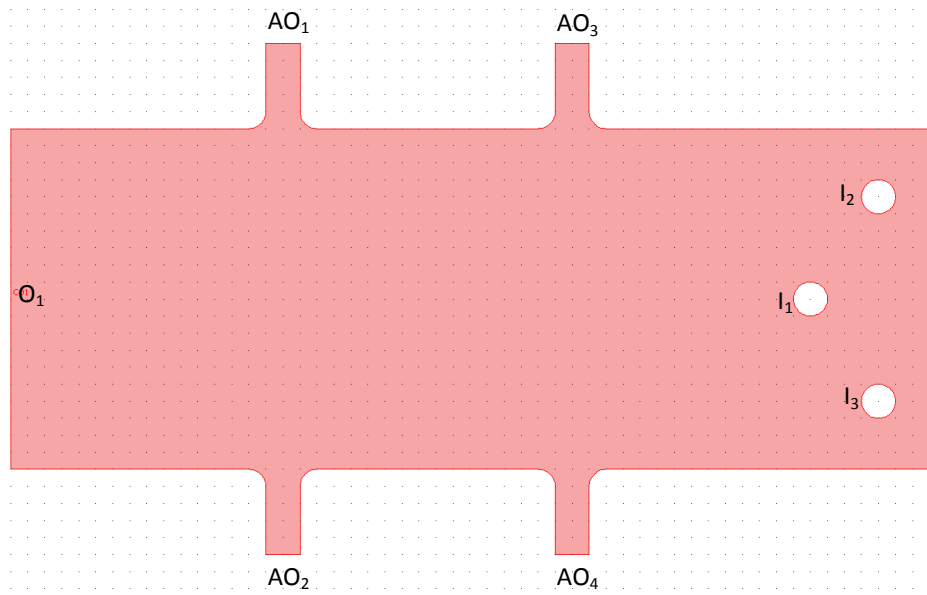


Figure 40: Test of gate-like with outlets rounded entrance with an open-end outlet.

Inlets	I ₁	I ₂	I ₃
Velocity	$2 \cdot 10^{-4} \text{ m} \cdot \text{s}^{-1}$	$2 \cdot 10^{-4} \text{ m} \cdot \text{s}^{-1}$	$2 \cdot 10^{-4} \text{ m} \cdot \text{s}^{-1}$
HCl Concentration	0.1M	0	0
Outlets	O ₁	AO ₁₋₄	
Velocity	Pressure = 0, no viscous stress	Pressure = 0, no viscous stress	
Concentration	Convective flux	Convective flux	
Applied modes	Incompressible Navier-Stokes Convection and diffusion		

Table 14: Boundary conditions for experimental setup shown in Figure 40.

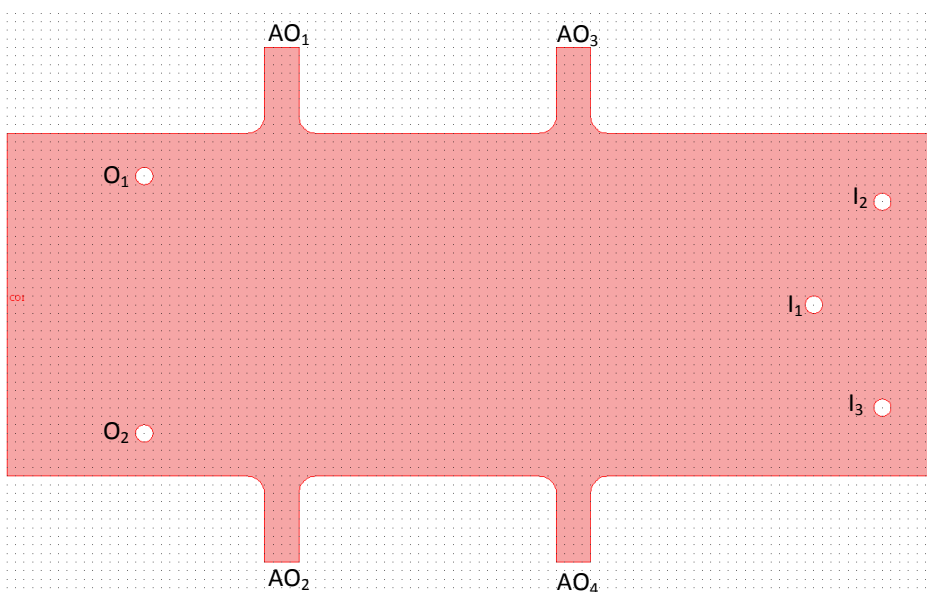


Figure 41: Test of gate-like with outlets rounded entrance with two main outlets located side-by-side.

Inlets	I_1	I_2	I_3
Velocity	$2 \cdot 10^{-4} \text{ m} \cdot \text{s}^{-1}$	$2 \cdot 10^{-4} \text{ m} \cdot \text{s}^{-1}$	$2 \cdot 10^{-4} \text{ m} \cdot \text{s}^{-1}$
HCl Concentration	0.1M	0	0
Outlets	O_{1-2}		AO_{1-4}
Velocity	Pressure = 0, no viscous stress		Pressure = 0, no viscous stress
Concentration	Convective flux		Convective flux
Applied modes	Incompressible Navier-Stokes Convection and diffusion		

Table 15: Boundary conditions for experimental setup shown in Figure 41.

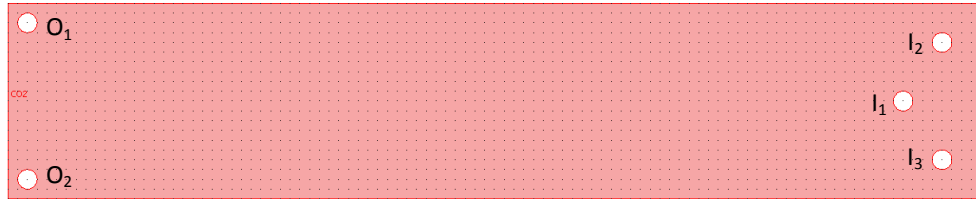


Figure 42: Test of long separation chamber with two main outlets located aside each other.

Inlets	I_1	I_2	I_3
Velocity	$1 \cdot 10^{-4} \text{ m} \cdot \text{s}^{-1}$	$1 \cdot 10^{-4} \text{ m} \cdot \text{s}^{-1}$	$1 \cdot 10^{-4} \text{ m} \cdot \text{s}^{-1}$
HCl Concentration	0.1M	0	0
Outlets	O_1		O_2
Velocity	Pressure = 0, no viscous stress		Pressure = 0, no viscous stress
Concentration	Convective flux		Convective flux
Applied modes	Incompressible Navier-Stokes Convection and diffusion		

Table 16: Boundary conditions for experimental setup shown in Figure 42.

3.1.3.8. Models incorporating pressure-drive flow and electromigration with the selected chip layout

Investigation of different inlet and outlet layouts for pressure driven flow (presented in the Section 3.1.3.7.) gave a potential layout candidate for focussing attempts with both pressure- and electro-driven flow. Limitations imposed by fabrication process lead to few adjustments in the chip design. The new chip based on preliminary experiments and investigation of the multi-outlet chip was designed and is presented in Figure 43.

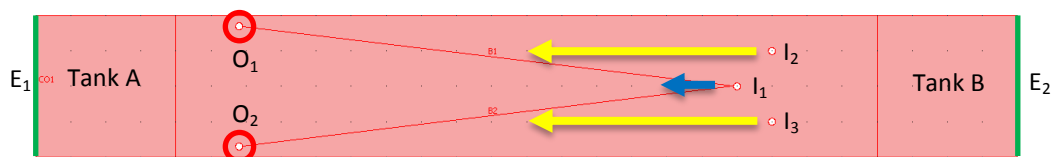


Figure 43: Schematic drawing of new chip for testing of simultaneous pressure- and electro-driven flow.

All three inlets (I_1 , I_2 and I_3) were shifted to a distance of 1.5cm from the agarose gel tank by 1 cm (compared to model of original chip). In this model only two outlets were present as shown in Figure 43. Also test substance (malachite green, MG) was introduced through the central inlet I_1 . By making these adjustments, the distance between the inlets and outlets was increased, which should improve the separation performance. Using presented outlet location (two outlets located aside each other) should allow for the formation of the trapezoidal region of high conductivity fluid and thus enabling EHD focusing. This model was developed using “Brinkman Equations” and “Nernst-Planck” modes.

Inlets	I_1	I_2	I_3
Velocity	$2 \cdot 10^{-5} \text{ m} \cdot \text{s}^{-1}$	$2 \cdot 10^{-4} \text{ m} \cdot \text{s}^{-1}$	$2 \cdot 10^{-4} \text{ m} \cdot \text{s}^{-1}$
MG Concentration	1mM	0	0
Tris-HCl Concentration	20mM	0	0
Outlets	O_1		O_2
Velocity	Pressure = 0, no viscous stress		Pressure = 0, no viscous stress
Concentration	Convective flux		Convective flux
Electrodes	E_1		E_2
Potential	200V, 1400V and 2000V		0V
Applied modes	Brinkman Equations, Nernst-Planck (with electroneutrality)		

Table 17: Boundary conditions for experimental setup shown in Figure 43.

3.1.3.9. The first model of EHDF

In the next series of simulations chip layout remained unchanged (see Figure 43) malachite green was introduced through inlets I_2 and I_3 and other parameters remained unchanged (see Table 18). This model was developed using “Brinkman Equations” and “Nernst-Planck” modes.

Inlets	I_1	I_2	I_3
Velocity	$2 \cdot 10^{-5} \text{ m} \cdot \text{s}^{-1}$	$2 \cdot 10^{-4} \text{ m} \cdot \text{s}^{-1}$	$2 \cdot 10^{-4} \text{ m} \cdot \text{s}^{-1}$
MG Concentration	0	0.1mM	0.1mM
Tris-HCl Concentration	20mM	0	0
Outlets	O_1		O_2
Velocity	Pressure = 0, no viscous stress		Pressure = 0, no viscous stress
Concentration	Convective flux		Convective flux
Electrodes	E_1		E_2
Potential	0V to 600s, 280V from 600s		0V
Applied modes	Brinkman Equations Nernst-Planck (with electroneutrality)		

Table 18: Boundary conditions for experimental setup shown in Figure 43.

3.1.3.10. The second model for EHDF

In the second model for EHDF boundary condition for walls was changed from “Insulation/Symmetry” implying no flux through the boundary to “Concentration = 0” (see Figure 44 and Table 19). This model was developed using “Brinkman Equations” and “Nernst-Planck” modes.

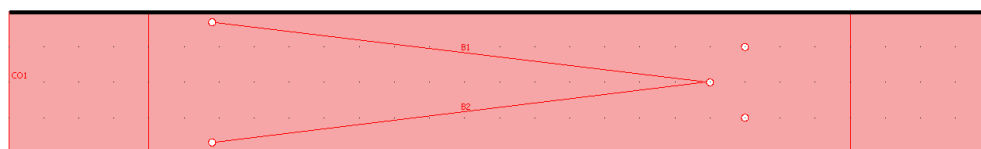


Figure 44: Boundaries with changed boundary condition are marked with black line. All other settings as in figure Figure 43.

Inlets	I ₁	I ₂	I ₃
Velocity	2·10 ⁻⁵ m·s ⁻¹	2·10 ⁻⁴ m·s ⁻¹	2·10 ⁻⁴ m·s ⁻¹
MG Concentration	0	0.1mM	0.1mM
Tris-HCl Concentration	20mM	0	0
Outlets	O ₁	O ₂	
Velocity	Pressure = 0, no viscous stress	Pressure = 0, no viscous stress	
Concentration	Convective flux	Convective flux	
Electrodes	E ₁	E ₂	
Potential	0V to 600s, 300V from 600s	0V	
Applied modes	Brinkman Equations Nernst-Planck (with electroneutrality)		

Table 19: Boundary conditions for experimental setup shown in Figure 44.

3.2. Experiments with microfluidic systems

This section provides information about instrumentation, materials and procedures used during experiments with microfluidic chips.

3.2.1. Instrumentation

3.2.1.1. Microfluidic chips

The microfluidic chip used for fluid focusing experiments was custom made in-house from polymethyl methacrylate (PMMA) sheet, 10 mm thick, bought from Goodfellow, UK. The PMMA sheet was cut into 160mm × 40mm rectangles, to form the upper and the lower part of the chip body. Both parts of the chip were drilled with fourteen threaded 5mm diameter holes to allow both pieces to be clamped together. In the upper part, two 20mm × 20mm square openings (to act as agarose gel tanks) and

nine microfluidic ports (inlets, outlets and electrode ports) were machined. Three ports were used to act as inlets, four as outlets (with possibility of blocking them independently, depending on the tested chip layout) and two as openings for electrodes (see Figure 45a). Full technical drawings of the microfluidic chip and the port fabrication process are presented in Appendix D.

PMMA layers were separated by a spacer made from polytetrafluoroethylene (PTFE) bought from Goodfellow, UK. PTFE sheets were cut into 160mm × 40mm rectangles with fourteen holes and with a 140mm × 20mm rectangular internal cutout (see Figure 45b). PTFE spacers used were of 50µm, 100µm, 200µm and 500µm thickness to provide the microfluidic chambers with variable thickness.

Agarose gel tanks were covered with a layer of 12.7µm (0.5mil) transparent polyester self-adhesive film ARcare® 92712 which came with a 17.78µm (0.7mil) MA-78 acrylic medical grade adhesive (giving a total combined thickness of 30.48µm). This film was bought from Adhesives Research, Ireland.

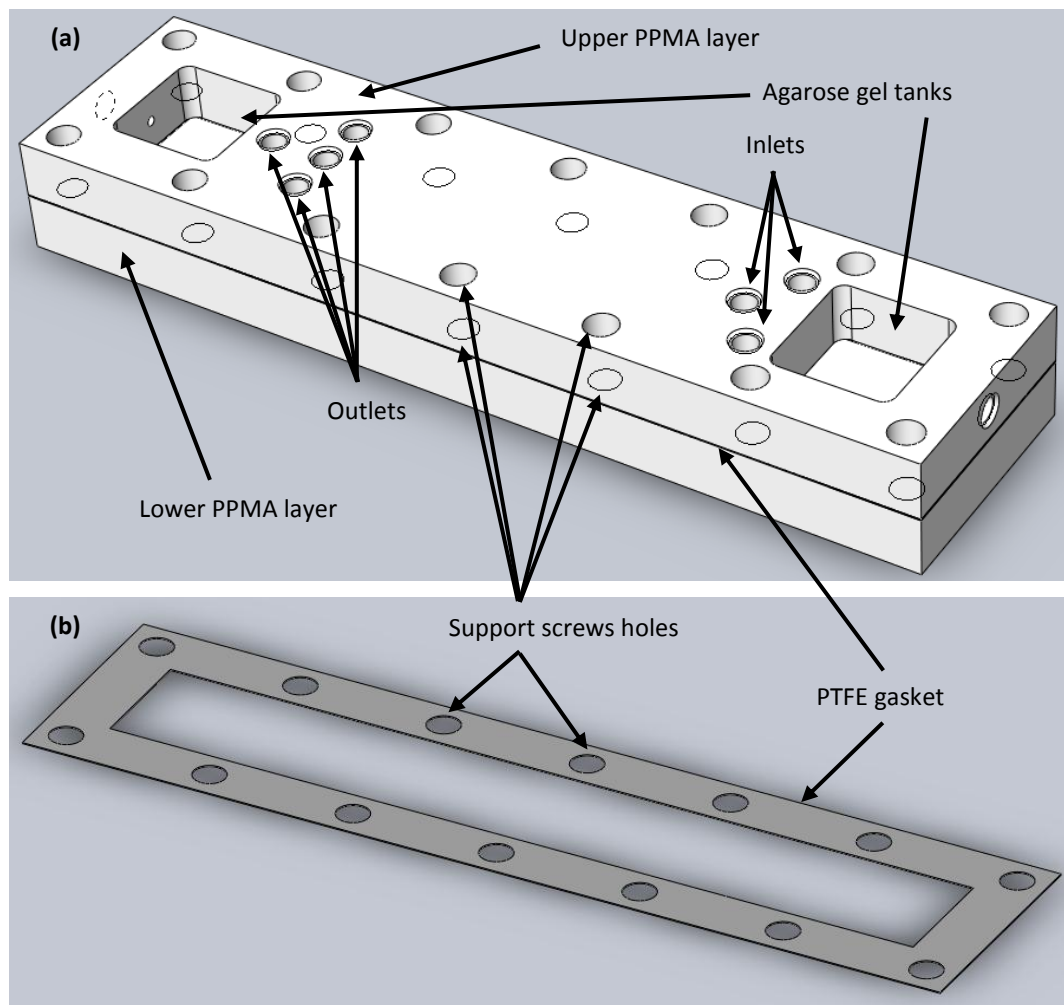


Figure 45: (a) 3D schematic of the assembled microfluidic chip and (b) PTFE gasket.

3.2.1.2. Pumps used

For fluidic experiments two HPLC pumps were used. The first one was Waters 600E Gradient Module HPLC system bought from AGB Scientific, Germany and the second one was Knauer Smartline Pump 100 bought from Kinesis Ltd. Cambs, UK.

Visualisation experiments were conducted using a milliGAT[®] pump, bought from Global FIA, Fox Island, WA, USA.

3.2.1.3. High voltage source

EMCO High Voltage USB20P (HVUSB20P) high voltage source, USB connected with 0 to +2000V output, bought from Condatas AG, Zürich, Switzerland was used as a voltage source in conjunction with PMMA microfluidic chip. The HVUSB20P was connected to the two electrodes immersed in the agarose gel tanks.

3.2.1.4. HPLC tubing, fittings and connectors

Upchurch Scientific universal PEEK HPLC fittings 1/16" diameter, thread 10-32 size bought from Sigma-Aldrich Ireland were used. Specifically F-120X fingertight fittings, P-890 microtee, 5-9722 slip-on filter and 1/16" PEEK tubing with 250µm inner diameter were used with these fittings.

3.2.1.5. Optical detection equipment

Ocean Optics MayaPRO spectrophotometer, coupled with Ocean Optics various diameter fibre optic waveguides, and Ocean Optics Spectrasuite software were used. The conditions of specific spectrum measurements are described later in details for all setups. The MayaPRO spectrophotometer was also used as an absorbance detector (working in absorbance mode) during experiments with focusing. Integrating sphere Ocean Optics FOIS-1 and calibrated light source Ocean Optics LS-1 tungsten halogen light source were used for radiometric measurements.

3.2.1.6. Microscopes

A LabSmith SVM340 Synchronised Video Microscope, digital microscope fitted with Zeiss 4x and 10x magnifying lens (DIN standard) connected by Hauppauge WinTV television tuner and uScope Software for image capturing and video recording, program version 1.013 was used for visualisation of the capillary end in the experiments with photopolymerisation of monoliths.

Olympus BH-2 BHSP microscope fitted with a 20x magnifying lens and an ImagingSource 1.2 megapixel USB camera was used to capture images for the light intensity distribution inside the capillary filled with a light absorbing dye.

Veho Discovery VMS-001 USB digital microscope with adjustable magnification ranging from 20x to 200x was used for real-time visualisation of the fluorescent dye in the microfluidic chip.

3.2.1.7. Camera

Panasonic DMC FZ-30 digital camera with 8 megapixel CCD matrix fitted with 35-420mm lens (35mm frame equivalent) mounted on a TD-1932 tripod was used for whole-chip imaging during experiments in PMMA microfluidic chip. The parameters for taking photos were: 1/50s exposure time, f/6.3 aperture, ISO 100 sensitivity, and uncompressed JPEG file with 3264x2448 pixels resolution output.

3.2.1.8. Power supply unit

Switching mode power supply unit N93CX bought from Maplin, Ireland was used to drive the LED at constant current 20 mA.

3.2.1.9. Computer used in microfluidic experiments

A Sony Vaio FZ-11z laptop was used for data acquisition and driving various devices (microscopes and high voltage source). This laptop contained a processor Intel® Centrino™2 Duo T7300, 2GB SO-DIMM PC2-5300, graphic card GeForce 8400M GT 256MB, hard disk drive 200GB 5400RPM 4MB cache and was run under Microsoft XP Professional operating system.

3.2.1.10. Other equipment

An A4 size lightbox (part number 948088) with 20W compact fluorescent lamps installed and illumination area of 292mm by 197mm bought from LightboxUK.net was used for bright field imaging and the illumination of the dye distribution during the electrohydrodynamic focusing experiments.

3.2.2. Materials (chemicals and consumables)

The chemical reagents used during the EHD focusing experiments are listed in the Table 20.

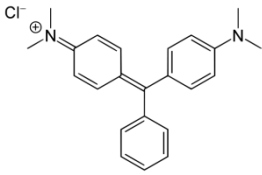
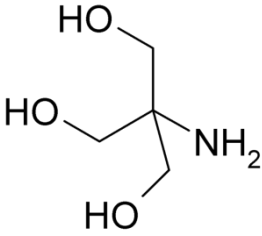
Chemical	Structure	Manufacturer	Purity	CAS Number
Malachite Green		Sigma-Aldrich®	>96.0%	569-64-2
TRIS		Sigma	>99%	77-86-1
HCl	H-Cl	Sigma	37% solution	7647-01-0

Table 20: Table of chemicals used during experiments on EHD focusing.

The LED (type LED430-06) of 5mm diameter and 430 nm central wavelength (violet) was purchased from Roithner Lasertechnik, GmbH, Vienna, Austria. The white LED of 5 mm diameter manufactured by Nichia (type NSPW500GS-K1), was purchased from Dotlight, Jülich, Germany.

3.2.3. Description of the general experimental setup

The microfluidic chip presented in 3.2.1.1 was connected to two pumps. The first pump (Waters system) was used to pump the low conductivity (0.039 S/m) 100µM malachite green solution in deionised water at pH 7.0 through two auxiliary inlets (both off-centre inlets) at a flowrate ranging from 10 to 40µl/min (see individual experimental setup description for details). The chip was connected to the pump using a microtee connector acting as a 50/50 flow splitter to provide flow to the two parts of the microfluidic chamber. Initially a 6 ml custom made sample loop and an injection valve were tested, but such large loop turned out to be ineffective and allowed diffusion played a significant role affecting the overall results. With this loop sample concentration was decreased with time. The sample was being diluted toward the end of the inject volume due to the relatively large loop volume and low flowrate applied

and one could not assume a constant concentration of the injected sample. The injection valve and the loop were therefore removed and the sample was pumped straight through the pump.

Pump number two (Knauer system) was used to pump the high conductivity (0.697 S/m) 20mM TRIS-HCl buffer of pH 4.9 at a flowrate ranging from 2 to 10 μ l/min, depending of the experiment. Initially the entire chip was primed with 100 μ M malachite green solution. After 10-20 minutes (see individual experiment description) the high voltage unit was turned on and the voltage was applied. Data points were gathered using the digital camera to capture at constant time intervals to capture the time evolution of the dye inside the chip. The experimental setup is shown in Figure 46.

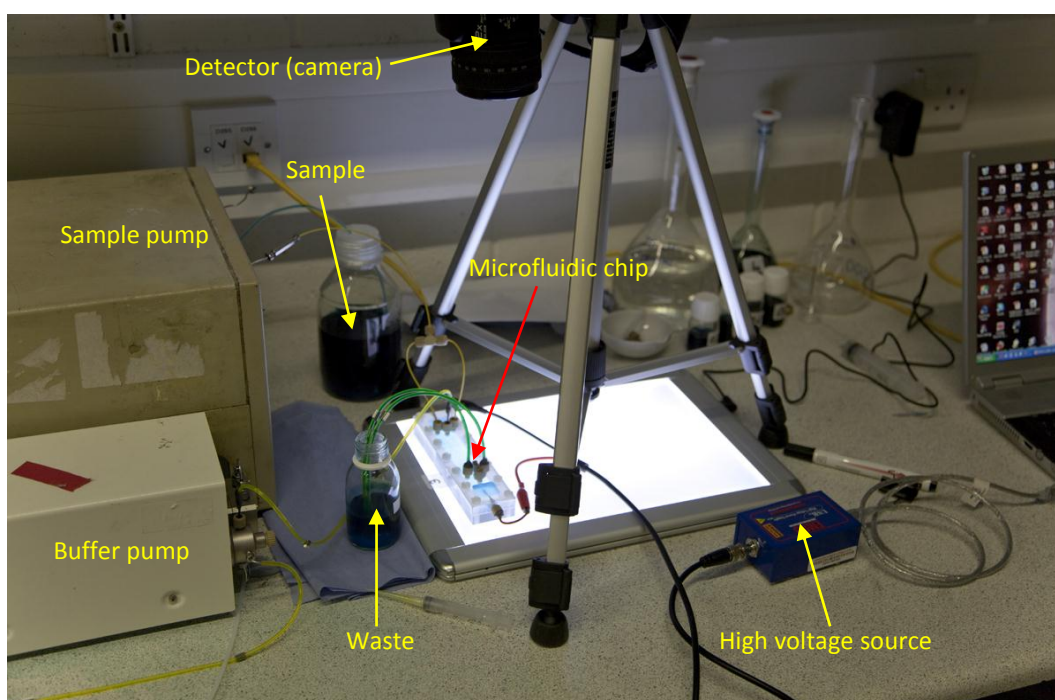


Figure 46: Photo of the experimental setup for the EHD focusing.

3.2.4. Procedure of the concentration and its error calculation using digital photos

The concentration measurements inside the chip were based on an absorbance photometry. The used test compound (malachite green) is a highly absorbing dye with a very intense blue-green colour even at a very low concentration. Entire chip was placed on a lightbox and was constantly illuminated with white light.

Due to the significant planar size of the chip (100mm \times 20mm) in order to acquire data over the entire chip chamber a two-dimensional sensor was needed.

Currently there are two major types of two-dimensional sensors available on the market: charged coupled device matrices (CCD) and complementary metal oxide semiconductor matrices (CMOS), both most commonly found as light-sensitive elements in digital cameras. Thus a camera was selected as the data recorder. It allowed visualising the entire chip at the same time which helped to observe and analyse the processes occurring inside the chip as well as directly comparing results to those from the modelling work. The rather low sensitivity of the camera matrix was complimented by direct measurement of the concentration changes using a fibre optic spectrophotometer working in absorbance measurement mode. A drawback associated with using a spectrophotometer is its one-point measurement mode. Thus it was used in later parts of experiments where focal points and flow paths were already identified.

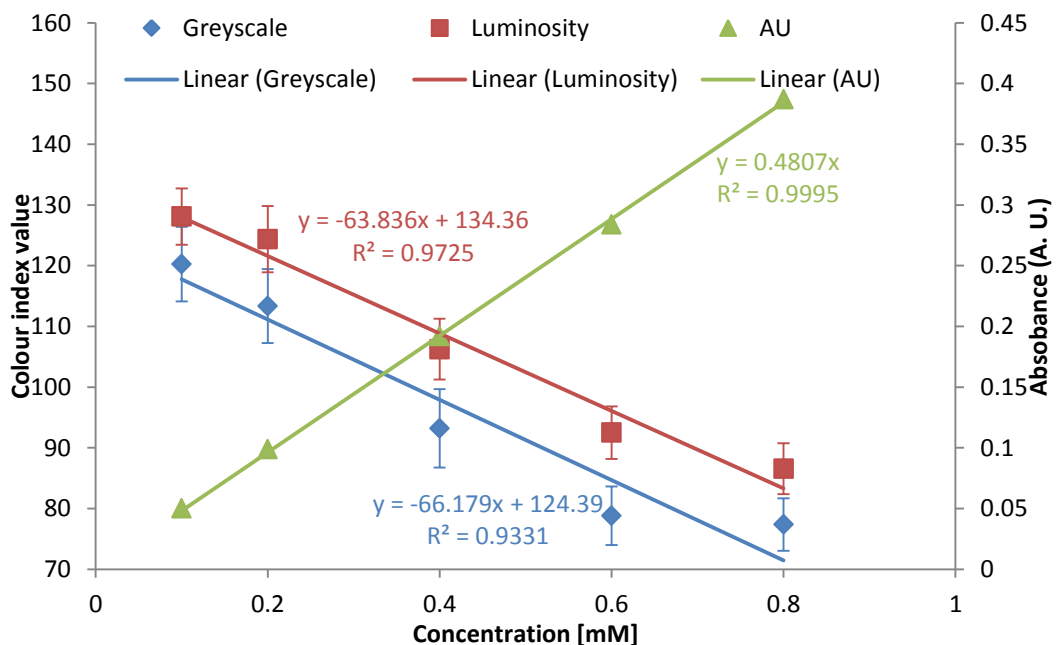


Figure 47: Calibration curves for the microfluidic chip with a 500µm gasket for images from digital camera (blue and red) and for spectrophotometer (green). AU stands for arbitrary unit.

The first tested method of calculating concentration values from photos involved picture conversion from colour RGB 8-bits per channel to 8-bit grayscale format and reading the light intensity value from the area of interest. Then a linear trend was fitted to the acquired data points.

As it can be seen from Figure 47, image conversion to grayscale lead to significant loss of precision and data (24-bit to 8-bit conversion) resulting data points lying further from the trend. R^2 value of 0.93 suggests that there is an error incorporated in the measurements. The second method using luminosity values of the selected area

of the chip interior proved to have a lower error ($R^2 = 0.979$) and the fitted line of linear trend remained within calculated errors. Basing on this result, the concentration calculation method involving grayscale conversion was abandoned. Data gathered with the spectrophotometer are much more precise lying on a nearly perfectly fitted line ($R^2 = 0.9995$) showing a high confidence level in the measurements.

For concentration measurements, standard calibration curves were made for each PTFE gasket thickness for each microfluidic chip set-up. The chip was filled with the malachite green of known concentrations (0.1, 0.2, 0.4, 0.6 and 0.8mM) and each one was photographed. Next the colour luminosity⁷ L (average luminosity of the selected region and its standard deviation S_L) was read using Adobe Photoshop CS3 software. An area of 20mm by 20mm close to the central outlet was selected during chip filling with the Tris-HCl buffer and a 3mm by 3mm area was selected of the focused dye to measure the real concentration inside the chip (see Figure 49).

Several picture-to-picture differences in luminosity measured from these areas were noted. The first pictures taken each day had lower average luminosity than those take later on. This was attributed to heating of the light box and stabilisation of the light output. The second observed problem was decreased luminosity after taking of a series of pictures and this was attributed to heating of the CCD matrix in the camera. In order to standardise luminosity values, to allow a direct picture comparison and to lower the error of the concentration calculation luminosity values were normalised. To do this a white area of typically 40mm by 80mm of the lightbox surface on each picture (a fragment typically located at the bottom of picture) was selected and its average luminosity W and its standard deviation S_W were measured (see Figure 48). Next the value of luminosity L measured from the selected test area was divided by white standard luminosity W . For combined luminosity variance evaluation from the luminosity standard deviation from the selected test area (given by S_L), and from the white area (S_W), a new combined standard deviation was calculated (D), as in the Eq. 20.

$$D = StDev\left(\frac{L - S_L}{W - S_W}, \frac{L + S_L}{W - S_W}, \frac{L - S_L}{W + S_W}, \frac{L + S_L}{W + S_W}\right) \quad \text{Eq. 20}$$

⁷ Defined as weighted nonlinear sum of each channel (red, green and blue) intensity
 $L = 0.299R + 0.587G + 0.114B$

After introduction of the reference white area was introduced, R^2 dropped from 0.979 to 0.973 and average dispersion calculated according to the Eq. 20 increased from 4.45% to 6.14% (see Figure 48).

The associated precision loss is inevitable as the introduced white standard is biased by its own error. Although theoretical precision dropped, the average concentration values calculated using this method were significantly closer to the actual values. After priming chip with 0.1mM malachite green and during the filling of the chip with high conductivity buffer calculated concentration values should be around 0.1mM and without normalisation with the white standard, these were often shifted by 0.2mM or even more from the actual values.

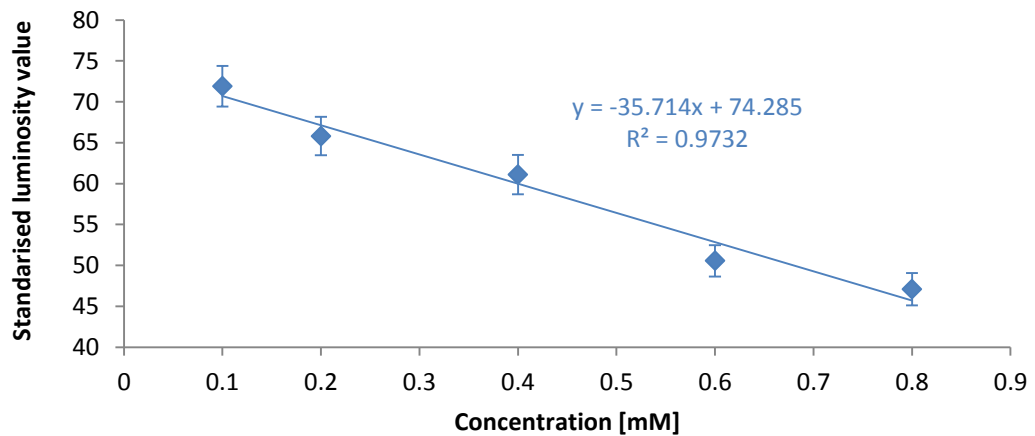


Figure 48: Calibration curve for 500µm gasket with light intensity correction based on luminosity of the reference white area.

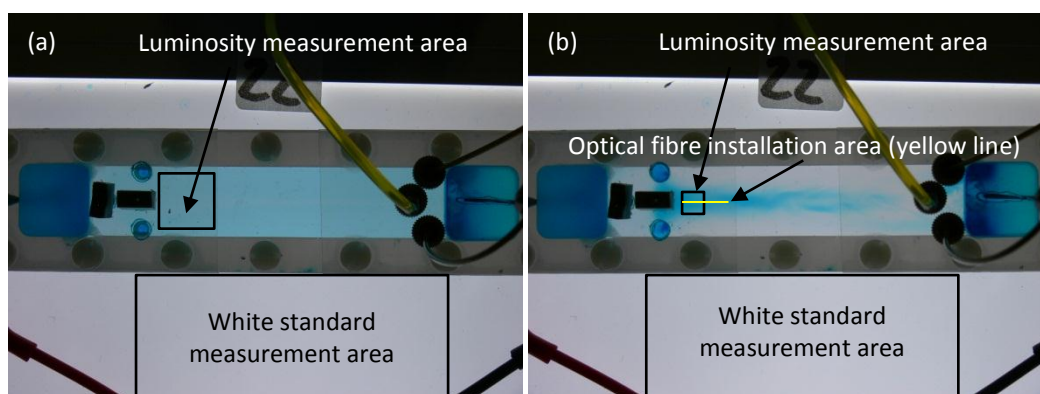


Figure 49: Localisations of the test areas for luminosity measurements and concentration calculations (a) 20x20mm area used during filling the chip with Tris-HCl buffer, (b) 3x3mm area used during focusing.

The difference between calculating concentration values using non-corrected luminosity values and luminosity values normalised against white area luminosity values

is presented in Figure 50. Until 900s (before applying the voltage) no significant changes in concentration should be observed, and this is concurrent with concentration values calculated using the mentioned normalisation method. For this period, the calculated concentration was within the error margin around the initial value (0.1mM). Also central points were closer to this value after normalisation. An increasing luminosity of the test area is visible as well.

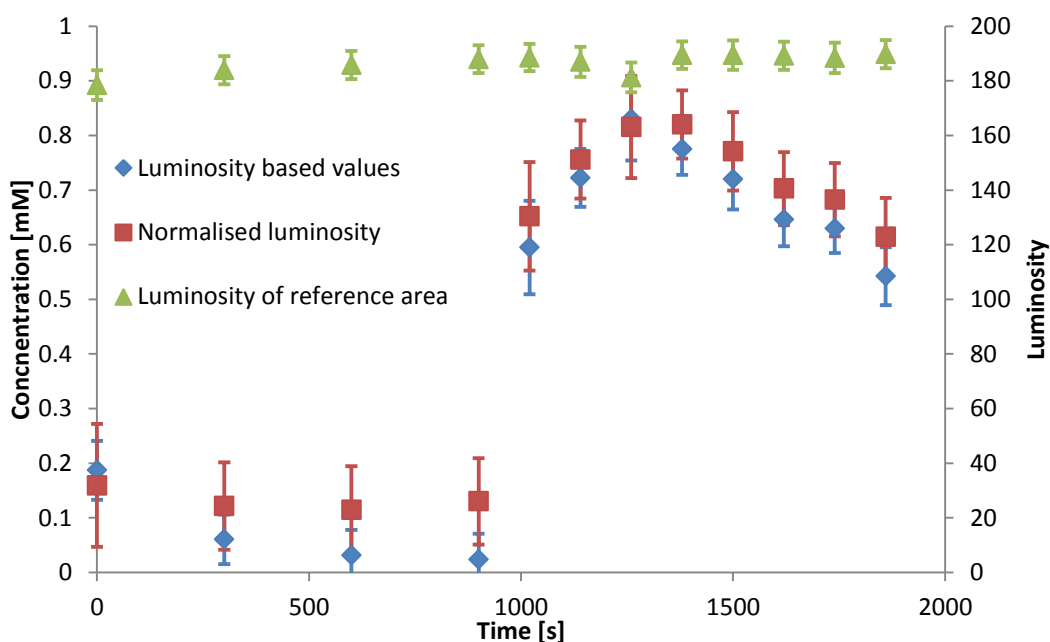


Figure 50: Comparison of the concentration calculations using non-corrected (blue points) and normalised luminosity (red point). Luminosity of the test area (green points) is presented as a reference.

3.2.5. Absorbance measurements in the chip

To check concentration measurements with those obtained from photos, a spectrophotometer Ocean Optics MayaPRO 2000 was used. A 50 μ m Premium Grade Optical Fibre QP50-2-UV/VIS, with numerical aperture 0.22, bought from Ocean Optics, UK was installed in a custom made aluminium holder above the chip (see Figure 51). Depending on the experiment (placement of fitting blocking outlets), the optical fibre was installed between 20mm and 35mm from the outlets in the centre of the chip (see Figure 49). Opposite to the collecting fibre a violet LED (type LED430-06) of 5mm diameter and 430nm central wavelength, purchased from Roithner Lasertechnik, GmbH, Vienna, Austria was installed. The 430nm LED was chosen due to the presence of the malachite green local absorbance maximum around that wavelength. See Figure 52 for LED emission spectrum and malachite green absorbance spectrum in the same wavelength range.

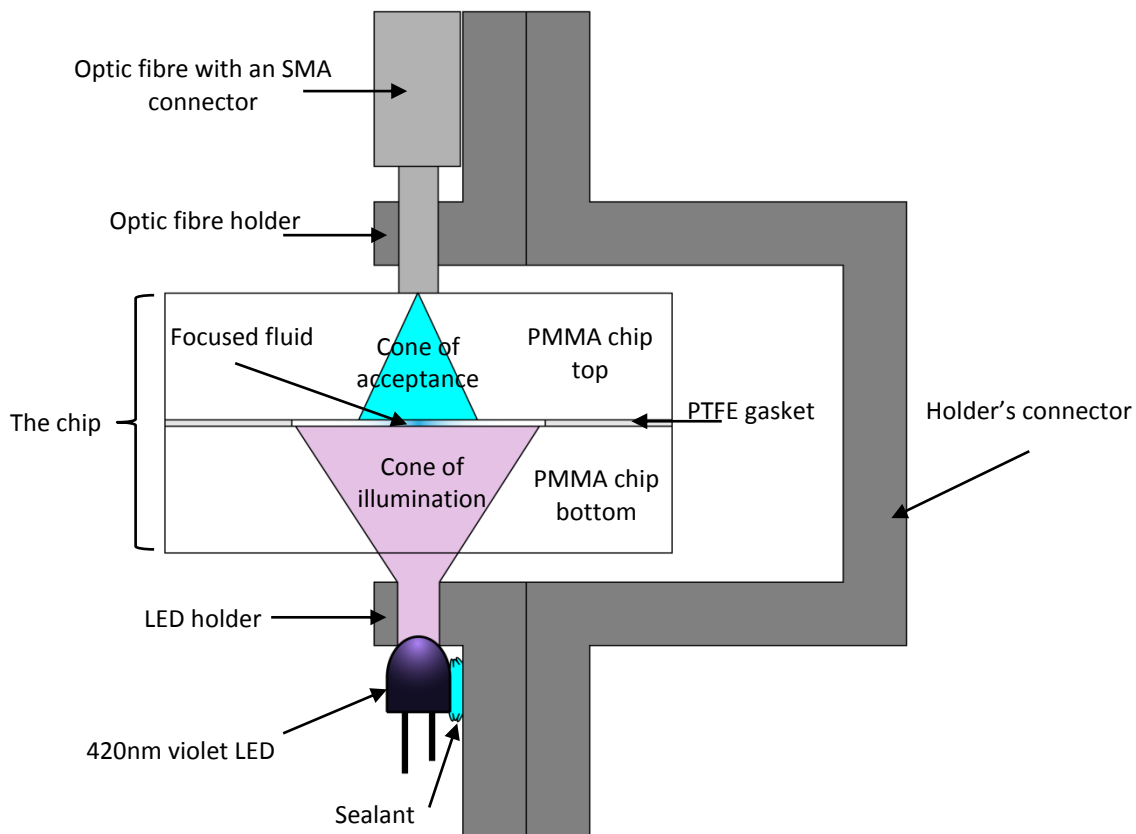


Figure 51: Schematic of the absorbance measurements setup using LED illumination and fibre optic spectrophotometer as absorbance detector (picture in scale).

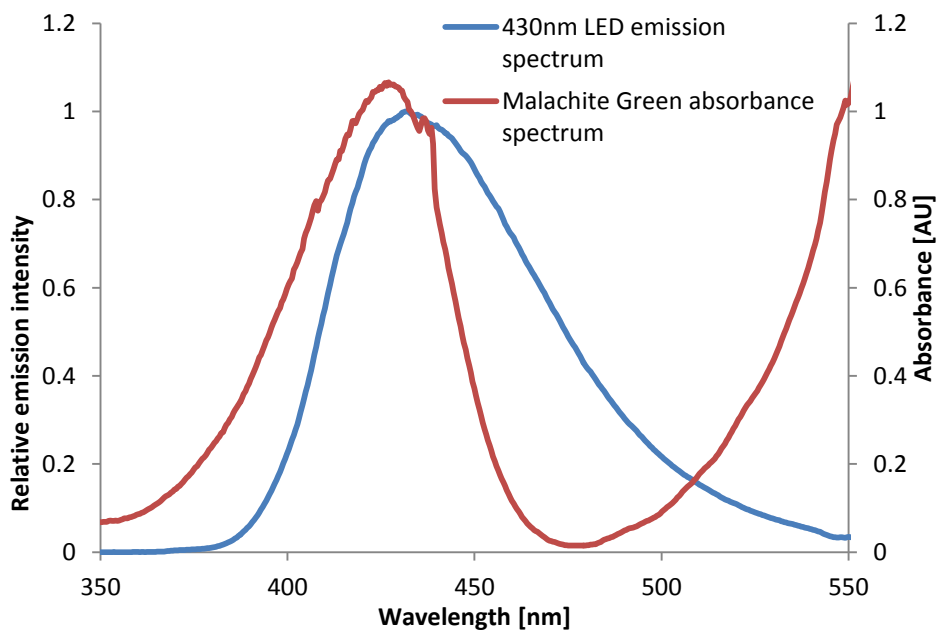


Figure 52: 430nm LED emission spectrum (blue line) for use as a light source in absorbance photometric detection of malachite green (red line).

3.2.6. Individual conditions for experiments on EHD focusing in microfluidic chip

The fabricated chip had three inlets and four outlets installed that could be enabled or disabled individually depending on the experimental setup (see Figure 53).

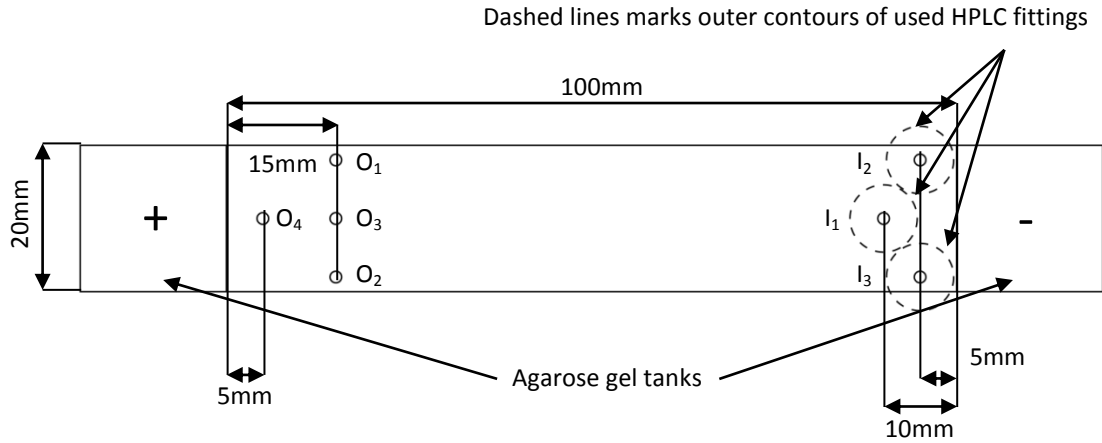


Figure 53: Plan schematic of the microfluidic chip used in focusing experiments.

Three general chip layouts were tested, which are named according to the outlet layouts used. The first series of experiments are named after using two peripheral outlets (O_1 and O_2) and was labelled 2P (see Figure 54). The second tested layout employed two outlets placed in line (O_3 and O_4) in the centre of the chip and was named 2L (see Figure 55). The third series employed application of three outlets placed in line transversally to the flow direction (O_1 , O_2 and O_3) and was labelled 3T (see Figure 56). The number following these prefix is the particular experiment number and can also be read from the presented photos documenting each experiment. Conditions for experiments 2P-14, 2P-22, 2P-30, 2P-47, 2L-15, 2L-16, 2L-17, 2L-26, 2L-40, 2L-41, 3T-20, 3T-21, 3T-24, 3T-31, 3T-36, 3T-43 AND 3T-58 are presented in Sections 3.2.6.1 to 3.2.6.17. Corresponding results are presented in Chapter 5 in Sections 5.1 to 5.17.



Figure 54: Schematic of the inlets and outlets and outlets used in the 2P-series experiments.

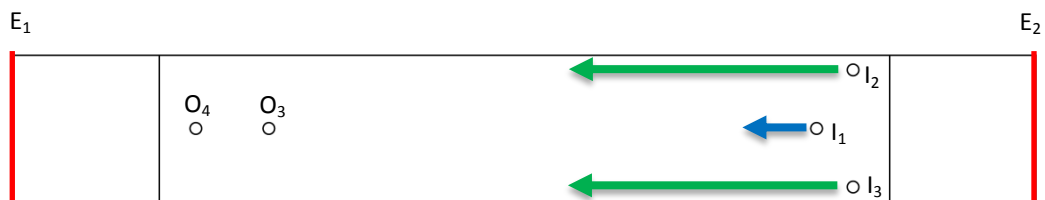


Figure 55: Schematic of the inlets and outlets and outlets used in the 2L-series experiments.

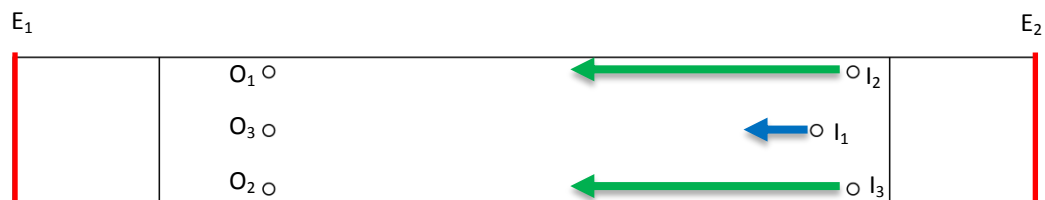


Figure 56: Schematic of the inlets and outlets and outlets used in the 3T-series experiments.

3.2.6.1. Problems observed during the initial stage of experiments

The initial experiments with the two peripheral outlets (2P experiment series) showed problems associated with the tubing used for waste collection. The two fingertight fittings with polymer tubing glued in were used to gather the outflowing fluid. Initial experiments showed that it was very difficult to maintain similar flow rates through each of these outlets. Even simple droplet counting showed significant discrepancies in the outflow rates. As even pressure distribution and equal outflow was regarded as a necessary condition to achieve the desired flow patterns, the fittings with tubing were removed and the outlets were left unrestricted. Overflowing liquid was gently removed with small piece of absorbing medium.

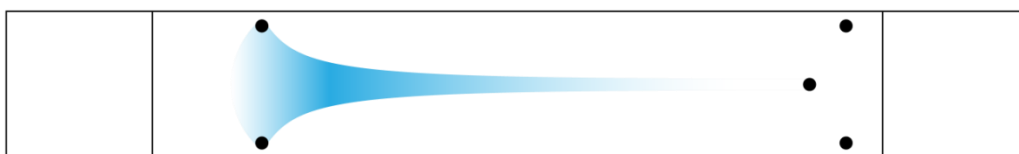


Figure 57: Schematic of the expected pattern of malachite green during a focusing experiment.

Figure 57 shows a schematic how a fluid would be expected to behave in the left part of the chip during a focusing experiment. A region of higher concentration should appear centrally in the chip, ideally along a symmetry axis of the chip and should start dispersing toward installed outlets. During experiments flow had tendency to divert toward one wall (e.g. to the bottom wall on the schematic, see Figure 58).

It was quite difficult to maintain even outflow even with tubing removed. Flow inside the chip showed tendencies to twist and turn instead of flowing smoothly. Comb-

like structures visible on Figure 58d are discussed later in this section. Typical problems associated with flow stability can be divided into categories:

- Oscillations of flow axis
- Uneven reach of the outlets
- Different wetting of the outlet

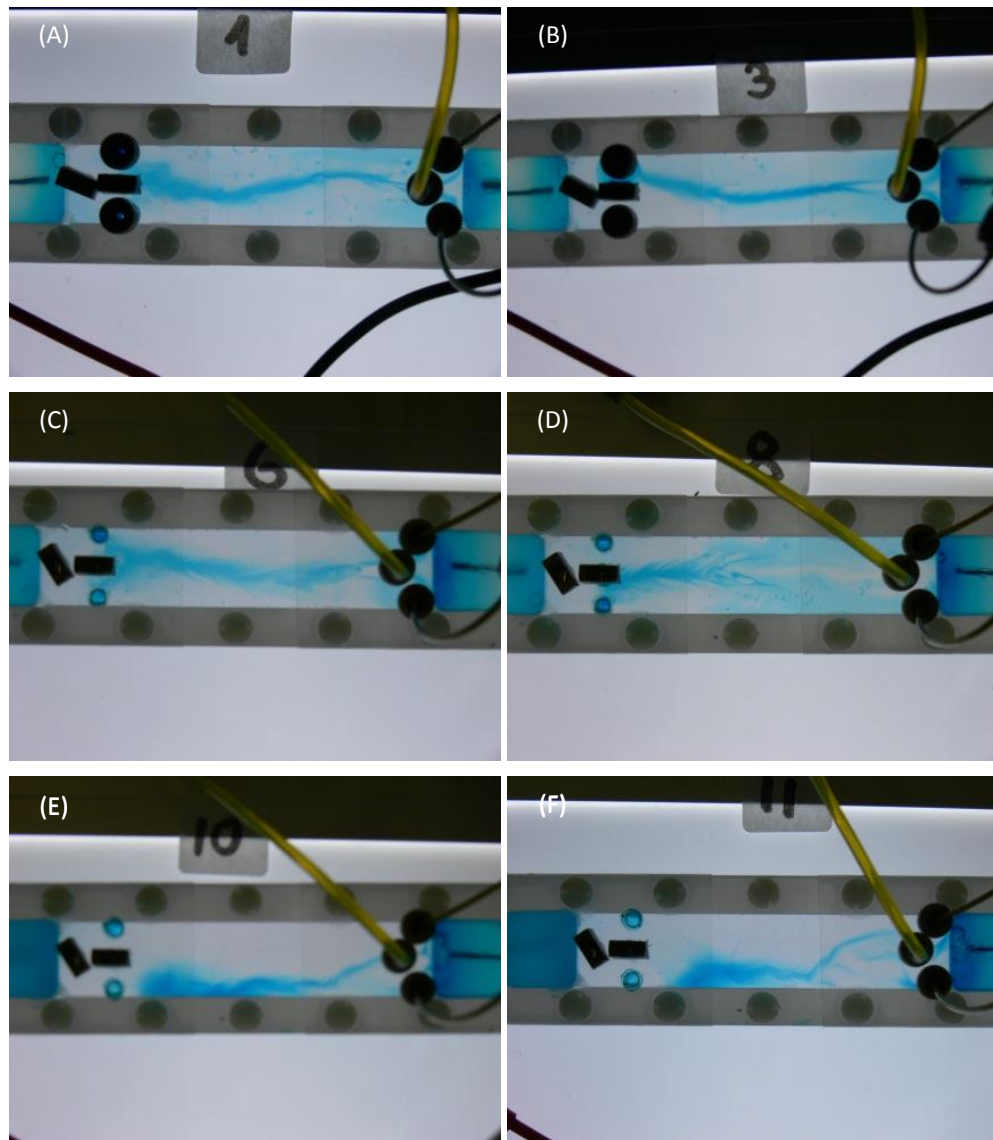


Figure 58a-f: Photos of observed problems with flow stability inside the chip.

The first two are attributed to unevenness in the surface morphology of the used chip. Occurrences did not appear random and repeated several times. Careful application of small pieces of tissue to simultaneously collect droplets forming in the outlets allowed minimising these effects. These effects intensified with reduction of the thickness of the used gasket. It was possible to maintain stable flow with 100 μ m thick gasket. The third problem was especially visible with thin gaskets (50 μ m and 100 μ m)

where the capillary action of the tissue was strong enough to drain completely one outlet, which diverted the flow after a while to the other outlet, which remained wet. The thinnest gasket (50 μ m) proved to be too thin to allow unrestricted flow and after several attempts to stabilise flow was abandoned.

3.2.6.2. Experiment 2P-14

The chip was primed with 0.1mM malachite green (MG). For 900s 20mM Tris-HCl buffer was pumped into the system at a flowrate of 4 μ l/min through the I₁ inlet. Malachite green at concentration of 0.1mM was pumped into the chip through the I₂ and I₃ inlets at a flowrate of 20 μ l/min. After 900s, a potential difference of 300V was applied. During the filling with Tris-HCl photos were taken every 300s, after applying the voltage photos were taken every 120s. The 500 μ m PTFE gasket was used. Figure 54 shows schematic of experimental setup and Table 21 provides summary of conditions.

Inlets	I ₁	I ₂	I ₃
Flowrate	4 μ l/min	20 μ l/min	20 μ l/min
Compound	20mM Tris-HCl	0.1mM MG	0.1mM MG
Gasket thickness	500 μ m		
Filling time	900s		
Voltage	300V after 900s		
Experiment time	1860s		

Table 21: Conditions for the experiment 2P-14.

3.2.6.3. Experiment 2P-22

The chip was primed with 0.1mM malachite green (MG). For 900s 20mM Tris-HCl buffer was pumped into the system at a flowrate of 5 μ l/min through the I₁ inlet. Malachite green at concentration of 0.1mM was pumped into the chip through the I₂ and I₃ inlets at a flowrate of 19 μ l/min. After 900s, a potential difference of 280V was applied. During the filling with Tris-HCl photos were taken every 300s, after applying the voltage photos were taken every 120s. 500 μ m PTFE gasket was used. Figure 54 shows schematic of experimental setup and Table 22 provides summary of conditions.

Inlets	I ₁	I ₂	I ₃
Flowrate	5 μ l/min	19 μ l/min	19 μ l/min
Compound	20mM Tris-HCl	0.1mM MG	0.1mM MG
Gasket thickness	500 μ m		
Filling time	900s		
Voltage	280V after 900s		
Experiment time	3060s		

Table 22: Conditions for the experiment 2P-22.

3.2.6.4. Experiment 2P-30

The chip was primed with 0.1mM malachite green (MG). For 1200s 20mM Tris-HCl buffer was pumped into the system at a flowrate of 2 μ l/min through the I₁ inlet. Malachite green at concentration of 0.1mM was pumped into the chip through the I₂ and I₃ inlets at a flowrate of 20 μ l/min. After 1200s, a potential difference of 300V was applied. During the filling with Tris-HCl photos were taken every 300s, after applying the voltage photos were taken every 120s. 500 μ m PTFE gasket was used. Figure 54 shows schematic of experimental setup and Table 23 provides summary of conditions.

Inlets	I ₁	I ₂	I ₃
Flowrate	2 μ l/min	20 μ l/min	20 μ l/min
Compound	20mM Tris-HCl	0.1mM MG	0.1mM MG
Gasket thickness	500 μ m		
Filling time	1200s		
Voltage	200V after 900s		
Experiment time	2520s		

Table 23: Conditions for the experiment 2P-30.

3.2.6.5. Experiment 2P-47

The chip was primed with 0.1mM malachite green (MG). For 600s 20mM Tris-HCl buffer was pumped into the system at a flowrate of 2 μ l/min through the I₁ inlet. Malachite green at concentration of 0.1mM was pumped into the chip through the I₂ and I₃ inlets at a flowrate of 20 μ l/min. After 600s, a potential difference of 300V was applied. During the filling with Tris-HCl photos were taken every 300s, after applying the voltage photos were taken every 120s. 200 μ m PTFE gasket was used. Figure 54 shows schematic of experimental setup and Table 24 provides summary of conditions.

Inlets	I ₁	I ₂	I ₃
Flowrate	2 μ l/min	20 μ l/min	20 μ l/min
Compound	20mM Tris-HCl	0.1mM MG	0.1mM MG
Gasket thickness	200 μ m		
Filling time	600s		
Voltage	300V after 600s		
Experiment time	2760s		

Table 24: Conditions for the experiment 2P-47.

3.2.6.6. Experiment 2L-15

The chip was primed with 0.1mM malachite green (MG). For 1200s 20mM Tris-HCl buffer was pumped into the system at a flowrate of 2 μ l/min through the I₁ inlet.

Malachite green at concentration of 0.1mM was pumped into the chip through the I₂ and I₃ inlets at a flowrate of 10µl/min. After 1200s, a potential difference of 300V was applied. During the filling with Tris-HCl photos were taken every 300s, after applying the voltage photos were taken every 120s. 500µm PTFE gasket was used. Figure 55 shows schematic of experimental setup and Table 25 provides summary of conditions.

Inlets	I ₁	I ₂	I ₃
Flowrate	2µl/min	10µl/min	10µl/min
Compound	20mM Tris-HCl	0.1mM MG	0.1mM MG
Gasket thickness	500µm		
Filling time	1200s		
Voltage	300V after 1200s		
Experiment time	2520s		

Table 25: Conditions for the experiment 2L-15.

3.2.6.7. Experiment 2L-16

The chip was primed with 0.1mM malachite green (MG). For 900s 20mM Tris-HCl buffer was pumped into the system at a flowrate of 4µl/min through the I₁ inlet. Malachite green at concentration of 0.1mM was pumped into the chip through the I₂ and I₃ inlets at a flowrate of 20µl/min. After 900s, a potential difference of 300V was applied. During the filling with Tris-HCl photos were taken every 300s, after applying the voltage photos were taken every 120s. 500µm PTFE gasket was used. Figure 55 shows schematic of experimental setup and Table 26 provides summary of conditions.

Inlets	I ₁	I ₂	I ₃
Flowrate	4µl/min	20µl/min	20µl/min
Compound	20mM Tris-HCl	0.1mM MG	0.1mM MG
Gasket thickness	500µm		
Filling time	900s		
Voltage	300V after 900s		
Experiment time	2140s		

Table 26: Conditions for the experiment 2L-16.

3.2.6.8. Experiment 2L-17

The chip was primed with 0.1mM malachite green (MG). For 1200s 20mM Tris-HCl buffer was pumped into the system at a flowrate of 2µl/min through the I₁ inlet. Malachite green at concentration of 0.1mM was pumped into the chip through the I₂ and I₃ inlets at a flowrate of 20µl/min. After 1200s, a potential difference of 300V was applied. During the filling with Tris-HCl photos were taken every 300s, after applying the

voltage photos were taken every 120s. 500 μ m PTFE gasket was used. Figure 55 shows schematic of experimental setup and Table 27 provides summary of conditions.

Inlets	I ₁	I ₂	I ₃
Flowrate	2 μ l/min	20 μ l/min	20 μ l/min
Compound	20mM Tris-HCl	0.1mM MG	0.1mM MG
Gasket thickness	500 μ m		
Filling time	1200s		
Voltage	300V after 1200s		
Experiment time	2160s		

Table 27: Conditions for the experiment 2L-17.

3.2.6.9. Experiment 2L-26

In this experiment the outlet O₁ was blocked. The chip was primed with 0.1mM malachite green (MG). For 900s 20mM Tris-HCl buffer was pumped into the system at a flowrate of 2 μ l/min through the I₁ inlet. Malachite green at concentration of 0.1mM was pumped into the chip through the I₂ and I₃ inlets at a flowrate of 20 μ l/min. After 900s, a potential difference of 295V was applied. During the filling with Tris-HCl photos were taken every 300s, after applying the voltage photos were taken every 120s. 500 μ m PTFE gasket was used. Figure 55 shows schematic of experimental setup and Table 28 provides summary of conditions.

Inlets	I ₁	I ₂	I ₃
Flowrate	2 μ l/min	20 μ l/min	20 μ l/min
Compound	20mM Tris-HCl	0.1mM MG	0.1mM MG
Gasket thickness	500 μ m		
Filling time	900s		
Voltage	295V after 1200s		
Experiment time	2940s		

Table 28: Conditions for the experiment 2L-26.

3.2.6.10. Experiment 2L-40

The chip was primed with 0.1mM malachite green (MG). For 600s 20mM Tris-HCl buffer was pumped into the system at a flowrate of 2 μ l/min through the I₁ inlet. Malachite green at concentration of 0.1mM was pumped into the chip through the I₂ and I₃ inlets at a flowrate of 20 μ l/min. After 600s, a potential difference of 595V was applied. During the filling with Tris-HCl photos were taken every 300s, after applying the voltage photos were taken every 120s. 200 μ m PTFE gasket was used. Figure 55 shows schematic of experimental setup and Table 29 provides summary of conditions.

Inlets	I ₁	I ₂	I ₃
Flowrate	2µl/min	20µl/min	20µl/min
Compound	20mM Tris-HCl	0.1mM MG	0.1mM MG
Gasket thickness	200µm		
Filling time	600s		
Voltage	595V after 600s		
Experiment time	2640s		

Table 29: Conditions for the experiment 2L-40.

3.2.6.11. Experiment 2L-41

In this experiment the outlet O₁ was blocked. The chip was primed with 0.1mM malachite green (MG). For 900s 20mM Tris-HCl buffer was pumped into the system at a flowrate of 2µl/min through the I₁ inlet. Malachite green at concentration of 0.1mM was pumped into the chip through the I₂ and I₃ inlets at a flowrate of 20µl/min. After 600s, a potential difference of 750V was applied. During the filling with Tris-HCl photos were taken every 300s, after applying the voltage photos were taken every 120s. 200µm PTFE gasket was used. Figure 55 shows schematic of experimental setup and Table 30 provides summary of conditions.

Inlets	I ₁	I ₂	I ₃
Flowrate	2µl/min	20µl/min	20µl/min
Compound	20mM Tris-HCl	0.1mM MG	0.1mM MG
Gasket thickness	200µm		
Filling time	600s		
Voltage	750V after 600s		
Experiment time	2160s		

Table 30: Conditions for the experiment 2L-41.

3.2.6.12. Experiment 3T-20

The chip was primed with 0.1mM malachite green (MG). For 900s 20mM Tris-HCl buffer was pumped into the system at a flowrate of 2µl/min through the I₁ inlet. Malachite green at concentration of 0.1mM was pumped into the chip through the I₂ and I₃ inlets at a flowrate of 20µl/min. After 900s, a potential difference of 280V was applied. During the filling with Tris-HCl photos were taken every 300s, after applying the voltage photos were taken every 120s. 500µm PTFE gasket was used. Figure 56 shows schematic of experimental setup and Table 31 provides summary of conditions.

Inlets	I ₁	I ₂	I ₃
Flowrate	2µl/min	20µl/min	20µl/min
Compound	20mM Tris-HCl	0.1mM MG	0.1mM MG
Gasket thickness	500µm		
Filling time	900s		
Voltage	280V after 900s		
Experiment time	3540s		

Table 31: Conditions for the experiment 3T-20.

3.2.6.13. Experiment 3T-21

The chip was primed with 0.1mM malachite green (MG). For 600s 20mM Tris-HCl buffer was pumped into the system at a flowrate of 2µl/min through the I₁ inlet. Malachite green at concentration of 0.1mM was pumped into the chip through the I₂ and I₃ inlets at a flowrate of 20µl/min. After 600s, a potential difference of 250V was applied. During the filling with Tris-HCl photos were taken every 300s, after applying the voltage photos were taken every 120s. 500µm PTFE gasket was used. Figure 56 shows schematic of experimental setup and Table 32 provides summary of conditions.

Inlets	I ₁	I ₂	I ₃
Flowrate	2µl/min	20µl/min	20µl/min
Compound	20mM Tris-HCl	0.1mM MG	0.1mM MG
Gasket thickness	500µm		
Filling time	600s		
Voltage	250V after 600s		
Experiment time	1920s		

Table 32: Conditions for the experiment 3T-21.

3.2.6.14. Experiment 3T-24

The chip was primed with 0.1mM malachite green (MG). For 600s 20mM Tris-HCl buffer was pumped into the system at a flowrate of 5µl/min through the I₁ inlet. Malachite green at concentration of 0.1mM was pumped into the chip through the I₂ and I₃ inlets at a flowrate of 20µl/min. After 600s, a potential difference of 350V was applied. During the filling with Tris-HCl photos were taken every 300s, after applying the voltage photos were taken every 120s. 500µm PTFE gasket was used. Figure 56 shows schematic of experimental setup and Table 33 provides summary of conditions.

Inlets	I ₁	I ₂	I ₃
Flowrate	5µl/min	20µl/min	20µl/min
Compound	20mM Tris-HCl	0.1mM MG	0.1mM MG
Gasket thickness	500µm		
Filling time	600s		
Voltage	350V after 600s		
Experiment time	2280s		

Table 33: Conditions for the experiment 3T-24.

3.2.6.15. Experiment 3T-31

The chip was primed with 0.1mM malachite green (MG). For 900s 20mM Tris-HCl buffer was pumped into the system at a flowrate of 2µl/min through the I₁ inlet. Malachite green at concentration of 0.1mM was pumped into the chip through the I₂ and I₃ inlets at a flowrate of 20µl/min. After 900s, a potential difference of 310V was applied. During the filling with Tris-HCl photos were taken every 300s, after applying the voltage photos were taken every 120s. 500µm PTFE gasket was used. Figure 56 shows schematic of experimental setup and Table 34 provides summary of conditions.

Inlets	I ₁	I ₂	I ₃
Flowrate	2µl/min	20µl/min	20µl/min
Compound	20mM Tris-HCl	0.1mM MG	0.1mM MG
Gasket thickness	500µm		
Filling time	900s		
Voltage	310V after 900s		
Experiment time	2340s		

Table 34: Conditions for the experiment 3T-24.

3.2.6.16. Experiment 3T-36

The chip was primed with 0.1mM malachite green (MG). For 600s 20mM Tris-HCl buffer was pumped into the system at a flowrate of 2µl/min through the I₁ inlet. Malachite green at concentration of 0.1mM was pumped into the chip through the I₂ and I₃ inlets at a flowrate of 20µl/min. After 600s, a potential difference of 300V was applied. During the filling with Tris-HCl photos were taken every 300s, after applying the voltage photos were taken every 120s. 500µm PTFE gasket was used. Figure 56 shows schematic of experimental setup and Table 35 provides summary of conditions.

Inlets	I ₁	I ₂	I ₃
Flowrate	2µl/min	20µl/min	20µl/min
Compound	20mM Tris-HCl	0.1mM MG	0.1mM MG
Gasket thickness	500µm		
Filling time	900s		
Voltage	300V after 900s		
Experiment time	1860s		

Table 35: Conditions for the experiment 3T-36.

3.2.6.17. Experiment 3T-43

The chip was primed with 0.1mM malachite green (MG). For 600s 20mM Tris-HCl buffer was pumped into the system at a flowrate of 2µl/min through the I₁ inlet. Malachite green at concentration of 0.1mM was pumped into the chip through the I₂ and I₃ inlets at a flowrate of 20µl/min. After 600s, a potential difference of 600V was applied. During the filling with Tris-HCl photos were taken every 300s, after applying the voltage photos were taken every 120s. 200µm PTFE gasket was used. Figure 56 shows schematic of experimental setup and Table 36 provides summary of conditions.

Inlets	I ₁	I ₂	I ₃
Flowrate	2µl/min	20µl/min	20µl/min
Compound	20mM Tris-HCl	0.1mM MG	0.1mM MG
Gasket thickness	200µm		
Filling time	600s		
Voltage	600V after 600s		
Experiment time	1800s		

Table 36: Conditions for the experiment 3T-43.

3.2.6.18. Experiment 3T-58

The chip was primed with 0.1mM malachite green (MG). For 300s 20mM Tris-HCl buffer was pumped into the system at a flowrate of 2µl/min through the I₁ inlet. Malachite green at concentration of 0.1mM was pumped into the chip through the I₂ and I₃ inlets at a flowrate of 20µl/min. After 300s, a potential difference of 1200V was applied. During the filling with Tris-HCl photos were taken every 300s, after applying the voltage photos were taken every 120s. 100µm PTFE gasket was used. Figure 56 shows schematic of experimental setup and Table 37 provides summary of conditions.

Inlets	I ₁	I ₂	I ₃
Flowrate	2µl/min	20µl/min	20µl/min
Compound	20mM Tris-HCl	0.1mM MG	0.1mM MG
Gasket thickness	100µm		
Filling time	300s		
Voltage	1200V after 300s		
Experiment time	2580s		

Table 37: Conditions for the experiment 3T-58.

3.2.6.19. Reproducibility of the EHDF

The chip was primed with 0.1mM malachite green (MG). For 1200s 20mM Tris-HCl buffer was pumped into the system at a flowrate of 2µl/min through the I₁ inlet. Malachite green at concentration of 0.1mM was pumped into the chip through the I₂ and I₃ inlets at a flowrate of 20µl/min. After 1200s, a potential difference of 250V was applied. During the filling with Tris-HCl photos were taken every 300s, after applying the voltage photos were taken every 120s. 500µm PTFE gasket was used. Six series of experiment with the same set of conditions were conducted. Figure 54 shows schematic of the experimental setup used and Table 38 provides a summary of the conditions.

Inlets	I ₁	I ₂	I ₃
Flowrate	2µl/min	20µl/min	20µl/min
Compound	20mM Tris-HCl	0.1mM MG	0.1mM MG
Gasket thickness	500µm		
Filling time	1200s		
Voltage	250V after 1200s		
Experiment time	3120s		

Table 38: Conditions for the experiment on repeatability.

3.3. Modelling and experiments of the light propagation in microfluidic systems

3.3.1. Software used

The Light propagation and light intensity distribution models were developed under LabVIEW™ 8.2, 8.5.1 and 2009 (9.0.1) graphical programming environment developed by National Instruments. Graphic-related work, such as generation of multi-colour maps, reading pixel colours etc. were conducted with Adobe Photoshop CS 3 ver. 10.0.1. Dimension and angle measurements on taken photos were performed using ImageJ 1.43u software.

3.3.2. Materials and chemicals used in experiments on light propagation

Two sets of macroscale experiment with the polymer tubes made of polymethylmetacrylate (PMMA) and polycarbonate (PC) were purchased from Access Plastic Company, Ireland. The two sets of concentric plastic cylinders were made with outer and inner diameter as follows Set A: 80x74mm PC and 70x60mm PMMA and Set B: 80x70mm PMMA and 70x64mm PC. The refractive indices used in the developed models for PMMA and PC were 1.495 and 1.592 respectively (255).

The used Polymicro Technologies transparent PTFE coated fused silica capillaries of 100 μm internal diameter were purchased from Composite Metal Services Ltd (UK).

The LED (type LED430-06) of 5mm diameter and 430 nm central wavelength violet was purchased from Roithner Lasertechnik, GmbH, Vienna, Austria. The white LED of 5 mm diameter was manufactured by Nichia (type NSPW500GS-K1), was purchased from Dotlight, Jülich, Germany.

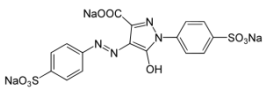
Name	Structure	Manufacturer	Purity	CAS Number
Tartrazine	 The chemical structure shows a central pyrazolone ring system. One nitrogen atom is substituted with a sodium sulfonate group (-SO ₃ Na). The other nitrogen atom is substituted with a 4-sulfonatephenyl group (-C ₆ H ₄ -SO ₃ Na). The ring also has a carboxylate group (-COO ⁻ Na ⁺) and a hydroxyl group (-OH) attached to the carbon atoms.	Sigma-Aldrich®	>85%	1934-21-0

Table 39: List of chemicals used in experiments on light propagation.

3.3.3. Materials and chemicals used in experiment with photopolymerisation of monoliths in capillaries

Polymicro Technologies Inc. (Phoenix, AZ, USA) transparent polytetrafluoroethylene (PTFE) coated fused silica capillaries (100 μm i.d.) were purchased from Composite Metal Services Ltd, UK. 365 nm light emitting diodes were purchased from Roithner Lasertechnik, GmbH (Vienna, Austria). HPLC pump (Waters 510) was used to flush the capillaries after the polymerisation.

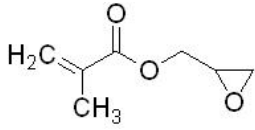
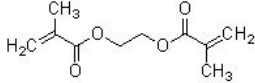
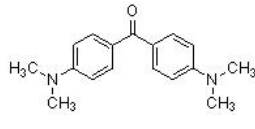
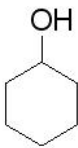
Name	Structure	Manufacturer	Purity	CAS Number
Glycidyl methacrylate		Sigma-Aldrich®	97%	106-91-2
Ethylene dimethacrylate		Sigma-Aldrich®	98%	97-90-5
Michler's ketone		Sigma-Aldrich®	98%	90-94-8
Cyclohexanol		Riedel-de Haën	≥99%	108-93-0
1-decanol	$\text{CH}_3(\text{CH}_2)_8\text{CH}_2\text{OH}$	Sigma-Aldrich®	≥98%	112-30-1

Table 40: List of chemicals used for photopolymerisation of monoliths in capillaries for verification of the light propagation model.

3.3.4. Procedure of development of the light propagation model

Whenever light is incident on the boundary of two transparent dielectrics part of it is reflected and part is transmitted, see Figure 59. The angle of incidence is related with the angle of transmittance by Snell's Law (Eq. 21). In the case of cylindrical symmetry, as in capillaries, it is possible that the exiting ray will not be parallel with the incident, see Figure 60.

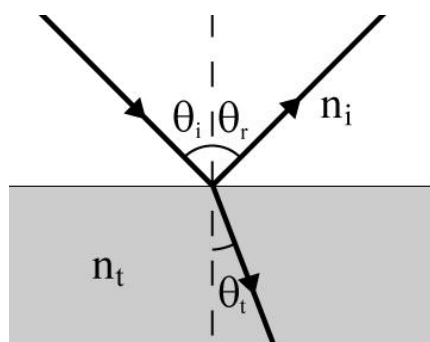


Figure 59: Light incident on boundary of two different dielectrics.

(b)

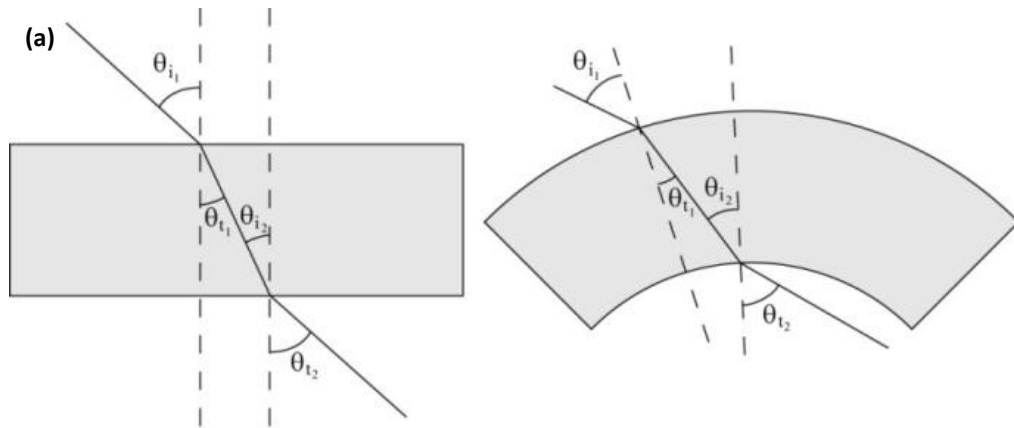


Figure 60: Schematic of light transmission through, (a) a flat transparent material and (b) a cylindrical capillary, showing curvature affects on angle of incidence and transmittance.

$$n_i \cdot \sin \theta_i = n_t \cdot \sin \theta_t \quad \text{Eq. 21}$$

where n_i is the refractive index of the incident ray transmission medium, θ_i is the angle between incident wavevector and the normal to surface, n_t is the refractive index of the material through with the transmitted ray passes and θ_t is the angle between transmitted wavevector and normal to the surface. Light attenuation inside the absorbing medium is governed by Beer-Lambert law (Eq. 15).

$$I = I_0 \cdot e^{-\alpha cl} \quad \text{Eq. 15}$$

where I is the initial light intensity, I_0 is the light intensity behind the sample, α is the molar absorptivity coefficient, c is concentration of the compound and l is length is the absorption path length.

The numerical modelling software was developed to calculate the light ray path through multi-layered cylinders, and the light intensity distribution map through the cylinder cross-sectional area. Light propagation within multimode optical fibres occurs by the phenomena of total internal reflection, where the values of refractive indices and fibre diameter remain within the limits of geometrical optics. The size of the capillary used in this work was comparable with the size of multimode optical fibres. It was assumed that capillary body, coating and bore were perfectly cylindrical and concentric. A second assumption was that the incident light had the form of parallel rays (spatially collimated), similar to laser beam light. Only the right half of the capillary cross-section is displayed in the developed model, as the diameter acts as the modelled axis of

symmetry and no light ray could propagate through from left to right side. In general such occurrence is possible, but only for higher values of refractive indices approximately twice those of glass and PTFE which were used in this work.

The programmed model calculated the light ray path equations in the Cartesian coordinate system. Separate linear functions to describe each of the light ray path segments were used (for example between air/tube, tube/tube or tube/liquid). Each light path segment was calculated in a separate subroutine calculating the light path in each zone. Incident light was in the form of rays parallel to y-axis, see Figure 61. The first subroutine calculated the coordinates of the light incident from infinity on the air/coating boundary. This point of incidence of the ray a_1 on outermost circle c_1 was assigned as p_1 . An extended radius r_1 going from (0, 0) through p_1 was drawn for calculation of angle of incidence θ_{i1} and in turn angle of transmission θ_{t1} was calculated from Eq. 21, for the use inputted values of refractive indices n_i and n_t . A line a_2 through p_1 was drawn representing the refracted ray in the coating with θ_{t1} as the angle between a_2 and r_1 , *ending the first program subroutine*, see Figure 61A. The next subroutine began with calculation of point p_2 (where line a_2 crossed boundary c_2) and the drawing of extended radius r_2 from (0, 0) through p_2 . Angle of incidence θ_{i2} was calculated as the angle bounded by r_2 and a_2 , see Figure 61B. Angle of transmittance θ_{t2} was calculated from Eq. 21 and the line a_3 was drawn where θ_{t2} was and angle between r_2 and a_3 , *ending the second program subroutine*, see Figure 61B. This subroutine was iterated a further three times to calculate light ray paths segments along lines a_4 , a_5 and a_6 after refraction on each encountered boundary. These next subroutines of the light path formation are illustrated in Figure 61C to E and the complete generated light path is presented in Figure 61F without reference lines. The entire light path was represented as a sum of individual rays calculated separately according to the symbolic algorithm:

$$r = \sum_{k=1}^{2n} (a_k \cap c_k \rightarrow p_k \rightarrow r_k \rightarrow \theta_{i_k} \rightarrow \theta_{t_k} \rightarrow a_{k+1})$$

where r is a light ray path, k is a step number; n is a number of layers; a , c , p , r , θ_i and θ_t are as described earlier.

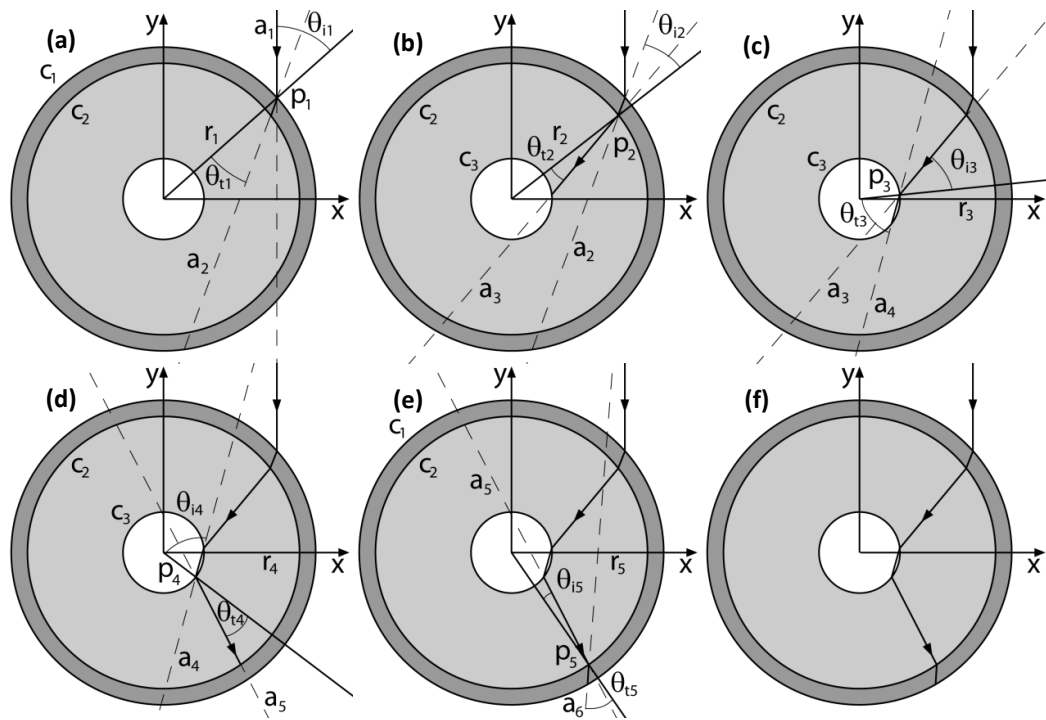


Figure 61: Schematic of reference lines and points, and light ray path calculated by each sub-routine for light passing through a three layer system in which the light ray path is passing through a coated hollow capillary

For light intensity calculations the entire capillary bore (100 μm inner diameter which was modelled) was divided into a $0.1 \times 0.1 \mu\text{m}$ grid and assigned with initial light intensity values of zero, see Figure 62. This resolution was determined to be adequate giving 500 cells along capillary radius and 1000 cells across capillary diameter. The external capillary surface was illuminated by a set of parallel light rays spaced $0.1 \mu\text{m}$ apart. Each individual light ray was propagated through the entire capillary, giving a single light path for each incident light ray at each x-value. Modelled light ray incidence direction and x-axis direction are the same as shown in Figure 61 and Figure 62. Note a new origin (0, 0) and y-axis direction are shown in Figure 62. For light intensity modelling it was assumed that there was no light absorption or attenuation in the capillary coating and capillary wall. Cell references for each light ray inside capillary bore were calculated to allow attribution of light intensity values from each ray to related cells, see Figure 62. Along each ray path, the light intensity at each cell was calculated as a percentage of initial intensity from Eq. 15. The intensity contribution from each ray to each cell was calculated separately and summed to give the total light intensity value in each cell. Due to the finite size of the cells and finite distance between incident rays, digitisation of the light intensity values across the capillary resulted. To visualise a more physically correct result all values were averaged using a 19 point moving average calculation along the x-

axis. By using this 19 point moving average method, there was a loss of accurate information for a $1.9 \mu\text{m}$ region (i.e. $19 \times 0.1\mu\text{m}$) at the outer diameter of the $100 \mu\text{m}$ bore (for x-values from 231 to 250).

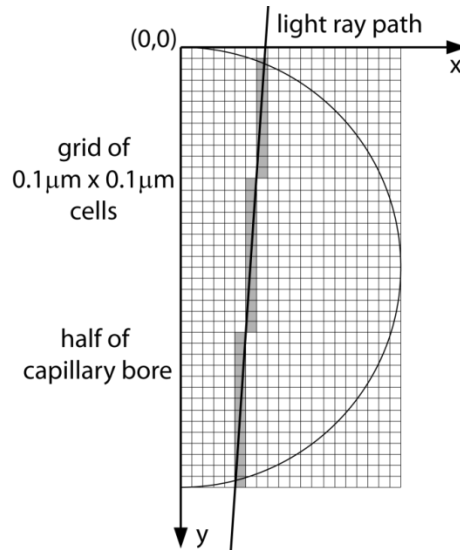


Figure 62: Scheme of method used by algorithm for allocation of cell x and y reference values to a light ray for calculation of related light intensity values at each location.

3.3.5. Light propagation model verification procedure

The green laser of 5 mW with wavelength of 532nm which was used as the light source was mounted on a micrometric stage pointing parallel to the axis of symmetry (y-axis) as shown in Figure 63. The laser was aligned to shine exactly along the longitudinal axis of symmetry of the tube and then moved 40mm along the x-axis such that the laser line formed a tangent to the outer cylinder. During the experiment the laser was moved by 1mm increments toward the cylinder's centre.

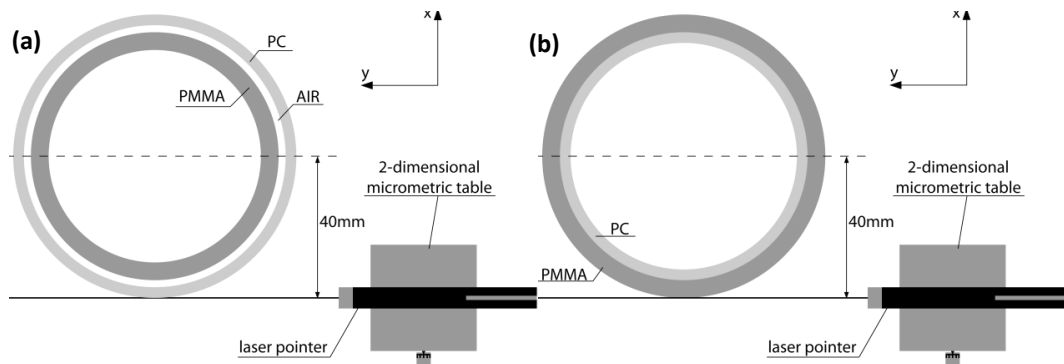


Figure 63: Schematic plan view of initial positions of laser with the (a) 80x74mm PC and 70x60mm PMMA concentric cylinders (Set A) and the (b) 80x70mm PMMA and 70x64mm PC concentric cylinders (Set B).

At each increment a picture, taken with a Panasonic LUMIX DMC-FZ30 digital camera mounted vertically overhead, was taken to measure the reflection and transmission angles in each cylinder for comparison with the corresponding numerical model results. Measurements were taken for points between from 15 to 40mm from the central axis point. These tests were repeated three times with average reflectance and transmission angles being recorded. Confidence intervals for these results using a 95% level and t-distribution were calculated.

The microscale experimental measurements of the optical light intensity in a 100 μm internal diameter capillary were recorded. These measurements were compared with the theoretical values as determined from numerical simulations. The capillary of 1 cm length was filled with 0.01M solution of tartrazine and illuminated with white and 430nm violet LEDs. Tartrazine is a yellow food dye with the maximum absorbance for which was measured around 425 nm, and thus an LED with emission maximum in the range where tartrazine is highly absorbing was chosen, see Figure 64. The experimental setup is presented in Figure 65.

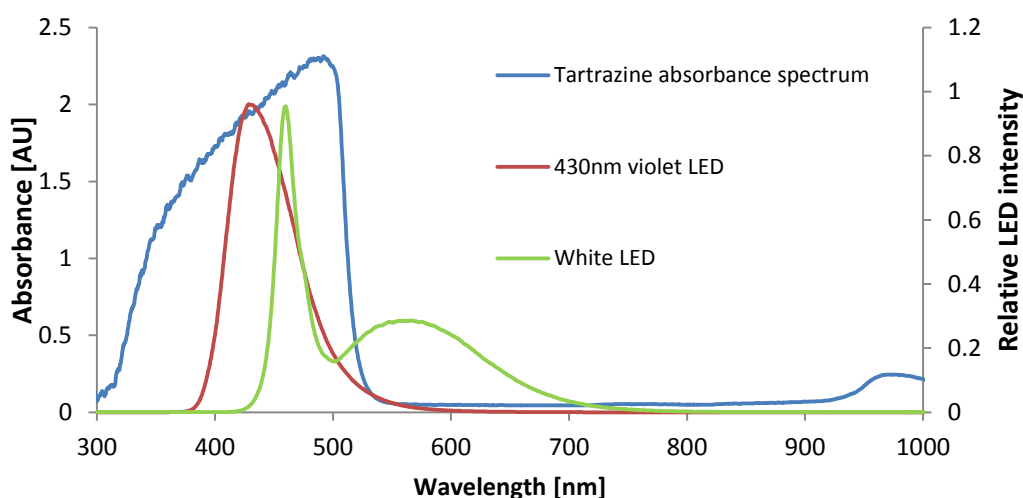


Figure 64: (a) Absorbance spectrum of tartrazine, (b) relative emission spectrum of the 430nm violet LED, and (c) relative emission spectrum of the white LED.

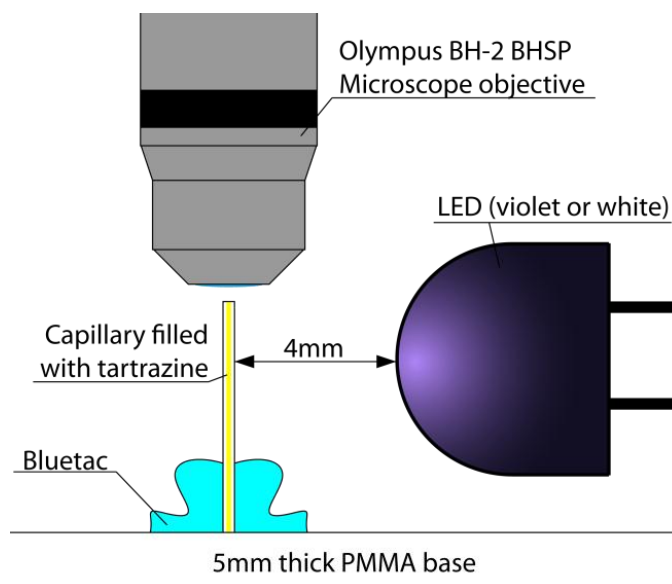


Figure 65: Schematic of the experimental setup for the light intensity distribution measurements inside the 100 μ m inner bore capillary.

3.3.6. Procedure of obtaining monoliths by photopolymerisation in capillaries for observation of light propagation changes

Methacrylic monoliths were synthesised using glycidyl methacrylate (GMA) and ethylene dimethacrylate (EDMA) (1/1 v/v). Cyclohexanol and decanol (1/2 v/v) were used as porogens. The photopolymerisation experiments are described in (256) with details briefly summarized as follows. The polymerisation mixture (400 μ l) consisted of 60 μ l GMA, 60 μ l EDMA, 1.26 mg (1% to monomer) photoinitiator MK, 95 μ l of cyclohexanol, and 185 μ l of decanol (1/2 v/v). After sonication and purging with nitrogen polymerisation mixture was filled into the silanized fused silica capillary and both ends were sealed with a rubber septum. In order to have sharp edges of monolith, the capillary was masked using a black tape.

An experiment demonstrating the real-time visualisation of the fluorescent dye is presented separately in the Appendix F.

3.4. Summary of experimental approach

The final goal of this work was the development of a novel microfluidic platform for preconcentration of analytes. The experimental approach was based on development of theoretical models of microfluidic systems that were verified experimentally. During this study a need for deeper understanding of the optical

properties of the used systems emerged. This section of work was studied using the same experimental approach: development of appropriate numerical model that followed by its experimental cross-examination.

The analysis of microfluidic systems was conducted using COMSOL Multiphysics software. The development of the numerical model of EHDF allowed for verification of the first research hypothesis: ability to attain the flow pattern needed to observe the EHDF. Although the initial assumptions on application of multiple additional outlets were discarded after an extensive study of the numerical models, a new chip was developed with the flow pattern properties remaining unchanged.

During the investigation of flow properties using numerical models the second and the third research hypotheses were confirmed: that the presence of trapezoidal flow pattern allows for formation of the electric field gradient and focusing of at least one compound.

To confirm the fourth research hypothesis a numerical model of light propagation and light intensity distribution in capillaries and microfluidic chips was developed. This model was positively verified experimentally and used to optimise the detection system in the chip for EHDF.

Chapter 4 – Modelling of microfluidic systems: results and discussion

Following chapter presents results of numerical simulations using COMSOL Multiphysics® and experiments with microfluidic chips. The modelling results includes comparison with previously conducted and published experiments, as well as studies of completely new designs, investigation how installation of multiple outlets affects flow pattern and preliminary results of preconcentration of analyte. The experimental results show different approaches to EHDF using different outlet layouts and gasket thicknesses. Final part concerns experimental results with on-line fluorescent detection in microfluidic chips.

4.1. Analysis of mesh density impact on simulation results

Although meshing is just a step during model development if inadequate it can seriously affect overall model quality and final results. Used mesh density should be as high as the parameters of the used computer can allow. One model discussed late in details was chosen as an example how mesh quality influence modelled result. Later models were developed using mesh at the computational limit of the used computer. Five different mesh densities were tested, namely: extremely coarse, coarser, normal, finer and extremely fine.

The first tested mesh density was extremely coarse, and as it can be seen from Figure 66 results were very inadequate. The maximum recorded concentration is 0.487M, while it should not exceed the initial concentration of 0.1mM, as the model involves only flow, convection and diffusion. A large part of the graph is white – these are areas where calculated concentration is either above initial value of 0.1M or below 0. The calculation error of almost 400% shows very significant inadequacy of used mesh density. The modelled negative concentration of -0.134M also informs about very significant numerical oscillations in the chip (white and blue stripes oppositely).

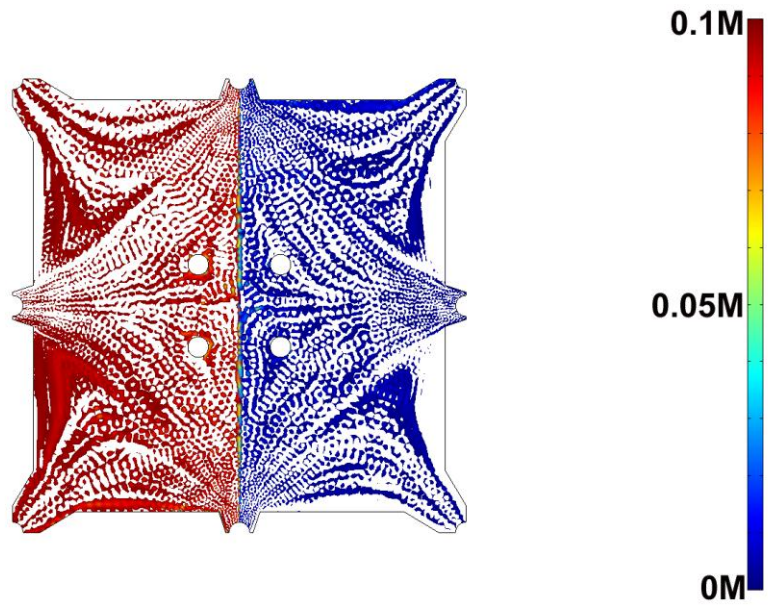


Figure 66: Modelling result for extremely coarse mesh grind. The colour to concentration assignment is on the left. White areas show where calculated concentration exceeds given range from 0 to 0.1M.

The second tested mesh density was named coarser. This mesh (presented in Figure 67) despite increase of the mesh elements number by 20% shows even more erroneous results with observed maximum of 0.570M and minimum of -0.384M. Even though absolute values of incorrectly calculated concentration are higher than in the extremely coarse mesh case, white area is noticeably smaller. This implies that with mesh refinement overall quality of the simulation is increasing.

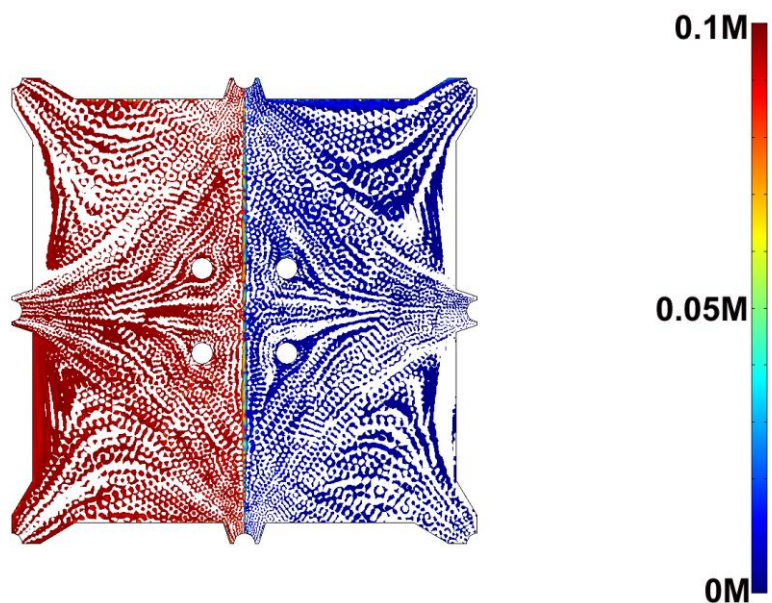


Figure 67: Modelling result for coarser mesh grid. The colour to concentration assignment is on the left. White areas show where calculated concentration exceeds given range from 0 to 0.1M.

Further mesh refinement (mesh density “normal”, see Figure 68), doubling initial number of mesh elements increased modelling quality and reduced error to 56% with maximum recorded concentration of 0.156M (0.1M initial). The observed minimum of -0.05M and large white area shows that numerical oscillations are still very significant and further mesh refinement is needed. Noticeably white areas are taking less surface than in previous simulations.

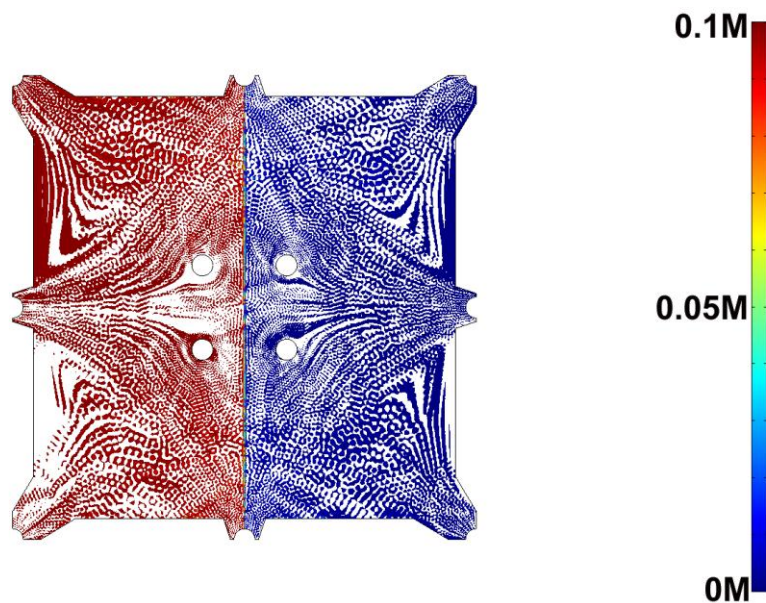


Figure 68: Modelling result for normal mesh grid. The colour to concentration assignment is on the left. White areas show where calculated concentration exceeds given range from 0 to 0.1M.

Figure 69 and Figure 70 are presenting modelling results for finer mesh and extremely fine respectively. Increasing mesh the density to maximum (using pre-defined settings) allowed reducing the concentration error to 40% and the value of negative concentration error to 20%. Such results were still unsatisfactory and significant improvements were needed. With further refinement of the mesh amount of data exceeding realistic values dropped visibly. To achieve this manual meshing was used and grid consisting over 119,000 elements was used to reduce error below 2% for positive (1.02mM) and 1.5% for negative concentration (-0.015mM).

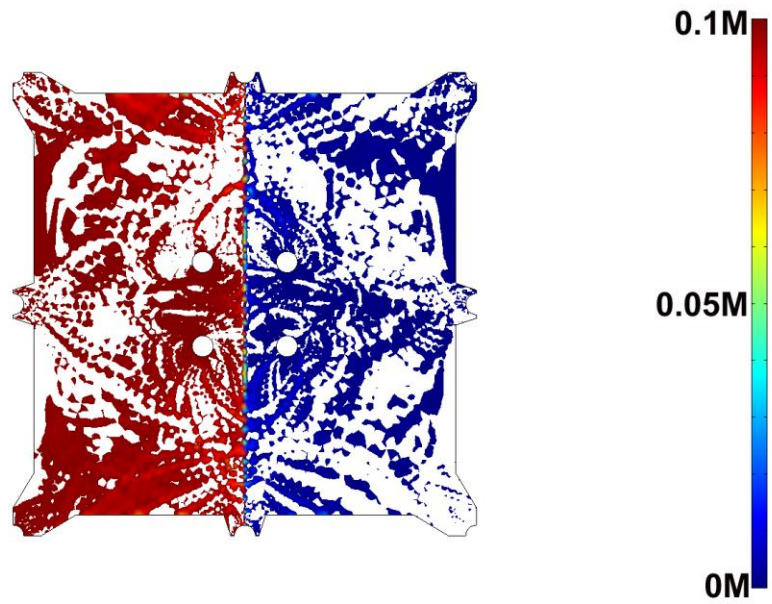


Figure 69: Modelling result for finer mesh grid. The colour to concentration assignment is on the left. White areas show where calculated concentration exceeds given range from 0 to 0.1M.

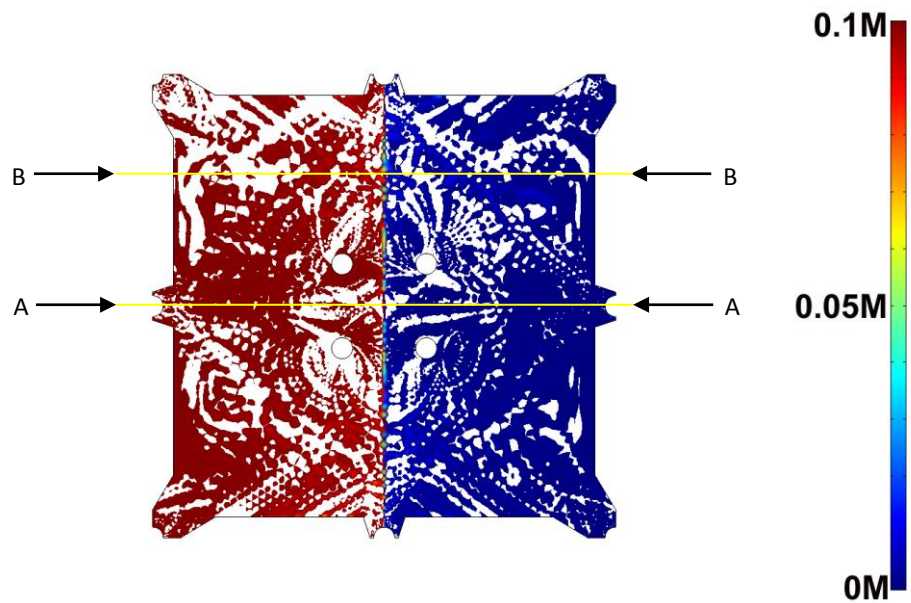


Figure 70: Modelling result for extremely fine mesh grid. The colour to concentration assignment is on the left. White areas show where calculated concentration exceeds given range from 0 to 0.1mM.

The progressing mesh refinement resulted in improved simulation performances but also increased time needed to find solution as well as operating memory requirements. Figure 71 summarises time needed to obtain full solution depending on the used mesh density.

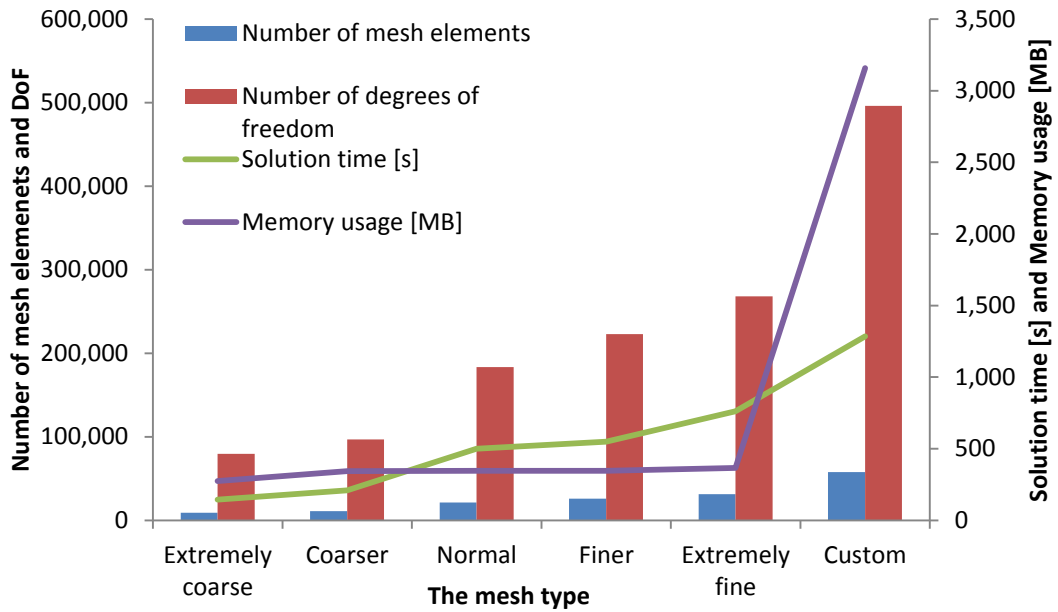


Figure 71: Graph showing comparison of number of mesh elements, degrees of freedom, solution times and memory usage for different mesh densities.

Concentration profiles measured on both profiles (along A-A and B-B, presented in Figure 72 and Figure 73) show significant influence of numerical oscillations affecting calculations of the concentration. With refinement of the mesh grid oscillations are reduced what can be measured by comparing a standard deviation values for each graph (see Figure 74). The more significant reduction of the oscillations along A-A compared to B-B is attributed to the I_2 and I_5 inflows location. The flow leaving both I_2 and I_5 inflows travels directly along A-A profile to meet each other in the centre. There is no flow parallel to B-B, only under angle coming from I_1 and I_4 and that may complicate overall result in that area. Cross-section B-B was chosen as particularly disturbed region for evaluation. The drop of oscillations can be assessed quantitatively by comparison of the standard deviation values along both profiles for all used mesh types. In both cases there is a downward trend, with more slope for A-A than for B-B.

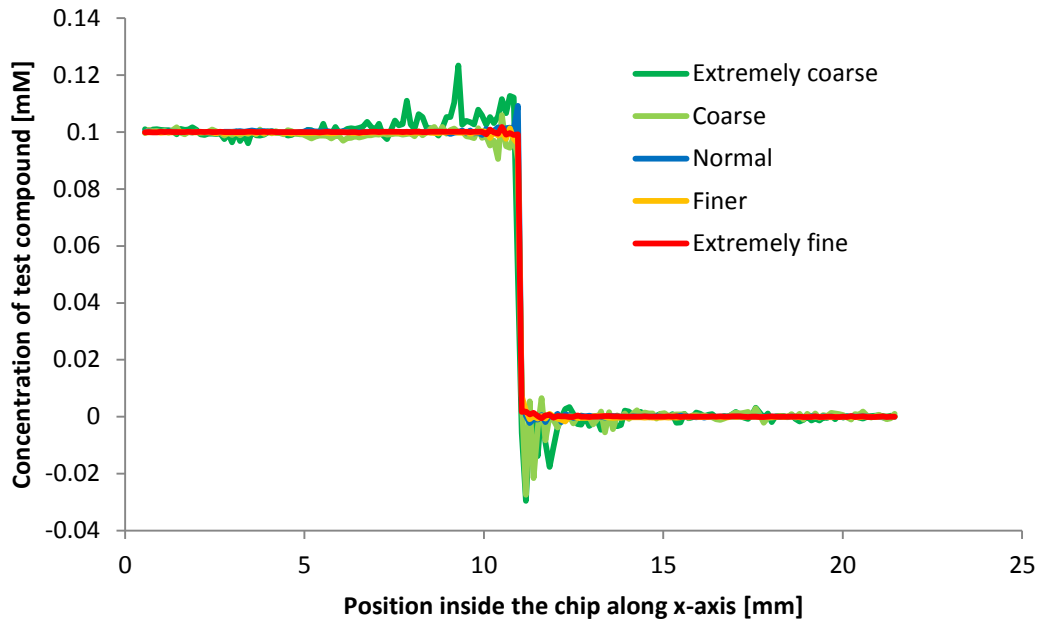


Figure 72: Comparison of the concentration values along A-A (Figure 70) for different mesh densities.

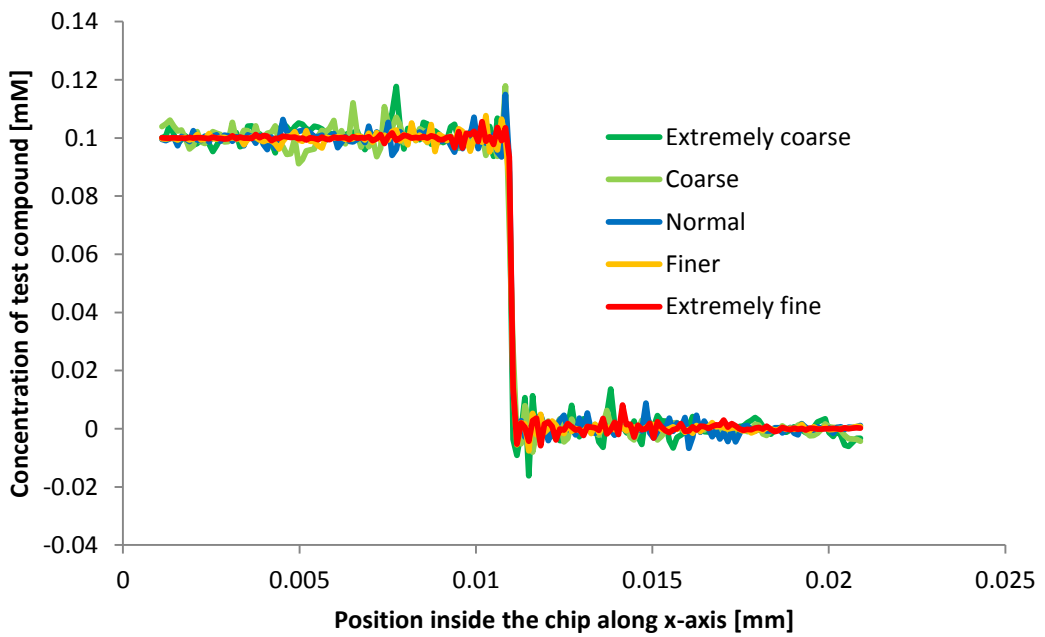


Figure 73: Comparison of the concentration values along B-B (Figure 70) for different mesh densities.

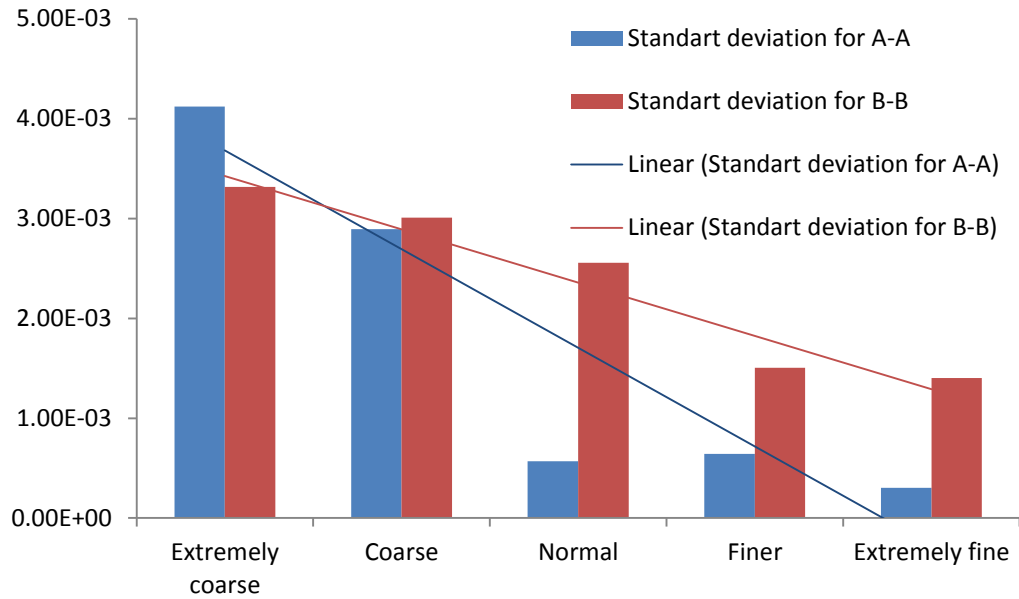


Figure 74: Comparison of standard deviations for different mesh densities.

The different mesh settings were tested to provide information about the optimal settings. The relation between mesh density and simulation quality was investigated. The growing mesh density resulted in reduction of local error, as well as in increasing smoothness of the results. The relation between the number of mesh elements and the time needed to complete the calculation was linear for models that required less RAM than amount of the memory installed. Significant increase of the time needed to complete the simulation was observed for larger models.

4.2. 1st Navier-Stokes flow with convection and diffusion in multi-outlet chip

The first step in project was to assess qualitatively numerical simulations of microfluidic systems. In general approach microfluidic chip is a three dimensional structure of defined width, length and depth (channel or chamber thickness). Three dimensional simulations are much more complicated and demanding from technical point of view. The second objective of modelling of shown chip was to assess accuracy of two-dimensional approximation of 3-D problem. Test compound (1M solution of malachite green) was introduced through NE inlet (marked with yellow arrow) and water through remaining (blue arrows). COMSOL can display concentration of one compound at a time, thus as three different colour regions are visible in the experiment

(see Figure 75a) in simulation test compound was introduced to form the central blue region and water was selected to fill white and pink regions.

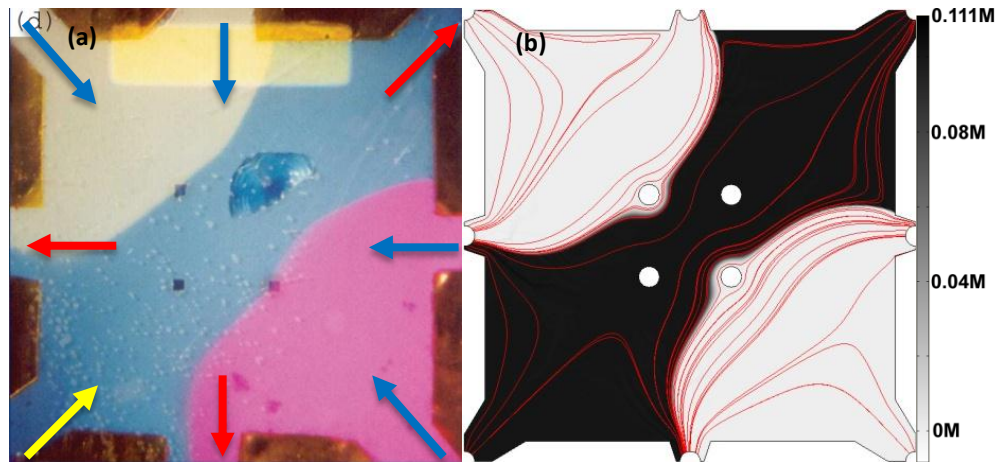


Figure 75: Comparison of (a) experimentally achieved flow pattern with (b) numerical simulation. Yellow arrow indicates inlet of the test compound for the model, blue arrows inlets of water and red arrows outlets.

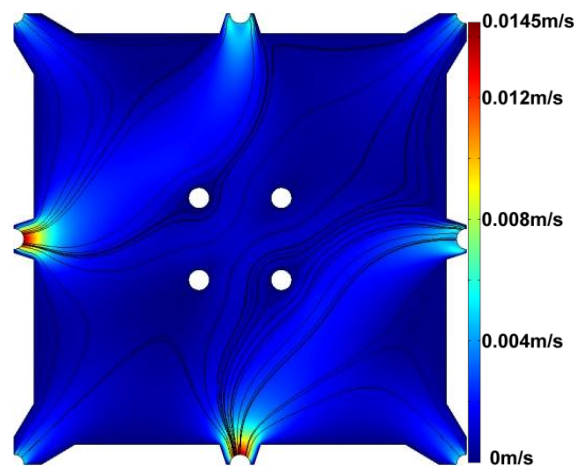


Figure 76: Velocity field map associated with the experiment shown in Figure 75. Blue colour represents the minimum, red the maximum.

As it can be observed, the modelled distribution of test compound is very similar to one presented in Figure 75a. Main discrepancies are around outlets O1 and O3 – these outlets are modelled as voids in chip due to limitations of two-dimensional modelling. There is no flow through or over central outlets what results in alteration of flow streamlines around obstacle. Modelled concentration near outlets S and W are showing very high similarity to the picture – blue dye is entering both outlets in very alike manner. Differences observed in distribution of test compound along walls are attributed to the noticeable lack of the perfect symmetry of the chip used in the experiments, while the numerical model possessed such symmetry. It is especially visible around inlets N, NE, SE and S. As it can be read from Figure 76 velocity near outlets is

roughly three times higher than of the inlets. This is expected value provided installation of six inlets and two outlets.

4.3. 2nd Navier-Stokes flow with convection and diffusion in a multi-outlet chip

The second selected pattern obtained experimentally (fig. Figure 77a) was successfully recreated numerically. In this simulation all inlets and outlet O4 were turned on. Test compound (again 1M solution of malachite green) was introduced through inlets NW, N, E and SE (marked with yellow arrows) while water through other (blue arrows). Linear velocity of fluid for all inlets was set to $5 \text{ mm}\cdot\text{s}^{-1}$ normal to curve. Figure 77a show photo of experiment and Figure 77b result of numeric simulation. In Figure 78 velocity field of that simulation is presented.

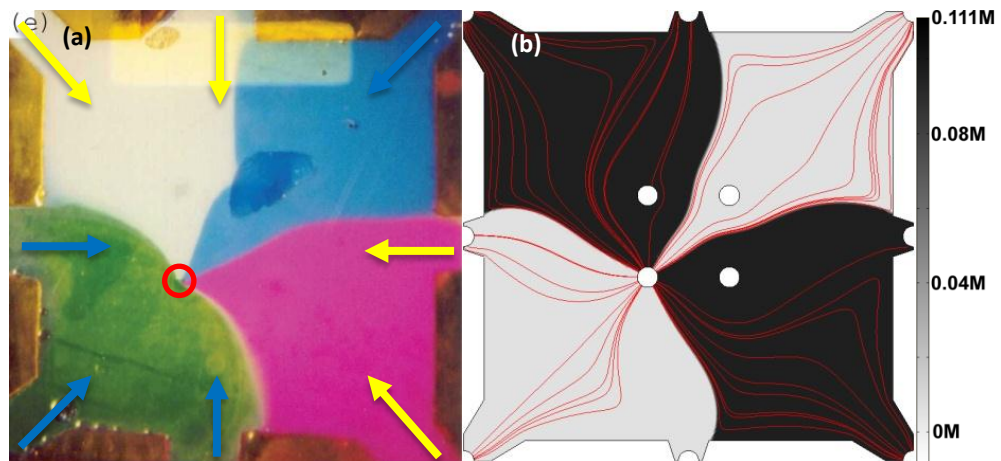


Figure 77: Comparison of (a) experimentally achieved flow pattern with (b) numerical simulation. Yellow arrow indicates inlet of the test compound for the model, blue arrows inlets of water and red circle localises used outlet.

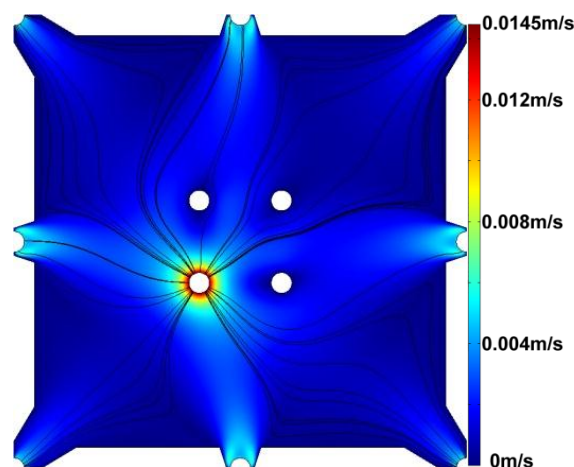


Figure 78: Velocity field map associated with the experiment shown in Figure 77. Blue colour represents the minimum, red the maximum.

As it can be seen from comparison of Figure 77a and Figure 77b the result of modelling is highly similar to the experiment. The main difference can be observed in the vicinity of O4 (active) outlet. On the photo one can see boundaries between fluids disappearing in one point. Due to the model limitations the region inside circle is not simulated and cannot be observed. Differences in fluids' flow near N inlet are attributed to different viscosity of used liquids – in the experiment white liquid was diluted coffee creamer while in simulation all liquids have dynamic viscosity of water $\eta = 0.001 \text{ Pa}\cdot\text{s}$. Also it is possible that pressure around N inlet was lower or not equal to the pressure of the NE inlet resulting in a shift of a boundary between liquids.

Simulations of microfluidic systems with only pressure-driven flow gave satisfactory results. Small discrepancies can be observed depending on complexity of model, accuracy of drawing and precision of devices used in experiments. Schemes used for modelling represent ideal systems and often do not take into account imperfectness of real apparatuses.

4.4. The mesh type assessment: comparison of triangular and quadrangle meshes

The first tested mesh density (an extremely coarse) did not converge and no stable solution was found in case of both triangular and quad mesh. Simplifications in the mesh outlook (squares instead of circles for inlets and outlets) and large size of individual mesh cell resulted in too large error value to achieve solution convergence. All other tested mesh densities (normal, extremely fine, 10% maximum growth of the adjacent element, and 2% maximum growth of the adjacent element) allowed for stable solution. In normal mesh density there were numerical oscillation present and overall solution accuracy was not satisfactory. In case of the triangular mesh minimum noted concentration was -0.204 (20.4% error, see Figure 79) and in case of the quad mesh it was -0.157 (15.7% error, see Figure 80).



Figure 79: Modelling result for normal density triangular mesh.

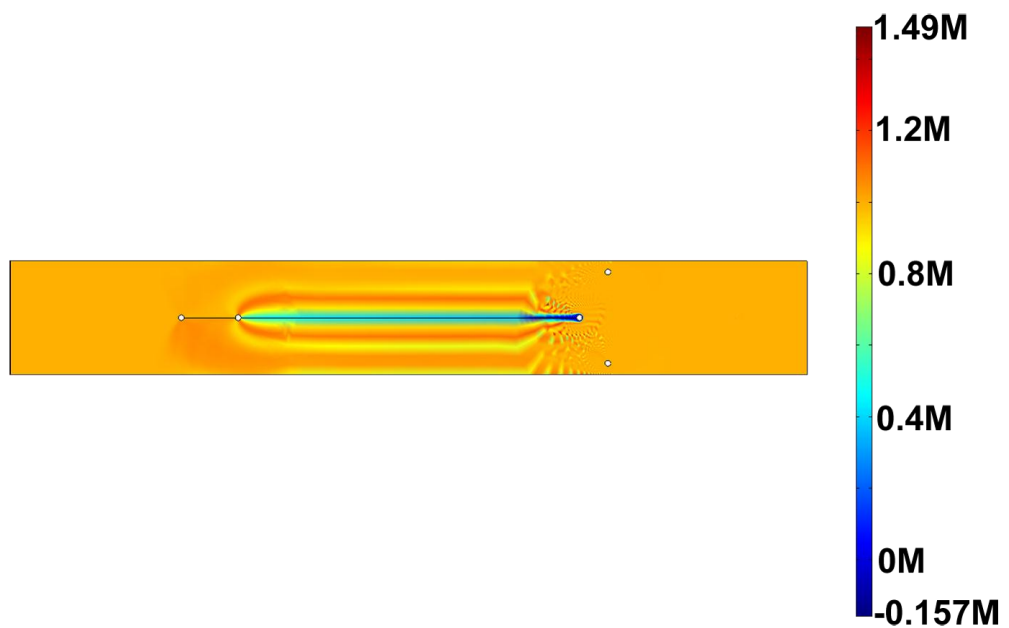


Figure 80: Modelling result for normal density quad mesh.

The extremely fine mesh had a number of errors reduced but they were still visible. To achieve satisfactory result and model quality, manual definition of the mesh parameters was required. The growth of a single mesh cell was limited to maximum 10% while generating the mesh grid, limiting the maximal size of a single mesh cell and increasing their total number. Measured concentration error was 0.6% for triangular mesh (see Figure 81) and 3% for quad mesh (see Figure 82). Further mesh refinement lead to reduction of error to 0.01% for triangular mesh and 0.04% for quad mesh.

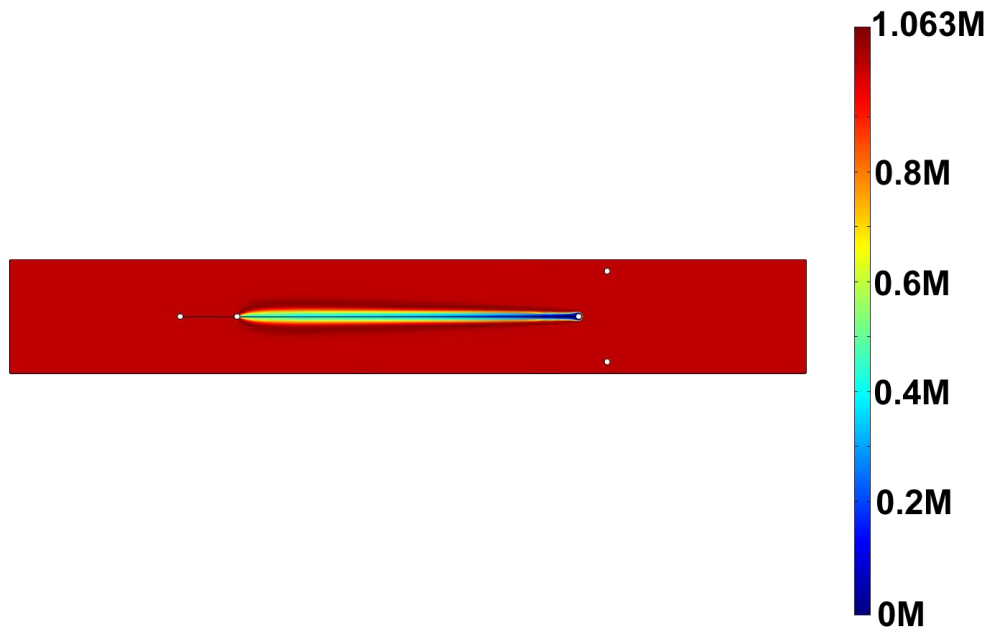


Figure 81: Modelling result for "10% growth" density triangular mesh.

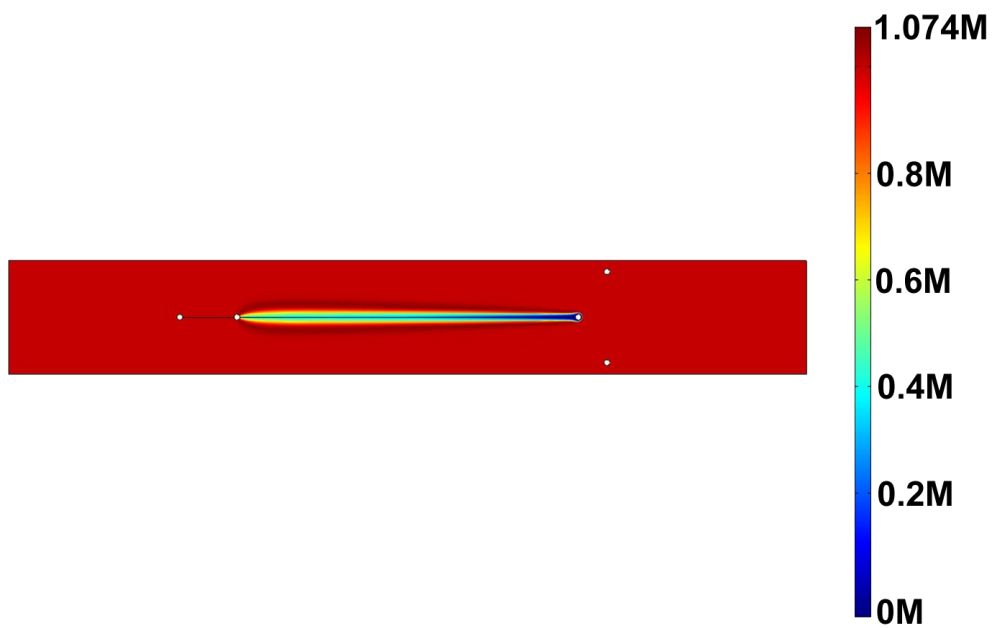


Figure 82: Modelling result for "10% growth" density quad mesh.

Figure 83 and Figure 84 shows comparison of model parameters and calculation performance of four different mesh densities using triangular and quadrangular meshes. Tested problem was complicated enough that "extremely coarse" mesh did not allow for achieving convergence and produced no result at all for both meshing types. Used mesh types "normal" and "extremely fine" are pre-set in COMSOL, "10% growth" and "2% growth" were manually set and have all other properties of "extremely fine" meshing,

except mesh element growth rate which are as given. Detailed parameters of used mesh grids are attached in Appendix E.

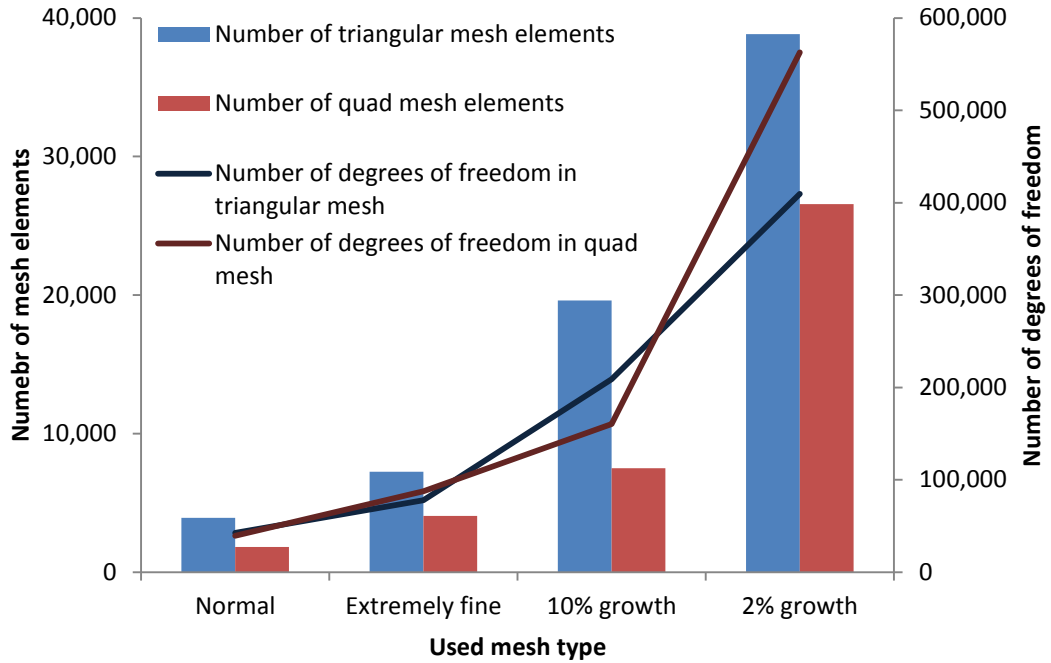


Figure 83: Comparison of model properties for four mesh densities using two different meshing methods.

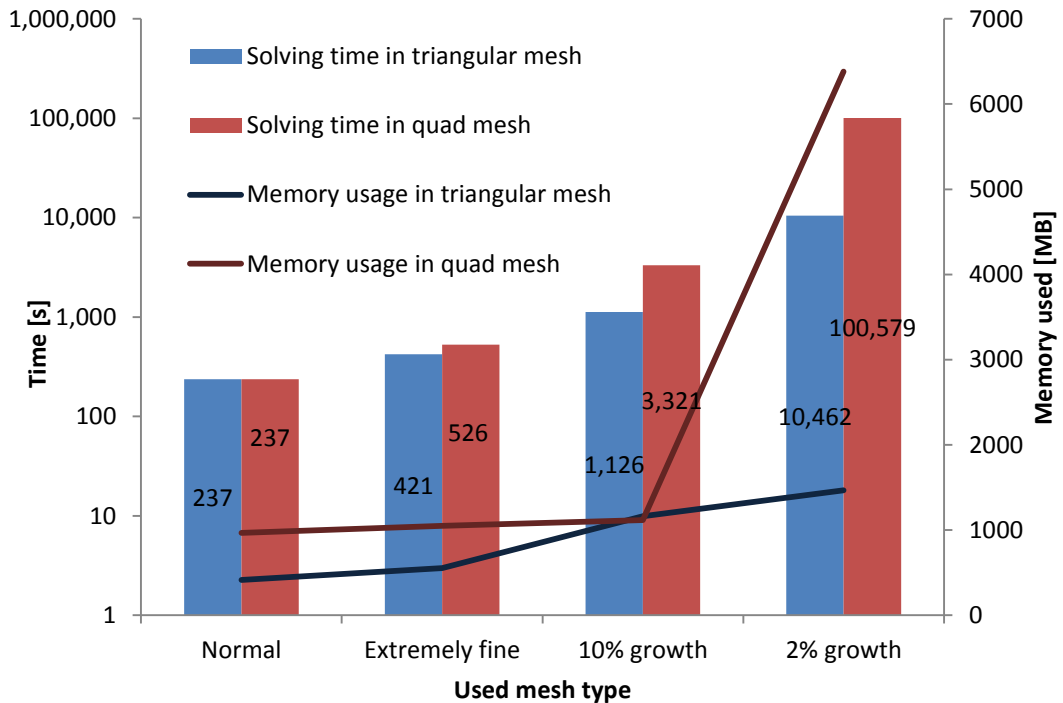


Figure 84: Comparison of calculation performances for four mesh densities using two different meshing methods.

The first visible tendency is that triangular mesh produces lower errors. The second observed feature is that application of quad mesh typically requires more system memory and is more time consuming. It is especially visible when model size exceeded amount of installed physical memory (4GB) and data swap between physical and virtual memory was required. In this case time to complete calculations was approximately ten times longer in case of quad mesh than for triangular one. Despite these deficiencies quad mesh allowed for to achieve model convergence and stable result in some cases where triangular mesh did not. All further models were developed using triangular mesh at the computer performance limit.

4.5. Modelling of the Conductivity Gradient Focusing

Conducted simulation shows concentration of model dye in central region of microfluidic device similar to this obtained in experiments. The highest concentration of MG was observed after 930 seconds from starting the experiment (330 after turning on voltage). The distribution of MG at the moment of the highest concentration is shown in Figure 85. Figure 86 shows concentration profile along cross-section A-A.

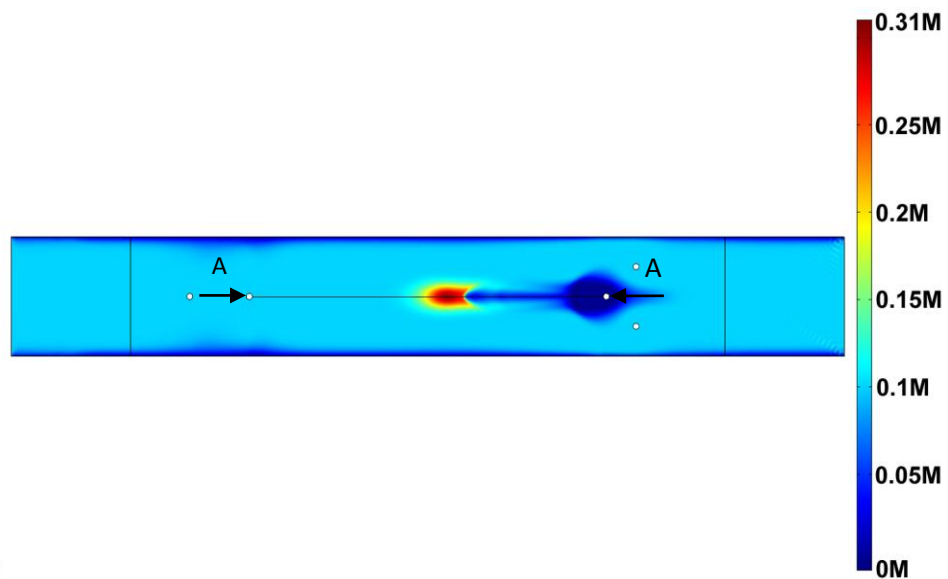


Figure 85: Concentration of Malachite Green after 930 s from beginning of simulation – moment when the highest concentration was observed.

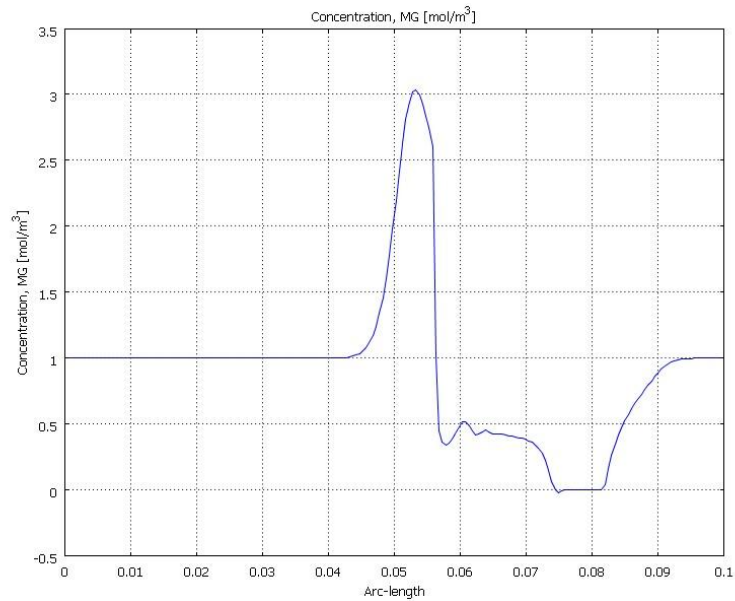


Figure 86: Concentration profile along A-A from Figure 85.

In conducted simulation movement due to pressure-driven flow was higher than electromigration induced by applied potential difference. After 1730 seconds concentrated MG in central channel reaches outlet and starts to escape system. At this moment area of complete depletion of the MG replaced by Tris pumped through central inlet takes significant part of microfluidic chamber near inlets (Figure 87a). At 2000 s (time at which simulation stops) this region is slightly larger (Figure 87b).

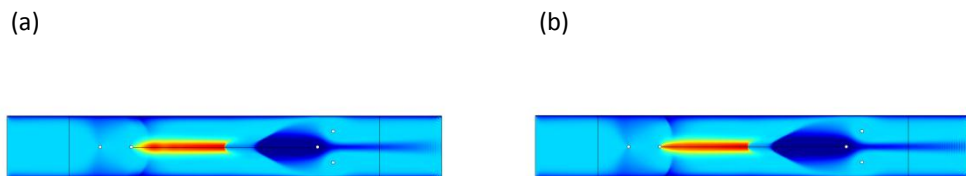


Figure 87: Concentration of MG (a) after 1730s and (b) after 2000s. Concentration scale as in Figure 85

Conducted simulation shows results qualitatively very similar to those obtained experimentally by Potter *et al.* Region of increased concentration forms in same place – central channel and behaves similarly (8). The main difference between experiment and simulation is that the highest concentration of the dye was observed at the end of the experiment, while simulated occurred significantly earlier. This fact is attributed to number of simplifications in the model. Noteworthy is that the concentration drops from the highest recorded to the end of the simulation is small (around 10%).

20mM Tris buffer introduced through the central inlet had significantly higher conductivity than the surrounding 1mM MG. Until 600s Tris formed a region approximately 40mm long from the central inlet toward the outlets (Figure 88). When voltage was applied, region filled with Tris presented lower resistivity thus diverting current into it rather than passing through regions filled with MG. As a result a non-zero potential gradient is observed. Figure 89 shows spatial distribution of electric field intensity at 600s.

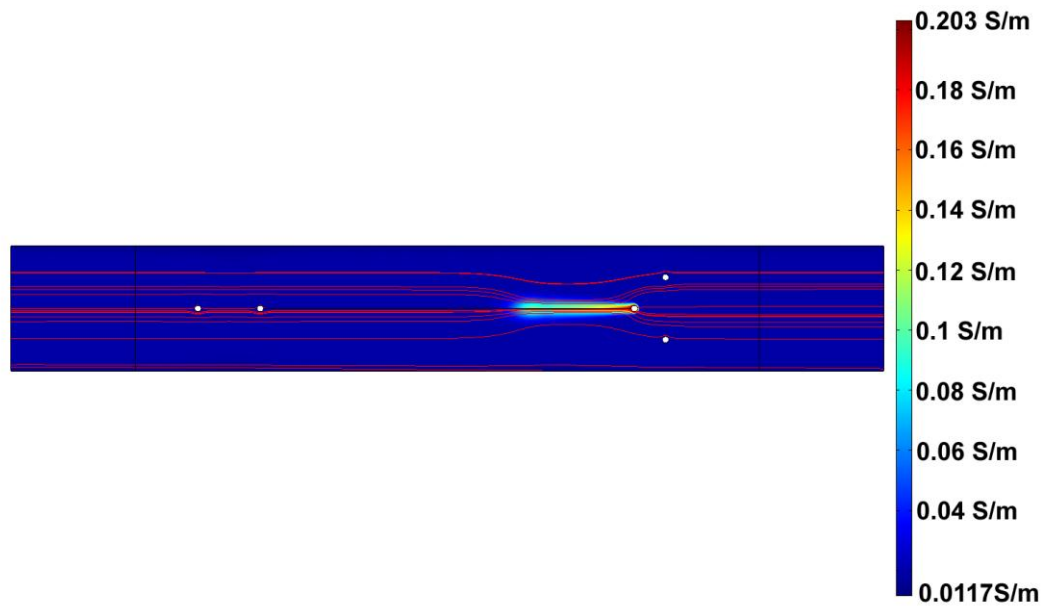


Figure 88: Graph of ionic conductivity [S/m] at 600s with overlay of lines of electric field.

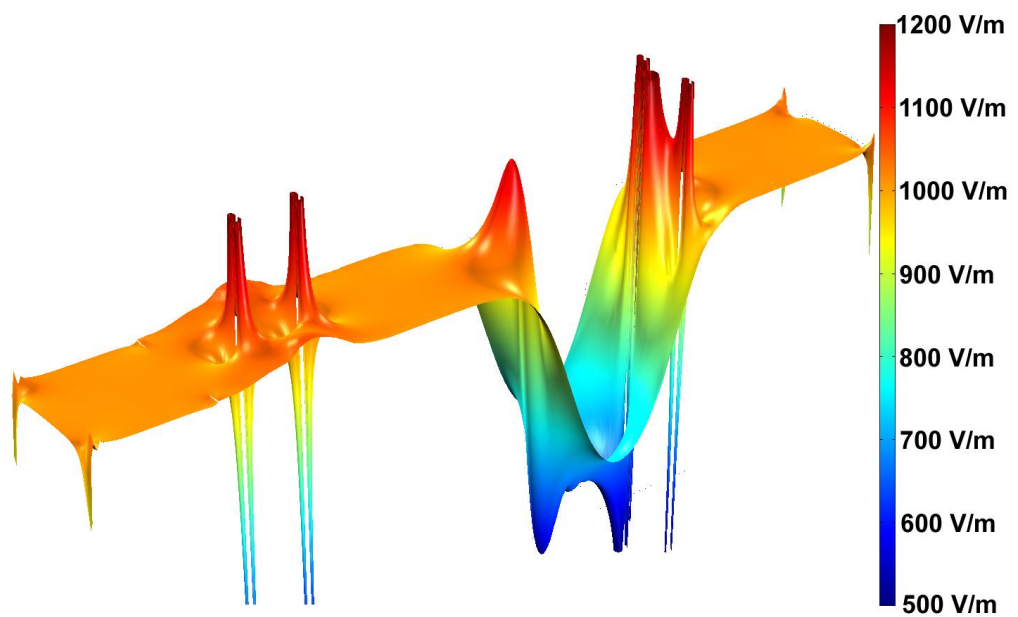


Figure 89: Spatial distribution of electric field intensity at 600s.

The largest difference in conductivity near the central inlet results in the highest changes in the electric field (Figure 89). The electric field intensity is more than two times higher outside high conductivity region than in it. In front of Tris filled area one can observe high electric field intensity in which malachite green is starting to concentrate. Strange formations around corners are results of different boundary conditions that overlap in one vertex. Inlets and outlets are modelled as void regions and there is no valid solution inside it. This results $\pm\infty$ values and should be neglected.

Presence of a small area with higher conductivity than surrounding solution results in deformations in electric field. One can observe as lines of electric field are deflected toward the high conductivity region. Because voltage applied to the electrode is positive and MG is cationic, there is repulsion between electrode and analyte. Figure 90 shows how electric field compress MG into narrow region in front of high conductivity area filled with Tris. Concentration of MG is represented with colour map, lines of electric field are marked black continuous lines and arrow plot shows direction of electric repulsion. As it can be seen lines are convergent toward the line of symmetry of the device. Positively charged particles of malachite green are therefore focused along y-axis. Shape of electric field in presented device is entirely dependent on flow pattern of low and high conductivity solutions. In order to achieve better focusing along y-axis different placements of inlets, outlets and flow velocities were investigated and are described in later part of this work. Main contribution to focusing along x-axis is a result of the applied potential difference. Due to the high symmetry of the modelled microfluidic device electric field has only x-component along symmetry axis. Differences in conductivity will result in local changes in the electric field x-component that may lead to different retardation speed of analyte. Region of increased concentration does not remain stable because permanent equilibrium between electromigration and pressure was not achieved. Constant flow of Tris buffer results in pushing plaque of focused analyte out of the system.

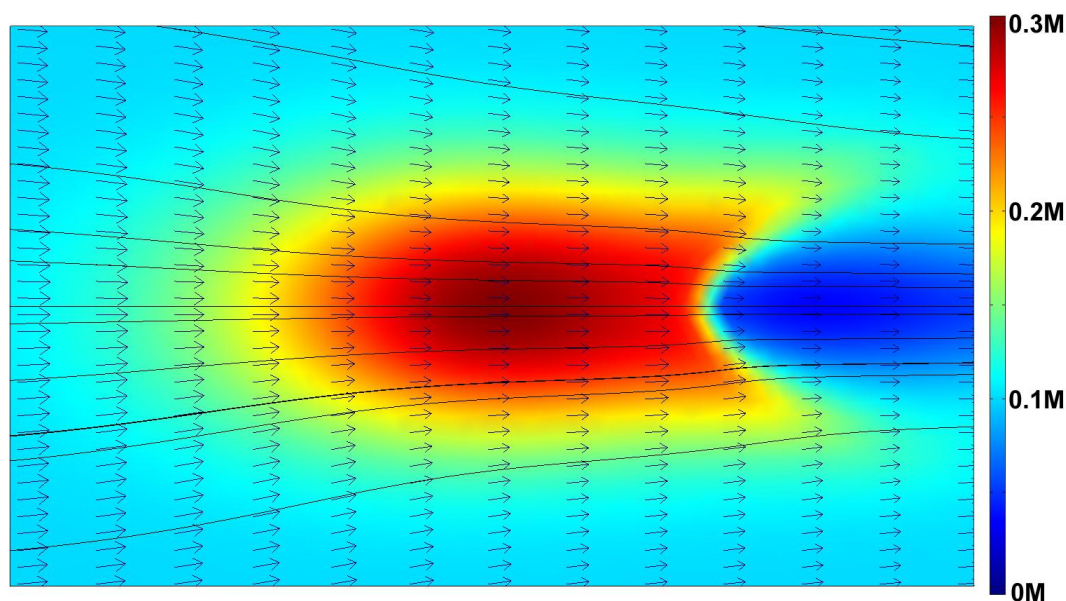


Figure 90: Formation of region of increased concentration of analyte. Arrows show direction of electric force focusing cationic dye (MG) in front of high conductivity buffer (Tris). Black lines are lines of electric field.

The developed model was used to recreate the experiment with conductivity gradient focusing (CGF) described in reference (8). The numerically calculated concentration distribution of the malachite green (see Figure 91) shows a three times concentration increase compared to the initial value. The area of increased concentration was formed between the first outlet and the central inlet, similarly as in the experiments. Figure 92 shows the experimentally obtained zone of focused malachite green using CGF. The authors of (8) noted concentration increase of approximately 3.2 times. This good correlation between the model and the published experiment indicated correct performance of the developed simulation. Similarly to the model, in the experiment there was a wide central stream of high conductivity transparent buffer and two flowstreams of MG at the walls.

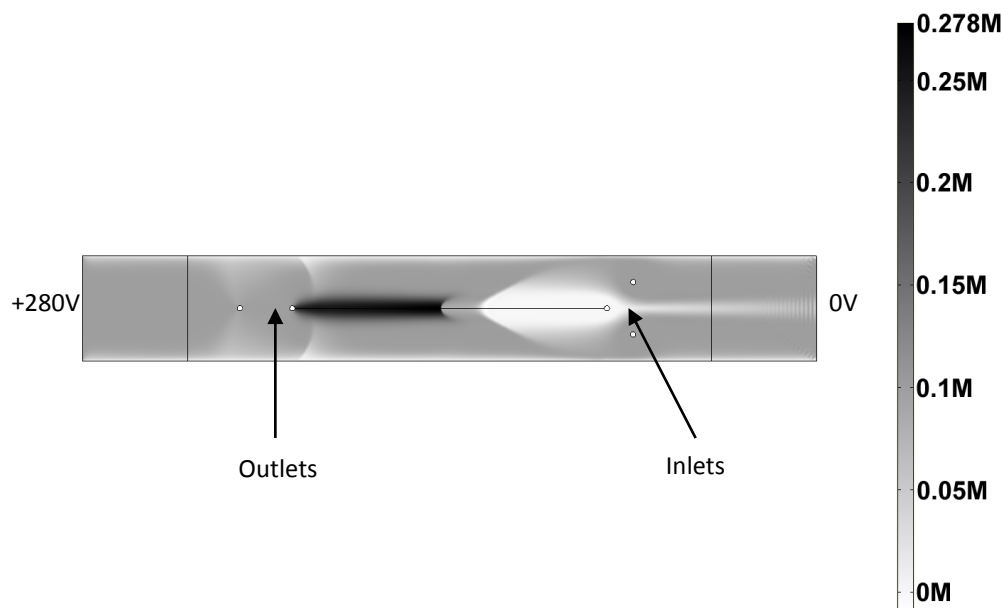


Figure 91: Modelled concentration distribution after 2000s in CGF.

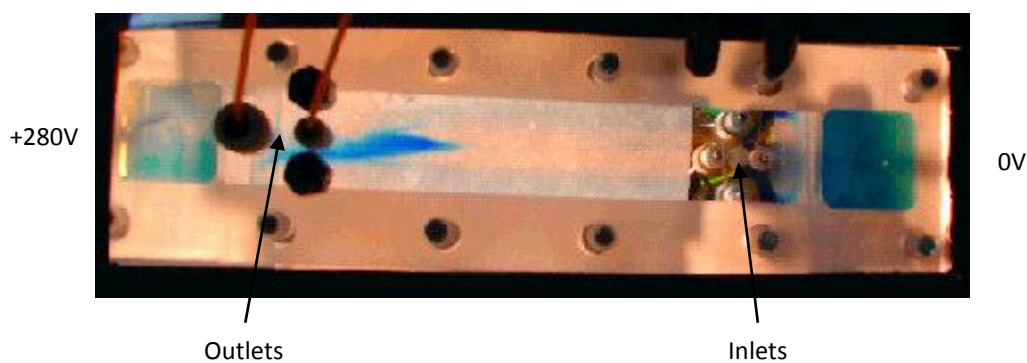


Figure 92: Photo of the CGF experiment at a time of 1980s.

4.6. Investigation of the multi-outlet chip properties

The development of several models of different chips with multiple outlets allowed concluding that although in principle this layout produces the required flow characteristic, it has a few imperfections. In order to achieve trapezoidal-like flow pattern, different flow rates ratios were tested and compared. Inlet fluid velocity for auxiliary inlets was set to $0.2 \text{ mm}\cdot\text{s}^{-1}$ (velocity normal to inlet contour) and for the central inlet, simulations were carried out at a range of velocities from 0.02 to $0.2 \text{ mm}\cdot\text{s}^{-1}$. To observe behaviour of formed flow pattern mass transport model including convection and diffusion was implemented. The possibility of observation of test substance allowed for conclusive comparison of different flow rate ratios. Attempts to simulate velocities above $0.5 \text{ mm}\cdot\text{s}^{-1}$ did not give satisfactory results because simulation

became unstable and convergence was not achieved – relative and absolute errors were too high to calculate solution.

In the chip with no auxiliary outlets ratio between flow rates defines a ratio of widths of central and side streams. In the chip with auxiliary outlets amount of fluid being flushed away from system depends on throughput of the outlet. All outlets were modelled similarly as free outlets (boundary condition pressure=0, no viscous stress). The most interesting results are shown below for discussion in Figure 93, Figure 94, Figure 95 and Figure 96. All graphs are showing concentration distribution of a constantly introduced model compound when the hydrodynamic equilibrium is reached.

Observed regions of zero concentration for distance of 5cm from the left wall of the chip are result of two-dimensional simplification of the problem. Concentrations profiles are read along defined lines where outlets are designed as void spaces and thus no concentration can be calculated inside.

Combination of mass transport mode with momentum transport allowed for studying diffusion effects. To observe the trapezoidal flow pattern, flow from the central inlet must reach any outlet beside O_1 (central main outlet, see Figure 35 for numbers). As it can be seen in Figure 93, Figure 94, Figure 95 and Figure 96 this principle is satisfied in all simulations, yet flow patterns differs significantly, as the diffusion plays an important role in compound distribution, and a high concentration of the test compound is recorded in the stationary state. For the lowest tested flow rate of $0.02 \text{ mm}\cdot\text{s}^{-1}$ (10% of auxiliary inflow) concentration does not drop on a distance of few millimetres only (Figure 93a). 4 cm from further (Figure 93b, profile “4cm”) drops to 20% of the initial, and in vicinity of main outlets (Figure 93b, profile “8cm”) is around 17%. Noteworthy is that behind the last auxiliary outlet diffusion is strong enough to distribute model substance across entire chip. This occurs even despite the fact that flow from auxiliary inlets is reaching central main outlet (there are streamlines connecting I_3 and O_1). As it can be seen on subsequent graphs (Figure 94, Figure 95 and Figure 96) with increased central inlet velocity streamlines from auxiliary inlets I_2 and I_3 are no longer able to reach central main outlet (O_1). For higher central inflow velocities (40% and 100% of auxiliary inflow velocity, Figure 95 and Figure 96 respectively) already at distance of 5cm from the inlet I_1 (roughly half of chip length) the concentration of model compound near walls was above zero. For case illustrated in Figure 95a compound concentration 5cm from inlet I_1 is slightly above zero (Figure 95b, profile “5cm” shows it precisely). There is a flow coming from auxiliary inlet reaching side main

outlet (shown with streamlines connecting inlet I_2 and outlet O_2). When central inlet velocity is equal to the velocity of the auxiliary inflows flow from auxiliary inlets is completely diverted to auxiliary outlets – there is no streamline connecting inlets I_2 or I_3 with outlets O_2 or O_3 . A strong flow from central inflow I_1 combined with diffusion results in a high concentration of the model substance between $AO_{1/2}$ and main outlets. Simulation predicts that for given conditions in outlet area it will be around 70% of initial, as it can be seen on Figure 96b, profile “9cm”.

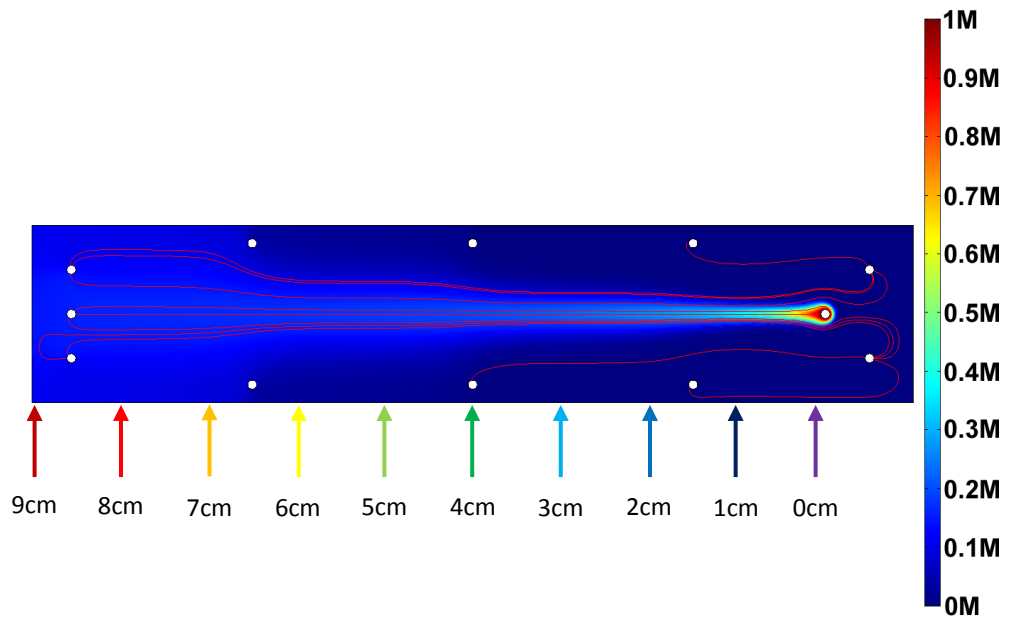


Figure 93a: Graph of flow pattern for velocities ratio 1:10.

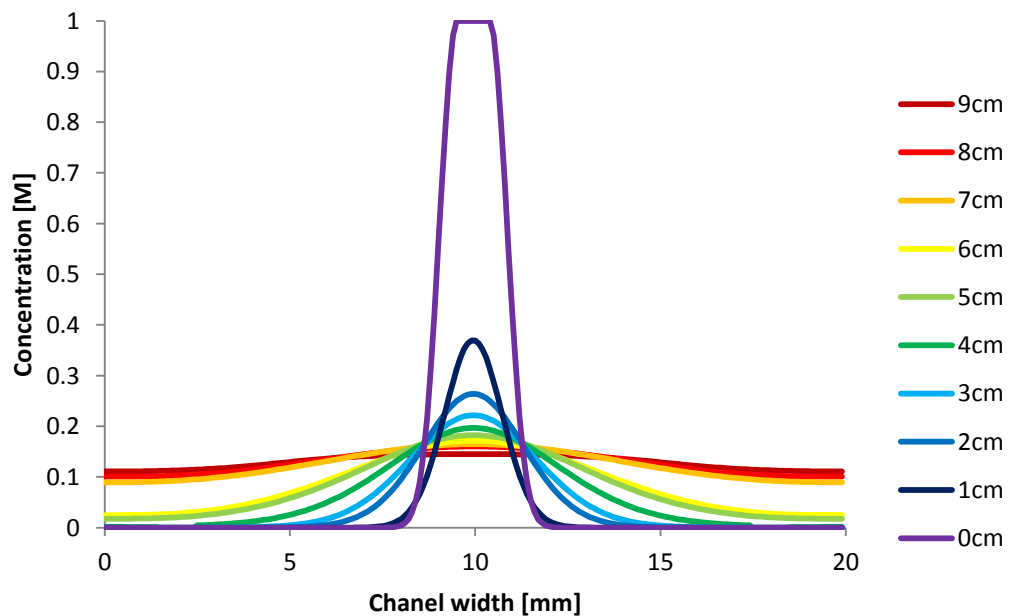


Figure 93b: Concentration profiles across the chip for given distance from the inlet. Distances provided in Figure 93a.

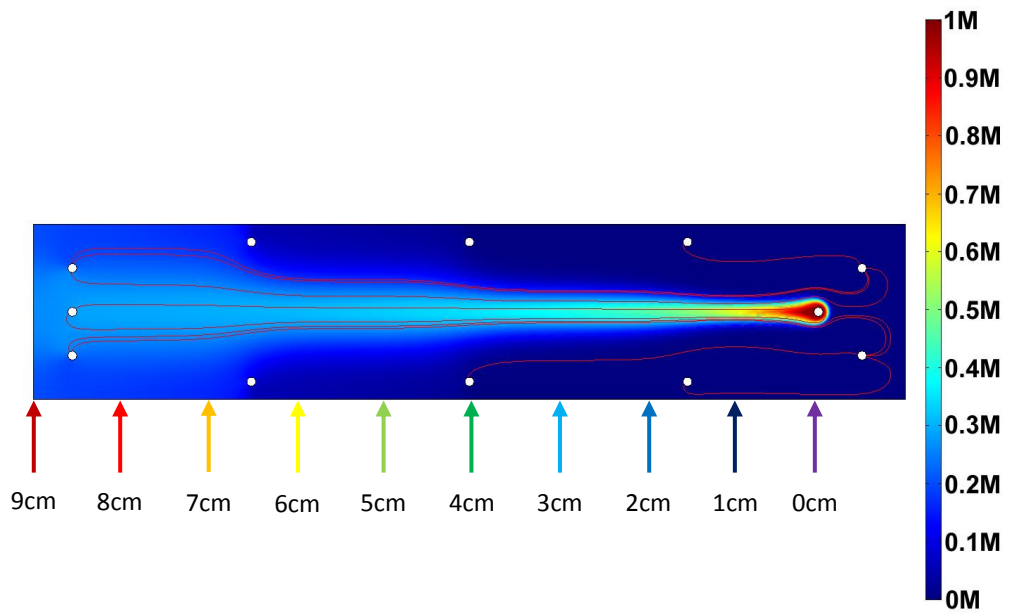


Figure 94a: Graph of flow pattern for velocities ratio 2:10.

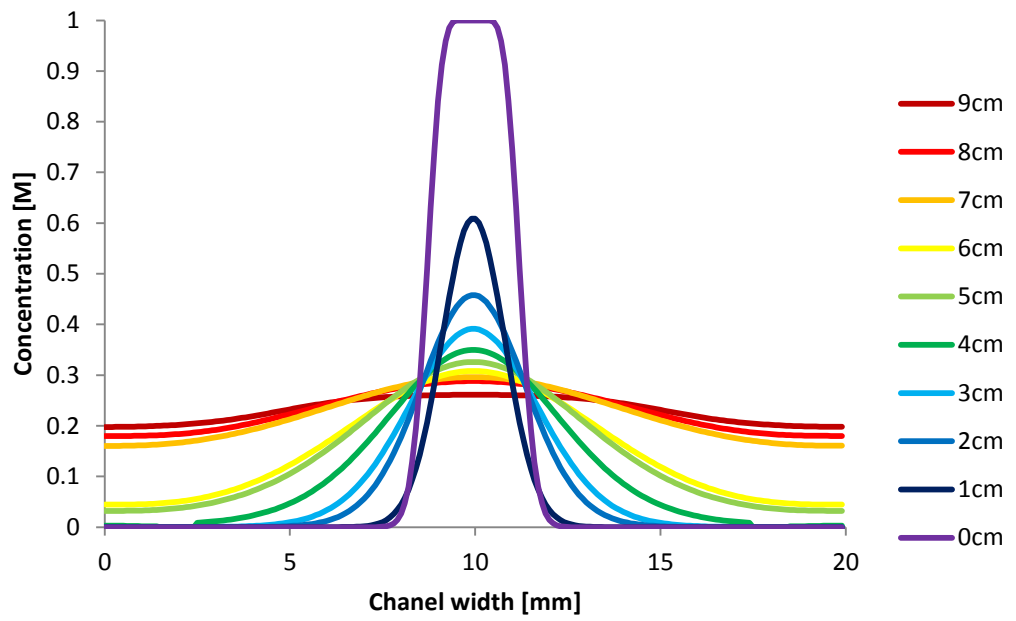


Figure 94b: Concentration profiles across the chip for given distance from the inlet. Distances provided in Figure 94a.

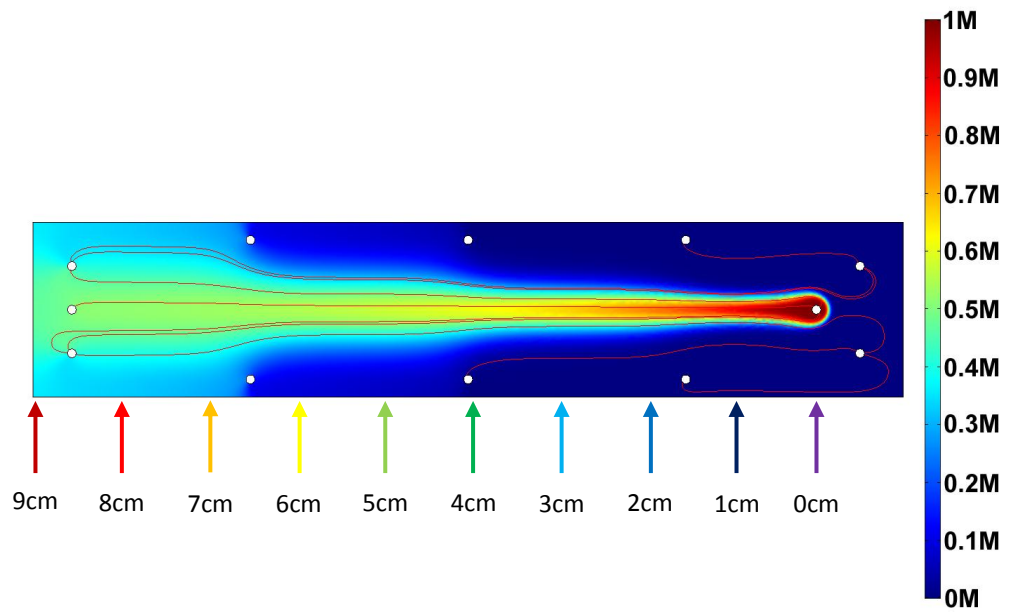


Figure 95a: Graph of flow pattern for velocities ratio 4:10.

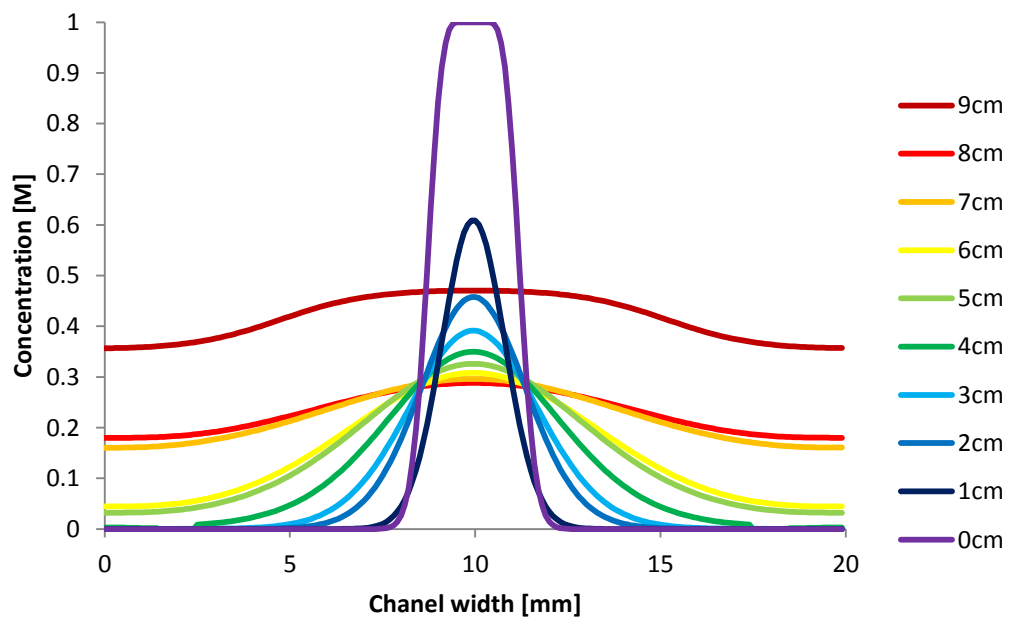


Figure 95b: Concentration profiles across the chip for given distance from the inlet. Distances provided in Figure 95a.

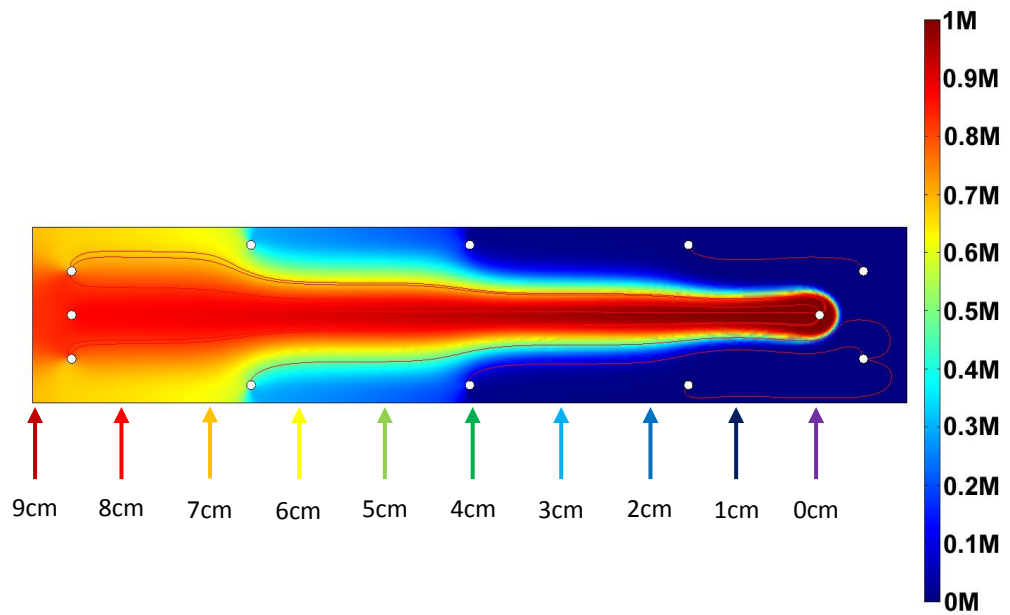


Figure 96a: Graph of flow pattern for velocities ratio 1:1.

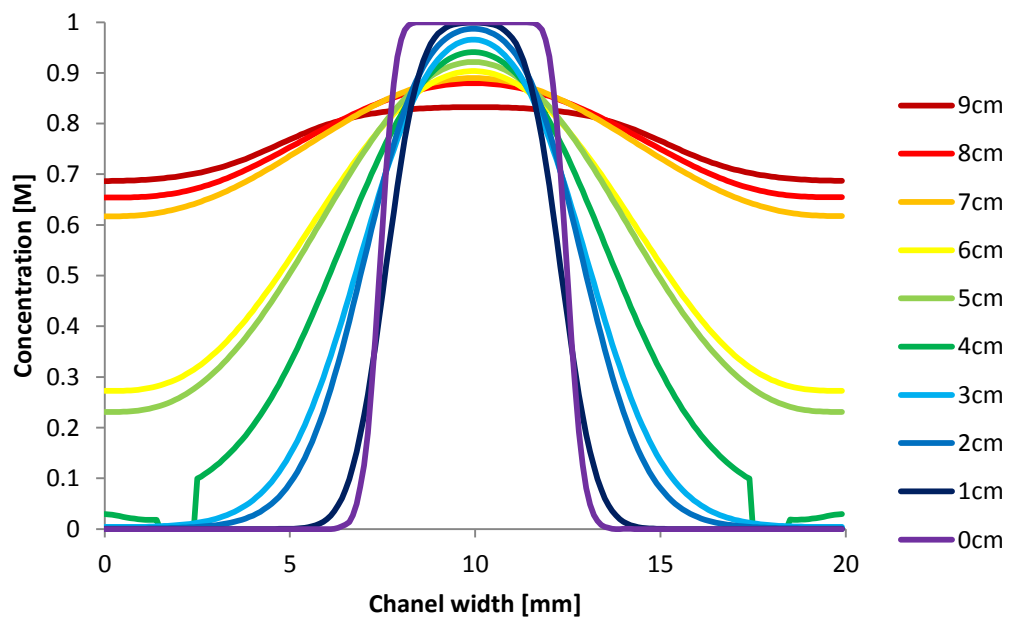


Figure 96b: Concentration profiles across the chip for given distance from the inlet. Distances provided in Figure 96a.

The second observed problem is the shape of flow in vicinity of auxiliary outlets. Theoretically the best flow pattern would have a shape of a trapezoid with a narrow end at the inlet and wide and on the opposite side of the chip. As one can see this is generally realised quite well in region from inlet to second auxiliary outlet (Figure 93, Figure 94 and Figure 95). Too high inlet velocity, (Figure 96a) makes already the first

transition steep. The presence of second pair of outlets ($AO_{2/4}$) affects flow pattern more noticeably. Figure 97a and b are showing x- and y-component of velocity vector respectively measured nearby ao_2 for simulation shown in Figure 97b (2mm from AO_2 toward chip centre, 12,5mm each side). Velocity vector x-component is negative due to direction of velocity vector.

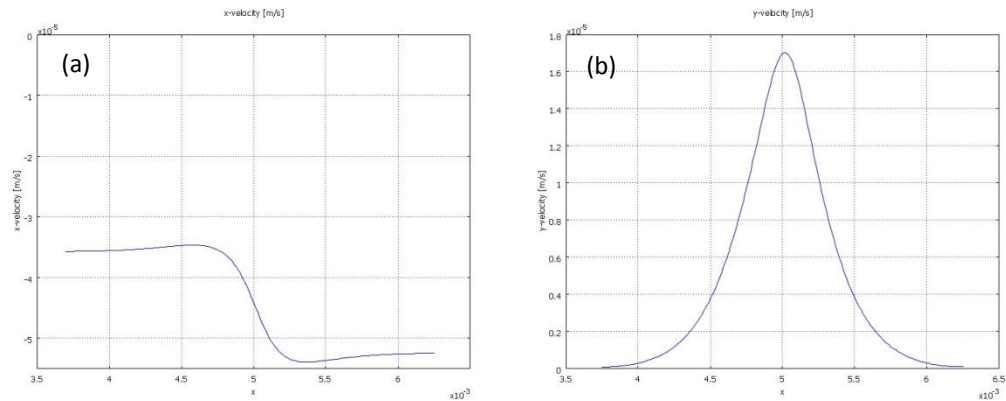


Figure 97: Velocity (a) x-component near auxiliary outlet and (b) y-component near auxiliary outlet.

Figure 97a shows that x-component of the velocity vector, changes considerably in the proximity of the outlet. Limited number of auxiliary outlets (only three implemented in this model) results in formation of step-like flow pattern, especially visible for higher velocities of central inlet. For lower velocities diffusion compensates presence of outlets making flow pattern smoother.

The third problem that had to be considered is shape and location of outlet. In this model, outlets (and inlets) were modelled as void spaces, and no equation was solved inside. For flow analysis this did not affect significantly overall results. Electric field will be applied to the model and the presence of void zones in main chip area could have significant impact on overall results – due to requirements of the COMSOL software boundary condition have to be the electric insulation around such object. Presence of such zone would affect local parameters of electric field and could lead to either wrong conclusions or prevent successful solving of the problem. Installation of additional auxiliary outlets has reduced problems. There are slight improvements in overall performance but steepness of the flow pattern can still be observed. Figure 98 and Figure 99 are showing comparative results for four and five pairs of auxiliary outlets installed. To achieve significant improvement the number of outlets would have to be increased to eight or even ten pair what is rather inconvenient from engineering point of view.

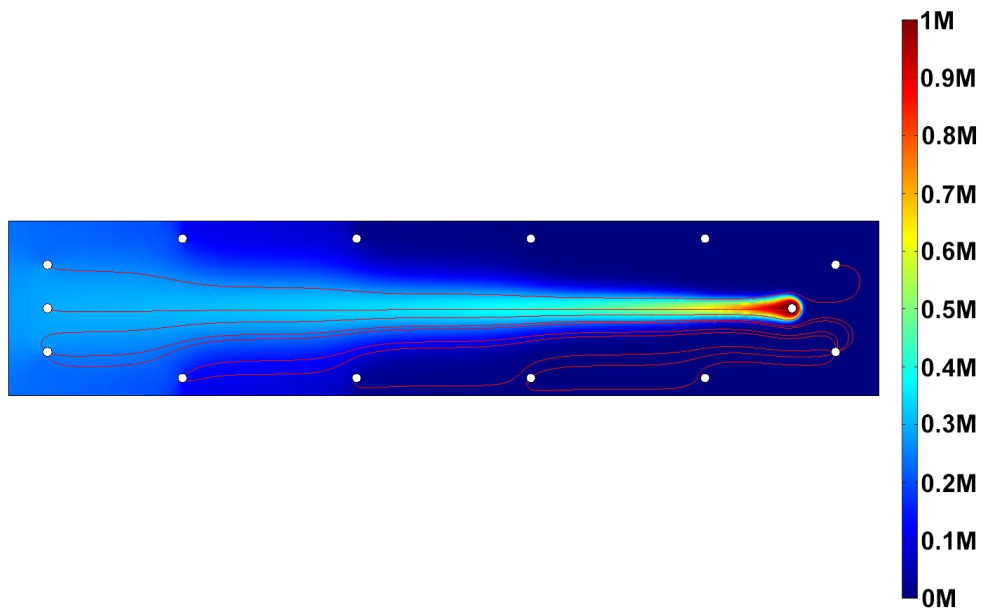


Figure 98: Graph of flow pattern for velocities ratio 2:10 with 4 pairs of auxiliary outlets.

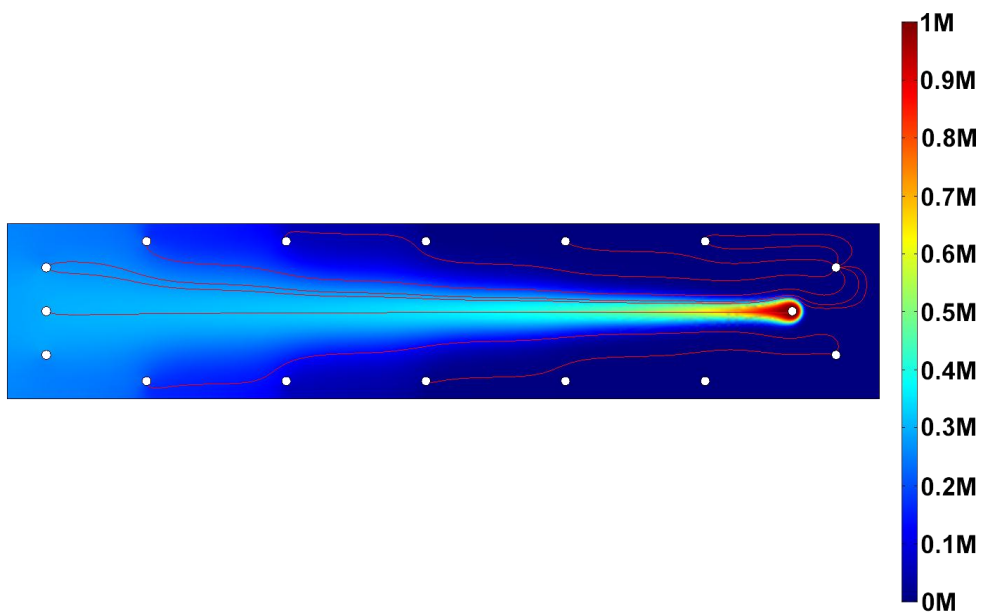


Figure 99: Graph of flow pattern for velocities ratio 2:10 with 5 pairs of auxiliary outlets.

Three chips with additional outlets (six, eight and ten) located along the chip side walls were investigated. The anticipated trapezoidal flow pattern and velocity gradient were achieved. With increased number of additional outlets, the flow pattern was smoother, and the velocity drop in the vicinity of the additional outlet was lower, producing a more uniform flow pattern. The different ratios of flow velocity between the central and auxiliary inlets were investigated. Increasing the flow velocity at the central inlet allowed for formation of the trapezoidal flow pattern to fill a larger part of

the chip. With more substance introduced into the chip within a given time unit, diffusion played a more significant role which was recognised as an undesired feature. Precise spatial distribution of the analyte introduced through the central inlet was regarded as a key element for EHDF and thus utilising multiple additional outlets was recognised as an inadequate approach for further work on EHDF.

4.7. The development of an optimal chip for the EHDF

Based on the presented simulations and observations of Dasgupta's results (15), a different approach to inlets and outlets was tested. Instead of modelling circle that represented tubing collecting fluid, gate-like structures with short collection channels along walls were implemented. Different shapes and positions were tested until optimal design was chosen.

The result of the first tested layout is presented in Figure 100 and it shows the first attempt of modelling side outlets with channels replacing circular inlets and outlets. Two different approaches were tested simultaneously: three rectangular inlets (marked with "R" in Figure 100) and outlets with trapezoidal channel. Semi-circles in channels are a representation of tubing pumping in or collecting solutions and inlet/outlet boundary conditions are applied only there. One can see completely incorrect value of concentration on the walls between inlets (marked with arrows). There are clearly visible problems with calculation in large part of the model (marked with an ellipse). There is a lot of numerical "artefacts" on the verge of two streams where is boundary between high concentration of test substance and pure solvent. Refining mesh to the computational limits of the used machine did not solve that problem. These erroneous calculation results are propagating along boundary of fluid stream but with distance diffusion plays more significant role and flow pattern stabilise.

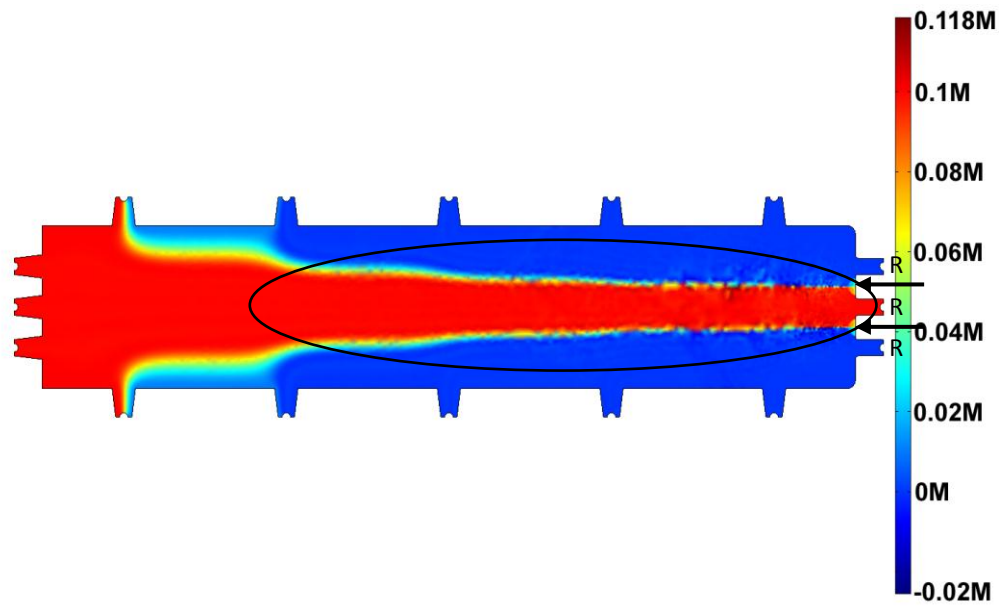


Figure 100: Test of circular inlets and outlets replaced by side channels with semi-circles.

The second tested layout is presented in Figure 101. Presence of numerical errors and incorrect values visible in Figure 100 was attributed to right angle between wall and channel leading to semi-circular inlet. All rectangular inlets were adjusted to match geometry of outlets and got trapezoidal shape. Also side outlets were shifted to the corners of the chip to improve capability of achieving trapezoidal flow pattern. Replacement of rectangular inlets reduced numerical problems very significantly. Small variations of concentration distribution are observable but they are occurring only for first 5 mm from the inlets and are disappearing completely afterwards. Flow pattern presented in Figure 101 is much more stable than the one presented in Figure 100. As it can be seen concentration of test substance at walls gradually increases away from inlets and with each outlet that increment is clearly visible. It is difficult to discuss any flow pattern behind the last pair of side outlets as differences in concentration levels are around 20% only. Also flow pattern achieved using mentioned outlets placement did not balance diffusion to sufficient degree.

Basing on simulations presented in Figure 100 and Figure 101 a completely different approach was tested: a chip with unrestricted broad outlet. Chip proportions were changed from 1:5 (width to length) to 1:3. Its schematic is shown in Figure 102. Inlets were remodelled due to previously observed problems. Auxiliary outlets got rectangular form with arcs connecting outlet channel wall with the main chamber wall to allow smooth continuous flow. Results of this simulation were encouraging to go

further, close the unrestricted open boundary but with implementation two main outlets (in form of circles).

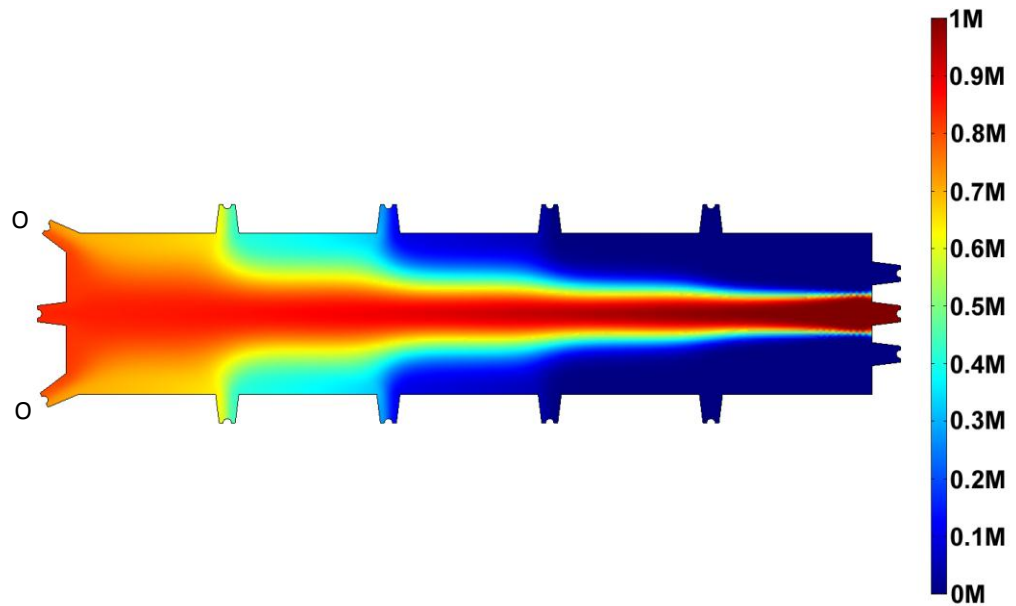


Figure 101: Test of trapezoidal side channels with semi-circles. Position of end outlets (O) was shifted compared to previous test.

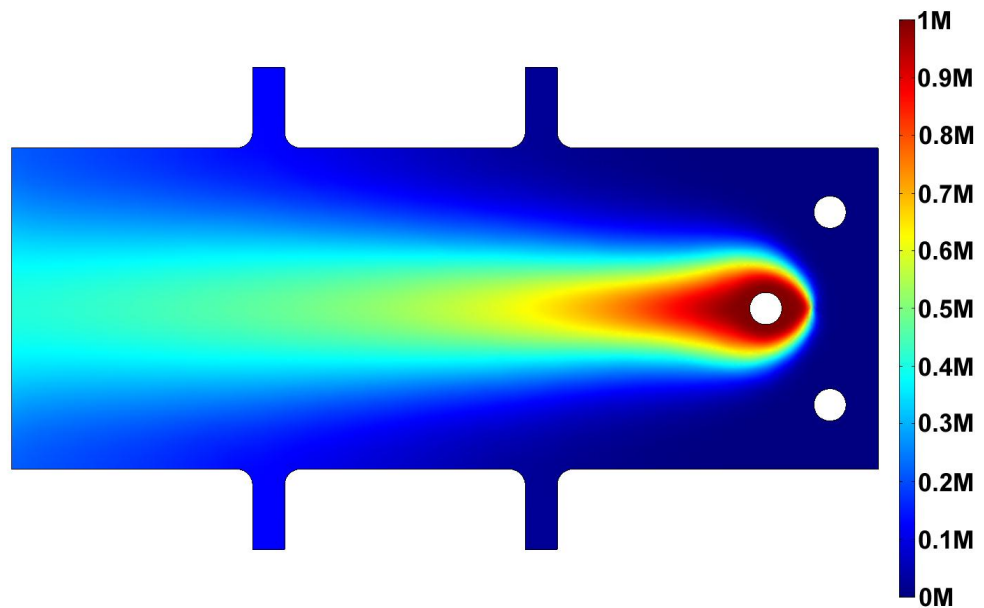


Figure 102: Test of the unrestricted outflow with auxiliary outlets. Trapezoidal side outlets were replaced with rectangular with smooth arcs connecting channel with main chamber.

Results of previously mentioned simulation were encouraging to go further, close the unrestricted open boundary, with implementation two main outlets (in form of circles). Achieved flow pattern and concentration distribution (Figure 103) shows trapezoid-like figure with small deformations due to the diffusion. This flow pattern was

regarded as potentially the one that will be used to simulate electrohydrodynamic focusing.

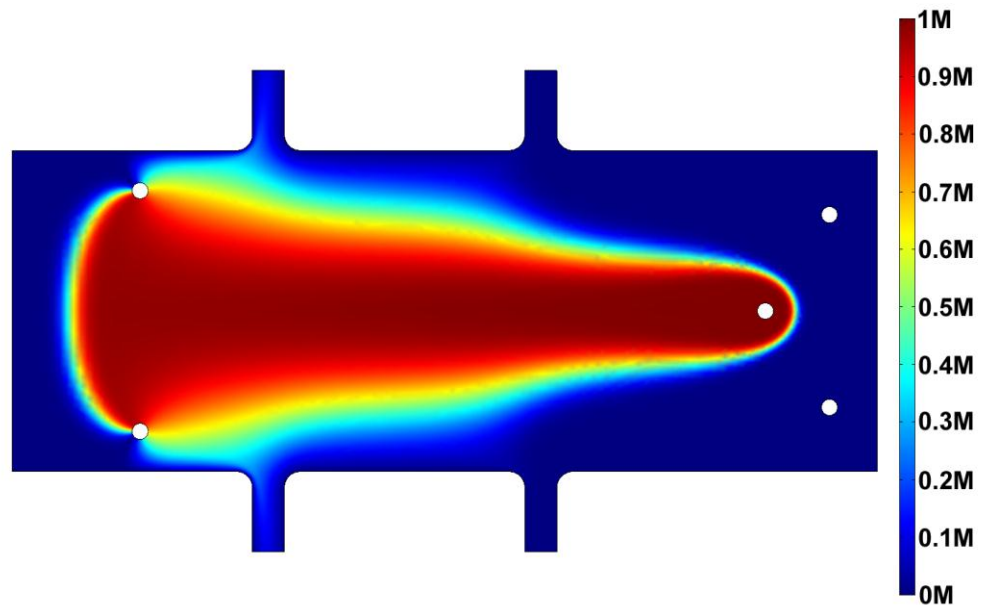


Figure 103: Test of the chip with two main and four auxiliary outlets.

The last tested model was a simplification of multi-outlet layout and somehow return to original idea of chip used for conductivity gradient focusing. All auxiliary outlets were removed and chip was elongated again (returned to 1:5 proportions) and two outlets located aside at the opposite end of the chip were located. Although achieving of the trapezoidal pattern was main goal, length of the separation channel (or separation chamber) has important role on separation efficiency. As it can be seen in Figure 104, flow is nicely stabilised and trapezoidal-like concentration distribution with low dispersion to the diffusion was achieved. Velocities in all inlets were same and equal $0.2 \text{ mm}\cdot\text{s}^{-1}$, diffusion coefficient was taken for chloride and equal $2.032\cdot 10^{-9} \text{ m}^2\cdot\text{s}^{-1}$.

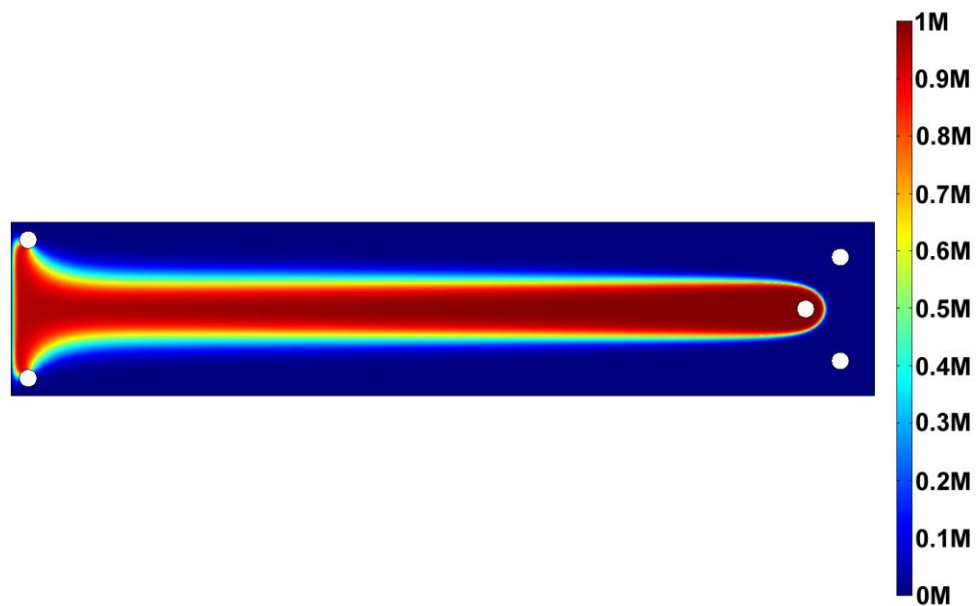


Figure 104: Test of the chip with only two main outlets located aside.

Five different chip layouts were investigated to produce an optimal chip with adequate properties for EHDF. An interesting relation between shape of the inlet/outlet and number of numerical errors was observed (see Figure 100 and Figure 101). An optimal chip with velocity gradient along x-axis (separation dimension) and low flow pattern broadening due to the diffusion was developed (see Figure 104). This chip layout was used for further work on EHDF.

4.8. Models incorporating pressure-drive flow and electromigration with the selected chip layout

Several different simulations were run to test how new layout performs in terms of achieved preconcentration and spatial stability of formed higher concentration region. First simulations were run for applied potential difference of 200V, 600 seconds after begin of the simulation. At around 900s region increased concentration can be clearly visible, and at 980s it exceeds 1.5 times of the initial concentration of malachite green (Figure 105). Maximum concentration is achieved at 1420s (Figure 106 – overlay of streamlines graph of pressure-driven flow). Figure 107 shows close-up of focused region. Total flux (vector sum of convective, diffusive and electrophoretic flux) of malachite green is marked with arrows. As it can be observed arrows on both sides of high concentration region are directed oppositely proving focusing along x-axis. However tested flow pattern constrain anti-focusing along y-axis – flux vectors are directed away from each other. This is result of convective flux (result of pressure driven

flow) and diffusive flux toward outlets (high concentration region in centre). A mid-point between outlets was taken as a reference point for the concentration profile (see Figure 108). The concentration shows initial drop after applying voltage (at 600s), then rapid increase, maximum at 1420s, and rapid drop afterwards. As it can be seen time when concentration is two times higher than initial is only 80s leaving very small window for any operations such as analyte extraction.

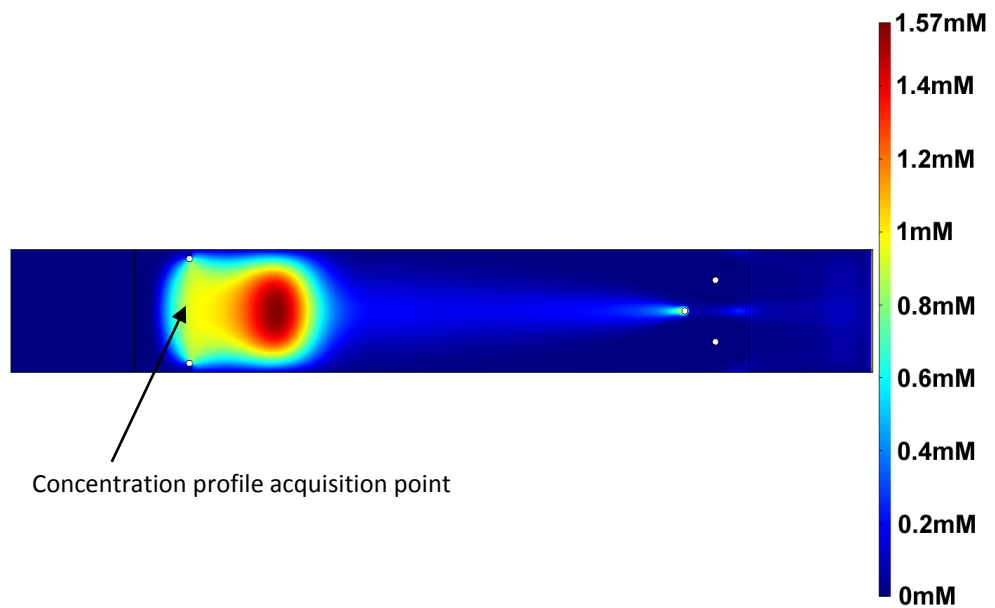


Figure 105: Concentration distribution of MG in new chip at 980s.

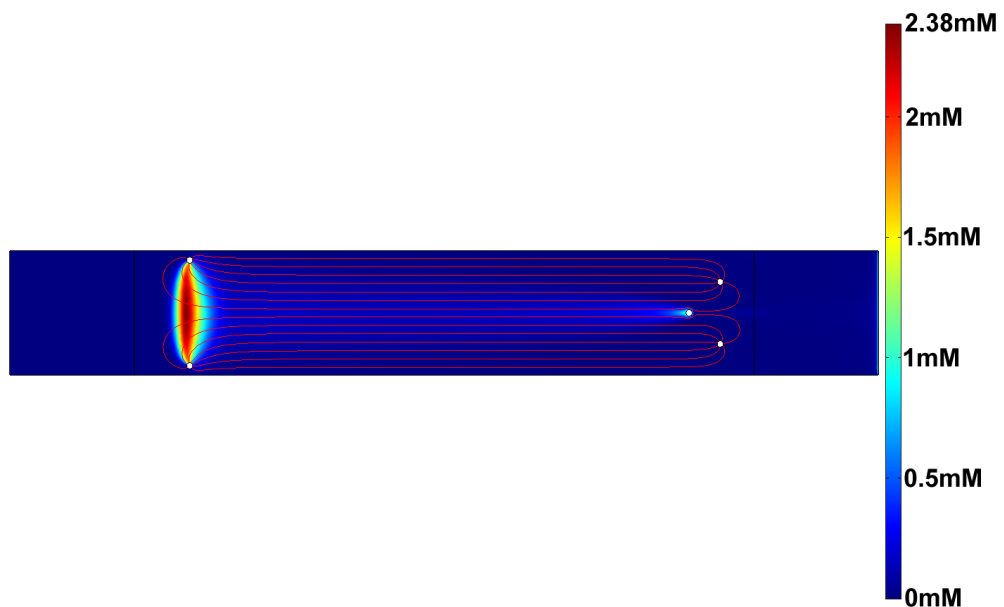


Figure 106: Concentration distribution of MG in new chip at 1420s overlay of pressure-driven flow streamlines.

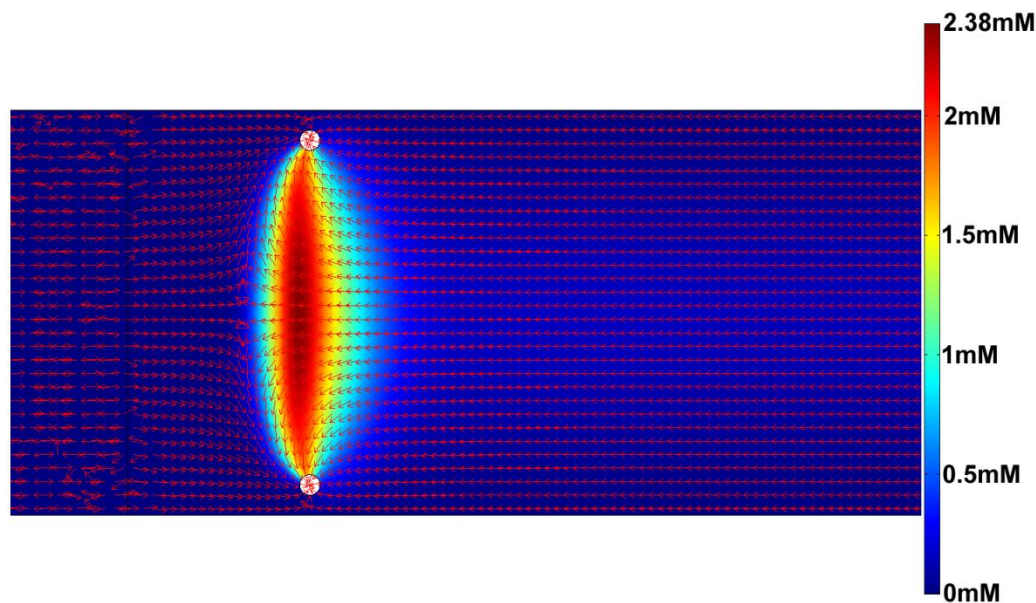


Figure 107: Close-up of high concentration region from Figure 106. Arrows are showing direction of total flux for malachite green at 1420s.

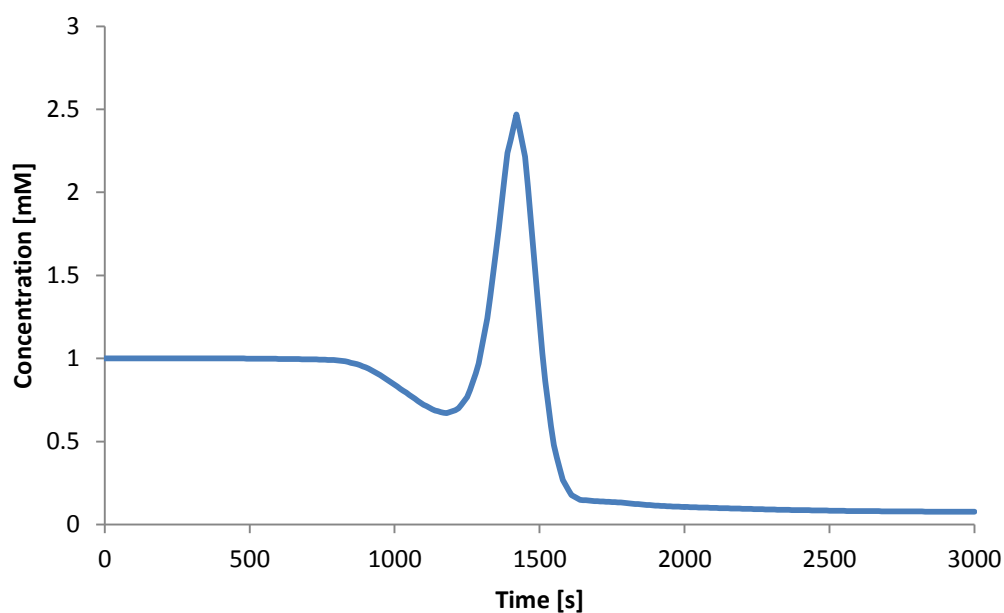


Figure 108: Concentration profile in the centre of the chip between outlets.

The selected chip layout was tested for different values of applied voltage. For potential difference of 1400V an interesting pattern has been observed – single central region of high concentration has been divided into two regions along symmetry axis of the chip (Figure 109). Unusual shape of preconcentrated analyte is a result of inlets shape. Applied voltage is strong enough to completely block significant amount of malachite green behind the central inlet. This can be observed after long experiment time (Figure 110). Inlets are modelled as circles but two dimensional models do not

allow any flow through it. As a result in front and behind the central inlet a zone of significantly lower velocity for pressure driven flow is formed (Figure 109c). Total migration of species is a result of convective flux due to applied pressure and electrophoretic flux due to applied voltage, corrected by diffusion. For 1400 V electromigration is almost equal modelled convection resulting formation of unusual high concentration area near central inlet for prolonged experiment (see Figure 110). Zone of high concentration of model compound on the right side of the central inlet is small – flow from auxiliary outlet is too weak to prevent MG build-up (see Figure 111). For higher voltages (2000V) electromigration dominates convection and MG cannot escape region of low velocity (Figure 112).

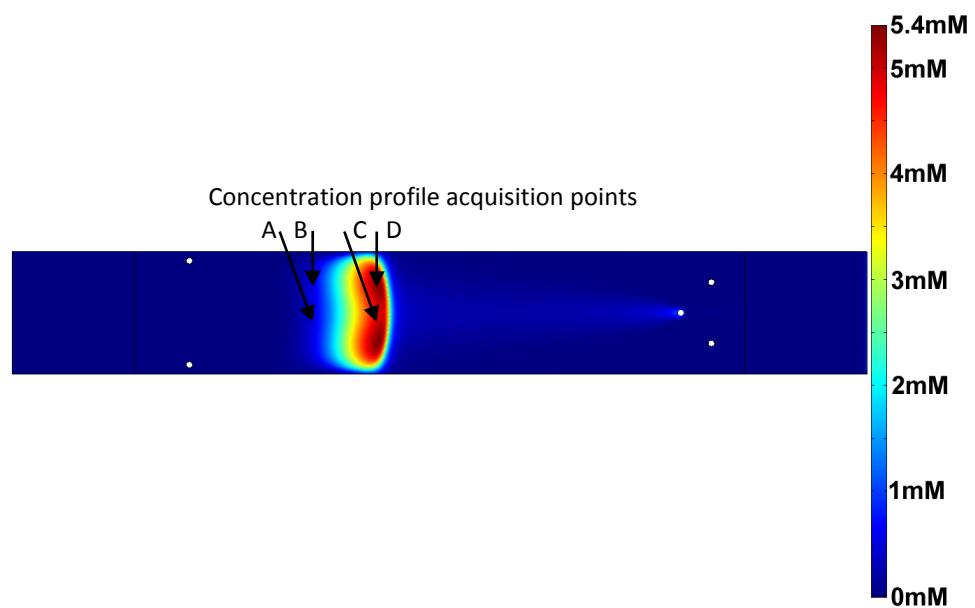


Figure 109: Distribution of concentration of MG after 960s, for 1400V.

To evaluate precisely achieved preconcentration four points were selected – 50mm and 60mm from the left wall of the chip in the middle (10mm from upper wall) and where maximum concentration was recorded (4.5mm from upper wall), see Figure 109 where these points are marked.

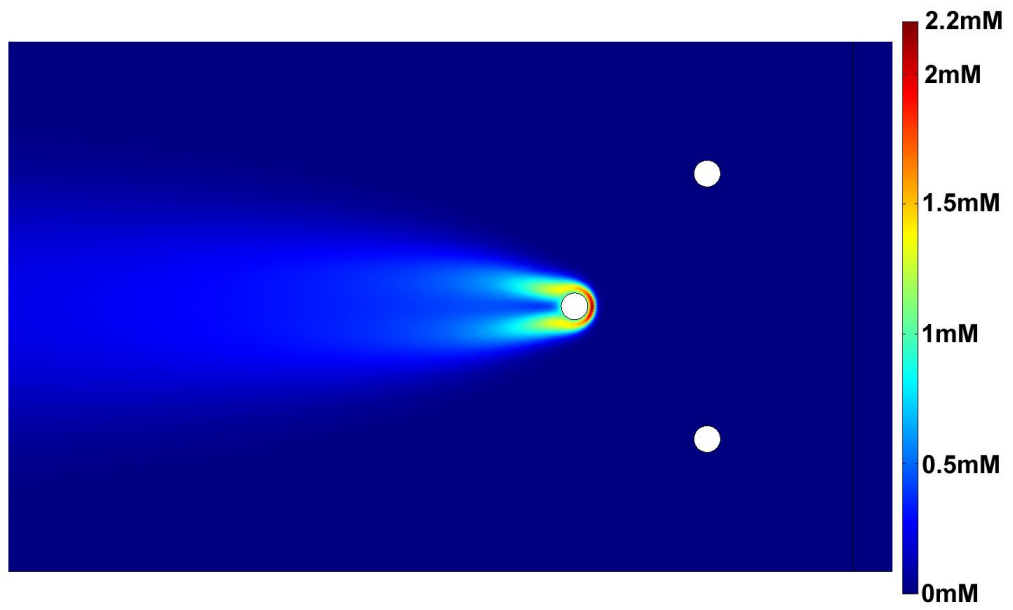


Figure 110: Distribution of concentration of MG after 3000 s, for 1400V.

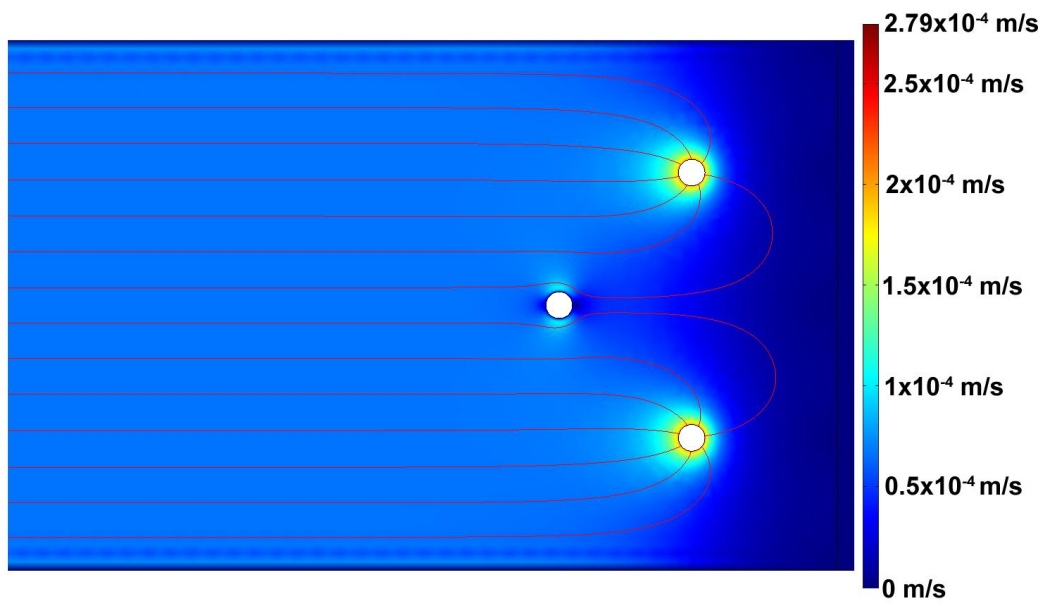


Figure 111: Map of the velocity value with streamlines for pressure driven flow.

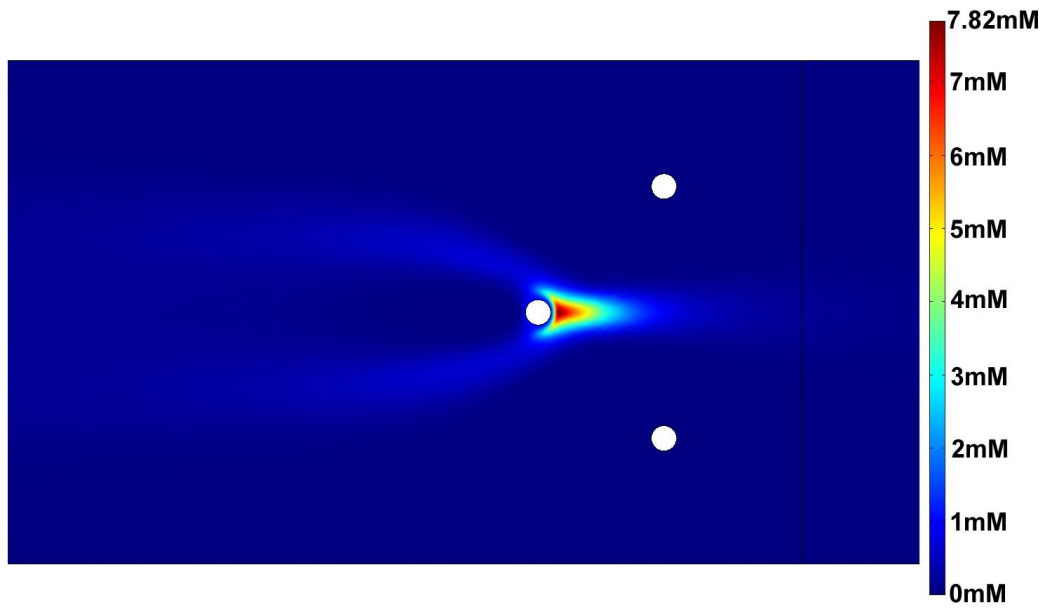


Figure 112: Distribution of concentration of MG after 3000 s, for 2000V applied.

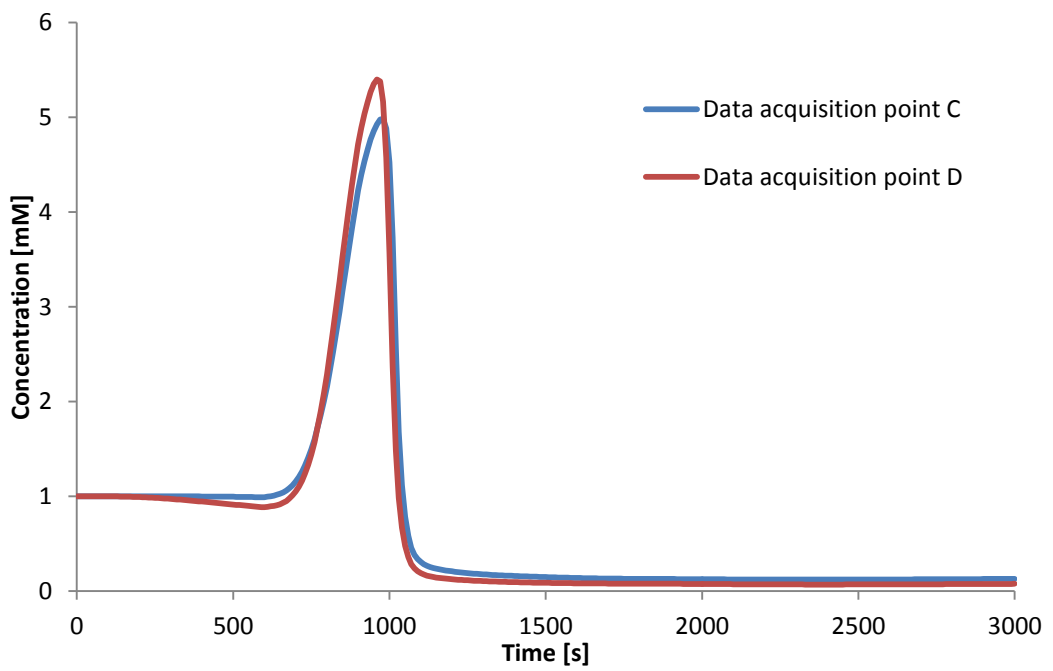


Figure 113: Concentration profiles for points located 60mm from the left chip wall.

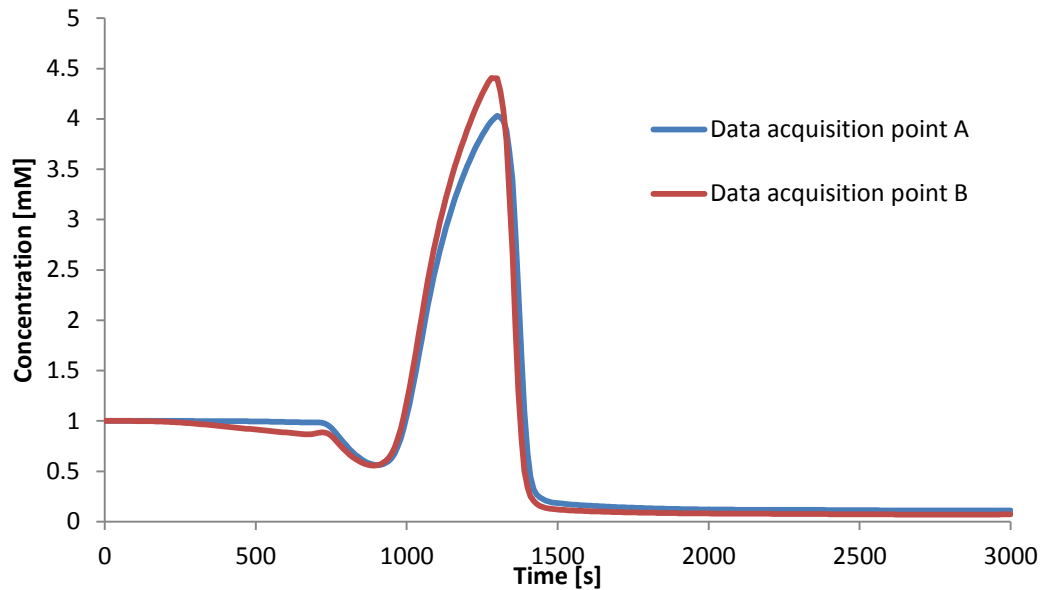


Figure 114: Concentration profiles for points located 50mm from the left chip wall.

Concentration profiles for points located 60mm from the left wall show similar tendency as it was demonstrated in Figure 108. In these conditions almost 5.5 times concentration increase was recorded (see Figure 113), however achieved zone did not remain completely stable. Region of increased concentration travels toward outlets and predominant diffusion start to disperse the analyte. It would be possible to install microfluidic ports suitable for the extraction of the analyte in the central region, however relatively short period of time of good preconcentration (roughly 120s for four times concentration increase, see Figure 114). Also location of the highest increase of the concentration shifted from the middle of the chip suggests that a better optimisation of the chip is needed.

The model incorporating electromigration and pressure driven flow was developed. A five-fold concentration increase was observed, although no equilibrium between the hydrodynamic and electromagnetic forces was achieved. The observed stable zone in the vicinity of the central inlet was the result of the two-dimensional approximation of three-dimensional problem. In the used approach the fluid cannot pass underneath the inlet what creates an artificial zone of very low velocity due to the pressure-driven flow. Although this result is regarded as an undesired in this thesis, it might be used in other experiments with such features fabricated in the chip. The general principle of EHDF was observed and obtained results suggested a need of further optimisation of modelling conditions.

4.9. The first model of EHDF

In the following series of simulations malachite green was introduced through inlets I_2 and I_3 as in previously published papers. For applied potential difference of 280V a quasi-stable focusing was observed. A region of 2.5 times increased concentration was formed. The maximum recorded concentration was 2.7 times of the initial at 1220s after begin of the experiment. After time of 1220s concentration dropped to around 2.5 times of the initial. The zone of increased concentration was slowly shifted toward the left wall of the microfluidic chip, even behind the outlets. There are noticeable numeric oscillations on the border of high and low concentration of the malachite green, but their overall influence is rather negligible as they are located in very limited area. Two points for acquisition of the concentration profiles were selected: one 5mm in front of the line connecting outlet centres and one 5mm behind that line (see Figure 115 and Figure 116).

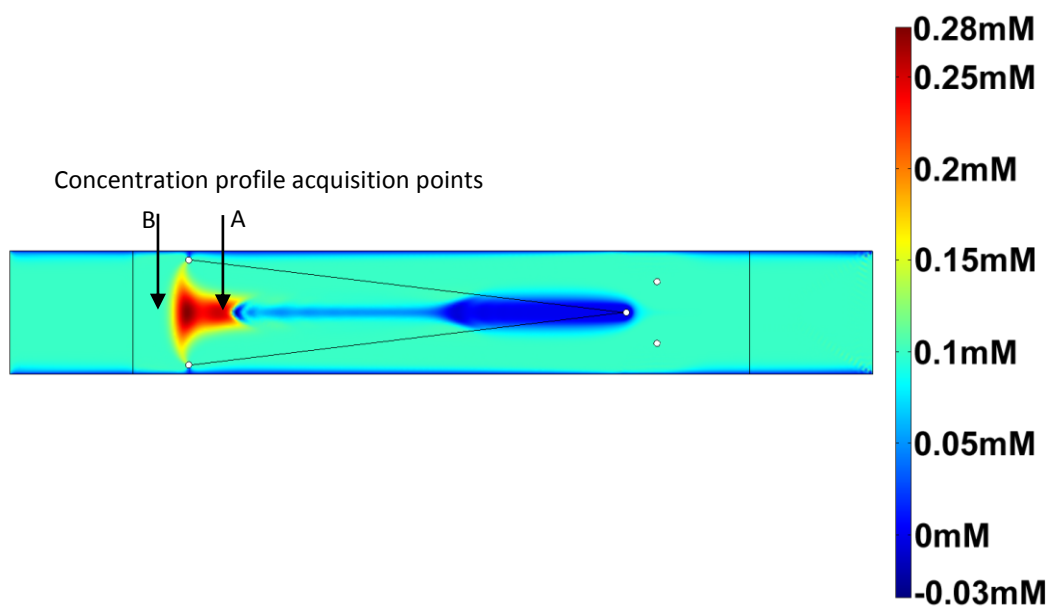


Figure 115: Concentration distribution of MG at 1220s.

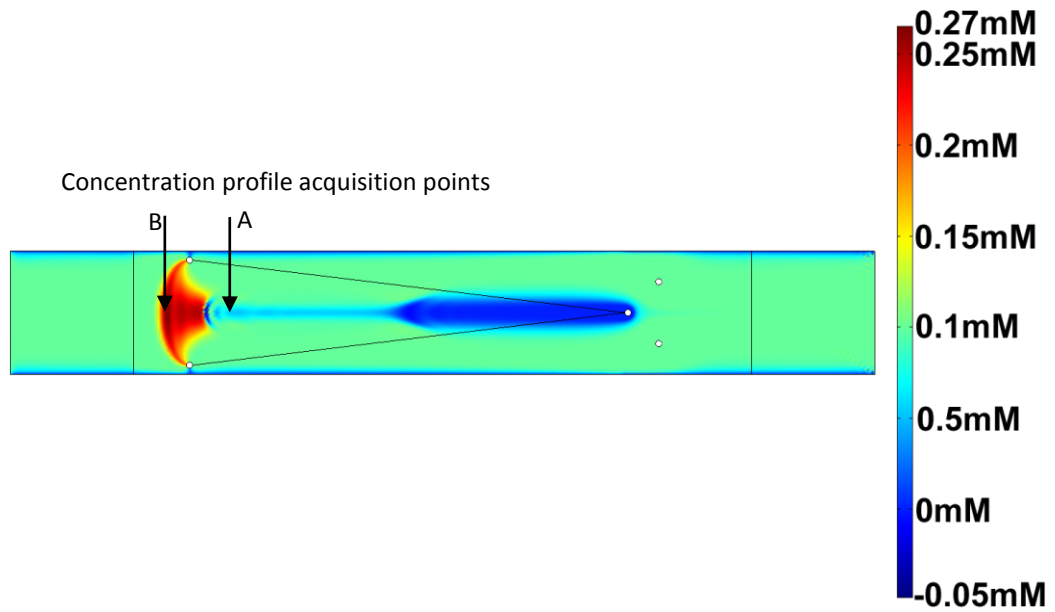


Figure 116: Concentration distribution of MG at 1390s.

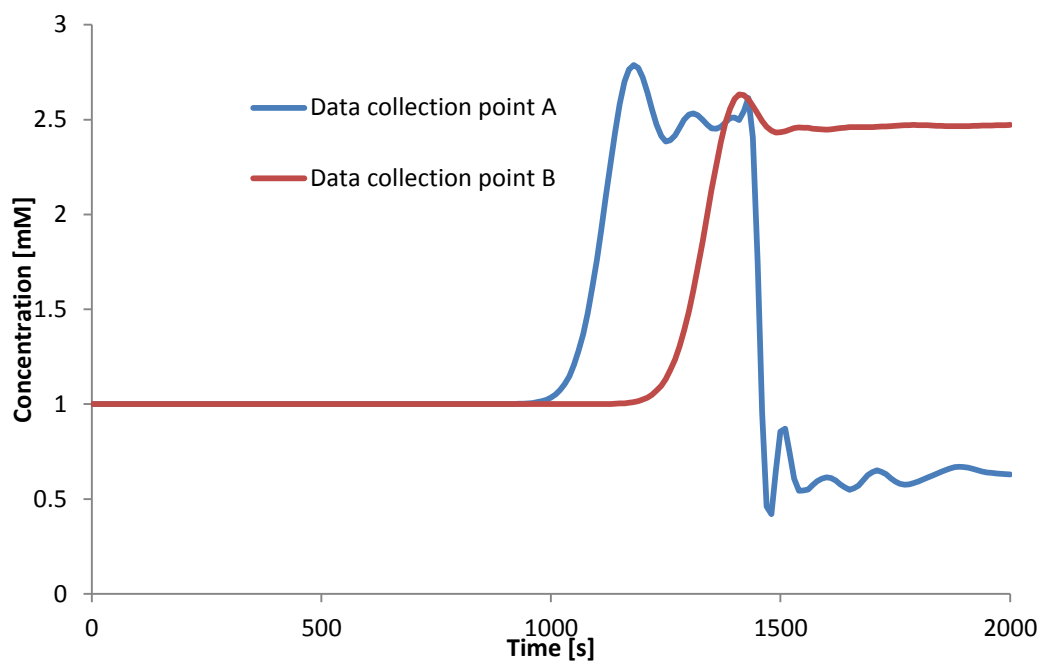


Figure 117: Concentration profiles for points located 5mm in front and behind outlets line.

As it can be read from concentration profiles (see Figure 117) it would be recommended to locate the collection valve close to the outlets line, preferably behind it. Although the highest recorded concentration occur in front of the outlets, but region of alleviated concentration is pushed behind that line after roughly 400s. Obtained flow pattern stabilises around 1600s and there are no major shifts in the position of the high concentration area.

4.10. The second model for EHDF

As previous model looked very promising it was used to theoretically optimise the performance of EHDF. The model was redesigned, virtual lines were removed and applied meshing was pushed to the limits of the used computer. A region of 2.4 times of increased concentration was recorded, moreover with stable region where an extraction valve could be located. Figure 118 and Figure 119 shows time evolution of focused MG zone in time of 700s. The displacement is small ($\approx 1\text{cm}$) and this result can be regarded as a stable solution for EHDF.

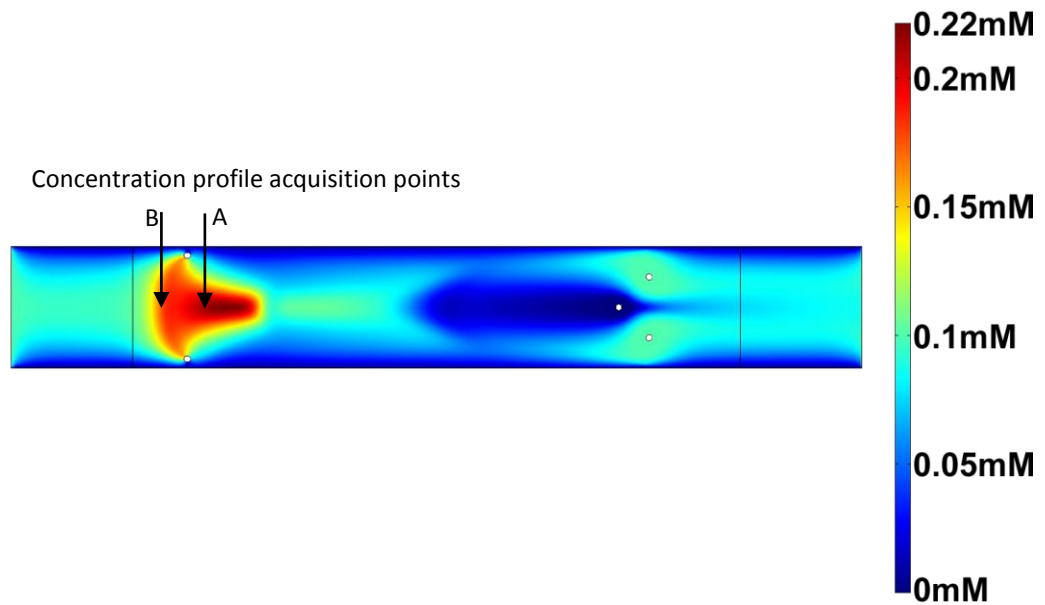


Figure 118: Concentration distribution of MG at 1600s.

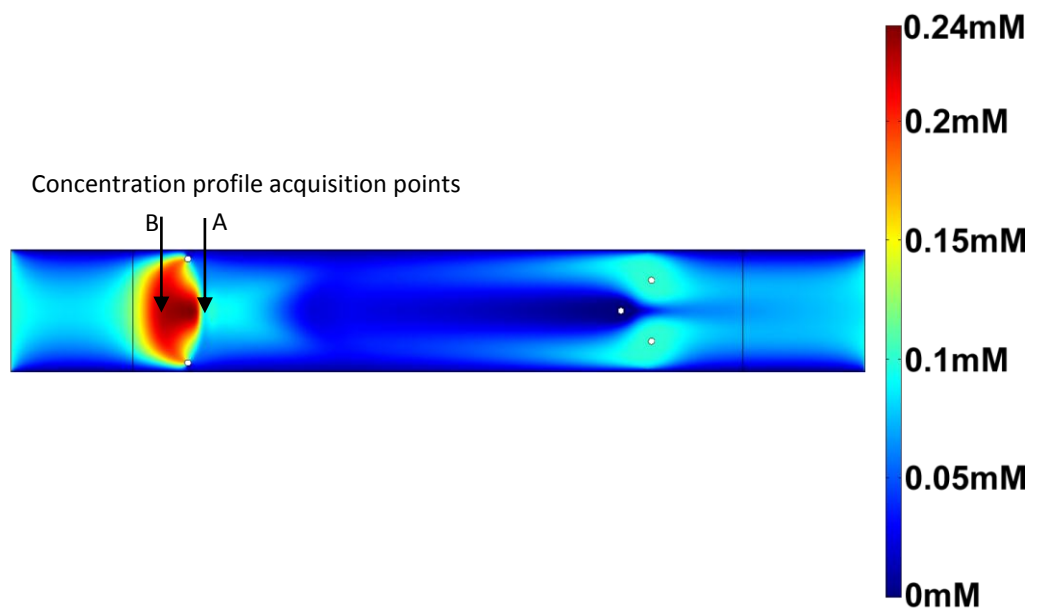


Figure 119: Concentration distribution of MG at 2300s.

Concentration profiles graph (see Figure 120) shows stable region of over two times concentration increase, giving large area where extraction valve could be located allowing for simultaneous collection of large amounts of pre-concentrated analyte.

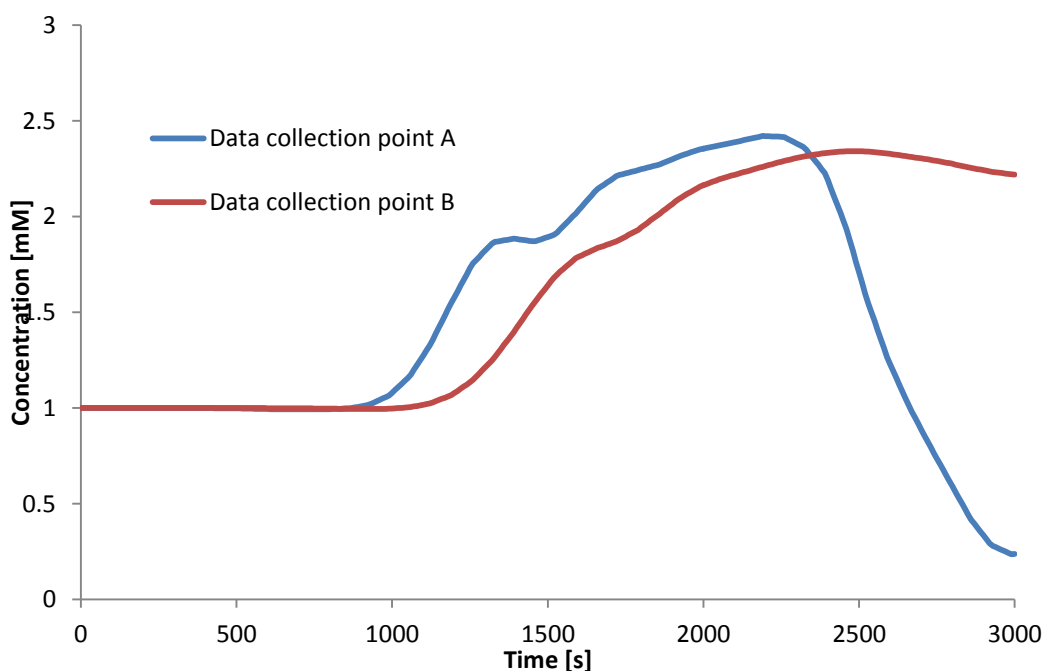


Figure 120: Concentration profiles for points located 2mm in front and 3mm behind outlets line.

A working model of quasi-stable electrohydrodynamic focusing (EHDF) was developed. Two and half times concentration increase was observed in the model and of focused analyte moved around 10mm in time of 900s. The zone of focused analyte remained in a well-defined region of the chip allowing for determination of a possible extraction outlet (not implemented) in the fabricated chip. The used chip layout reduced the influence of the diffusion hence improving the focusing performance. The results were found satisfactory, and the used chip layout was selected for fabrication and further experimental work, which results are presented in Chapter 5.

4.11. Conclusions and the key modelling results

This chapter presents a summary of the modelling of the EHDF. Initially, the basic properties of fluidic models developed in COMSOL were investigated, together with its numerical parameters such as mesh shape, density, and boundary conditions. Results of these simulations allowed for determination of key computing parameters combining consideration for the time needed to solve the presented problem with

quality of the results. In the next step COMSOL was tested for its accuracy of flow pattern prediction and cross-examined with previously published experiments.

The positive recreation of conductivity gradient focusing (CGF) was a starting point for the work on the optimal chip for electrohydrodynamic focusing (EHDF). COMSOL was used to test the initially presented hypothesis on a multi-outlet chip and investigate its properties. The results of these simulations revealed a need of different chip design as the presence of undesired flow properties were found unsatisfactory. COMSOL was used to develop an optimal chip for EHDF that was characterised by a trapezoidal flow pattern, a low influence of the diffusion, and a velocity gradient along the separation dimension. For simplicity of engineering of the chip a compromise between all these factors had to be established. Finally, the optimal chip layout was used for modelling of the EHDF. Results of these simulations are presented in Sections 4.9 and 4.10. Two and a half times concentration increase was observed from the model and the spatial distribution of the analyte was found to be adequate. The modelled chip was then verified experimentally.

Chapter 5 – Experiments in microfluidic systems: results and discussions

Based on the results of conducted simulations presented in Chapter 4 a new chip was fabricated, which is described in detail in section 3.2.6 and technical drawing are in Appendix D. Three inlets (I_1 , I_2 and I_3) were located in one end of the chip and four outlets (O_1 , O_2 , O_3 and O_4) on the opposite end. All inlets in the fabricated chip were shifted 5mm toward the agarose gel tank compared to the numerical model to increase length of the separation chamber. This way the inlet I_1 was located 10mm from the right agarose gel tank and inlets I_2 and I_3 were located 5 mm from the right tank. Inlets I_2 and I_3 were shifted 3mm apart from the chip symmetry axis to provide enough space for standard fingertight HPLC fittings used to secure the tubing. After this adjustment, inlets I_2 and I_3 were located 2mm from the chip long wall.

Four outlets were installed: two main outlets (O_1 and O_2) close to the chip walls (2mm from the wall) and the central collection outlets (O_3 and O_4 , 10mm apart from each other), O_3 in line with outlets O_1 and O_2 and O_4 10mm behind them, 5mm from the left agarose gel tank. The positive electrode (anode) was immersed in the agarose gel tank close to the outlets (left). The ground was immersed in the right tank, close to the inlets.

5.1. Description of experiments

The experiments on EHDF conducted in the microfluidic chip are arranged in three groups according to the implemented layouts of outlets. The exact conditions and precise description of each layout is presented in the section 3.2.6. Below, a table summarises used chip outlet layouts.

In the 2P-series, two peripheral outlets located close to the chip walls were used to form the flow pattern that was modelled. During these experiments a novel phenomenon named lateral electrohydrodynamic focusing was observed, which is discussed in greater detail in the later part of this thesis. The investigation of the lateral EHDF led to employment of two following chip layouts.

In the 2L-series of experiments the formation of lateral EHDF was investigated using two central outlets located on the chip symmetry axis. This chip layout was employed to verify any relation between the location of the outlets and the formation of the highly concentrated flowstream of the test analyte.

In the 3T-series further study of more practical applications of lateral EHDF were investigated. Three outlets were open to allow for formation of three parallel flowstreams within the chip. This layout was used to positively identify key parameters of lateral EHDF. All the experimental setups are summarised in the Table 41.




Experiment series	Experiment number	Used outlets	Chip layout schematic
2P	14, 22, 30, 47	O ₁ and O ₂	
2L	15, 16, 17, 26, 40, 41	O ₃ and O ₄	
3T	20, 21, 24, 31, 36, 43, 58	O ₁ , O ₂ and O ₃	

Table 41: Summary of the experiment series, experiment numbers and relevant chip layout.

5.2. Results of the experiment 2P-14

Experimental set-up for the experiment 2P-14 is presented in section 3.2.6.2. After solving problems with the flow stability, a series of experiments to achieve successful focusing was conducted. Different flow rates were tested to find that optimal ratio between the central and auxiliary inflows. This was found to be 1:5 – half as was used in the COMSOL model (see section 4.9 and 4.10). For these initial tests the 500 μ m gasket was used. Sometimes a higher ratio of flow velocities resulted in an unstable flow and focused stream tend to stick to the wall (Figure 58f) in the early stage of experimental work.

Figure 121 presents six chosen time moments of the experiment 2P-14, labelled according to the time from the moment of introduction of the high conductivity buffer into the chip. Concentration values were read according to the method described in section 3.2.4 and are presented in Figure 122. There was initially a slight concentration drop (transparent buffer slowly reaching detection point diluting the MG) and after applying voltage a significant concentration increase was observed. The highest registered concentration was 0.82mM \pm 0.094mM what was 8 times concentration increase compared to the concentration of the compound introduced into the chip at

0.1mM MG. Concentration profile obtained experimentally was similar to that predicted using numerical modelling. The most important differences were higher performance of the focusing (8 times, compared to a maximum of 4.5 times predicted from the model), and size of the focused area. The size of the focused area was larger than that found from the model. Instead of forming a single focused zone, focusing occurred not only along the chip symmetry line, but also perpendicularly to this, thus narrowing the zones of MG into a thin concentrated line.

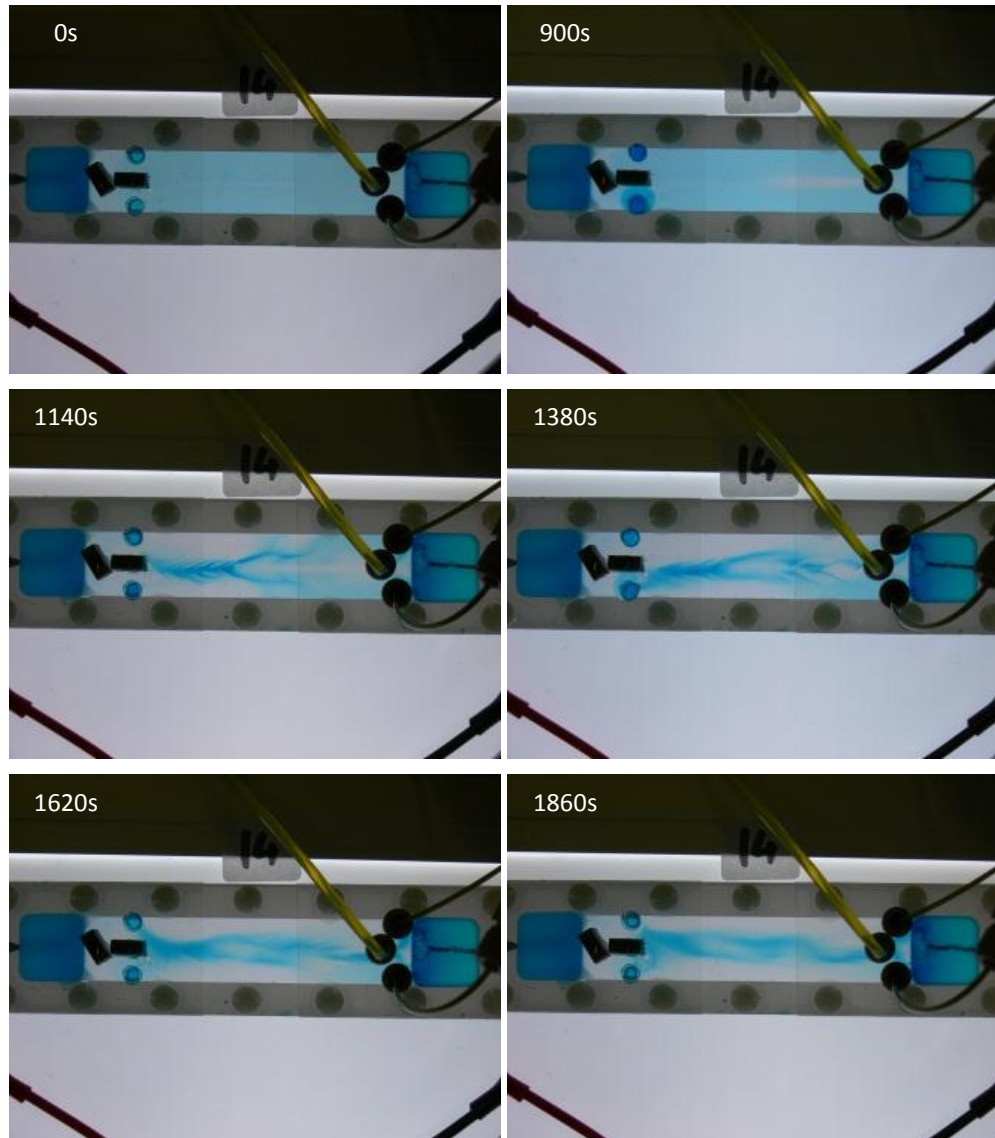


Figure 121: Focusing in the microfluidic chip, experiment 2P-14.

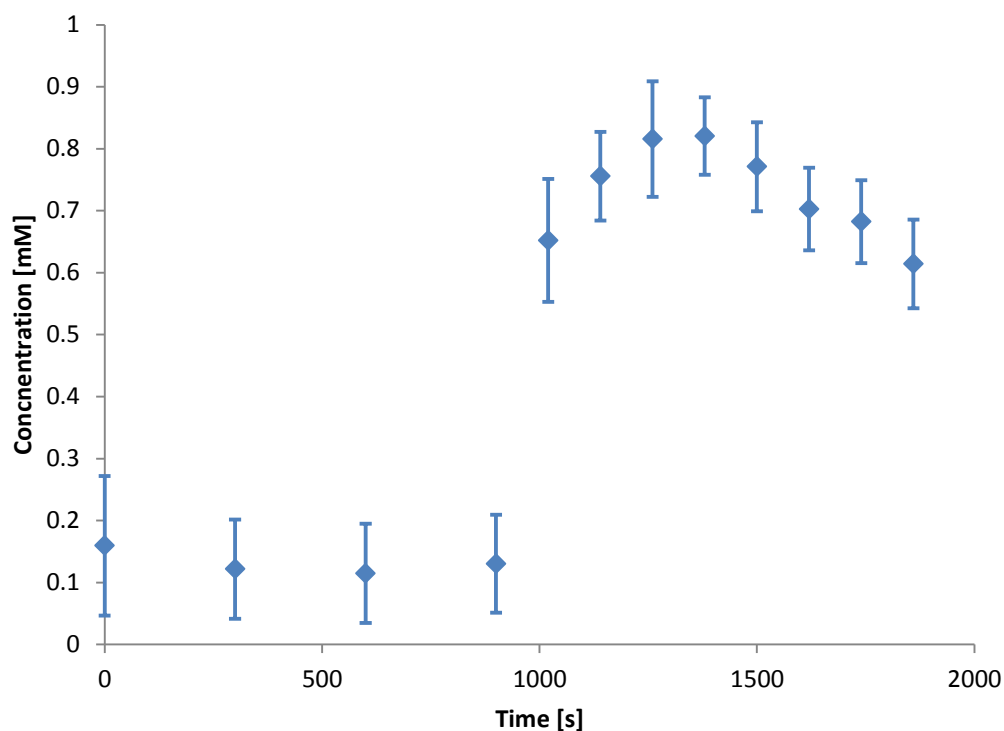


Figure 122: Graph of concentration vs. time of the focused analyte from experiment 2P-14 shown in Figure 121.

5.3. Results of the experiment 2P-22

With the changing of flowrates for the central and auxiliary inflows and decreasing of the applied voltage, a higher focusing ratio was achieved. This experiment is especially important as high flow stability was maintained successfully. The process of formation of the focused zone is documented (see Figure 123). The chip was primed with 0.1mM MG (Figure 123 – 600s) and at 900s filling with Tris-HCl took place. During the filling the flow was stable and a clear area of transparent fluid was slowly travelling along the chip. The flow was stable and only colour gradient between MG and Tris-HCl due to the diffusion could be observed (Figure 123 – 600s).

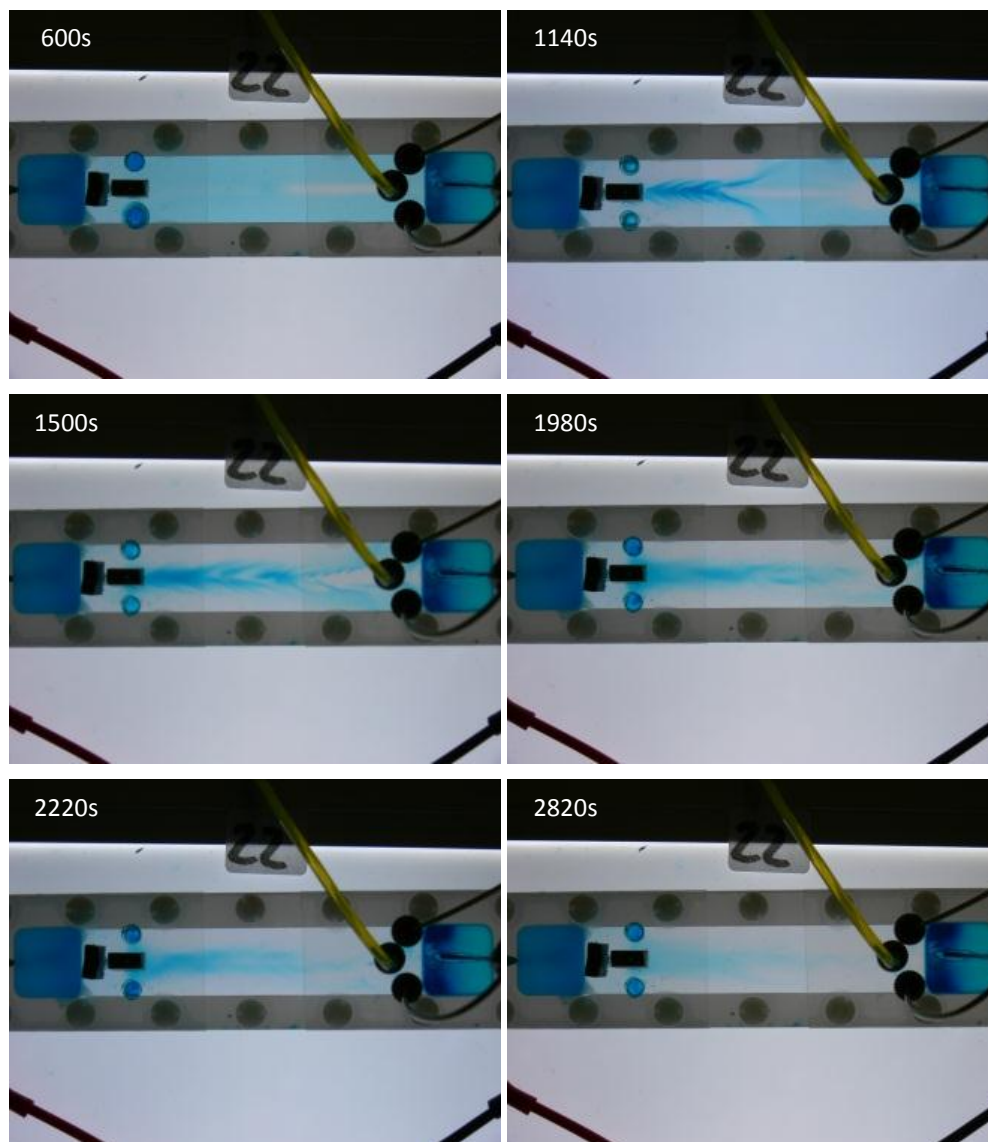


Figure 123: Focusing in the microfluidic chip, experiment 2P-22.

Almost immediately after applying the voltage an interesting situation developed. The MG filling the chip was pushed toward right side of the chip with inlets more rapidly near walls than in the centre of the chip forming a plough-shaped front of highly concentrated dye (Figure 123 – 1140s). With time the high concentration of MG migrated visibly to the central stream of high conductivity buffer. The desired flow patten with equal outflow through both outlets was maintained well during the experiment. There were clearly visible comb-like structures and tiny vortices on the boundary between MG and the solvent shortly after applying the voltage (Figure 123 – 1140s). Their formation is attributed to the rapid movement of the MG toward the centre of the chip. With increased time diffusion stabilised that effect and it was no longer observed. Shortly after applying the voltage there was a significant concentration

increase (Figure 123 – 1140 to 1900s) which dropped with time. Eventually when entire MG stored in the chip in the beginning of the experiment was either diverted to the central stream and flushed away from chip, or migrated beyond the inlets. The inflow of MG was too low compared to the inflow of the high conductivity buffer and therefore a reduction in focusing was observed with increased time. Figure 124 presents the concentration versus time graph for experiment 2P-22. A Seven to nine fold concentration increase for about 1000s was observed followed by flushing the MG from the chip as the MG inflow quantity was insufficient to susustain continuous focusing.

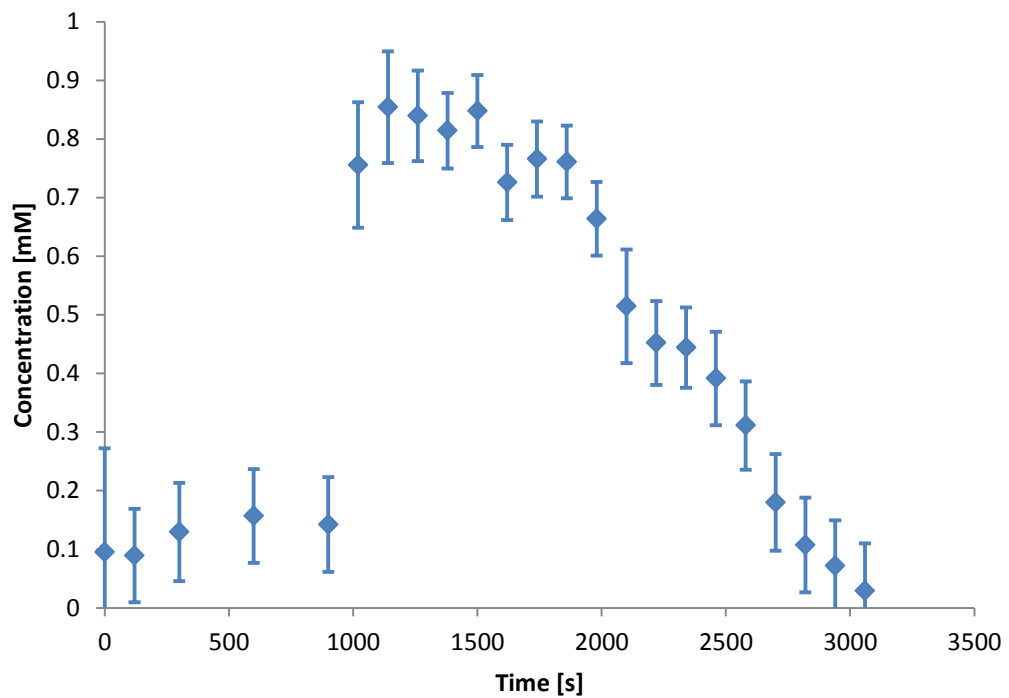


Figure 124: Concentration profile for experiment 2P-22 shown in Figure 123.

5.4. Results of the experiment 2P-30

Reducing the inflow of the Tris-Hcl to 2 μ l/min, increasing the inflow of MG to 40 μ l/min and increasing voltage to 300V allowed for achieving a flow pattern with continuous focusing of the inflowing test compound. The MG remained focused despite problems with flow pattern stability and non-equal outflow through both outlets.

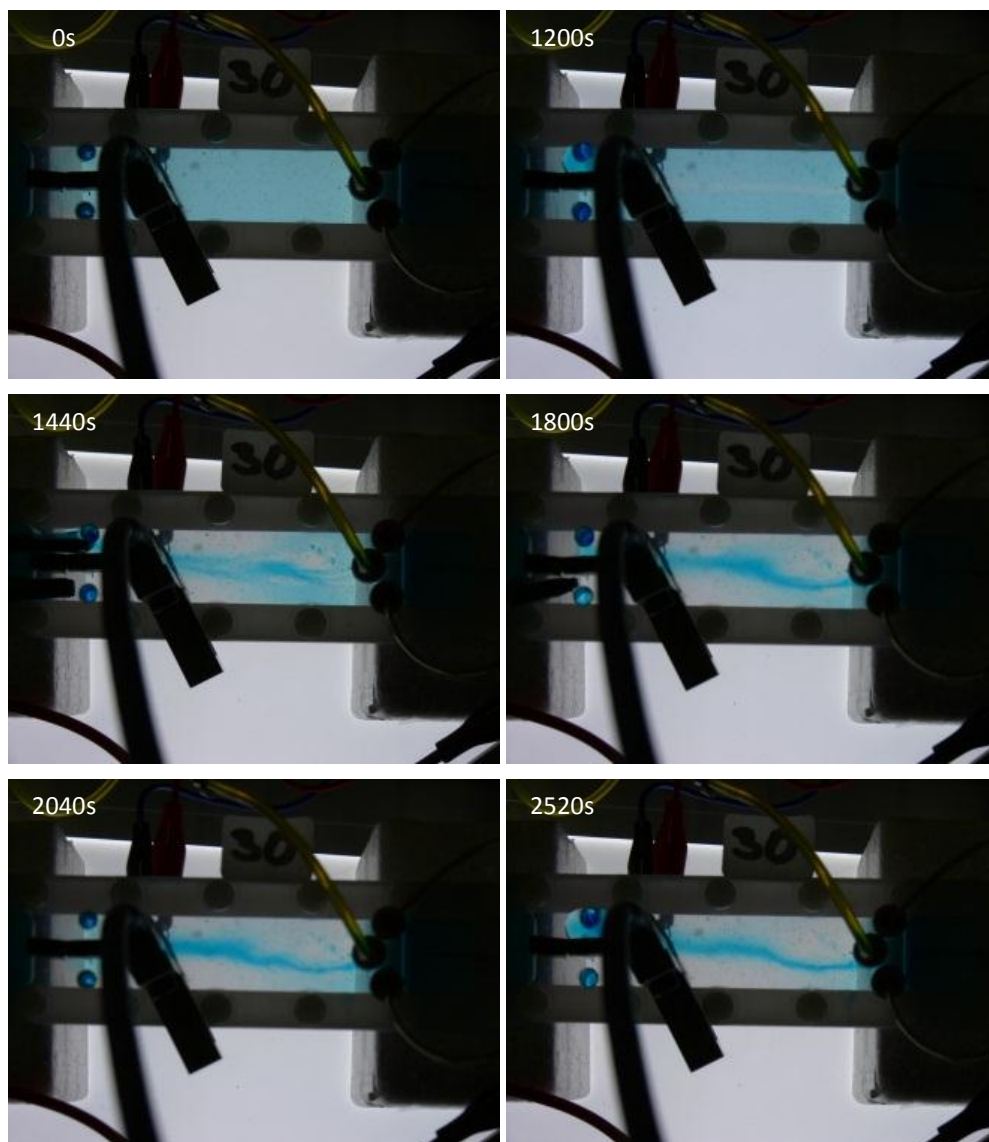


Figure 125: Focusing in the microfluidic chip, experiment 2P-30.

After filling the chip for 1200s with high conductivity buffer a potential difference of 300V was applied. As it can be observed in Figure 125 at 1440s, formation of the highly concentrated central stream was turbulent and flow was diverted toward O_1 outlet. Despite numerous attempts to stabilise flow with draining mostly outlet O_2 to divert flow to its original path, the flow pattern remained almost unchanged. Concentration calculations using taken photos allowed for selecting any set of data point within initially selected region. Concentration measurements with the fibre optic spectrophotometer required installing the illuminating LED and collecting fibre at one point. Recalibration of the sensor at each point of the chip was necessary as each point has slightly different transmittance (scratches, stains, etc.). A numerical aperture of 0.22 ± 0.02 of the used $50\mu\text{m}$ fused silica optical fibre resulted in the formation of cone of

acceptance with a 4.74 ± 0.24 mm base radius (see Figure 51). When a fluid is highly focused or diverted from its path, an area of transparent solvent can take up significant part of the set detection area limiting its usefulness. As it can be seen in most of the time steps in Figure 125, the flow has an asymmetric pattern and a significant part of the detection area was taken by the solvent, reducing the usefulness of data acquired from the spectrophotometer.

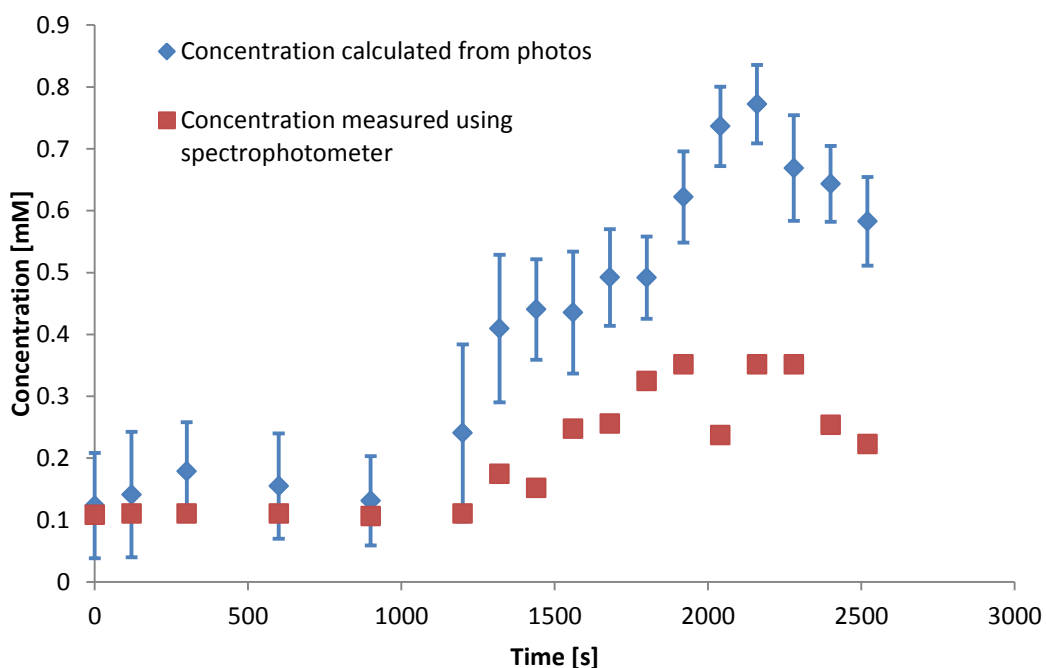


Figure 126: Comparison of the concentration of MG in experiment 2P-30.

Both methods (spectrophotometer and image analysis of photos) agree in concentration measurements during the filling with Tris-HCl (see Figure 126). Concentration values read with the spectrophotometer were far more precise than those read from photos, however calculated concentration values from photos remain correct within error margins. When transparent Tris-HCl reached the detection zone and analyte started focusing fluctuations could be observed. The lower reading from the spectrophotometer at 1320s could be explained as the width of focused MG zone was around 5-6mm at this stage, which left around 25% of detection area for transparent solvent. There were similar tendencies in concentration for both detection methods – increase from 1200s to 1920s, stabilisation to 2280s and drop afterwards. The concentration drop observed from the spectrophotometer at the 2040s time step, was observed to be due to a flow shift away from the detection point. Despite problems with the flow stability, MG was focused by at least 3.5 times (spectrophotometer data).

Moreover, the most important observation was this experiment was the successful achievement of a continuous flow of focused analyte, which lead to investigation of different flow patterns.

5.5. Results of the experiment 2P-47

The same set of conditions as in the experiment 2P-30 was tested on the 200 μ m PTFE gasket. Results are presented in Figure 127. The achieved flow pattern is very chaotic. There are visible regions of focused malachite green separated by low concentration regions (see Figure 127 – 840s). The flow pattern stabilised around a time of 1320s (720s after voltage application). Uneven flow was observed: the stream of focused MG shifted from one outlet to the other.

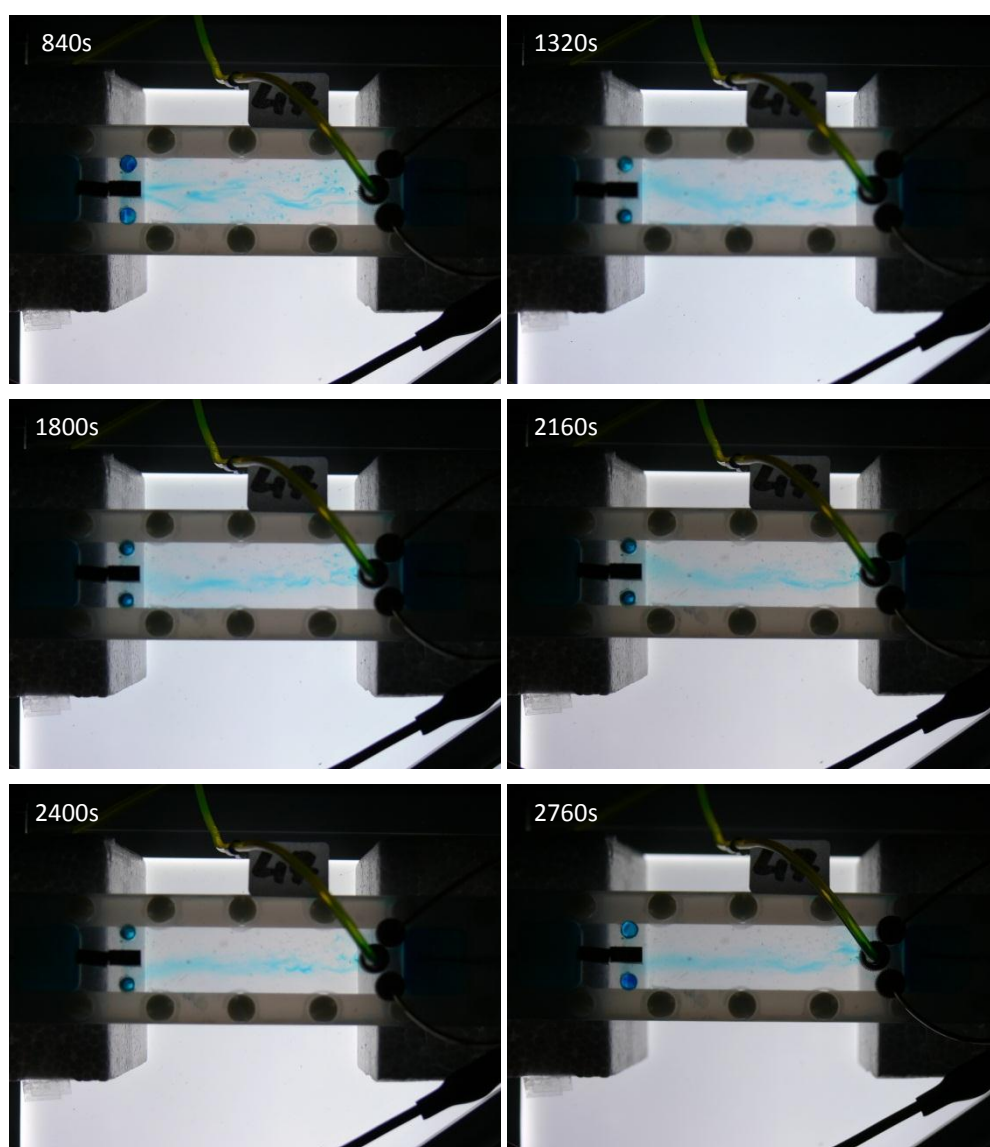


Figure 127: Focusing in the microfluidic chip, experiment 2P-47.

The acquired concentration profile shows a high dispersion of results (see Figure 128). This was a result of the thinner gasket reducing the light absorption path by 60% (comparing to the 500 μ m gasket) and low focusing performance, which gave a high standard deviation of the luminosity measurement. The applied voltage was too low to compensate for the pressure driven flow and focusing was only marginally observable.

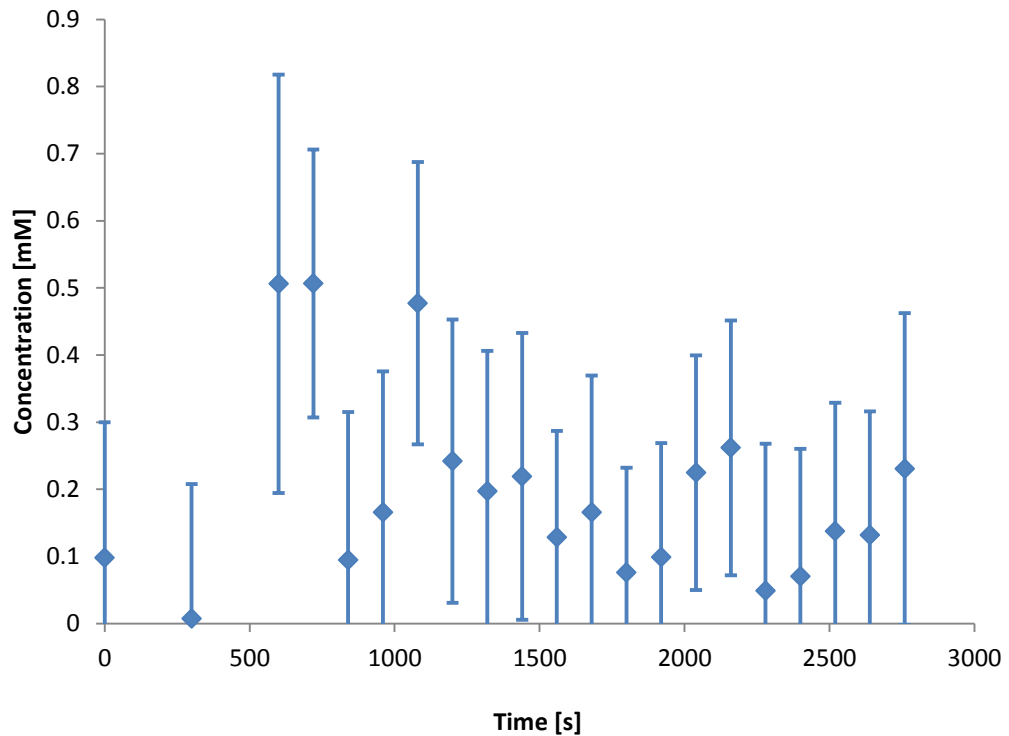


Figure 128: Concentration profile for experiment 2P-47.

5.6. Results of the experiment 2L-15

During experiments in 2P-series with outlets O_1 and O_2 open (see Figure 53) an interesting property of the flow pattern was observed – focusing of the MG already in the vicinity of the inlets. According to the developed COMSOL models MG should start focusing a few centimetres from the inlets. A series of experiments was conducted to investigate unpredicted before behaviour of the MG. With two outlets open (O_1 and O_2) problems with flow stability were observed. To enforce flow stability a different layout of outlets was selected for 2L-series of experiments - O_1 and O_2 were closed and O_3 and O_4 were open. Open outlets lying on the chip axis of symmetry should increase flow stability as the entire flow has to move toward the chip centre. This outlet layout was used by Potter (8) and allowed for the comparison of results.

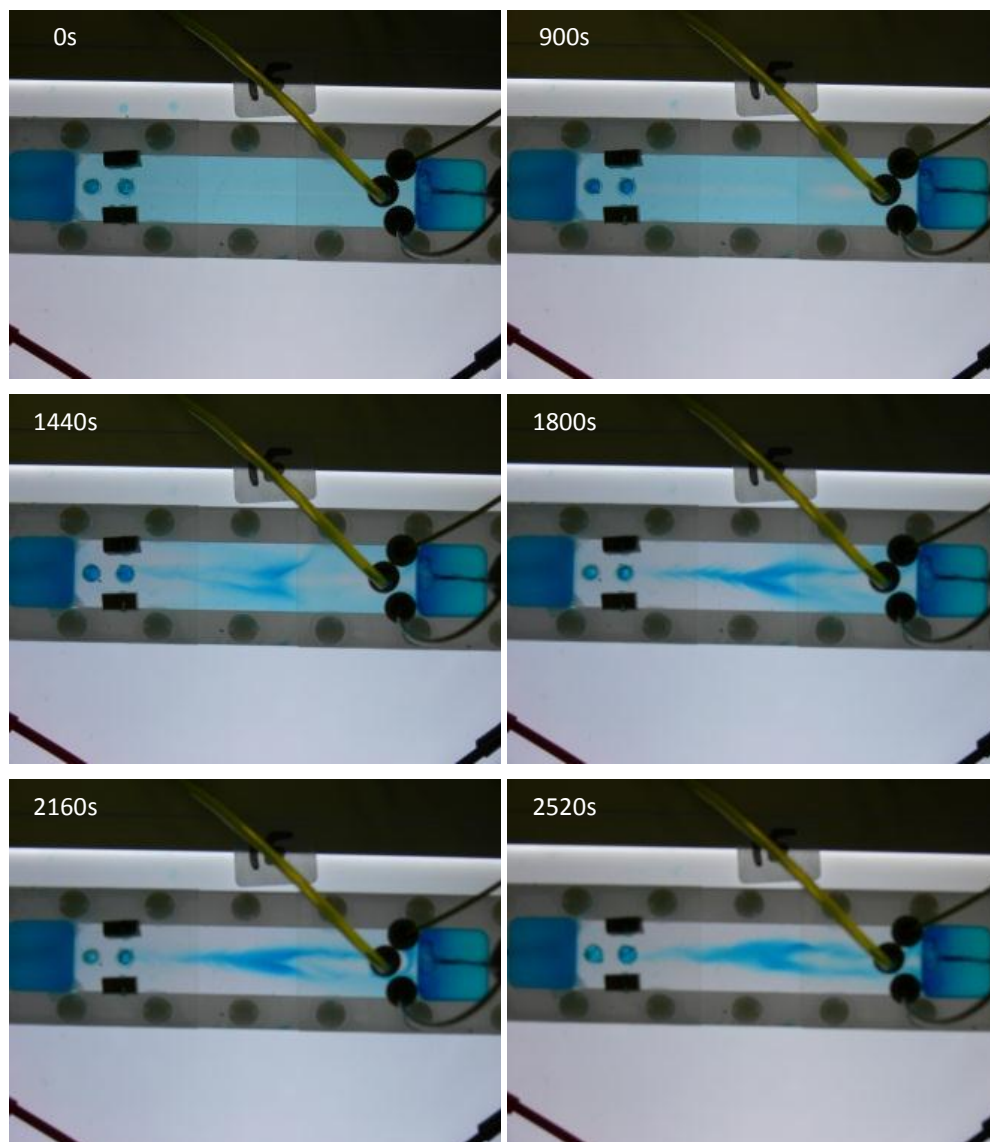


Figure 129: Experiment 2L-15 - focusing in the central flowstream.

Figure 129 shows the formation of the highly concentrated MG in the central part of the chip where high conductivity buffer was flowing. The equilibrium between opposing forces imposed by pressure driven flow and electromigration was established at a time of 1800s – 600s after applying the voltage. Since that time, the flow pattern did not change significantly. Initially MG was migrated toward the inlets (Figure 129 – 1440s). During the entire experiment a transparent region of clear high conductivity Tris-HCl buffer was visible for around 2cm from the I_1 inlet. After that distance MG was forced into the central stream and then moved toward the open outlet.

5.7. Results of the experiment 2L-16

Increase of the flowrate of the Tris-HCl to $4\mu\text{l}\cdot\text{min}^{-1}$ in this experiment was compensated by reduction of the filling time to 900s to have a similar length of high conductivity buffer (Tris-HCl) in the chip compared to the experiment 2L-15.

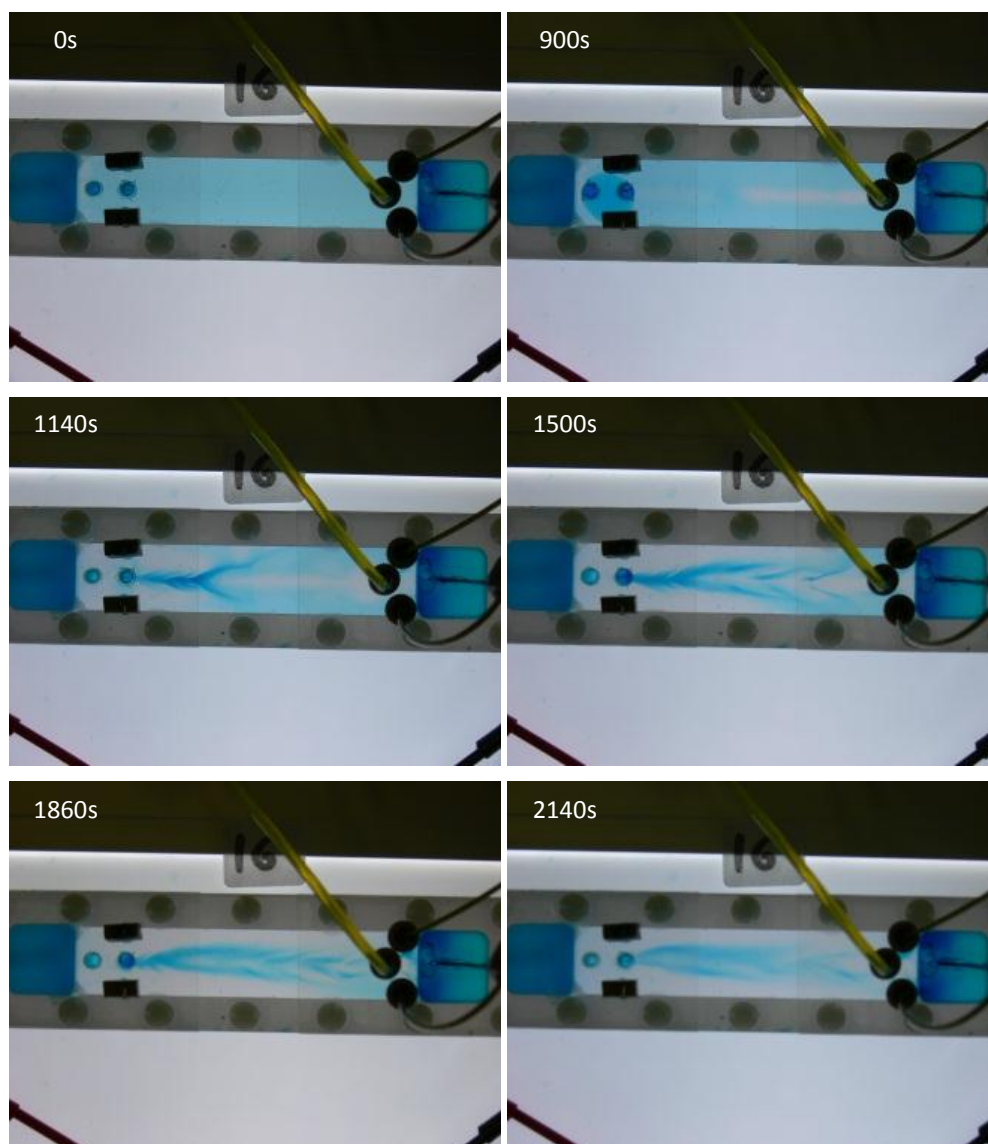


Figure 130: Experiment 2L-16 - focusing in the central flowstream.

Doubling the flow rates for all inlets in this experiment, compared to the previous tests yielded very interesting results. The observed flow pattern (Figure 130) was similar to the one presented in Figure 129. The “Y” shaped region near first outlet formed quickly but did not move toward the inlets. Comb-like structures can be observed on the edge between the focused MG and the clear solvent (Figure 130 – 1140s). The turbulences are significant and focused MG formed in several small regions before the flow pattern stabilised (Figure 130 – 1500s). Around a time of 1860s,

diffusion overcame the initial separation of MG patches and a more uniform flow pattern was observed. Again a region of lower concentration of MG from the central inlet I_1 to the focused zone is visible – at these conditions MG was not forced completely into the high conductivity buffer but only partially. Also it is visible that equilibrium was not reached. The initial pattern resembling the letter “Y” (Figure 130 – 1140s) was slowly pushed out of the chip and at time of 1900s the flow pattern resembled letter “V”.

5.8. Results of the experiment 2L-17

In this experiment the flowrate of the Tris-HCl was reduced in order to maintain flowrate ratio of 1:10 between central (Tris-HCl) and auxiliary inflows (MG). Also the applied voltage was reduced by 20% (compared to experiment 2L-16) to observe the behaviour of the MG.

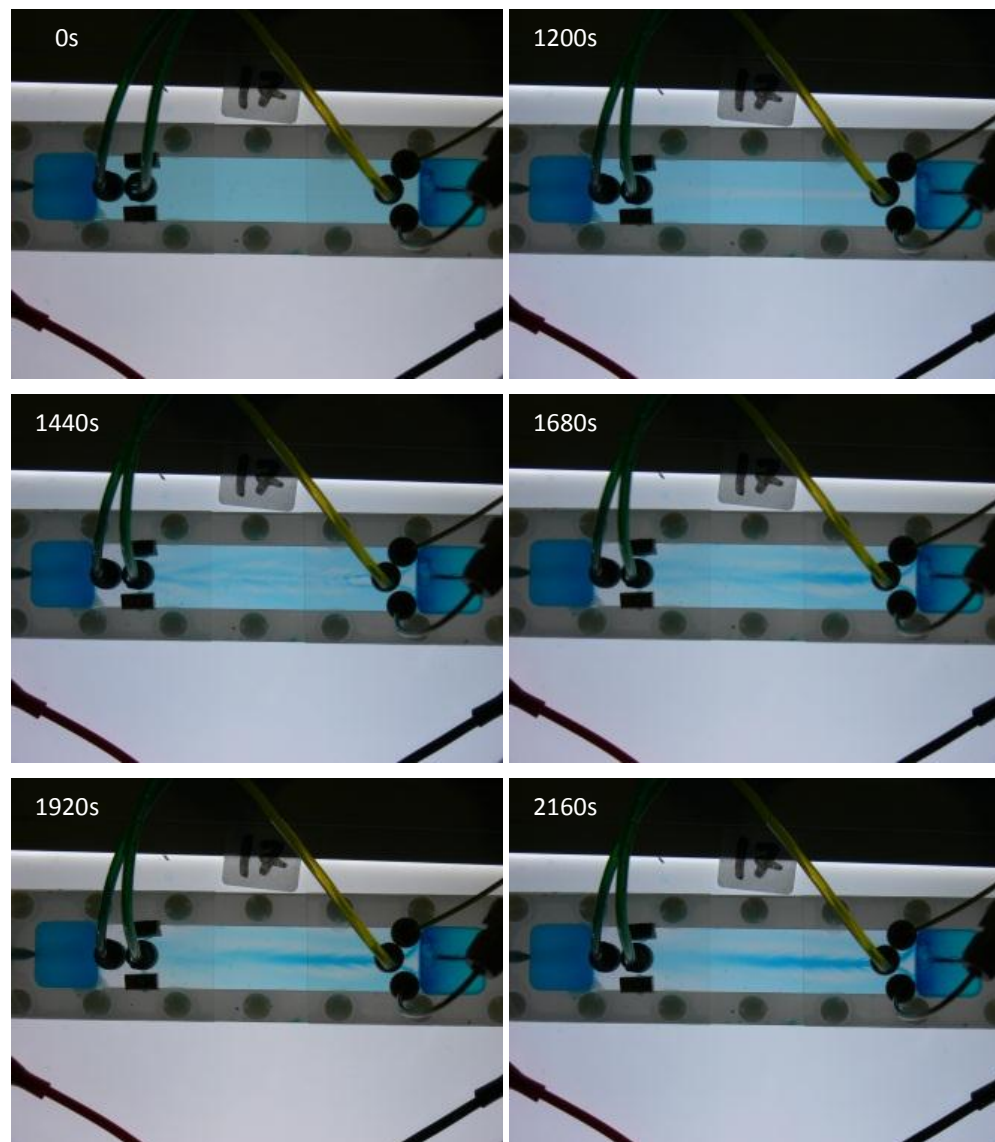


Figure 131: Experiment 2L-17 - focusing in the central flowstream.

After applying the voltage, MG was slowly pushed from the outlet region toward the inlets. The applied voltage was too weak to compensate for inflow of the MG thus in no chip region was completely depleted of MG. The inflow of Tris-HCl visibly darkens with time as more and more MG was pushed into it. After 2160s a well visible stream of concentrated MG in a stable flow pattern was observed. There were also some remains of the initial MG close to the walls.

Concentrations calculated from the obtained photos showed the visible tendencies in the concentration values. Figure 132 provides a comparison of concentration values from three experiments (2L-15, 2L-16 and 2L-17). In experiment 2L-15 (see Figure 129), concentration slowly rose, reached maximum and eventually started decreasing. In experiment 2L-16 (see Figure 130), there was a rapid concentration rise after applying the voltage followed by a small drop and then, a quasi-equilibrium formed as a region of stable concentration was slowly pushed out of the chip resulting in an acceleration in drop of the concentration. In experiment 2L-17 (see Figure 131) there was initial concentration drop as the transparent Tris-HCl reached the measurement area followed by slow and constant rise in concentration. The concentration increased between five to nine times.

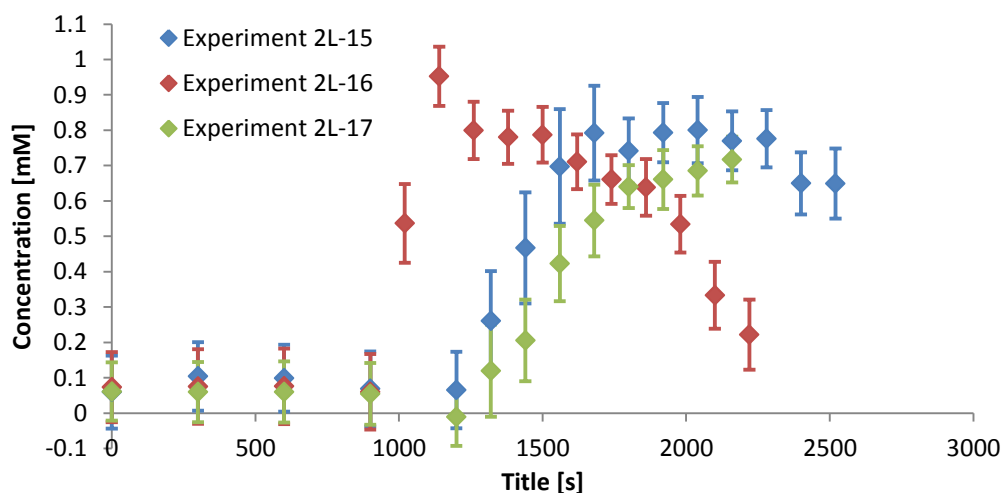


Figure 132: Comparison of concentration changes in three experiments (2L-15, 2L-16 and 2L-17) involving focusing of the MG in the central flowstream.

5.9. Results of the experiment 2L-26

Knowing conditions required to observe the malachite green focusing in the central flowstream, another series of experiments were conducted with the spectrophotometer installed for additional precise concentration measurements.

Compared to the previously mentioned experiments, tubing in outlet O_3 (see Figure 53) was blocked to minimise the influences of the uneven outflow. This experiment was conducted to establish how a stable focusing in the central flowstream occurs.

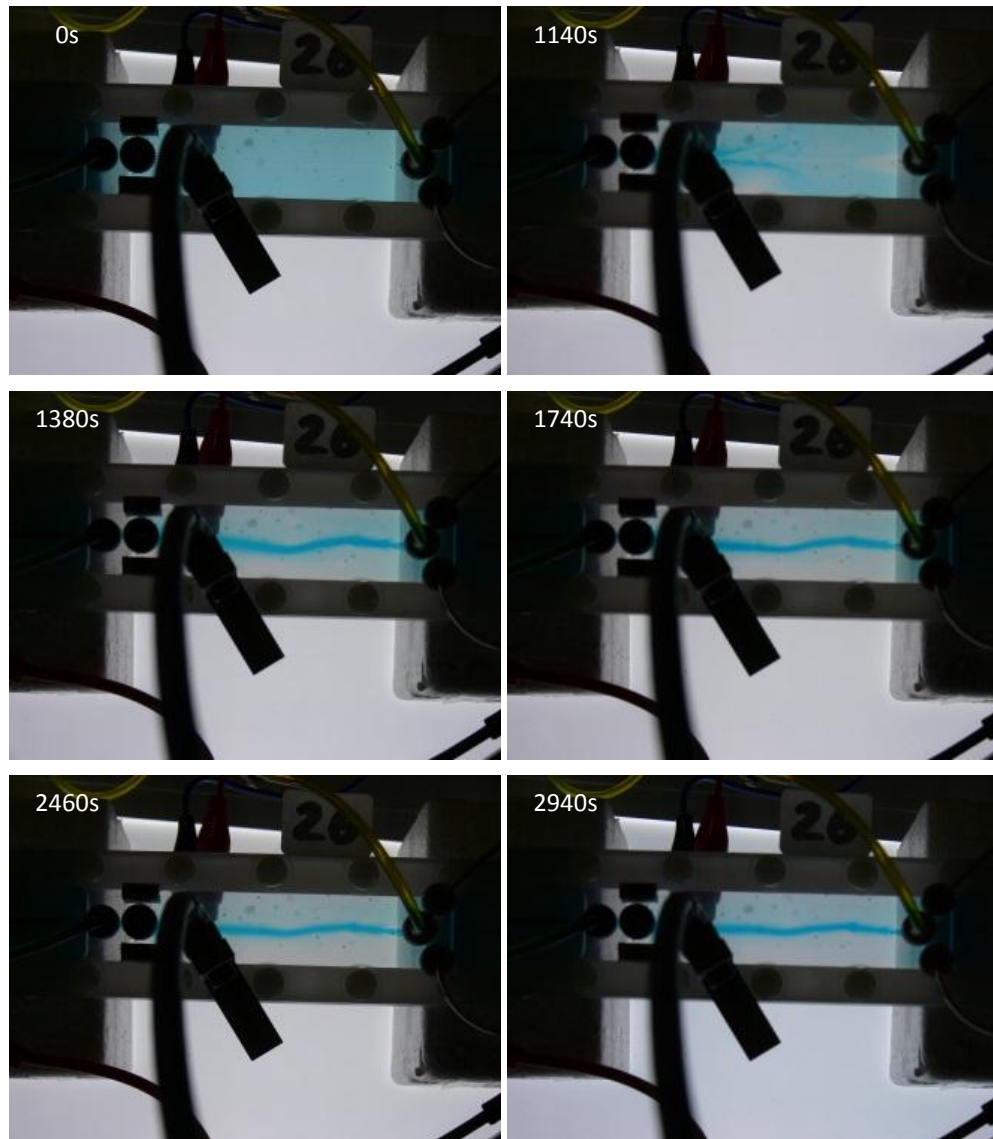


Figure 133: Experiment 2L-26 - focusing in the central flowstream.

The chip was primed with malachite green and filled for 900s with Tris-HCl buffer. After 900s a 295V was applied. MG located outside the central flowstream was pushed from the outlet region toward the inlets (Figure 133 – 1380s), but it can be considered as completely depleted 600 seconds later – at around 1980s. During the stabilisation time there were two regions of higher MG concentration lying on both sides of the central flowstream (Figure 133 – 1380s). At time mark of 1620s diffusion was already prevalent and there was one stream of MG visible. There were two turns in the central flowstream visible, which straightened with time and at time mark 2940s the

central flowstream was almost straight. These turns are attributed to unevenness of both the upper and bottom chip surface as the flow tries to flow through the line of the lowest resistance. This result is important as the focusing occurred perpendicularly to applied potential difference. A possible explanation of this observed phenomenon is presented later in this thesis in section 5.19.

One point on the chip axis of symmetry, close to outlet O₃ (see Figure 49), was selected and an optical fibre leading to the spectrophotometer was installed to provide concentration measurements of the test compound. The schematic of the optical fibre holder is presented in Figure 51. Initially the concentration of the MG was stable at 0.1mM. Concentration calculated from the photos shows some problems with calibration, but generally agrees within error margin (see Figure 134).

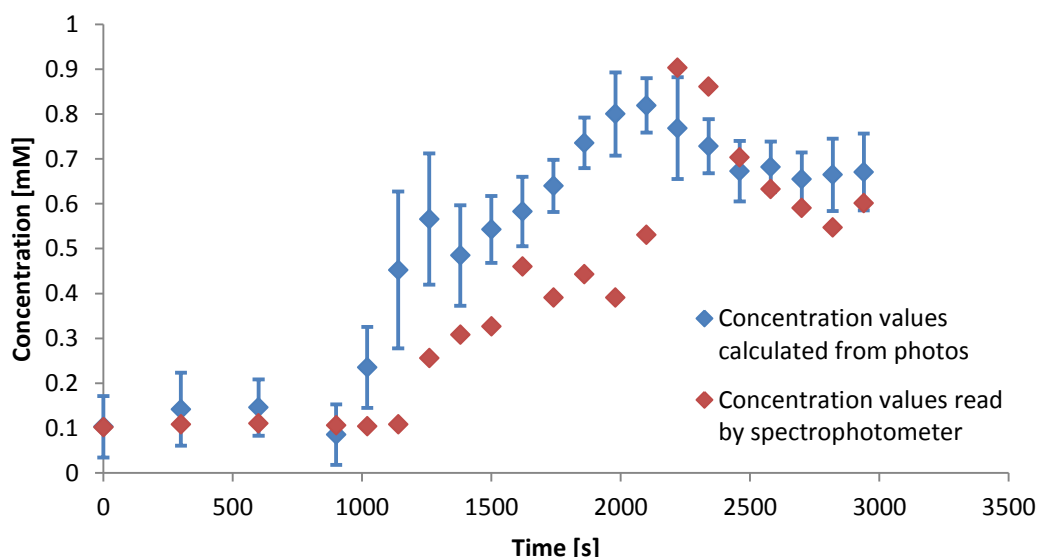


Figure 134: Comparison of concentration values calculated from photos (blue points) with read from spectrophotometer (red points).

After applying voltage there was a slow constant increase of the concentration to time mark of 2100s, which was followed by small drop and stabilisation. The maximum was reached when there was still some MG from initial chip priming not flushed away. After the time mark of 2100s, the only MG in the chip was introduced through inlets. The concentration of MG does not vary significantly after time step 1740s. This experiment shows that a stable focusing of a test compound five to six times of the initial concentration perpendicularly to the applied electric field can be achieved using fluids of different conductivity. Once it is known that this is possible, only conditions for convenient extraction of the test compound are needed for effective pre-concentration.

5.10. Results of the experiment 2L-40

The experiments with the two in-line outlets open were conducted using the 200 μ m gasket. Employment of this gasket highlighted surface unevenness as there was a clearly visible bend in the flow pattern around 20mm from the central inlet (see Figure 135). There were also visible spots of malachite green close to the inlets, which did not migrate during the experiment. Generally the flow pattern was stable and focusing in the central flowstream was achieved successfully.

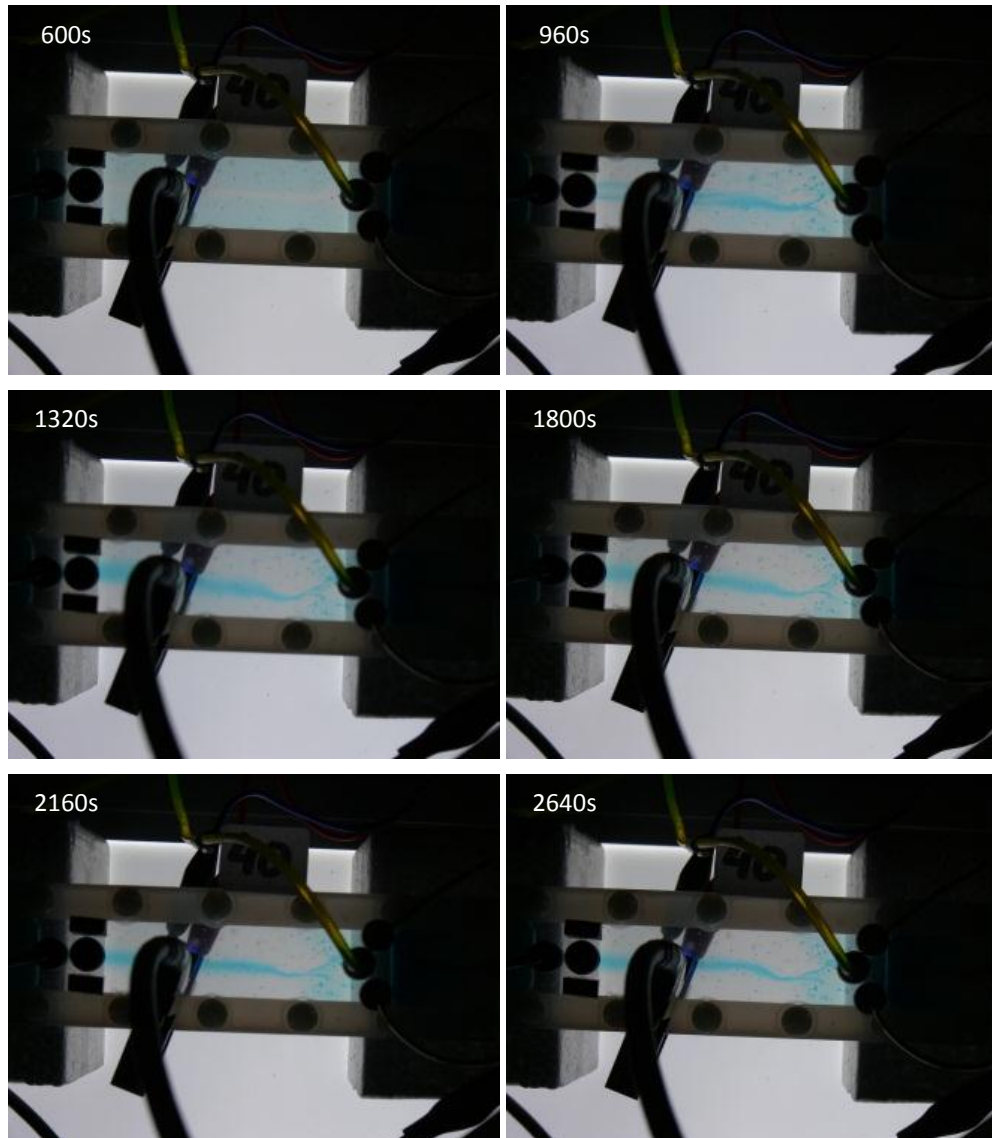


Figure 135: Experiment 2L-40 – focusing in the central flowstream with 200 μ m gasket used.

The graph presented in Figure 136 shows a comparison of the concentration values measured with the spectrophotometer and calculated from the photos. After applying the voltage at 600s there was a significant rise (four to five times depending on the method of measurement) of the concentration of MG to 1080s followed by

stabilisation at this concentration level. Only a slow rise between 1080s and end of the experiment at 2640s was. Variations in spectrophotometric measurements are attributed to flow fluctuations and movement of the flow of highly concentrated MG from the detection area.

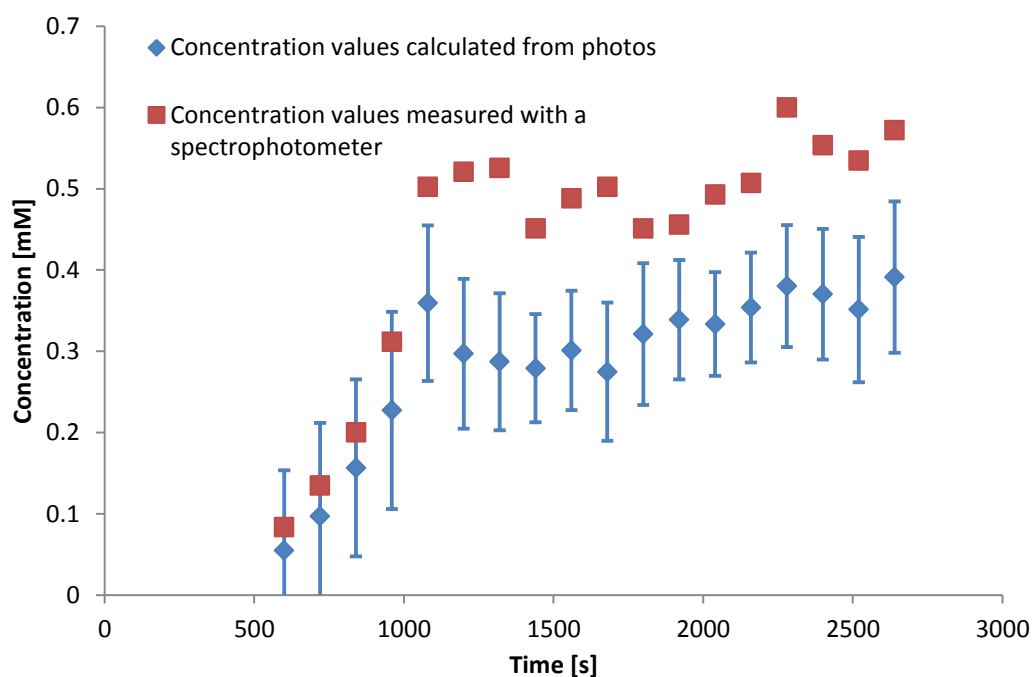


Figure 136: Comparison of concentration values calculated from photos with values acquired using a spectrophotometer in experiment 2L-40.

5.11. Results of the experiment 2L-41

In this experiment the value of applied voltage was increased to observe focusing performance. The increase of voltage by 25% (compared to the experiment 2L-40) resulted in the formation of a stable stream of malachite green in the central flowstream of the high conductivity Tris-HCl. The observed average increase in concentration was six times compared to the initial value. Lower readings from the spectrophotometer are attributed to the presence of a narrow central flowstream that did not cover entirely data acquisition field. The concentration drops observed at 1320s and 2040s are a result of flow instability and movement of the focused fluid from the acquisition field (see Figure 137 and Figure 138).

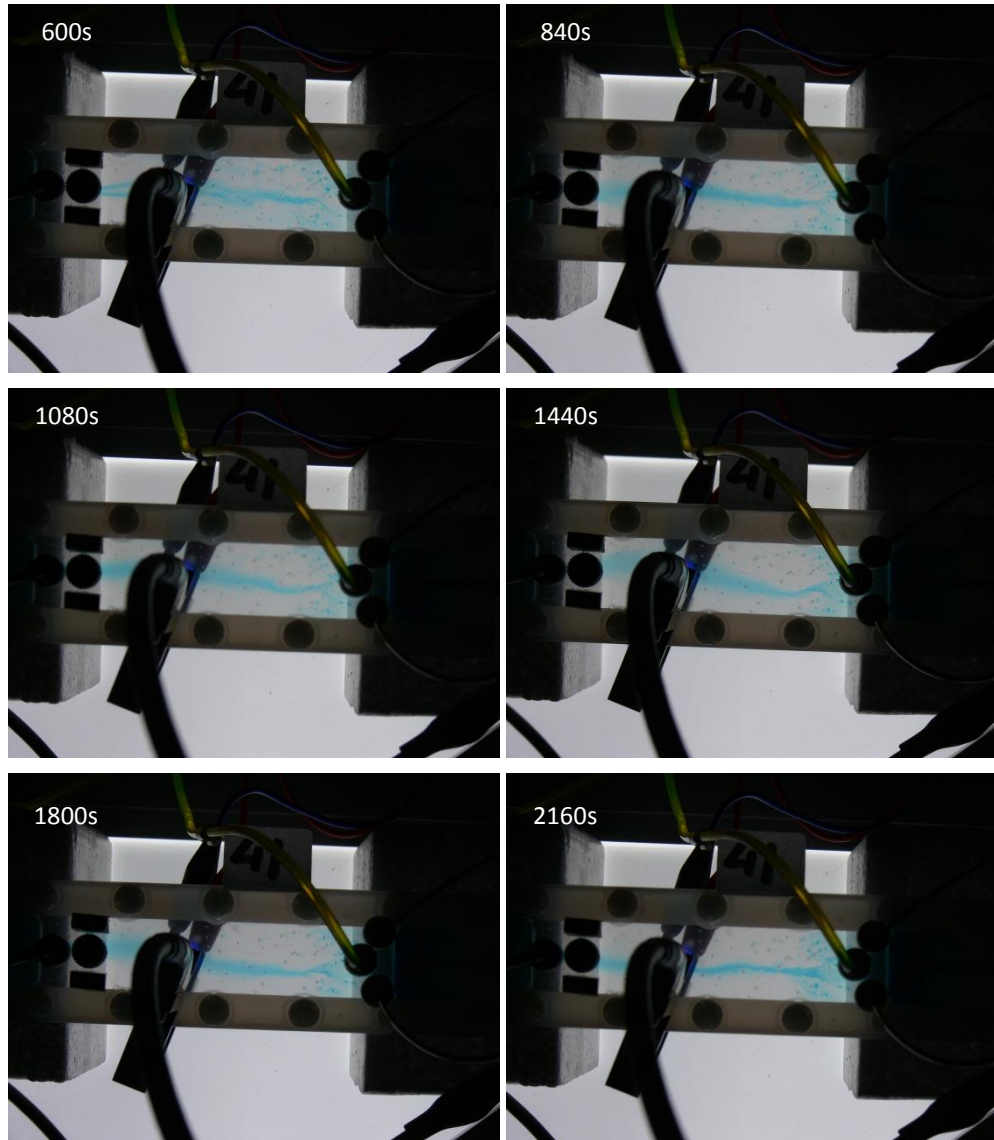


Figure 137: Experiment 2L-41 – focusing in the central flowstream with 200 μ m gasket used.

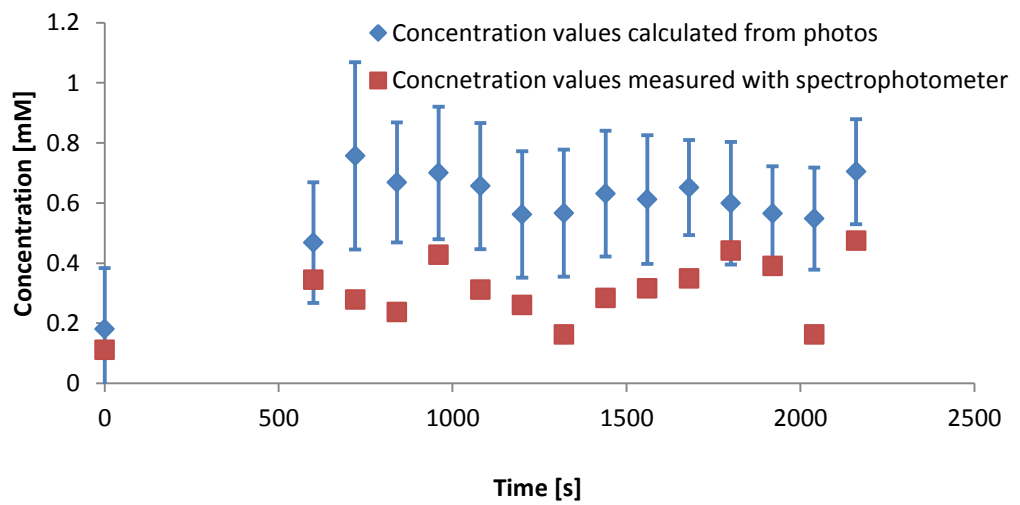


Figure 138: Comparison of concentration values calculated from photos with values acquired using a spectrophotometer in experiment 2L-41.

5.12. Results of the experiment 3T-20

The observation of an unexpected phenomenon of lateral focusing in the central flowstream perpendicular to the applied voltage led to investigation how to exploit it for practical use. Both tested chip outlet layouts showed that lateral focusing can occur already after a few millimetres from inlets. Knowing the behaviour of laminar flow an attempt was made to achieve three parallel flowstreams inside the microfluidic chamber leading to three separate outlets. With employment of this observed focusing mode a test compound introduced as diluted solution through two auxiliary inlets (I_2 and I_3 , see Figure 53) should be focused into the central stream of a high conductivity buffer and flushed away from chip through the central outlet (O_3). Outlet O_4 was blocked for these experiments. The schematic of the expected result is shown in Figure 139.

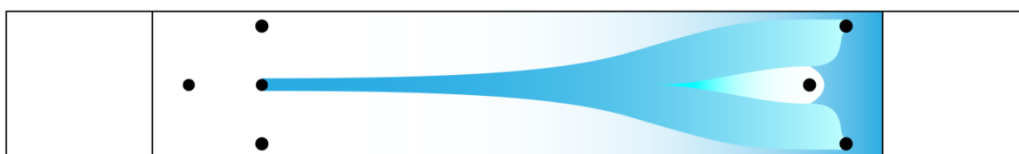


Figure 139: Expected flow pattern for successful lateral electrohydrodynamic focusing.

Initial experiments were dedicated to find a set of optimal conditions where previously observed lateral focusing was the most efficient. Figure 140 shows the result of the first experiment in 3T-series (see Figure 56) employing three parallel flowstreams.

After applying voltage, the malachite green migrated toward the central flowstream. The initial MG present in the chip after priming depletes around the time mark of 2460s. The observed concentration rose at 900s. After the initial rise to the maximum of 0.42mM, concentration in the focused stream slowly decreased indicating that no equilibrium between pressure driven flow and electromigration was achieved. The observed flow pattern was stable and the stream of the focused MG was flushed away only through the central outlet O_3 (see Figure 141).

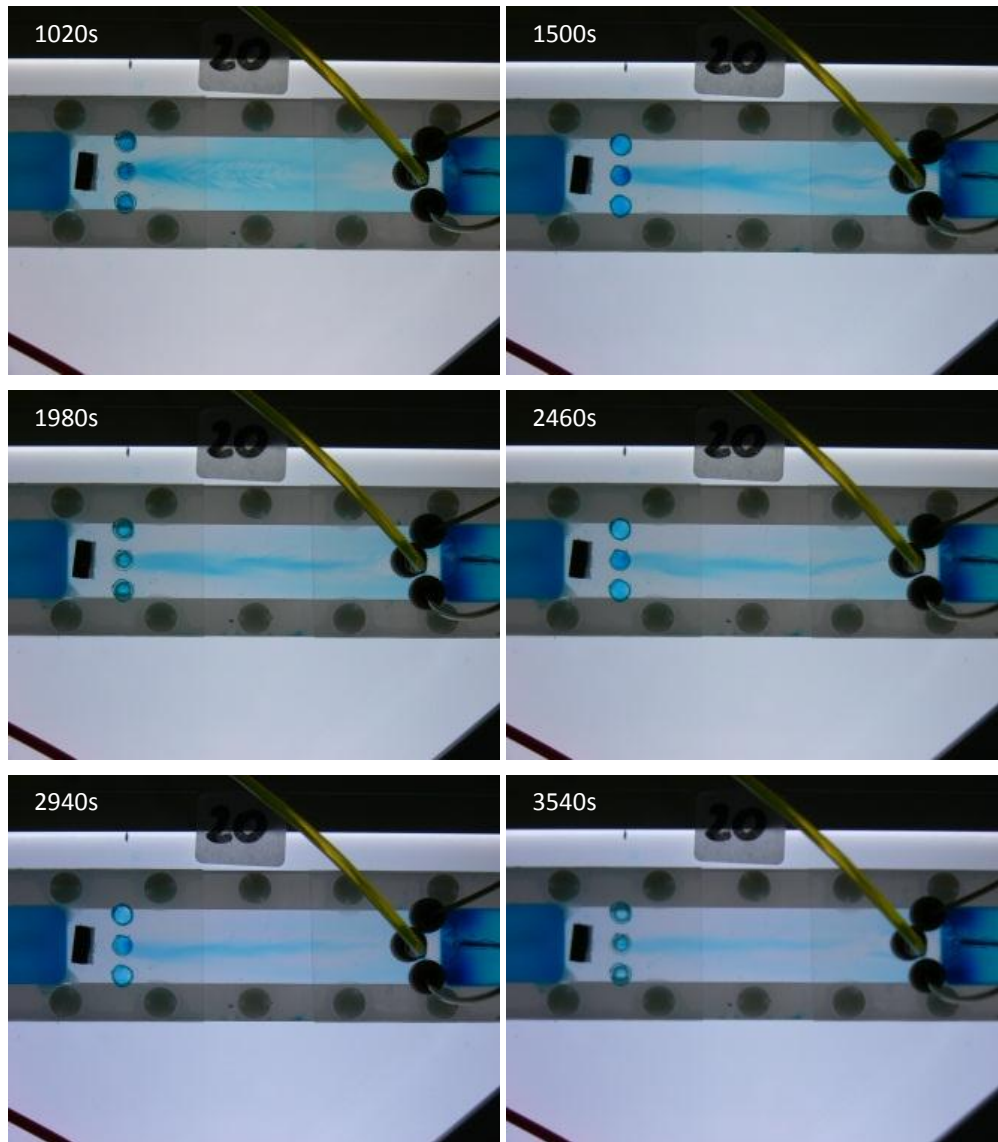


Figure 140: Experiment 3T-20 – lateral focusing in the microfluidic chip.

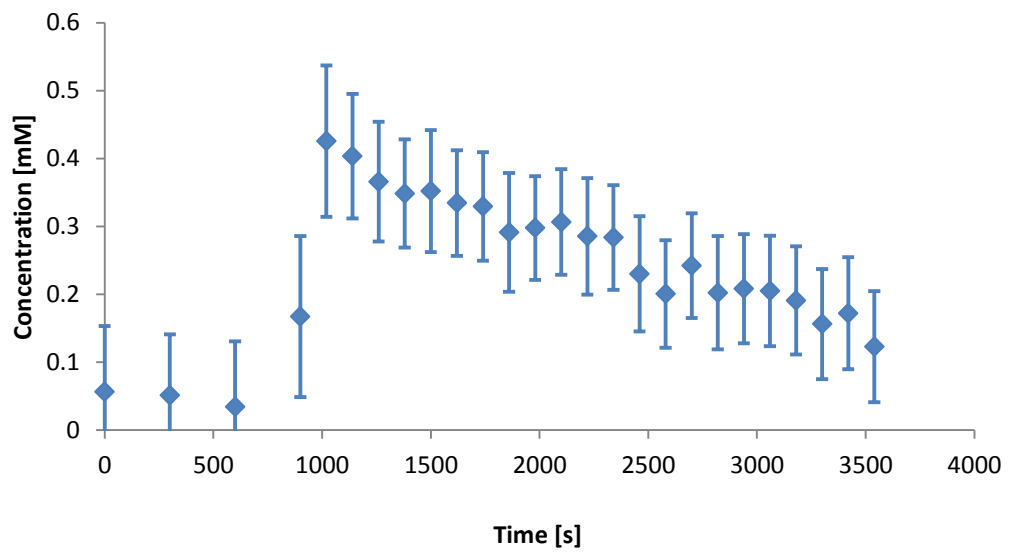


Figure 141: Concentration profile for the experiment 3T-20.

5.13. Results of the experiment 3T-21

In this experiment (3T-21) the applied voltage level (250V) was reduced compared to the experiment 3T-20 (280V)(see Figure 142).

The applied voltage was too low for substantial concentration increase and malachite green did not migrate into the central flowstream. The front of MG present in the chip after priming moved only around 20mm from the central outlets. The central flowstream (Tris-HCl) was still transparent throughout the majority of the distance between I_1 and O_3 . Compared to the experiment 3T-20, in the experiment 3T-21 the applied voltage was too low and Tris was not migrated toward the right gel tank right after entering the chip. Presence of the positively charged Tris inhibited MG migrating into the central flowstream what reduced focusing performance to the minimum.

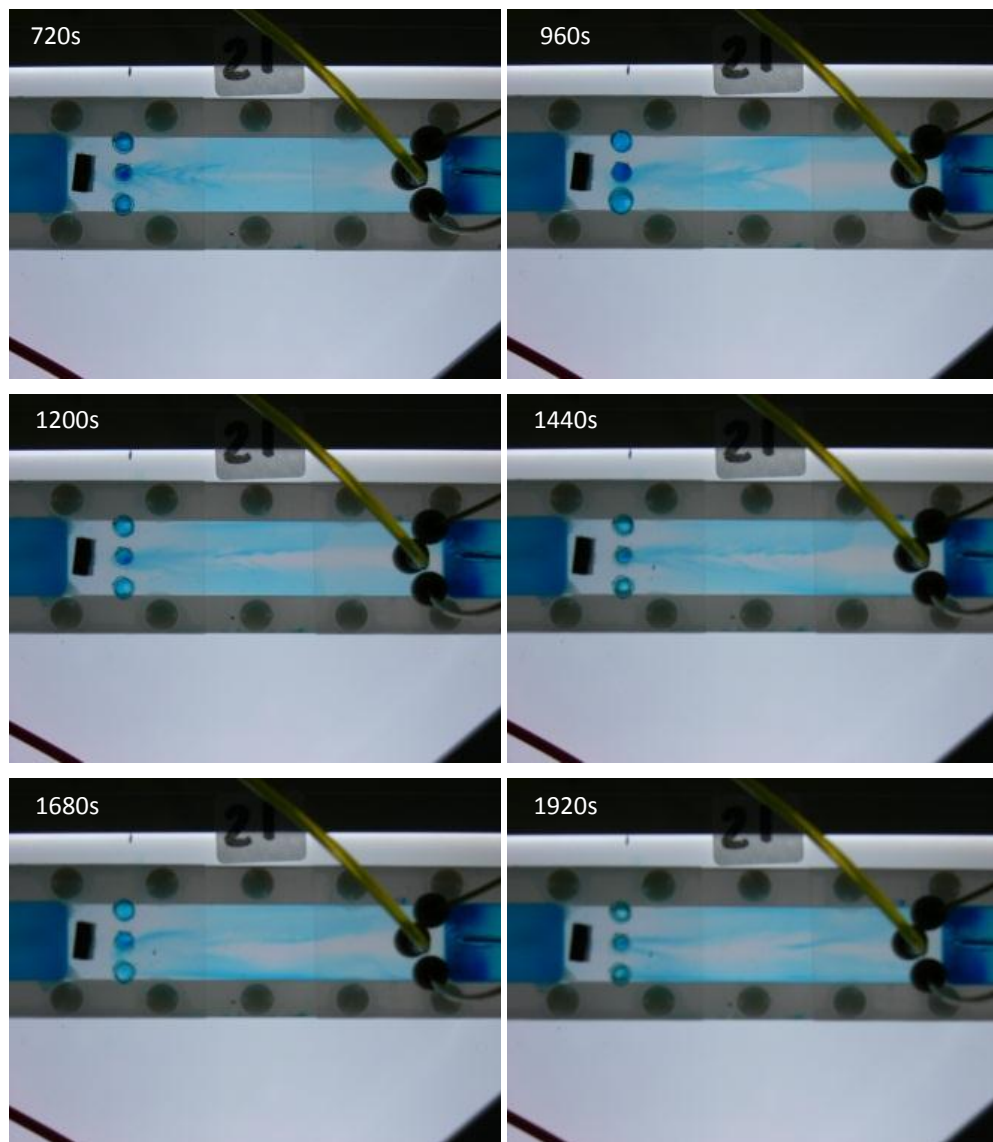


Figure 142: Experiment 3T-21 – lateral focusing in the microfluidic chip.

5.14. Results of the experiment 3T-24

In experiment 3T-24 the value of applied voltage (350V) was increased compared to the experiment 3T-20 (280V)(see Figure 143).

After applying voltage the malachite green present in the chip after priming was quickly moved into the central flowstream. However, the value of applied voltage was too high and all malachite green coming through the inlets was migrated toward the right side of the chip and no MG was delivered to sustain the focusing. After exhausting the initial supply no focusing was observed.

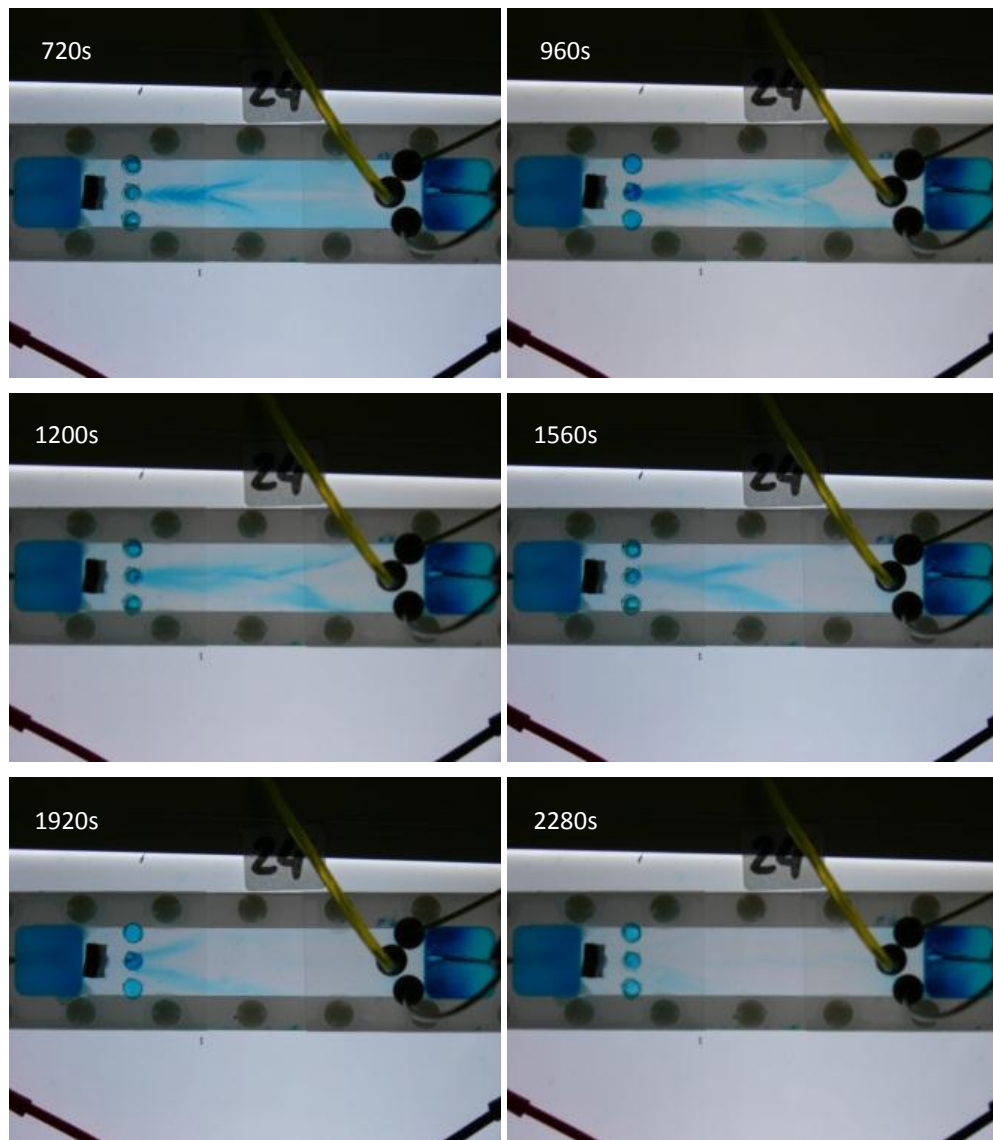


Figure 143: Experiment 3L-24 – lateral focusing in the microfluidic chip.

Experiments 3L-21 (see Figure 142) and 3L-24 (see Figure 143) showed how delicate the equilibrium between opposing forces is. The comparison of the results from

experiment 3L-21 and 3L-24 (see Figure 144) showed in both cases an initial rise of MG concentration, as MG initially present in the chip was migrated into the central flowstream which was followed by a decline in concentration. In experiment 3L-21 (blue points) recorded concentration rise was around 5.3 times the initial value (see Figure 144). A quasi-stable region between 960s and 1680s (concentration drop is within error margin) was reached, followed by a significant drop. In the experiment 3L-24 (red points) the concentration rise was very high (8.5 times from the initial value), but was followed by a fast drop. At a time of 1440s, average concentration in the test area was the same for both experiments, despite a 60% higher focusing ratio in the experiment 3L-24. This is attributed to a presence of too high electric field – applied voltage was 40% higher in 3L-24 than in 3L-21. As a result MG was very quickly migrated from the inlet toward the right side and the applied pressure driven flow was too weak to counteract it resulting in a lack of material to focus.

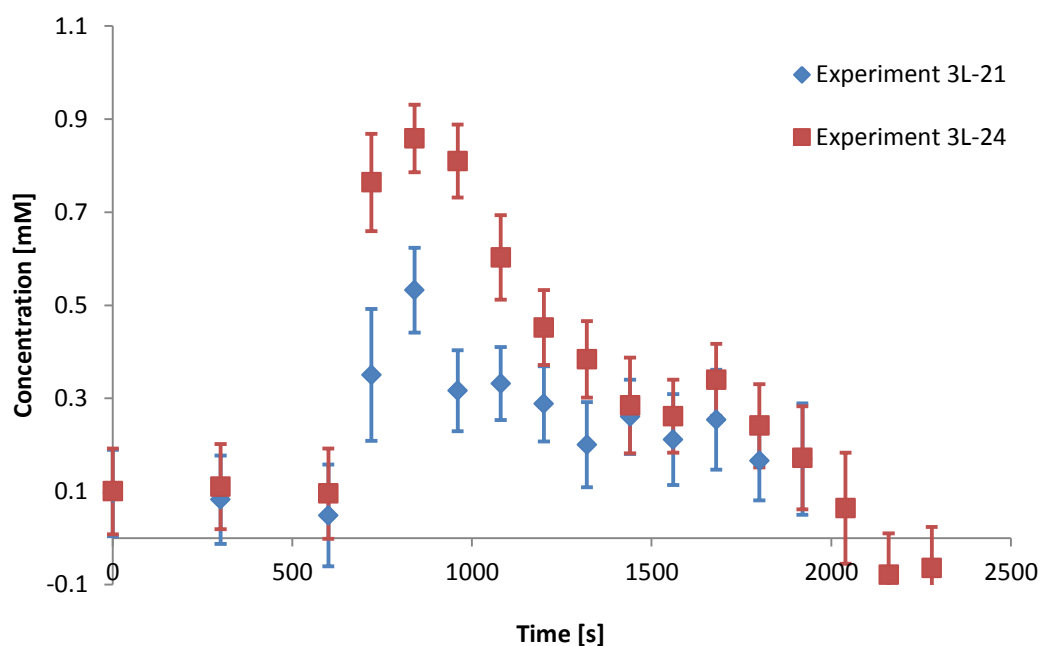


Figure 144: Comparison of achieved focusing in experiment 3L-21 (Figure 142) and 3L-24 (Figure 143).

5.15. Results of the experiment 3T-31

Experiments 3T-20, 21 and 24 provided with a good range of the experimental conditions in which the lateral focusing should occur (Figure 145).

Application of the potential difference of 310V yielded a stable flow pattern of the focused dye. The voltage value provided constant inflow of the malachite green to the central part of the chip, which allowed for sustained focusing (see Figure 146). A six

fold increase in concentration was recorded on average for times over 1500s. Shifts in concentration values recorded with the spectrophotometer are attributed to the lateral flow instability allowing regions of significantly lower absorptivity to enter the detection field and thus reduce the overall measured absorbance.

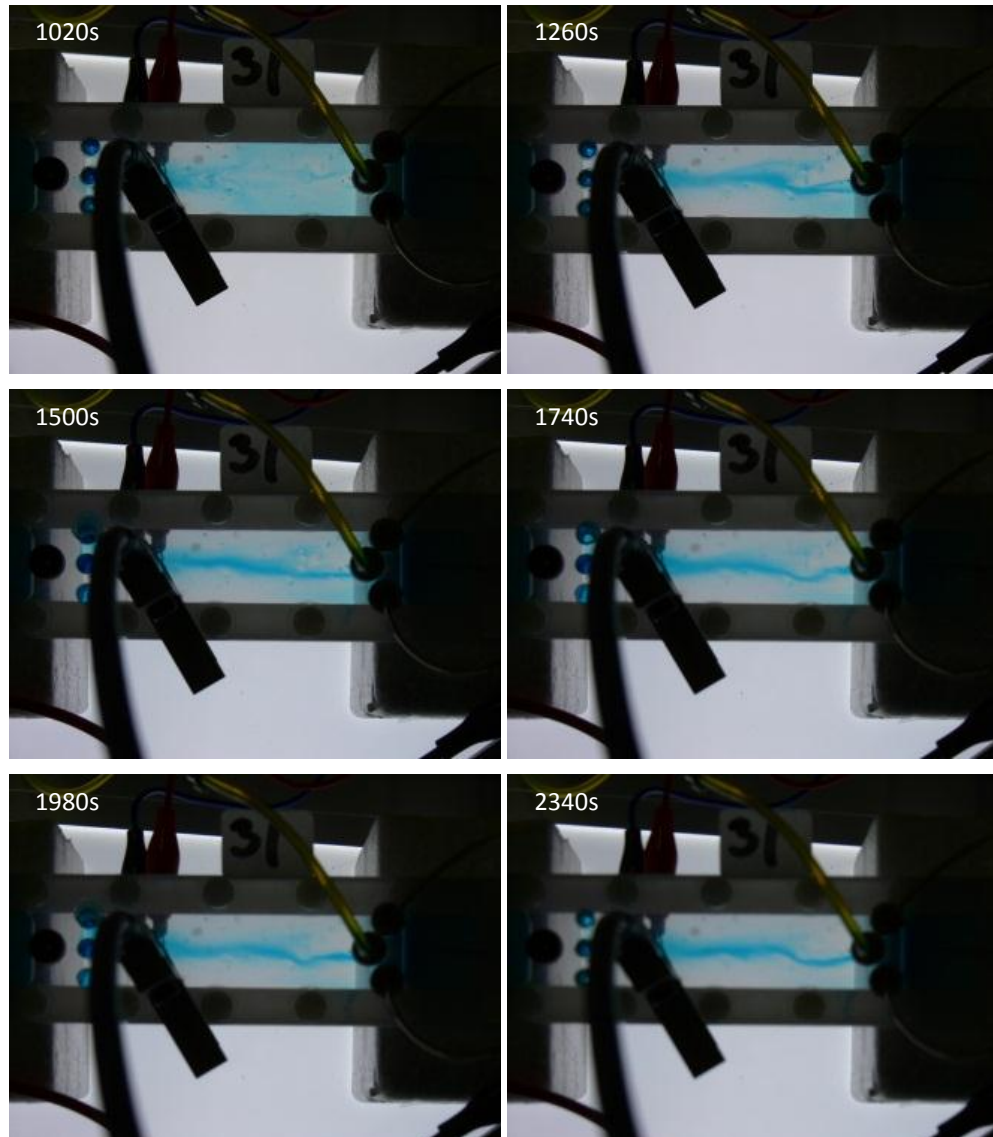


Figure 145: Experiment 3T-31 – lateral focusing in the microfluidic chip.

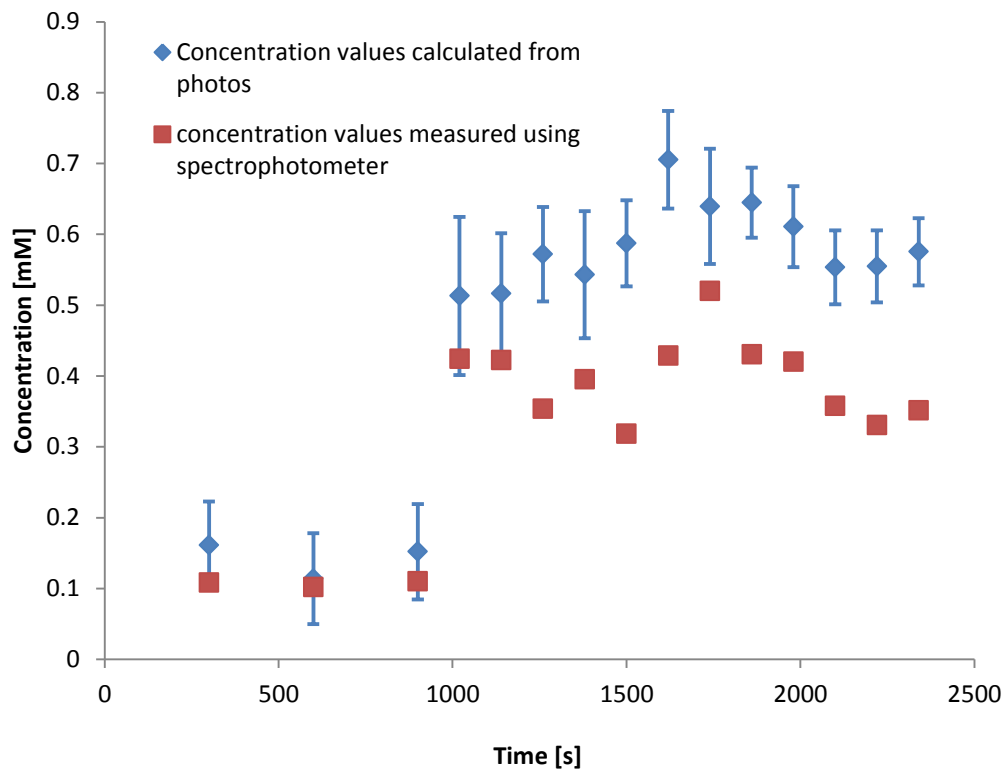


Figure 146: Comparison of concentration values calculated from photos (blue points) with values measured using spectrophotometer (red points) in the experiment 3L-31.

5.16. Results of the experiment 3T-36

In the experiment 3T-36 the application of slightly lower voltage value (300V) compared to the experiment 3T-31 slightly improved achieved focusing performance. Also there were fewer problems with flow stability recorded during the experiment which improved the overall focusing. Experiments 3L-31 (Figure 145) and 3L-36 (Figure 147), showed almost perfect lateral electrohydrodynamic focusing of malachite green.

The achieved flow pattern was stable in the sense that the focused MG reached only the central outlet throughout the entire experiment. A six to seven fold concentration increase was recorded and it did not drop with time (see Figure 146 and Figure 148). Small fluctuations of the position and width of the central flowstream still occurred, which were especially evident from the photometric detection. In the experiment 3L-36 at a time mark 1380s, a larger patch reached the detection area which is visible with the sudden concentration surge (see Figure 148). Obtained results show sustained concentration raise four to six times depending on the measurement method and experiment.

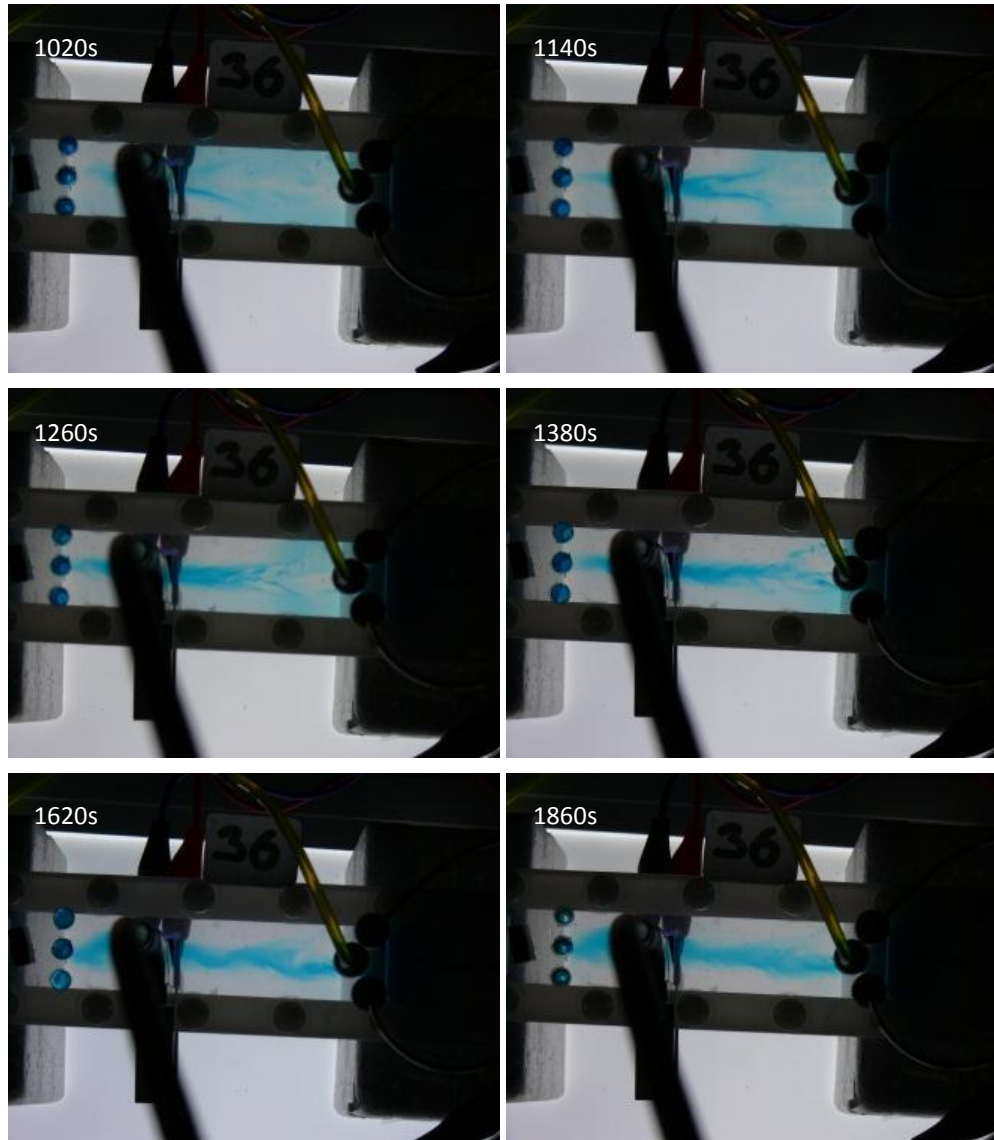


Figure 147: Experiment 3L-36 – lateral focusing in the microfluidic chip.

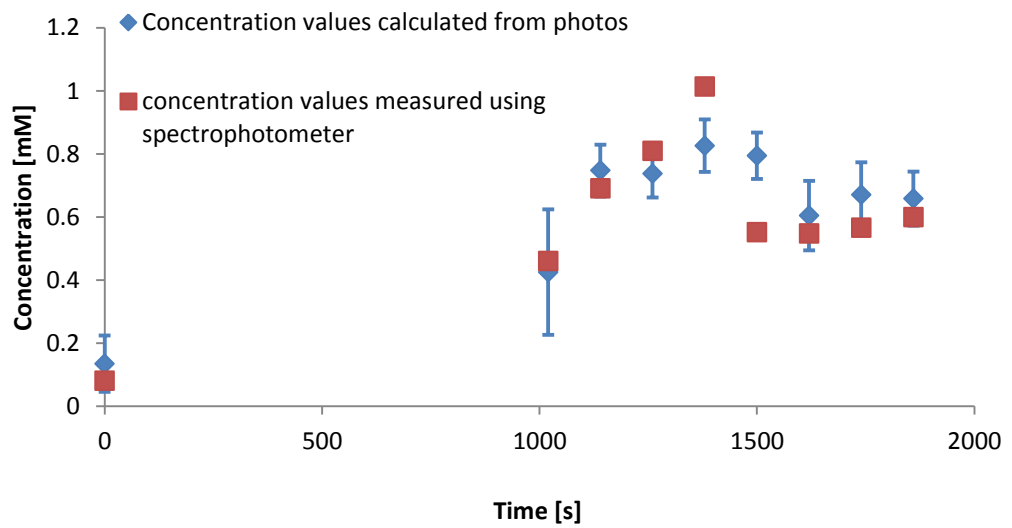


Figure 148: Comparison of concentration values calculated from photos (blue points) with values measured using spectrophotometer (red points) in the experiment 3L-36.

5.17. Results of the experiment 3T-43

In the experiment 3L-43, the 500 μm thick PTFE gasket was replaced with the 200 μm thick gasket. Lateral focusing was observed even though the flow was unstable and stream of focused MG often shifted between outputs O_1 and O_3 (see Figure 149). The flow pattern fluctuations are especially visible in comparison of the concentration measurements (see Figure 150). The central flowstream shifting its position did not cover the spectrophotometer detection area consistently producing significant variations of the recorded values. Concentration values calculated from the photos were more consistent. As the flowrate could not be set to lower values and still provide stable flow, the linear velocity of the fluids inside the chip increased approximately 2.5 times, the voltage value was increased, in order to compensate for this pressure driven flow.

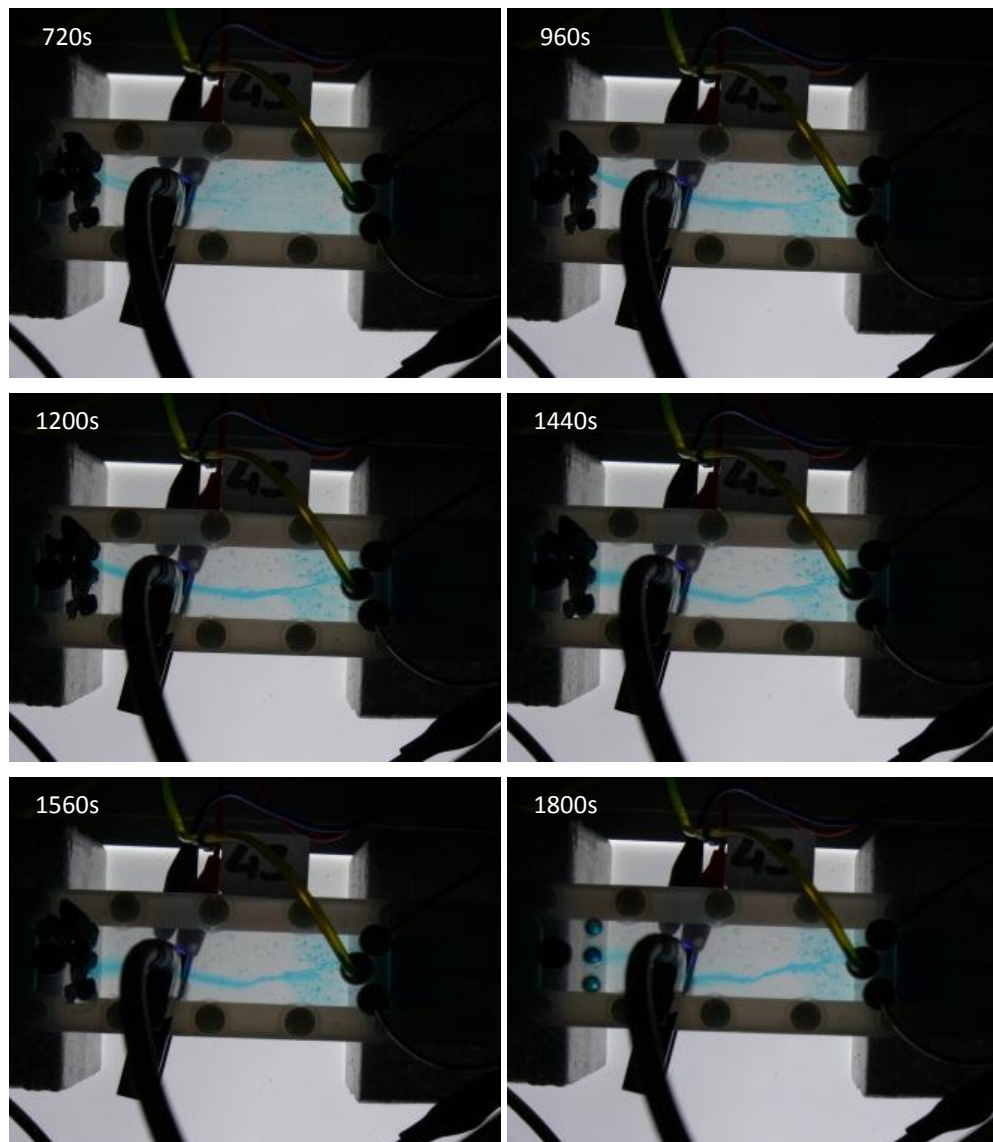


Figure 149: Experiment 3L-43 – lateral focusing in the microfluidic chip.

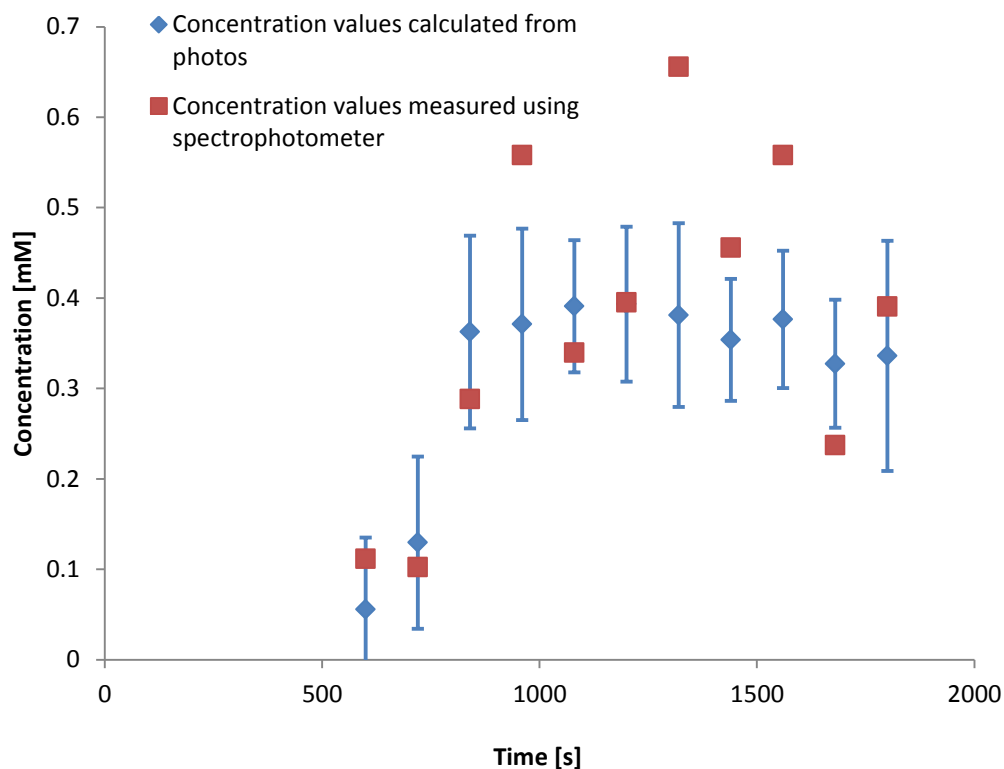


Figure 150: Comparison of concentration values calculated from photos (blue points) with values measured using spectrophotometer (red points) in the experiment 3L-43.

5.18. Results of the experiment 3T-58

In experiment 3L-58, the 200 μ m PTFE gasket was replaced with the 100 μ m thick gasket. After testing a series of different voltage values no fully successful lateral focusing was observed (see Figure 151). The central flow stream was not filled completely with MG although regions of visibly higher concentration formed on the border between the central flowstream (coming from inlet I_1) and side flowstreams (coming from inlets I_2 and I_3). As in the case of the 200 μ m gasket the flow instabilities were observed.

The concentration of MG recorded was around 0.8mM (see Figure 152), but this was not a continuous flow, but rather patches or regions forming locally on the border between central and side flowstreams. The high dispersion of calculated concentration values was a result of the applied method. Measured luminosity of the selected area was the average value for the region with given standard deviation. As there were regions of high concentration separated by region of visibly lower concentration a high standard deviation in the measurement was introduced for this experiment.

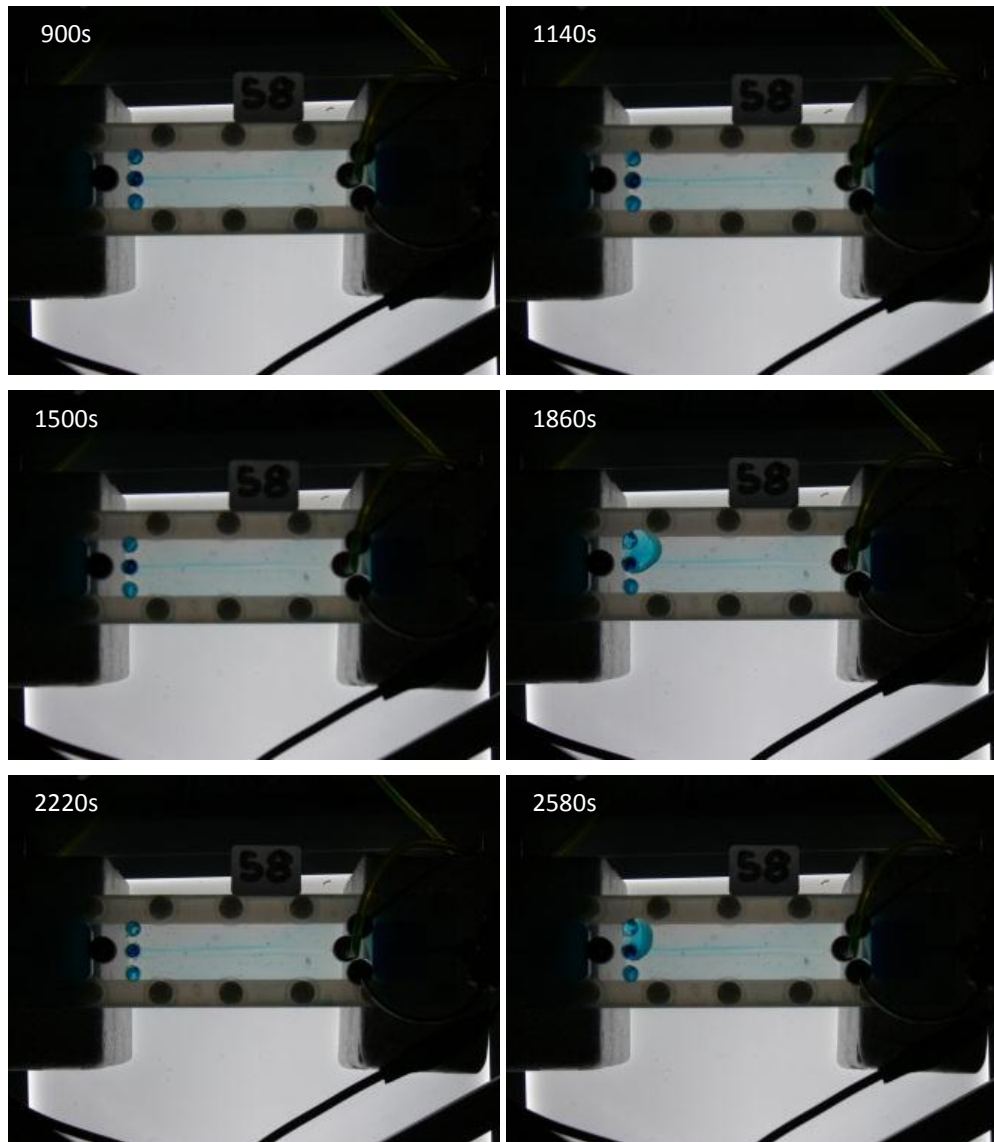


Figure 151: Experiment 3L-58 – lateral focusing in the microfluidic chip.

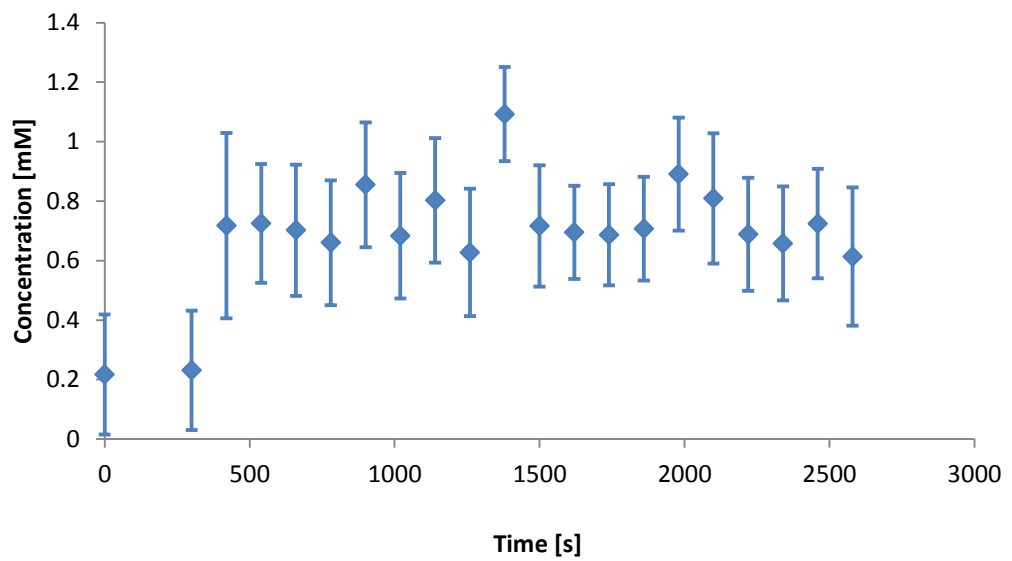


Figure 152: Experiment 3L-58 – concentration values calculated from photos.

5.19. Repeatability of the EHDF

Series of five consecutive experiments using exactly the same experimental conditions was conducted in order to determine the repeatability of the observed fluid behaviour in the fabricated chip.

For this experiment the layout with the two peripheral (2P) outlets open was selected (Figure 54) as the most difficult one to provide a stable flow pattern. Using this layout it was easier to determine the contribution of each element: chip flatness, wetting of the outlets, or the focusing mechanism itself.

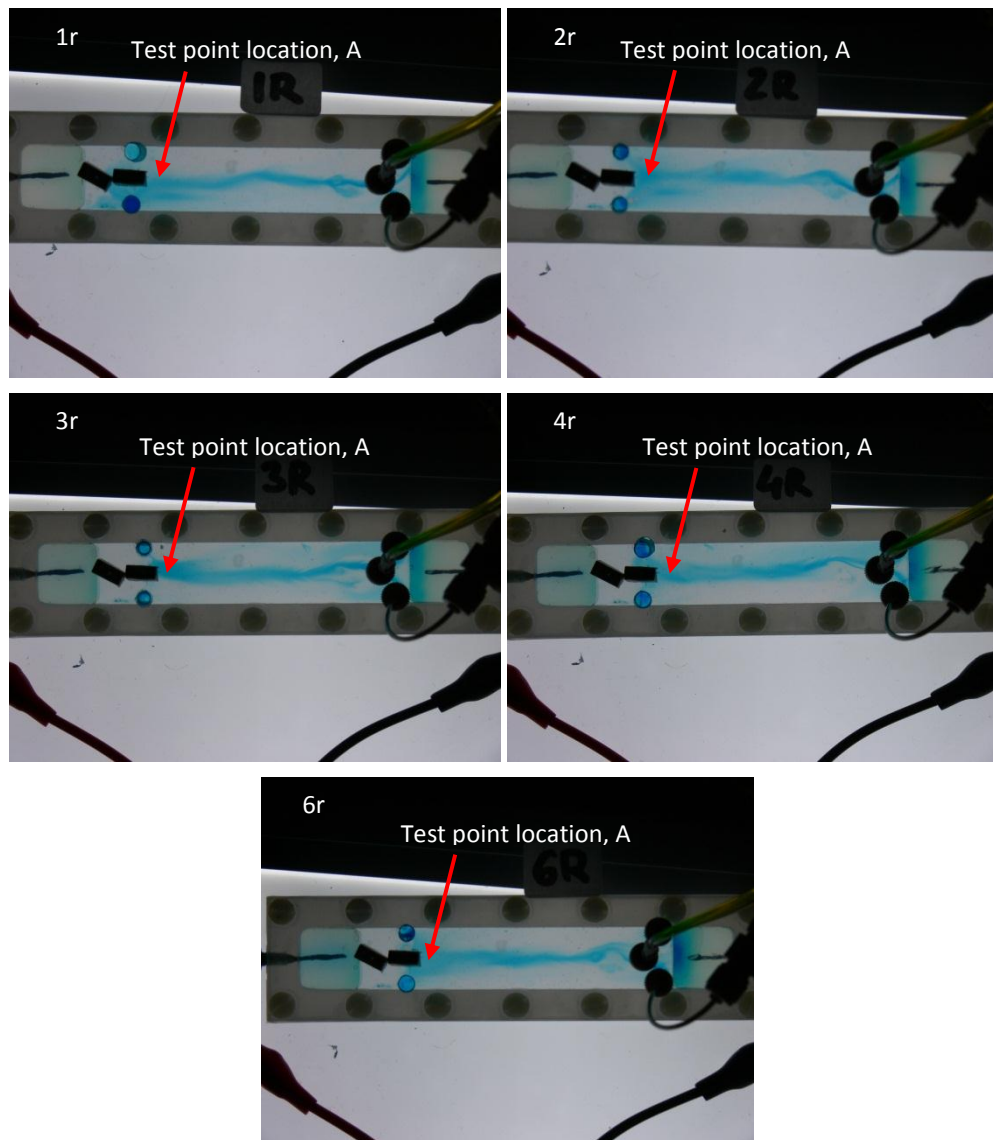


Figure 153: Picture of the microfluidic chip at 2040s in each experiment under same conditions to observe repeatability of the EHDF.

Typical observed problems were related to the flow stability. The central flowstream had a tendency to shift between the open outlets (see Figure 153 –

experiments 1r and 3r). One point for concentration measurements was chosen, the same location as point A in section 4.10 (see Figure 118 and Figure 119).

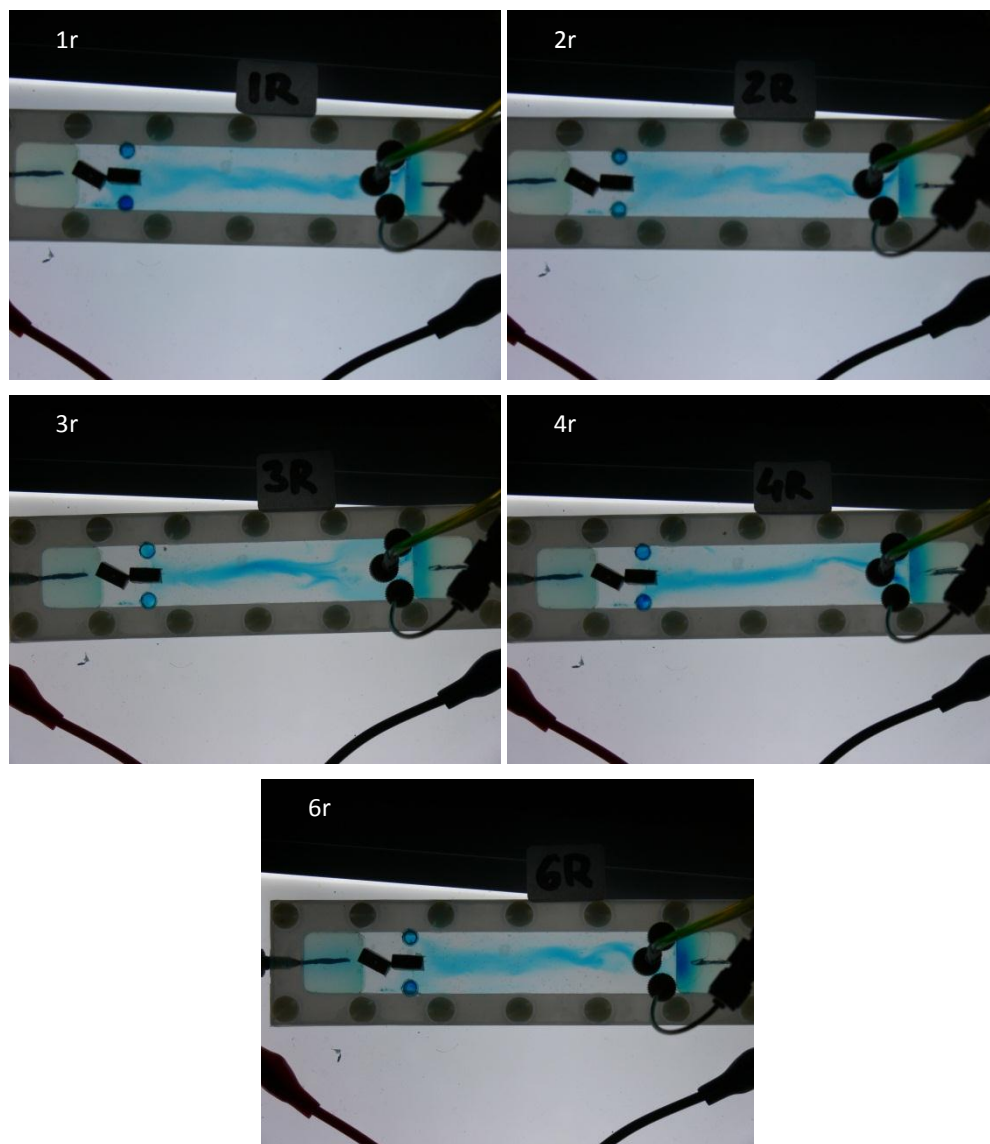


Figure 154: Picture of the microfluidic chip at 3120s in each experiment under same conditions to observe repeatability of the EHDF.

During the early stage of focusing – 240 to 480 seconds after voltage application there were discrepancies observed in the distribution of the malachite green. This is attributed to uneven distribution of the high conductivity buffer which could be affected the same way as was shown in Figure 153. The uneven outflow of the Tris-HCl buffer could result in one-sided focusing and removal of the material from the test area. During the filling of the chip with the Tris buffer, the concentration of MG was 0.1mM, after chip priming. The measured concentration values showed results typically shifted by of 0.07 to 0.1 mM depending on the experiment.

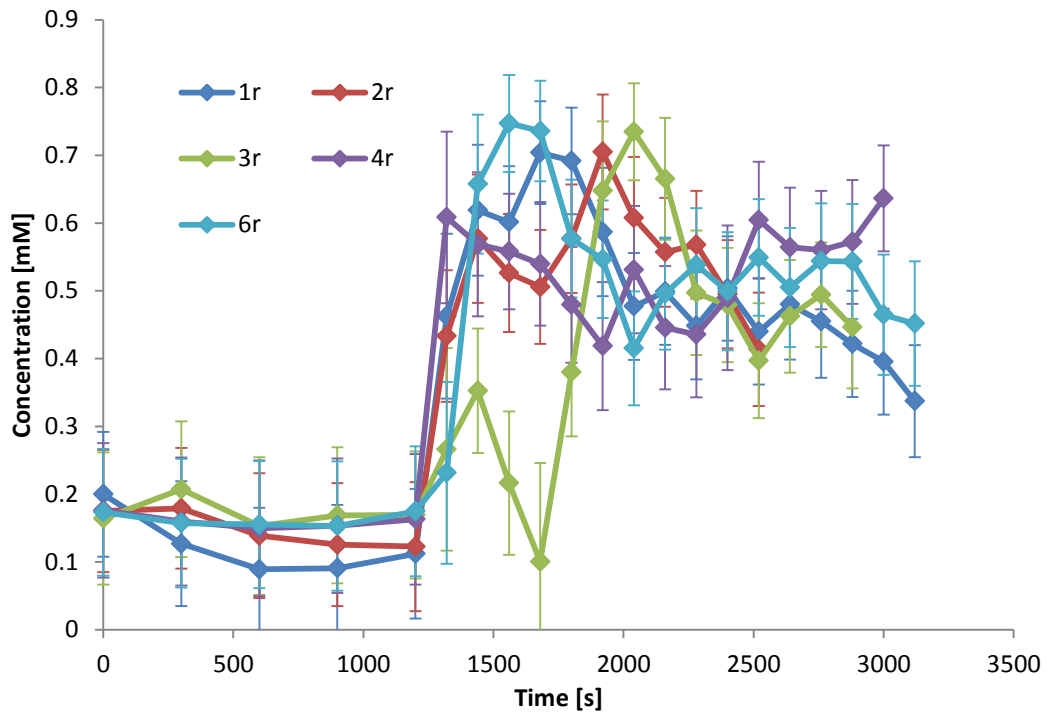


Figure 155: Concentration profiles for all six experiments (labeled 1r, 2r, etc.) on repeatability of the focusing.

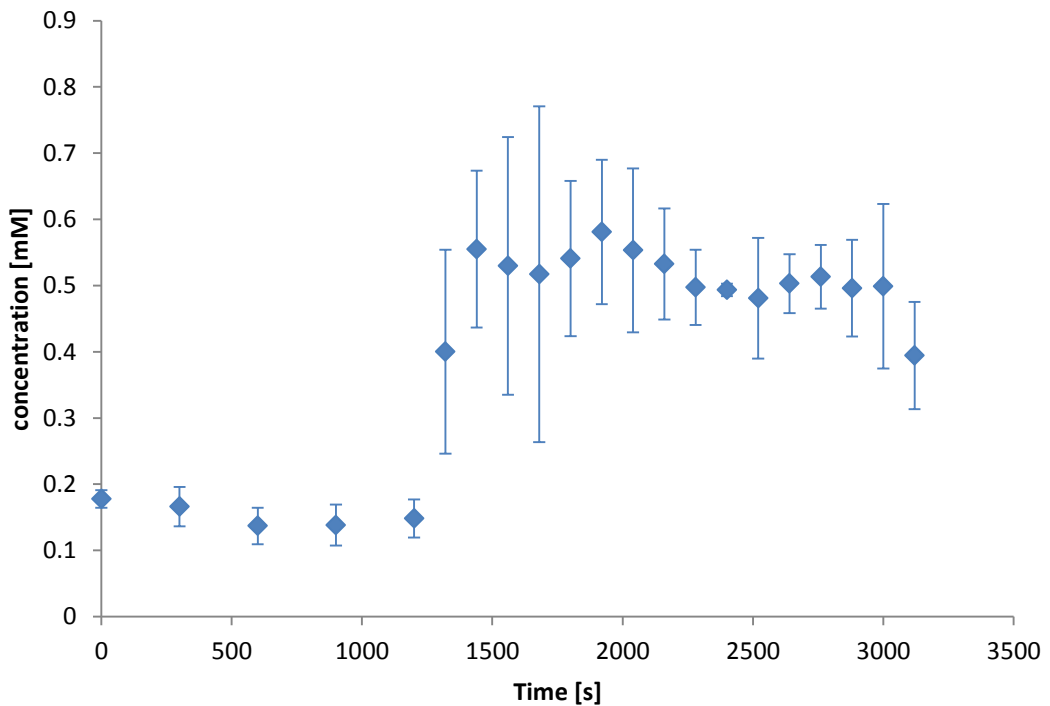


Figure 156: Average concentration (with exclusion of the experiment 5r). Error bars represents the standard deviation of concentration values.

All acquired concentration profiles presented the same tendencies (see Figure 155). There was an initial rise observed immediately after applying the voltage typically six to eight times. In the experiment 3r some turbulence was observed and the flow

pattern stabilised around 600s after the voltage application. Figure 156 shows the average of measured concentration values. The highest error observed at 1680s was a result of the very low concentration value at the acquisition point in experiment 3r.

Lateral focusing was observed in all experiment. Typically a stream of the highly focused malachite green in the central flowstream was observed from time of 1700s (500s after the voltage application). Even the presence of an obstacle (small piece of agarose gel that separated from the tank) affecting the flow stability problems did not prevent formation of the highly focused stream of MG in the vicinity of inlets, which slowly propagated through the chip. For photos of these experiments see Appendix H.

5.20. Comparison of the modelling and experimental results

The first series of experiments was focused on recreation of the numerical simulations discussed in chapter 4. At the start there was only one chip outlet layout to be tested and additional outlets were installed for possible extraction of the concentrated species.

The electrohydrodynamic focusing in its most general form can be regarded as a focusing technique that allows two dimensional focusing employing the counteracting forces of pressure and electromigration. Numerical models were designed to form a stable equilibrium where the net force acting on the target analyte was zero rendering it immobile in one point. An ion leaving this place, for example due to the diffusion would be exposed to non-zero force pushing it back into the focusing area. This EHDF mode was modelled and successfully experimentally replicated (see sections 4.10 and 5.3).

There are two main items that are compared simultaneously when discussing results of numerical simulations and experiments. The first is the actual concentration distribution across the microfluidic chip during the EHDF obtained from modelling and from experiments. The second important comparison criterion is the information of concentration values and focusing performance.

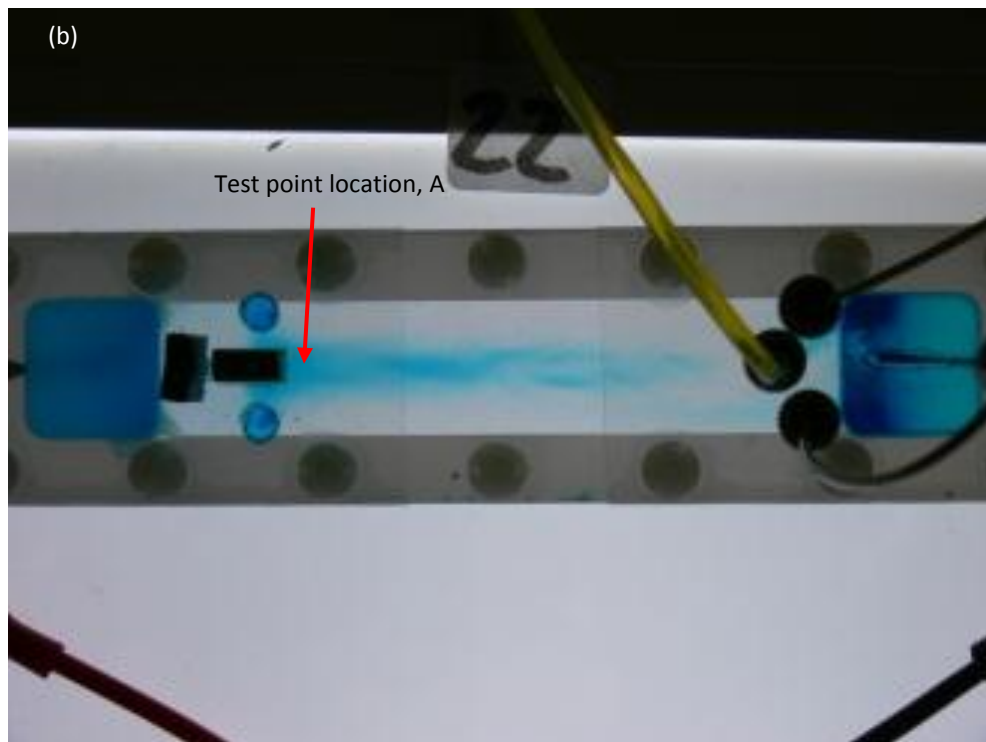
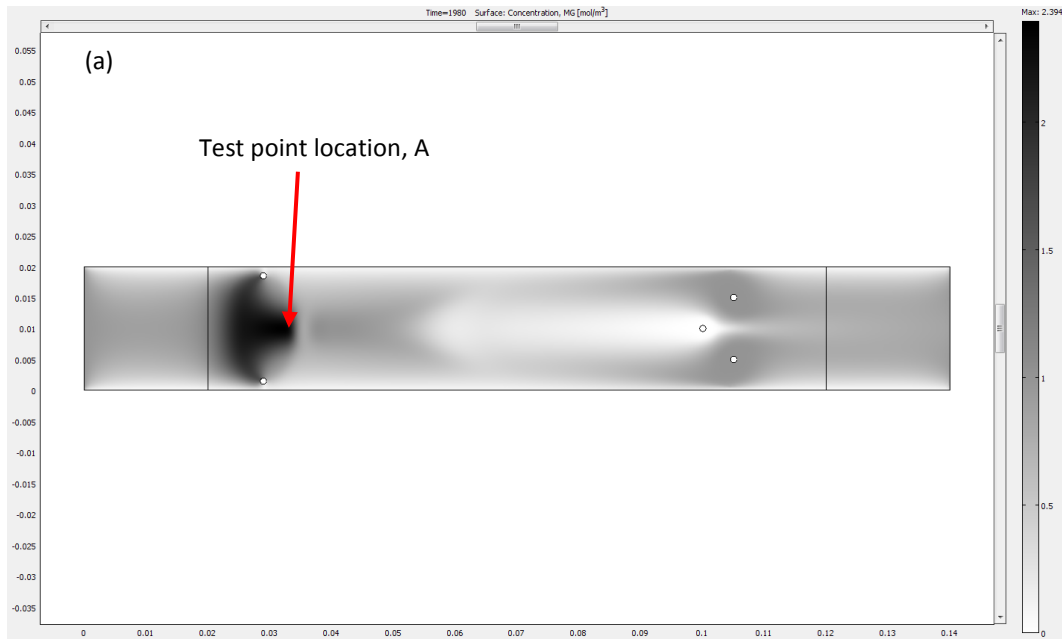


Figure 157: Comparison of the malachite green concentration (a) obtained by simulation and (b) experimentally.

The concentration distribution shows significant similarities in the vicinity of outlets and is clearly different in the central part of the chip. In the developed model malachite green moved in two flowstreams parallel to the central flowstream and the concentration value drops with distance from the inlets. In the vicinity of the outlets there was a crescent-shaped region of high concentration of MG (see Figure 157a). In the fluidic experiment, with the same set of conditions a different behaviour of MG was

observed compared to the numerical model. The malachite green was migrating into the central flowstream already at a distance close to inlets (up to 20mm) forming a one stream of alleviated concentration. The crescent-shaped area near the outlets was observed similar to the model. In the model this crescent-shaped region was pushed toward the left agarose gel tank for up to 10mm more than in the experiments.

The discrepancies in concentration distribution between the developed model and the experimental result make direct comparison of the concentration value complicated. In the model the region of increased concentration was pushed approximately to the line connecting outlet centres which prevents easily comparing with the experimental results, as this region was obscured by the fitting blocking installed outlet. The modelled outlet diameter was 1mm. The microfluidic port installed in the upper PMMA layer of the chip had the diameter of 1/16" (1.58mm) on the side contacting the fluids, but over 4mm on the side of the camera. It resulted in reduction of the available field of view for concentration measurements.

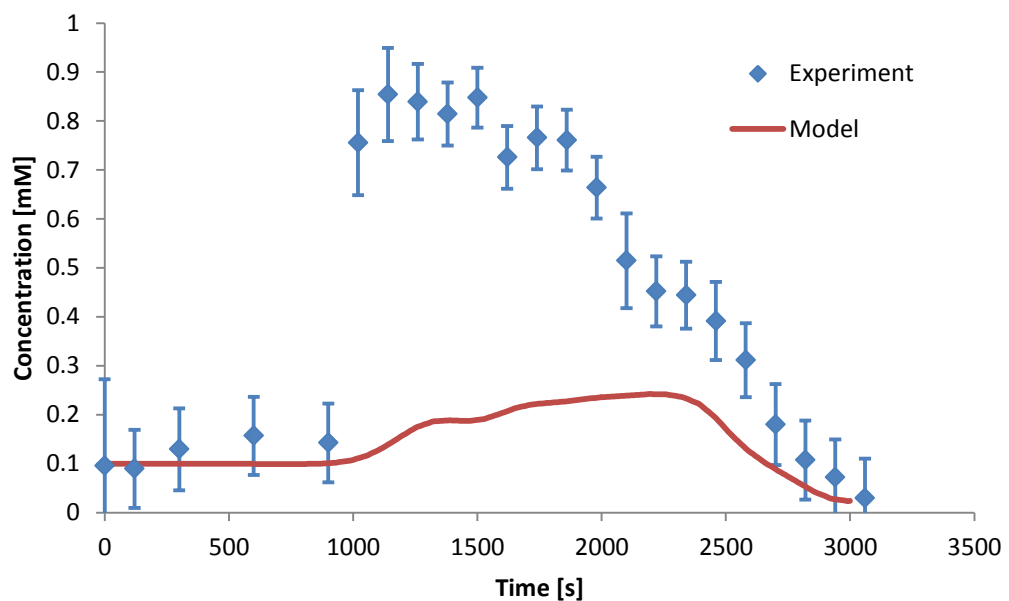


Figure 158: Comparison of the performance of modelled EHDF (red line) and experimental values (blue points)

One point was selected to compare the concentration value (see Figure 157a and b). The concentration values during the experiment were approximately three to four times higher than those numerically predicted. In the model, a region of higher concentration of MG formed and was pushed into the area where test point is located. The MG was in a quasi-stable state. From 2000s it was slowly pushed behind outlets. In

the experiment, the highly concentrated region formed much quicker, then a quasi-stable situation similarly to the model was formed, and after around 2000s inflow of the MG was too weak to sustain the focusing and the MG was washed away from the system. This comparison shows that generally such model developed using COMSOL contains too many simplifications to accurately predict the observed concentration distribution, however trends in concentration distribution have been predicted.

5.21. Proposed mechanism of microdrople electrohydrodynamic focusing

During the fluidic experiments a new mode of electrohydrodynamic focusing was discovered and tested extensively. Instead of creating a stationary zone of focused analyte a constant stream of analyte focused laterally to the applied electric field without application of physical boundaries or multiple electrodes was achieved. It is a novel method which was not predicted by computer modelling that was tested and proved successful.

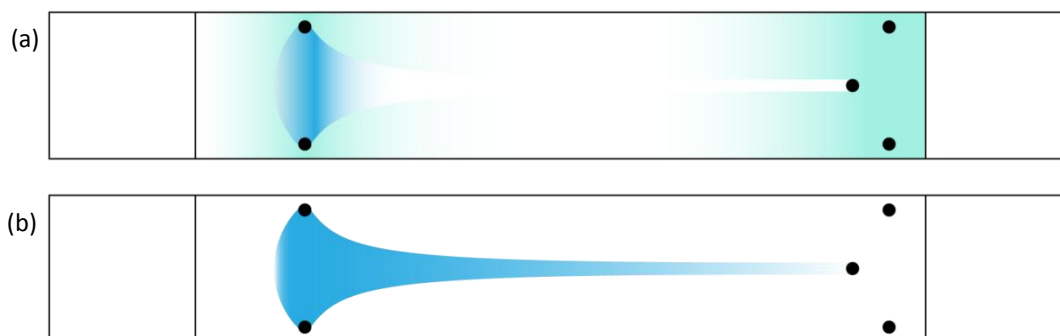


Figure 159: The comparison of schematics of (a) a modelled flow pattern and (b) obtained experimentally.

Simulations conducted in COMSOL are in agreement with experiments in the vicinity of the outlets (see Figure 159). Concentration values obtained during simulations were lower than the values measured experimentally. According to the conducted simulations expected concentration increment should be in range between two to five times. Experimentally registered concentration rise was up to eight times for the maximum values and from four to six times for sustained flow conditions.

The most unexpected result was the formation of a highly concentrated stream of malachite green along the entire chip that led to experiments with outlets aligned on the chip axis of symmetry and the development of the second mode of

electrohydrodynamic focusing. Series of experiments in the prototype chip for lateral focusing yielded successful results. During these experiments MG was focused four to six times compared to the initial concentration with continuous outflow. Initially the anticipated EHDF would operate according to the schematics: priming chip with analyte, introduction of the high conductivity buffer, application of voltage, focusing, extraction, and flushing the chip with solvent. The discovered mode of lateral focusing allows for continuous operation allowing for much easier automation of the process.

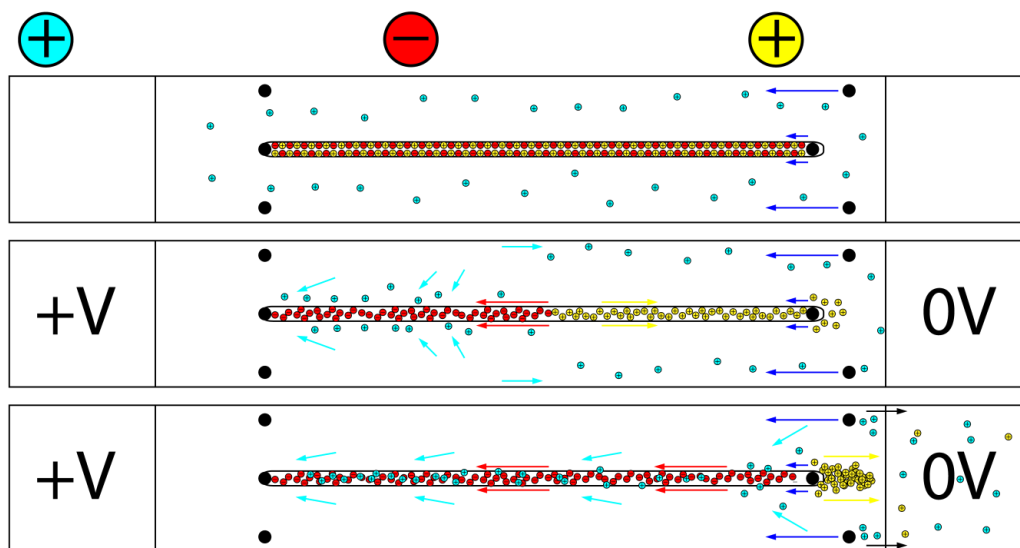


Figure 160: Schematic of the mechanism leading to lateral electrohydrodynamic focusing: (a) initial state with MG present in the chip and Tris-HCl filling the central flowstream, (b) situation shortly after applying positive voltage, (c) stabilised lateral focusing. Deep blue arrows mark force imposed by pressure driven flow, light blue arrows mark net force acting on MG, red arrows mark net force acting on chlorine, and yellow arrows mark net force acting on Tris.

Figure 160 shows a schematic of the proposed mechanism that has led to the observed lateral focusing and which is concurrent with conducted experiments. Initially the chip was filled with low conductivity malachite green (0.1mM), which was constantly pumped into the chip at high flowrate and highly conductive Tris-HCl buffer was introduced at low flowrate through the central inlet. Shortly after applying a positive voltage (see individual experiment condition for specific values) positively charged Tris (counter-ion) was retarded and for low flow rates for I_1 it was prevented to reach outlet (electromigration prevailed over pressure). Negatively charged chlorine (a supporting ion) was accelerated toward the outlet. In short time, Tris and chlorine were separated. For low flow rates of Tris-HCl only chlorine ions are present in the zone between I_1 and O_3 . As the electric field is diverted into the region of higher conductivity it decreases the diffusion effect acting as a stabilising mechanism and focusing chlorine. Malachite green

is exposed to three separate forces: pressure pushing toward outlets (and anode), electromigration pushing away from the anode and electrostatic attraction toward the negatively charged chlorine. As a result near the walls MG is predominantly pushed toward the inlets. The distance of 10mm between the walls and central flowstream was long enough to mitigate MG and Cl attraction. In the central part of the chip MG was quickly moved into the central flowstream. This explains the observed plough-like shape of the MG front during the stabilisation phase. For higher flow rates of the Tris-HCl (see Figure 131) the applied voltage was too weak to counteract the pressure and as a result positively charged Tris was still present in the central flowstream nullifying the attraction created by the negative chlorine. In order to achieve successful lateral electrohydrodynamic focusing several criteria must be met at the same time:

- It can only be performed on charged species.
- Only one charge sign species might be focused at a time (either positively or negatively) determining the supporting ion sign to be present in the central flowstream.
- The analyte and supporting ion must have opposite signs.
- Velocity of the analyte imposed by electromigration must be lower than the velocity imposed by the pressure.
- Velocity of the counter-ion in the central flowstream imposed by electromigration must be higher than the velocity imposed by the pressure driven flow to ensure the presence of only one ion in the central flowstream.

The major problem associated with the tested chip design is flow stability, which is crucial for the focusing process and the extraction of the focused analyte. To improve focusing performance a high degree of precision of chip flatness is required. The tolerance for the chip flow region thickness of $7.5\mu\text{m}$, to ensure maximum error of 3% error in the chip chamber height (for $500\mu\text{m}$ gasket), is suggested. For thinner gaskets the tolerance should be even higher.

The second problem discovered during experiments was related to the method of isolating electrodes. The high pressure present in the chip resulted in deterioration of the polymer layer and leaks coming through agarose gel tanks. Especially the tank close to inlets was vulnerable to this problem. This problem could be solved if the gel tanks were not present in a milled cavity which exposed the agarose gel through the entire

upper chip layer, but for a part of it. Such an approach would remove the problem of using transparent polymer film to cover the gel tanks.

5.22. Conclusions from the conducted experiments

The developed numerical model of EHDF, presented in the Section 3.1 and in the Chapter 4, was verified experimentally. The appropriate microfluidic chip was engineered, assembled and tested. The initial employed chip layout was directly transferred from the model. During these experiments the basic principle of EHDF was confirmed. The performance of the manufactured chip exceeded the modelled performance, allowing for up to nine fold concentration increase. In order to generate the flow pattern needed to establish the electric field gradient, the conflicting requirements between, influence of the diffusion and velocity gradient resulted in difficulties with maintaining the perfect equilibrium between the hydrodynamic and electromagnetic forces. Despite this occurrence, a quasi-stable equilibrium was achieved, and was presented in the Section 5.4.

Some discrepancies in the spatial distribution of the test compound in the vicinity of the inlets between the developed model and fabricated chip were observed. The further study of these divergences led to observation of an unexpected and previously unreported phenomenon named lateral EHDF. Two series utilizing two other chip layouts were conducted to investigate this phenomenon further. In the second series the possible relation between the used chip layout and the occurrence of the lateral EHDF was explored and eventually ruled out. The third series of the experiments was an attempt to exploit the lateral EHDF for possible practical uses. The experiments on lateral EHDF exhibited a four to six fold concentration increase with the constant outflow of the preconcentrated analyte.

The lateral EHDF presents an interesting method of rapid preconcentration with relatively simple process of possible automation. The major benefit of the lateral EHDF is possibility of the continuous outflow of the preconcentrated target analyte as long as it is supplied to the system, simplifying the experimental protocol. Also it is possible to employ the lateral EHDF for the role of purification. Instead of preconcentrating the analyte, the two auxiliary outflows could provide the original solvent with reduced number of ionic impurities.

Chapter 6 – Modelling and experiments for the light propagation: results and discussion

This chapter summarises all results of the light propagation modelling, results of the experimental verification of the developed model and results on photopolymerisation of the monolithic stationary phases in capillaries for verification of the theoretical models explaining observed problems associated with photoinitiated polymerisation in capillaries.

6.1. The experimental verification of the developed light propagation model

A series of photos of the polymer cylinders illuminated by green laser were used to measure angle of reflectance and transmittance as light propagates through the material and compare it with theoretical predictions from the developed numerical model of light propagation. Procedure of data acquisition and angle measurement is described in section 3.3.4.

6.1.1. Experimental and model results for first macro-simulation tests (set A)

Figure 161 shows a picture of the laser light (532 nm) passing through the macro experimental configuration as per experimental set A (see 3.3.4). The reflection and transmission angles (θ_{R1} , θ_{T1} and θ_{T2}) presented in this picture were those selected for comparison with the numerical model results. The results of the angle measurements of θ_{R1} , θ_{T1} and θ_{T2} from these experiments and the numerical models are presented in Figure 162, Figure 163 and Figure 164 respectively.

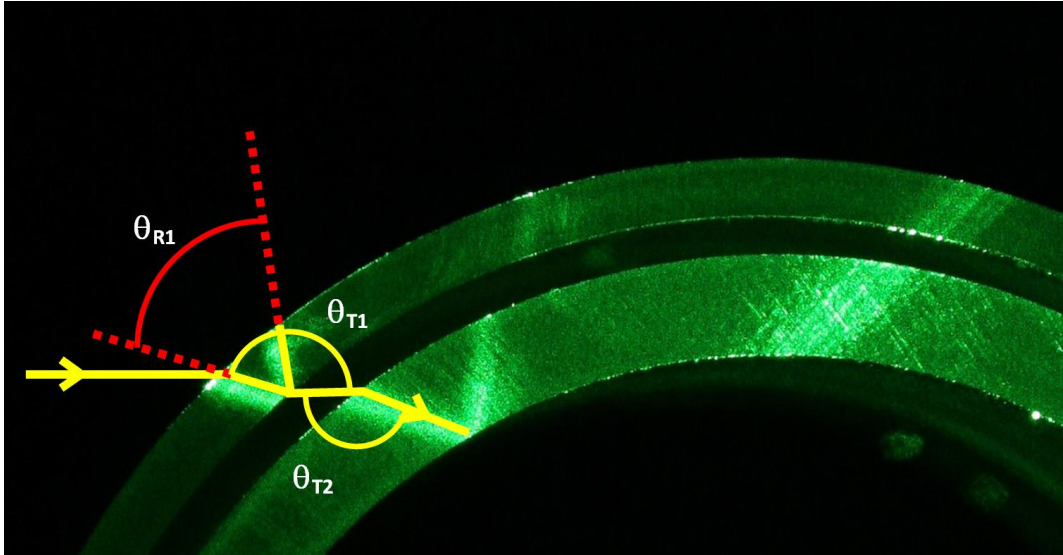


Figure 161: Picture showing plan view of laser light passing through the outer cylinder made PC, then air and then the inner cylinder made of PMMA. The drawn solid arrow lines (yellow) show the laser path and construction lines (red) show the location of reflection and transmission angles (θ_{R1} , θ_{T1} and θ_{T2}).

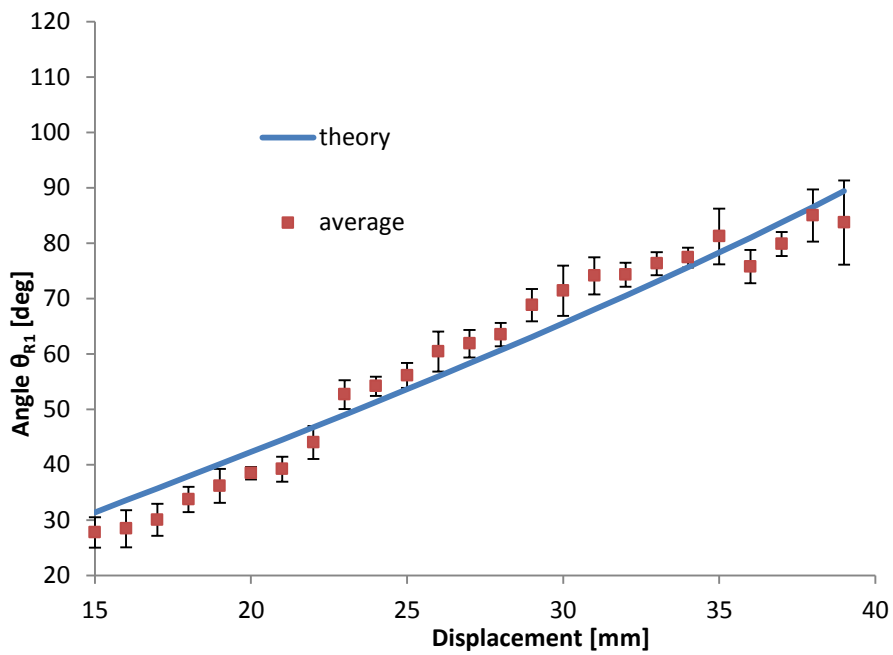


Figure 162: Comparison of theoretical calculations from the developed software (solid blue line) with experimentally measured values for the reflection angles inside the outer cylinder (angle θ_{R1} in Figure 161).

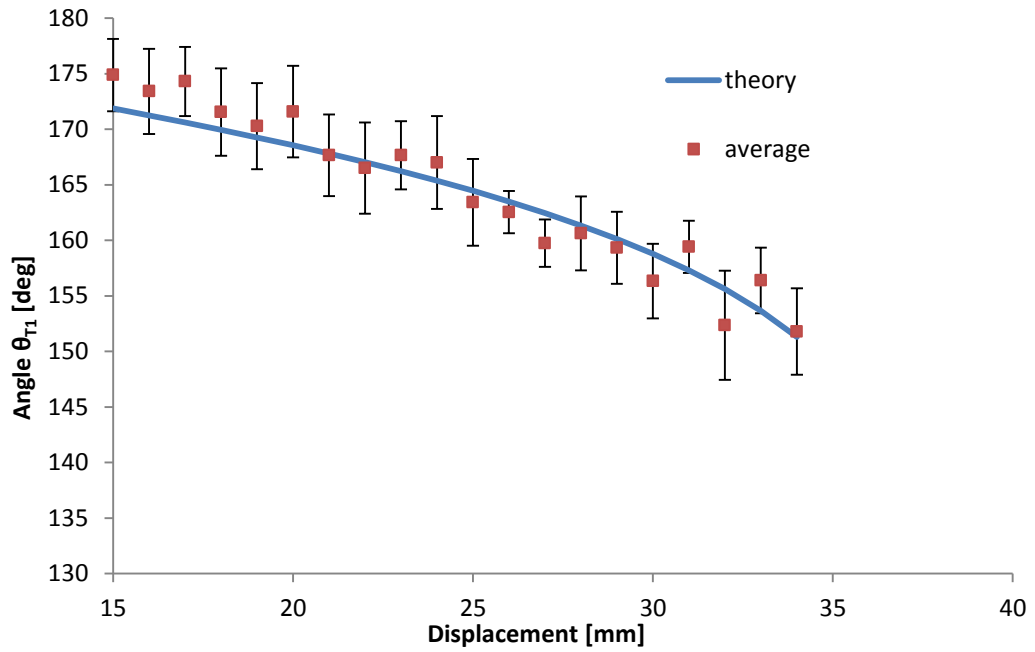


Figure 163: Comparison of theoretical calculations from developed software (solid blue line) with experimentally measured values for the transmission angles between the first cylinder and air (angle θ_{T1} in Figure 161).

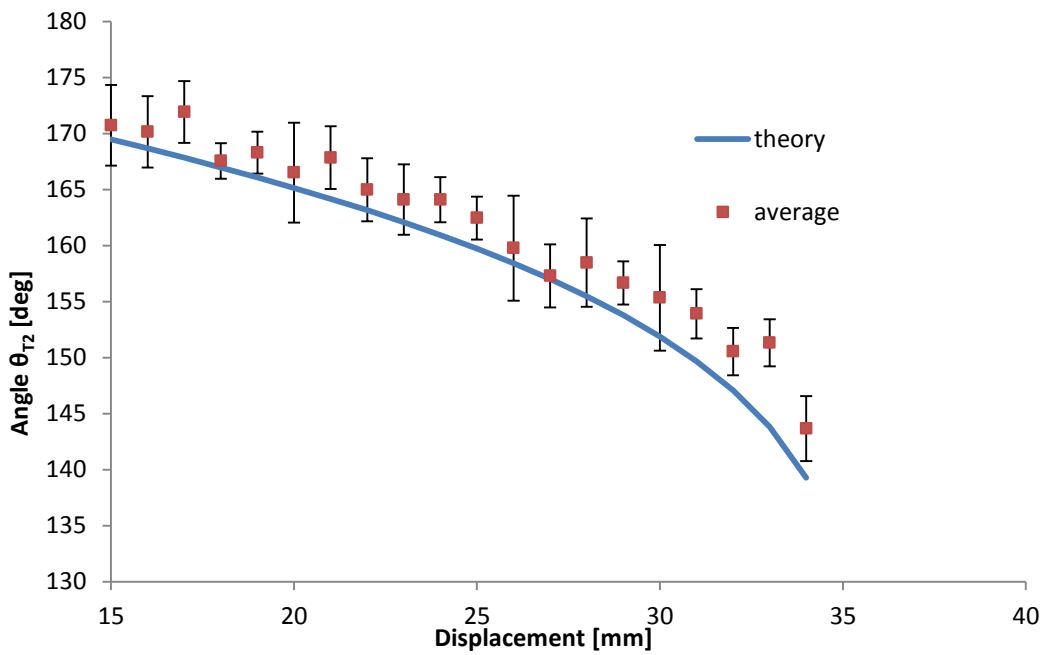


Figure 164: Comparison of theoretical calculations from developed software (solid blue line) with experimentally measured values for the transmission angles from air to the inner cylinder (angle θ_{T2} in Figure 161).

6.1.2. Experimental and model results for second macro-simulation tests (set B)

Figure 165 shows a picture of the laser light (532 nm) passing through the macro experimental configuration as per experimental set B. The reflection and transmission angles (θ_{R1} , θ_{T1} and θ_{T2}) presented in this picture were those selected for comparison with the numerical model results. The results of the angle measurements of θ_{R1} , θ_{T1} and θ_{T2} from these experiments and the numerical models are presented in Figure 166, Figure 167 and Figure 168 respectively.

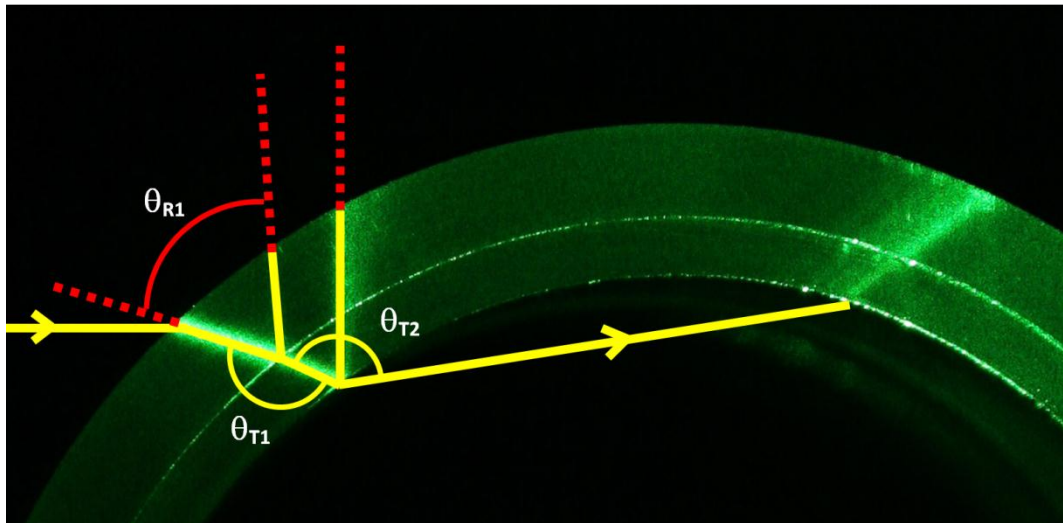


Figure 165: Picture showing plan view of laser light passing through the outer cylinder made PMMA and then the inner cylinder made of PC. The drawn solid arrow lines (yellow) show the laser path and construction lines (red) show the location of reflection and transmission angles (θ_{R1} , θ_{T1} and θ_{T2}).

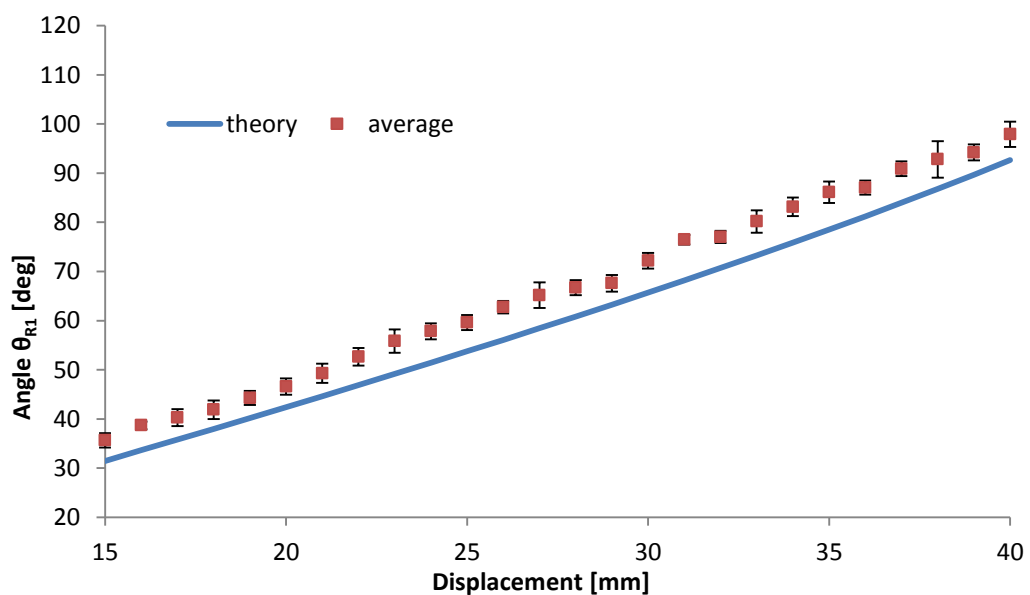


Figure 166: Comparison of theoretical calculations from the developed software (solid blue line) with the experimentally measured values for the reflection angles inside outer cylinder (θ_{R1} angle in Figure 165).

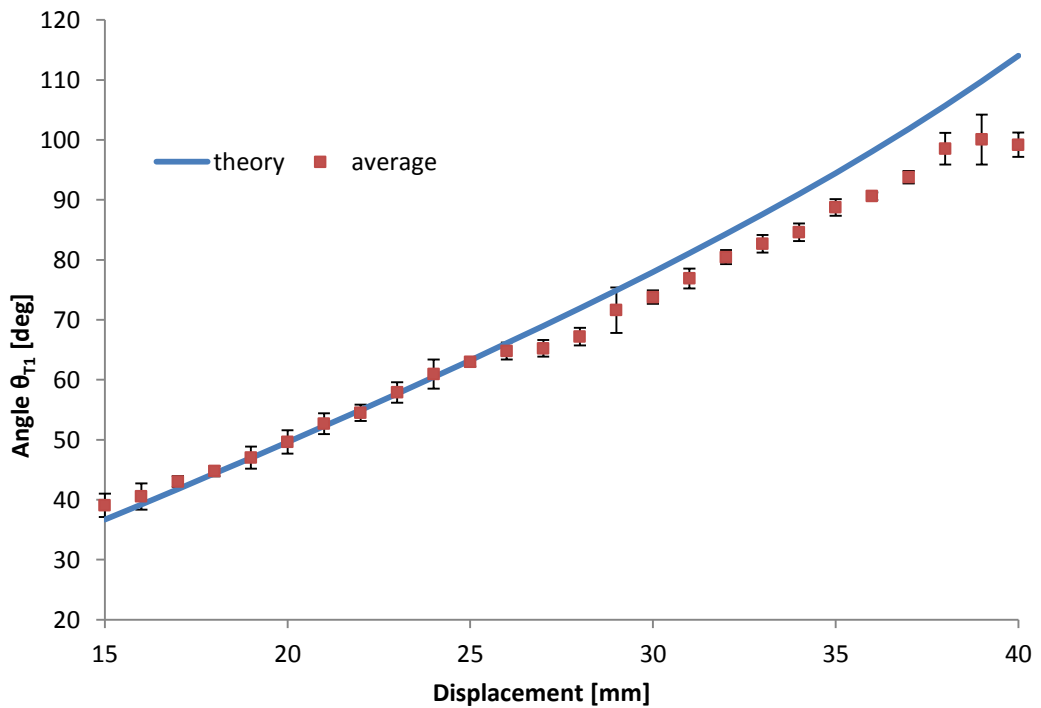


Figure 167: Comparison of theoretical calculations from the developed software (solid blue line) with experimentally measured values for the transmission angles through air (θ_{T2} angle in Figure 165).

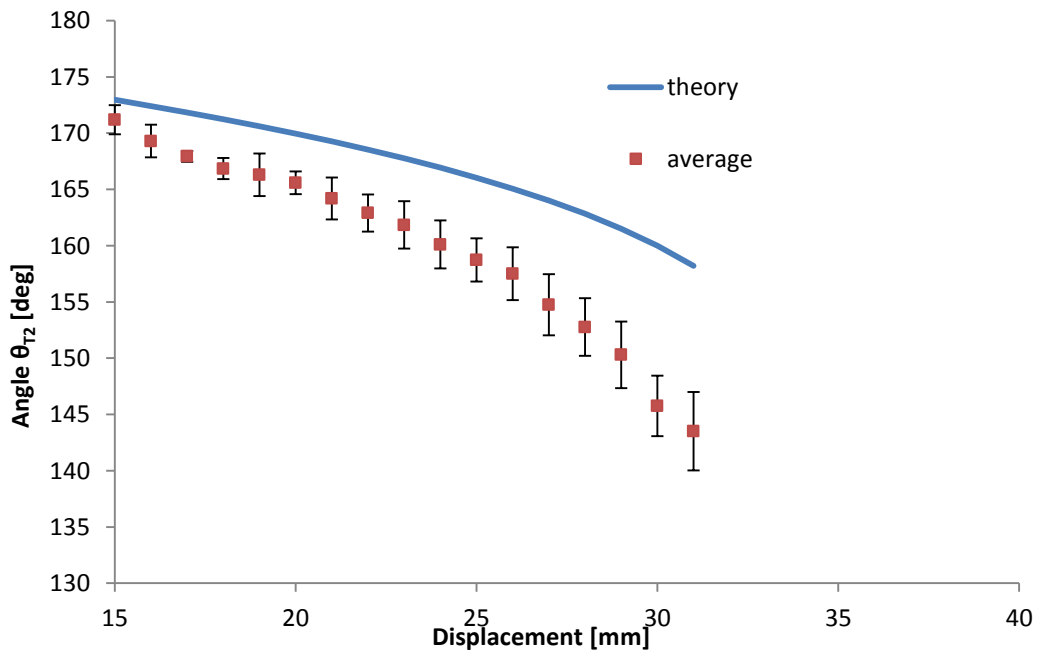


Figure 168: Comparison of theoretical calculations from the developed software (solid blue line) with experimentally measured values for the transmission angles through air (θ_{T2} angle in Figure 165).

6.1.3. Micro-scale experiments and model results for intensity distribution tests

Figure 169 shows the 3D theoretically calculated light intensity distribution inside half of the 100 μm capillary filled with light absorbing solution and its 2D plan view projection. As the capillary was optically symmetrical and light ray paths could not pass from one half to the other, only half of the capillary is shown here. The light intensity values recorded in the model were divided into six ranges as represented by the colour map shown in Figure 169. The values from the model were scaled to fall within the range of intensity values from 135 to 255. The values shown against each colour represent the mid-point value for a range of 20 on the colour intensity with values above 255 being assigned within the 255 to 236 range. This scaling allowed for direct comparison with the experimental results shown in Figure 170b. The range of 20 on the colour map represents a span of 7.8% in light intensity values on the scale of 0 to 255. Light was incident along the y- axis (i.e. from the left side in Figure 169b).

A series of colour photos were taken of the tartrazine filled 100 μm inner bore diameter capillary under illumination of the LEDs. These images were saved as 256 level, gray scale, '.PSD' format images. Such images directly indicate light intensity values. All pixels of intensity within a ± 10 grey scale range were selected together and a colour was assigned. For example, level 225 included all pixels within grey scale intensity level range from 216 to 235. Theoretical predictions were compared with these experimentally measured light intensity maps. Figure 170a shows the photograph of the light intensity distribution inside a capillary filled with tartrazine and illuminated with the white LED and Figure 170b shows the same image processed into a colour map representing light intensity distribution inside the capillary. Figure 171a shows the same capillary illuminated with the 430 nm violet LED Figure 171b and shows the same image processed into a colour map representing light intensity distribution inside the capillary. A small shadow effect is present in the upper part of the photographs (Figure 170b and Figure 171b) as a result of the capillary not being perfectly cut. When compared to theoretical predictions, shown in Figure 169, similar profiles can be observed.

An interesting feature clearly displayed in the theoretical model is the location of a highest intensity point at the capillary wall. Its location is a result of capillary focusing, where the capillary walls act like a lens. Although this point is not directly measured from experiment (due to too low a detector sensitivity) the layers of crescent-like distributions of the same intensity concurs well with the theoretical predictions.

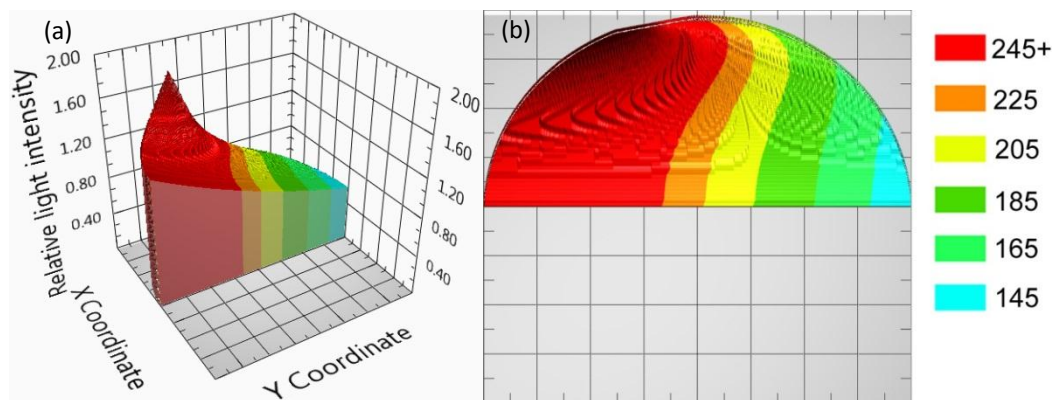


Figure 169: (a) 3D theoretically calculated light intensity distribution inside the 100 μm inner diameter capillary filled with light absorbing solution (b) and its 2D top view projection. Light was incident along the y- axis (from the left side in (b)).

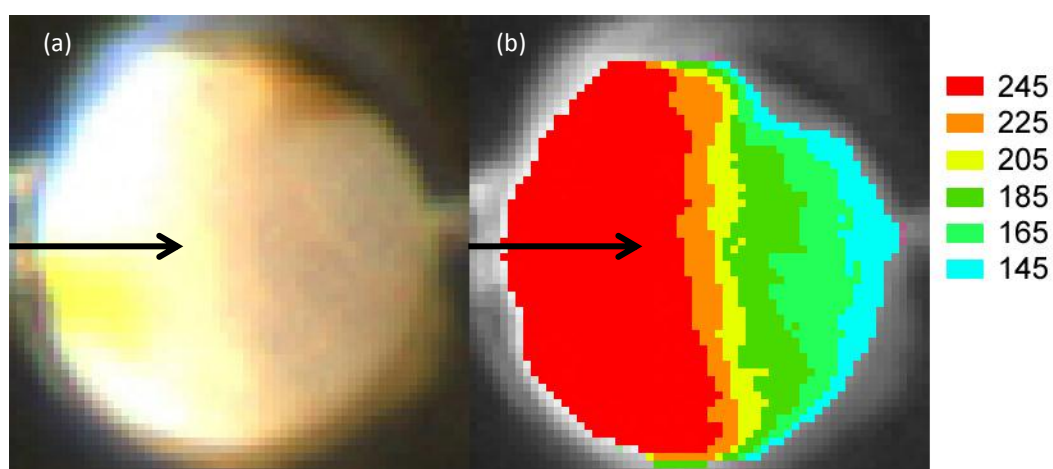


Figure 170: (a) Capillary filled with 0.01M tartrazine solution illuminated with white LED and (b) a colour map representing light intensity distribution inside the capillary. Arrows represent direction of illumination.

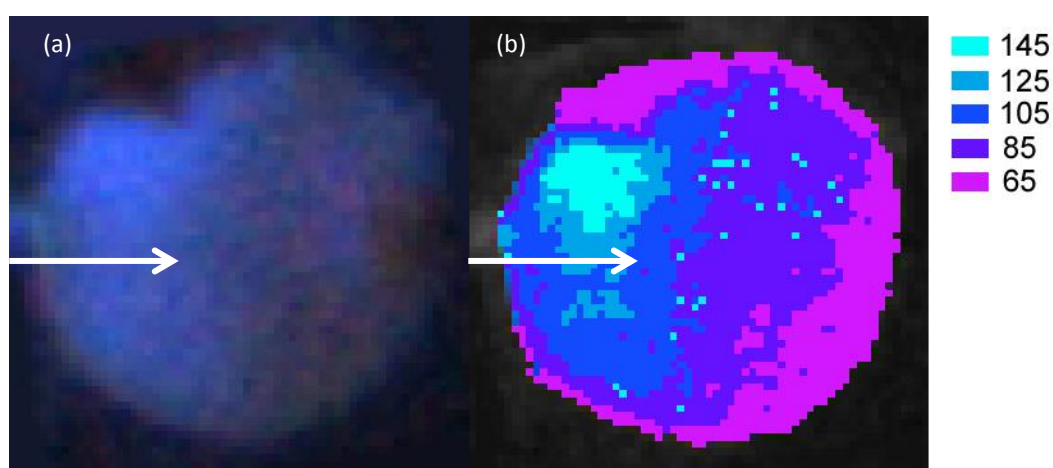


Figure 171: (a) Capillary filled with 0.01M tartrazine solution illuminated with 430nm violet LED and (b) a normalised colour map representing light intensity distribution inside the capillary. Arrows represent direction of illumination.

6.1.4. Discussion of the developed light propagation model

For set A macro tests, comparison of the experimental and model results for the reflection and transmission angles (θ_{R1} , θ_{T1} and θ_{T2}) showed good agreement between these with model values largely lying within the 95% confidence intervals of the experimental results. The results from the models and experiments also trended well together. For set B macro tests, the θ_{R1} and θ_{T1} experimentally measured results were found to match only reasonably well with the theoretical results. These results were found to largely lie within the confidence intervals if a 2mm additional displacement was applied to the incident light. The correlation coefficients for the set B results were higher than the values for set A indicating the closer trending of the experimental data with the model values despite higher absolute error. Reasons for observed discrepancies between theoretical and measured values are most likely due to experimental error. Much effort was invested to ensure alignment of the individual components, including mounting the experiment on an optical bench, attaching the laser on a micrometre stage which in turn was set up perpendicular to the edge of the cylinder's base plate, checking alignment of the reflected beams before measurement for height and perpendicularity adjustments and mounting the camera on an optical bench stand perpendicular to the top of the cylinders. However, over the scale of the experiment, alignment errors could be present due to imperfect alignment of the camera resulting in slight tilt of the incident laser beam; imperfect alignment of the laser pointer in the x-y plane resulting in a tilt of the beam; imperfect alignment of the laser pointer parallel to the x-axis of the micrometric stage; and difficulties in determination of laser beam edges in photographs resulting in inaccurate angle measurements. A slight shift and tilt of the beam from the true theoretical position could therefore be present along with some inaccurate edge detection in used image analysis routines.

From the light intensity distribution simulation an interesting focusing lens behaviour effects of the capillary were detected. The model clearly displayed the highest intensity location point at the capillary wall. These simulation results also predicted light intensities of similar magnitude in crescent-like regions emanating from the capillary walls. These distributions corresponded well with the light intensity distribution regions as measured experimentally. The shape of regions of equal intensity, their numerical values and the relative percentage changes are almost identical between the simulation and experimental results. These experimental validations show encouragingly good agreement between theoretical predictions and measured results which could allow for

optimisation of associated regions for monolith synthesis and use in fluidic chromatography, optical detection systems and flow cells for capillary electrophoresis and flow injection analysis.

6.1.5. Conclusions from the model verification

A numerical model of light propagation and intensity distribution for coated fused silica capillaries was developed. Theoretical predictions of the light paths are concurrent with previous publications, and are presented with improved capability allowing taking into account the presence of coating materials and their optical properties. The model itself has high flexibility allowing calculations for multiple coatings and capillary body materials with differing dimensions (coating, capillary wall thickness, and bore diameters) and optical properties (refractive indices and light absorptivities). The model has been tested experimentally and showed good agreement between theoretical predictions and measured results.

The numerical model was developed to provide a limited alternative to commercially available software such as Zemax or Optica Software. The model uses a simple geometrical approach to calculate the actual light path through a multilayered system with cylindrical symmetry. The results obtained from this model were cross-examined with the experiments to verify accuracy of the developed model.

The macro-scale verification process yielded positive results, with only one minor discrepancy between theoretical and experimental values. This was attributed to misalignment of the experimental setup affecting values of the measured angles. In all other cases theoretical values calculated using the developed model were in good agreement with the measured values. The micro-scale experiments on the light intensity distribution concurred with the theoretical prediction. A counter-intuitive result from the theoretical model is localisation of the highest intensity point within the capillary bore. Due to the lensing effect of the capillary, the highest light intensity is not located precisely on the illumination axis, but is shifted away from it. This effect may be exploited further for optimisation of the capillary-based optical detection systems, as well as for alignment and localisation of the light sources in the photo-induced polymerisation inside capillaries. The developed model could be easily adapted for such an application.

6.2. Growth of the monolithic polymers in photoinitiated polymerisation in non-illuminated region

6.2.1. Results of the monoliths growth

A series of experiments were conducted in order to evaluate the degree of monolith growth under the masked region of a capillary where direct light should not enter. Observed results in experiments with photopolymerisation using same mixture and light sources showed that monolith can grow few millimetres under the mask. Such growth is considered undesired. Table 42 and Figure 173 shows average of three results of photoinitiated polymerisation of monolith with measured distance of the part formed under the photomask – in a region where direct light should not reach and therefore polymerisation would not be anticipated or well controlled. There was a clear trend of increased length of monolith grown under the mask as the LED was placed closer to the capillary. Also when the LED was tilted by an angle of 45° growth was significantly larger that side compared to when the LED was held perpendicularly. The light source was located directly over the edge of the photomask as shown in Figure 172.

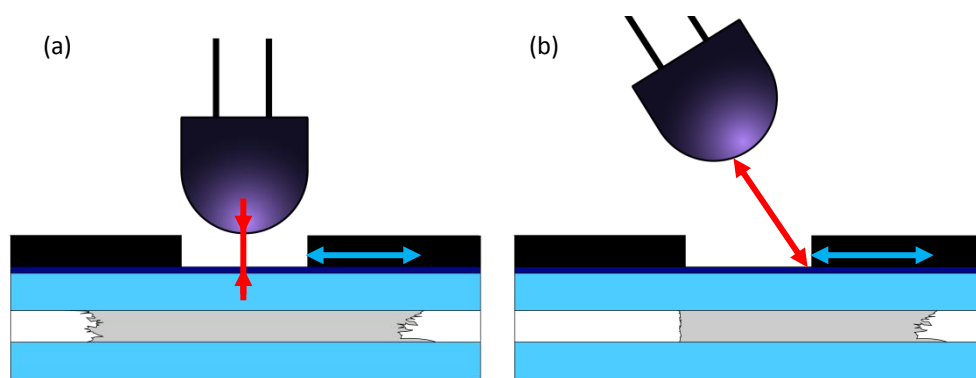


Figure 172: (a) schematic of the LED placement versus the capillary for perpendicular illumination and (b) for illumination under 45° angle. Red arrow marks distance from capillary to the LED, blue arrows marks distance of the monolith growth.

LED perpendicular		LED tilted by 45°	
LED distance from capillary	Growth length	LED distance from capillary	Growth length
0 cm	1.1 mm	0 cm	2.3 mm
1 cm	0.7 mm	1 cm	1.9 mm
2.5 cm	0.5 mm	2.5 cm	1.7 mm
4 cm	0 mm	4 cm	1.4 mm

Table 42: Monolith growth depending on light source position.

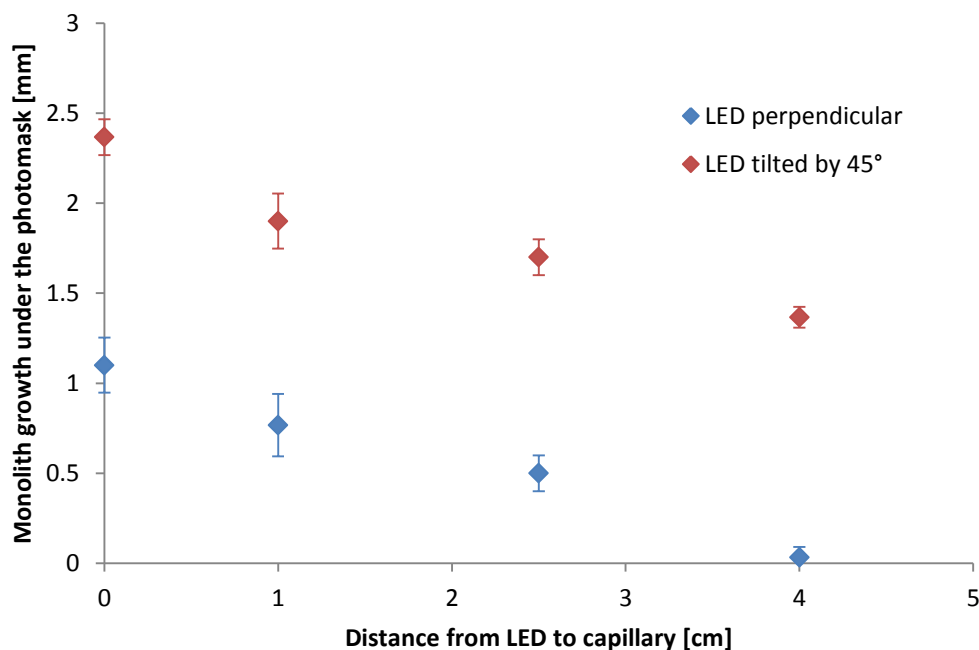


Figure 173: Graph showing relation between distance from the light source and monolith growth in non-illuminated region for LED shining perpendicularly to the capillary and under angle 45°.

6.2.2. Discussion of the results

Previously described theoretical model for light propagation was used in order to understand what is happening during photopolymerisation with light, solution and monolith. Tilting of the LED and thus delivering significantly more light to one side of the monolith suggest that capillary geometry plays significant role.

When the light is incident on a boundary of two dielectrics with different dielectric constant (e.g. PTFE/fused silica, fused silica / polymerization mixture) a portion of it undergoes reflection reducing the intensity of transmitted light. The intensity of the reflected and transferred light is given by Fresnel's equations (Eq. 22) separately for each polarisation of light:

$$R_s = \left[\frac{\sin(\theta_i - \theta_t)}{\sin(\theta_i + \theta_t)} \right]^2 \quad R_p = \left[\frac{\tan(\theta_i - \theta_t)}{\tan(\theta_i + \theta_t)} \right]^2 \quad \text{Eq. 22}$$

The uncollimated light is mixture of all possible polarisations, that is combination of linear polarisations and can be separated for *p* polarisation (vector of the electric field is parallel to plane of incidence) and *s* polarisation (vector of the electric field is perpendicular to plane of incidence). Graph on Figure 174 shows percentage of light being reflected on boundary PTFE/fused silica (light coming from medium with lower refractive index to medium with higher one) versus angle of incidence for both polarisations calculated from Eq. 22.

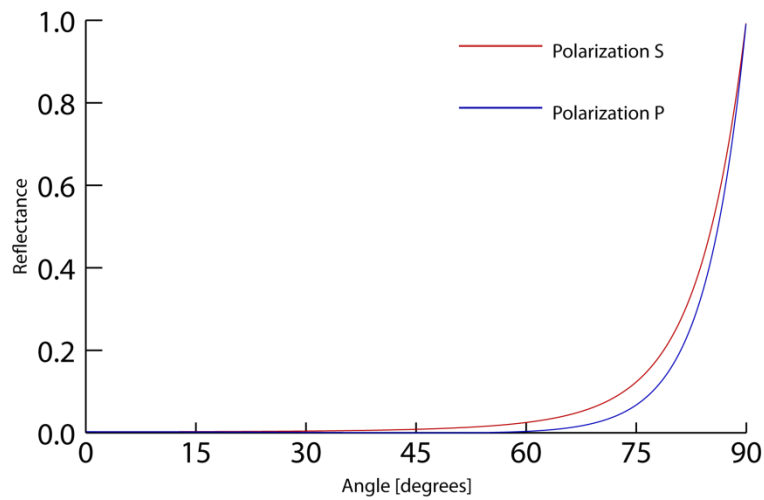


Figure 174: Graph of theoretical reflectance of s and p polarised light incident on boundary PTFE/fused silica vs. angle of incidence calculated from Eq. 22.

The light that reflects multiple times on dielectric boundary quickly loses intensity. The developed numerical model showed that incidence angles that are present in a capillary at the fused silica/PTFE boundary illuminated from outside do not provide significant reflectance and light is quickly transmitted outside of the capillary. Figure 175 provide information with upper limits of the light intensity that can be reflected by the capillary assuming total lack of absorption at this stage.

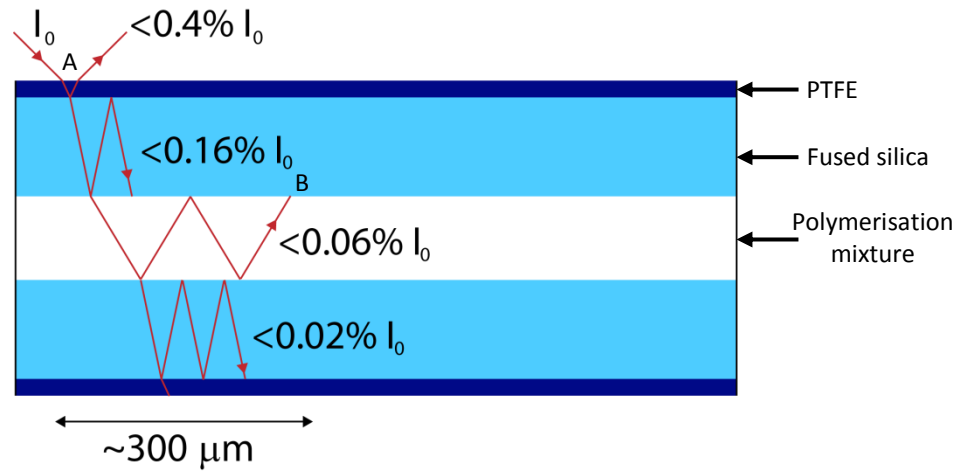


Figure 175: Schematic of the light propagation by multiple reflections inside PTFE-coated fused silica capillary with upper limit of the initial intensity I_0 (no more than). Dark blue – PTFE, light blue – fused silica, white – polymerisation mixture, red – light path

Figure 175 shows schematic cross-section of capillary with sample light ray. After two reflections (first on boundary fused silica/polymerisation mixture, second on boundary fused silica/PTFE) not more than 0.16% of intensity from point A is delivered to point B. The real value of the light intensity in point A is already lower than I_0 due to reflection on boundary air/PTFE and boundary PTFE/fused silica, but these effects are neglected and rounded to I_0 is this discussion. After three reflections intensity drops to not more than 0.06% of initial, and after four to not more than 0.02%. Dimensions of the capillary and refractive indices of PTFE, fused silica and polymerisation mixture are enforcing angles in further reflections and transmittances – after around 300 μm from initial point of illumination total delivered light intensity is below 0.2% of the initial light intensity I_0 delivered to the capillary is available. This calculations are based on assumption that all materials (air, PTFE, fused silica and polymerisation mixture) are completely transparent and do not absorb any light. Because their transmission coefficients are below 1 total amount of light available will be significantly lower, making impossible to penetrate distances observed in the experiments.

The size of a standard capillary is comparable with size of multimode optical fibres, where geometrical optics is sufficient to explain observations and calculate results. Capillaries and coating have form of coaxial cylinders. The basic principle of optical (multimode) waveguide is total internal reflection (TIR). This phenomenon is occurring when dielectric with refractive index n_1 (e.g. fused silica (FS)) is covered with dielectric with refractive index $n_2 < n_1$ (e.g. PTFE, $n_{\text{PTFE}} < n_{\text{FS}}$). The light wave incoming from medium with higher refractive index to boundary can undergo TIR provided angle

of incidence is high enough. The graph on Figure 176 shows dependence of intensity of reflected light versus angle of incidence (for fused silica/PTFE boundary).

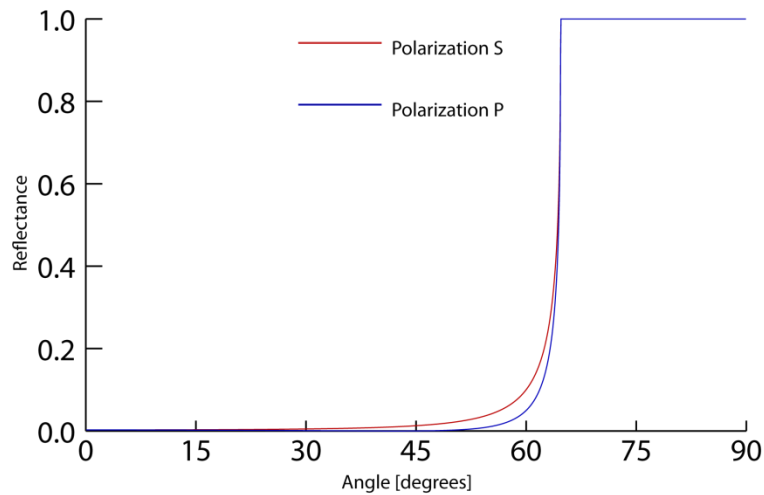


Figure 176: Graph showing the theoretical reflectance on boundary fused silica/PTFE vs. angle of incidence. Reflectance of 1 (starting at 64.8°) shows where total internal reflection occurs and no light is transmitted through the boundary (from Eq. 22).

In order to observe total internal reflection for light incident on fused silica/PTFE boundary, angle of incidence must be higher than 64.8°, otherwise some light will be transmitted through the boundary resulting with loss of the light intensity. The developed numerical model showed that no angle higher than 44.7° is available in any part of the capillary meaning that no light introduced to capillary from source placed above the capillary can achieve angle sufficient to reflect totally within the fused silica.

Capillaries are made of fused silica and have very similar diameters to optical fibres. PTFE has lower refractive index than fused silica. Initially a hypothesis about the capillary acting as an optical waveguide was discussed to explain occurrences of monolith growth under the photomask. There were two major contradictions: light coming from outside of cone of acceptance (i.e. from source located above the capillary) for optical fibre it cannot be transmitted over longer distance. The value of the highest possible angle of incidence on boundary fused silica/PTFE for light interacting with capillary content obtained from the developed model is significantly lower than required for the TIR. Graph on Figure 176 shows that for angles of incidence below 45°, reflectance is very low, and light is mostly transmitted through the boundary.

The last possibility was reflection on boundary PTFE/air – the highest possible ratio of refractive indices. In order to observe TIR on this boundary the incidence angle

of light must not be lower than 49.25° ⁸. The highest incidence angle on fused silica/PTFE boundary calculated using light propagation model gives angle of 44.57° . Although amount of light reflected on that boundary is around 10% it does not satisfy the condition to observe total internal reflection and could not explain growth of few millimetres.

These attempts mentioned above to explain observed result were based on a static system with constant time-independent properties. A capillary with on-going polymerisation reaction is a dynamic system, which changes its physical and optical properties in time. A hypothesis that a monolith forming inside capillary is changing optical properties of the setup during the polymerisation was posed. To prove this hypothesis, new photographs of capillary filled with polymerisation mixture and monolith were taken to show the transmission of light when the LED was shining on the capillary. The capillary was installed vertically above the digital microscope. In order to prevent any undesired light, a black cardboard separated the microscope objective from the rest of the setup and photos were taken in total darkness. Any possible openings near capillary wall were covered with a sealant. Schematic of that setup is shown on Figure 177.

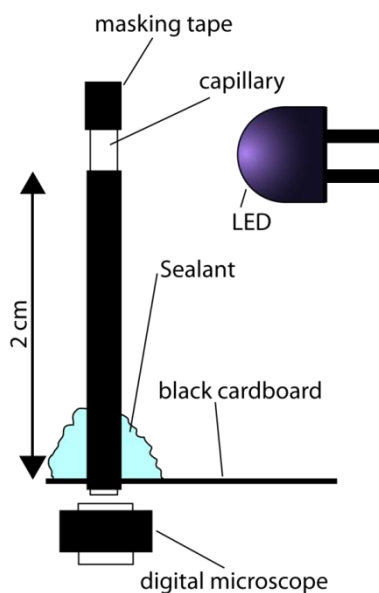


Figure 177: Schematic of experimental setup for observing light waveguiding inside the capillary with monolith.

⁸ Calculated from Eq. 22, refractive index of PTFE $n_{\text{PTFE}} = 1.32$ and refractive index of air $n_{\text{air}} = 1$

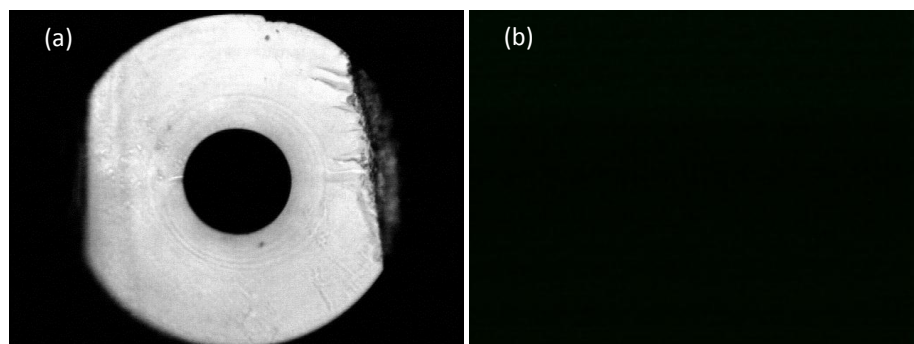


Figure 178: (a) capillary with monolith and (b) empty capillary. Image collected by digital microscope using setup from Figure 177.

It can be clearly seen in the Figure 178a that light was transmitted through the fused silica. The distance from the light source to the microscope was 20 mm to prevent any other discussed method than waveguiding to propagate light toward the end of capillary. To confirm that the observed effect has nothing to do with collimation of the light the experiment was repeated using 532 nm green laser as light source. Result is shown on Figure 179. Black spots are effect of destructive interference of laser beam with itself after multiple reflections inside fused silica. LED light is non-collimated thus the interference effect was not observed.

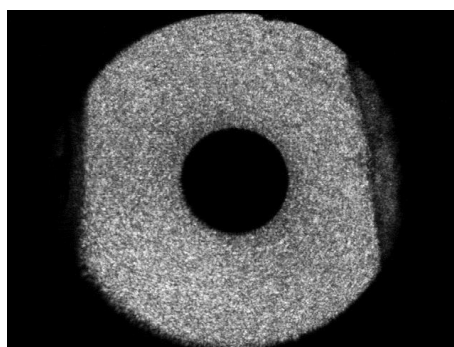


Figure 179: Image observed when 532 nm green laser is used as light source (setup same as on Figure 177).

The monolith inside the capillary has a very irregular surface. Moreover the refractive index of a polymer is higher than of the fused silica. The incident light was scattered on the monolith surface (polymerisation mixture/monolith boundary) and due to the morphology of the monolith surface it was scattered in all directions (Figure 180). This type of reflection is called diffuse reflection or diffuse scattering. In this situation light can be reflected under an angle sufficient to undergo total internal reflection on boundary fused silica/PTFE. These angles are not available for light that is not a subject to diffuse reflection. The refractive index of polymethacrylic polymer is higher than

fused silica and ranges from 1.472 to 1.506 (255). Light reflected diffusively in one part of monolith can propagate through the monolith, cross the boundary monolith/fused silica, and then remain in the TIR regime in regions where no monolith is present, effectively turning capillary into an optical waveguide.

Also diffuse scattering allows photons entering fused silica under angles higher than for those coming directly from light source. Wherever total internal reflection is occurring, on opposite side of boundary an evanescent field appears strong enough to initiate photopolymerisation. Figure 181 shows a schematic of that principle.

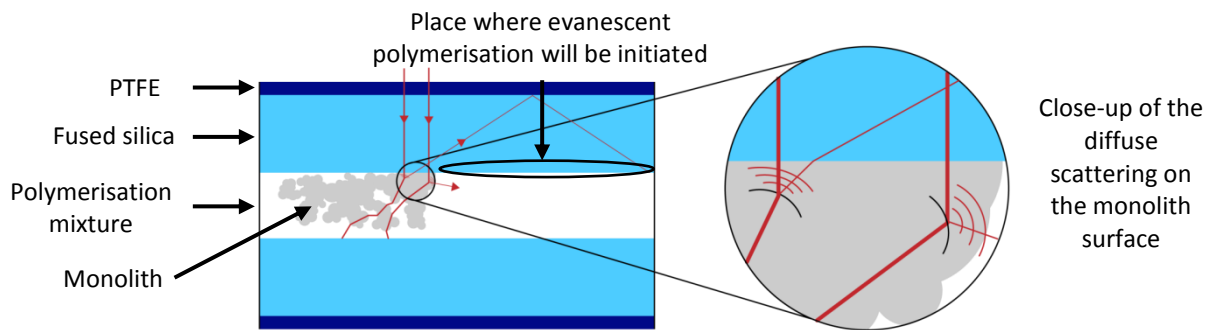


Figure 180: Schematic of the diffuse scattering of incident light on the porous surface of the monolith that has formed inside the capillary.

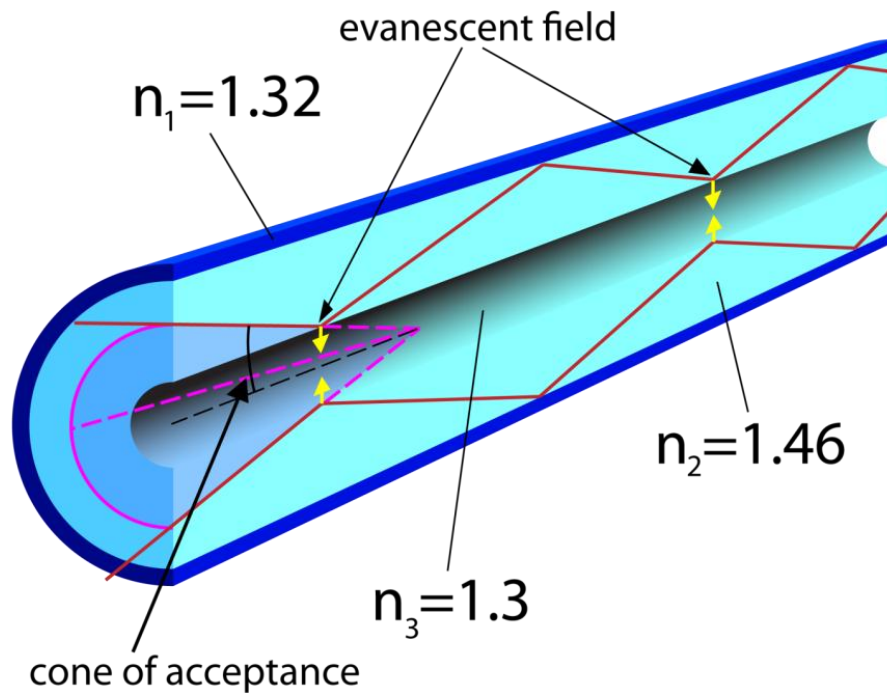


Figure 181: Schematic showing formation of the evanescent field (yellow arrow) outside dielectric inside which light undergoes total internal reflection. Dark blue – PTFE, light blue – fused silica, transparent – polymerisation mixture.

6.2.3. Conclusions from the monolith photopolymerisation

The developed numerical model was used for investigation of the capillary optical properties during the photopolymerisation reaction. The main goal was finding a relation between alignment of the light source versus the capillary and the shape and size of polymerised monoliths. The previous observations suggested that a light transmission through the capillary fused silica body occurs in a similar manner as in an optical fibre. The numerical model was used to determine conditions necessary for total internal reflection of the light used to initiate the polymerisation reaction, which in consequence would lead to waveguiding of the light through the capillary and enabled evanescent polymerisation in an obscured region under the photomask.

Studies of the empty capillary and capillary filled with photopolymerisation mixture yielded conclusive results that the light does not propagate in the system under the photomask. The minimum required angle to observe total internal reflection was not present in the system. This result is concurrent with basic knowledge of the optical fibres: the light must be introduced into the waveguide under a sufficient angle to remain within total internal reflection regime. If the initial angle of incidence is higher than required the beam will eventually escape the waveguide. This hypothesis was tested using an empty and filled with polymerisation mixture capillary illuminated perpendicularly and a photodetector that was recording light emitted through the capillary cross-section. The results were in both cases negative. Meanwhile the conducted experiments relating position of the light source and its distance from the capillary clearly suggested that such a relation exists.

During this investigation a dynamics of the polymerisation process affecting optical properties was studied. The polymerisation process and thus the formation of a monolith inside the capillary could affect the optical properties of whole system. An organic monolith is a highly porous, amorphous structure, that when illuminated reflects significant amount of light. Presence of the monolith formed during the reaction changes the optical properties of the capillary that may longer be regarded as a uniform cylindrical structure with constant refractive indices across its whole cross-section. The experiment with a capillary with monolith formed inside proved dramatic changes of the optical properties of the capillary, resulting in the light transmission through the fused silica capillary body. The monolith inside the capillary bore provided a surface for diffuse light reflection. The monolith's surface morphology allowed for presence of the angle that are normally unavailable inside the capillary system, but with monolith the

waveguiding of the light becomes possible. As the light can be transmitted along the capillary for significant distances (measured distance was 20mm) utilising the total internal reflection mechanism. On the side opposite to the light reflecting of the boundary evanescent field forms, strong enough to initiate the reaction of photopolymerisation. The increase of the distance between the capillary and the light source significantly reduces amount of light reflected from the monolith surface and thus amount of light that can propagate through the capillary. Placing the light source too close to the capillary may result in over-illumination of the region of interest and allow for some light to propagate through the capillary body.

Chapter 7 – Conclusions

Presented thesis contains several separate work packages that can be divided into three sections: computer modelling of the microfluidic processes, experimental verification of developed models and the study of the light propagation for microfluidic devices. Two main areas of interest studied were the fluid dynamics with electroseparations and the optical detection via designated and tested visualisation methods.

7.1. Conclusions form the scientific work

In the area of fluid dynamics, a microfluidic platform for separation and preconcentration was investigated. The initial idea based on previously published experiments was modelled and tested experimentally; see results in section 4.10 and 5.3. The electrohydrodynamic focusing (EHDF) was designed as an equilibrium separation method of analyte preconcentration. The designed platform had to be easily automated allowing a continuous mode of operation “sample in – selected preconcentrated substance out”. Numerous advantages of microfluidics suggested its application for the design. Small scales, compliance with miniaturisation, possibility of full automation of the process and potential of integrating sample handling, separation and detection in one device were regarded as key elements during this research.

A typical microfluidic device design resembles often an electronic circuit. Numerous tanks containing reagents are connected by micrometre-scale width and height channels with micro-reactors, inlets and outlets. The majority of microfluidic devices rely only on electromigration, though there are platforms using pressure-driven flow as well (e.g. Agilent Bioanalyser 2100). In this project a novel idea of planar two dimensional microfluidic devices with multiple parallel flow streams present at the same time was investigated. EHDF was designed as a development of other methods: Conductivity Gradient Focusing and Electric Field Gradient Focusing. The novelty was in the application of adjustable geometry created by different conductivity regions instead of using a fabricated device with defined geometry.

At the start of the project, a numerical model of occurring processes inside the chip using COMSOL Multiphysics was developed. Initial models provided results concurrent with those previously published indicating applicability of this method for

the simulation of this process. During the modelling work several different chip layouts were investigated and one was selected for manufacturing of the chip used for focusing experimental work. The model theoretical predictions suggested the presence of a quasi-stationary zone of analyte with a two to five fold increase of concentration that could be extracted for further applications.

The microfluidic chip based on the developed model was manufactured and used to cross reference results of numerical simulations with results of experiments, see sections 5.1, 5.2, 5.3, 5.4, and 5.19. During the experiments the performance of the fabricated microfluidic chip exceeded predictions from the conducted modelling. The observed concentration increase was as high as nine times compared to the initial value, making it two to three times more efficient than estimated by simulations. The modelled flow pattern was in general achieved and there were observed problems with flow stability. To maintain the necessary flow pattern in the chip the same outflow rate through both outlets where peripheral outlets were used had to be maintained. This proved to be difficult but possible.

Testing of different gasket thicknesses exposed the necessity of surface flatness and maintaining a constant thickness throughout the flow chamber. Variable chamber height can decrease flow stability and as the device relies on symmetry of the different conductivity solution distributions. This requirement can completely prevent the device from working as was the case with the thinnest gasket used. Also difficulties with installation of electrodes in the agarose gel tanks were noted. Tanks were machined throughout the upper layer of the chip and then blocked with an adhesive polymer. The presence of the increased pressure resulted in deterioration of the agarose gel and the adhesive layer itself leading to leaks and reduced overall performance of the device.

The developed numerical model of EHDF displayed parallel flowstreams (two streams of low conductivity test compound separated by a stream of the high conductivity buffer) up to the focusing zone and was in agreement with previously published work. During the experiments a novel unexpected mode of focusing was discovered. Immediately after applying voltage to the system the test compound (malachite green) started migrating into the central flowstream and forming a thin line along the chamber. This phenomenon was investigated to try to understand the reasons of such behaviour. This was unexpected as the focusing occurred along the line perpendicular to the applied electric field more so than along the applied field. The chip geometry and flow pattern variability were dismissed as causes, as repeated experiments

produced highly similar results. The observed occurrence of lateral electrohydrodynamic focusing was tested as a potential method for separation and preconcentration of analytes. A series of experiments with multiple parallel flowstream in the same microfluidic chamber was conducted to present a possible theoretical explanation for this event. Two flowstreams of a low conductivity analyte (malachite green) were separated by a stream of a high-conductivity buffer (Tris-HCl). After applying the voltage, Tris was migrated on the other side of the chip, while Cl was accelerated toward the outlets. The central flowstream had an excess of negatively charged Cl ions, which were attracting positively charged MG ions. As a result MG was migrated into the central flowstream (perpendicularly to the applied field).

A similar effect was observed in thin channel microfluidic chips as a result of interaction with charge located on the walls (257; 258). The observed lateral EHDF works in a very simple routine allowing continuous extraction of preconcentrated analyte without pausing in the system flow. The observed lateral electrohydrodynamic focusing presents a novel opportunity as a separation and preconcentration technique which should be pursued.

The second part of this project was dedicated to the investigation of a solid state light sourced (mostly light emitting diodes) in the area of visualisation, optical detection and application for photoinitiated polymerisation of organic monoliths for separation sciences. A numerical model for light propagation and intensity distribution in multi-layered cylindrical systems was developed from first principles using the LabVIEW programming environment.

The model was initially design to provide answers about occurrences of photopolymerisation of monolith in capillaries in regions covered by the photomask. The model was designed to provide information as to the extent of photopolymerisation beneath the edges of the photomask. The completed model was used for simulation the actual light path in multilayer system with cylindrical symmetry and for simulating the light intensity distribution in such systems and was cross referenced with experimental results both on the macro and the micro-scales. The experiments validated the model calculations of the light paths geometry (ray-tracing) and calculations of light intensity distribution inside the capillary filled with the light absorbing medium.

Light emitting diodes (LEDs) were used extensively throughout the project as a main type of light source for both visualisation and optical detection. The unique

spectral properties combined with the small scale of the LEDs made them suitable for use during the experiments in the microfluidic chip where an LED coupled to the spectrophotometer was used as a light source for the optical absorbance detection. An LED was also used as a light source for light intensity distribution measurements in the light propagation experiments. A high-power LED was used for low-cost real-time visualisation of fluorescent dye in the chip. An UV-LED was also used for experiments to investigate polymerisation of the monoliths under the photomask. LEDs are currently regarded as a new generation of light sources with multitude of applications including photometric detection, fluorometry and visualization. A part of this project was related to imaging and data analysis from digital photos to determine concentration values in the microfluidic chip or the light intensity distribution inside the capillary. Two scientific papers were published from this work. The first paper was on the development and validation of the light propagation model (259), and the second one on the employment of the white LEDs as light sources for optical detection (260). This work highlights the usefulness and good applicability of both LEDs and light path and distribution modelling for μ -TAS system design and development. An example of the use of this photometric detection is given in the photo-absorption experimental validation work presented in Chapter 5 of this thesis.

7.1.1. Testing of the hypotheses

The work presented in this thesis was based on few research hypotheses:

- It is possible to attain a stable high conductivity stream of varying cross-section using multiple inlets and outlets (referred further in this thesis as the flow pattern) in a planar two-dimensional microfluidic chip
- The presence of such a flow pattern will allow for the formation of an electric field gradient and velocity gradient along the separation dimension
- A stable trapezoidal flow pattern based on this generated flow pattern will allow for focusing of at least one compound
- Simultaneous concentration measurements can be made across the whole chip with a developed photometric detection system, based and optimised on the investigation of simpler capillary-based microfluidic photometric detection systems

The first hypothesis as the base for EHDF was tested extensively with investigation of the numerical models and during the experiments. The initial assumption on application of multiple additional outlets that would withdraw auxiliary,

low-conductivity flowstreams and allowed for broadening of the central, high conductivity flowstream proved to be hindered by unwanted species distribution due to the diffusion. This approach was abandoned during the modelling stage. The second principle of this hypothesis, formation of triangular flow pattern, remained unchanged throughout the rest of the numerical modelling process. Eventually a different chip layout was developed that allowed for formation of the trapezoidal flow pattern needed for the formation of the electric field gradient. As a cost associated with the employed approach a velocity gradient along only x-axis resulted. This led to complexities with attaining a perfect equilibrium between the pressure-driven flow and the electromigration. The lack of perfect balance between these two forces yielded a quasi-stable EHDF that could still be employed practically. The developed model also could be used for better theoretical explanation of CGF presented in (8). The achieved EHDF presents a novel method for preconcentration of the analytes that is not based on fabricated features of the microfluidic chip, but rather on a balance between fluid flows.

The second hypothesis was tested positively and was used extensively both in modelling and during the experiments. The formation of the trapezoidal flow pattern is regarded as a key element for EHDF. In other approaches presented in Chapter 2 either specific geometry or multiple electrodes were employed to achieve electric field gradient. Application of a flowstream with adaptable cross-section and thus adjusting the electric field parameters using only two electrodes has not been published previously.

The third research hypothesis was verified positively. The focusing of the test compound was observed during the modelling stage and in the experiments on EHDF. The performance of the developed chip exceeded the numerically predicted values. Also during the experiments, an unexpected behaviour of the focused analyte was observed, named lateral EHDF. The investigation of this mode of EHDF yielded very encouraging results in terms of preconcentration efficiency, simplicity and robustness of the used chip and repeatability. The previously published works on lateral focusing occurred within narrow microfluidic channels and were based on particle-wall electrostatic interaction (257; 261).

The study of the optical properties during the experiments on EHDF led to the development of a numerical model of the light propagation and the light intensity distribution for microfluidic devices – mostly capillaries and chips. The model was successfully verified experimentally, and results were published in (259). The application

of this model was demonstrated in explanation of monolith photopolymerisation in theoretically impossible place.

7.2. Future work

The presented thesis structures research directions for future studies of the electrohydrodynamic focusing. This work should be regarded as the proof of concept of the EHDF and lateral EHDF. There are several objectives that have to be investigated to fully develop EHDF as a laboratory or industrial technique:

- A better control of the velocity gradient. Currently employed method proved to be not efficient enough, although allowed for the observation of the EHDF.
- A higher precision of the chip upper and lower surface flatness is required in order to test thinner gaskets. Suggested tolerance is $\pm 1\mu\text{m}$ for $50\mu\text{m}$ gasket, to have the maximal combined chamber thickness error of 4%.
- Materials harder than PTFE as gaskets could be tested, combined with torque measurement of the supporting screws to minimise the changes in the chamber thickness
- A more robust material than agarose gel should be used to support the electrodes. The deterioration of the agarose gel required its often replacement to minimise the undesired effects
- The electrode housings should not be drilled through the upper chip layer. Only a cavity instead of the hole is suggested to simplify the experimental procedure, reduction of leaks and undesired backflows
- At the current stage only one analyte was focused at the same time. In order to use EHDF in laboratory or industrial scale a focusing of several analytes is required
- A detection system based on a CCD or CMOS matrix should be integrated into one of the chip layers. It is suggested to use the opposite part than the one with fluidic ports.
- LEDs could be integrated in such chip to provide the illumination for the photometric detection
- Lateral EHDF could be used for purification of the solutions focusing all impurities in one flowstream

The EHDF presents novel, interesting method for preconcentration of the analytes. There are several obstacles to overcome but the potential for this technique, especially when automated can be enormous.

References

1. **Tabeling, P.** *Introduction to Microfluidics*. Oxford : Oxford University Press, 2006. ISBN 0-19-856864-9 978.
2. **Wilkes, J. O.** *Fluid Mechanics for Chemical Engineers*. Upper Saddle River : Prentice Hall PTR, 2006. ISBN: 0-13-148212-2.
3. **Li, D., [ed.]**. *Encyclopedia of Microfluidics and Nanofluidics*. New York : Springer Science+Business Media LLC., 2008. ISBN: 978-0-387-489998-8.
4. **Bruus, H.** *Theoretical Microfluidics*. Oxford : Oxford University Press, 2008. ISBN 978-0-19-923-509-4.
5. *Several new electrofocusing techniques*. **Ivory, C. F.** 1-2, 2007, ELECTROPHORESIS, Vol. 28, pp. 15-25.
6. *Solid-phase trapping of solutes for further chromatographic or electrophoretic analysis*. **Fritz, J. S., Macka, M.** 1, 2000, JOURNAL OF CHROMATOGRAPHY A, Vol. 902, pp. 137-166.
7. *Sample preconcentration in microfluidic devices* . **Lin, C. C., Hsu, J. L., Lee, G. B.** 3, 2011, MICROFLUIDICS AND NANOFUIDICS, Vol. 10, pp. 481-511.
8. *Conductivity Gradient Focusing*. **Potter, O. G. Guijt, R. M. Corney, S. Haddad, P. R. Macka, M.** Malmö, Sweden : s.n., 26-30 September 2004. Proceedings of Conference on Micro Total Analysis Systems. pp. 81-83. ISBN 0-85404-643-7.
9. *Eigenmobilities in background electrolytes for capillary zone electrophoresis: IV. Computer program PeakMaster*. **Jaros, M., Hruska, V., Stedry, M., Zuskova, I., Gas, B.** 18-19, 2004, ELECTROPHORESIS, Vol. 25, pp. 3080-3085.
10. *Simul 5 - Free dynamic simulator of electrophoresis*. **Hruska, V., Jaros, M., Gas, B.** 5-6, 2006, ELECTROPHORESIS, Vol. 27, pp. 984-991.
11. *Solid-state lighting - a benevolent technology*. **Schubert, E. F., Kim, J. K., Luo, H., Xi, J. Q.** 12, 2006, REPORTS ON PROGRESS IN PHYSICS, Vol. 69, pp. 3069-3099.
12. *Status and future of high-power light-emitting diodes for solid-state lighting*. **Krames, M. R., Shchekin, O. B., Mueller-Mach, R., Mueller, G. O., Zhou, L., Harbers, G., Craford, M. G.** 2, 2007, JOURNAL OF DISPLAY TECHNOLOGY, Vol. 3, pp. 160-175.
13. *Absorbance based light emitting diode optical sensors and sensing devices*. **O'Toole, M., Diamond, D.** 4, 2008, SENSORS, Vol. 8, pp. 2453-2479.

14. *History, development, and applications of high-brightness visible light-emitting diodes.* **Dupuis, R. D., Krames, M. R.** 9-12, 2008, JOURNAL OF LIGHTWAVE TECHNOLOGY, Vol. 26, pp. 1154-1171.
15. *Flow of multiple fluids in a small dimension.* **Dasgupta, P. K., Surowiec, K., Berg, J.** 7, 2002, ANALYTICAL CHEMISTRY, Vol. 74, pp. 208A-213A.
16. *Gas-Chromatographic Air Analyzer Fabricated on a Silicon-Wafer.* **Terry, S. C., Jerman, J. H. and Angell, J. B.** 12, 1979, IEEE TRANSACTIONS ON ELECTRON DEVICES, Vol. 26, pp. 1880-1886.
17. *Portable gas chromatograph with tunable retention and sensor array detection for determination of complex vapor mixtures.* **Lu, C. J., Whiting, J. and Zellers, E. T.** 6, 2003, ANALYTICAL CHEMISTRY, Vol. 75, pp. 1400-1409.
18. *Hand-Portable Gas Chromatograph-Toroidal Ion Trap Mass Spectrometer (GC-TMS) for Detection of Hazardous Compounds.* **Contreras, J. A., et al., et al.** 10, 2008, JOURNAL OF THE AMERICAN SOCIETY FOR MASS SPECTROMETRY, Vol. 19, pp. 1425-1434.
19. *Micro Total Analysis Systems. 1. Introduction, Theory, and Technology.* **Reyes, D. R., Iossifidis, D., Auroux, P. A. Manz, A.** 12, 2002, ANALYTICAL CHEMISTRY, Vol. 74, pp. 2623-2636.
20. *Engineering flows in small devices: Microfluidics toward a lab-on-a-chip.* **Stone, H. A., Stroock, A. D., Ajdari, A.** 2004, ANNUAL REVIEW OF FLUID MECHANICS, Vol. 36, pp. 381-411.
21. *The fluid mechanics of microdevices - The Freeman Scholar Lecture.* **Gad-el-Hak, M.** 1, 1999, JOURNAL OF FLUIDS ENGINEERING-TRANSACTIONS OF THE ASME, Vol. 121, pp. 5-33.
22. *Flow Transport in Plants.* **Canny, M. J.** 1977, ANNUAL REVIEW OF FLUID MECHANICS, Vol. 9, pp. 275-296.
23. *Miniaturized Total Chemical-Analysis Systems - A Novel Concept For Chemical Sensing.* **Manz, A., Graber, N., Widmer, H. M.** 1-6, 1990, SENSORS AND ACTUATORS B-CHEMICAL, Vol. 1, pp. 244-248.
24. *Micro total analysis systems: Latest achievements.* **West, J., Becker, M., Tombrink, S., Manz, A.** 12, 2008, ANALYTICAL CHEMISTRY, Vol. 80, pp. 4403-4419.
25. *Electroosmotic Pumping Within a Chemical Sensor System Integrated on Silicon.* **Harrison, D. J., Manz, A., Glavina, P. G.** San Francisco, CA , USA : s.n., 24-27 Jun 1991 . Solid-State Sensors and Actuators, 1991. Digest of Technical Papers, TRANSDUCERS '91., 1991 International Conference on . pp. 792 - 795.

26. *Integrated Electroosmotic Pumps and Flow Manifolds for Total Chemical Analysis Systems.* **Manz, A., Harrison, D. J., Fettingner, J. C., Verpoorte, E., Ludi, H., Widmer, H. M.** San Francisco, CA , USA : s.n., 24 - 27 Jun 1991. Solid-State Sensors and Actuators, 1991. Digest of Technical Papers, TRANSDUCERS '91., 1991 International Conference on. pp. 939 - 941.
27. *Planar Chips Technology for Miniaturization and Integration of Separation Techniques into Monitoring Systems - Capillary Electrophoresis on a Chip.* **Manz, A., Harrison, D. J., Verpoorte E. M. J., Fettingner, J. C., Paulus, A., Ludi, H., Widmer, H. M.** 1-2, 1992, JOURNAL OF CHROMATOGRAPHY, Vol. 593, pp. 253-258.
28. *Capillary Electrophoresis and Sample Injection Systems Integrated on a Planar Glass Chip.* **Harrison, D. J., Manz, A., Fan, Z. H., Ludi, H., Widmer, H. M.** 17, 1992, ANALYTICAL CHEMISTRY, Vol. 64, pp. 1926-1932.
29. *The origins and the future of microfluidics.* **Whitesides, G. M.** 7101, 2006, NATURE, Vol. 442, pp. 368-373.
30. *Patterning Self-Assembled Monolayers Using Microcontact Printing - a New Technology for Biosensors.* **Mrksich, M., Whitesides, G. M.** 6, 1995, TRENDS IN BIOTECHNOLOGY, Vol. 13, pp. 228-235.
31. *Fabrication of three-dimensional micro-structures: Microtransfer molding.* **Zhao, X. M., Xia, Y. N., Whitesides, G. M.** 10, 1996, ADVANCED MATERIALS, Vol. 8, pp. 837-&.
32. *Low temperature bonding for microfabrication of chemical analysis devices.* **Wang, H. Y., Foote, R. S., Jacobson, S. C., Schneibel, J. H., Ramsey J. M.** 3, 1997, Sensors and Actuators B: Chemical, Vol. 45, pp. 199-207.
33. *SU-8: a low-cost negative resist for MEMS.* **Lorenz, H., Despont, M., Fahrni, N., LaBianca, N., Renaud, P., Vettiger, P.** 3, 1997, Journal of Micromechanics and Microengineering, Vol. 7, pp. 121-124.
34. *Simple and low cost fabrication of embedded micro-channels by using a new thick-film photoplastic.* **Guerin, L. J., Bossel, M., Demierre, M., Calmes, S., Renaud, P.** Chicago, IL, USA : s.n., 16-19 June 1997. Solid State Sensors and Actuators, 1997. TRANSDUCERS '97 Chicago., 1997 International Conference on. Vol. 2, pp. 1419 - 1422.
35. *Features of Gold Having Micrometer to Centimeter Dimensions can be Formed Through a Combination of Stamping with an Elastomeric Stamp and an Alkanethiol Ink Followed by Chemical Etching.* **Kumar, A., Whitesides, G. M.** 14, 1993, APPLIED PHYSICS LETTERS, Vol. 63, pp. 2002-2004.

36. *Fabrication of microfluidic systems in poly(dimethylsiloxane)*. **McDonald, J. C., Duffy, D. C., Anderson, J. R., Chiu, D. T., Wu, H. K., Schueller, O. J. A., Whitesides, G. M.** 1, 2000, ELECTROPHORESIS, Vol. 21, pp. 27-40.
37. *Rapid prototyping of microfluidic systems in poly(dimethylsiloxane)*. **Duffy, D. C., McDonald, J. C., Schueller, O. J. A., Whitesides, G. M.** 23, 1998, ANALYTICAL CHEMISTRY, Vol. 70, pp. 4974-4984.
38. *Microfluidic large-scale integration*. **Thorsen, T., Maerkl, S. J., Quake, S. R.** 298, 2002, SCIENCE, Vol. 5593, pp. 580-584.
39. *Lab-on-a-chip: microfluidics in drug discovery*. **Dittrich, P. S., Manz, A.** 3, 2006, NATURE REVIEWS DRUG DISCOVERY, Vol. 5, pp. 210-218.
40. **Publishing, RSC.** About Lab on a Chip. *Royal Society of Chemistry*. [Online] 2001. [Cited: 9 March 2011.] <http://www.rsc.org/Publishing/Journals/LC/about.asp>.
41. **Bird, R. B., Stewart, W. E., Lightfoot, E. N.** *Transport phenomena*. Yew York/ Chichester/ Weinheim/ Brisbane/ Singapore/ Toronto : Johny Wiley & Sons, Inc., 2002. ISBN: 0-471-36474-6.
42. *Scaling and the design of miniaturized chemical-analysis systems*. **Janasek, D., Franzke, J., Manz, A.** 7101, 2006, NATURE, pp. 374-380.
43. Lennard-Jones-Potential. *Academic dictionaries and encyclopedias*. [Online] [Cited: 10 3 2011.] <http://de.academic.ru/dic.nsf/dewiki/840173>.
44. *Microfluidics: Fluid physics at the nanoliter scale*. **Squires, T. M., Quake, S. R.** 3, 2005, REVIEWS OF MODERN PHYSICS, Vol. 77, pp. 977-1026.
45. *Biotechnology at low Reynolds numbers*. **Brody, J. P., Yager, P., Goldstein, R. E., Austin, R. H.** 6, 1996, BIOPHYSICAL JOURNAL, Vol. 71, pp. Source: BIOPHYSICAL JOURNAL Volume: 71 Issue: 6 Pages: 3430-3441 Published: DEC 1996 .
46. **Jaworski, B. M., Dietlaf, A. A.** *Fizyka poradnik encyklopedyczny*. [trans.] W. Skubiszak, L. Komar. Warszawa : Wydawnictwo Naukowe PWN, 1995. ISBN 83-01-11858-X.
47. *Chaotic mixer for microchannels*. **Stroock, A. D., Dertinger, S. K. W., Ajdari, A., Mezic, I., Stone, H. A., Whitesides, G. M.** 5555, 2002, SCIENCE, Vol. 295, pp. 647-651.
48. *A Microfabricated Rotary Pump*. **Chou, H. P., Unger, M., Quake, S. R.** 4, 2001, Biomedical Microdevices, Vol. 3, pp. 323-330.
49. *Microfluidics: Honey, I shrunk the lab*. **Knight, J.** 6897, 2002, NATURE, Vol. 418, pp. 474-475.

50. *Single-molecule fluorescence detection in microfluidic channels-the Holy Grail in mu TAS?* **Dittrich, P., Manz, A.** 8, 2005, ANALYTICAL AND BIOANALYTICAL CHEMISTRY, Vol. 382, pp. 1771-1782.
51. *Microfluidics-based systems biology.* **Breslauer, D. N., Lee, P. J., Lee, L. P.** 2, 2006, MOLECULAR BIOSYSTEMS, Vol. 2, pp. 97-112.
52. *Micro Total Analysis Systems. Recent Developments.* **Vilkner, T., Janasek, D., Manz, A.** 12, 2004, ANALYTICAL CHEMISTRY, Vol. 76, pp. 3373-3386.
53. *Micro Total Analysis Systems. 2. Analytical Standard Operations and Applications.* **Auroux, P. A., Iossifidis, D., Reyes, D. R., Manz, A.** 12, 2002, ANALYTICAL CHEMISTRY, Vol. 74, pp. 2637-2652.
54. *DNA amplification in a microfabricated reaction chamber.* **Northrup, M. A., Ching, M. T., White, R. M., and Watson, R. T.** Yokohama : s.n., 7-10 June 1993. Transducers '93, Seventh International Conference on Solid Sensors and Actuators. pp. 924-927.
55. *Micromachined Multichannel Systems for the Measurement of Cellular Metabolism.* **Bousse, L., McReynolds, R. J., Kirk, G., Dawes, T., Lam, P., Bemiss, W. R., Parce, J. W.** Yokohama, Japan : s.n., 7 - 10 June 1993. Transducers '93, Seventh International Conference on Solid Sensors and Actuators. pp. 916-919.
56. *A microfabricated flow chamber for optical measurements in fluids.* **Sobek, D., Young, A. M., Gray, M. L., Senturia, S. D.** Fort Lauderdale, FL, USA : s.n., 7-10 Feb 1993. Micro Electro Mechanical Systems, 1993, MEMS '93, Proceedings An Investigation of Micro Structures, Sensors, Actuators, Machines and Systems. IEEE. pp. 219 - 224.
57. *Microchip Separations of Neutral Species via Micellar Electrokinetic Capillary Chromatography.* **Moore, A. W., Jacobson, S. C., Ramsey, J. M.** 22, 1995, ANALYTICAL CHEMISTRY, Vol. 67, pp. 4184-4189.
58. *Micellar Electrokinetic Chromatography Separations and Analyses of Biological Samples on a Cyclic Planar Microstructure.* **von Heeren, F., Verpoorte, E., Manz, A., Thormann, W.** 13, 1996, Analytical Chemistry, Vol. 68, pp. 2044–2053.
59. *Continuous Separation of High Molecular Weight Compounds Using a Microliter Volume Free-Flow Electrophoresis Microstructure.* **Raymond, D. E., Manz, A., Widmer, H. M.** 15, 1996, Analytical Chemistry, Vol. 68, pp. 2515–2522.
60. *PDMS free-flow electrophoresis chips with integrated partitioning bars for bubble segregation.* **Kohler, S., Weilbeer, C., Howitz, S., Becker, H., Beushausen, V., Belder, D.,** 2, LAB ON A CHIP, Vol. 11, pp. 309-314.

61. *Characterization of electrophoretic sample injection and separation in a gel-filled cyclic planar microstructure.* **von Heeren, F., Verpoorte, E., Manz, A., Thormann, W.** 6, 1996, *Journal of Microcolumn Separations*, Vol. 8, pp. 373–381.
62. *Characterization of dissolved organic carbon at low levels in environmental waters by microfluidic-chip-based capillary gel electrophoresis with a laser-induced fluorescence detector.* **Shen, S. L., Li, Y., Wakida, S.** 1-4, 2010, *ENVIRONMENTAL MONITORING AND ASSESSMENT*, Vol. 166, pp. 573-580.
63. *Functional integration of PCR amplification and capillary electrophoresis in a microfabricated DNA analysis device.* **Woolley, A. T., Hadley, D., Landre, P., deMello, A. J., Mathies, R. A., Northrup, M. A.** 23, 1996, *ANALYTICAL CHEMISTRY*, Vol. 68, pp. 4081-4086.
64. *Chip PCR .1. Surface passivation of microfabricated silicon-glass chips for PCR.* **Shoffner, M. A., Cheng, J., Hvichia, G. E., Kricka, L. J., Wilding, P.** 2, 1996, *NUCLEIC ACIDS RESEARCH*, Vol. 24, pp. 375-379.
65. *Chip PCR .2. Investigation of different PCR amplification systems in microfabricated silicon-glass chips.* **Cheng, J., Shoffner, M. A., Hvichia, G. E., Kricka, L. J., Wilding, P.** 2, 1996, *NUCLEIC ACIDS RESEARCH*, Vol. 24, pp. 380-385.
66. *Microchip electrophoretic immunoassay for serum cortisol.* **Koutny, L. B., Schmalzing, D., Taylor, T. A., Fuchs, M.** 1, 1996, *ANALYTICAL CHEMISTRY*, Vol. 68, pp. 18-22.
67. *Microfabrication of a planar absorbance and fluorescence cell for integrated capillary electrophoresis devices.* **Liang, Z. H., Chiem, N., Ocvirk, G., Tang, T., Fluri, K., Harrison, D. J.** 6, 1996, *ANALYTICAL CHEMISTRY*, Vol. 68, pp. 1040-1046.
68. *A microfabricated, electrochemiluminescence cell for the detection of amplified DNA.* **Hsueh, Y. T., Smith, R. L., Northrup, M. A.** 1-3, 1996, *SENSORS AND ACTUATORS B-CHEMICAL*, Vol. 33, pp. 110-114.
69. *Sub-microliter electrochemiluminescence detector - A model for small volume analysis systems.* **Arora, A., de Mello, A. J., Manz, A.** 12, 1997, *ANALYTICAL COMMUNICATIONS*, Vol. 34, pp. 393-395.
70. *Microchip Coulter particle counter.* **Larsen, U. D., Blankenstein, G., Branebjerg, J.** Chicago, IL , USA : s.n. *Solid State Sensors and Actuators*, 1997. *TRANSDUCERS '97 Chicago.*, 1997 International Conference on . Vol. 2, pp. 1319 - 1322.
71. *Lysing bacterial spores by sonication through a flexible interface in a microfluidic system.* **Taylor, M. T., Belgrader, P., Furman, B. J., Pourahmadi, F., Kovacs, G. T. A., Northrup, M. A.** 3, 2001, *ANALYTICAL CHEMISTRY*, Vol. 73, pp. 492-496.

72. *Extraction of nucleic acids from bacterial spores using bead-based mechanical lysis on a plastic chip.* Geissler, M., Beauregard, J. A., Charlebois, I., Isabel, S., Normandin, F., Voisin, B., Boissinot, M., Bergeron, M. G., Veres, T. 2, 2011, ENGINEERING IN LIFE SCIENCES, Vol. 11, pp. 174-181.
73. *A degassing plate with hydrophobic bubble capture and distributed venting for microfluidic devices.* Meng, D. D. S., Kim, J., Kim, C. J. 2, 2006, JOURNAL OF MICROMECHANICS AND MICROENGINEERING, Vol. 16, pp. 419-424.
74. *A membrane-based, high-efficiency, microfluidic debubbler.* Liu, C. C., Thompson, J. A., Bau, H. H. 9, 2011, LAB ON A CHIP, Vol. 11, pp. 1688-1693.
75. *Sub-second isoelectric focusing in free flow using a microfluidic device.* Xu, Y., Zhang, C. X., Janasek, D., Manz, A. 4, 2003, LAB ON A CHIP, Vol. 3, pp. 224-227.
76. *Microfluidic preparative free-flow isoelectric focusing in a triangular channel: System development and characterization.* Wen, J. A., Albrecht, J. W., Jensen, K. F. 10, 2010, ELECTROPHORESIS, Vol. 31, pp. 1606-1614.
77. *Microchip-based purification of DNA from biological samples.* Breadmore, M. C., Wolfe, K. A., Arcibal, I. G., Leung, W. K., Dickson, D., Giordano, B. C., Power, M. E., Ferrance, J. P., Feldman, S. H., Norris, P. M., Landers, J. P. 8, 2003, ANALYTICAL CHEMISTRY, Vol. 75, pp. 1880-1886.
78. *Rapid detection of bacterial cell from whole blood: Integration of DNA sample preparation into single micro-PCR chip.* Hwang, K. Y., Jeong, S. Y., Kim, Y. R., Namkoong, K., Lim, H. K., Chung, W. S., Kim, J. H., Huh, N. 1, 2011, SENSORS AND ACTUATORS B-CHEMICAL, Vol. 154, pp. 46-51.
79. *Microfluidic electrophoresis chip coupled to microdialysis for in vivo monitoring of amino acid neurotransmitters.* Sandlin, Z. D., Shou, M. S., Shackman, J. G., Kennedy, R. T. 23, 2005, ANALYTICAL CHEMISTRY, Vol. 77, pp. 7702-7708.
80. *Development of a PDMS-based microchip electrophoresis device for continuous online in vivo monitoring of microdialysis samples.* Nandi, P., Desaias, D. P., Lunte, S. M. 8, 2010, ELECTROPHORESIS, Vol. 31, pp. 1414-1422.
81. *Microfluidic separation of (S)-ibuprofen using enzymatic reaction.* Huh, Y. S., Jun, Y. S., Hong, Y. K., Hong, W. K., Kim, D. H. 1-4, 2006, JOURNAL OF MOLECULAR CATALYSIS B-ENZYMATIC, Vol. 43, pp. 96-101.

82. *On-Chip Drop-to-Drop Liquid Microextraction Coupled with Real-Time Concentration Monitoring Technique.* **Wijethunga, P. A. L., Nanayakkara, Y. S., Kunchala, P., Armstrong, D. W., Moon, H.** 5, 2011, ANALYTICAL CHEMISTRY, Vol. 83, pp. 1658-1664.
83. *Integrated sample preparation and MALDI mass spectrometry on a microfluidic compact disk.* **Gustafsson, M., Hirschberg, D., Palmberg, C., Jorndal, H., Bergman, T.** 2, 2004, ANALYTICAL CHEMISTRY, Vol. 76, pp. 345-350.
84. *Integrated microfluidic device for solid-phase extraction coupled to micellar electrokinetic chromatography separation.* **Ramsey, J. D., Collins, G. E.** 20, 2005, ANALYTICAL CHEMISTRY, Vol. 77, pp. 6664-6670.
85. *A simple, valveless microfluidic sample preparation device for extraction and amplification of DNA from nanoliter-volume samples.* **Legendre, L. A., Bienvenue, J. M., Roper, M. G., Ferrance, J. P., Landers, J. P.** 5, 2006, ANALYTICAL CHEMISTRY, Vol. 78, pp. 1444-1451.
86. *Development of PCR Microchip for Early Cancer Risk Prediction.* **Jha, S. K., Joo, G. S., Ra, G. S., Lee, H. H., Kim, Y. S.** 9, 2011, IEEE SENSORS JOURNAL, Vol. 11, pp. 2065-2070.
87. *A fully integrated microfluidic genetic analysis system with sample-in-answer-out capability.* **Easley, C. J., Karlinsey, J. M., Bienvenue, J. M., Legendre, L. A., Roper, M. G., Feldman, S. H., Hughes, M. A., Hewlett, E. L., Merkel, T. J., Ferrance, J. P., Landers, J. P.** 51, 2006, PROCEEDINGS OF THE NATIONAL ACADEMY OF SCIENCES OF THE UNITED STATES OF AMERICA, Vol. 103, pp. 19272-19277.
88. *A nanoliter-scale nucleic acid processor with parallel architecture.* **Hong, J. W., Studer, V., Hang, G., Anderson, W. F., Quake, S. R.** 4, 2004, NATURE BIOTECHNOLOGY, Vol. 22, pp. 435-439.
89. *A magnetic bead-based DNA extraction and purification microfluidic device.* **Azimi, S. M., Nixon, G., Ahern, J., Balachandran, W.** 2, 2011, MICROFLUIDICS AND NANOFUIDICS, Vol. 11, pp. 157-165.
90. *Single DNA molecule isolation and trapping in a microfluidic device.* **Kumemura, M., Collard, D., Yamahata, C., Sakaki, N., Hashiguchi, G., Fujita, H.** 12, 2007, CHEMPHYSICHEM, Vol. 8, pp. 1875-1880.
91. *Decoding Circulating Nucleic Acids in Human Serum Using Microfluidic Single Molecule Spectroscopy.* **Liu, K. J., Brock, M. V., Shin, L. M., Wang, T. H.** 6, 2010, JOURNAL OF THE AMERICAN CHEMICAL SOCIETY, Vol. 132, pp. 5793-5798.
92. *Emerging technologies in DNA sequencing.* **Metzker, M. L.** 12, 2005, GENOME RESEARCH, Vol. 15, pp. 1767-1776.

93. *Picoliter DNA sequencing chemistry on an electrowetting-based digital microfluidic platform.* **Welch, E. R. F., Lin, Y. Y., Madison, A., Fair, R. B.** 2, 2011, BIOTECHNOLOGY JOURNAL, Vol. 6, pp. 165-176.
94. *Microfluidic devices fabricated in poly(dimethylsiloxane) for biological studies.* **Sia, S. K., Whitesides, G. M.** 21, 2003, ELECTROPHORESIS, Vol. 24, pp. 3563-3576.
95. *Non-ionic, thermo-responsive DEA/DMA nanogels: Synthesis, characterization, and use for DNA separations by microchip electrophoresis.* **Lu, X. H., Sun, M. Y., Barron, A. E.** 2, 2011, JOURNAL OF COLLOID AND INTERFACE SCIENCE, Vol. 357, pp. 345-353.
96. *Microfluidic chips for clinical and forensic analysis.* **Verpoorte, E.** 5, 2002, ELECTROPHORESIS, Vol. 23, pp. 677-71.
97. *A multilevel Lab on chip platform for DNA analysis.* **Marasso, S. L., Giuri, E., Canavese, G., Castagna, R., Quaglio, M., Ferrante, I., Perrone, D., Cocuzza, M.** 1, 2011, BIOMEDICAL MICRODEVICES, Vol. 13, pp. 19-27.
98. *Integrated microfluidic devices.* **Erickson, D., Li, D. Q.** 1, 2004, ANALYTICA CHIMICA ACTA, Vol. 507, pp. 11-26.
99. *Whole gene amplification and protein separation from a few cells.* **Chueh, B. H., Li, C. W., Wu, H. L., Davison, M., Wei, H. B., Bhaya, D., Zare, R. N.,** 1, 2011, ANALYTICAL BIOCHEMISTRY, Vol. 411, pp. 64-70.
100. *A multifunctional micro-fluidic system for dielectrophoretic concentration coupled with immuno-capture of low numbers of Listeria monocytogenes.* **Yang, L. J., Banada, P. P., Chatni, M. R., Lim, K. S., Bhunia, A. K., Ladisch, M., Bashir, R.** 7, 2006, LAB ON A CHIP, Vol. 6, pp. 896-905.
101. *High-Throughput Selection, Enumeration, Electrokinetic Manipulation, and Molecular Profiling of Low-Abundance Circulating Tumor Cells Using a Microfluidic System.* **Dharmasiri, U., Njoroge, S. K., Witek, M. A., Adebisi, M. G., Kamande, J. W., Hupert, M. L., Barany, F., Soper, S. A.** 6, 2011, ANALYTICAL CHEMISTRY, Vol. 83, pp. 2301-2309.
102. *Self-contained, fully integrated biochip for sample preparation, polymerase chain reaction amplification, and DNA microarray detection.* **Liu, R. H., Yang, J. N., Lenigk, R., Bonnano, J., Grodzinski, P.** 7, 2004, ANALYTICAL CHEMISTRY, Vol. 76, pp. 1824-1831.
103. *Study of a novel cell lysis method with titanium dioxide for Lab-on-a-Chip devices.* **Wan, W. J., Yeow, J. T. W.** 3, 2011, BIOMEDICAL MICRODEVICES, Vol. 13, pp. 527-532.

104. *Analysis of single mammalian cells on-chip*. **Sims, C. E., Allbritton, N. L.** 4, 2007, LAB ON A CHIP, Vol. 7, pp. 423-440.
105. *High-content screening of drug-induced cardiotoxicity using quantitative single cell imaging cytometry on microfluidic device*. **Kim, M. J., Lee, S. C., Pal, S., Han, E., Song, J. M.** 1, 2011, LAB ON A CHIP, Vol. 11, pp. 104-114.
106. *Isolation of rare circulating tumour cells in cancer patients by microchip technology*. **Nagrath, S., Sequist, L. V., Maheswaran, S., Bell, D. W., Irimia, D., Ulkus, L., Smith, M. R., Kwak, E. L., Digumarthy, S., Muzikansky, A., Ryan, P., Balis, U. J., Tompkins, R. G., Haber, D. A., Toner, M.** 7173, 2007, NATURE, Vol. 450, pp. 1235-U10.
107. *Microfluidics for T-Lymphocyte Cell Separation and Inflammation Monitoring in Burn Patients*. **Rosenbach, A. E., Korias, P., Goverman, J., Kotz, K. T., Gupta, A., Yu, M., Fagan, S. P., Irimia, D., Tompkins, R. G.** 1, 2011, CTS-CLINICAL AND TRANSLATIONAL SCIENCE, Vol. 4, pp. 63-68.
108. *Microfabricated electrophoresis chip for bioassay of renal markers*. **Wang, J., Chatrathi, M. P.** 3, 2003, ANALYTICAL CHEMISTRY, Vol. 75, pp. 525-529.
109. *Development of healthcare chips checking life-style-related diseases*. **Oki A, Ogawa, H., Nagai, M., Shinbashi, S., Takai, M., Yokogawa, A., Horiike, Y.** 6-8, 2004, MATERIALS SCIENCE & ENGINEERING C-BIOMIMETIC AND SUPRAMOLECULAR SYSTEMS, Vol. 24, pp. 837-843.
110. *Microfluidic tectonics platform: A colorimetric, disposable botulinum toxin enzyme-linked immunosorbent assay system*. **Moorthy, J., Mensing, G. A., Kim, D., Mohanty, S., Eddington, D. T., Tepp, W. H., Johnson, E. A., Beebe, D. J.** 10-11, 2004, ELECTROPHORESIS, Vol. 25, pp. 1705-1713.
111. *Microdroplets: A sea of applications?* **Huebner, A., Sharma, S., Srisa-Art, M., Hollfelder, F., Edel, J. B., Demello, A. J.** 8, 2008, LAB ON A CHIP, Vol. 8, pp. 1244-1254.
112. **Giddings, J. C.** *Unified separation science*. New York/ Chichester/ Brisbane/ Toronto/ Singapore : John Wiley & Sons, Inc., 1991. ISBN 0-471-52089-6.
113. *O novoy kategorii adsorbtsionnykh yavleniy i o primenenii ikh k biokhimicheskomu analizu*. **Tsvet, M. S.** 6, 1905, Trudy Varhavskago Obshchestva Estestvoispytatelei, Otdelenie Biologii, Vol. 14, pp. 20-39.
114. *On-line sample preconcentration in capillary electrophoresis Fundamentals and applications*. **Simpson, S. L., Quirino, J. P., Terabe, S.** 1-2, 2008, JOURNAL OF CHROMATOGRAPHY A, Vol. 1184, pp. 504-541.

115. *Recent advances in enhancing the sensitivity of electrophoresis and electrochromatography in capillaries and microchips.* **Breadmore, M. C.** 1-2, 2007, ELECTROPHORESIS, Vol. 28, pp. 254-281.
116. **Fick, A.** 59, Leipzig : s.n., 1855, Ann. Phys., Vol. 170.
117. **Bronsztejn, I. N., Siemiendiajew, K .A.** *Matematyka, Poradnik Encyklopedyczny.* 14th. Warszawa : Wydawnictwo Naukowe PWN, 1997. ISBN 83-01-11658-7.
118. *Several new electrofocusing techniques.* **Ivory, C. F.** 1-2, 2007, ELECTROPHORESIS, Vol. 28, pp. 15-25.
119. **Meloan, C. E.** *Chemical separations. Principles, techniques and experiments.* New York/ Chichester/ Brisbane/ Singapore/ Toronto : John Wiley & Sons, 1999. ISBN: 0-471-35197-0.
120. **Landers, J. P.** *Handbook of capillary electrophoresis.* Boca Raton : CRC Press, 1994. ISBN 0-8493-8690-X.
121. **Camilleri, P., [ed.].** *Capillary electrophoresis. Theory and practice. Second edition.* 2nd. Boca Raton : CRC Press, 1998. ISBN 0-9493-9127-X.
122. *Gradient elution in non-linear preparative liquid-chromatography.* **Antia, F. D., Horvath, C.** 1989, JOURNAL OF CHROMATOGRAPHY, Vol. 484, pp. 1-27.
123. *Focusing proteins in an electric field gradient.* **Koehler, W. S., Ivory, C. F.** 1-2, 1996, JOURNAL OF CHROMATOGRAPHY A, Vol. 726, pp. 229-236.
124. *An agarose-gel resolving a wide-range of DNA fragment lengths.* **Boncinelli, E., Simeone, A., Defalco, A., Fidanza, V., Lavolpe, A.** 1, 1983, ANALYTICAL BIOCHEMISTRY, Vol. 134, pp. 40-43.
125. *Analytical and preparative electrophoresis in a non-uniform electric-field.* **Rolchigo, P. M., Graves, D. J.** 3, 1988, AIChE JOURNAL, Vol. 34, pp. 483-492.
126. **Pohl, H. A.** *Dielectrophoresis: The Behavior of Neutral Matter in Nonuniform Electric Fields.* Cambridge : Cambridge University Press, 1978.
127. *Field gradient focusing: A novel method for protein separation.* **Koehler, W. S., Ivory, C. F.** 6, 1996, BIOTECHNOLOGY PROGRESS, Vol. 12, pp. 822-836.
128. *Separation of yeast chromosome-sized DNAs by pulsed field gradient gel-electrophoresis.* **Schwartz, D. C., Cantor, C. R.** 1, 1984, CELL, Vol. 37, pp. 67-75.
129. *Multiscale phenomena in microfluidics and nanofluidics.* **Hu, G. Q., Li, D. Q.** 13, 2007, CHEMICAL ENGINEERING SCIENCE, Vol. 62.

130. **Ferziger, J. H., Peric, M.** *Computational methods for fluid dynamics*. Berlin/ Heidelberg/ New York : Springer, 2002. ISBN: 3-540-42074-6.
131. *Recent advances in computational simulation of macro-, meso-, and micro-scale biomimetics related fluid flow problems*. **Yan, Y. Y.** 2, 2007, JOURNAL OF BIONIC ENGINEERING, Vol. 4, pp. 97-107.
132. *An early history of the molecular modeling industry*. **Richon, A. B.** 15-16, 2008, DRUG DISCOVERY TODAY, Vol. 13, pp. 659-664.
133. **Akai, T. J.** *Applied numerical methods for engineers*. New York/ Chichester/ Brisbane/ Singapore/ Toronto : John Wiley & Sons, 1994. ISBN: 0-471-57523-2.
134. CFD-ACE+ Fluid dynamics package. *ESI*. [Online] [Cited: 30 March 2011.] <http://www.esi-group.com/products/Fluid-Dynamics/cfd-ace>.
135. ANSYS Products. *ANSYS*. [Online] ANSYS. [Cited: 30 March 2011.] <http://www.ansys.com/products/fluid-dynamics/cfx/>.
136. FLOW-3D - CFD Software. *FLOWScience*. [Online] [Cited: March 30 2011.] <http://www.flow3d.com/>.
137. COMSOL. *COMSOL*. [Online] [Cited: 30 March 2011.] <http://www.comsol.com/>.
138. *Towards numerical prototyping of labs-on-chip: modeling for integrated microfluidic devices*. **Erickson, D.** 4, 2005, MICROFLUIDICS AND NANOFUIDICS, Vol. 1, pp. 301-318.
139. **von Smoluchowski, M.** 1903, Bulletin International de L'Académie des Science de Cracovie, Vol. 184.
140. *Oscillating electrolytes*. **Hruska, V., Jaros, M., Gas, B.** 3, 2006, ELECTROPHORESIS, Vol. 27, pp. 513-518. Special Issue.
141. *Electrophoresis - mathematical-modeling and computer-simulation*. **Bier, M., Palusinski, O. A., Mosher, R. A., Saville, D. A.** 4590, 1983, SCIENCE, Vol. 219, pp. 1281-1287.
142. *Electrophoretic transport-equations - electrophoretic models based on migration only and their interrelationships*. **Thormann, W., Mosher R. A.** 9, 1985, ELECTROPHORESIS, Vol. 6, pp. 413-418.
143. *Theory of electrophoretic separations .1. Formulation of a mathematical-model*. **Saville, D. A., Palusinski, O. A.** 2, 1986, AIChE JOURNAL, Vol. 32, pp. 207-214.

144. *Theory of electrophoretic separations .2. Construction of a numerical-simulation scheme and its applications.* **Palusinski, O. A., Graham, A., Mosher, R. A., Saville, D. A.** 2, 1986, AICHE JOURNAL, Vol. 32, pp. 215-223.
145. *Computer-simulation and experimental validation of the electrophoretic behavior of proteins.* **Mosher, R. A., Dewey, D., Thormann, W., Saville, D. A., Bier, M.** 4, 1989, ANALYTICAL CHEMISTRY, Vol. 61, pp. 362-366.
146. *Wall adsorption in capillary electrophoresis - experimental study and computer-simulation.* **Ermakov, S. V., Zhukov, M. Y., Capelli, L., Righetti, P. G.** 1-2, 1995, JOURNAL OF CHROMATOGRAPHY A , Vol. 699, pp. 297-313.
147. *Computer simulations of electrokinetic transport in microfabricated channel structures.* **Ermakov, S. V., Jacobson, S. C., Ramsey, J. M.** 21, 1998, ANALYTICAL CHEMISTRY, Vol. 70, pp. 4494-4504.
148. *Isotachophoresis at pH extremes: Theory and experimental validation.* **Ermakov, S. V., Zhukov, M. Y., Capelli, L., Righetti, P. G.** 2, 1998, ELECTROPHORESIS, Vol. 19, pp. 192-205.
149. *Axial temperature effects in electromigration.* **Gas, B.** 1, 1993, JOURNAL OF CHROMATOGRAPHY, Vol. 644, pp. 161-174.
150. *Dynamics of peak dispersion in capillary zone electrophoresis including wall adsorption .1. Theoretical-model and results of simulation.* **Gas, B., Stedry, M., Rizzi, A., Kenndler, E.** 6, 1995, ELECTROPHORESIS, Vol. 16, pp. 958-967.
151. *Transient modelling of capillary electrophoresis Isotachophoresis.* **Martens, J. H. P. A., Reijenga, J. C., Boonkamp, J. H. M. T., Mattheij, R. M. M., Everaerts, F. M.** 1-2, 1997, JOURNAL OF CHROMATOGRAPHY A, Vol. 772, pp. 49-62.
152. *Microchannel protein separation by electric field gradient focusing.* **Petsev, D. N., Lopez, G. P., Ivory, C. F., Sibbett, S. S.** 6, 2005, LAB ON A CHIP, Vol. 5, pp. 587-597.
153. *Modeling and simulation of IEF in 2-D microgeometries.* **Shim, J., Dutta, P., Ivory, C. F.** 4, 2007, ELECTROPHORESIS, Vol. 28, pp. 572-586.
154. *Assessing the scalability of dynamic field gradient focusing by linear modeling.* **Tracy, N. I., Ivory, C. F.** 2, 2008, JOURNAL OF SEPARATION SCIENCE, Vol. 31, pp. 341-352.
155. *Design and construction of a preparative-scale dynamic field gradient focusing apparatus.* **Tracy, N. I., Huang, Z., Ivory, C. F.** 2, 2008, BIOTECHNOLOGY PROGRESS, Vol. 24, pp. 444-451.

156. *Engineering MEMS resonators with low thermoelastic damping.* **Duwel, A., Candler, R. N., Kenny, T. W., Varghese, M.** 6, 2008, JOURNAL OF MICROELECTROMECHANICAL SYSTEMS, Vol. 15, pp. 1437-1445.
157. *Numerical solution of critical state in superconductivity by finite element software.* **Hong, Z., Campbell, A. M., Coombs, T. A.** 12, 2006, SUPERCONDUCTOR SCIENCE & TECHNOLOGY, Vol. 19, pp. 1246-1252.
158. *Mathematical modeling of laser lipolysis.* **Mordon, S. R., Wassmer, B., Reynaud, J. P., Zemmouri, J.** 2008, BIOMEDICAL ENGINEERING ONLINE, Vol. 7. Article Number: 10.
159. *Simulations of heat and oxygen diffusion in UO₂ nuclear fuel rods.* **Ramirez, J. C., Stan, M., Cristea, P.** 3, 2006, JOURNAL OF NUCLEAR MATERIALS, Vol. 359, pp. 174-184.
160. *Electrokinetic fluid control in two-dimensional planar microfluidic devices.* **Lerch, M. A., Jacobson, S. C.** 19, 2007, ANALYTICAL CHEMISTRY, Vol. 79, pp. 7485-7491.
161. *10 000-fold concentration increase in proteins in a cascade microchip using anionic ITP by a 3-D numerical simulation with experimental results.* **Bottenus, D., Jubery, T. Z., Dutta, P., Ivory, C. F.** 5, 2011, ELECTROPHORESIS, Vol. 32, pp. 550-562.
162. *Simulation of hydrodynamics in microfluidic systems.* **Ilnicki, F., Wawro, B., Pijanowska, D., Torbicz, W.** 10, 2010, PRZEGLAD ELEKTROTECHNICZNY, Vol. 86, pp. 27-29.
163. **Landgraf, S.** Handbook of Luminescence Display Materials and Devices. [ed.] H. S., Rohwer, L. S. Nalwa. *Handbook of Luminescence, Display Materials and Devices.* Valencia : American Scientific Publishers, 2003, Vol. Volume 2. Inorganic Display Materials.
164. *Light emitting diode-based detectors absorbance, fluorescence and spectroelectrochemical measurements in a planar flow-through cell.* **Dasgupta, P. K., Eom, I. Y., Morris, K. J., Li, J. Z.** 1-2, 2003, ANALYTICA CHIMICA ACTA, Vol. 500, pp. 337-364.
165. *In pursuit of the ultimate lamp.* **Craford, M. G., Holonyak, N., Kish, F. A.** 2, 2001, SCIENTIFIC AMERICAN, Vol. 284, pp. 62-67.
166. Roithner Lasertechnik GmbH. *Roithner Lasertechnik GmbH.* [Online] Roithner Lasertechnik GmbH, 2011. [Cited: 1 April 2011.] <http://www.roithner-laser.com/>.
167. *Relation between delamination and temperature cycling induced failures in plastic packaged devices.* **Vandoorselaer, K., Dezeuw, K.** 4, 1990, IEEE TRANSACTIONS ON COMPONENTS HYBRIDS AND MANUFACTURING TECHNOLOGY, Vol. 13, pp. 879-882.

168. *Thermal and mechanical analysis of high-power LEDs with ceramic packages.* **Hu, J. Z., Yang, L. Q., Shin, M. W.** 2, 2008, IEEE TRANSACTIONS ON DEVICE AND MATERIALS RELIABILITY, Vol. 8, pp. 297-303.
169. *Mechanism and thermal effect of delamination in light-emitting diode packages.* **Hu, J. Z., Yang, L. Q., Shin, M. W.** 2, 2007, MICROELECTRONICS JOURNAL, Vol. 38, pp. 157-163.
170. *Thermal and mechanical analysis of delamination in GaN-based light-emitting diode packages.* **Hu, J. Z., Yang, L. Q., Hwang, W. J., Shin, M. W.** 1, 2006, JOURNAL OF CRYSTAL GROWTH, Vol. 288, pp. 157-161.
171. *Sixty thousand hour light output reliability of AlGaInP light emitting diodes.* **Grillot, P. N., Krames, M. R., Zhao, H.** 4, 2006, IEEE TRANSACTIONS ON DEVICE AND MATERIALS RELIABILITY, Vol. 6, pp. 564-574.
172. *Accelerated life test of high brightness light emitting diodes.* **Trevisanello, L., Meneghini, M., Mura, G., Vanz, i M., Pavesi, M., Meneghesso, G., Zanoni, E.** 2, 2008, IEEE TRANSACTIONS ON DEVICE AND MATERIALS RELIABILITY, Vol. 8, pp. 304-311.
173. *Novel Detection Schemes of Nuclear Magnetic Resonance and Magnetic Resonance Imaging: Applications from Analytical Chemistry to Molecular Sensors.* **Harel, E., Schroder, L., Xu, S. J.** 2008, ANNUAL REVIEW OF ANALYTICAL CHEMISTRY, Vol. 1, pp. 133-163.
174. *Optical sensing systems for microfluidic devices: A review.* **Kuswandi, B., Nuriman, Huskens, J., Verboom, W.** 2, 2007, ANALYTICA CHIMICA ACTA, Vol. 601, pp. 141-155.
175. *Broadband quantum dot micro-light-emitting diodes with parabolic sidewalls.* **Tanriseven, S., Maaskant, P., Corbett, B.** 12, 2008, APPLIED PHYSICS LETTERS, Vol. 92. Article Number: 123501.
176. *High-efficiency UV light-emitting diode.* **Kamiyama, S., Iwaya, M., Amano, H., Akasaki, I.** 2, 2002, PHYSICA STATUS SOLIDI A-APPLIED RESEARCH, Vol. 194, pp. 393-398.
177. *Stripe geometry ultraviolet light emitting diodes at 305 nanometers using quaternary AlInGaN multiple quantum wells.* **Khan, M. A., Adivarahan, V., Zhang, J. P., Chen, C. Q., Kuokstis, E., Chitnis, A., Shatalov, M., Yang, J. W., Simin, G.** 12A, 2001, JAPANESE JOURNAL OF APPLIED PHYSICS PART 2-LETTERS, Vol. 40, pp. L1308-L1310.
178. *Successful fabrication of white light emitting diodes by using extremely high external quantum efficiency blue chips.* **Narukawa, Y., Sano, M., Sakamoto, T., Yamada, T., Mukai, T.** 5, 2008, PHYSICA STATUS SOLIDI A-APPLICATIONS AND MATERIALS SCIENCE, Vol. 205, pp. 1081-1085.

179. *Solid-state lighting - a benevolent technology*. **Schubert, E. F., Kim, J. K., Luo, H., Xi, J. Q.** 12, 2006, REPORTS ON PROGRESS IN PHYSICS, Vol. 69, pp. 3069-3099.
180. **Hogan, Treacy**. Irishindependent.ie National News. *Irishindependent.ie*. [Online] 07 December 2007. [Cited: 12 July 2008.] <http://www.independent.ie/national-news/gormley-lights-the-way-with-ban-on-bulbs-1240074.html>.
181. *Alternating-current light emitting diodes with a diode bridge circuitry*. **Cho, J., Jung, J., Chae, J. H., Kim, H., Kim, H., Lee, J. W., Yoon, S., Sone, C., Jang, T., Park, Y., Yoon, E.** 45-49, 2007, JAPANESE JOURNAL OF APPLIED PHYSICS PART 2-LETTERS & EXPRESS LETTERS, Vol. 46, pp. L1194-L1196.
182. *Enhancement of detection sensitivity for indirect photometric detection of anions and cations in capillary electrophoresis*. **Johns, C., Macka, M., Haddad, P. R.** 12-13, 2003, ELECTROPHORESIS, Vol. 24, pp. 2150-2167.
183. *Double-beam laser indirect absorption detection in capillary electrophoresis*. **Xue, Y. J., Yeung, E. S.** 20, 1993, ANALYTICAL CHEMISTRY, Vol. 65, pp. 2923-2927.
184. *Design and performance of a light-emitting diode detector compatible with a commercial capillary electrophoresis instrument*. **Johns, C., Macka, M., Haddad, P. R.** 18-19, 2004, ELECTROPHORESIS, Vol. 25, pp. 3145-3152.
185. *Indirect photometric detection of anions in capillary electrophoresis using dyes as probes and electrolytes buffered with an isoelectric ampholyte*. **Johns, C., Macka, M., Haddad, P. R.** 7, 2000, ELECTROPHORESIS, Vol. 21, pp. 1312-1319.
186. *Simple double-beam absorption detection systems for capillary electrophoresis based on diode lasers and light-emitting diodes*. **Tong, W., Yeung, E. S.** 1, 1995, JOURNAL OF CHROMATOGRAPHY A, Vol. 718, pp. 177-185.
187. *Linearity evaluation in absorbance detection: The use of light-emitting diodes for on-capillary detection in capillary electrophoresis*. **Macka, M., Andersson, P., Haddad, P. R.** 12, 1996, ELECTROPHORESIS, Vol. 17, pp. 1898-1905.
188. *CE detector based on light-emitting diodes*. **Xiao, D., Zhao, S. L., Yuan, H. Y., Yang, X. P.** 1-2, 2007, ELECTROPHORESIS, Vol. 28, pp. 233-242.
189. *Capillary electrophoresis in bioanalysis*. **Kostal, V., Katzenmeyer, J., Arriaga, E. A.** 12, 2008, ANALYTICAL CHEMISTRY, Vol. 80, pp. 4533-4550.
190. *Capillary electrophoresis of proteins 2005-2007*. **Dolnik, V.** 1, 2008, ELECTROPHORESIS, Vol. 29, pp. 143-156.

191. *Light emitting diodes and phototransistors in photometric modules.* **Flaschka, H., McKeitha, C., Barnes, R.** 7, 1973, ANALYTICAL LETTERS, Vol. 6, pp. 585-594.
192. *Development of a novel fluorimeter based on superluminescent light-emitting diodes and acousto-optic tunable filter and its application in the determination of chlorophylls a and b.* **Alexander, T. A., Gao, G. H., Tran, C. D.** 11, 1997, APPLIED SPECTROSCOPY, Vol. 51, pp. 1603-1606.
193. *An aluminium nitride light-emitting diode with a wavelength of 210 nanometres.* **Taniyasu, Y., Kasu, M., Makimoto, T.** 7091, 2006, NATURE, Vol. 441, pp. 325-328.
194. **Zukauskas, A., Shur, M. S., Gaska, R.** *Introduction to Solid-State Lighting.* New York : John Wiley & Sons, 2002. ISBN: 0-471-21574-0.
195. Cree. Cree. [Online] [Cited: 22 July 2008.] www.cree.com.
196. *History, development, and applications of high-brightness visible light-emitting diodes.* **Dupuis, R. D., Krames, M. R.** 9-12, 2008, JOURNAL OF LIGHTWAVE TECHNOLOGY, Vol. 26, pp. 1154-117.
197. **Schubert, E. F.** *Light-emitting diodes.* Cambridge : Cambridge University Press, 2003. ISBN: 0-521-53351-1.
198. **Skoog, D. A., Holler, F. J., Crouch, S. R.** *Principles of instrumental analysis.* Belmont : Thomson Books/Cole, 2007. ISBN 13: 978-0-495-12570-9.
199. Beer-Lambert Law. *Wikipedia.* [Online] Wikimedia, 2011. [Cited: 06 09 2011.] http://en.wikipedia.org/wiki/Beer%E2%80%93Lambert_law.
200. *Highly sensitive flow-through phototransducer for unsegmented continuous-flow analysis demonstrating high-speed spectrophotometry at parts per 10⁹ level and a new method of refractometric determinations.* **Betteridge, D., Dagless, E. L., Fields, B., Graves, N. F.** 1230, 1978, ANALYST, Vol. 103, pp. 897-908.
201. *Probe photometer based on optoelectronic components for determination of total alkalinity in seawater.* **Anfalt, T., Graneli, A., Strandberg, M.** 2, 1976, ANALYTICAL CHEMISTRY, Vol. 48, pp. 357-360.
202. *High-performance optical absorbency detectors based on low-noise switched integrators.* **Liu, H. H., Dasgupta, P. K., Zheng, H. J.** 9, 1993, TALANTA, Vol. 40, pp. 1331-1338.
203. *Light-emitting diode based flow-through optical-absorption detectors.* **Dasgupta, P. K., Bellamy, H. S., Liu, H. H., Lopez, J. L., Loree, E. L., Morris, K., Petersen, K., Mir, K. A.** 1, 1993, TALANTA, Vol. 40, pp. 53-74.

204. *An affordable high-performance optical absorbance detector for capillary systems.* **Boring, C. B., Dasgupta, P. K.** 2-3, 1997, ANALYTICA CHIMICA ACTA, Vol. 342, pp. 123-132.
205. *Simultaneous photometric flow-injection determination of sulfide, polysulfide, sulfite, thiosulfate, and sulfate.* **Sonne, K., Dasgupta, P. K.** 5, 1991, ANALYTICAL CHEMISTRY, Vol. 63, pp. 427-432.
206. *Automated-determination of total phosphorus in aqueous samples.* **Shen, D., Dasgupta, P. K.** 2, 1991, TALANTA, Vol. 39, pp. 133-137.
207. *Dual-wavelength photometry with light-emitting-diodes - compensation of refractive-index and turbidity effects in flow-injection analysis.* **Liu, H. H. and Dasgupta, P. K.** 3, 1994, ANALYTICA CHIMICA ACTA, Vol. 289, pp. 347-353.
208. *A dual-wavelength light-emitting diode based detector for flow-injection analysis process analyzers.* **Huang, J. L., Liu, H. H., Tan, A. M., Xu, J. H., Zhao, X. N.** 6, 1992, TALANTA, Vol. 39, pp. 589-592.
209. *Optical fiber coupled light emitting diode based absorbance detector with a reflective flow cell.* **Jambunathan, S., Dasgupta, P. K., Wolcott, D. K., Marshall, G. D., Olson, D. C.** 3, 1999, TALANTA, Vol. 50, pp. 481-490.
210. *A renewable liquid droplet as a sampler and a windowless optical-cell - automated sensor for gaseous chlorine.* **Liu, H. H. and Dasgupta, P. K.** 23, 1995, ANALYTICAL CHEMISTRY, Vol. 67, pp. 4221-4228.
211. *Recent developments in detection methods for microfabricated analytical devices.* **Schwarz, M. A., Hauser, P. C.** 1, 2001, LAB ON A CHIP, Vol. 1, pp. 1-6.
212. *A photometric detector based on a blue-light-emitting diode.* **Hauser, P. C., Chiang, D. W. L.** 8, 1993, TALANTA, Vol. 40, pp. 1193-1200.
213. *Miniature flow-injection analysis manifold created by micromilling.* **Rainelli, A., Stratz, R., Schweizer, K., Hauser, P. C.** 5, 2003, TALANTA, Vol. 61, pp. 659-665.
214. *A multiwavelength photometer based on light-emitting-diodes.* **Hauser, P. C., Rupasinghe, T. W. T., Cates, N. E.** 4, 1995, TALANTA, Vol. 42, pp. 605-612.
215. *A simple device for quantitative colorimetric diffuse reflectance measurements.* **Matias, F. A. A., Vila, M. M. D. C., Tubino, M.** 1, 2003, SENSORS AND ACTUATORS B-CHEMICAL, Vol. 88, pp. 60-66.

216. *Simple double-beam absorption detection systems for capillary electrophoresis based on diode lasers and light-emitting diodes.* **Tong, W., Yeung, E. S.** 1, 1995, JOURNAL OF CHROMATOGRAPHY A, Vol. 718, pp. 177-185.
217. *Simultaneous separation of inorganic anions and cations using capillary electrophoresis with a movable contactless conductivity detector.* **Unterholzner, V., Macka, M., Haddad, P. R., Zemann, A.** 6, 2002, ANALYST, Vol. 127, pp. 715-718.
218. *Practical method for evaluation of linearity and effective pathlength of on-capillary photometric detectors in capillary electrophoresis.* **Johns, C., Macka, M., Haddad, P. R., King, M., Paull, B.** 1-2, 2001, JOURNAL OF CHROMATOGRAPHY A, Vol. 927, pp. 237-241.
219. *Determination of barium and strontium by capillary zone electrophoresis using an electrolyte containing sulfonazo III.* **Macka, M., Paull, B., Andersson, P., Haddad, P. R.** 1-2, 1997, JOURNAL OF CHROMATOGRAPHY A, Vol. 767, pp. 303-310.
220. *Separation of uranium(VI) and lanthanides by capillary electrophoresis using on-capillary complexation with arsenate III.* **Macka, M., Nesterenko, P., Andersson, P., Haddad, P. R.** 1-2, 1998, JOURNAL OF CHROMATOGRAPHY A, Vol. 803, pp. 279-290.
221. *Investigation of solute-wall interactions in separation of uranium(VI) and lanthanides by capillary electrophoresis using on-capillary complexation with arsenazo III.* **Macka, M., Nesterenko, P., Haddad, P. R.** 1, 1999, JOURNAL OF MICROCOLUMN SEPARATIONS, Vol. 11, pp. 1-9.
222. *Performance of a simple UV LED light source in the capillary electrophoresis of inorganic anions with indirect detection using a chromate background electrolyte.* **King, M., Paull, B., Haddad, P. R., Macka, M.** 12, 2002, ANALYST, Vol. 127, pp. 1564-1567.
223. *Sun photometer with light-emitting-diodes as spectrally selective detectors.* **Mims, F. M.** 33, 1992, APPLIED OPTICS, Vol. 31, pp. 6965-6967.
224. *How to monitor ultraviolet-radiation from the sun.* **Mims, F. M.** 2, 1990, SCIENTIFIC AMERICAN, Vol. 263, pp. 106-109.
225. *Light-emitting diodes as sensors for colorimetric analyses.* **Berry, R. J., Harris, J. E., Williams, R. R.** 10, 1997, APPLIED SPECTROSCOPY, Vol. 51, pp. 1521-1524.
226. *Novel fused-LEDs devices as optical sensors for colorimetric analysis.* **Lau, K. T., Baldwin, S., Shepherd, R. L., Dietz, P. H., Yezunis, W. S., Diamond, D.** 1, 2004, TALANTA, Vol. 63, pp. 167-173.

227. *Photometric detection in flow analysis systems using integrated PEDDs.* **O'Toole, M., Lau, K. T., Diamond, D.** 5, 2005, *TALANTA*, Vol. 66, pp. 1340-1344.
228. *Determination of phosphate using a highly sensitive paired emitter-detector diode photometric flow detector.* **O'Toole, M., Lau, K. T., Shepherd, R., Slater, C., Diamond, D.** 2, 2007, *ANALYTICA CHIMICA ACTA*, Vol. 587, pp. 290-294.
229. *Quantitative colorimetric analysis of dye mixtures using an optical photometer based on LED array.* **Lau, K. T., Yerazunis, W. S., Shepherd, R. L., Diamond, D.** 2, 2006, *SENSORS AND ACTUATORS B-CHEMICAL*, Vol. 114, pp. 819-825.
230. *Novel integrated paired emitter-detector diode (PEDD) as a miniaturized photometric detector in HPLC.* **O'Toole, M., Lau, K. T., Shazmann, B., Shepherd, R., Nesterenko, P. N., Paull, B., Diamond, D.** 8, 2006, *ANALYST*, Vol. 131, pp. 938-943.
231. *Development of a low-cost four-color LED photometer.* **Hamilton, J. R., White, J. S., Nakhleh, M. B.** 11, 1996, *JOURNAL OF CHEMICAL EDUCATION*, Vol. 73, pp. 1052-1054.
232. *A multichannel photometer based on an array of light emitting diodes for use in multivariate calibration.* **Fonseca, A., Raimundo, I. M.** 2, 2004, *ANALYTICA CHIMICA ACTA*, Vol. 522, pp. 223-229.
233. *A portable spectrophotometer using a white-color light-emitting diode and a charge-coupled device and its application to on-site determination of iron.* **Shimazaki, Y., Watanabe, S., Takahashi, M., Iwatsuki, M.** 10, 2000, *ANALYTICAL SCIENCES*, Vol. 16, pp. 1091-1093.
234. **Lakowicz, J. R.** *Principles of fluorescence spectroscopy.* Third Edition. New York : Springer, 2006.
235. *Elementary processes of photochemical reactions.* **Franck, J., Dymond, E. G.** February, 1926, *Journal Cover:Trans. Faraday Soc.*, 1926, 21, 536-542, Vol. 21, pp. 536-542.
236. *A Theory of Intensity Distribution in Band Systems.* **Condon, E.** 6, 1926, *Physical Reviews*, Vol. 28, pp. 1182-1201.
237. *Zasada Francka-Condana.* *Wikipedia.org.* [Online] Wikimedia.org, 23 July 2010. [Cited: 07 April 2011.] http://pl.wikipedia.org/wiki/Zasada_Francka-Condana.
238. **Johnson, I. D., Davidson, M. W.** *Jablonski energy diagram.* *Microscope Resource Center.* [Online] Olympus. [Cited: 07 April 2011.] <http://www.olympusmicro.com/primer/java/jablonski/jabintro/index.html>.
239. *Micro- and sub-nanosecond lifetime measurements using a UV light-emitting diode.* **Szmacinski, H., Chang, Q.** 1, 2000, *APPLIED SPECTROSCOPY*, Vol. 54, pp. 106-109.

240. *Frequency-domain fluorescence microscopy with the LED as a light source.* **Herman, P., Maliwal, B. P., Lin, H. J., Lakowicz, J. R.** 2001, JOURNAL OF MICROSCOPY-OXFORD, Vol. 203, pp. 176-181. Part 2.
241. *Frequency domain fluorometry with pulsed light-emitting diodes.* **Herman, P., Vecer, J.** [ed.] O. S. Wolfbeis. 2008, FLUORESCENCE METHODS AND APPLICATIONS: SPECTROSCOPY, IMAGING, AND PROBES, Vol. 1130, pp. 56-61. ANNALS OF THE NEW YORK ACADEMY OF SCIENCES.
242. *Long-lived visible luminescence of UV LEDs and impact on LED excited time-resolved fluorescence applications.* **Jin, D., Connally, R., Piper, J.** 3, 2006, JOURNAL OF PHYSICS D-APPLIED PHYSICS, Vol. 39, pp. 461-465.
243. *Recent developments in optical detection methods for microchip separations.* **Gotz, S., Karst, U.** 1, 2007, ANALYTICAL AND BIOANALYTICAL CHEMISTRY, Vol. 387, pp. 183-192.
244. *Ultrafast analysis of oligosaccharides on microchip with light-emitting diode confocal fluorescence detection.* **Dang, F., Zhang, L., Hagiwara, H., Mishina, Y., Baba, Y.** 4, 2003, ELECTROPHORESIS, Vol. 24, pp. 714-721.
245. *Characterization of electrophoretic behavior of sugar isomers by microchip electrophoresis coupled with videomicroscopy.* **Dang, F. Q., Zhang, L. H., Jabasini, M., Kaji, N., Baba, Y.** 10, 2003, asini M, Kaji N, Baba Y, Vol. 75, pp. 2433-2439.
246. *Rapid analysis of oligosaccharides derived from glycoproteins by microchip electrophoresis.* **Dang, F. Q., Kakehi, K., Nakajima, K., Shinohara, Y., Ishikawa, M., Kaji, N., Tokeshi, M., Baba, Y.** 2, 2006, JOURNAL OF CHROMATOGRAPHY A, Vol. 1109, pp. 138-143.
247. *Spectral filtering of light-emitting diodes for fluorescence detection.* **de Jong, E. P., Lucy, C. A.** 1, 2005, ANALYTICA CHIMICA ACTA, Vol. 546, pp. 37-45.
248. *Fabrication of an integrated PDMS microchip incorporating an LED-induced fluorescence device.* **Miyaki, K., Guo, Y. L., Shimosaka, T., Nakagama, T., Nakajima, H., Uchiyama, K.** 3, 2005, ANALYTICAL AND BIOANALYTICAL CHEMISTRY, Vol. 382, pp. 810-816.
249. *Light emitting diode excitation emission matrix fluorescence spectroscopy.* **Hart, S. J., Jiji, R. D.** 12, 2002, ANALYST, Vol. 127, pp. 1693-1699.
250. *Combined Contactless Conductometric, Photometric, and Fluorimetric Single Point Detector for Capillary Separation Methods.* **Ryvolova, M., Preisler, J., Foret, F., Hauser, P. C., Krasensky, P., Paull, B., Macka, M.** 1, 2010, ANALYTICAL CHEMISTRY, Vol. 82, pp. 129-135.

251. *Electrohydrodynamic preparation of particles, capsules and bubbles for biomedical engineering applications*. **Enayati, M., Chang, M. W., Bragman, F., Edirisinghe, M., Stride, E.** 1-3, 2011, COLLOIDS AND SURFACES A-PHYSICO-CHEMICAL AND ENGINEERING ASPECTS, Vol. 382, pp. 154-164.
252. *Onset condition of pulsating cone-jet mode of electrohydrodynamic jetting for plane, hole, and pin type electrodes*. **Kim, H., Song, J., Chung, J., Hong, D.** 10, 2010, JOURNAL OF APPLIED PHYSICS, Vol. 108, p. Article Number: 102804.
253. **Macka, M.** Electrohydrodynamic Focusing in 2-Dimensional Planar Microfluidic Devices for Preconcentration of Low Abundance Bioanalytes. *Full Proposal Research Frontiers Programme Grant*. Dublin, Ireland : Science Foundation Ireland, 2006.
254. **Levicky, R.** Flow through porous media. *ChE3110, Handout #15*.
255. **Brandrup, J., Immergut, E. H.** *Polymer Handbook*. New York : John Wiley & Sons, 1975.
256. *UV-LED photopolymerised monoliths*. **S. Abele, F.Q. Nie, F. Foret., B. Paull, M. Macka.** 2008, Analyst, Vol. 133, pp. 864-866.
257. *Wall-induced lateral migration in particle electrophoresis through a rectangular microchannel*. **Liang, L. T., Ai, Y., Zhu, J. J., Qian, S., Xuan, X. C.** 1, 2010, JOURNAL OF COLLOID AND INTERFACE SCIENCE, Vol. 347, pp. 142-146.
258. *Transverse electrokinetic and microfluidic effects in micropatterned channels: Lubrication analysis for slab geometries*. **Ajdari, A.** 1, 2002, PHYSICAL REVIEW E, Vol. 65, p. Article Number: 016301.
259. *Numerical model for light propagation and light intensity distribution inside coated fused silica capillaries*. **Piasecki, T., Macka, M., Paull, B., Brabazon, D.** 2011, Optics and Lasers in Engineering, Vol. 49, pp. 924-931.
260. *White LEDs as broad spectrum light sources for spectrophotometry: Demonstration in the visible spectrum range in a diode array spectrophotometric detector*. **Piasecki, T., Breadmore, M., Macka, M.** 2010, Electrophoresis, Vol. 31, pp. 3737-3744.
261. *Three-dimensional electrokinetic particle focusing in a rectangular microchannel*. **Liang, L. T., Qian, S., Xuan, X. C.** 1, 2010, JOURNAL OF COLLOID AND INTERFACE SCIENCE, Vol. 350, pp. 377-379.
262. *The benefits of Facebook "friends": Social capital and college students' use of online social network sites*. **Ellison, N. B., Steinfield, C., Lampe, C.** 4, 2007, JOURNAL OF COMPUTER-MEDIATED COMMUNICATION, Vol. 12.

263. **Campbell-Kelly, M. Aspray, W.** *Computer. A history of the information machine.* Oxford : Westview Press, 2004. ISBN: 978-0-8133-4264-1.
264. Ancient Discoveries Ancient Robots. *YouTube.* [Online] http://www.youtube.com/watch?v=cbW_xKRbt_M.
265. The ENIAC Team. *The Franklin Institute.* [Online] 2004-2011. [Cited: March 23 2011.] <http://www.fi.edu/learn/case-files/eckertmauchly/team.html>.
266. *How to make Zuse's Z3 a universal computer.* **Rojas, R.** 3, 1998, IEEE ANNALS OF THE HISTORY OF COMPUTING, Vol. 20, pp. 51-54.
267. *Atanasoff-Berry computer replica.* **Grier, D. A.** 1, 1998, IEEE ANNALS OF THE HISTORY OF COMPUTING, Vol. 20, pp. 77-78.
268. *Colossus: Its origins and originators.* **Copeland, B. J.** 4, 2004, IEEE ANNALS OF THE HISTORY OF COMPUTING, Vol. 26, pp. 38-45.
269. *The ENIAC, an electronic computing machine.* **Hartree, D. R.** 4015, 1946, NATURE, Vol. 158, pp. 500-506.
270. *SOP: What is it and why? A new micro system-integration technology paradigm-Moore's law for system integration of miniaturized convergent systems of the next decade.* **Tummala, R. R.** 2, 2004, IEEE TRANSACTIONS ON ADVANCED PACKAGING, Vol. 27, pp. 241-249.
271. **Beer, G., Watson, J. O.** *Introduction to finite and boundary element methods for engineers.* Ney York/ Chichester/ Brisbane/ Singapore/ Toronto : John Wiley & Sons, 1992. ISBN: 0-471-92813-5.
272. *The lattice Boltzmann equation method: theoretical interpretation, numerics and implications.* **Nourgaliev, R. R., Dinh, T. N., Theofanous, T. G., Joseph, D.** 1, 2003, INTERNATIONAL JOURNAL OF MULTIPHASE FLOW, Vol. 29, pp. 117-169.
273. *Overview of the lattice Boltzmann method for nano- and microscale fluid dynamics in materials science and engineering.* **Raabe, D.** 6, 2004, MODELLING AND SIMULATION IN MATERIALS SCIENCE AND ENGINEERING, Vol. 12, pp. R13-R46.
274. *Solid-state lighting - Lamps, chips, and materials for tomorrow.* **JY, Tsao.** 3, 2004, IEEE CIRCUITS & DEVICES, Vol. 30, pp. 28-37.
275. Luminescence: Oxford reference Online Premium. *Oxford reference Online Premium.* [Online] 2011. [Cited: 30 March 2011.] <http://www.oxfordreference.com/views/ENTRY.html?entry=t83.e1767&srn=2&ssid=552117169#FIRSTHIT>.

276. *A note on carborundum.* **Round, H. J.** 1908, *Electrical World*, Vol. 49, p. 309.
277. *The life and times of the LED - a 100-year history.* **N, Zheludev.** 4, 2007, *NATURE PHOTONICS*, Vol. 1, pp. 189-192.
278. **Losev, O. V.** 1928, *Phil. Mag.*, Vol. 6, pp. 1024-1044.
279. **Losev, O. V.** 1929, *Physik. Zeitschr.*, Vol. 30, pp. 920-923.
280. **Losev, O. V.** 1931, *Physik. Zeitschr.*, Vol. 32, pp. 692-696.
281. **Losev, O. V.** 1933, *Physik. Zeitschr.*, Vol. 34, pp. 397-403.
282. *Coherent light emission from GaAs junction.* **Hall, R. N. Carlson, R. O., Soltys, T. J., Fenner, G. E., Kingsley, J. D.** 9, 1962, *PHYSICAL REVIEW LETTERS*, Vol. 9, pp. 366-368.
283. *Coherent (visible) light emission from ga(as1-xpx) junctions.* **Holonyak, N., Bevacqua, S. F.** 4, 1962, *APPLIED PHYSICS LETTERS*, Vol. 1, pp. 82-83.
284. *Luminescent properties of GaN.* **Pankove, J. I., Berkeyhe., J. E., Maruska, H. P., Wittke, J.** 13, 1970, *SOLID STATE COMMUNICATIONS*, Vol. 8, pp. 1051-&.
285. *Optical absorption of gan.* **Pankove, J. I., Maruska, H. P., Berkeyhe, J. E.** 5, 1970, *APPLIED PHYSICS LETTERS*, Vol. 17, pp. 197-&.
286. *Electroluminescence in GaN.* **Pankove, J. I., Miller, E. A., Richman, D., Berkeyheiser, J. E.** 1, 1971, *Journal of Luminescence*, Vol. 4, pp. 63-66.
287. *Recent developments in light-emitting-diode technology.* **Craford, M. G.** 7, 1977, *IEEE TRANSACTIONS ON ELECTRON DEVICES*, Vol. 24, pp. 935-943.
288. *Research at lincoln-laboratory leading up to the development of the injection-laser in 1962.* **Rediker, R. H.** 6, 1987, *IEEE JOURNAL OF QUANTUM ELECTRONICS*, Vol. 23, pp. 692-695.
289. *Recombination radiation emitted by gallium arsenide.* **Keyes, R. J., Quist, T. M.** 8, 1962, *PROCEEDINGS OF THE INSTITUTE OF RADIO ENGINEERS*, Vol. 50, pp. 1822-&.
290. *Blue-green laser diodes.* **Haase, M. A., Qiu, J., Depuydt, J. M., Cheng, H.** 11, 1991, *APPLIED PHYSICS LETTERS*, Vol. 59, pp. 1272-1274.
291. *Stimulated-emission near ultraviolet at room-temperature from a gan film grown on sapphire by movpe using an ain buffer layer.* **Amano, H., Asahi, T., Akasak, I.** 2, 1990, *JAPANESE JOURNAL OF APPLIED PHYSICS PART 2-LETTERS*, Vol. 29, pp. L205-L206.
292. *High-Power GaN P-N Junction Blue-Light-Emitting Diodes.* **Nakamura, S., Mukai, T., Senoh, M.** 12A, 1991, *JAPANESE JOURNAL OF APPLIED PHYSICS PART 2-LETTERS*, Vol. 30, pp. L1998-L2001.

293. *A light-emitting future - Light-emitting diodes may ultimately replace lightbulbs.* **Cristol, H.** 5, 2002, *FUTURIST*, Vol. 36, pp. 6-7.
294. *Status and future of high-power light-emitting diodes for solid-state lighting.* **Krames, M. R., Shchekin, O. B., Mueller-Mach, R., Mueller, G. O., Zhou, L., Harbers, G., Craford, M. G.** 2, 2007, *JOURNAL OF DISPLAY TECHNOLOGY*, Vol. 3, pp. 160-175.
295. **Grosso, G., Parravicini, G. P.** *Solid state physics*. San Diego : Academic Press, 2000. ISBN: 0-12-304460-X.
296. *Internal quantum efficiency of laser-diodes.* **Claissse, P. R., Taylor, G. W.** 21, 1992, *ELECTRONICS LETTERS*, Vol. 28, pp. 1991-1992.
297. *Effect of V-shaped defects on structural and optical properties of AlGaN/InGaN multiple quantum wells.* **Jeon, S. R., Lee, S. J., Jung, S. H., Lee, S. H., Baek, J. H., Jeong, H., Cha, O. H., Suh, E. K., Jeong, M. S.** 13, 2008, *uh EK (Suh, Eun-Kyung)2, Jeong MS (Jeong, Mun Seok)3*, Vol. 41. Article Number: 132006.
298. *Laser beams and resonators.* **Kogelnik, H., Li, T.** 10, 1966, *APPLIED OPTICS*, Vol. 5, pp. 1550-&.
299. *Laser diode pumped solid-state lasers.* **Hughes, D. W., Barr, J. R. M.** 4, 1992, *JOURNAL OF PHYSICS D-APPLIED PHYSICS*, Vol. 25, pp. 563-586.
300. *Frequency domain fluorometry with pulsed light-emitting diodes.* **Herman, P., Vecer, J.** 2008, *FLUORESCENCE METHODS AND APPLICATIONS: SPECTROSCOPY, IMAGING, AND PROBES*, Vol. 1130, pp. 56-61.
301. *Absorbance based light emitting diode optical sensors and sensing devices.* **O'Toole, M., Diamond, D.** 4, 2008, *SENSORS*, Vol. 8, pp. 2453-2479.
302. *An integrated fluorescence detection system for lab-on-a-chip applications.* **Novak, L., Neuzil, P., Pipper, J., Zhang, Y., Lee, SH.** 1, 2007, *LAB ON A CHIP*, Vol. 7, pp. 27-29.

Appendix A – Brief history of computers

There is no other single invention that revolutionised our lives in the way that computers did. When looking back at the prognoses of the future from the beginning of the 20th century, the expansion of aviation and mechanics could have been foreseen. Historically in 1947 Bardeen, Brattain and Shockley had presented the transistor (196). Since then development of integrated circuits has revolutionised our lives affecting even the most basic phenomena such as interpersonal communication (262).

The word “computer” in the English language originally meant “one who computes; a calculator, reckoner; *specifically* a person employed to make calculations in an observatory, in surveying *etc.*” (263). The oldest machines designed to help counting, such as the abacus, dates back to ancient era; it was not until 17th century when William Oughtred developed a slide rule, a device based on logarithm theory that allowed not just simple adding but multiplication, division and calculating the logarithm of a number. Different scientists throughout the ages tried to develop a computing machine, such as Blaise Pascal, Gottfried Leibnitz, Charles Babbage, Alan Turing, Konrad Zuse and George Stibitz. Although the first programmable devices are reported as early as 12th century (264), the first programmable machines that really affected the world were mechanical looms designed by Joseph Marie Jacquard. His design relied on a mechanical system of handles and cogs deciphering a demanded pattern from perforated cards. Notably perforated cards remained in use until late 1970s already in era of semiconductor computers (263).



Figure 182: Members of the ENIAC team at work in the 1940s (265).

Machines developed to solve difficult mathematical problems were somehow already designed for simulations and modelling. Formulated laws could be processed with ease, allowing personal manipulation, even things difficult or impossible to change in experimental practice. This made modelling and simulations an integral part of the applications of the early computational machines which led to development of modern computers during the 1940's. From the viewpoint of the history of computers the most important events occurred during World War II and early-post war years. The first machine that was able to perform universal computation was the electromechanical Z3 computer, made by Zuse in Berlin in 1941 (266). Meanwhile in 1937 in US a non-programmable computer (calculator) made by Atanasoff and Berry (Atanasoff-Berry Computer, ABC) were displayed (267). In UK a secretly developed series of "Colossus" electronic computers was introduced in 1943 (268) and ENIAC (Electronic Numerical Integrator And Computer) in the 1946 (269). What made ENIAC different from other machines was the combination of design and non-specified purpose. The Z-series were not purely electronic and ABC were not programmable, ENIAC was. While "Colossus" computers were designed to break codes, ENIAC was intended for different tasks. Those features made ENIAC the predecessor of modern computers from table-top PCs to mainframes and supercomputers. Some of very famous quotes related to computers and computer industry:

- "Future computers will have only around 1000 vacuum tubes, and should weigh less than 1.5 ton", Article in "Popular Mechanics", march 1949

- “I think there is a world market for maybe five computers”, Thomas Watson, Chairman of IBM, 1943
- “What the hell it might be useful for...?”, Robert Lloyd, Dept. of Advanced Computational Systems, IBM, c.a. 1968 referring to microprocessor
- “There is no reason anyone would want a computer in their home”, Ken Olson , President, Chairman and founder of Digital Equipment Corp., 1977

Rapid developments in computers in last two decades of 20th century resulted in the popularisation of personal computers and the increased availability of the computer to average researcher. A law predicted by Gordon Moore in 1965 stating that the number of transistors per surface unit will double every 18 months, interpolated to doubling the computational power every 24 months still remains valid (see Figure 183) (270). With quickly escalating accessible computational power, problems that a few years earlier required a supercomputer could then be performed with a table-top PC allowing the individual researcher to use software that was unavailable for the average user just a few years previously. Also it allowed an increased complication of models, increased number of parameters, and increased precision of solutions.

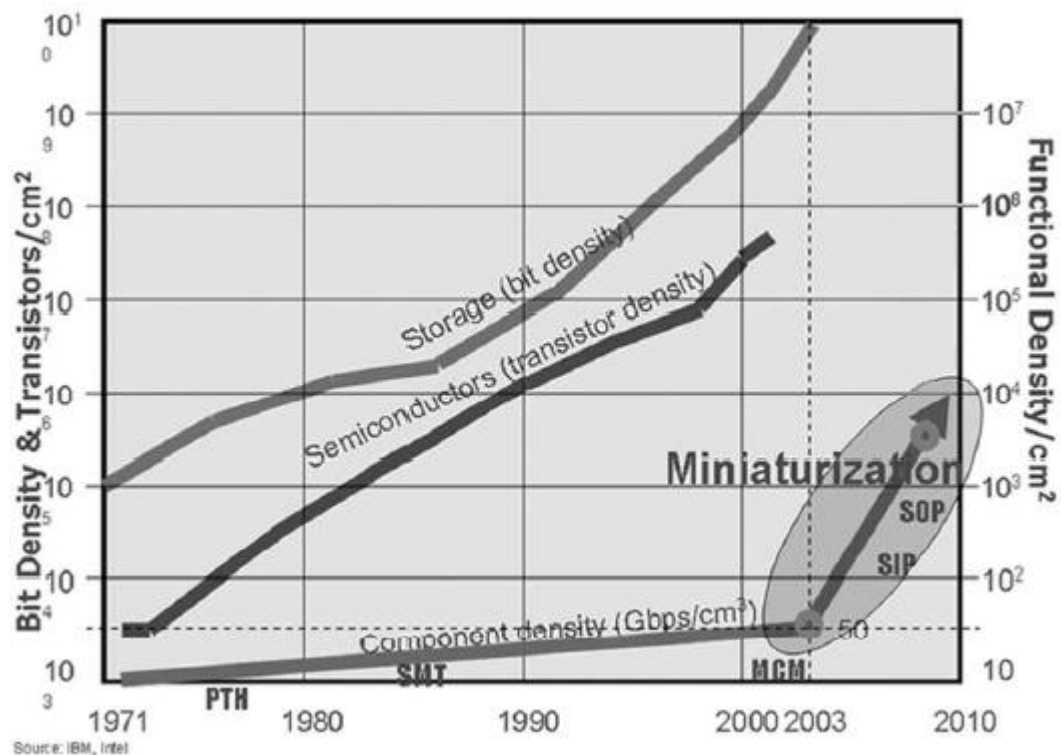


Figure 183: Graph showing evolution of Moore's law from 1972 to 2003 on semiconductors and data storage density (270).

Appendix B – Description of different methods used in CFD

8.1. Finite Difference Method (FDM)

This is the oldest known computationally designed method of numerical solving PDEs, which introduction is attributed to Leonhard Euler in the 18th century. FDM is started as all numerical methods with a construction of the grid over the solution space. At each node point the differential equation is approximated, typically by Taylor series expansion or polynomial fit to approximate first and second derivative of the variable with respect of the coordinates system. The main problem is that although FDM can be applied to any mesh type, the only known applications are to structured mesh, where grid lines serve as coordinate systems. The second disadvantage associated with FDM is that special attention has to be paid for securing conservation laws and boundary settings (130; 138).

8.2. The Finite Volume Method (FVM)

The FVM divides the computational domain into a finite number of test volumes, each being equivalent to a single point located at a centroid. These points serve as nodes for solving the governing equations where values of variables are calculated with the respect of the coordinates system. The FVM differs from FDM in that it uses an integral form of conservation equations. Calculated variables values for the centres of test volumes are then interpolated. The FVM can work with any type of mesh and works well for complex geometries. The grid defines how test volumes are located and is independent of the coordinates system. The FVM is regarded as the easiest one to implement programmably. FVM is also known for its difficulties in dealing with equations which have non-zero viscous terms somewhat reducing its usefulness for microfluidics (130; 138).

8.3. The Finite Elements Method (FEM)

A FEM has similar structure to FVM but equations are multiplied by a weight function prior to the integration. A typical feature of the FEM is the application of unstructured grids – triangles and quadrangles (in two dimensions) and tetrahedrons and hexahedrons (in three dimensions) to produce a mesh with rather circumstantial shape depending on preferred mesh density. In the simplest approach the solution and weight are approximated by a linear function with a secured continuity condition set between each mesh cell. The approximation is replaced by a weighted integral function of the conservation function and solved such that the

derivative of the integral with respect to each mesh cell value is zero. As a result a set of non-linear algebraic equations is produced. FEM works well with flux or gradient based boundary conditions making it very useful for microfluidic applications. Also it excels in difficult geometries that can be easily refined with a more dense or simplified grid. One difficulty with FEM is in handling geometries with dimensions which differ by several orders of magnitude (130; 138).

8.4. Other methods

There are other numerical methods that are employed in seeking solutions of PDEs. All previously mentioned methods were based on some form of anchor points filling the entire solution domain. The Boundary Element Method (BEM) represents a different approach. Approximations are made only on the perimeter of the computational area – the circumference in case of 2D problems and the surface of the test volume for 3D. There are two basic types of BEMs: indirect and direct. Indirect BEMs are characterised by an intensity distribution (density) function over which superposition of fundamental solutions is sought. The boundary integral equation analytical solution that cannot be found in general is replaced by an approximate solution of the varying density function over the boundaries. For direct BEMs the integral equation is calculated using the divergence theorem⁹. With appropriate substitutions and use of arbitrary functions, an integral equation over the boundary is obtained. This approach is called “direct” because functions appearing in the equation are physically meaningful equations contrary to the density function in indirect method (271).

A relatively new and not yet fully explored method is called Lattice Boltzmann Method (LBM). LBM was developed from kinetic gas theory where the primary variability described by one-particle probability distribution function, Boltzmann’s H theorem, stating that for fixed volume entropy never decreases and collision interval theory. LBM employs mathematical description of pseudo particles, that represent no single molecules but rather clusters of them. LBM is considered a molecular technique rather than continuum but is still under development (272; 273).

⁹ Also known as Gauss theorem, Ostrogradsky theorem or Gauss-Ostrogradsky theorem:

$$\oint_{\Sigma} \mathbf{v} d\mathbf{S} = \int_V \nabla \cdot \mathbf{v} dv$$

Appendix C – Brief history of Solid State Lighting

The Solid State Light (SSL) presents a new quality resource in the world of illuminating techniques. SSL is composed of light sources belonging to a fourth generation of light sources: after burning a fuel and using bare fire (1st), passing current through metallic fibre to induce light through thermoluminescence (2nd), and inducing fluorescence in gases (3rd), light can be generated directly from the electric current carriers passing through a semiconductor (4th generation). The underlying physical phenomenon is called the electroluminescence – semiconductors emit a stream of electromagnetic energy – photons, when they return to the ground state after being excited by electrons (274; 275).

The first documented observation of electroluminescence comes from Henry Joseph Round in 1907 (276). During an investigation of silica carbide he observed light emission as a result of radiative recombination of electrical carriers. The first publication concerning the theory on which this phenomenon is based was brought out by a little known Russian scientist Oleg Vladimirovich Losev who published several papers in British and German journals between 1928 and 1933 (277; 278; 279; 280; 281). Lack of co-workers, his premature death in 1941 and the situation after the World War II resulted in his works being forgotten. The first demonstration of coherent light emission from a semiconductor (first laser diode) was conducted by Hall and his team in 1962 (282). Later the same year, visible red light emission from semiconductor diode (the first light emitting diode) was demonstrated by Holonyak (283). In 1969 Maruska and Pankove studied fundamental properties of gallium nitride (GaN) (284; 285) which resulted in the first solid state source of blue light from a metal-insulator-semiconductor structure (MIS-structure) (286). Their light source, although working, was far from perfect. Development of vapour-phase epitaxy allowed Crawford in 1970 to produce high-performance amber, yellow and yellow-green electroluminescent sources (287). Solid state infrared emitters based on GaAs were constructed in 1950, before the first visible light emitting diode (288). In 1962 extremely efficient infrared emissions with energies close to bandgap energy were observed in the infrared range (289).

In 1991 the world first blue laser was demonstrated by Haase and co-workers at the 3M Company (290). Their achievement however was only a proof of a theoretical concept, but not a technically optimal solution for a blue solid state light source. Another design based on ZnSe/CdZnSe junction was toxic and therefore short lived. In 1992, Akasaki demonstrated stimulated light emission from a GaN semiconductor (291), but it was Nakamura who

introduced around the same time a method of mass production of high luminosity, long life-time and non-toxic blue LEDs (292). From that moment the world turned its attention to a new era of illumination, the era of solid-state lighting. Continuous developments in the area of semiconductors and material physics working their way through the light spectrum down into the UV-spectral range allowed in 2006 an LED with peak emission at 210 nm to be constructed (193). Meanwhile a silent revolution took place in the world of red LEDs – the luminous efficacy reached up to 80 lumens per watt. In 2008 white LEDs for the first time exhibited a luminous efficacy higher than red LEDs, namely 169 lumens per watt (178). While there is no official definition of ‘ultra-bright’ LEDs, generally it is assumed that such diodes have luminous efficacy at least 150 lm/W (196). With continuous development of new LED technologies and constant increases in LED manufacturing volumes, which brought the lowering of the costs per unit, the transition to solid state lightning has begun (293). Among many other benefits, environmental impact due to the reduced energy consumption is important. It was estimated in the USA in 2006 that with 80% market penetration by solid state lighting the total electrical energy consumption would be lowered by approx. 11% (179).

Appendix D – Physical principles of LEDs

A light emitting diode (LED) is a semiconductor diode that emits specific light when electrical current is flowing in forward bias. The energy (or wavelength, Eq. 24) of the emitted photon depends on the physical properties of the used semiconductors (bandgap energy E_g). A range of semiconductor materials have been developed for particular wavelength ranges. Most commonly used materials are gallium arsenide (GaAs) for infrared emission (wavelength of emitted radiation $\lambda > 760$ nm); aluminium gallium arsenide (AlGaAs) (610-760nm); gallium (III) phosphide (GaP) (500-760nm); indium gallium nitride (InGaN) (400-570nm when combined with gallium (III) nitride (GaN)); aluminium gallium nitride (AlGaN) and indium aluminium gallium nitride (AlInGaN) both below 400nm (294).

LEDs can be built from semiconductors with a straight bandgap only. Bandgap is defined as straight when the maximum energy of the valence band equals the minimum energy of the conduction band in momentum space (see Figure 184). Only the vertical transitions are radiative. The horizontal transitions results in increased oscillations of the crystal lattice (phonons) and contributes only toward heat generation. Therefore it is not possible to create LED from pure silicon as it has indirect bandgap. GaAs, the first material to be used in massive scale for LED construction has a direct bandgap (295). This can be schematically represented as in Figure 184. Band energy extremum mismatch results in increased non-radiative transitions and lowers overall light generation efficiency.

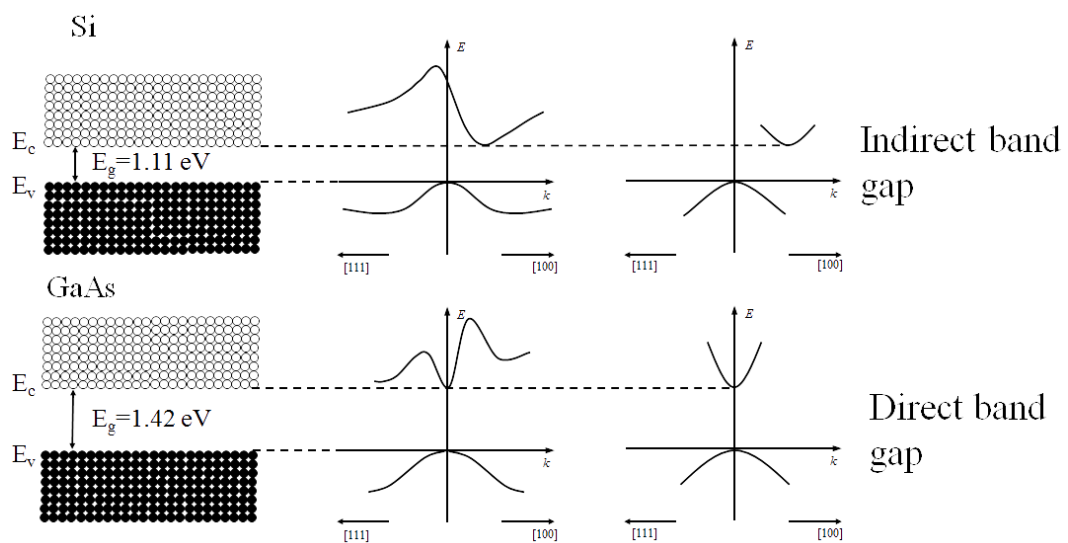


Figure 184: Schematic comparison of the population of charge carriers at 0K in semiconductor with indirect bandgap (Si) and with direct bandgap (GaAs).

Maximising the light output and at the same time minimising the undesirable heat production and overall energy consumption are major considerations for all LED developments. As photons are created at the contact of the two semiconductors they can be easily lost by being absorbed by the overlaying material. A major engineering challenge to produce an efficient high-luminosity LED is to extract as many photons as possible from the place of the electron-hole recombination and deliver them outside of the chip. It is easier to increase the LED luminosity by increasing the extraction efficiency, than by improving the internal quantum efficiency (ratio of radiative transitions to all transitions in a junction) (296). The most important factor to improve the internal quantum efficiency is to reduce the amount of heat generated by the LED.

For a semiconductor in the thermodynamic equilibrium above 0K some electrons have enough energy to transfer from the valence band to the conductivity band. Contrary to metals, with increased temperature, semiconductors display better conductivity. Increase of the carrier density in the conductivity band with temperature is greater than losses due to crystal lattice oscillations. The density distribution of electrons in the valence band is governed by the Fermi-Dirac distribution (Eq. 23) (see Figure 184 and Figure 185):

$$f(E) = \frac{1}{e^{-\left(\frac{E-E_f}{kT}\right)} + 1} \quad \text{Eq. 23}$$

where $f(E)$ is the electron density function, E is energy, E_f is Fermi's energy¹⁰, k is Boltzmann constant, T is the absolute temperature.

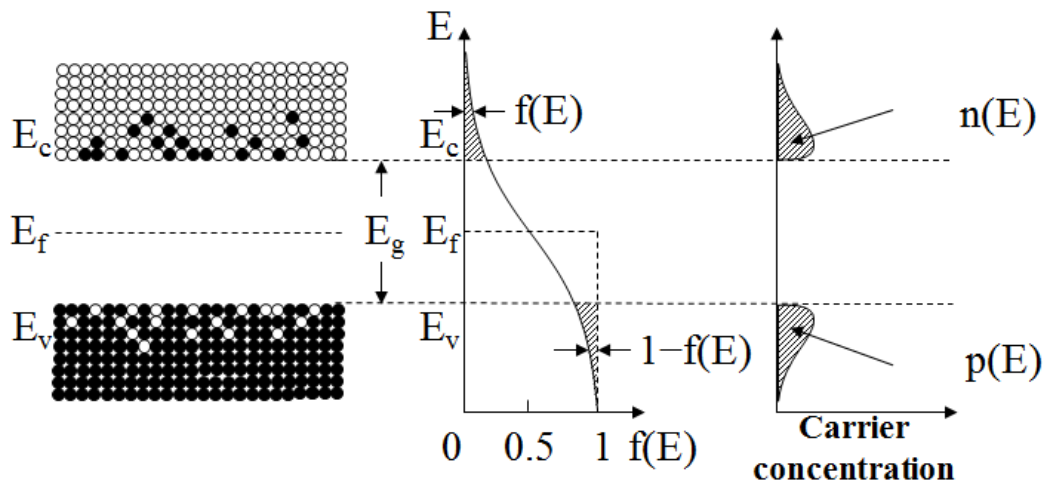


Figure 185: Graphical representation of a carrier density distribution at $T > 0K$; $n(E)$ and $p(E)$ are density functions for negative and positive carriers.

¹⁰ Defined as maximal energy of an electron at 0K (35).

To improve achieve appropriate electrical properties semiconductors are admixed with different elements, see Figure 186, Figure 187 and Figure 188. There are two types of doping semiconductors:

- Type N (negative) when a semiconductor is admixed with an element with more valence electrons – phosphor (V) doping silica (IV)
- Type P (positive) when a semiconductor is admixed with an element with less valence electrons – indium (III) doping silica (IV)

▪ type n P(V) → Si(IV)

▪ type p In(III) → Si(IV)

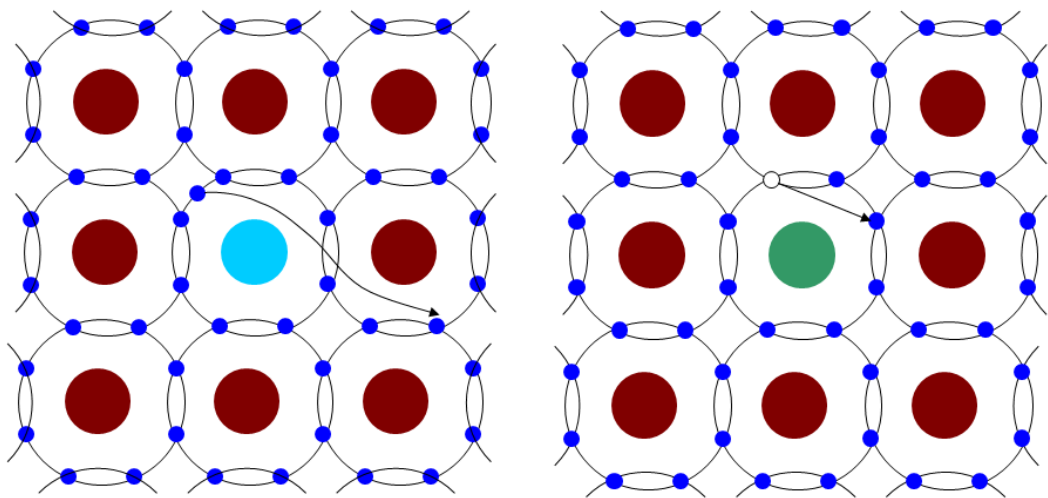


Figure 186: Scheme of the crystal lattice in doped semiconductor: type n on the left, type p on the right.

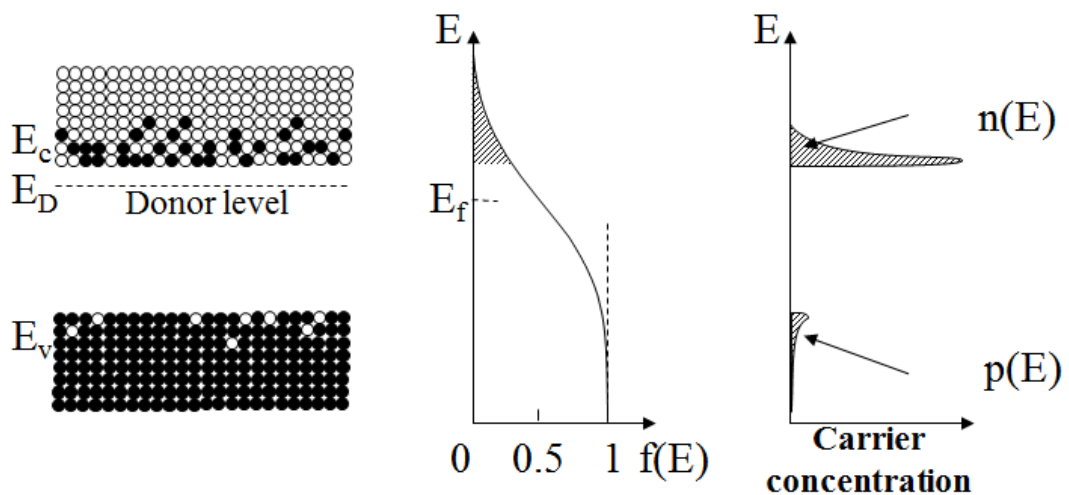


Figure 187: Carrier density distribution for n-type doped semiconductor.

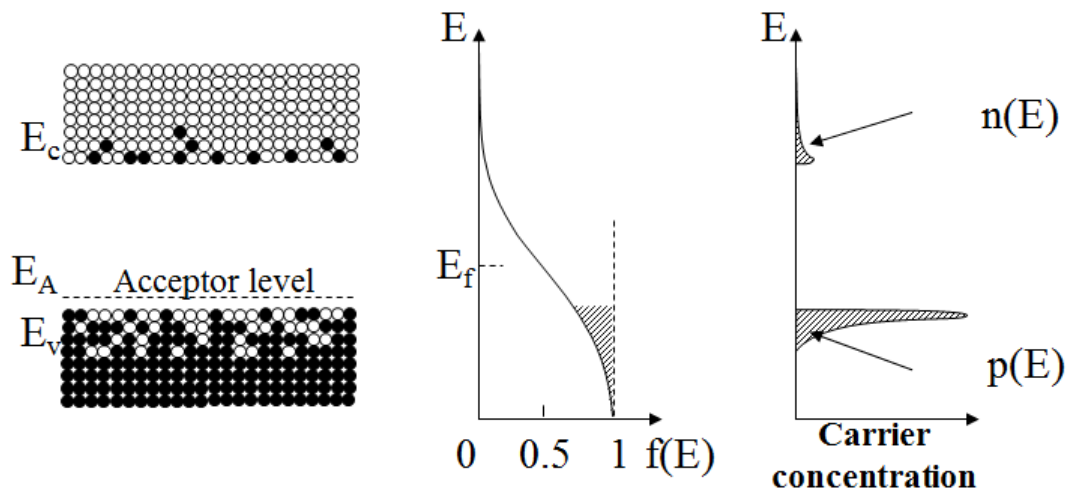
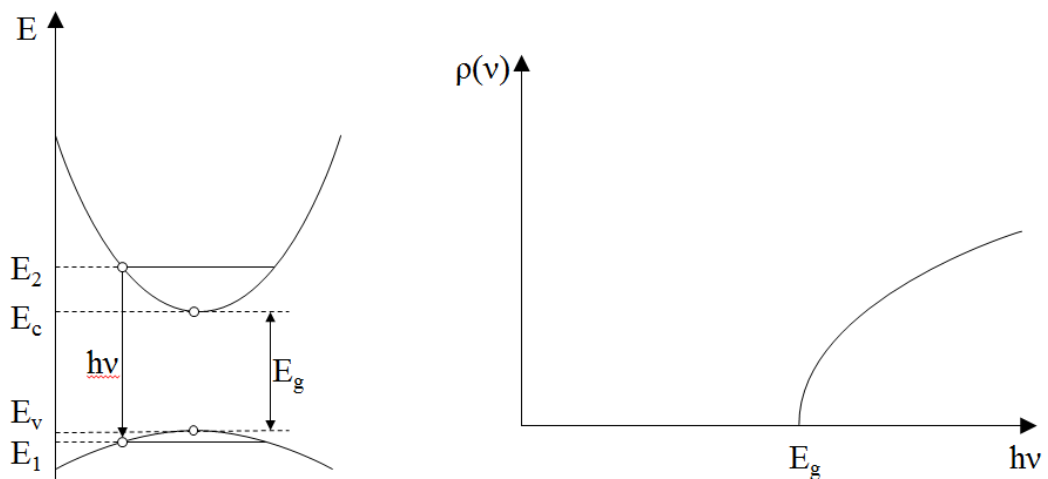


Figure 188: Carrier density distribution for p-type doped semiconductor.

Bandgap energy defines minimum frequency (maximum wavelength) of the emitted by Planck's relation (Eq. 24):

$$\Delta E = h\nu \quad \text{Eq. 24}$$

No transition might occur with $\Delta E < E_g$, thus E_g is minimal energy of emitted photon, defining minimal frequency of the emitted light. The LED spectrum is result of the carrier concentration function. Also with increasing temperature (for example due to inadequate cooling) emission spectrum from the LED will broaden, and colour will have tendency to shift toward blue, as bandgap energy defines maximum wavelength of the emitted light, peak emission is shifted toward lower wavelengths (see Figure 189 and Figure 190).



$$E_2 - E_1 = h\nu \geq E_g$$

Figure 189: Energies of possible transitions between conductivity band and valence band in a semiconductor and resulting spectrum.

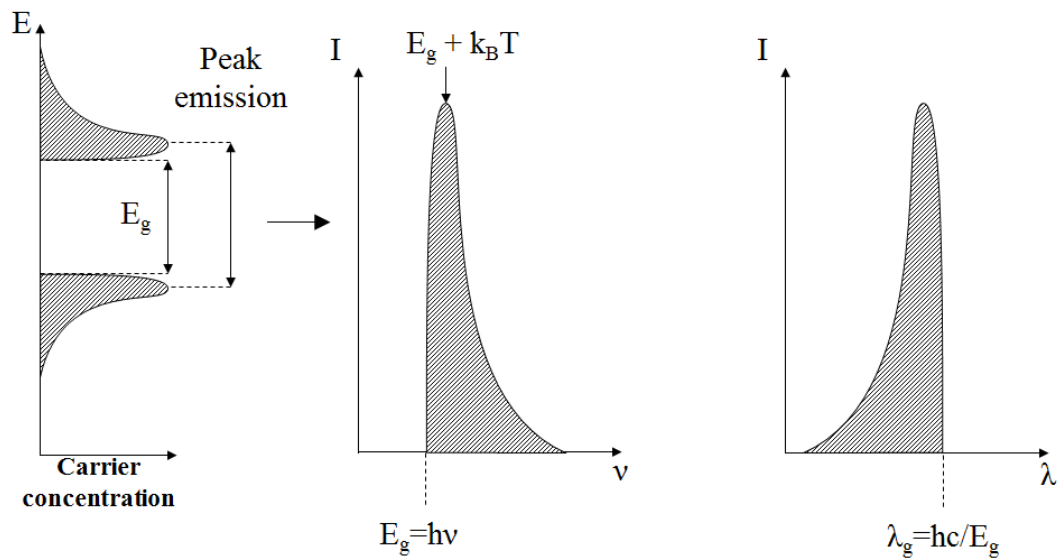


Figure 190: Spectrum shape of the emitted light from LED chip, due to carrier distribution.

Semiconductors typically have rather high refractive indices, making light extraction from the place of origin even more challenging due to the total internal reflection phenomenon. To maximise the Overall Energy Conversion Efficiency (OECE, mW of optical power for mW of electric power, also called Wall Plug Efficiency/WPE) (178) and luminosity of LEDs several technologies have been developed as follows: flip-chip construction (contacts are placed in bottom part of chip), patterned chips (engraved 3 dimensional structures on upper surface of chip), implementation of distributed Bragg mirrors (mirrors composed of layers of different dielectrics), thin film epitaxy (thickness of active layer is much lower than planar dimensions), using high reflectance contacts, minimising the surface of the contacts and removing base material used for the growth of the semiconductor layer (Figure 191 and Figure 192). The highest OECE is displayed by blue LEDs and can reach up to ca. 68.5 % (294). It typically goes down with wavelength and while it is possible to manufacture blue LEDs with WPE above 50%, commercially available UV-LEDs are still far less efficient, although the first UV-LEDs with WPE just above 20% were reported (297). The portion of supplied electrical energy not converted to light ends up as heat that must be effectively dissipated for the LED to avoid too high rise in temperature resulting in LED damage and reduced optical output. Figure 193 shows schematically loss sources for of delivered power converted in the LED chip.

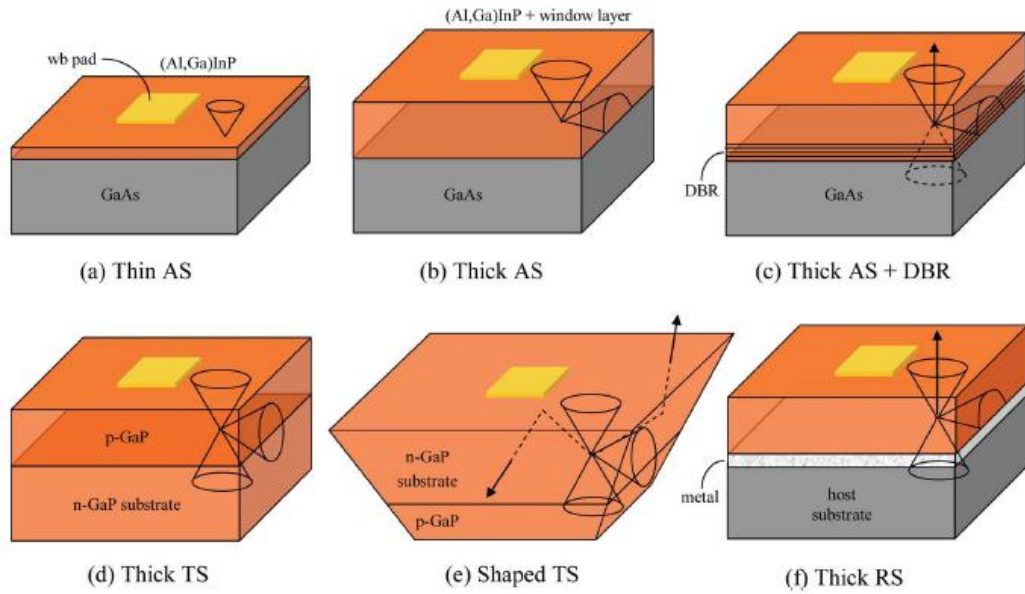


Figure 191: Different approaches to maximise light extraction from LED chip: AS – absorbing substrate, TS – transparent substrate, DBR – Distributed Bragg Reflector, RS – Reflective Substrate. Black cones represent angle values for which photon can may escape the chip and will not be lost due to total internal reflection (294).

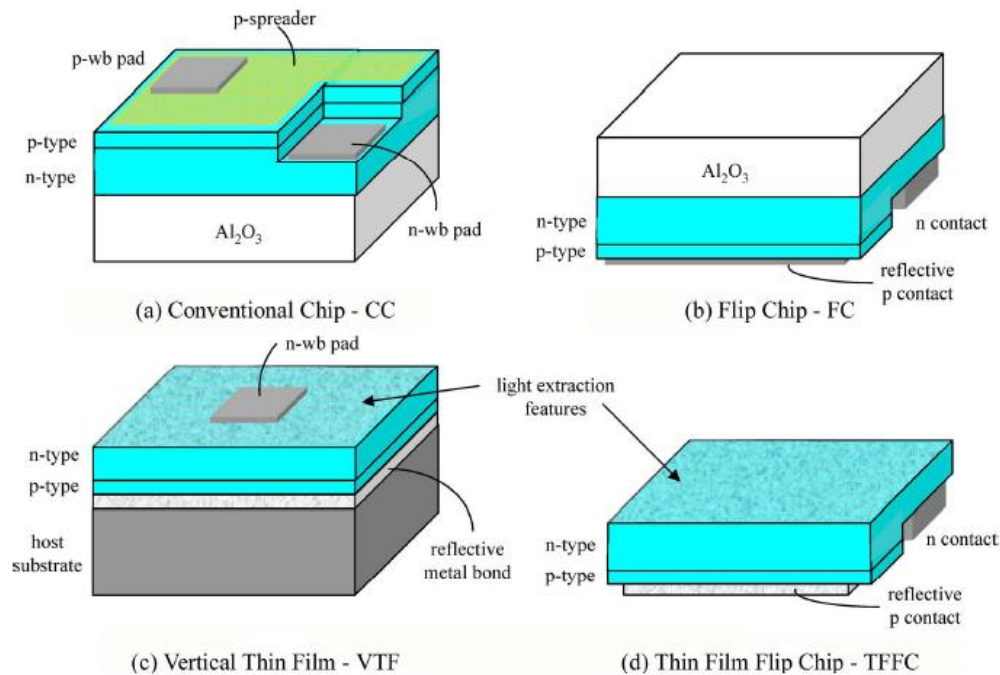


Figure 192: More modern approaches to manufacture LED chips: (a) application of semi-transparent contacts, (b) reflective p-contact, (c) application of reflective layer between host substrate and semiconductor, (d) combination of techniques used in (b) and (c).

Increase of the light emission can be divided into two regions: increased efficiency of photon creation and increased efficiency of extracting photons from place of origin outside. The resistive losses are of purely electrical origin, and are regarded as the most difficult to overcome. The nonradiative losses are mostly due to bandgap extremum mismatch and presence of horizontal transitions. This can be improved by application of semiconductors with

lower number of defects per unit volume. The extraction losses can be compensated by employing more efficient chip design such as textured surface, shaped chip or flip-chip technologies (294).

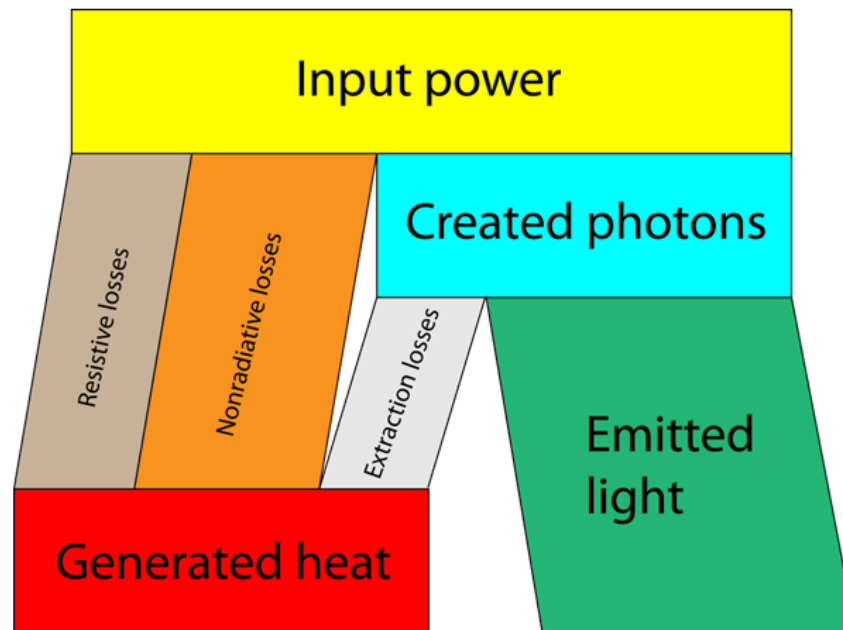


Figure 193: Graph illustrating losses in LED chip, after (294).

Laser diodes (LDs) are based on the same principle as LEDs (p-n junction and carrier recombination). Stimulated emission and optical gain are achieved by shaping active region of the chip into a form of optical waveguide closed by parabolic mirrors forming an optical resonator. Laser diodes are often used as a pumping laser for other laser devices. By principle laser diode is a semiconductor laser (Light Amplification by Stimulated Emission of Radiation (298)) device. The main differences between LDs and LEDs are in spectra, coherent emission pattern, and output power. LDs emit a much narrower spectrum than LEDs in the range of few nm. Compared to LEDs, LDs emitted light has higher time and spatial coherence. Laser diodes of near infrared region can have output power reaching even 15kW (165). Probably the most common application of LDs is usage as an optical pumping device for other lasers (197; 299).

Appendix E – Experiments on real time visualisation of fluorescent dye in a microfluidic chip

Visualisation experiments were performed in a thinkXXS Snake Mixer Slide SMS 0104 microfluidic chip, bought from thinkXXS Microtechnology, Zweibrücken, Germany, see Figure 194.



Figure 194: Photo of thinkXXS Snake Mixer Slide SMS 0104 microfluidic chip.

The following chemical reagents were used during the visualisation of fluorescent dye experiments.

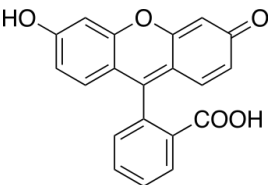
Chemical	Structure	Manufacturer	Purity	CAS Number
Fluorescein		Aldrich®	>95%	2321-07-5

Table 43: Table of chemicals used during experiments on real-time visualisation of the fluorescent dyes in microfluidic chip.

Real-time on-line visualisation of fluorescent dye (fluorescein) was performed in a SMS0104 microfluidic chip. Sample of known concentration was introduced to the injection valve sample loop, and afterwards was pumped through the chip with low pressure pump (6 bars max pressure) at low flow rate (<2-5 μ l/min). The chip channel was illuminated with Luxeon LED and emitted light was collected by a small USB microscope. The experimental setup is presented in Figure 195 and Figure 196. Luxeon LED was driven at 700mA (maximum allowed stable current for that model). The current was reduced during picture taking to 290mA to reduce brightness of the LED. Two different excitation filters were used to test the

system efficiency. Their transmission spectra overlaying excitation and emission spectrum of used fluorescent dye are shown on Figure 197. Emission filter was fitted directly to the USB microscope objective to prevent registration of any parasitic light from the used light source or environment (e.g. light emitted by laptop screen). Experiments were conducted in a dark room. Data was recorded in the form of pictures and movies by microscope software and stored in the form of *.jpg and *.mov files.

The sample was introduced to the system using a Rheodyne 7125 Injector valve, fitted with a custom made 10 μ l loop. The used LED was a 3W Luxeon V Star, bought from Dotlight, Jülich, Germany. Excitation filter used was BrightLine Basic Fluorescence Filter 460/60 F39-461, purchased from AHF Analysentechnik, Tübingen, Germany with 460nm central wavelength and 60 nm full width at half maximum (FWHM) and Edmund Optics NT-62-081 442nm CWL, 10nm bandwidth filter. Emission filter was Edmund Optics NT-46-057 GG-475 12.5mm long pass filter, with cut-off wavelength at 475 \pm 6 nm.

A switching mode power supply unit N93CX bought from Maplin, Ireland was used to drive the LED and constant current 700 mA.

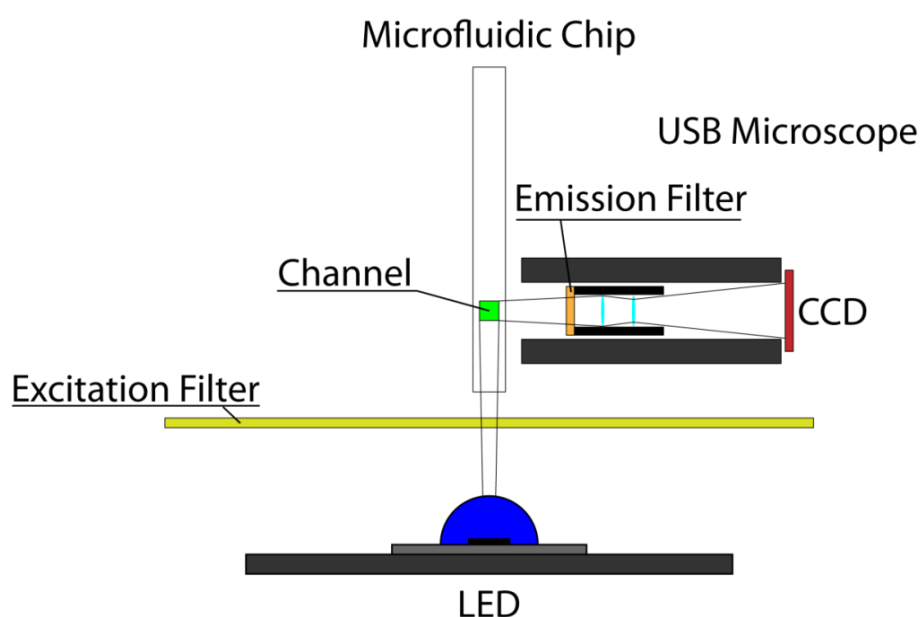


Figure 195: Schematic of the experimental setup for real-time visualisation of a fluorescent dye in the SMS0104 microfluidic chip.

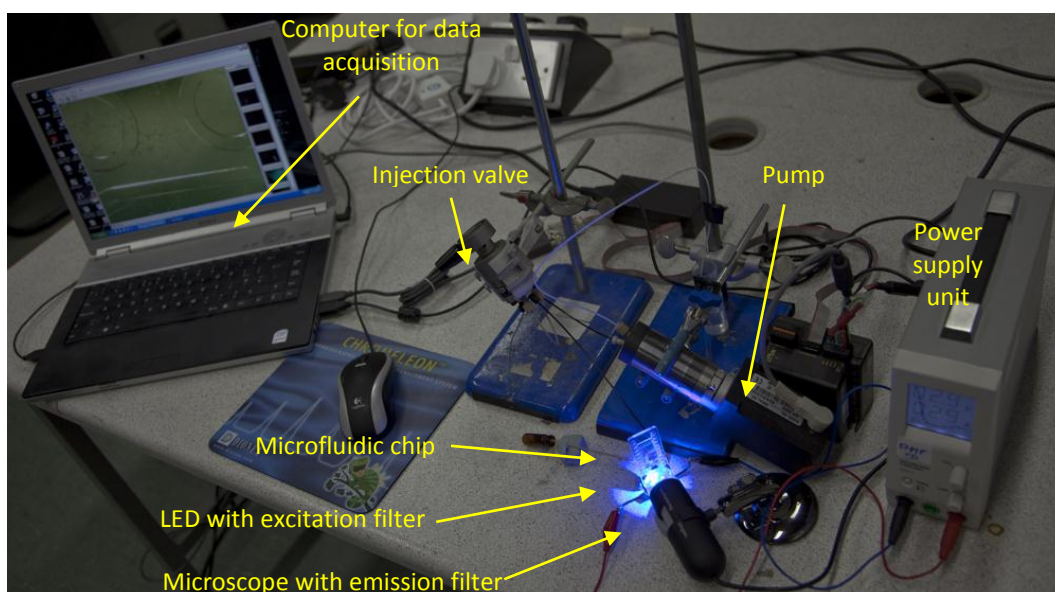


Figure 196: Photography of the experimental setup for visualisation of a fluorescent dye in the SMS0104 microfluidic chip.

A series of simple experiments was conducted to find a cheap alternative for real-time on-chip fluorescent imaging. The fluorometric detection was discussed as an alternative method for experiments with EHD focusing in microfluidic chips. This method was not selected as the used chip dimensions were significantly larger than the used microscope field of view (FOV) and whole chip imaging was not possible. Nevertheless this method could be employed in other fluidic experiments where the area of interest is smaller than the FOV of the used microscope.

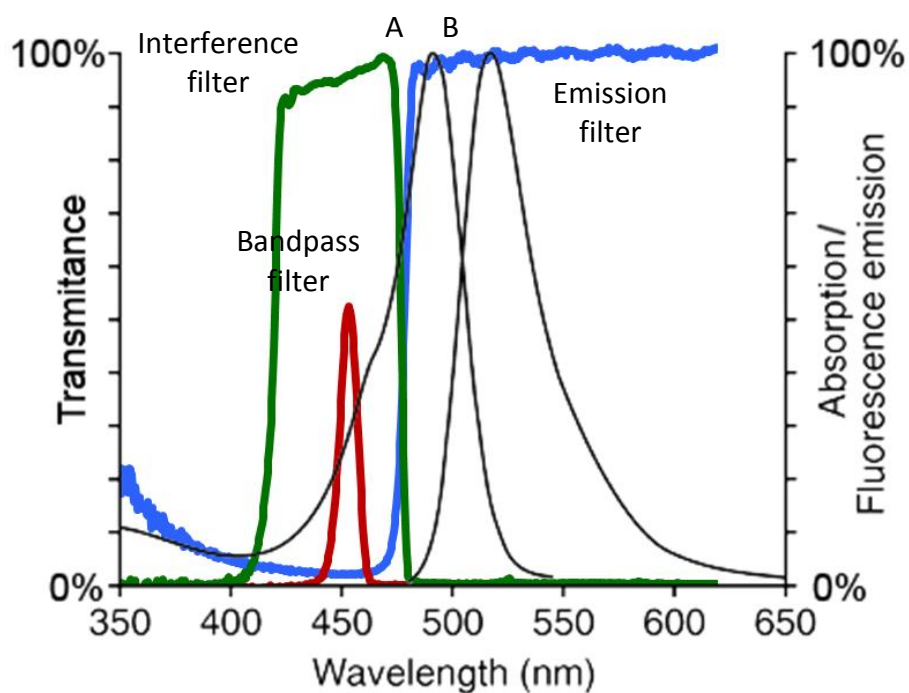


Figure 197: Absorption (a) and emission (b) spectra of fluorescein with overlaying transmission spectra for two excitation filters: red line – bandpass filter, green line – interference filter and blue line – emission filter

Figure 198 and Figure 199 shows difference in the amount of light reaching the detector if different filters are employed. The difference is one order of magnitude – fluorescein at 10^{-7}M is easily visible. The LED was installed 12mm from the chip channel (marked with white arrow in Figure 198 and Figure 199). Measured radiometric power of the used LED was 24mW, the channel width 600 μm and channel length was 6mm giving a total cross-sectional area of 3.6mm², which is equivalent to provide a solid angle of 0.0062sr. As the energy emission is close to a maximum along the illumination axis, assuming uniform energy distribution it gives 152 μW of energy delivered to the chip channel (without filter). After calculating transmission loss due to filter presence, energy delivered with the bandpass filter was 12 μW and with the interference filter it is 53 μW . The amount of energy delivered to the chip channel with the interference filter is over four times higher. The emitted light was collected 44mm from the chip by a 3mm diameter objective. This gave solid angle of only 0.0073sr. Assuming 100% efficient isotropic fluorescence gives 0.7 μW delivered to the CCD matrix in the microscope for the bandpass filter and 3 μW for the interference filter.

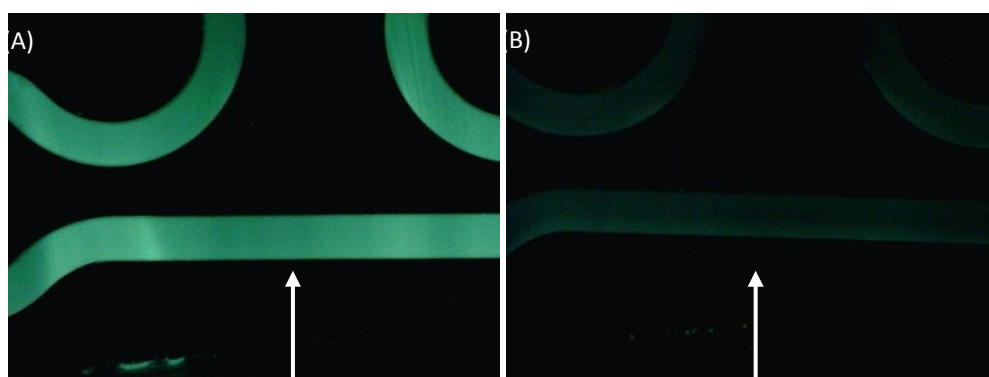


Figure 198: Images of the fluorescein at (a) 10^{-5}M and (b) 10^{-6}M recorded with used bandpass filter. White arrow indicated direction of the illumination in the picture plane.

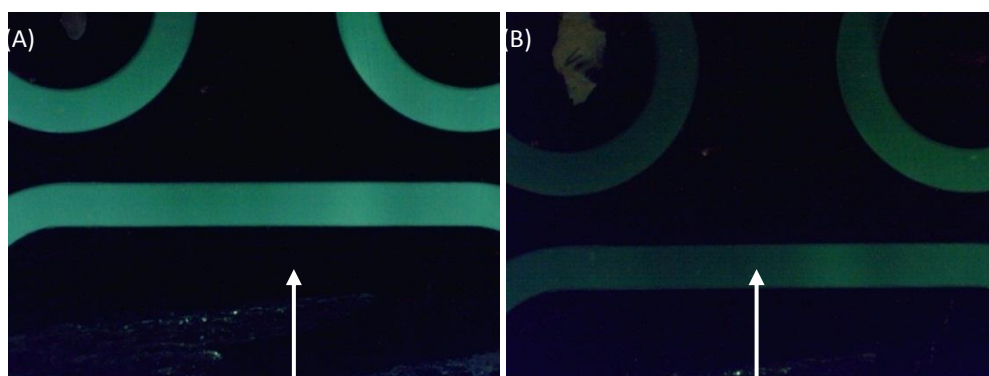


Figure 199: Images of the fluorescein at (a) 10^{-6}M and (b) 10^{-7}M recorded with used interference filter. White arrow indicated direction of the illumination in the picture plane.

Traditionally visualisation of fluorescent compounds is conducted using large and expensive optical microscopes. Also it is typically conducted with shutter-equipped digital

cameras that are gathering light for a predefined period of time. In this experiment a real-time visualisation was demonstrated using significantly cheaper and portable equipment. Although visualisation of fluorescein at concentration of 10^{-7} is not setting a new record, conducted calculations show where to look for improvements in energy transfer. Fluorescent detection is very sensitive and the possibilities of integrating it into a portable μ -TAS device should be explored thoroughly.

Appendix F – Mesh structures and convergence graphs

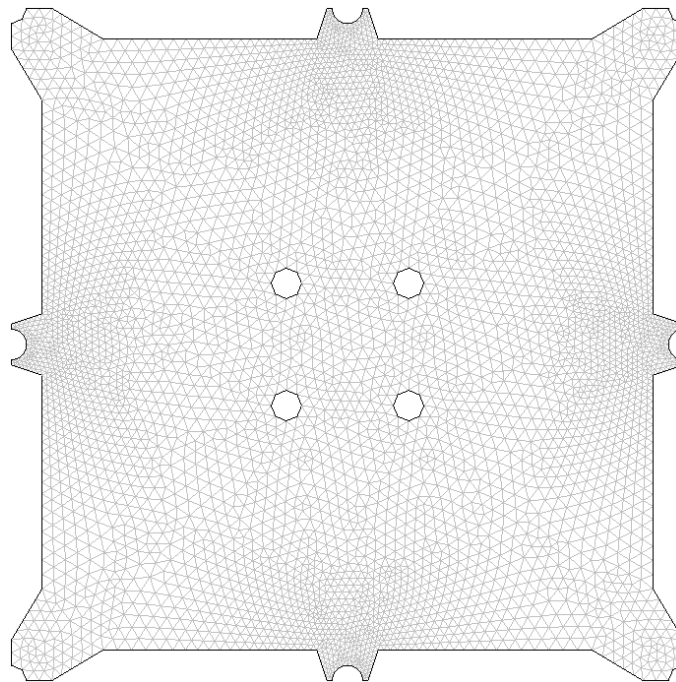


Figure 200: Extremely coarse mesh grid.

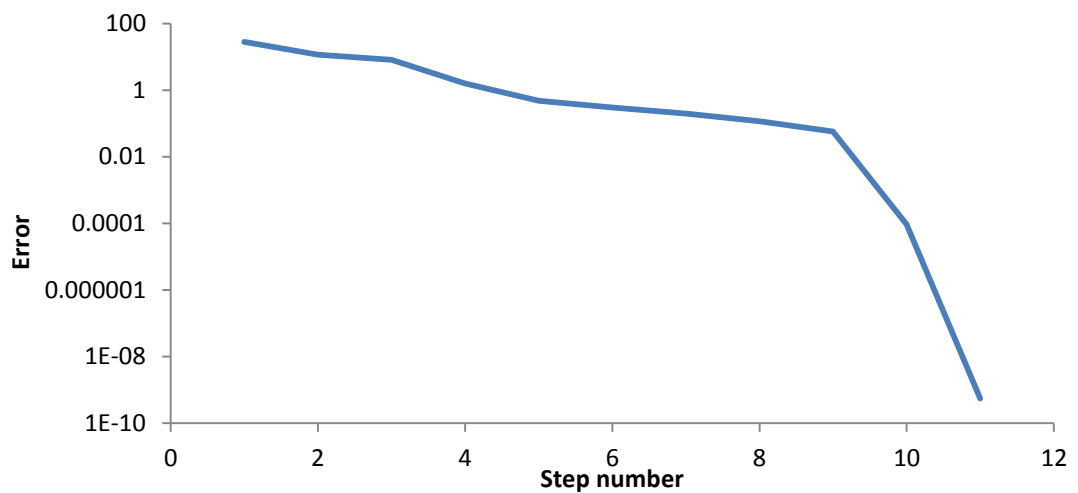


Figure 201: Convergence graph for extremely coarse mesh.

Extremely coarse mesh grid parameters:

Mesh:	9,178 elements
Degrees of Freedom:	79,636
Solution time:	145.02s
Memory usage:	275MB

Table 44: Summary of the extremely coarse mesh.

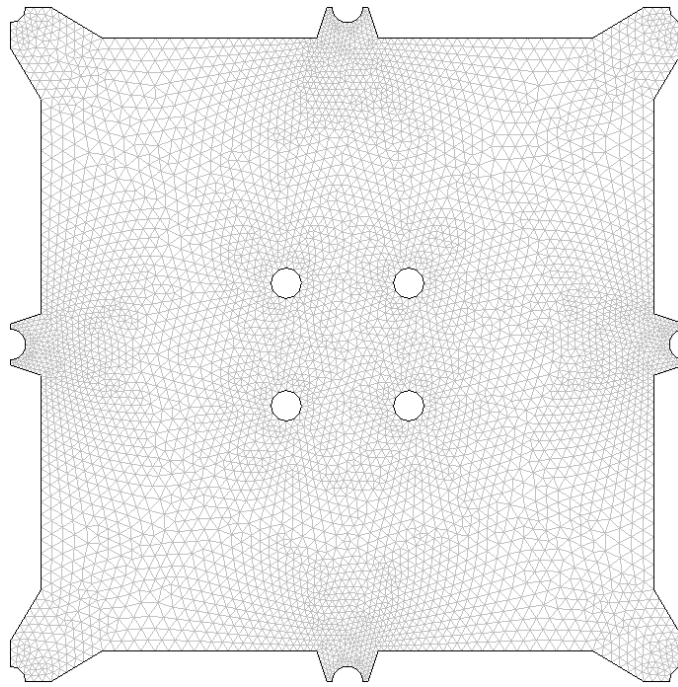


Figure 202: Coarser mesh grid.

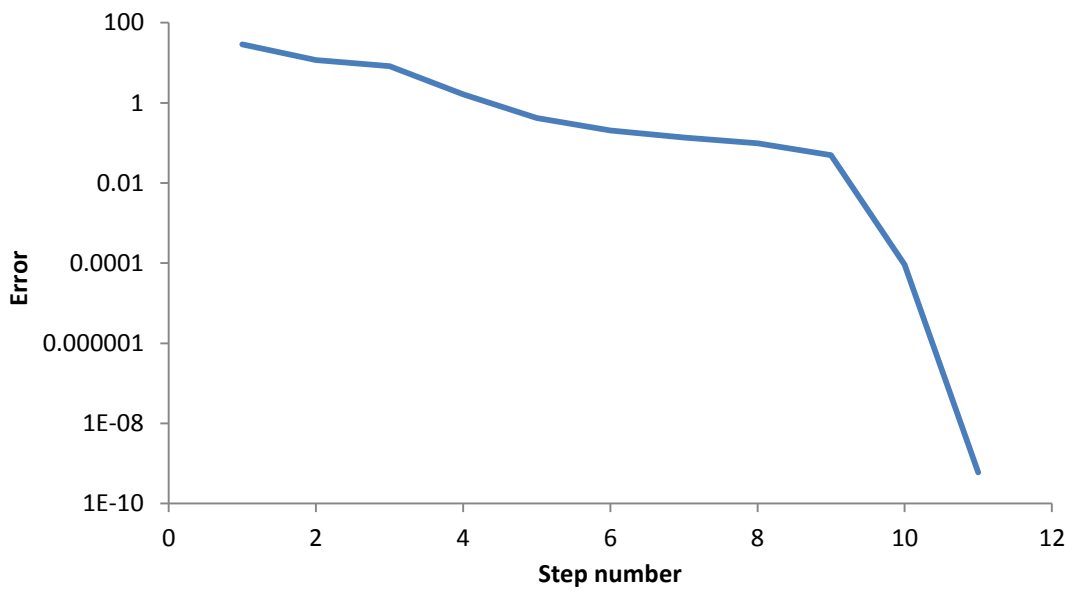


Figure 203: Convergence graph for coarser mesh.

Coarser mesh grid parameters:

Mesh:	11,188 elements
Degrees of Freedom:	96,892
Solution time:	209.19s
Memory usage:	344MB

Table 45: Summary of the coarser mesh.

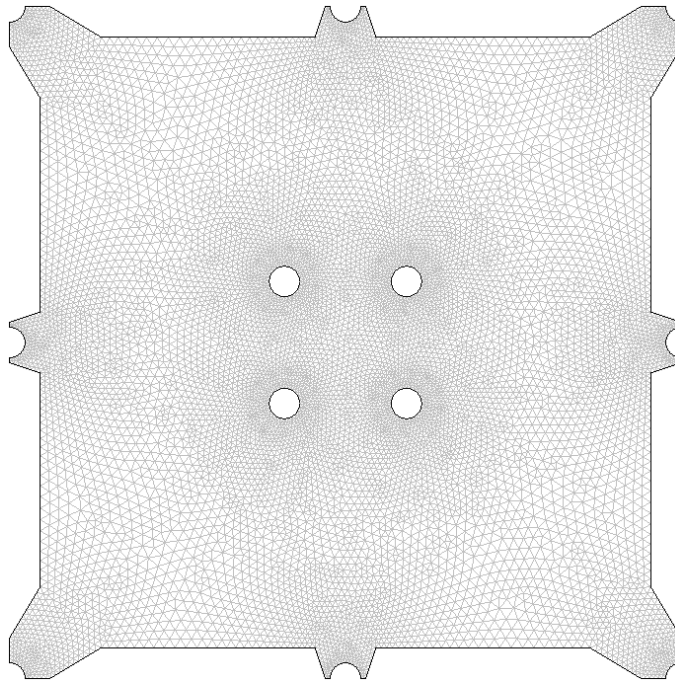


Figure 204: Normal mesh grid.

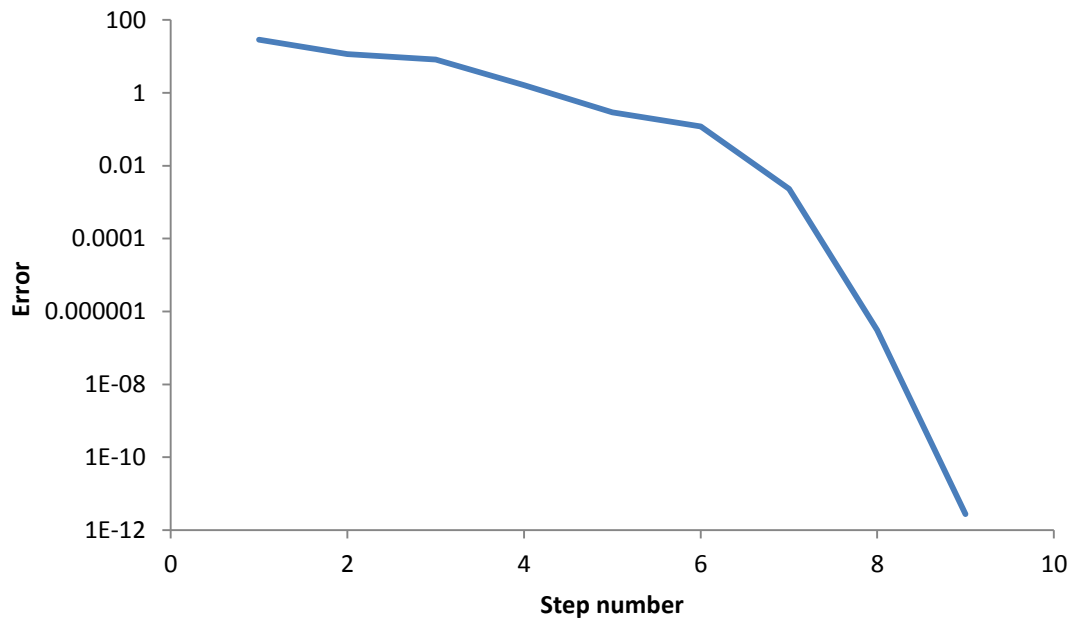


Figure 205: Convergence graph for normal mesh.

Normal mesh grid parameters:

Mesh:	21,284 elements
Degrees of Freedom:	183,473
Solution time:	499.951s
Memory usage:	347MB

Table 46: Summary of the normal mesh.

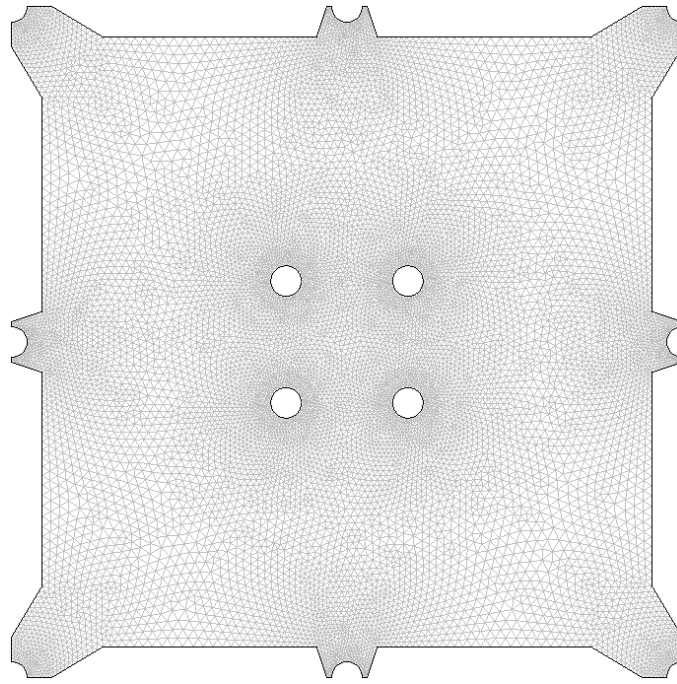


Figure 206: Finer mesh grid.

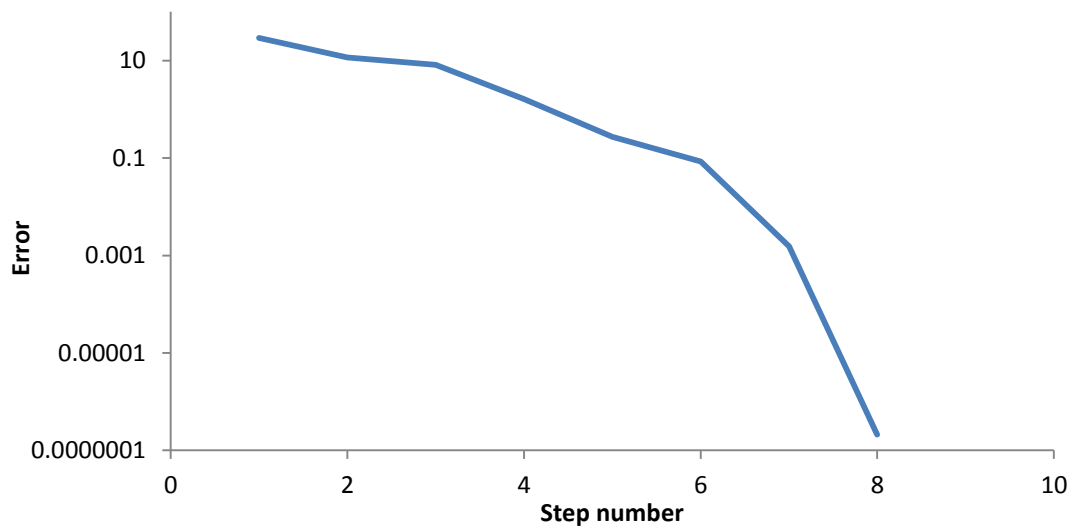


Figure 207: Convergence graph for finer mesh.

Finer mesh grid parameters:

Mesh:	25,886 elements
Degrees of Freedom:	223,022
Solution time:	550.551s
Memory usage:	345MB

Table 47: Summary of the finer mesh.

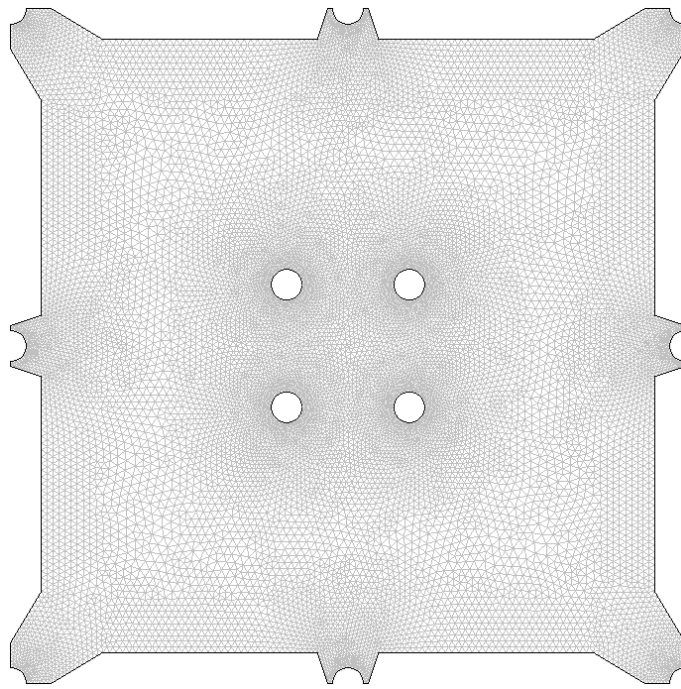


Figure 208: Extremely fine mesh grid.

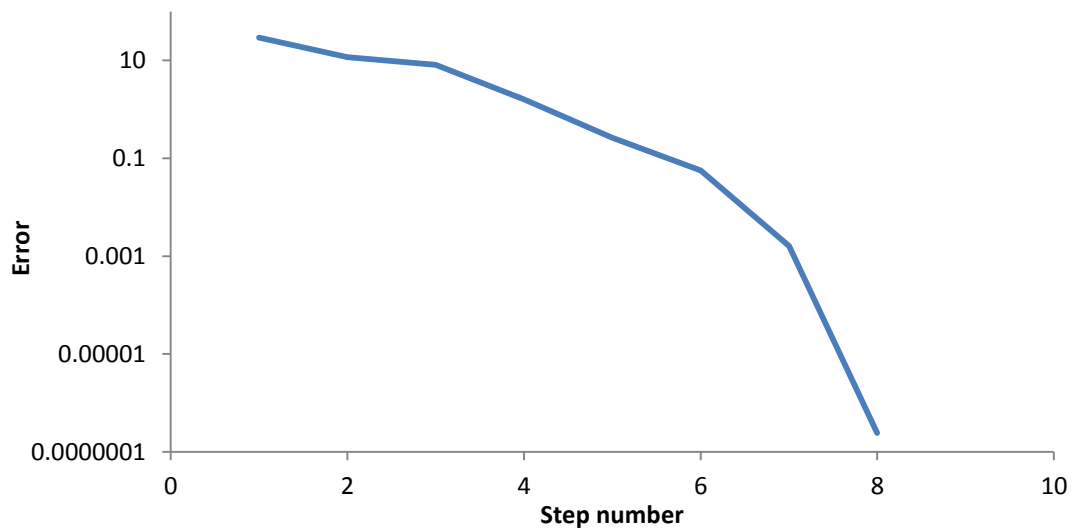


Figure 209: Convergence graph for extremely fine mesh.

Extremely fine mesh grid parameters:

Mesh:	31,166 elements
Degrees of Freedom:	268,298
Solution time:	761.551s
Memory usage:	366MB

Table 48: Summary of the extremely fine mesh.

Appendix G – Technical drawings for the microfluidic chip for EHDF

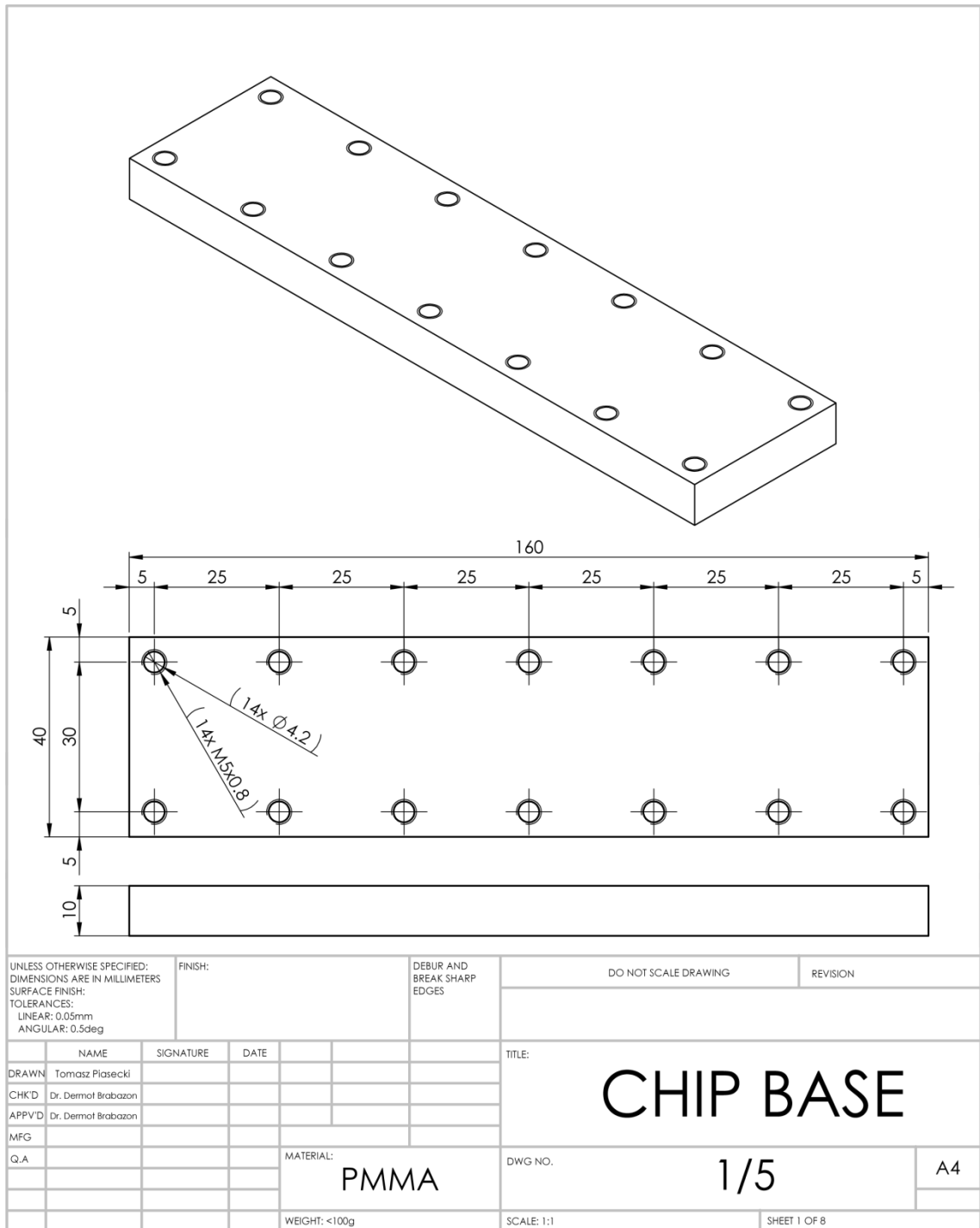


Figure 210: Lower layer of PMMA chip for EHDF.

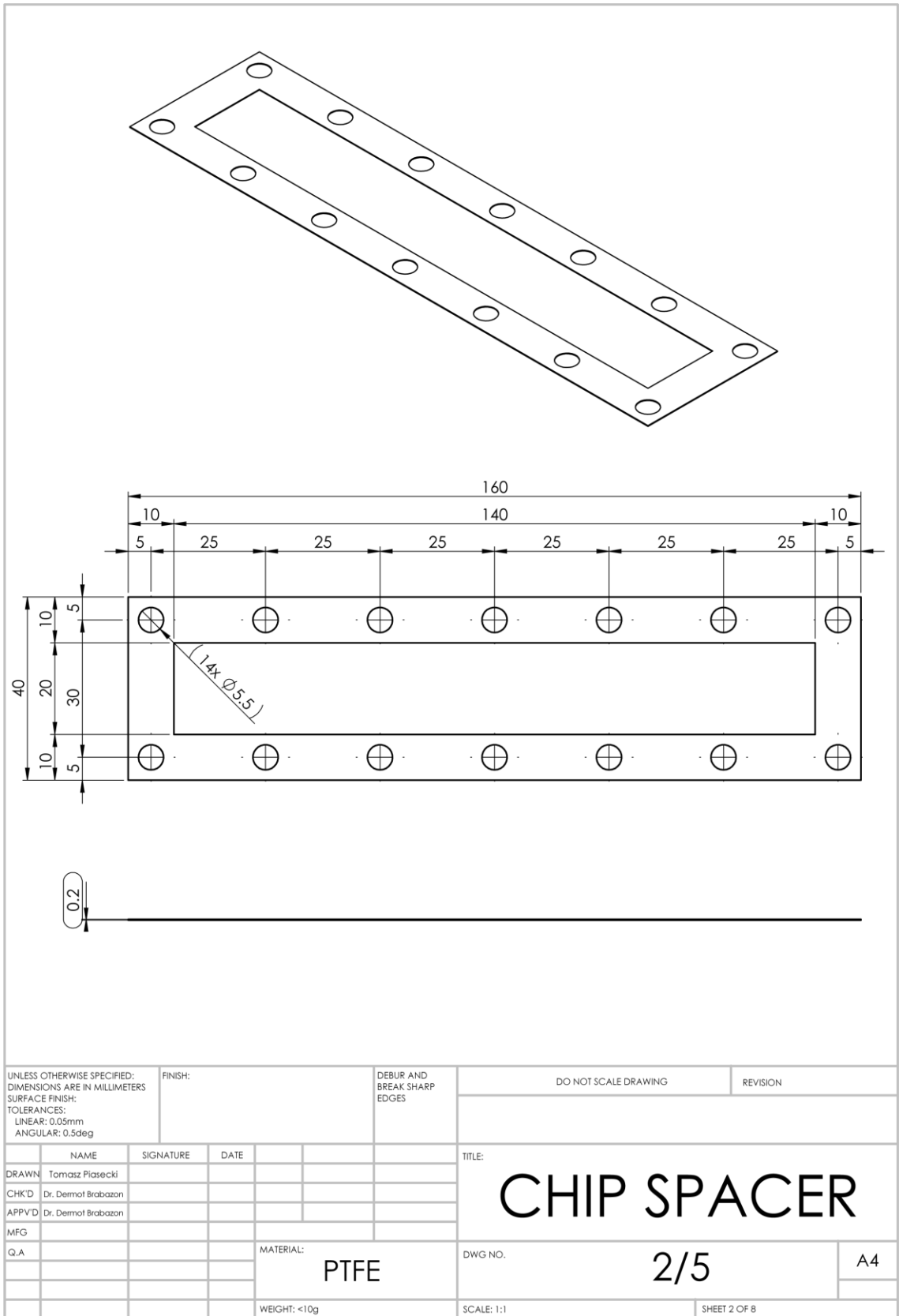


Figure 211: The PTFE gasket (thickness varies) used in the PMMA chip for EHDF.

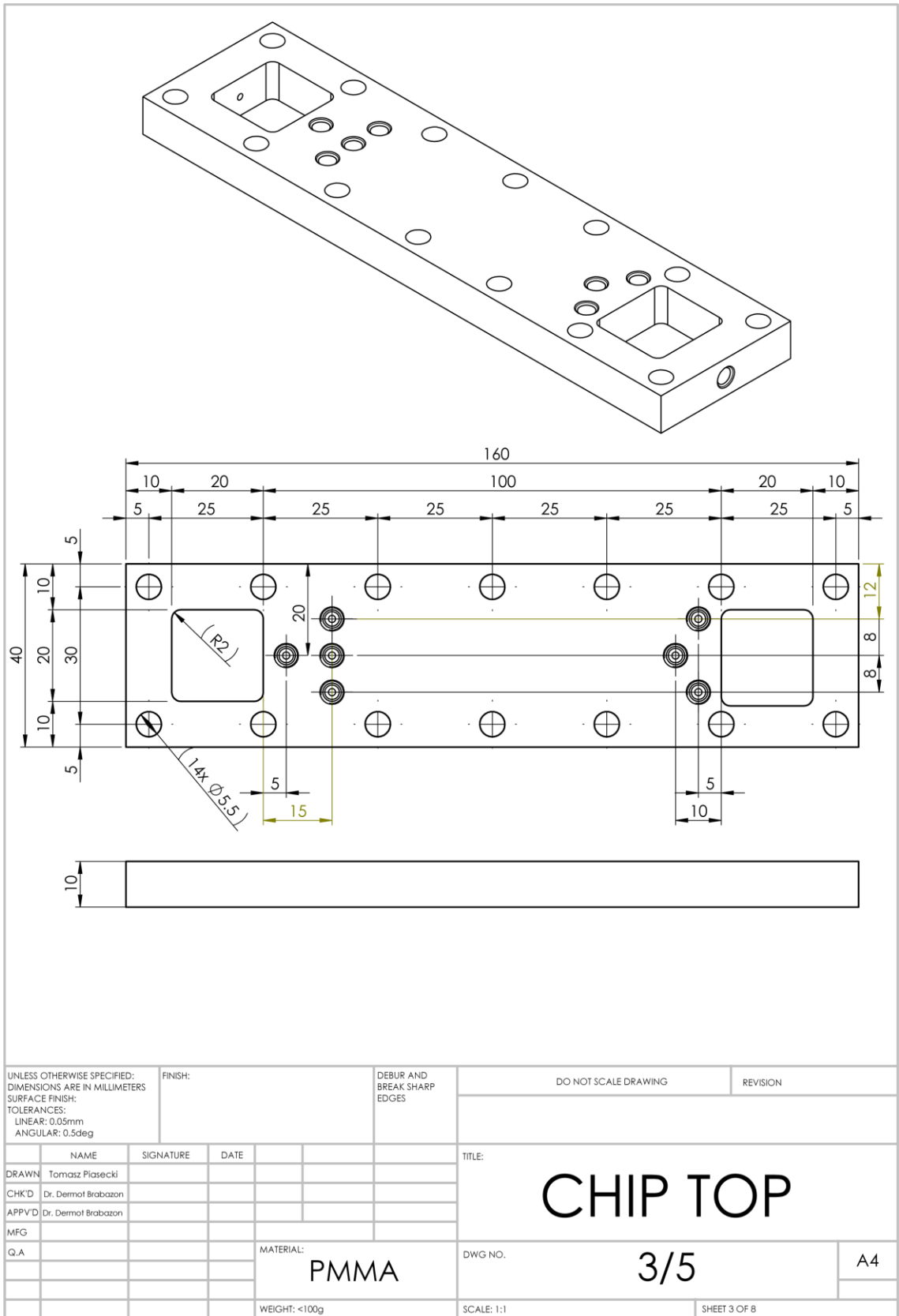


Figure 212: upper layer of the PMMA chip used for EHDF.

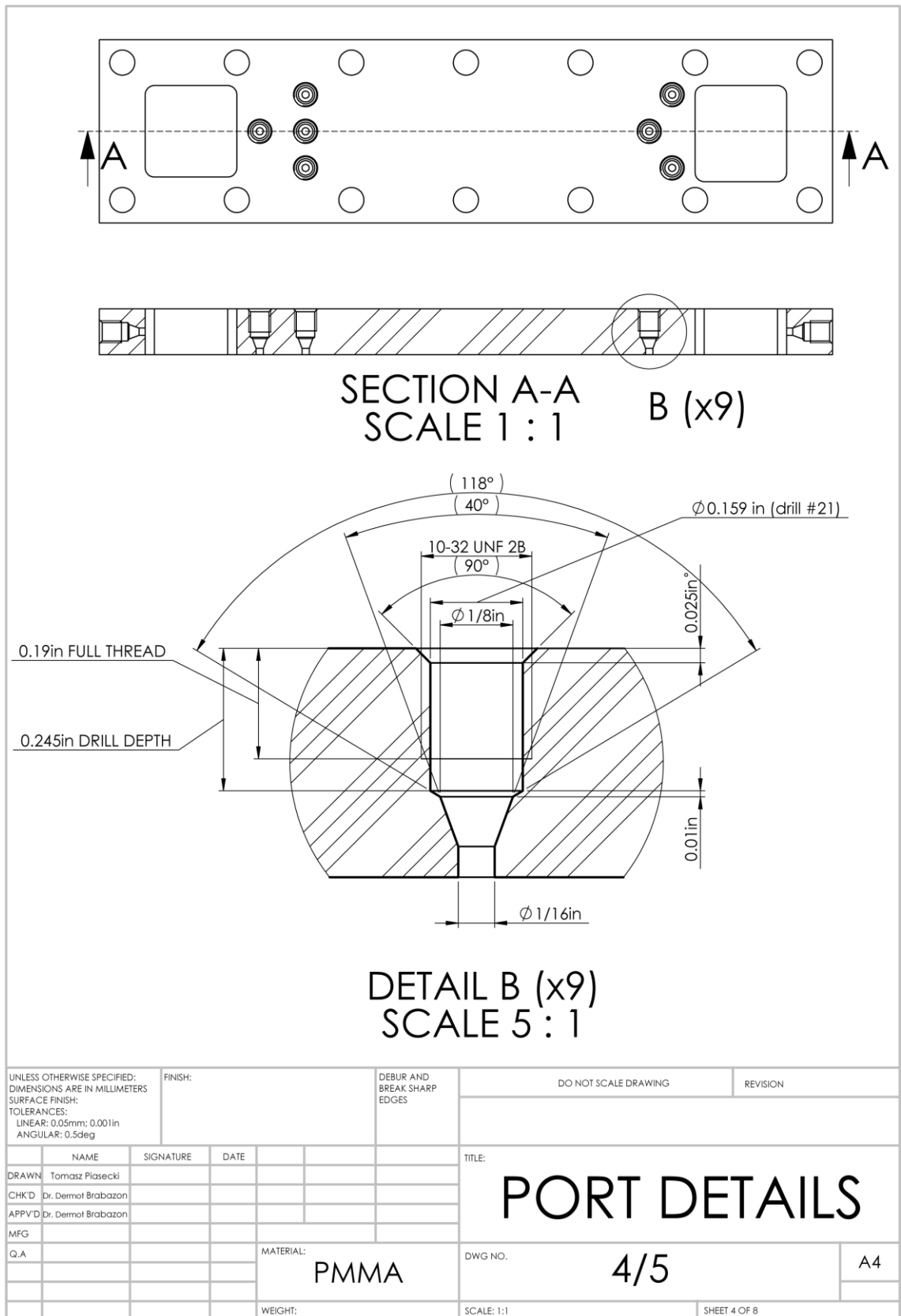


Figure 213: Details of standard 10-32 microfluidic port (nine installed in the upper layer).

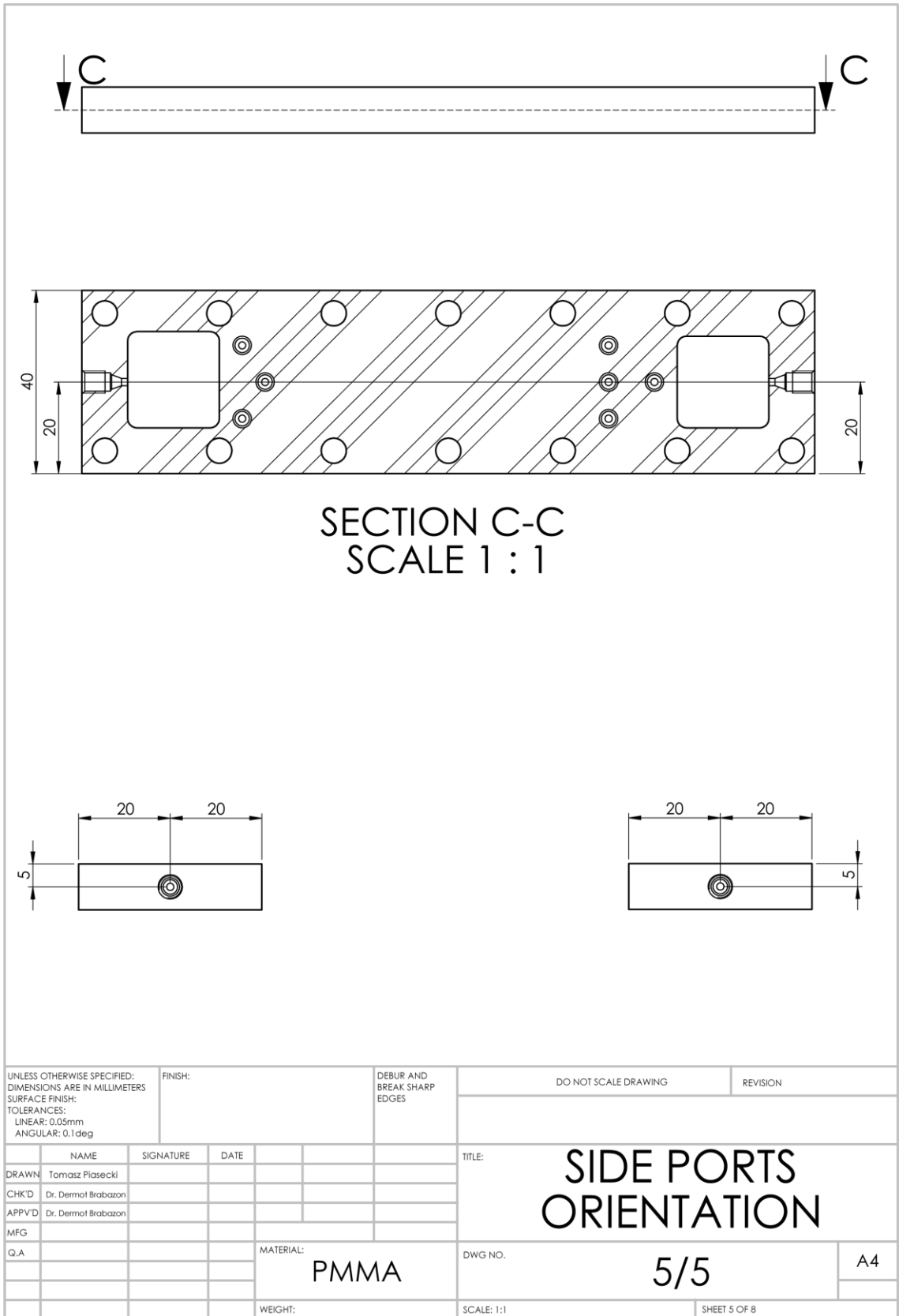


Figure 214: Side ports orientation.

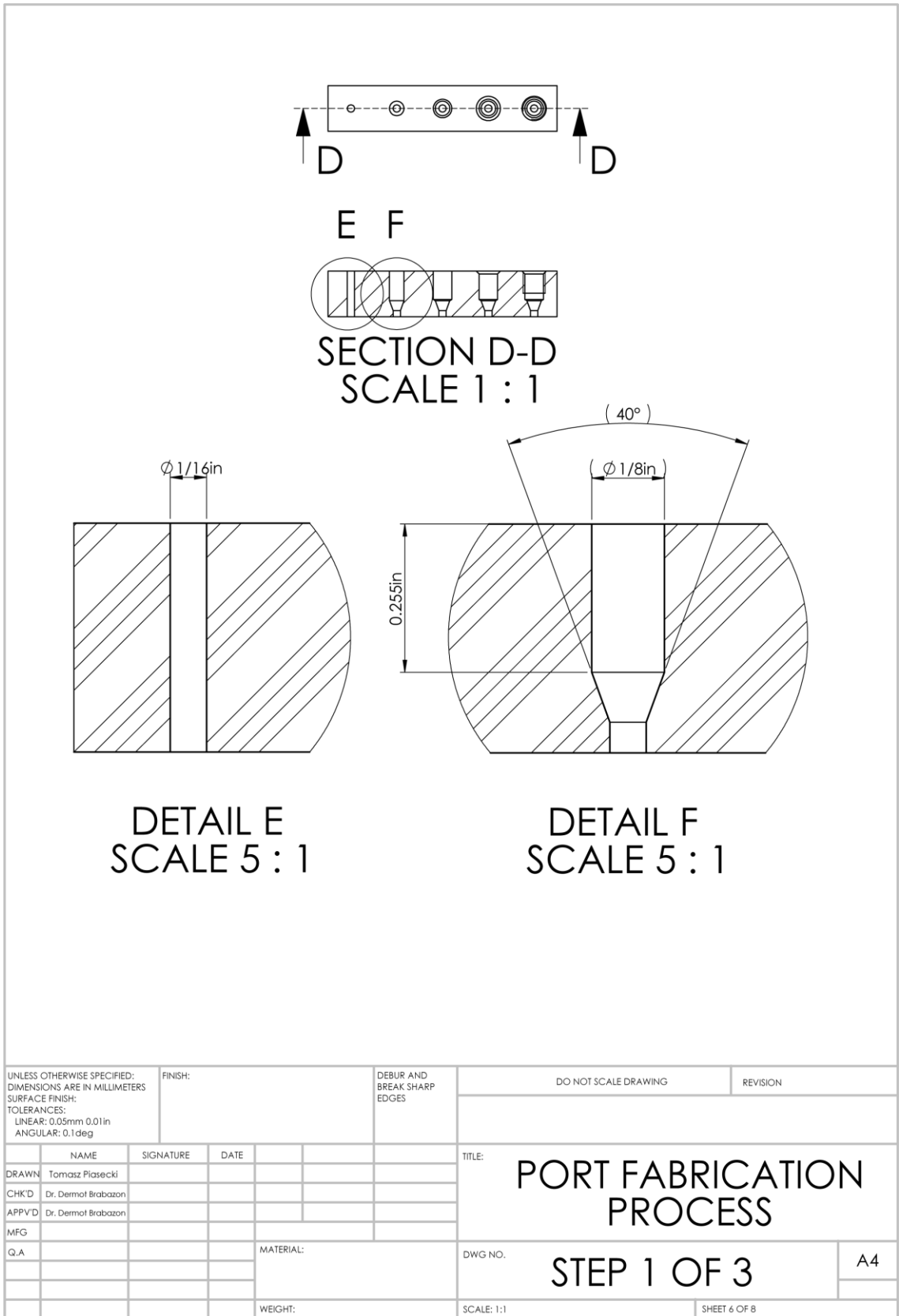


Figure 215: Details of technological process of the microfluidic port fabrication (steps one and two).

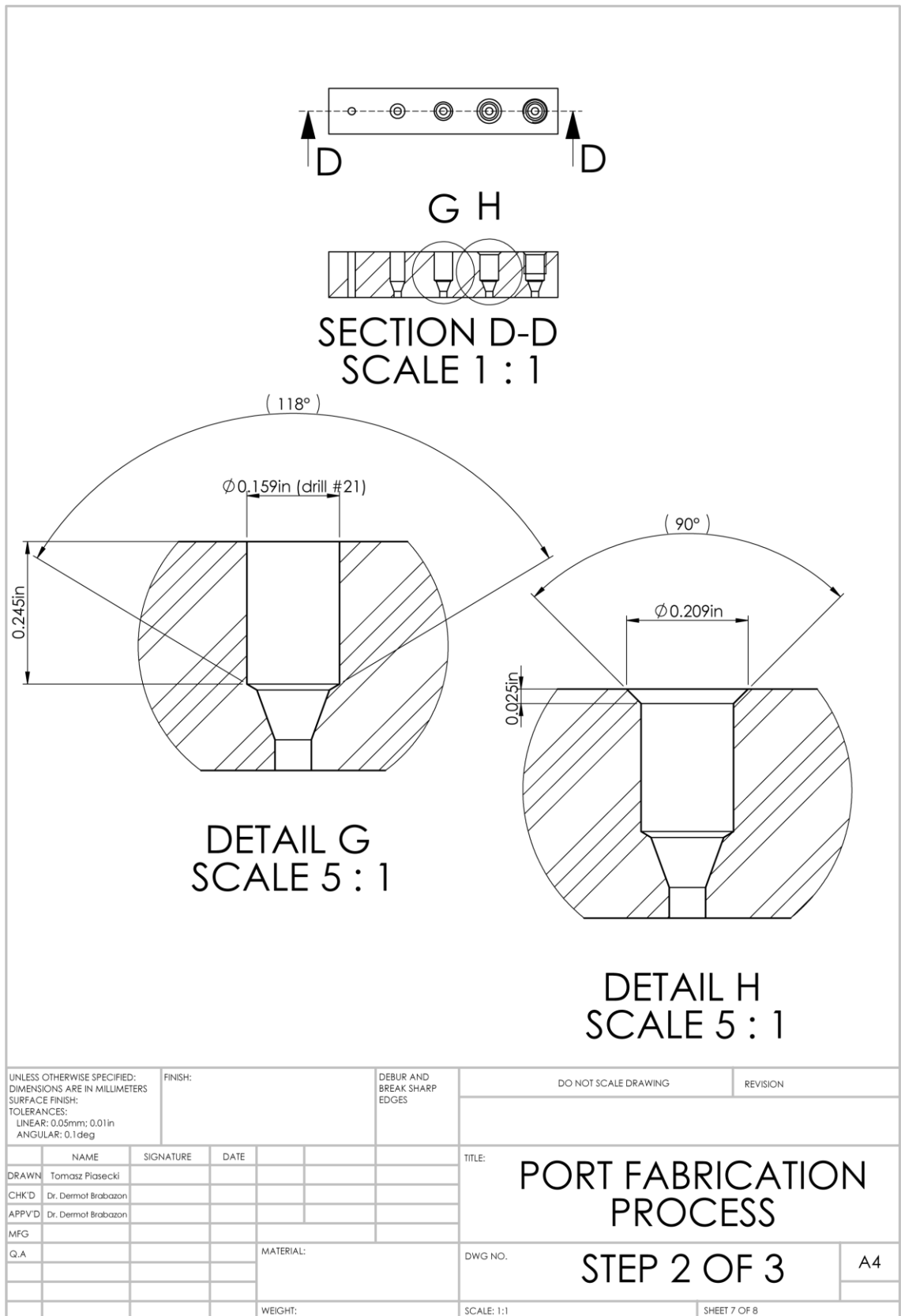
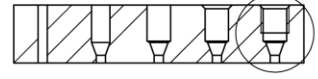
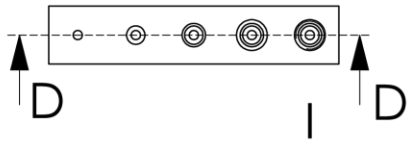
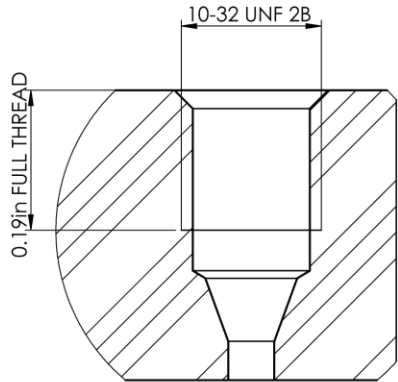


Figure 216: Details of technological process of the microfluidic port fabrication (steps three and four).



SECTION D-D
SCALE 1 : 1



DETAIL I
SCALE 5 : 1

UNLESS OTHERWISE SPECIFIED: DIMENSIONS ARE IN MILLIMETERS SURFACE FINISH: TOLERANCES: LINEAR: 0.05mm; 0.01in ANGULAR: 0.1deg		FINISH:		DEBUR AND BREAK SHARP EDGES		DO NOT SCALE DRAWING		REVISION	
DRAWN Tomasz Piasecki		SIGNATURE		DATE		TITLE: PORT FABRICATION PROCESS		DWG NO. STEP 3 OF 3	
CHK'D Dr. Dermal Brabazon									
APPV'D Dr. Dermal Brabazon									
MFG									
Q.A				MATERIAL:		SCALE: 1:1		SHEET 8 OF 8	
				WEIGHT:				A4	

Figure 217: Details of technological process of the microfluidic port fabrication (step five).

Appendix H – Mesh parameters used for comparison of mesh types

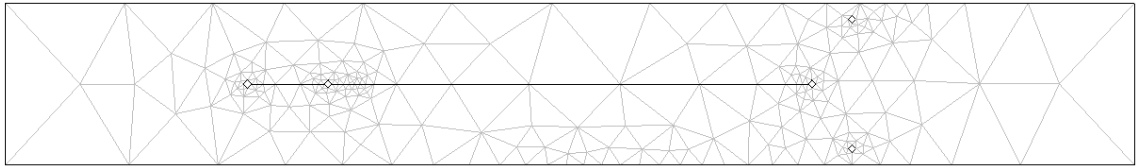


Figure 218: Extremely coarse triangular mesh.

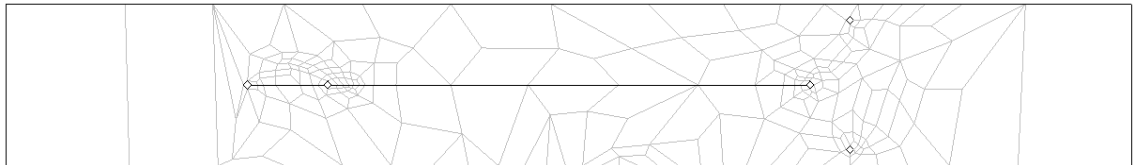


Figure 219: Extremely coarse quad mesh.

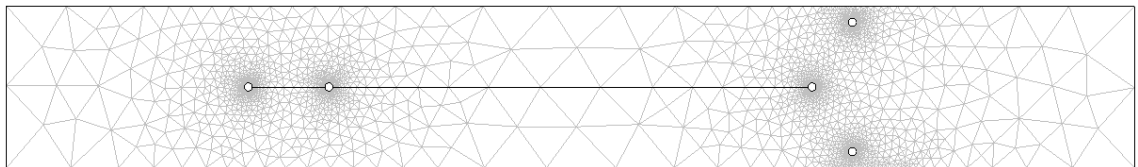


Figure 220: Normal triangular mesh.

Normal triangular mesh grid parameters:

Mesh:	3,927 elements
Degrees of Freedom:	42,469
Solution time:	237.29s
Memory usage:	413MB

Table 49: Summary of the normal triangular mesh.

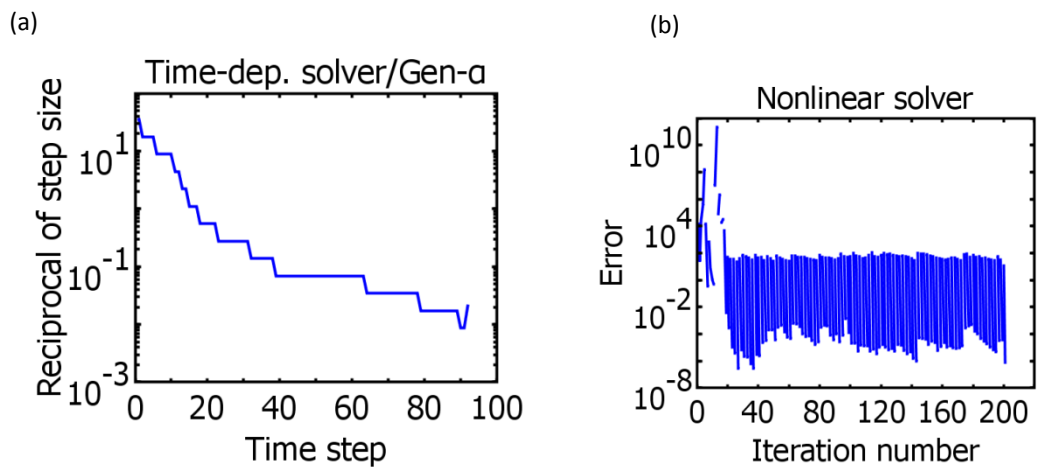


Figure 221: (a) Reciprocal of time step and (b) error in each iteration for normal triangular mesh.

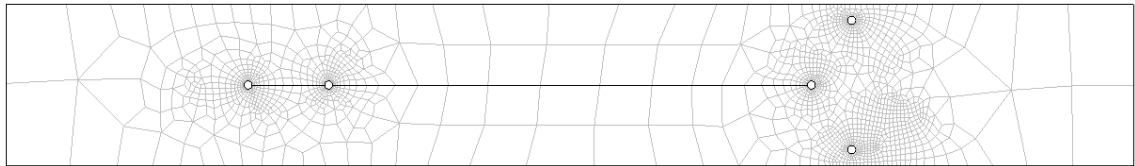


Figure 222: Normal quad mesh.

Normal quad mesh grid parameters:

Mesh:	1,814 elements
Degrees of Freedom:	39,335
Solution time:	236.681s
Memory usage:	965MB

Table 50: Summary of the normal quad mesh.

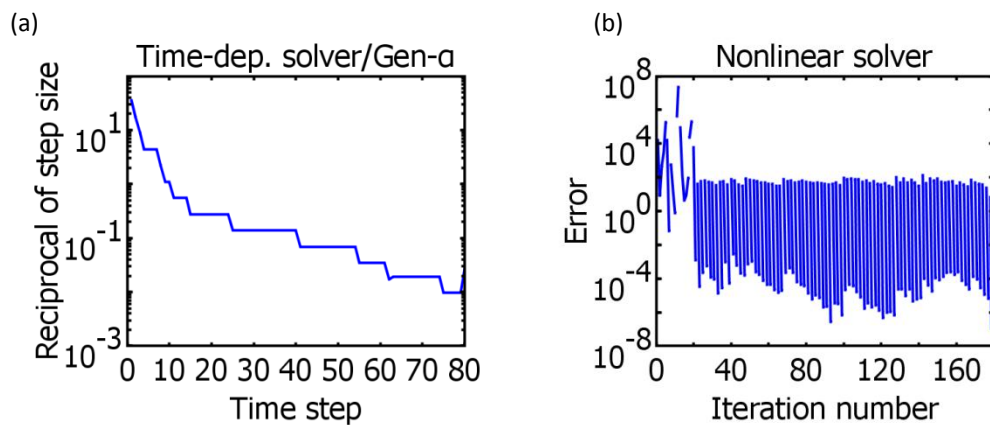


Figure 223: (a) Reciprocal of time step and (b) error in each iteration for normal quad mesh.

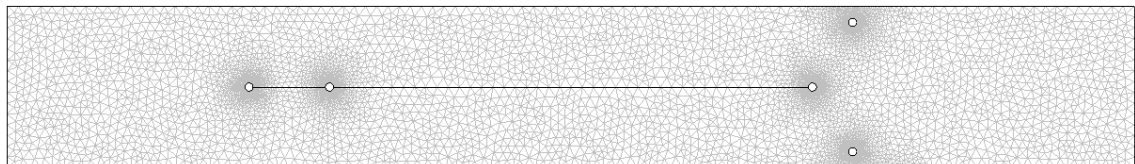


Figure 224: Extremely fine triangular mesh.

Extremely fine triangular mesh grid parameters:

Mesh:	7,248 elements
Degrees of Freedom:	77,829
Solution time:	421s
Memory usage:	552MB

Table 51: Summary of the extremely fine triangular mesh.

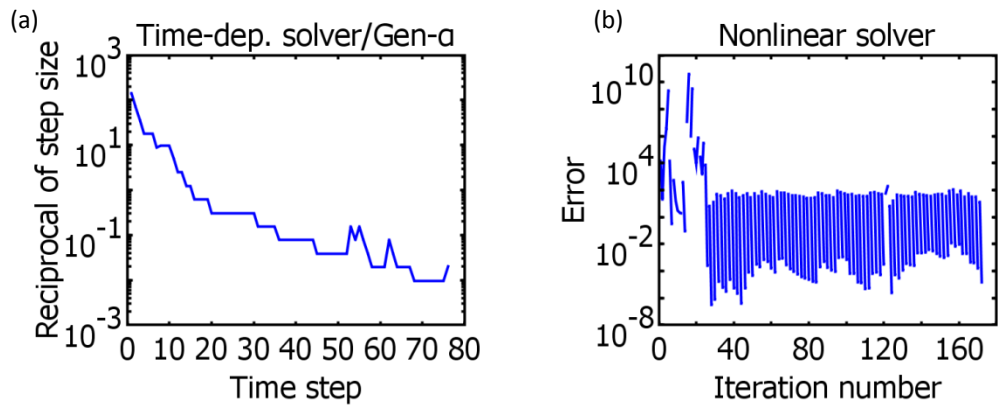


Figure 225: (a) Reciprocal of time step and (b) error in each iteration for the extremely fine triangular mesh.

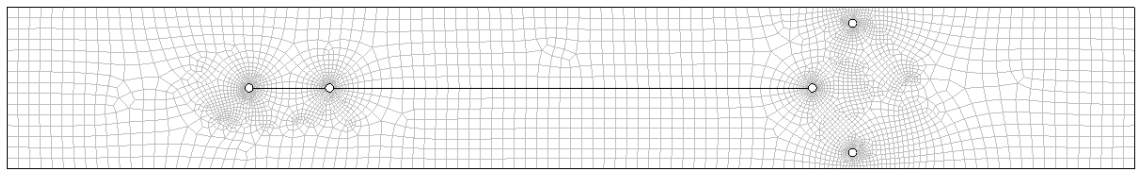


Figure 226: Extremely fine quad mesh.

Extremely fine quad mesh grid parameters:

Mesh:	4,057 elements
Degrees of Freedom:	87,538
Solution time:	526.441
Memory usage:	1,049MB

Table 52: Summary of the extremely fine quad mesh.

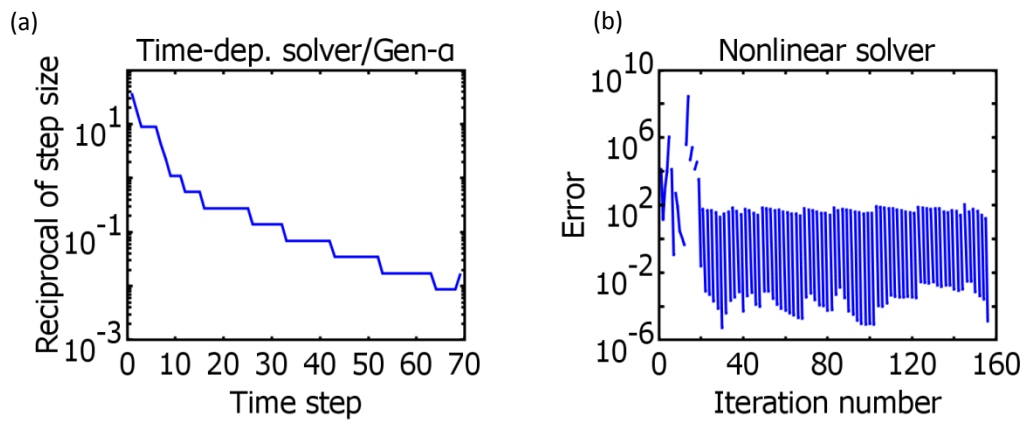


Figure 227: (a) Reciprocal of time step and (b) error in each iteration for extremely fine quad mesh.

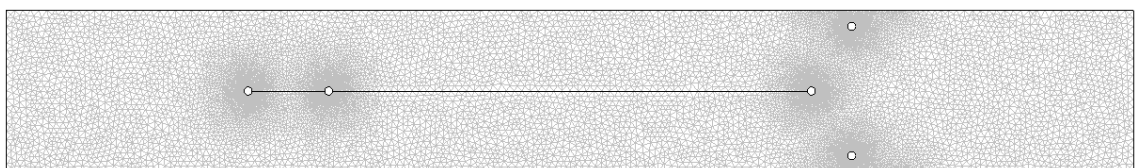


Figure 228: 10% growth triangular mesh.

“10% growth” triangular mesh grid parameters:

Mesh:	19,620 elements
Degrees of Freedom:	208,879
Solution time:	1,126.221s
Memory usage:	1,161MB

Table 53: Summary of the “10% growth” triangular mesh.

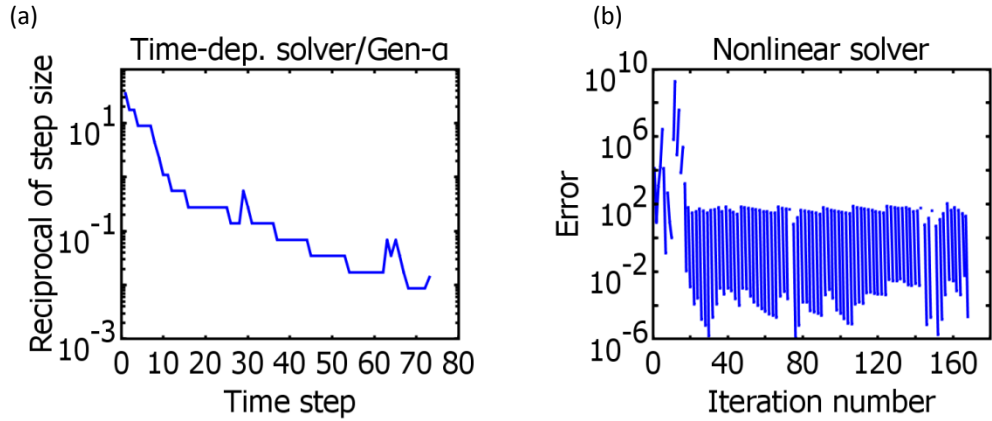


Figure 229: (a) Reciprocal of time step and (b) error in each iteration for the “10% growth” triangular mesh.

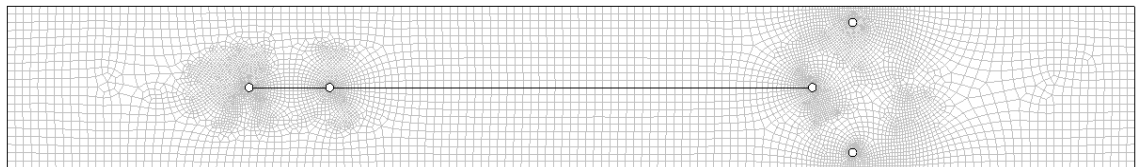


Figure 230: 10% growth quad mesh.

“10% growth” quad mesh grid parameters:

Mesh:	7,516 elements
Degrees of Freedom:	160,573
Solution time:	3,321.3s
Memory usage:	1,116MB

Table 54: Summary of the “10% growth” quad mesh.

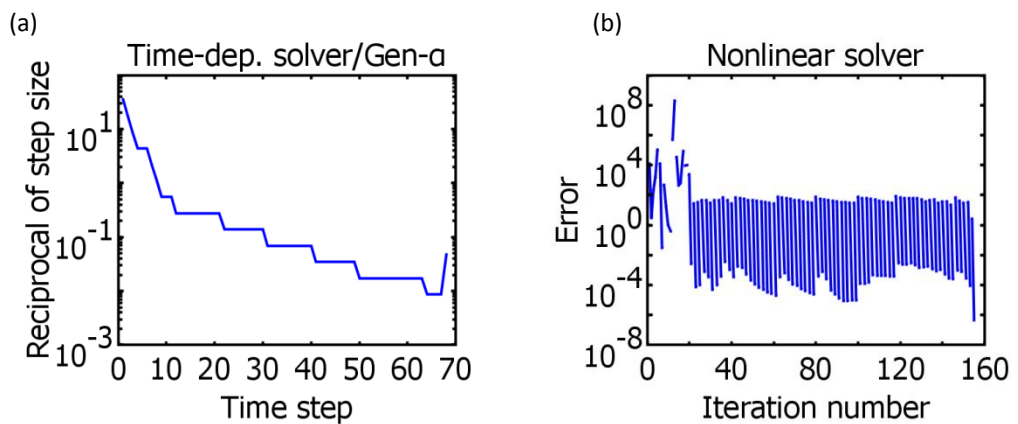


Figure 231: (a) Reciprocal of time step and (b) error in each iteration for the “10% growth” quad mesh.

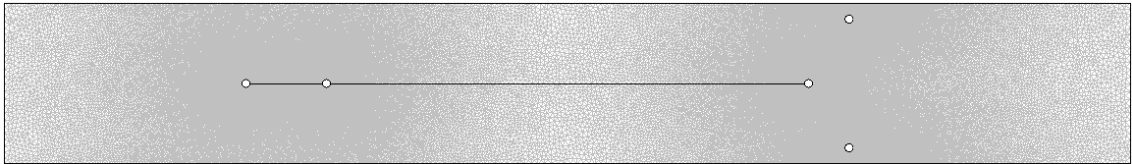


Figure 232: 2% growth triangular mesh.

“2% growth” triangular mesh grid parameters:

Mesh:	38,825 elements
Degrees of Freedom:	409,619
Solution time:	10,462.445s
Memory usage:	1,467MB usage

Table 55: Summary of the “2% growth” triangular mesh.

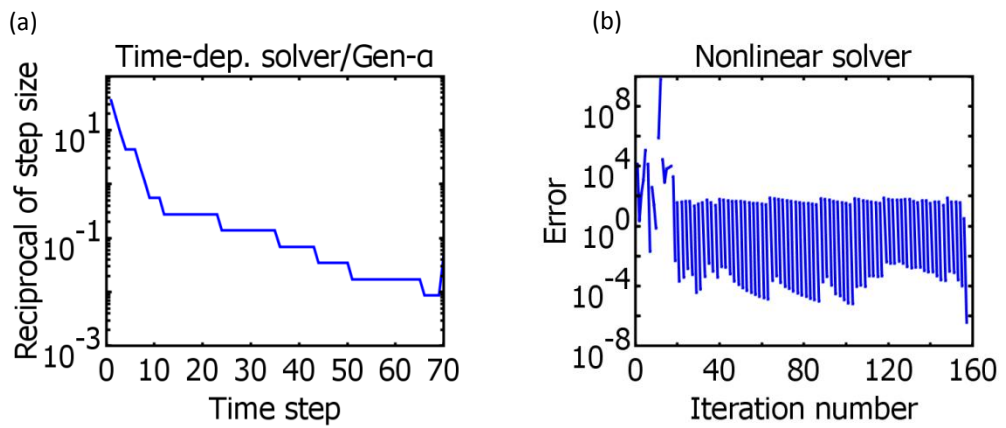


Figure 233: (a) Reciprocal of time step and (b) error in each iteration for the “2% growth” triangular mesh.

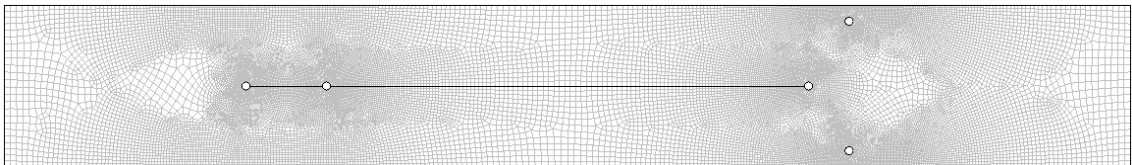


Figure 234: “2% growth” quad mesh.

“2% growth” quad mesh grid parameters:

Mesh:	26,561 elements
Degrees of Freedom:	562,729
Solution time:	100,579.331s
Memory usage:	6,382MB

Table 56: Summary of the “2% growth” quad mesh.

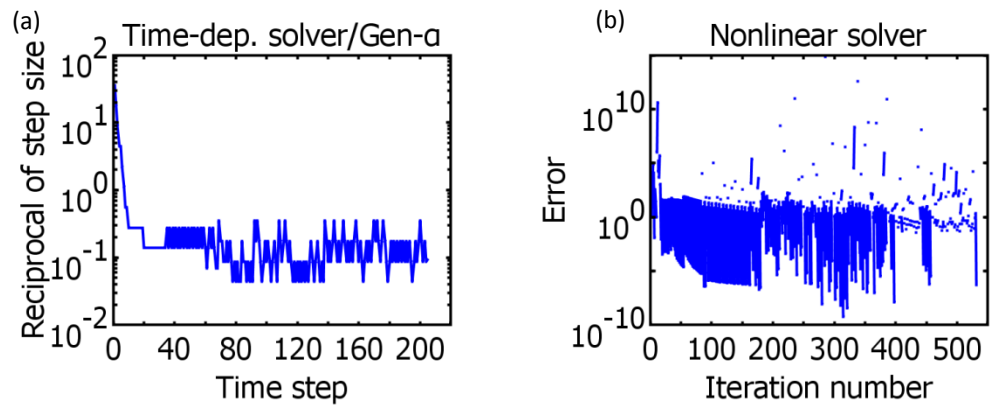
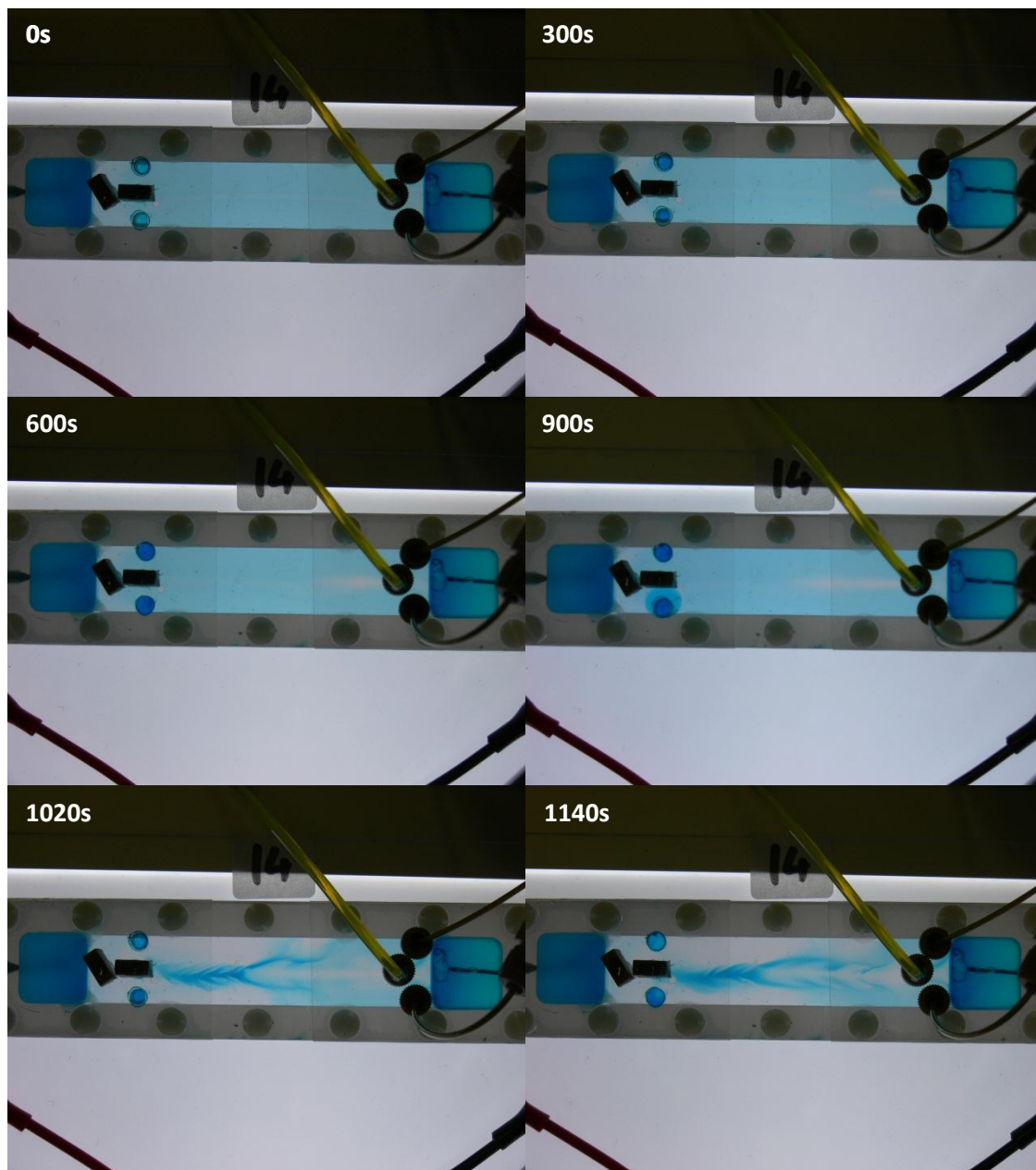
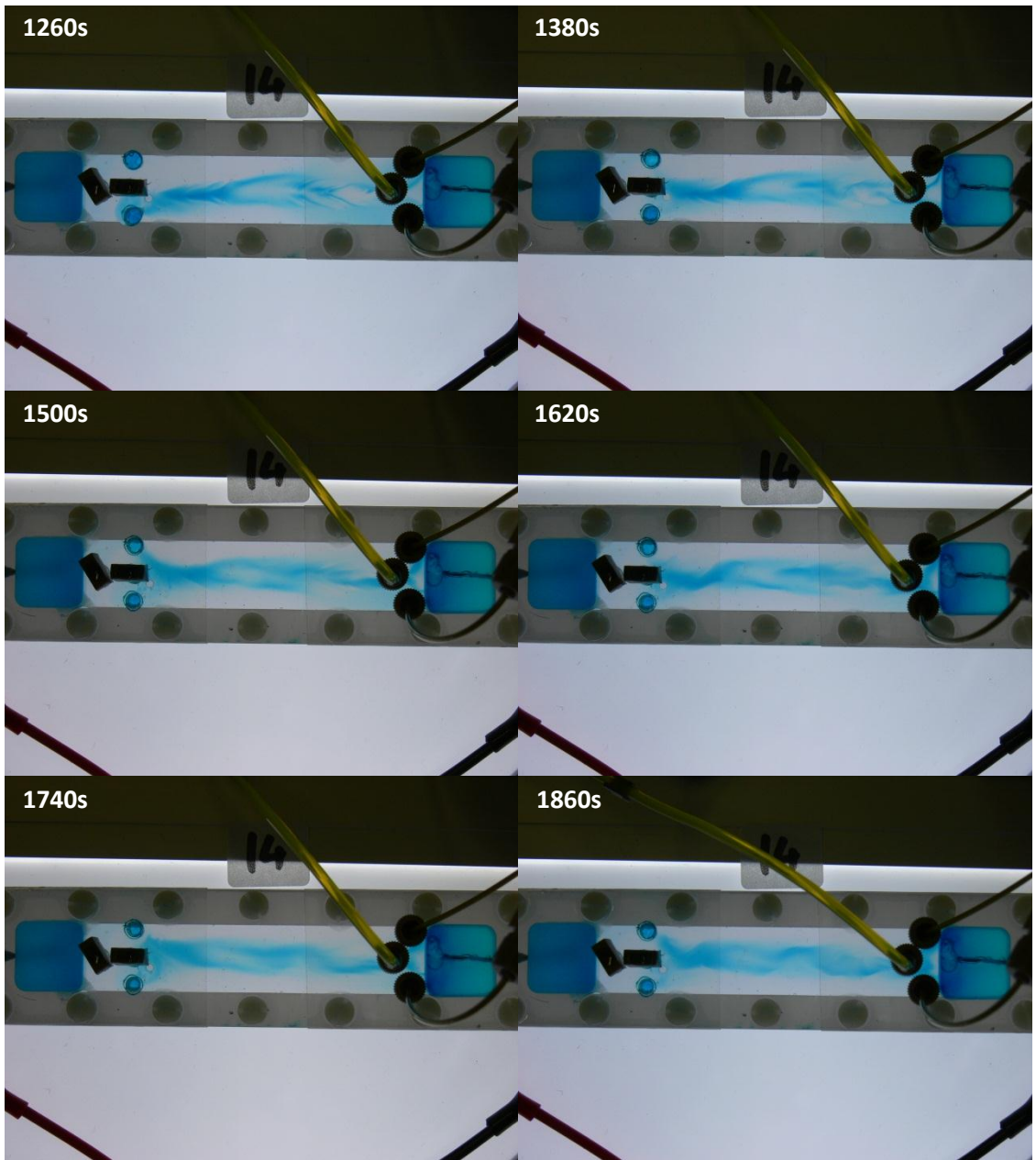


Figure 235: (a) Reciprocal of time step and (b) error in each iteration for the 2% growth” quad mesh.

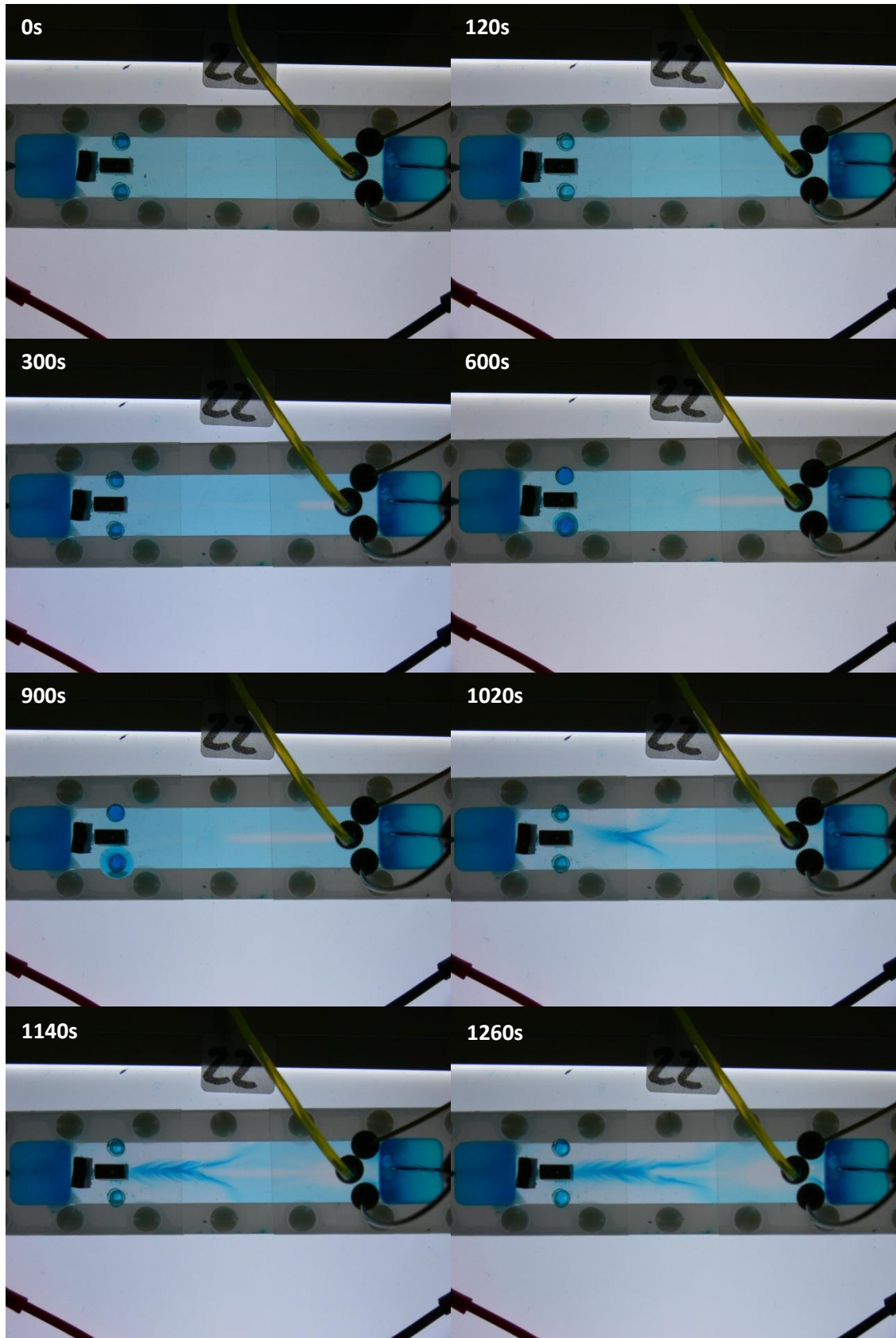
Appendix I – Photos of all presented microfluidic experiments

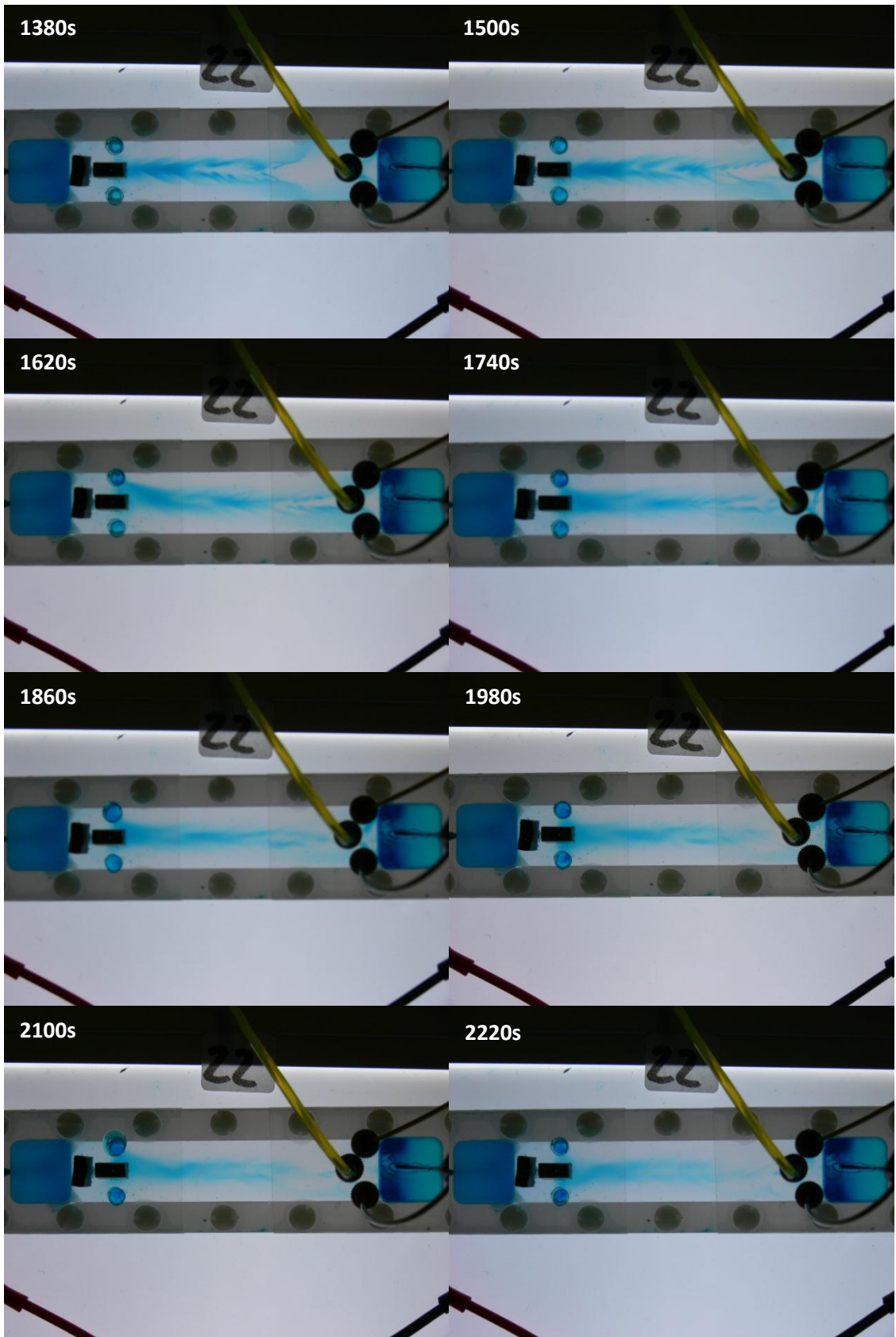
1. Experiment 2P-14

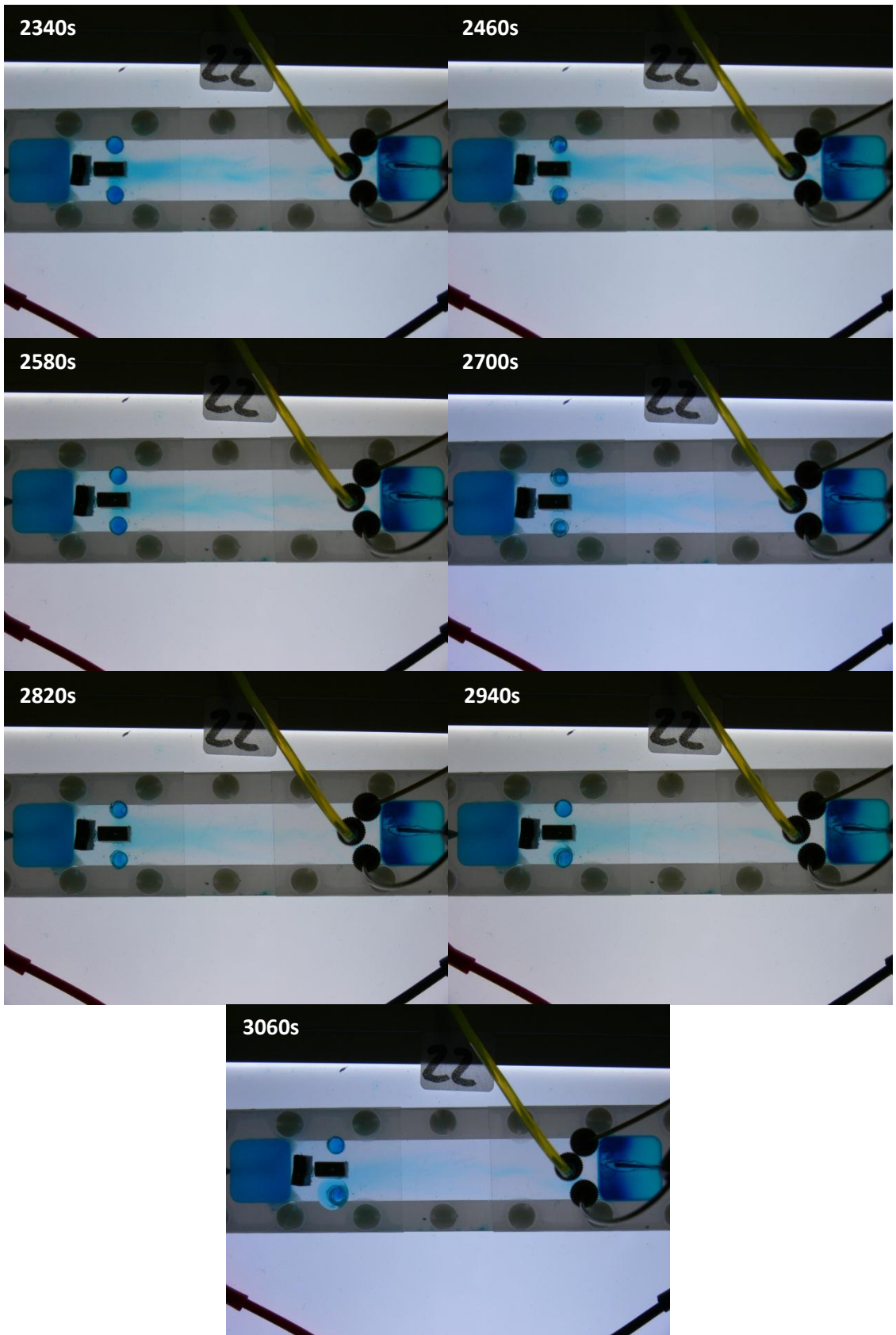




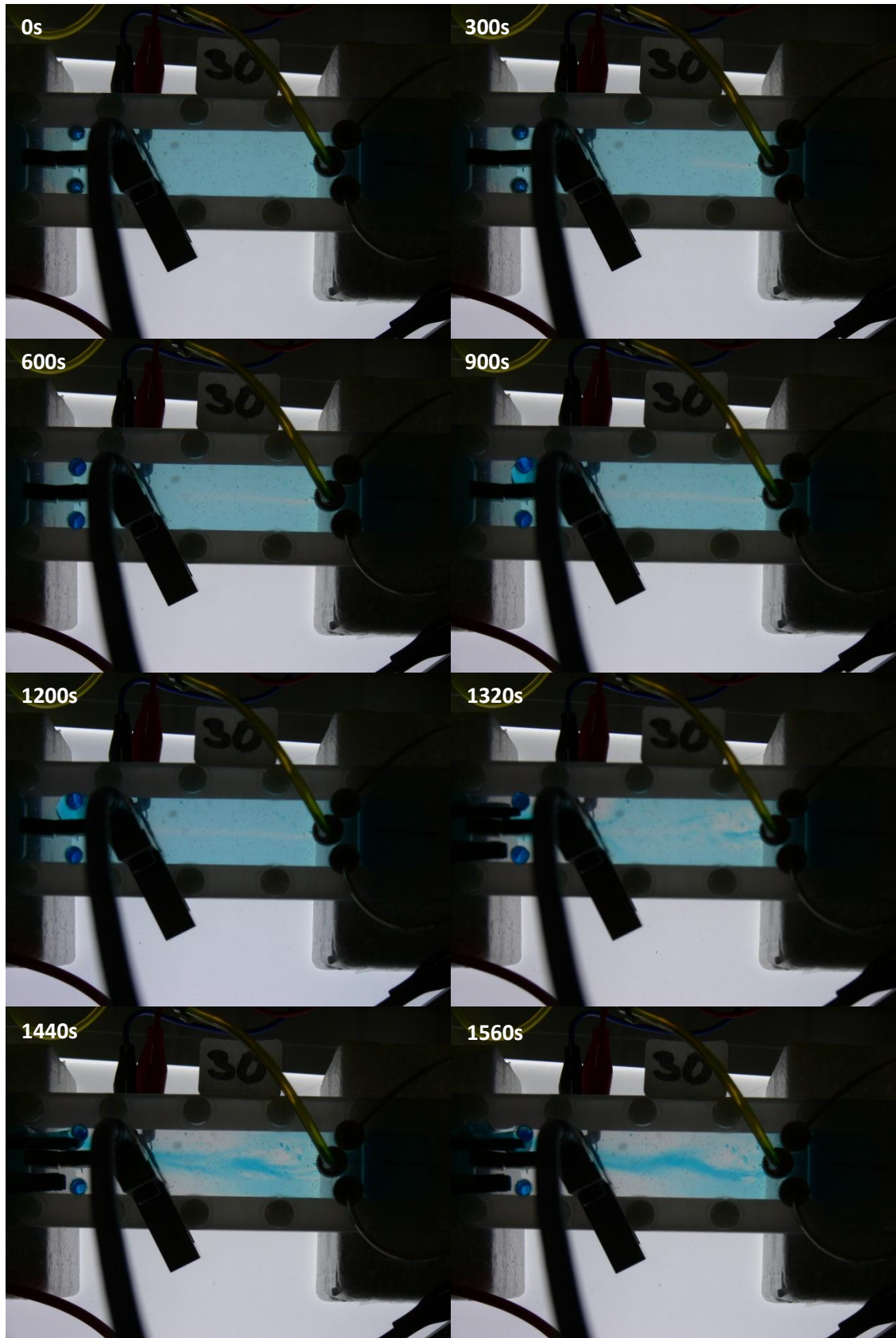
2. Experiment 2P-22

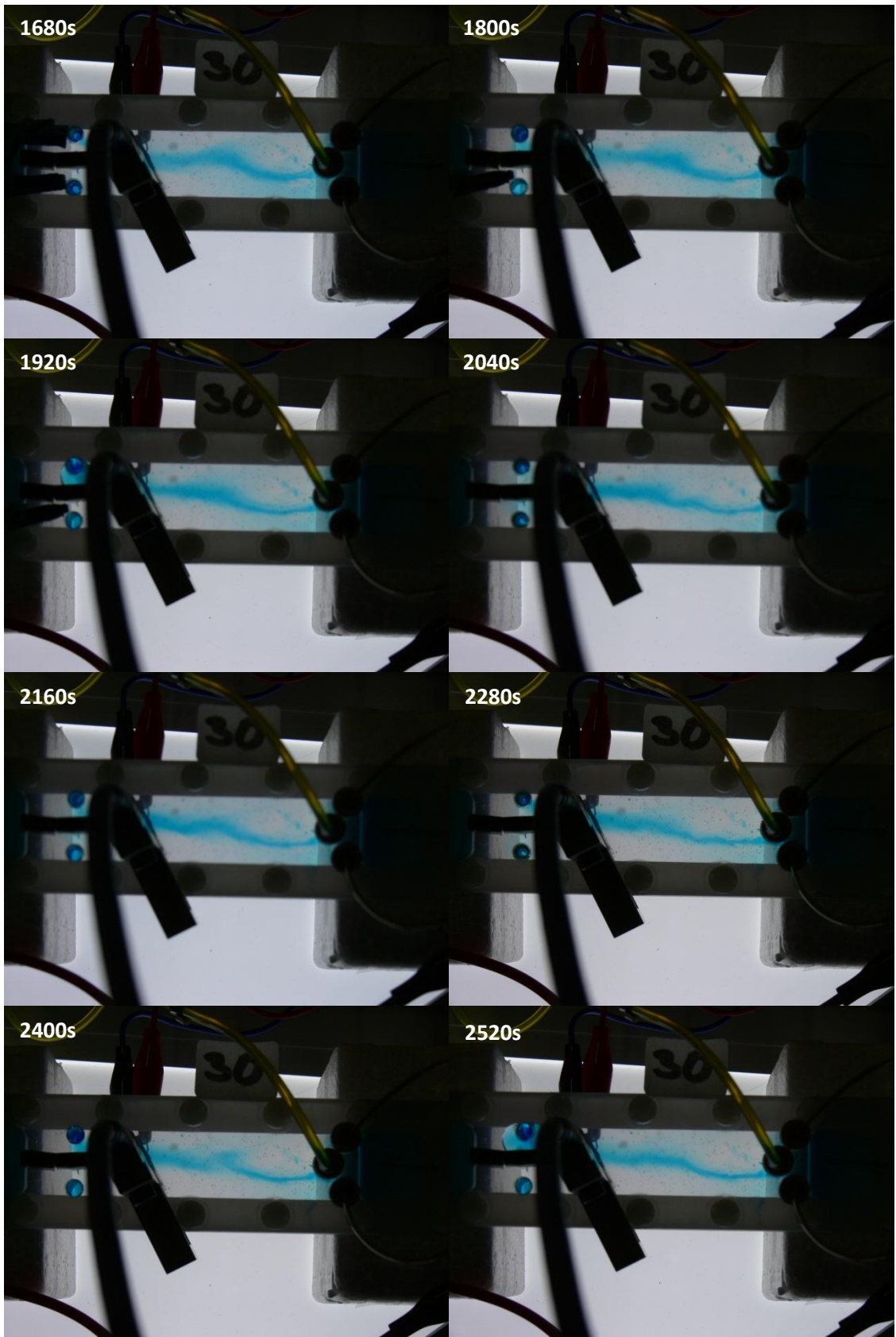




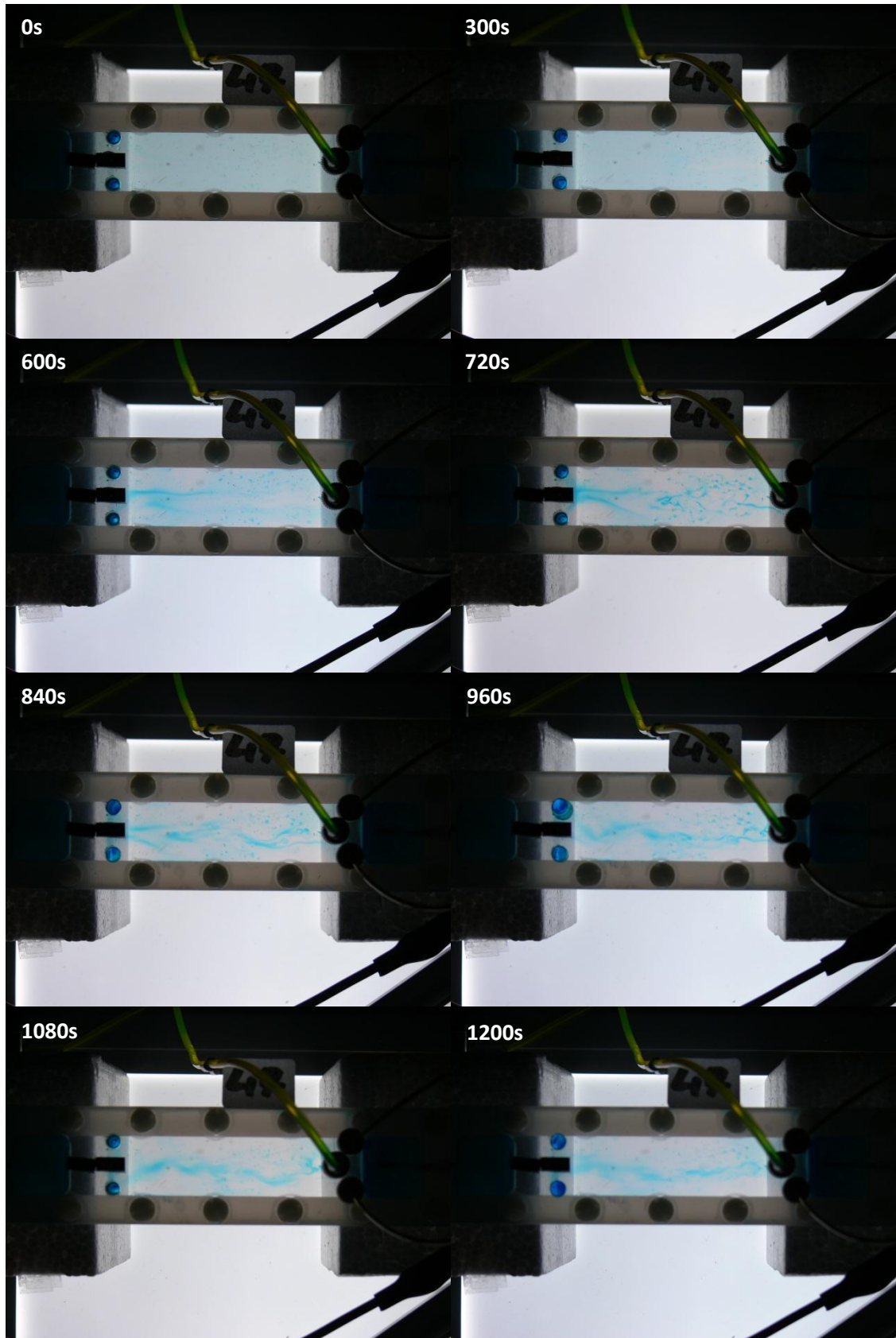


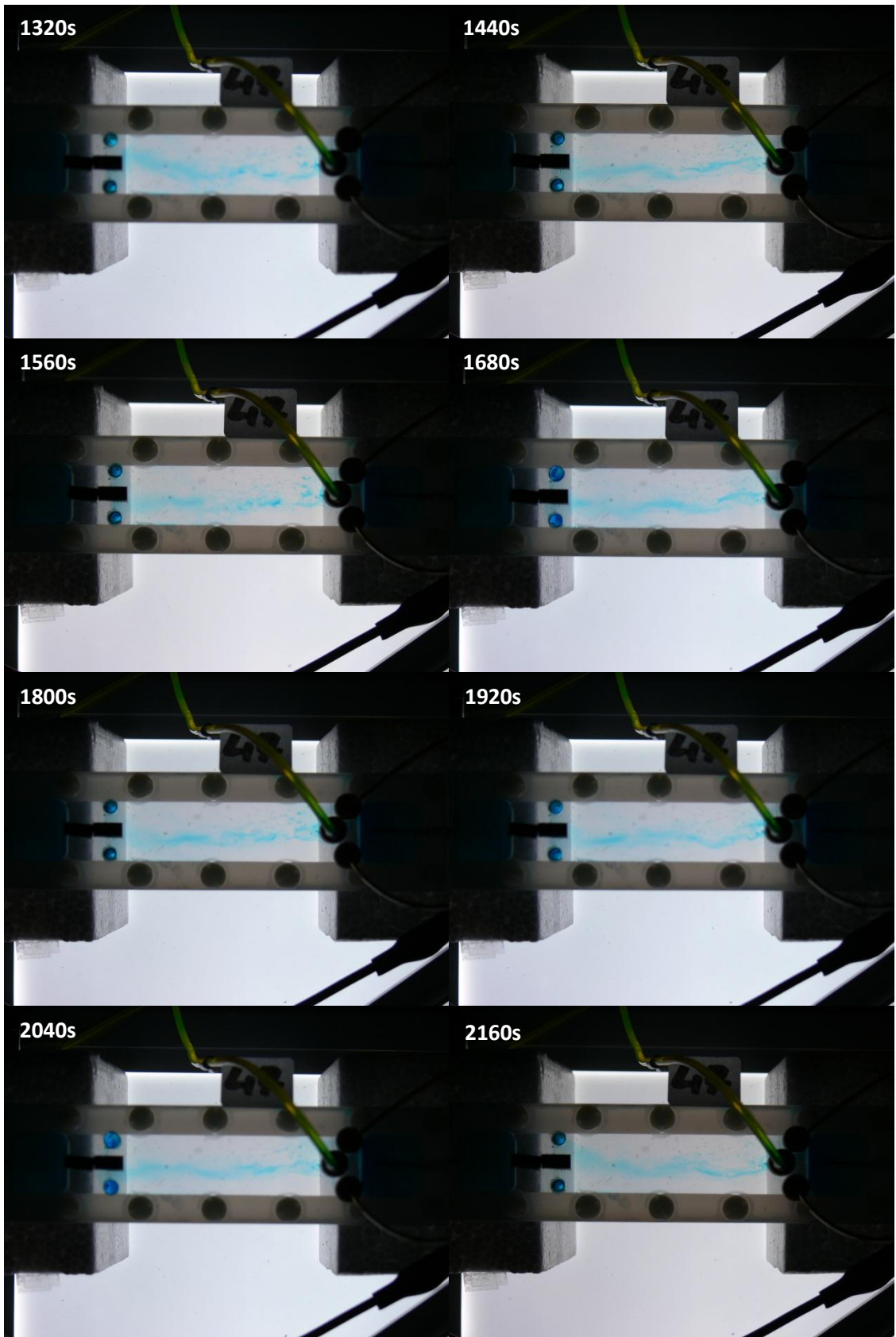
3. Experiment 2P-30

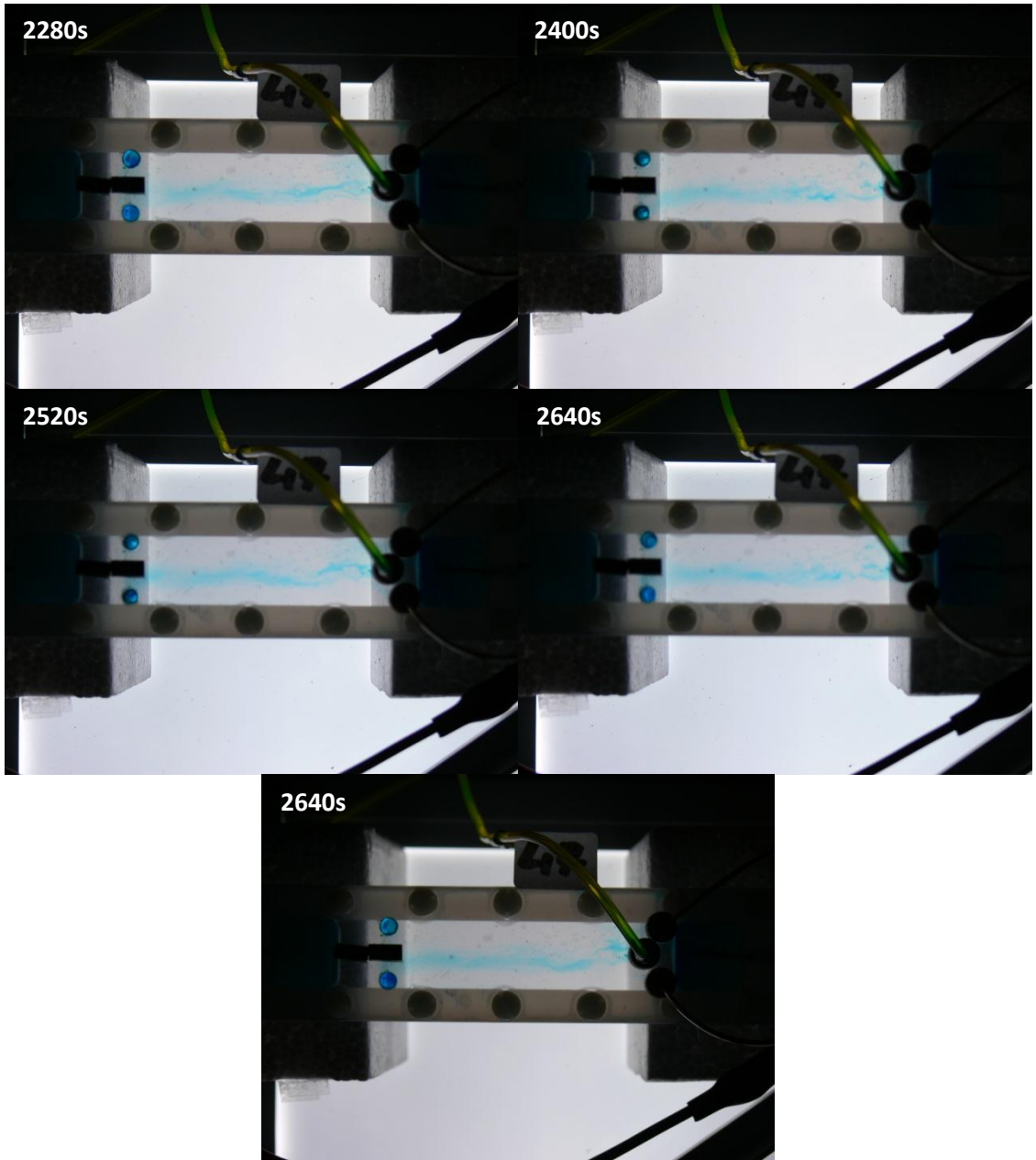




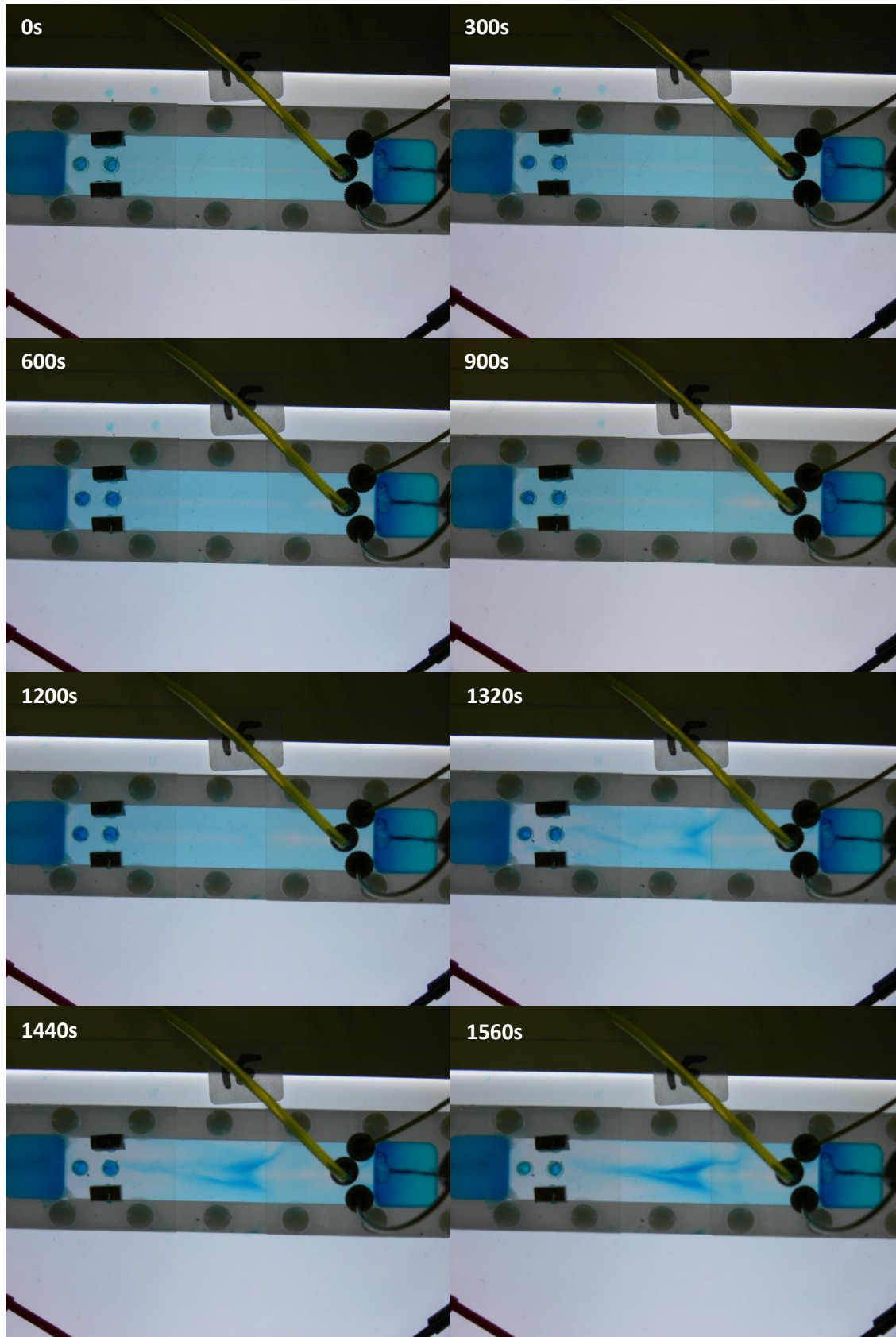
4. Experiment 2P-47

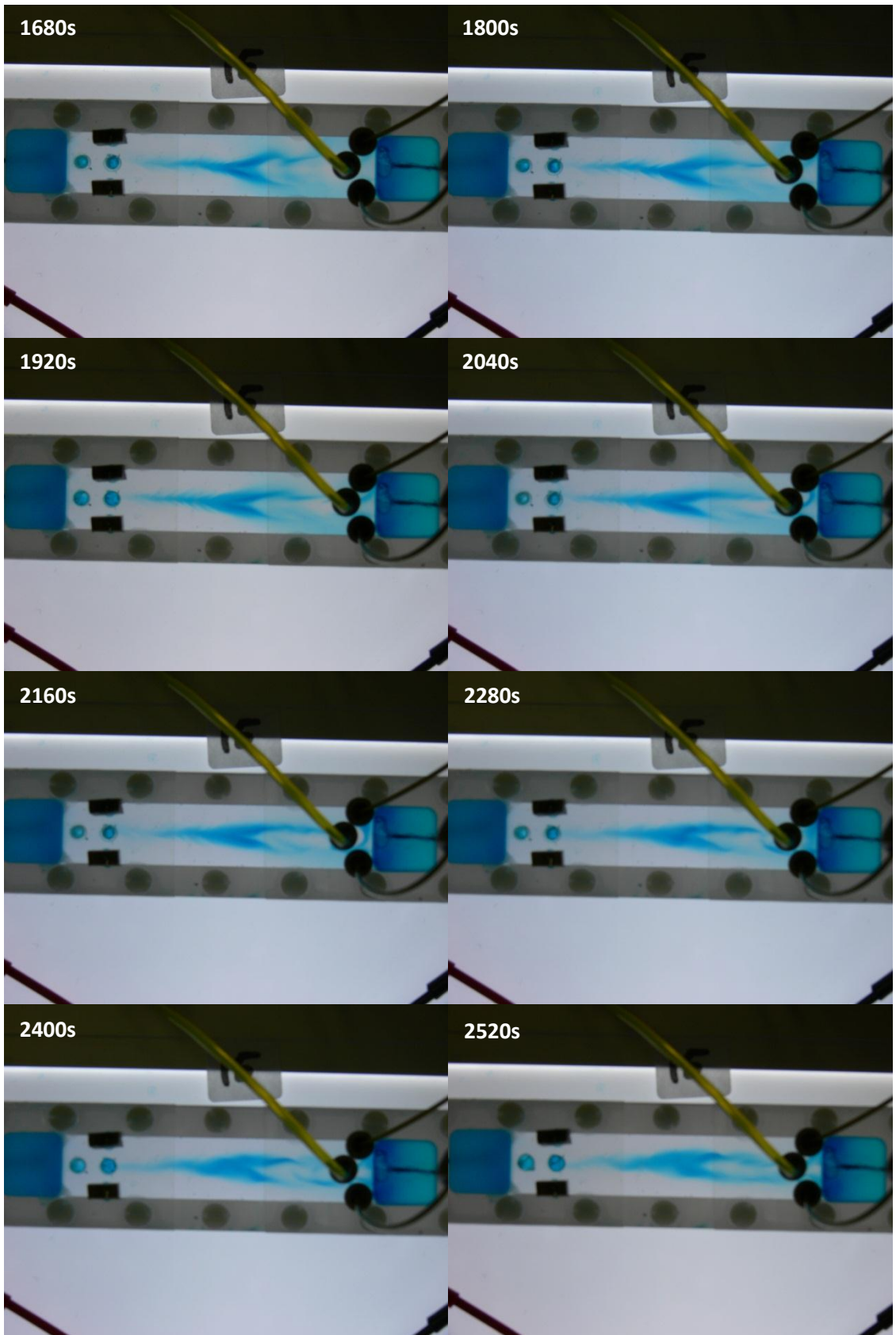




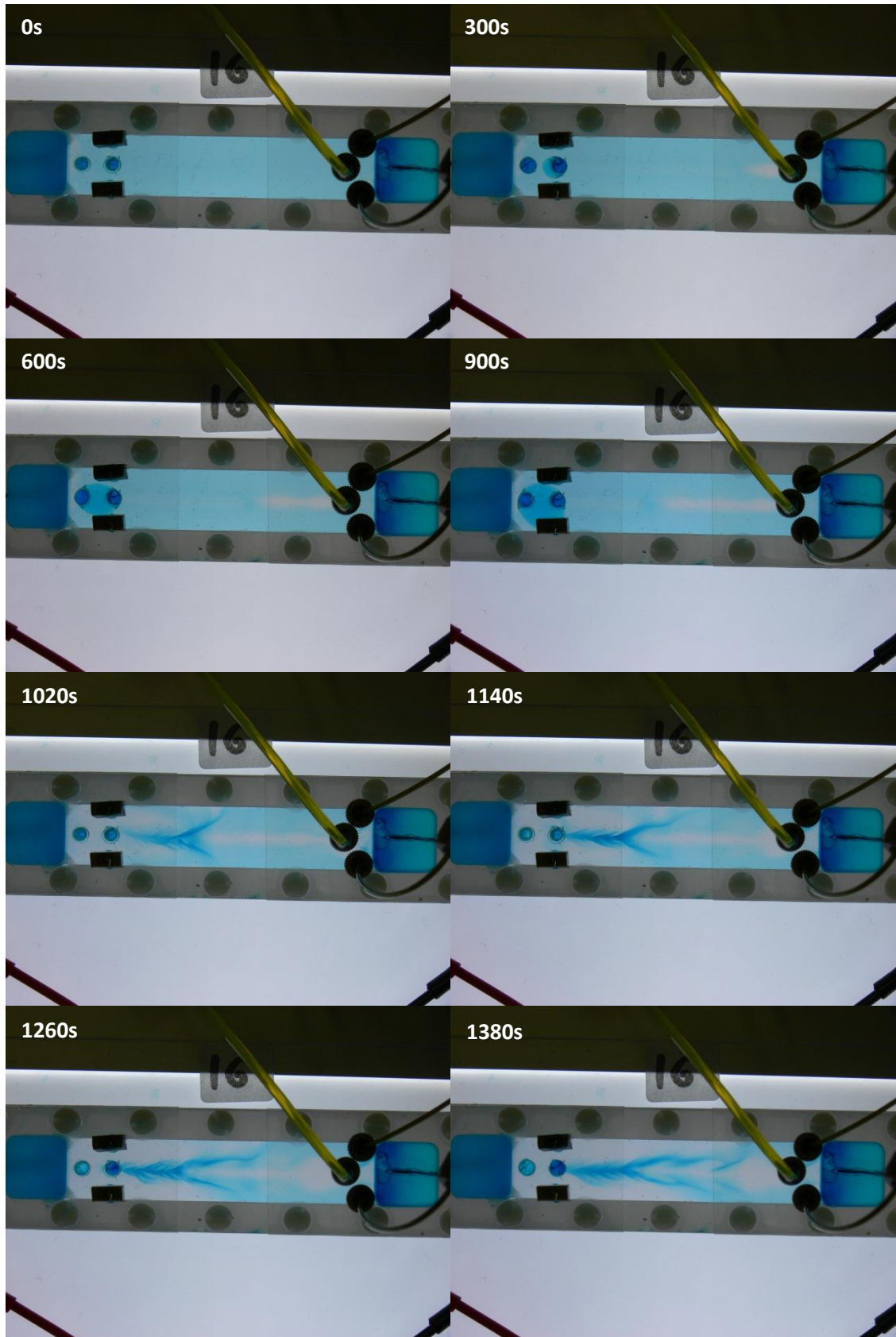


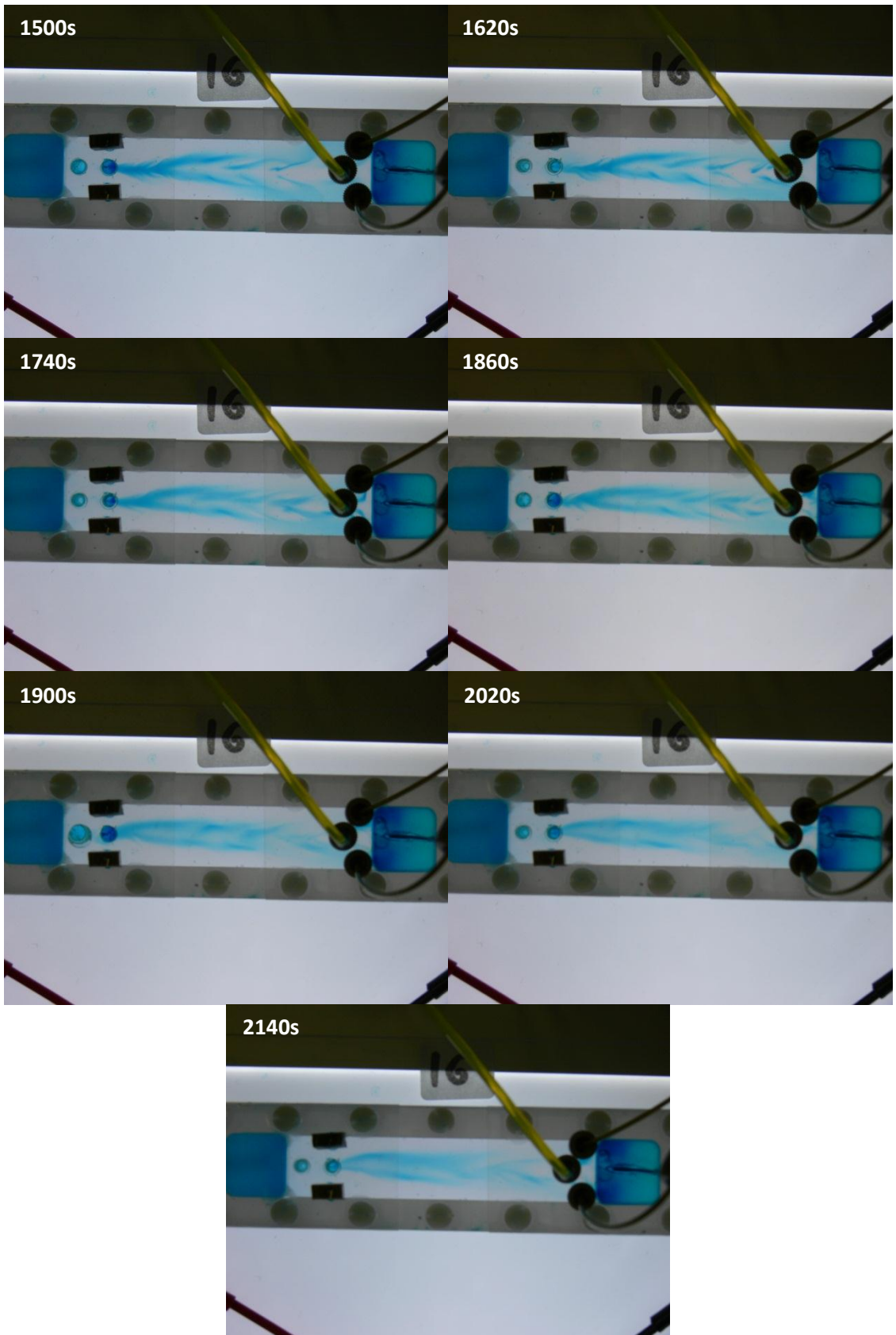
5. Experiment 2L-15



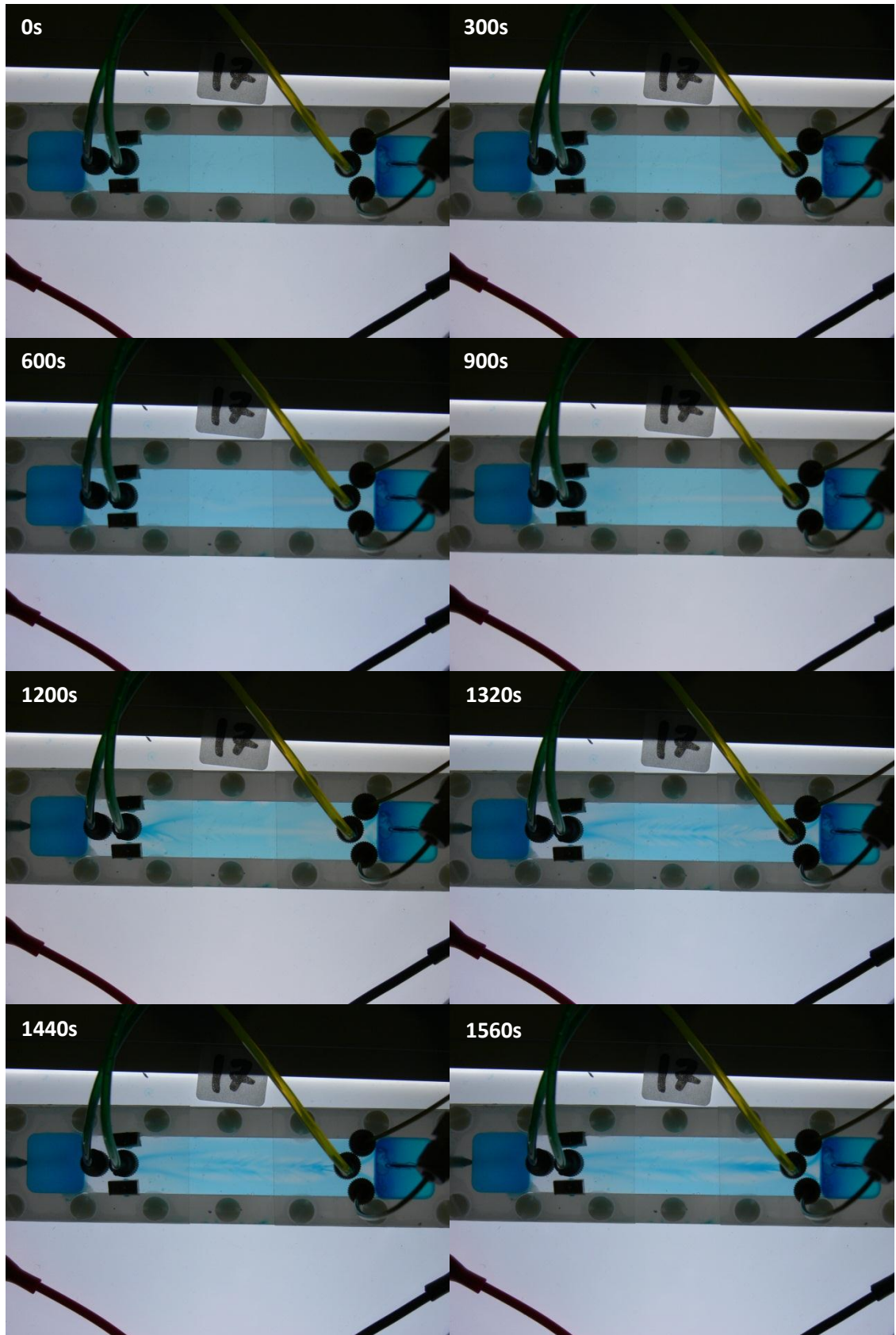


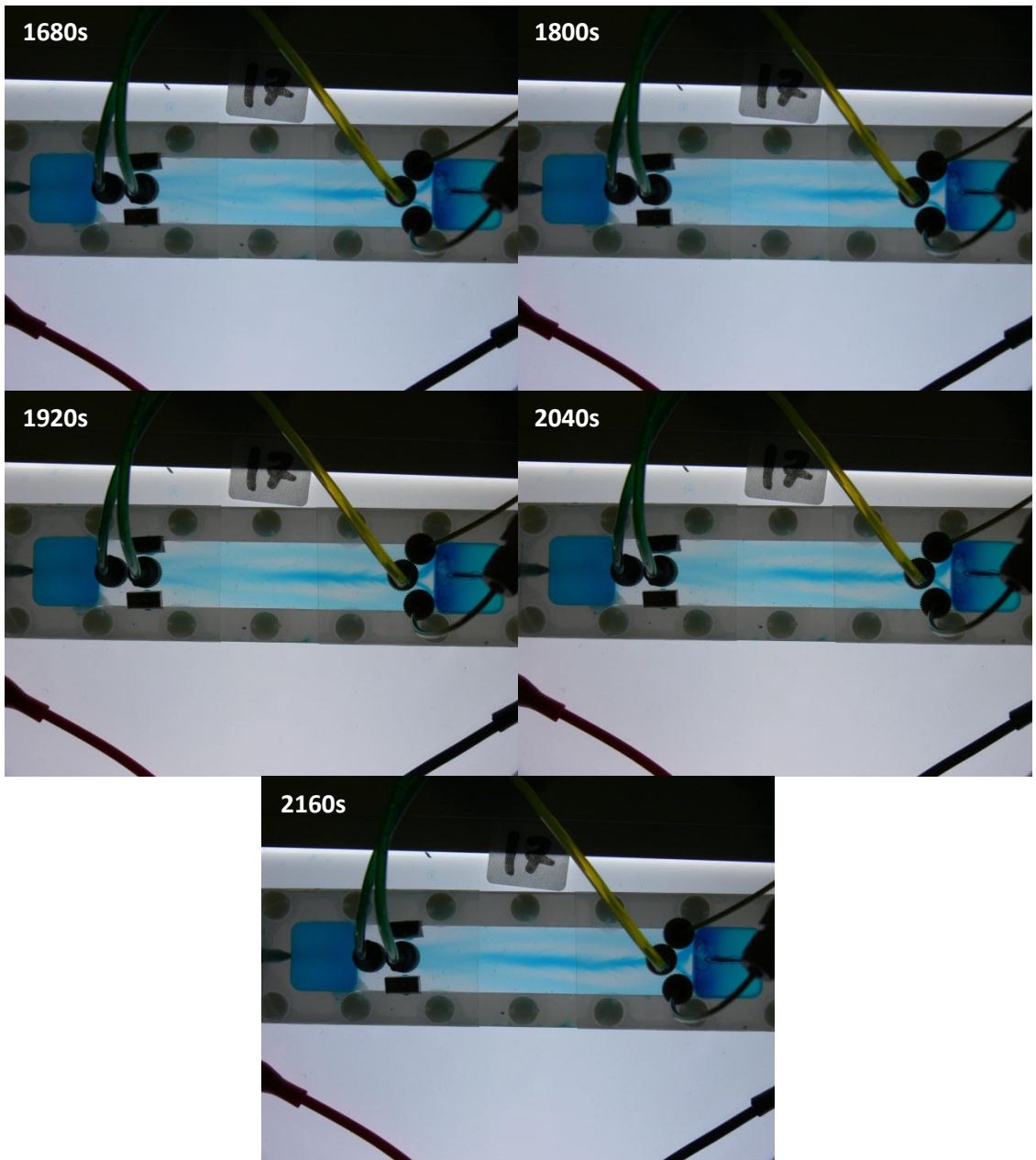
6. Experiment 2L-16



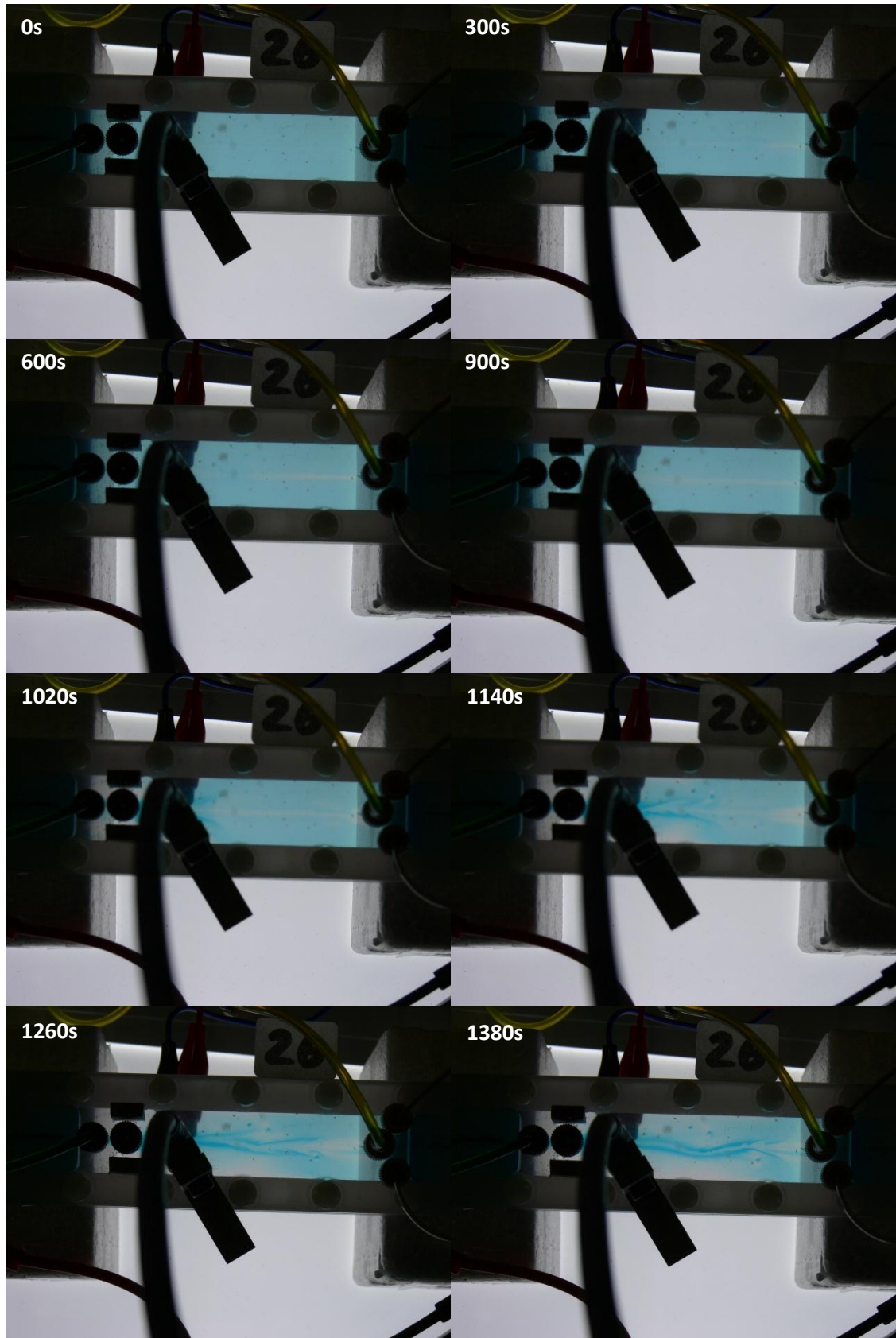


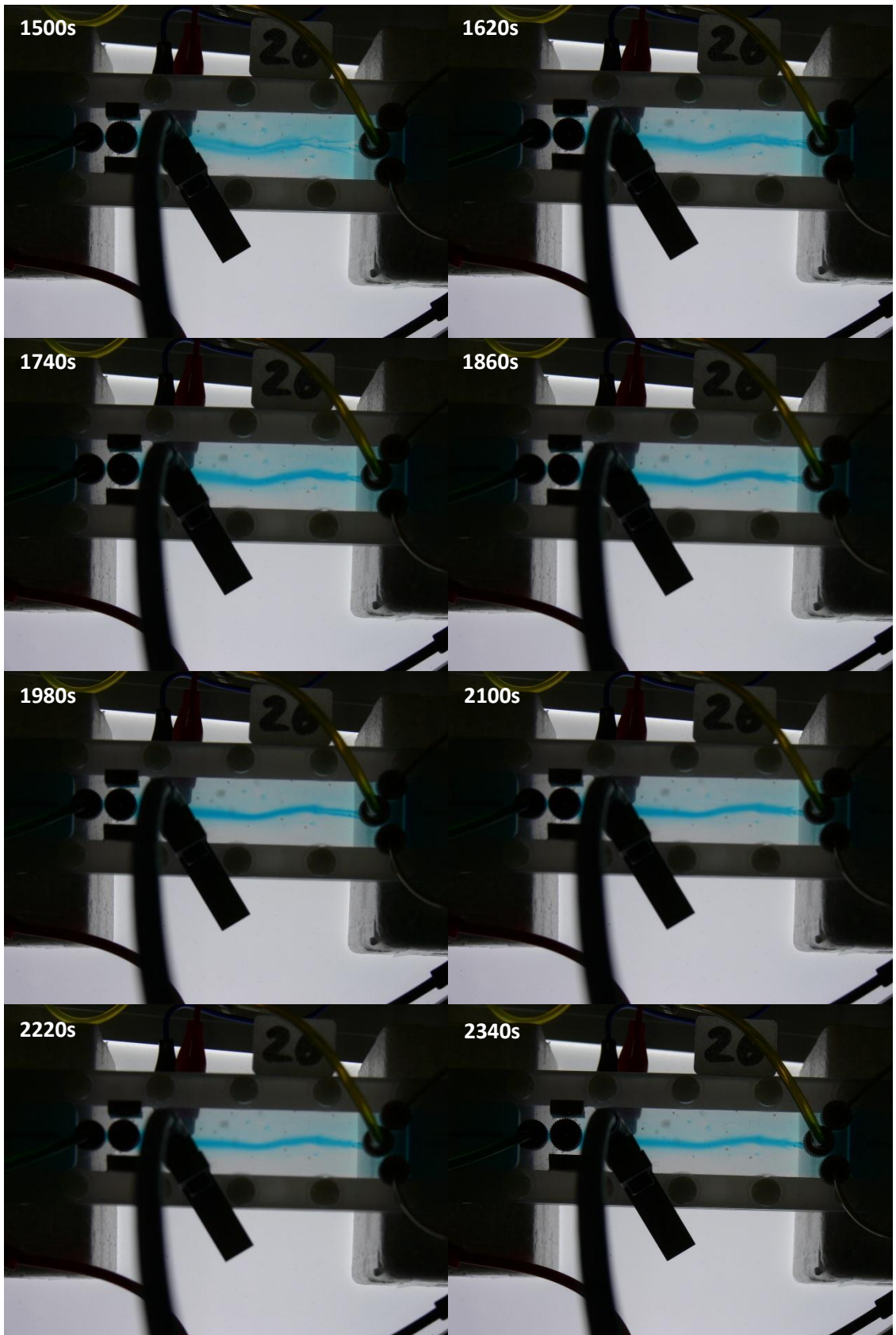
7. Experiment 2L-17

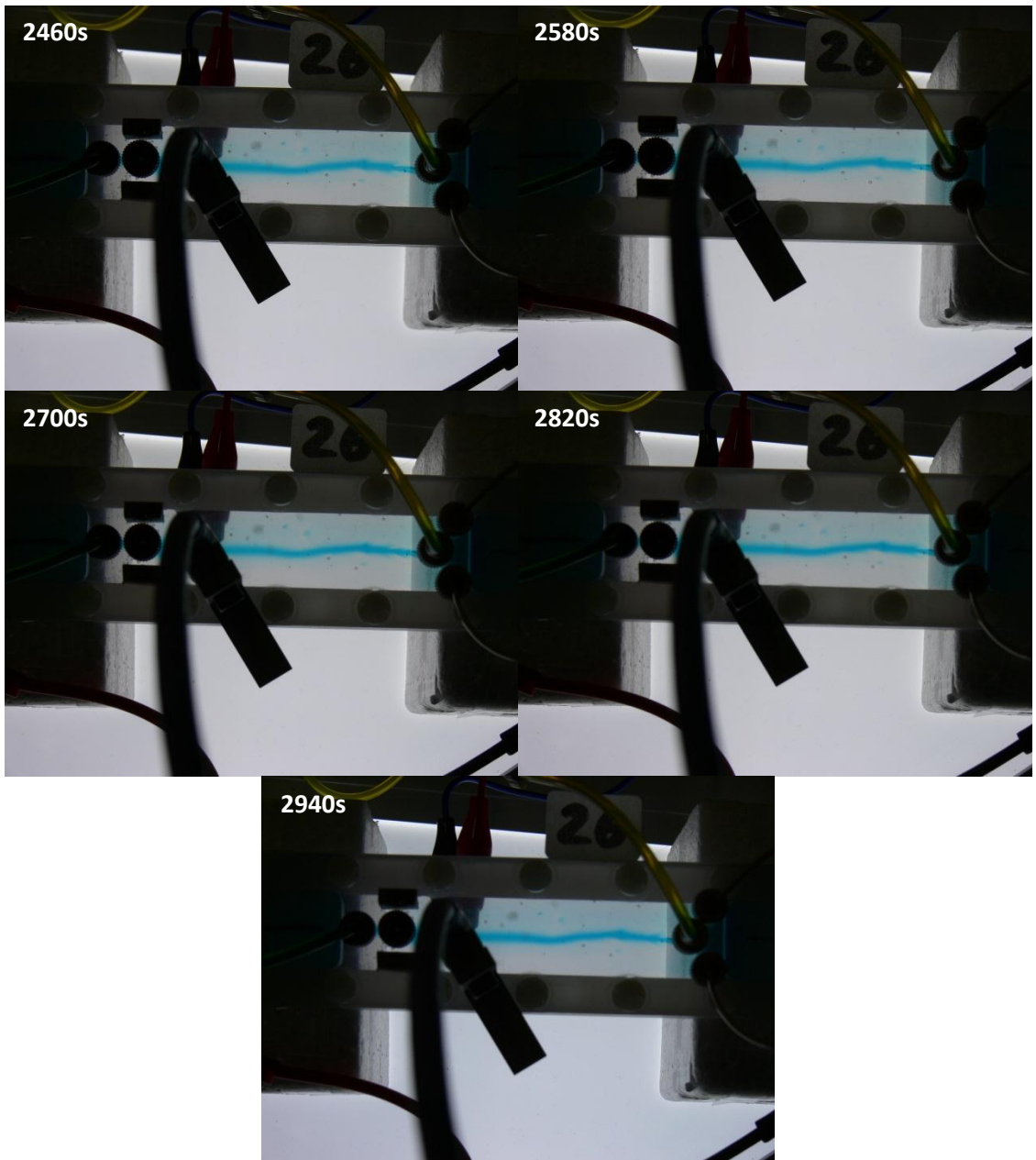




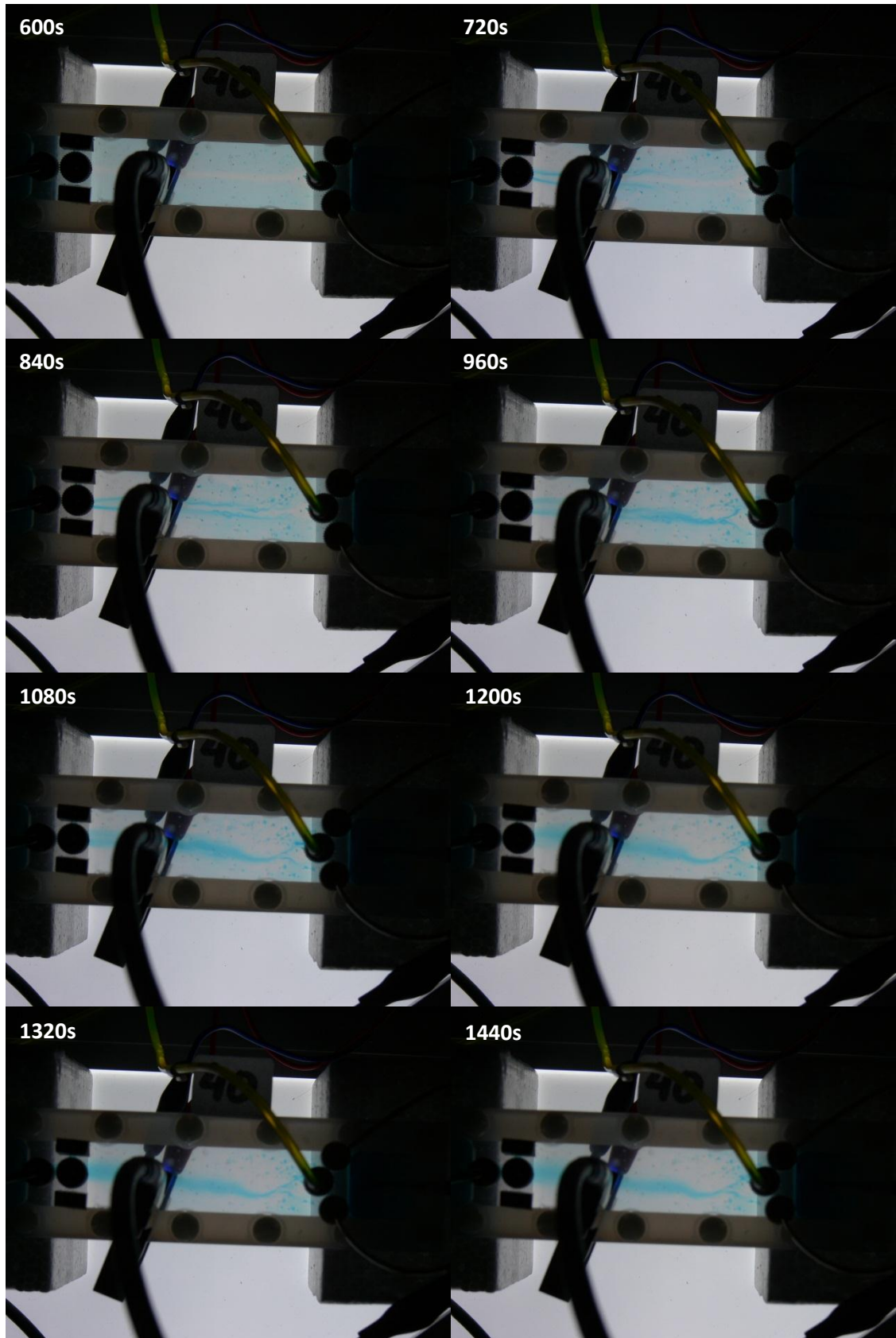
8. Experiment 2L-26

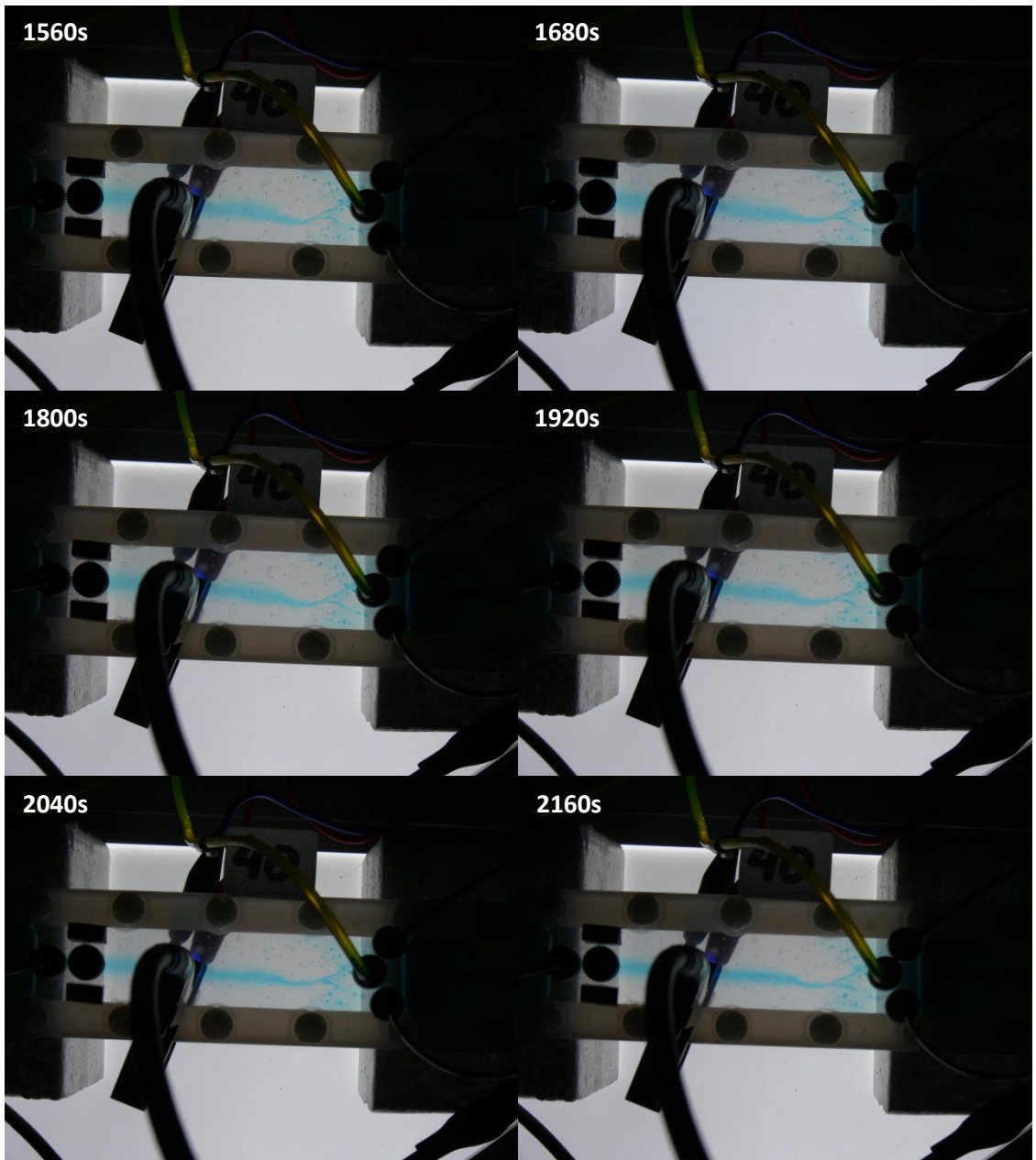


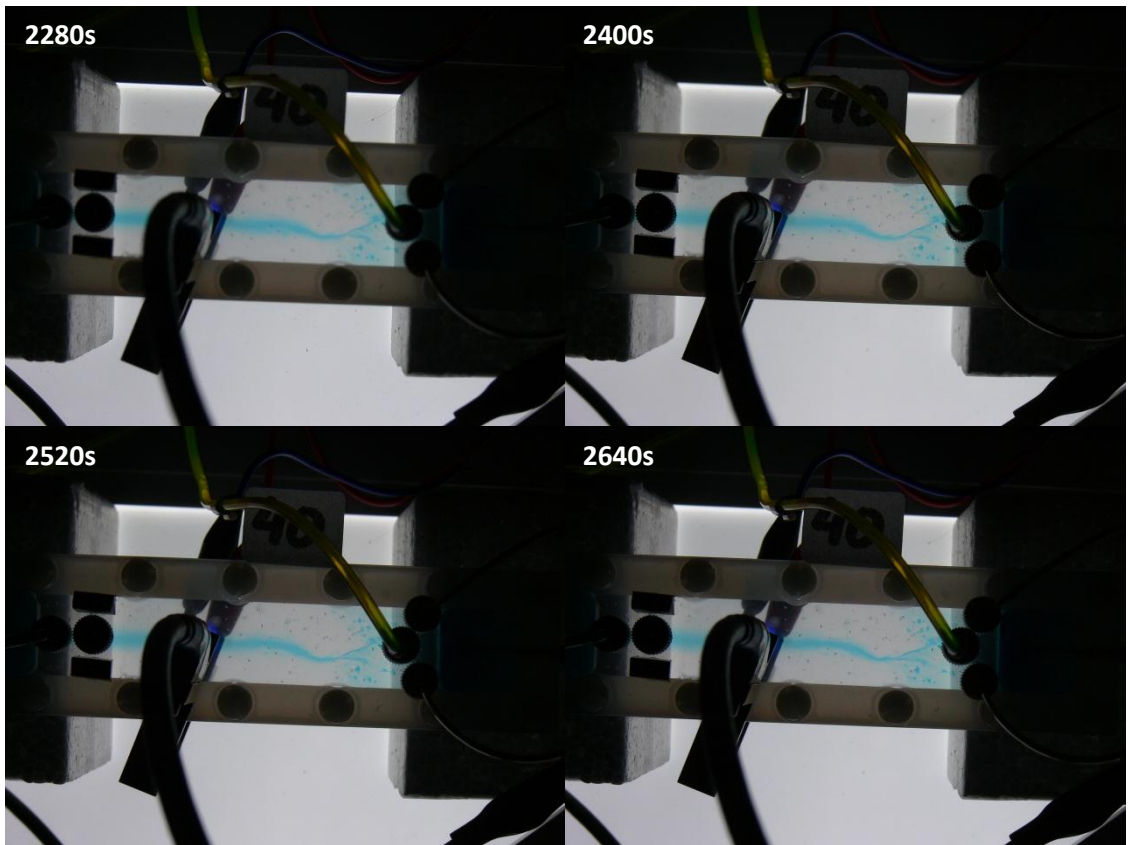




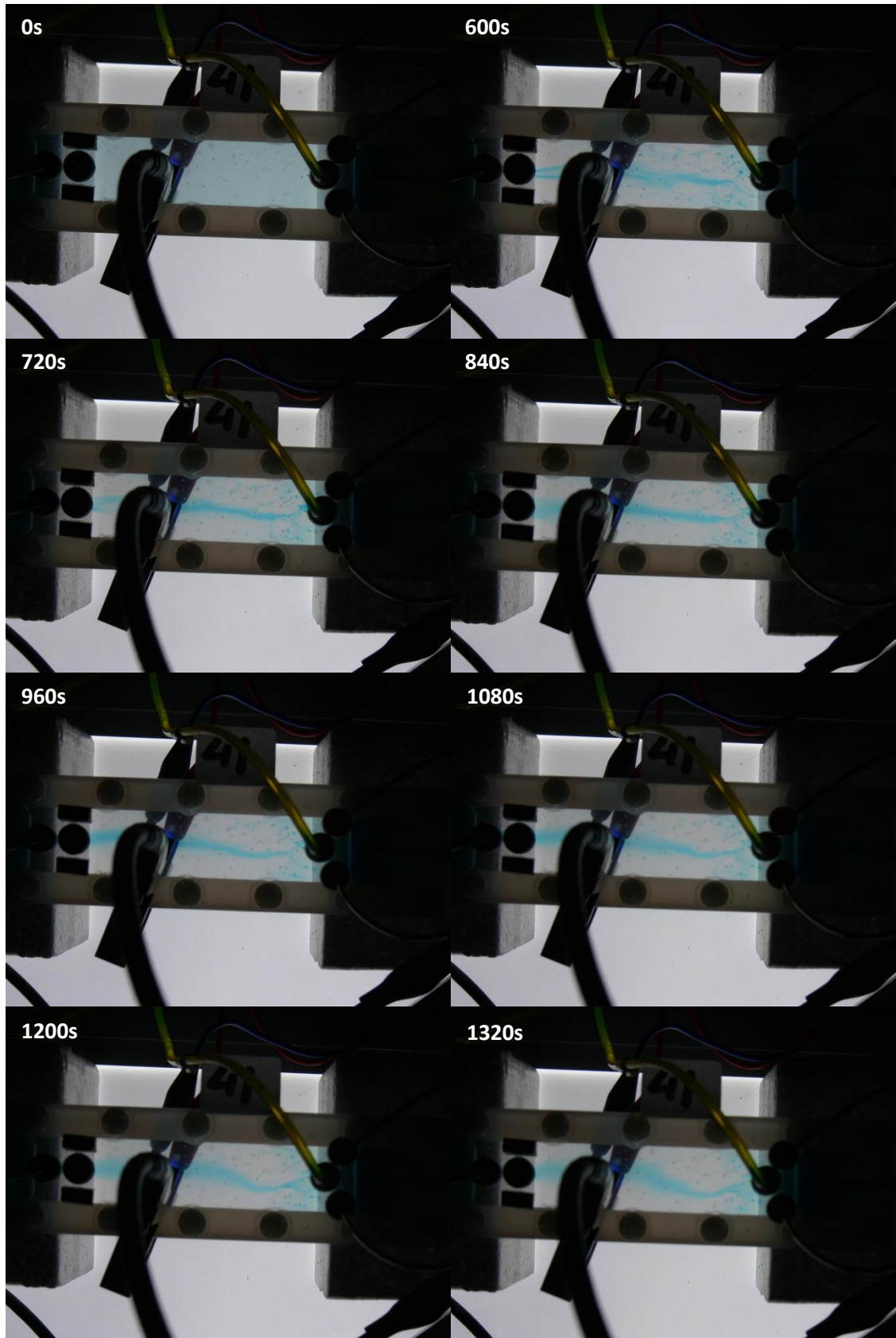
9. Experiment 2L-40

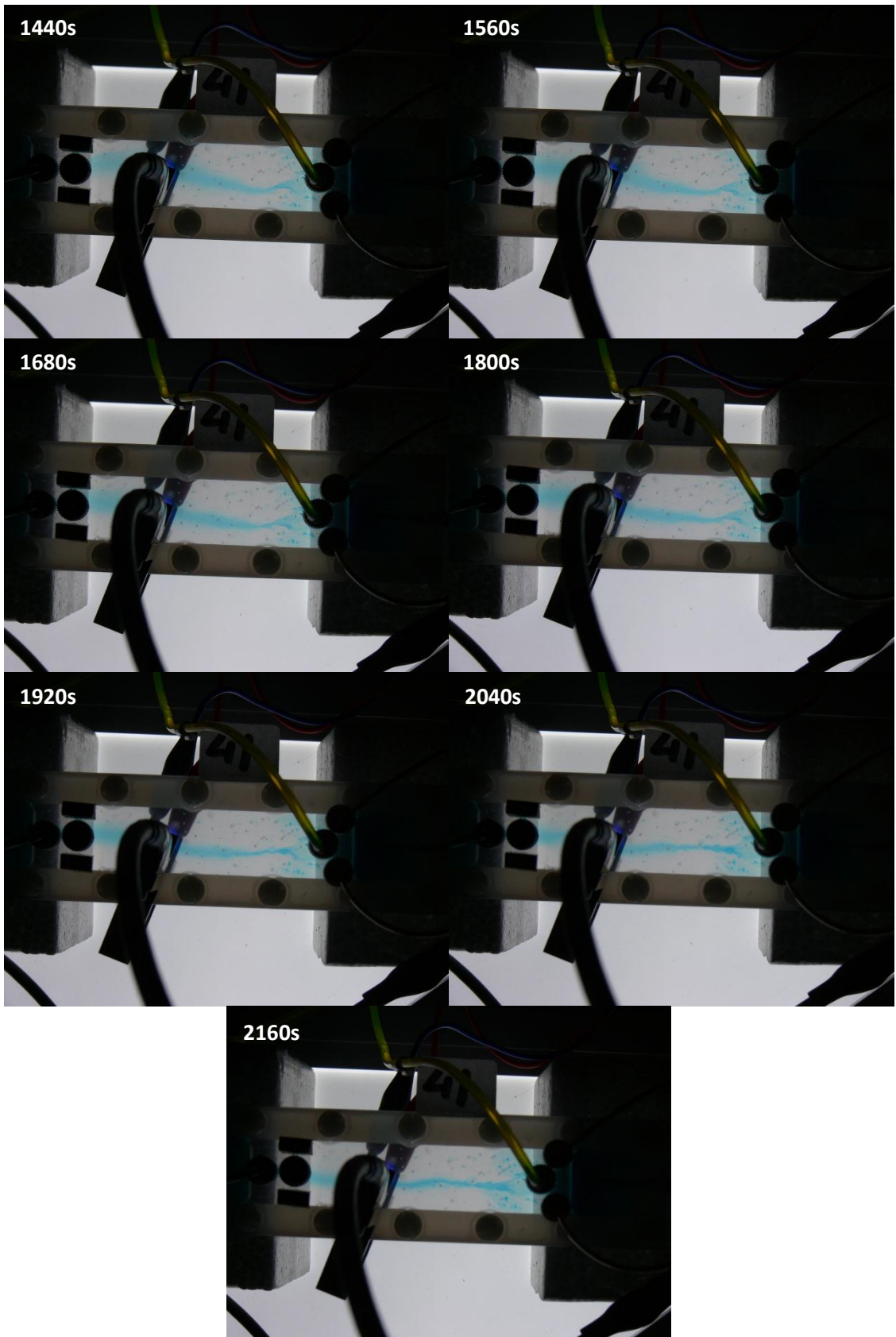




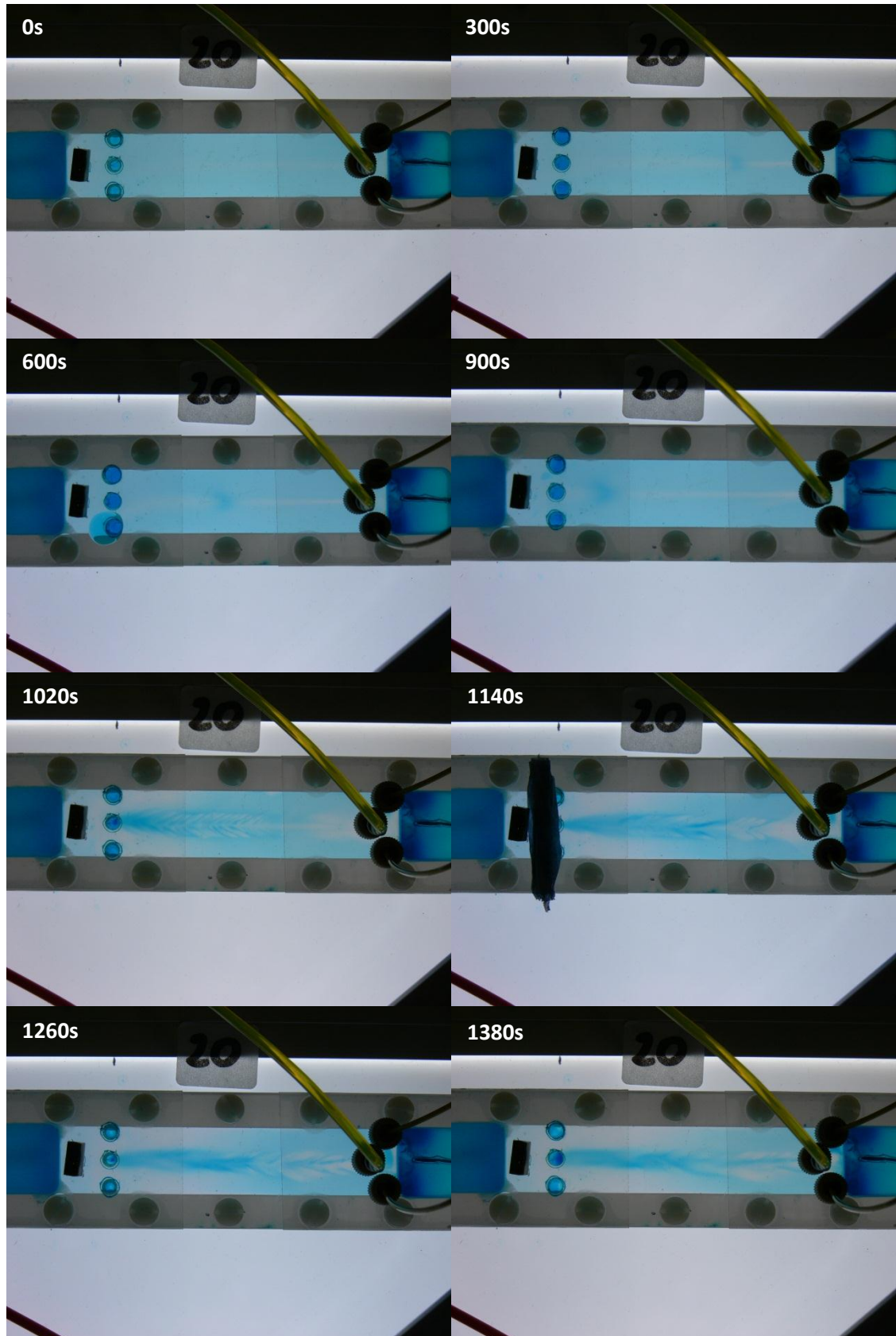


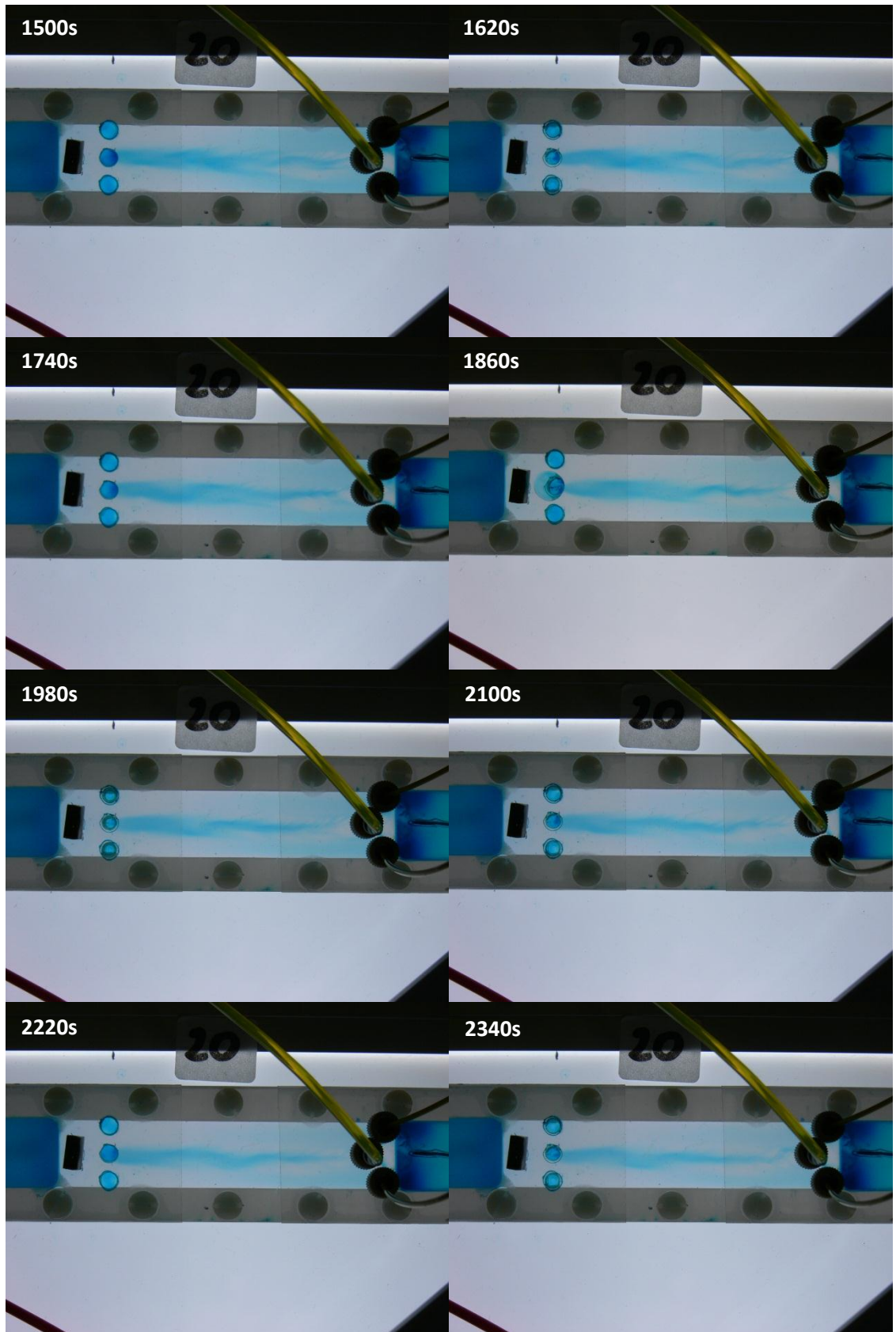
10. Experiment 2L-41

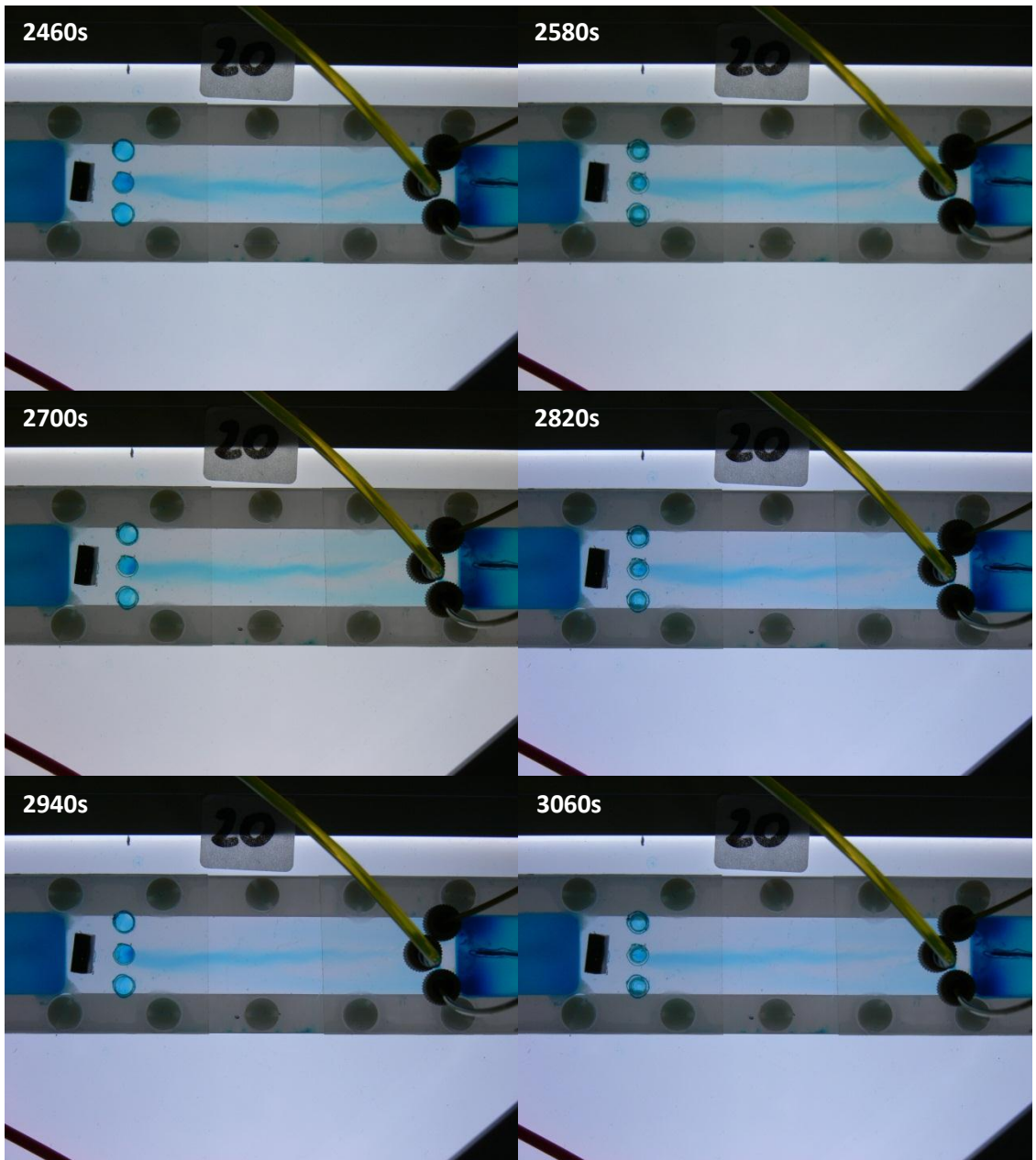


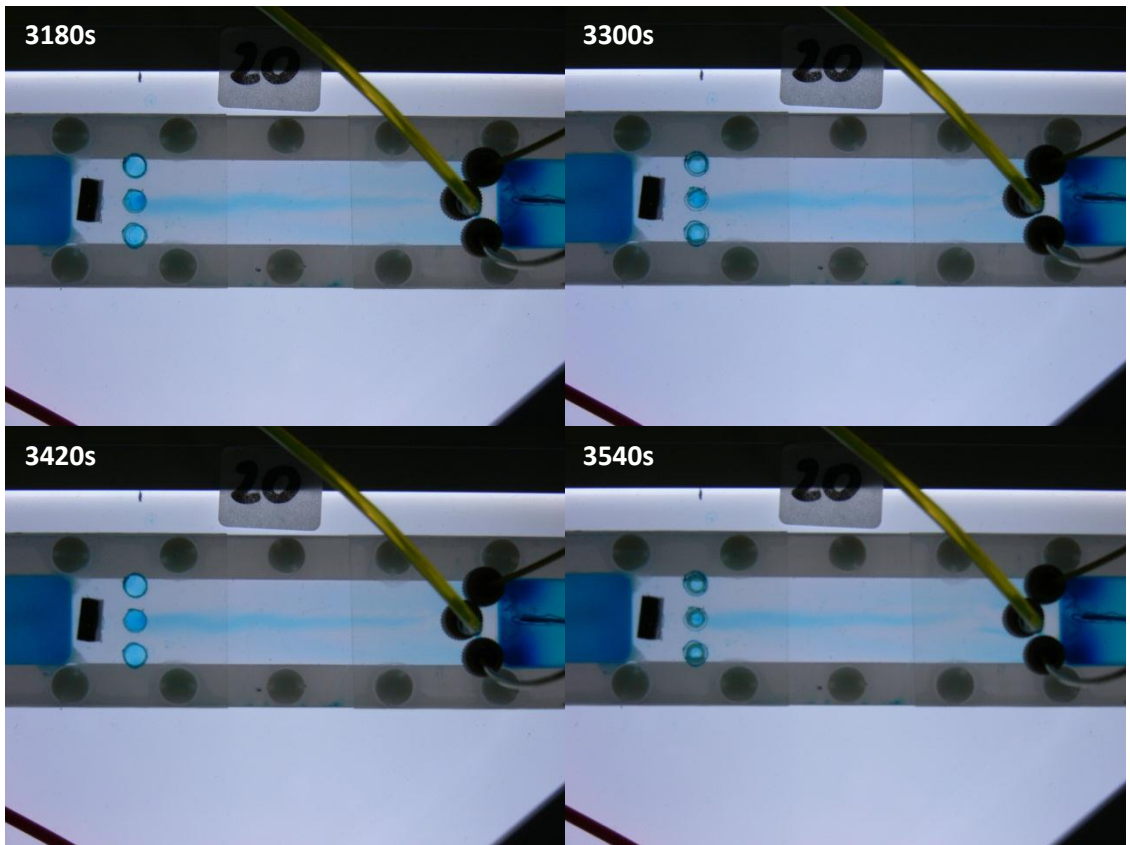


11. Experiment 3T-20

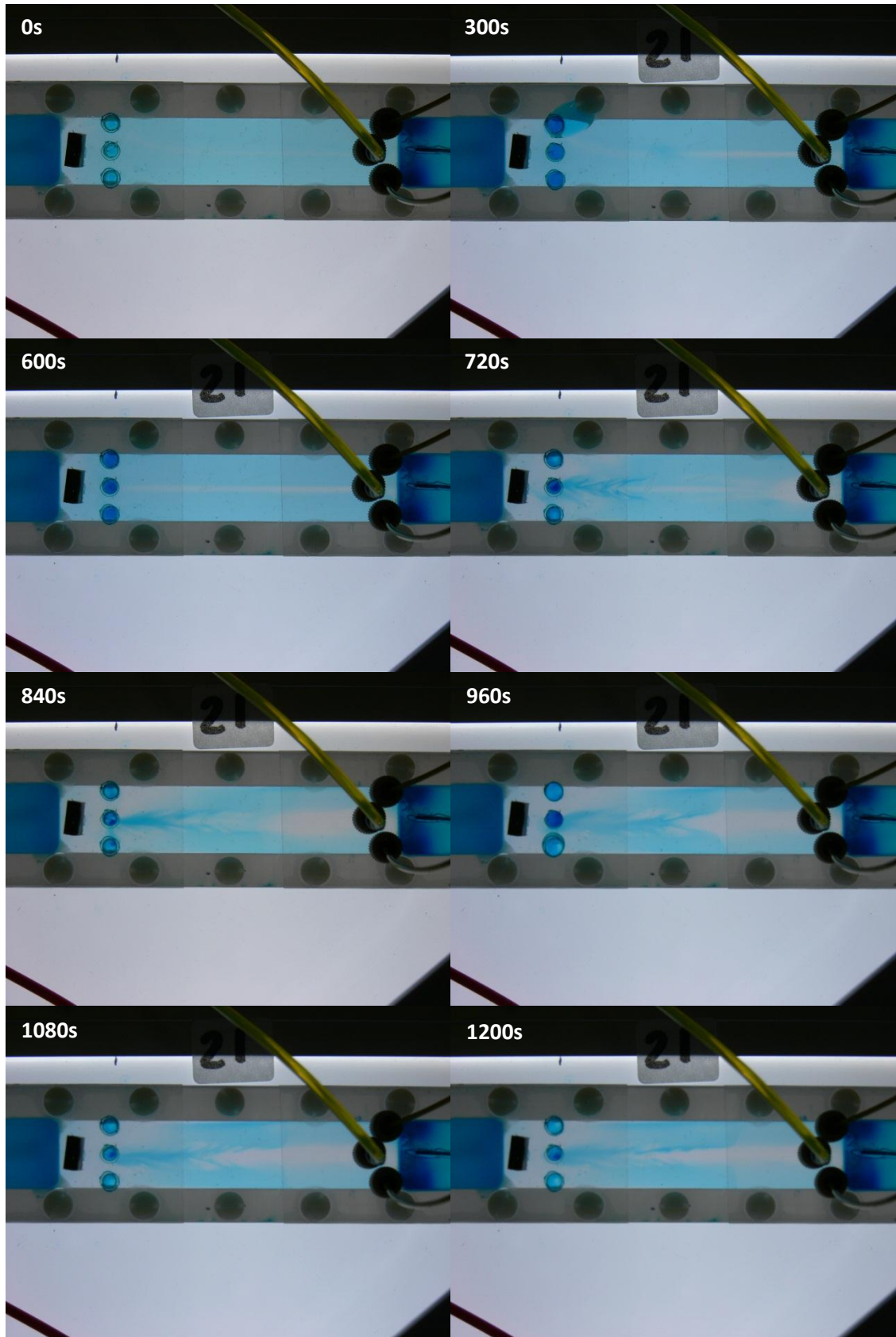


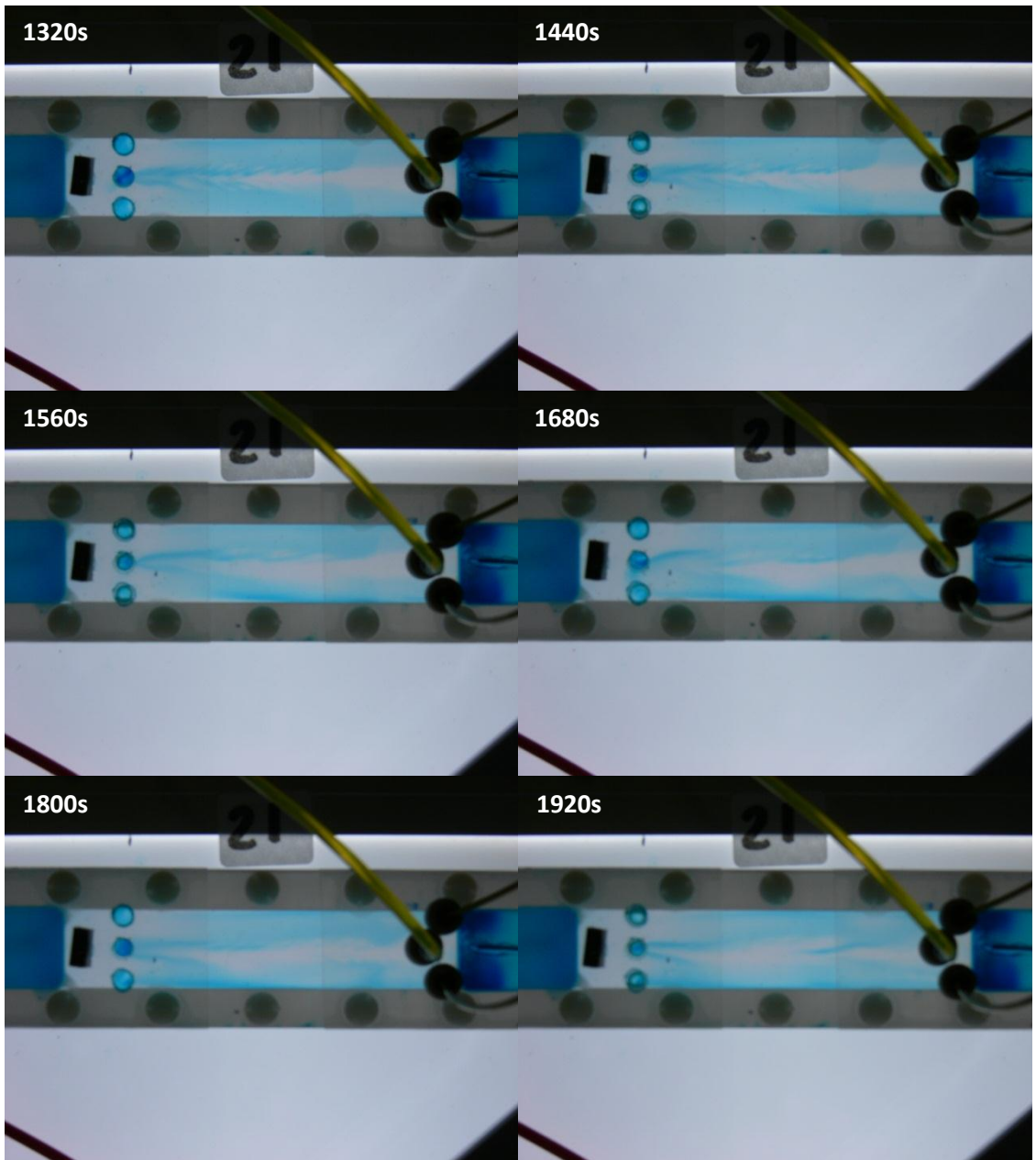




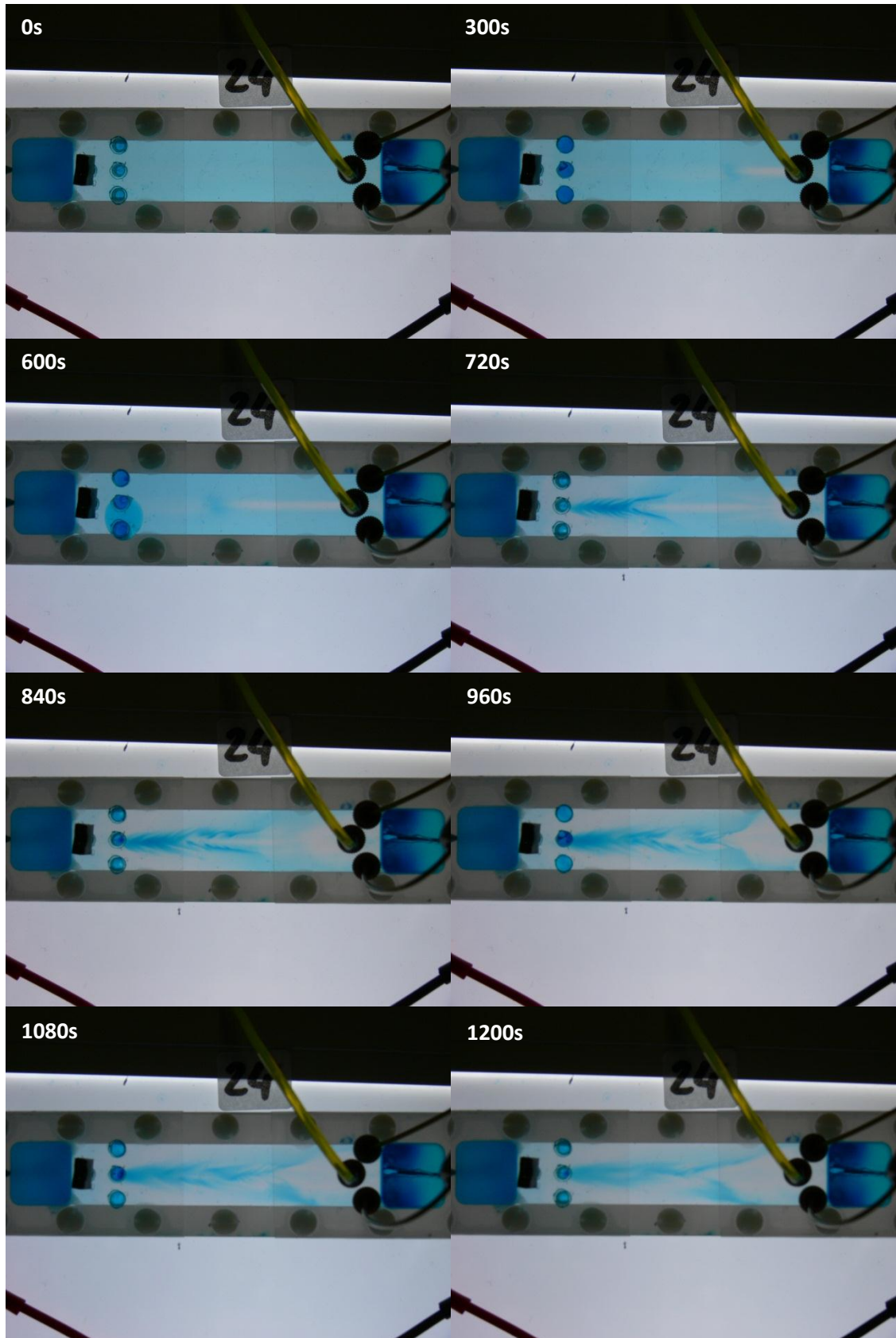


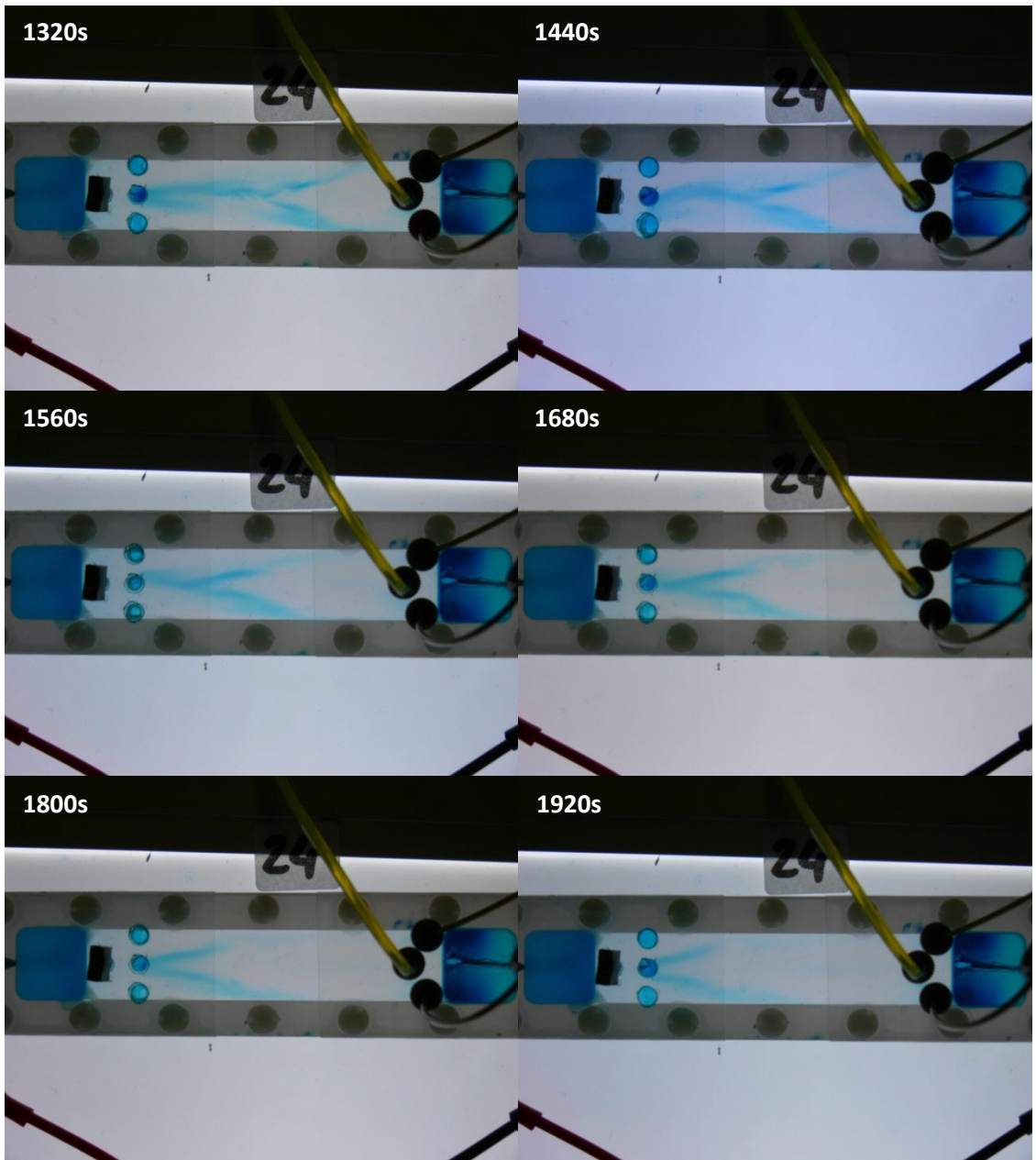
12. Experiment 3T-21

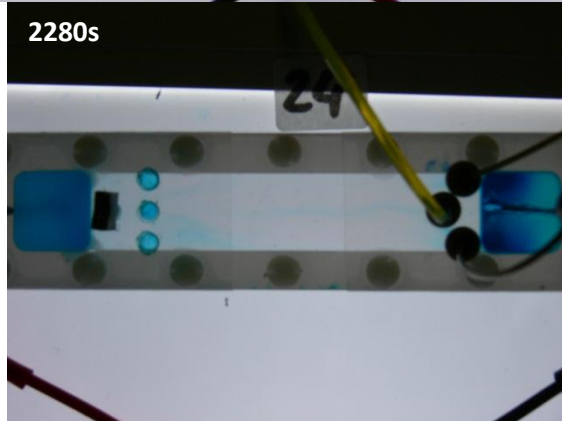
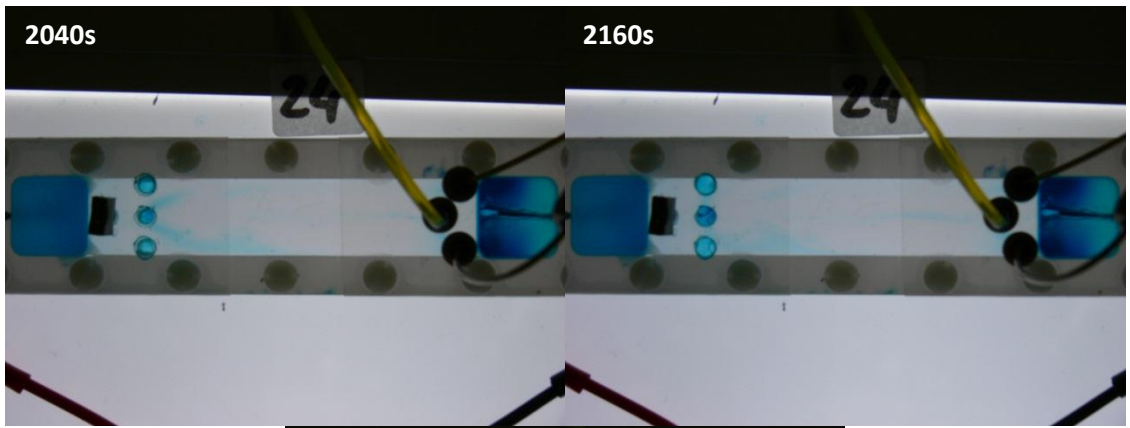




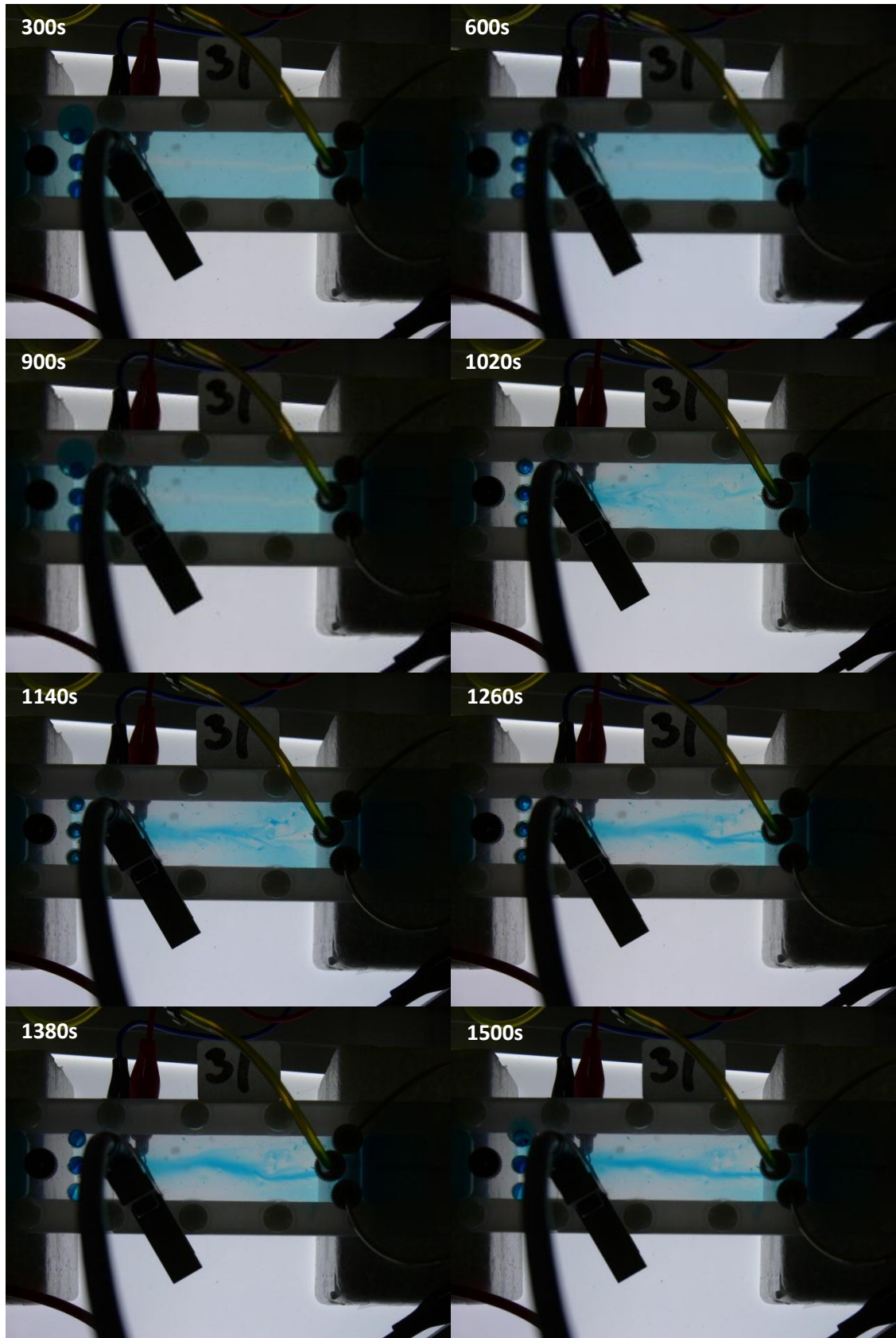
13. Experiment 3T-24

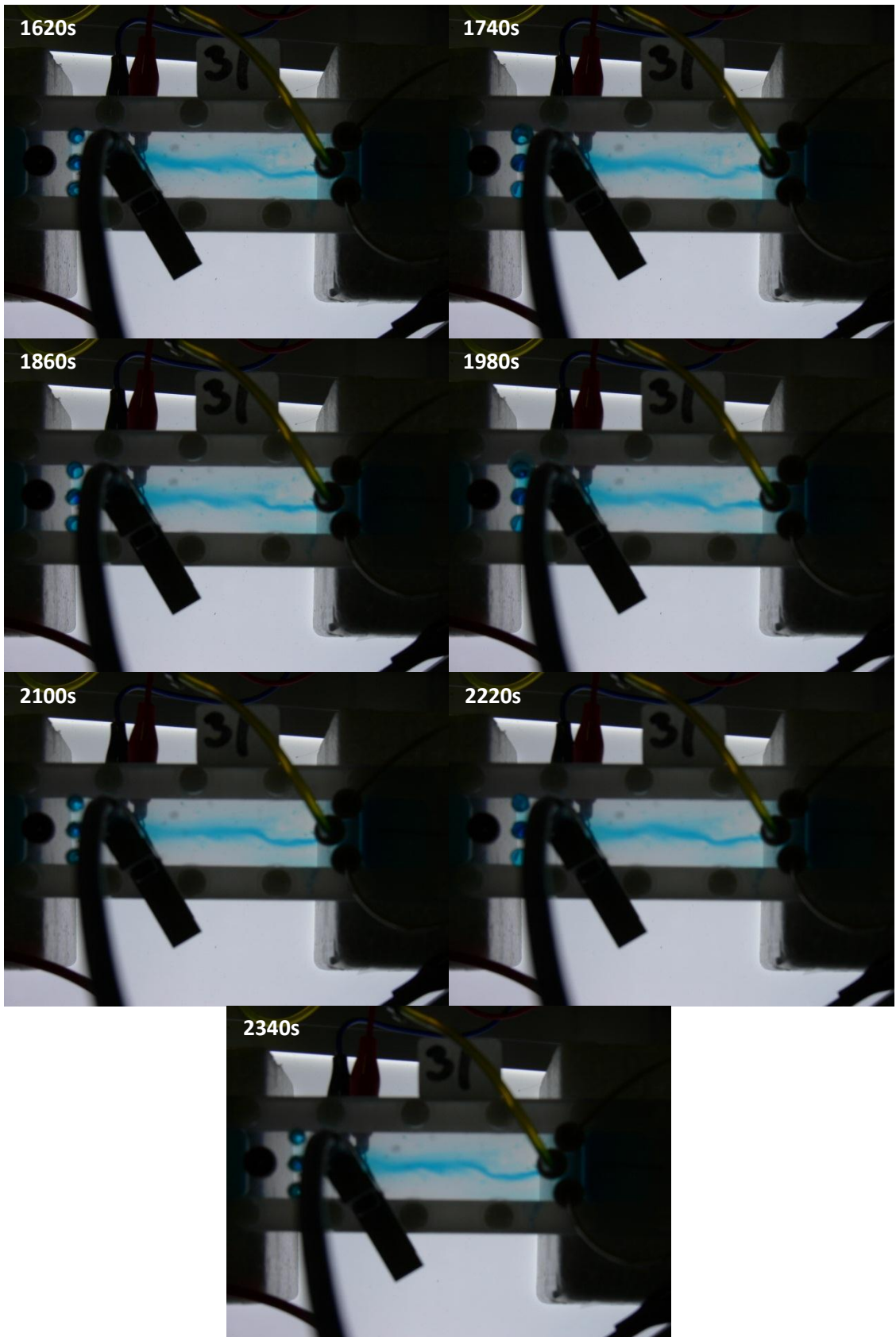




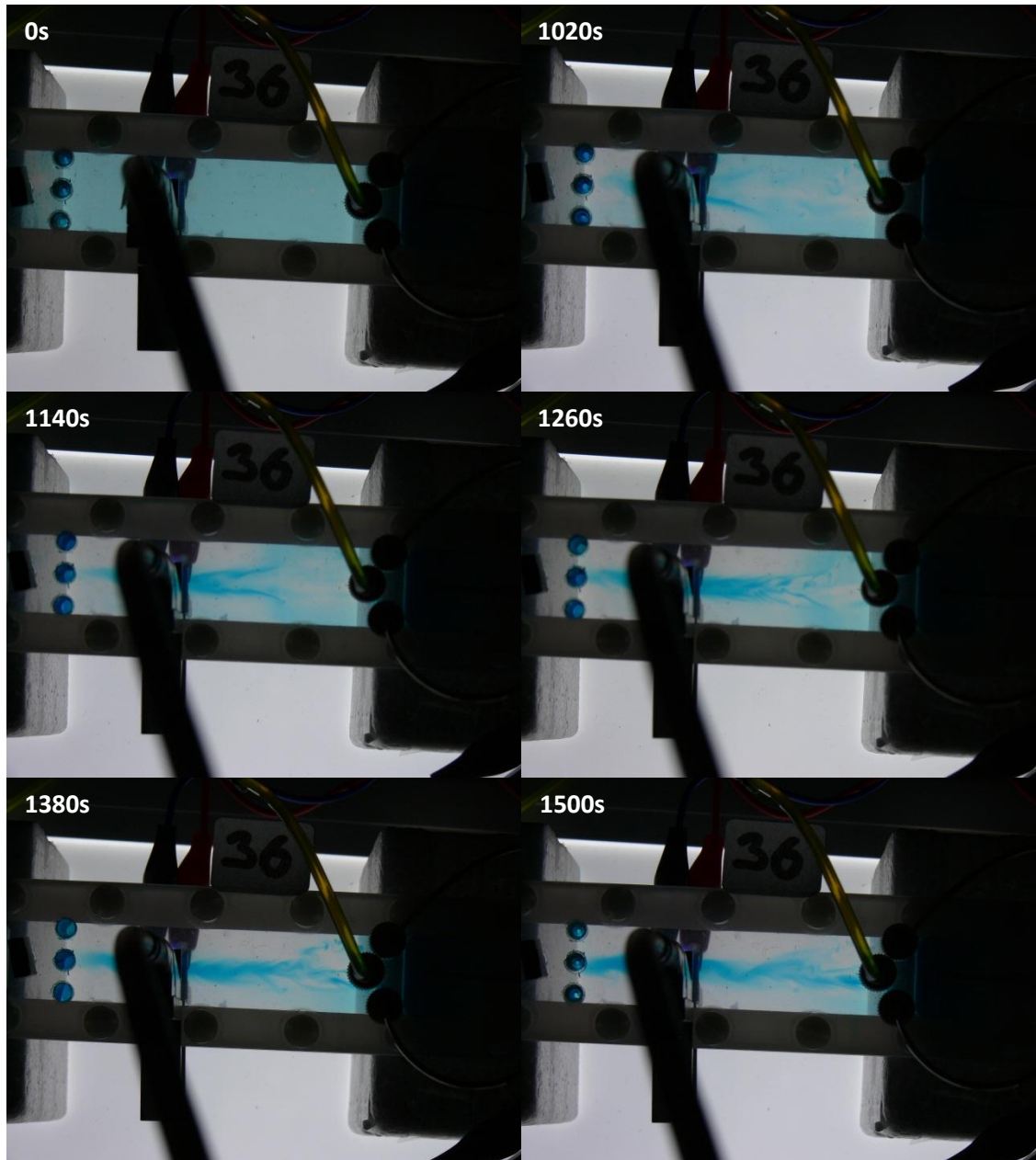


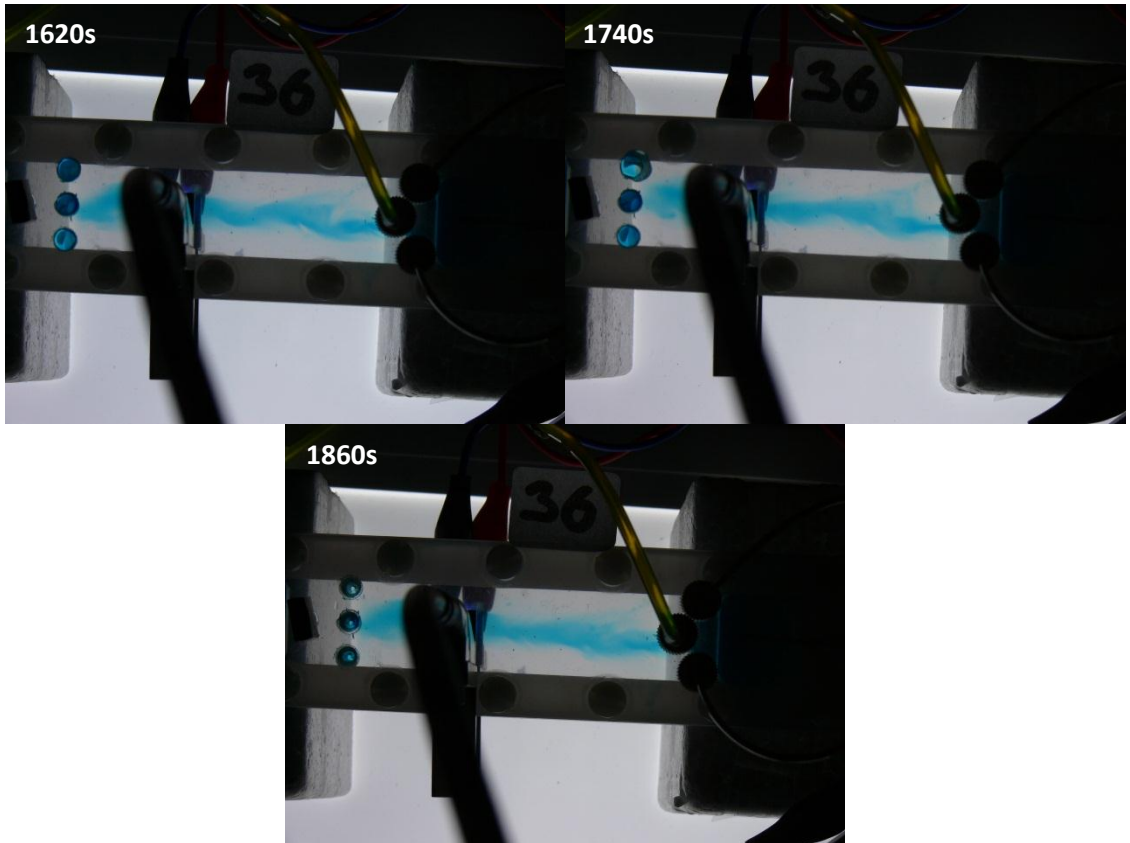
14. Experiment 3T-31



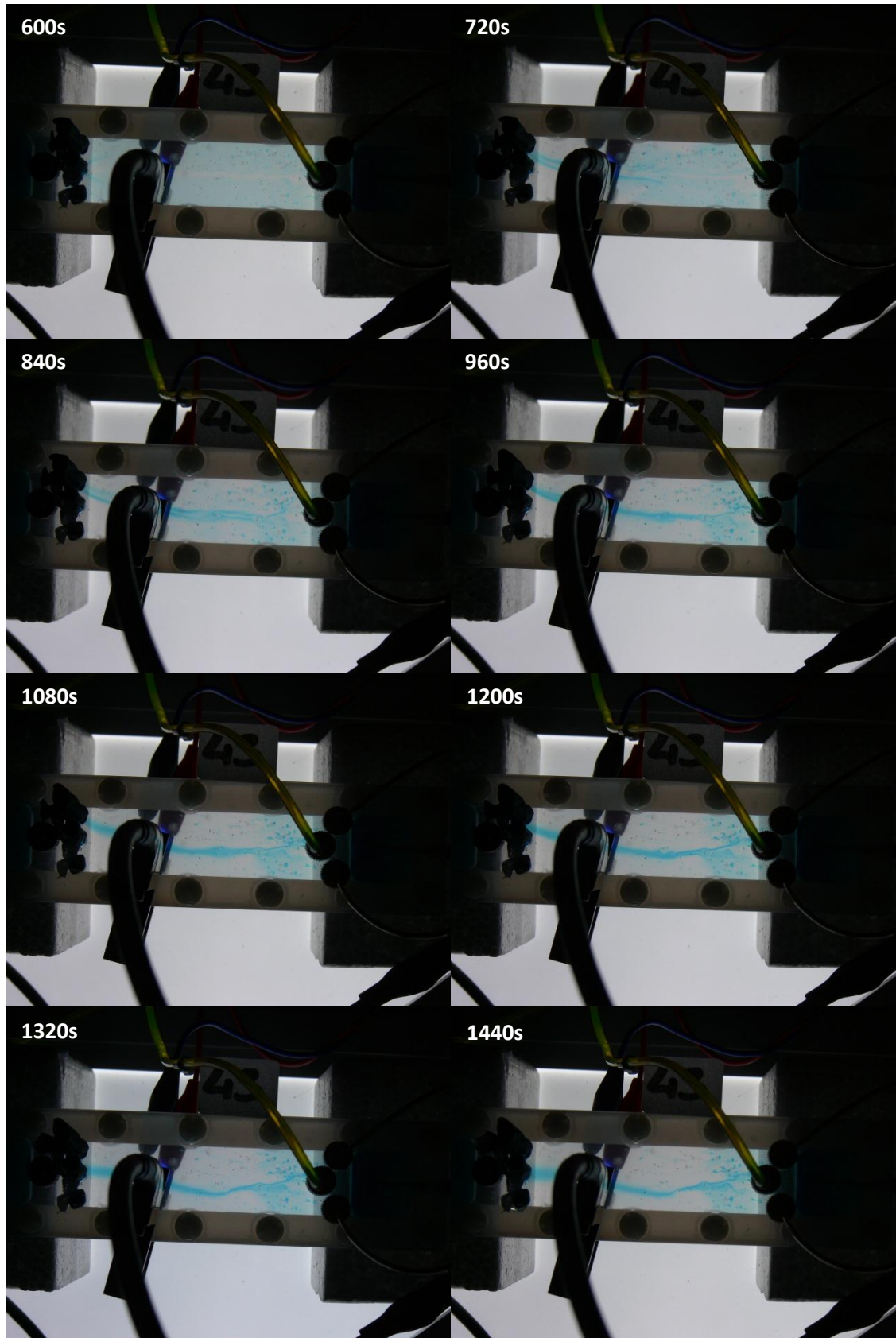


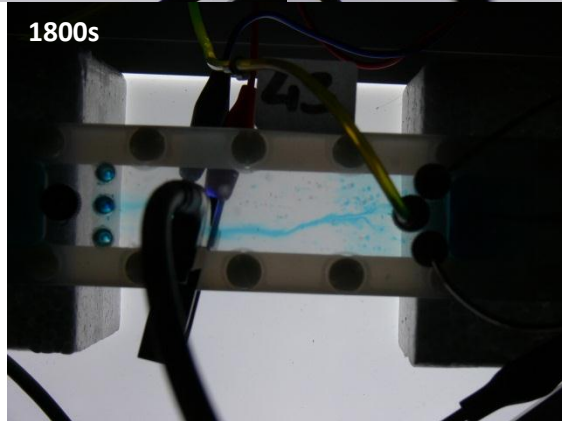
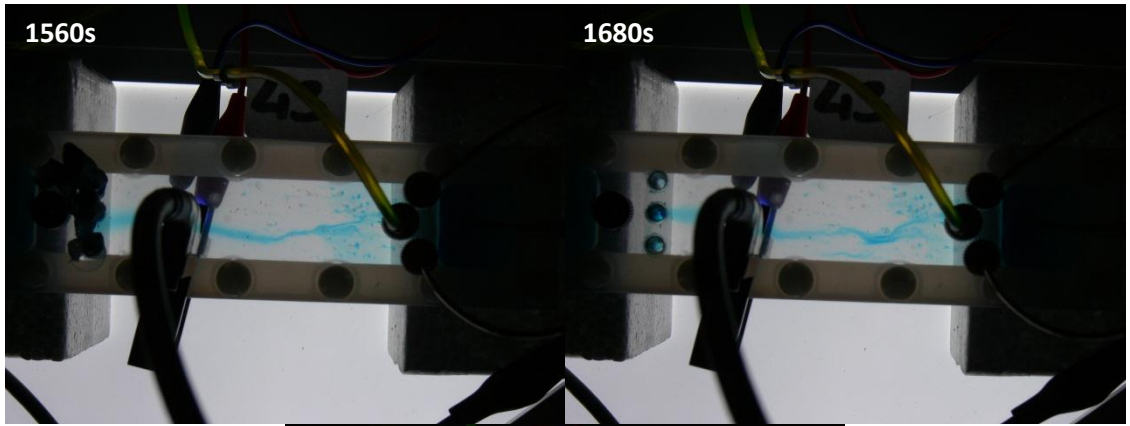
15. Experiment 3T-36





16. Experiment 3T-43





17. Experiment 3T-58

